Cooperative Redox Chemistry Utilizing Bioinspired Dipyrrin Pacman Complexes

HARVARD UNIVERSITY
Graduate School of Arts and Sciences

DISSERTATION ACCEPTANCE CERTIFICATE

The undersigned, appointed by the

Department of Chemistry & Chemical Biology

have examined a dissertation entitled:

Cooperative Redox Chemistry Utilizing Bioinspired Dipyrrin Pacman Complexes

presented by: Elizabeth J. Johnson

candidate for the degree of Doctor of Philosophy and hereby certify that it is worthy of acceptance.

Signature _____
Typed name: Professor Theodore A. Betley

Signature _____
Typed name: Professor Eric N. Jacobsen

Signature _____
Typed name: Professor Daniel G. Nocera

Date: 3 May 2021

Cooperative Redox Chemistry Utilizing Bioinspired Dipyrrin Pacman Complexes

A dissertation presented

by

Elizabeth J. Johnson

to

The Department of Chemistry and Chemical Biology

in partial fulfillment of the requirements

for the degree of

Doctor of Philosophy

in the subject of

Chemistry

Harvard University

Cambridge, MA

May 2021

Cooperative Redox Chemistry Utilizing Bioinspired Dipyrrin Pacman Complexes

Polynuclear active sites are a common motif employed by enzymes to facilitate cooperative redox chemistry. For instance, diiron enzymes serve a variety of purposes in nature, including the promotion of C–H functionalization (soluble methane monooxygenase) and small molecule activation (ribonucleotide reductase) reactivity in biological systems. Inspired by the cooperativity of these and similar enzymes, we aim to derive a functional mimic utilizing a bimetallic scaffold to promote metal–metal interaction, isolate reactive intermediates, and ultimately perform challenging multi-electron reactions. Specifically, we propose the use of dipyrrinato Pacman structures, wherein the dinucleating architecture can support two metals proximally oriented to maximize their ability to perform cooperative chemistry. To this end, we have developed strategies to tether two dipyrromethene motifs in a cofacial manner utilizing organic backbones and have incorporated late transition metals into this framework.

With this platform in hand, we demonstrate the accessibility of a series of diiron bridging hydroxo and oxo complexes in multiple oxidation states, analogous to the reactive intermediates observed in enzymatic active sites. This includes a rare diiron(II) μ-oxo with distinct bond metrics from the few other reported examples. Spectroscopic, crystallographic, and computational methods have been employed to examine the effect of molecular oxidation state on the acid-base reactivity of these motifs. The concurrent findings that the basicity of the bridging oxo unit decreases upon oxidation are consistent with observations that hemerythrin, a diiron dioxygen transport enzyme, undergoes a decrease in the pK_a of the bridging hydroxide proton concomitant with oxidation.

To gain insight into the effect of the metal identity on the reactivity of these complexes, we extende this system to cobalt, targeting the analogous dicobalt bridging hydroxo species. As such, we have synthesized dicobalt(II) bridging mono- and bis-hydroxide species that display unique reactivity from the diiron system. Specifically, lability of the hydroxide bridges of the bis-hydroxo complex by acid-base or redox reactions allows for interconversion between these species. Furthermore, both hydroxide bridges are expelled when the bis-hydroxide species undergoes two-electron oxidation by an inner-sphere oxidant, such as Ph_3CCl, to yield the corresponding dicobalt(II) dichloride species and generate Ph_3COH as the organic byproduct. Computational studies are utilized to model potential higher valent intermediates operative in this reaction, which demonstrate the roles of ligand/metal oxidation and spin accumulation at the bridging hydroxides that likely contribute to this unique reactivity.

Finally, we hypothesize that these bimetallic units can also be used to perform cooperative redox chemistry, in which the proximal metal centers work together to manage the redox load of multielectron reactions. As such, we demonstrate the capability of this dinuclear system to mediate the reduction of nitrite to nitric oxide without the requirement of external substrates (e.g., reductants, proton sources, or oxophillic substrates) to help initiate the reduction. The major iron-containing products of this transformation include the first reported four-coordinate diiron bis-nitrosyl species, as well as a diiron(III) μ-oxo organometallic species that is unique within the dipyrrin framework. We have also explored the facilitation of multielectron reductions, to which we observe promising evidence of the deoxygenation chemistry of pollutants such as perchlorate and periodate and the reduction of aryl-nitro substrates to the corresponding aniline complexes with the dipyrrin Pacman complexes.

Table of Contents

List of Figures and Schemes

List of Tables

List of Chemical Abbreviations

Δ9D	stearoyl-ACP Δ^9-desaturase
^{Ad}L	5-mesityl-1,9-(adamantyl)-dipyrromethene
^{Ad}L′	1,9-di-adamantyl-5-(2,6-dichlorophenyl)-dipyrromethene
^{Ar}L	5-mesityl-1,9-(2,4,6-$Ph_3C_6H_2$)-dipyrromethene
BAr^F	3,5- bis(trifluoromethyl)phenyl) borate
Boc_2O	di-*tert*-butyl decarbonate
BPP	*N*,*N*-bis(2-pyridylmethyl)-3-aminopropionate
Bu	butyl
Cd_1NiR	cytochrome d_1-containing nitrite reductase
CoOEP	cobalt(II) octaethylporphyrin
CHD	cyclohexadiene
Cp	cyclopentadienyl
CuNiR	copper-containing nitrite reductase
dbabh	2,3:5,6-Dibenzo-7-azabicyclo[2.2.1]hepta-2,5-diene
DBA	dibenzofuran-4,6-diacetic acid
DCM	dichloromethane
DDQ	2,3-dichloro-5,6-dicyano-1,4-benzoquinone
DMPO	5,5-dimethyl-1-pyrrolidine-*N*-oxide
DPD	diporphyrin dibenzofuran
DPDF	*meso*-tripentafluorophenyl porphyrin dibenzofuran
DPX	diporphyrin xanthene
Et	ethyl
Et_2O	diethylether
Fc	ferrocene
Fc^+	ferrocenium
hDOHH	deoxyhypusine hydroxlase
HPTB	*N,N,N′,N′*-tetrakis(2-benzylimidazolylmethyl)-2-hydroxo-1,3-diaminopropane
Hr	hemerythrin
^{i}Pr	isopropyl
L	ligand
L^{tBu}	(2,6-diisopropylphenyl)NC(^{t}Bu)CHC(^{t}Bu)N(2,6-diisopropylphenyl)$^-$
Lut	lutidine
Me	methyl
Mes	mesityl or 2,4,6-trimethylphenyl
MeCN	acetonitrile
MMO	methane monooxygenases
^{n}Bu	*n*-butyl
ODP	oxygen-binding diiron protein
OEC	oxygen evolving complex
OEP	octaethylporphyrin
NADH	protonated nicotinamide adenine dinucleotide

N_2OR	nitrous oxide reductase
NIR	nitrite reductase
OTf	trifluoromethylsulfonate or triflate
P	porphyrin
PAP	purple acid phosphatase
PCET	proton-coupled electron transfer
Ph	phenyl
PO	propylene oxide
PPTS	pyridinium *para*-toluenesulfonate
py	pyridine
pz	pyrazolyl
sMMO	soluble methane monooxygenase
R2	protein within RNR containing diiron active site
RNR	ribonucleotide reductase
tacn	1,4,7-triazacyclononane
TPA	tris(pyridylmethyl)amine
Tr	trityl
^{Tr}L	5-mesityl-1,9-(trityl)-dipyrromethene
^{t}Bu	*tert*-butyl
(^{tBu}dmx)H_2	1,9-(*tert*-butyl)$_2$-5-dipyrromethene units bridged by 9,9-dimethyl-*9H*-xanthene
^{tBu}L	1,9-di-*tert*-butyl-5-(2,6-dichlorophenyl)-dipyrromethene
thf or THF	tetrahydrofuran
TACN	triazacylononane
TMEDA	tetramethylethylenediamine
TMS	trimethylsilyl

List of Acronyms, Symbols, and Units

•	radical
^{13}C	carbon-13
^{1}H	proton
^{19}F	fluorine-19
Å	angstrom, 10^{-10} meters
A	hyperfine coupling constant
BDE	bond dissociation energy
CHN%	combustion analysis percentages for carbon, hydrogen, and nitrogen
CV	cyclic voltammetry or cyclic voltammogram
cm^{-1}	wavenumbers or inverse centimeters
D	axial zero field splitting parameter
d	doublet in NMR
D or ^{2}H	deuterium
dc	direct current
DFT	density functional theory
d_n	deuterated (*n* is the number of positions where ^{2}H replaces ^{1}H)
DPV	differential pulse voltammetry or differential pulse voltammogram
E	rhombic zero field splitting parameter
$E_{1/2}$	half-wave potential
e^-	electron
ENDOR	electron nuclear double resonance
EXAFS	extended X-ray absorption fine structure
EPR	electron paramagnetic resonance
ESI^+	positive ion electron spray ionization
FT	Fourier transform
FWHM	full width at half maximum
G	gauss
g	Landé g-factor (but may also refer to the anomalous gyromagnetic ratio, 2.0023)
GHz	gigahertz, 10^9 Hertz or 10^9 s^{-1}
GpdQ	glycerophosphodiesterase
H	magnetic field
H^+	proton
HAA	hydrogen atom abstraction
HOMO	highest occupied molecular orbital
IR	infrared spectroscopy
J	coupling constant
J_{HH}	proton–proton coupling constant
k	Boltzmann constant, 0.695 cm^{-1}/K
K	kelvin
M	molar, moles per liter
MCD	molecular circular dichromism

m	multiplet in NMR
m/z	mass to charge ratio
MetAP	methionine aminopeptidase
MHz	megahertz, 10^6 Hertz or 10^6 s^{-1}
mmol	millimole, 10^{-3} moles
MO	molecular orbital
mV	millivolt, 10^{-3} volts
N	Avogadro constant, 6.022 x 10^{23} mol^{-1}
nm	nanometer, 10^{-9} meters
NMR	nuclear magnetic resonance
Oe	oersted
p-	*para* position on an aryl ring, indicating a 1,4 relationship
ppm	parts per million
pK_a	negative log of the acid dissociation constant, or K_a
s	singlet in NMR or second
S	spin
S	spin operator
SQUID	superconducting quantum interference device
T	tesla
t	triplet in NMR
T or T	temperature
UV/Vis	ultraviolet-visible absorption spectroscopy
V	potential in mV or V
V	volt
XAS	X-ray absorption spectroscopy
XRD	X-ray diffraction
δ	delta, chemical shift in ppm
δ	isomer shift for ^{57}Fe Mössbauer spectroscopy in $^{mm}/_{s}$
ΔE_Q	quadrupole splitting for ^{57}Fe Mössbauer spectroscopy in $^{mm}/_{s}$
ΔG	entropy
ε	epsilon, extinction coefficient or molar absorptivity in M^{-1} cm^{-1}
η^n	eta, hapticity or the number of, n, contiguous atoms in a ligand bound to a metal
κ^n	kappa, denticity or the number of, n, atoms in a polydentate ligand bound to the metal
μ	mu, a single atom bridging to metals
μ_B	Bohr magneton, 9.274 x 10^{-21} erg/G
μ_{eff}	mu effective, effective magnetic moment in Bohr magnetons
µmol	micromole, 10^{-6} moles
λ	lambda, wavelength in nm
ρ	density
ν	frequency
χ	magnetic susceptibility
χ_M or χ_m	molar magnetic susceptibility in cm^3/mol

For My Family, Given and Chosen

Thank you for your encouragement, support, and unwavering belief in me

Graduate school has been one of the most challenging, exciting, and transformative experiences that I have been blessed to encounter. The research, resources, and people at Harvard have made this opportunity extremely rewarding and motivated me to come in every day for these six years. First and foremost, I need to thank my advisor Ted for his guidance, patience, and mentorship throughout the years. After meeting Ted six years ago, I knew I wanted to have him as my Ph.D. advisor almost immediately. Even when I have struggled to believe in myself and my research, Ted has acted as the support I needed to begin to have confidence in my abilities and has pushed me to find my voice amidst a competitive field. Thank you also for all the tissues and real conversations – I could not be more appreciative for the support and solace I received when I most needed it. Thank you to my thesis committee members, Prof. Eric Jacobsen and Prof. Dan Nocera, for being so invested in my research and success. It was a pleasure learning from you, teaching with you, and seeking your advice and input as I progressed throughout graduate school.

The other major pull towards coming to Harvard was the Betley lab, and I could not be more thankful for some extremely amazing lab mates and friends. From the beginning, I was blessed to have a supportive and engaged mentor, Claudia, who taught me everything I needed to know and helped me start off in a great spot. While we did not work together, Diana was always someone I could go to for help and advice. Even since leaving our group, she has maintained a mentorship role by checking in frequently, chatting with me on the phone about science, and reading countless drafts. I cannot believe I can still be so supported from someone who lives so far away! Thank you to all of the other Betley lab group members past and present for fun times and great scientific conversations while you were in the lab, with special thanks to Lisa, Brian, Amymarie, Benji, Tonia, Ryan, and Claire for the shopping trips, game nights, coffee outings, Bachelor nights in the loft, basketball games, and general good times.

I wish to give an extra special thank you to Becca, who I was fortunate enough to have as a collaborator, mentor, and friend. I am so appreciative for the many fancy dinners, nights in, nights out, long walks, and Boston explorations we were able to do together. Thank you for being a great colleague, role model, and lifetime friend. Thank you to Justin, who I clicked with right away from our NJ connection and has become one of my closest friends. It was so helpful to always be able to ask for your advice on everything related to science, grad school, teaching, or life, and for you to always find a way to make me laugh regardless of how upset or nervous or confused I was. You have been such a great and supportive friend to me at Harvard and beyond, and I am looking forward to future travels with you, Carew, and Ben. P.S. Thank you for helping me stay well-fed and taking some time to relax as I wrote my thesis! Last, I need to thank Yun for being the best hood mate, box mate, and just mate. You were always the first person I turned to whenever I got any result, needed help deciding which reaction to do next, or needed to vent about something that happened inside or outside of lab. I seriously could not have made it through grad school without you (or George) to help me cheer up and find my step!

There are many other wonderful people in the department who made my time here much more enjoyable and, quite honestly, much easier! Thank you to Gabi for being an amazing lab administrator – I have missed having you and your smile every single day. Thanks to Joe, Edison, Marvin, Helena, and the many other custodians I got to interact with daily. Thank you to John, Mike, Bob, and the receiving folks for your constant help, support, and conversations. Thank you to Caitlin, Helen, Kathy, Joe, Elizabeth, Barbara, and all of the other wonderful people in the front office who always greet me with a smile and keeps everything moving in the department! Thank you to the members of the GPC, HWIC, and CCB Community Committee for giving me the opportunity to help guide department culture and organize fun events for CCB members! I also

want to thank Gregg, Sirinya, Lu, Nick, Zach, Ron, David, Heidi, Austin, Marty, and Emily for the opportunity to serve as a pedagogy fellow, grow as a teacher, and mentor first year graduate students. I am also grateful to the many mentors I had at Harvard, including Prof. Cassandra Extavour, Tamara Pico and Jess Knawal for being an amazing HGWISE mentoring group and helping me persevere as a woman in STEM.

Thank you to the many other CCB members who were extremely helpful in giving me advice and chatting about chemistry. In particular, thank you to David, Moriana, Prithvi, and Matt for being great resources throughout the years. Thank you also to David for the countless coffee and food excursions, conversations, and for hosting so many football Sundays! Thanks to Amymarie, Ben, Benji, Brian, Carew, Charlie, Justin, Lisa, Matt, Nina, Ryan, and the other members of our volleyball team for great times and chances to get in some physical activity and express my competitiveness in a healthy way! Thank you to the core cohort, Chris, Ethan, and Ben, for our birthday celebrations, game nights, and picnics. Shout out to Ethan and Sophie for being fantastic roommates and helping me find a happy home to come home to after hard days at lab. And thank you immensely to my running buddies and amazing friends, Sandhya, Martell, and Nina! The countless miles, workouts, and conversations we had on the trails, roads, and steps meant the world to me. Thank you to my supportive and wonderful friends from home, Alyssa, Jillian, Megan, Kayla, and Julie, for all of the check-ins, Zoom catch-ups, and visits. Your continued support and friendship meant so much and helped me stay grounded during this whirlwind of an experience!

Thank you to all of the teachers, professors, and advisors I met earlier in life that taught me about science and encouraged me to pursue advanced degrees in chemistry. Thank you especially to Mrs. White, Mr. Robold, Mrs. Gangel, Mr. Coon, Dr. Abourahma, Dr. O'Connor, and Margaret Scheuermann for your roles in guiding me towards science and ultimately towards going to

graduate school. A huge thank you to my family: my parents, Diane and Justin; my grandparents, Evelyn and Roland Johnson and Charlene and Jay Warren; my sisters, Julia and Erica; Aunt June, Uncle Dave, Stacey, Eric, Aunt Joyce; Aunt Shannon, Uncle John; and Aunt Blip. You have all supported me in my journey towards becoming a scientist and taught me how to use drive, motivation, and a solid work ethic to pursue my dreams. Thank you for always encouraging me to prioritize education and helping me financially and emotionally throughout these many years of schooling!

Last, and in many ways most, I need to thank Ben for being a great friend throughout graduate school and my rock during the toughest years. You have always been one of the most fun people to let off steam with. Your kind heart, patience, and great listening abilities have been essential for encouraging me to persevere and gain the confidence and self-sufficiency I needed to finish my degree. I am especially grateful for you expanding my bubble and helping me to begin to see the world. You are the most fun person to travel and experience life with, and I cannot wait to see what adventures are in store for us. In addition to all of the wonderful things Harvard has taught me, I am most thankful for having met my best friend and life partner at this institution.

Bioinspired Bimetallic Constructs for Small Molecule Activation

1.1 Introduction

Earth-abundant small molecules, such as H_2, N_2, CO_2, CO, O_2, N_2O, NO, and CH_4, are reservoirs for chemical energy, and as such, their interconversion holds promise as an energy-storage strategy. These simple compounds can be utilized for a variety of purposes, for instance toward synthesizing complex molecular structures, acting as important signaling molecules for initiating biological processes, and supporting processes such as respiration. One challenge associated with these molecules is their thermodynamic stability and the high kinetic barriers associated with their activation. Metal complexes have been utilized by biological systems to overcome such feats, allowing for facile capture and activation of these small molecules.[1] Structures and functions of such metalloenzymes are diverse, ranging from mononuclear centers (i.e., cytochrome P450,[2] cobalamin,[3] nickel superoxide dismutase[4]) to polynuclear metal clusters (i.e., the oxygen evolving complex (OEC) in photosystem II,[5] Cu_z^* in nitrous oxide reductase

[1] Tolman, W. B. in *Activation of Small Molecules, Organometallic and Bioinorganic Perspectives* (Ed.: W. B. Tolman), Wiley-VCH Verlag GmbH & Co, KGaA **2006**.

[2] Rittle, J.; Green, M. T. *Science*. **2010**, *330*, 933–937.

[3] Matthews, F. S.; Gordon, M. M.; Chen, Z.; Rajashankar, K. R.; Ealick, S. E.; Alpers, D. H.; Sukumar, N. *Proc. Natl. Acad. Sci.* **2007**, *104*, 17311–17316.

[4] Abreu, I. A.; Cabelli, D. E. *Biochim. Biophys. Acta. Proteins Proteom.* **2010**, *1804*, 263–274.

[5] Umena, Y.; Kawakami, K.; Shen, J.-R.; Kamiya, N. *Nature* **2011**, *473*, 55–60.

(N_2OR),[6,7] the iron-molybdenum cofactor in nitrogenase[8]), that feature a variety of first-row transition metals to facilitate selective processes with small molecules (**Figure 1.1**). In particular, the latter multimetallic systems feature proximal metal centers that employ synergy to achieve selective activation and/or functionalization, through storage of required electron equivalents in

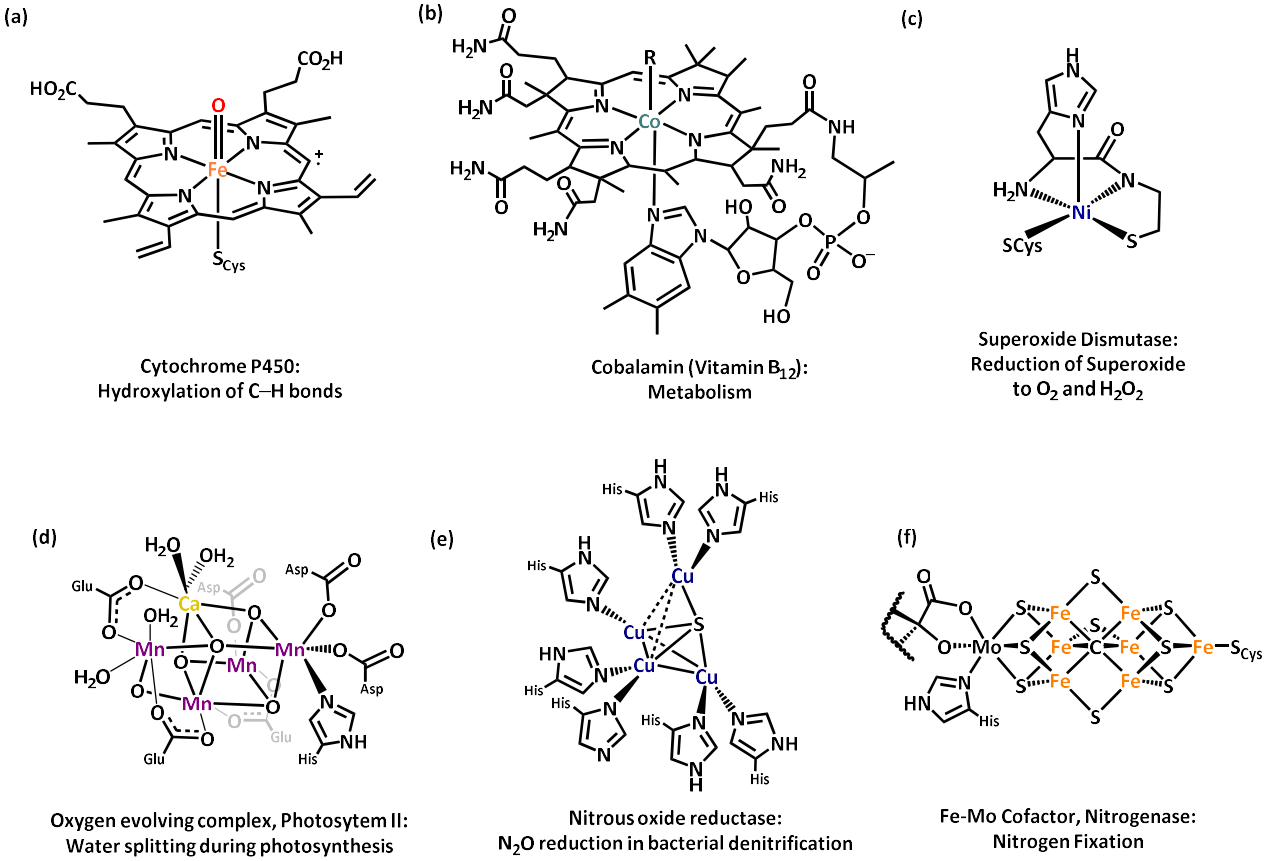

Figure 1.1. Structures and functions of well-studied metalloenzyme active sites. Mononuclear examples include (a) cytochrome P450,[2] (b) vitamin B12,[3] and (c) nickel superoxide dismutase.[4] Polynuclear sites include (d) the OEC of photosystem II,[5] (e) Cu_z^* in N_2OR,[6] and (f) the iron-molybdenum cofactor in nitrogenase.[8]

[6] (a) Brown, K.; Tegoni, M.; Prudêncio, M.; Pereira, A. S.; Besson, S.; Moura, J. M.; Moura, I.; Cambillau, C. *Nature Struct. Bio.* **2000**, *7*, 191–195. (b) Ghosh, S.; Gorelsky, S. I.; Chen, P.; Cabrito, I.; Moura, J. J. G.; Moura, I.; Solomon, E. I. *J. Am. Chem. Soc.* **2003**, *125*, 15708–15709.

[7] Ghosh, A. C.; Duboc, C.; Gennari, M. *Coord. Chem. Rev.* **2021**, *428*, 213606.

[8] Einsle, O.; Tezcan, F. A.; Andrade, S. L. A.; Schmid, B.; Yoshida, M.; Howard, J. B.; Rees, D. C. *Science.* **2002**, *297*, 1696–1700.

the multiple metal centers or by cooperatively binding and manipulating the substrate.[7]

Inspired by such metalloenzymes, chemists have sought to synthesize bioinspired analogues to better understand these complex biological systems, aiming to develop functional biomimetic systems to perform challenging transformations in laboratories and, in some cases, even on industrial scales.[1,7,9] For example, the groups of Peters,[10] Holland,[11] Murray,[12] and Tomson[13] have developed multiiron systems inspired by nitrogenase to bind dinitrogen, and in some cases, reduce dinitrogen to ammonia in the presence of external reductants. Models of the OEC include $CaMn_3O_4$ cubanes developed by Agapie and coworkers which have provided insight into the role of redox-inactive metals in OEC reactivity,[14] as well as $MnCo_3O_4$ cubanes by Tilley *et al.* for water oxidation catalysis.[15] Synthetic analogues of N_2OR include multicopper-sulfur complexes that active and reduce nitrous oxide developed by the groups of Tolman,[16] Torelli,[17] and Mankad.[18] Design of systems featuring earth-abundant and biologically-relevant metals has led to better

[9] Kandemir, T.; Schuster, M. E.; Senyshyn, A.; Behrens, M.; Schlögl, R. *Angew. Chem. Int. Ed.* **2013**, *52*, 12723 – 12726.

[10] Creutz, S. E.; Peters, J. C. *J. Am. Chem. Soc.* **2015**, *137*, 7310–7313.

[11] (a) Rodriguez, M. M.; Bill, E.; Brennessel, W. W.; Holland, P. L *Science* **2011**, *334*, 780–783. (b) Macleod, K. C.; Holland, P. J. *Nat. Chem.* **2013**, *5*, 559–565.

[12] Lee, Y.; Sloane, F. T.; Blondin, G.; Abboud, K. A.; Garcia-Serres, R.; Murray, L. J. *Angew. Chem. Int. Ed.* **2015**, *54*, 1499–1503.

[13] Liu, T.; Gau, M. R.; Tomson, N. C. *J. Am. Chem. Soc.* **2020**, *142*, 8142–8146.

[14] (a) Kanady, J. S.; Tsui, E. Y.; Day, M. W.; Agapie, T. *Science* **2011**, *333*, 733–736. (b) Tsui, E. Y.; Tran, R.; Yano, J.; Agapie, T. **2013**, *5*, 293–299. (c) Tsui, E. Y.; Agapie, T. *Proc. Natl. Acad. Sci. U. S. A.* **2013**, *110*, 10084–10088.

[15] Nguyen, A. L.; Suess, D. L. M.; Darago, L. E.; Oyala, P. H.; Levine, D. S.; Ziegler, M. S.; Britt, R. D.; Tilley, T. D. *J. Am. Chem. Soc.* **2017**, *139*, 5579–5587.

[16] Bar-Nahum, I.; Gupta, A. K.; Huber, S. M.; Ertem, C. J.; Tolman, W. B. *J. Am. Chem. Soc.*, **2009**, *131*, 2812–2814.

[17] Esmieu, C.; Orio, M.; Torelli, S.; Le Pape, L.; Pécault, J.; Lebrun, C.; Ménage, S. *Chem. Sci.* **2014**, *5*, 4774–4784.

[18] (a) Johnson, B. J.; Antholine, W. E.; Linderman, S. V.; Graham, M. J.; Mankad, N. P. *J. Am. Chem. Soc.* **2016**, *138*, 13107–13110. (b) Hsu, C.-W.; Rathnayaka, S. M.; Islam, S. N.; MacMillan, S. N.; Mankad, N. P. *Angew. Chem. Int. Ed.* **2020**, *59*, 627–631.

comprehension of the active sites evolved by nature and provided critical understanding required to develop cutting-edge and broadly accessible catalysts competent for small molecule activation.[19]

1.2 Diiron Active Sites in Nature

One specific class of polynuclear enzymes are those containing bimetallic active sites, which utilize two metals in proximity to perform cooperative multielectron chemistry.[20] Diiron units are ubiquitous throughout biological systems and are responsible for performing a wide variety of functions.[21] Key examples include soluble methane monooxygenase, ribonucleotide reductase, hemerythrin, and purple acid phosphatase. Critical to the reactivity of these diiron centers is their ability to communicate through a monoatomic hydroxo or oxo bridge that allows for cooperative chemistry as well as to access multiple oxidation states to enable multielectron reactivity. Herein is an overview of key findings by the bioinorganic community toward understanding the structure and reactivity of such diiron enzymes, followed by discussion of bioinspired model complexes that have elucidated further comprehension and emulation of these motifs.

1.2.1. Soluble Methane Monooxygenase

Methane monooxygenases (MMO) catalyze the selective oxidation of strong, unactivated C–H bonds, such as those in methane (105 $^{kcal}/_{mol}$) to form methanol in the first step of anaerobic

[19] Artero, V. *Nature Energy.* **2017**, *2*, 17131. (b) Milani, B.; Clot, E.; Albrecht, M. *Dalton Trans.* **2016**, *45*, 14419–14420.

[20] Vigato, P. A.; Tamburini, S.; Fenton, D. E. *Coord. Chem. Rev.* **1990**, *106*, 25–170.

[21] van den Beuken, E. K.; Feringa, B. L. *Tetrahedron,* **1998**, *54*, 12985–13011.

metabolism by methanotrophic bacteria.[22,23] Two types of MMO have evolved to perform this reactivity; most methanotrophs contain the membrane-bound, copper particulate MMO (pMMO) while many methanotrophs utilize the diiron soluble MMO (sMMO) in copper-limited conditions.[24] While pMMO is the primary form found in nature, sMMO has proven to be more easily purified and has thus been studied in great detail over the last four decades.[23,25] In fact, the extensive study of this enzyme has led to one of the most comprehensive dioxygen activation descriptions for any oxygenase or oxidase enzyme.[23] The two primary bacterial sources of sMMO that have been studied originate from the *Methylococcus capsulatus* Bath (*Mc*)[24,26] and the *Methylosinus trichosporium* OB3b (*Mt*)[27] methanotrophs. In both instances, the overall enzyme structure consists of three components: a hydroxylase (MMOH) where substrate oxidation occurs, a reductase (MMOR) which provides electrons for the transformation, and a regulatory protein (MMOB). MMOH features an $\alpha_2\beta_2\gamma_2$ architecture with the diiron active site located deep within the α manifold.[25]

[22] Merkx, M.; Kopp, D. A.; Sazinsky, M. H.; Blazyk, J. L.; Müller, J,; Lippard, S. J. *Angew. Chem. Int. Ed.* **2001**, *40*, 2782–2807.

[23] Banerjee, R.; Jones, J. C.; Lipscomb, J. D. *Annu. Rev. Biochem.* **2019**, *88*, 409–431.

[24] Tinberg, C. E.; Lippard, S. J. *Acc. Chem. Res.* **2011**, *44*, 280–288.

[25] Wang, V. C.-C.; Maji, S.; Chen, P. P.-Y.; Lee, H. K.; Yu, S. S.-F.; Chan, S. I. *Chem. Rev.* **2017**, *117*, 8574–8621.

[26] Pilkington, S. J.; Dalton, H. *Methods Enzymol.* **1990**, *188*, 181–190.

[27] Fox, B. G.; Froland, W. A.; Dege, J. E.; Lipscomb, J. D. *J. Biol, Chem.* **1989**, *264*, 10023–10033.

The resting state of the enzyme (H_{ox}) has been crystallographically characterized in many reports.[28,29,30] The binuclear iron cluster is coordinated by two histidine residues, four glutamate residues, an aquo ligand, a bridging hydroxide ligand, and another bridging hydroxide or aquo ligand depending on the crystallization conditions (**Scheme 1.1a**).[30] ^{57}Fe Mössbauer (**Table 1.1**),[31,32] EXAFS, and EPR studies have indicated a diamagnetic ground state of two anti-ferromagnetically coupled high-spin iron(III) centers with $J \approx -15$ cm^{-1} in which the μ-OH/μ-OH($_2$) ligands are believed to mediate the spin exchange.[32] NADH reduces MMOR, which binds to MMOH and concurrently reduces the active site to the diiron(II) state (H_{red}), a form which has also been extensively studied crystallographically.[29,30] The structure features a carboxylate-shift of one of the previously terminal glutamine residues to displace one of the μ-OH units (**Scheme 1.1b**) Extensive studies on the electronic structure of H_{red} reveal a weakly ferromagnetically coupled high-spin diiron(II) center, showing a diagnostic $S = 4$ EPR signal with $g = 16$,[32,33] an

[28](a) Rosenzweig, A. C.; Frederick, C. A.; Lippard, S. J.; Nordlund, P. *Nature* **1993**, *366*, 537–543. (a) Elango, N.; Radhakrishnan, R.; Froland, W. A.; Wallar, B. J.; Earhart, C. A.; Lipscomb, J. D.; Ohlendorf, D. H. *Prot. Sci.* **1997**, *6*, 556–558.

[29] (a) Rosenzweig, A. C.; Nordlund, P.; Takahara, P. M.; Frederick, C. A.; Lippard, S. J. *Chem. Biol.* **1995**, *2*, 409–418. (b) Whittington, D. A.; Lippard, S. J. *J. Am. Chem. Soc.* **2001**, *123*, 827–838.

[30] Merkx, M.; Kopp, D. A.; Sazinsky, M. H.; Blazyk, J. L.; Müller, J.; Lippard, S. J. *Angew. Chem. Int. Ed.***2001**, *40*, 2782–2807.

[31] Fox, B. G.; Surerus, K. K.; Münck, E; Lipscomb, J. D. *J. Biol. Chem.***1988**, *283*, 10553–10556.

[32] (a) DeWitt, J. G.; Bentsen, J. G.; Rosenzweig, A. C.; Hedman, B.; Green, J.; Pikington, S.; Papaefthymiou, G. C.; Dalton, H.; Hodgson, K. O.; Lippard, S. J. *J. Am. Chem. Soc.* **1991**, *113*, 9219–9235. (b) Fox, B. G.; Hendrich, M. P.; Surerus, K. K.; Andersson, K. K.; Froland, W. A.; Lipscomb, J. D.; Münck, E. *J. Am. Chem. Soc.* **1993**, *115*, 3688–3701.

[33] Hendrich, M. P.; Münck, E; Fox. B. G.; Lipscomb, J. D. *J. Am. Chem. Soc.* **1990**, *112*, 5861–5865.

MCD-derived coupling of $J \approx 0.3\text{-}0.5$ cm^{-1},[34] and ^{57}Fe Mössbauer features of $\delta \sim 1.3$ mm s^{-1} and $|\Delta E_Q| \sim 3$ mm s^{-1} (**Table 1.1**).[31,32,35]

Beyond the two crystallized forms of the enzyme, the proposed mechanistic pathway following dioxygen reaction with H_{red} has been extensively studied and debated. A number of various intermediates have been proposed, some detected spectroscopically and others suggested by stopped-flow kinetics data. The first detected intermediate, termed H_{peroxo} for Mc[24] or P for Mt[23], is assigned to contain a diiron(III) peroxo unit due to its broad electronic absorption spectrum ($\lambda = 720$ nm, $\varepsilon = 1350$ M^{-1} cm^{-1} for Mc; $\lambda = 725$ nm, $\varepsilon = 2500$ M^{-1} cm^{-1} for Mt).[36] ^{57}Fe Mössbauer data confirms an overall diamagnetic state with two similar diiron(III) centers (**Table 1.1**).[35,37] Resonance Raman data for this intermediate has not been obtained, which would be informative towards assigning the binding mode of the peroxo bridge. Rather, spectroscopic similarities of H_{peroxo}/P to other structurally characterized diiron peroxo active sites with μ-(1,2)-peroxo modes demonstrated by Raman spectroscopy (**Table 1.1**, *vide infra*) and high-level theoretical calculations support a μ-(1,2)-peroxo binding mode;[38,39] furthermore, spectroscopic comparisons to crystallographically characterized model complexes suggest this intermediate potentially features a *trans* μ-(1,2)-peroxo mode (**Table 1.2**, *vide infra*).[24] En route to H_{peroxo} formation in Mc, an additional transient intermediate has been proposed called P*, potentially consisting of a iron(II)

[34] Pulver, S.; Froland, W. A.; Fox, B. G.; Lipscomb, J. D.; Solomon, E. I. *J. Am. Chem. Soc.* **1993**, *115*, 12409–12422.

[35] Liu, K. E.; Valentine, A. M.; Wang, D.; Huynh, B. H.; Edmondson, D. E.; Salifoglou, A.; Lippard, S. J. *J. Am. Chem. Soc.* **1995**, *117*, 10174–10185.

[36] (a) Tinberg, C. E.; Lippard, S. J. *Biochem.* **2009**, *51*, 12145–12158. (b) Lee, S.-K.; Lipscomb, J. D. *Biochem.* **1999**, *38*, 4423–4432.

[37] Shu, L.; Nesheim, J. C.; Kauffmann, K.; Münck, E.; Lipscomb, J. D.; Que, L., Jr. *Science* **1997**, *275*, 515–518.

[38] (a) Dunietz, B. D.; Beachy, M. D.; Cao, Y.; Whittington, D. A.; Lippard, S. J.; Friesner, R. A. *J. Am. Chem. Soc.* **2000**, *122*, 2828–2839. (b) Han, W.-G.; Noodleman, L. *Inorg. Chem*. **2008**, *47*, 2975–2986. (c) Bochevarov, A. D.; Li, J.; Song, W. J.; Friesner, R. A.; Lippard, S. J. *J. Am. Chem. Soc.* **2011**, *133*, 7384–7397.

[39] Siegbahn, P. E. M.; Crabtree, R. H. *J. Am. Chem. Soc.* **1997**, *119*, 3103–3113.

iron(III) superoxo or a related diiron(III) *cis* μ-(1,2)-peroxo.[22] Meanwhile, toward formation of intermediate P in Mt, the existence of two intermediates have been implicated by kinetics data. EPR studies indicate that both intermediates are diiron(II) in character, leading to their tentative assignment as dioxygen bound in the active site (intermediate O) and dioxygen binding to the diiron core (P*).[23]

Decay of H_{peroxo}/P leads to the formation of intermediate Q, which can react directly with methane to insert an oxygen atom into one of the C–H bonds.[23] Q exhibits intense electronic absorption features at λ ~ 330-350 nm (ε = 9800 M^{-1} cm^{-1}) and λ ~ 420-430 nm (ε = 7500 M^{-1} cm^{-1}).[23,24] Oxidation to diiron(IV) centers has been implicated by ^{57}Fe Mössbauer data, in which Mc monooxygenase exhibits two equal intensity features (δ = 0.21 mm s^{-1} , $|\Delta E_Q|$ = 0.68 mm s^{-1} ; δ = 0.14 mm s^{-1}, $|\Delta E_Q|$ = 0.55 mm s^{-1}) suggesting iron(IV) centers in slightly distinct electronic environments[35] while Mt has one quadrupole doublet (δ = 0.17 mm s^{-1}, $|\Delta E_Q|$ = 0.53 mm s^{-1}) indicative of a symmetric core (**Table 1.1**).[40] Initial extended X-ray absorption fine structure (EXAFS) studies collected in 1997 led to the proposal of a diiron bis-μ-oxo diamond core structure due to the short iron–iron distance of 2.46 Å with Fe–O bond lengths in the range of single bonds (1.77 Å and 2.05 Å) (**Scheme 1.1d**).[37] However, recent EXAFS data utilizing more sophisticated X-ray absorption spectroscopy (XAS) techniques have implicated longer Fe–Fe distances and demonstrated better data reproducibility with an open-core formulation.[41] Furthermore,

[40] Lee, S.-K.; Fox, B. G.; Froland, W. A.; Lipscomb, J. D.; Münck, E. *J. Am. Chem. Soc.* **1993**, *115*, 6540–6541.

[41] Cutsail, G. E., III; Banerjee, R.; Zhou, A.; Que, L., Jr.; Lipscomb, J. D.; DeBeer, S. *J. Am. Chem. Soc.* **2018**, *140*, 16807–16820.

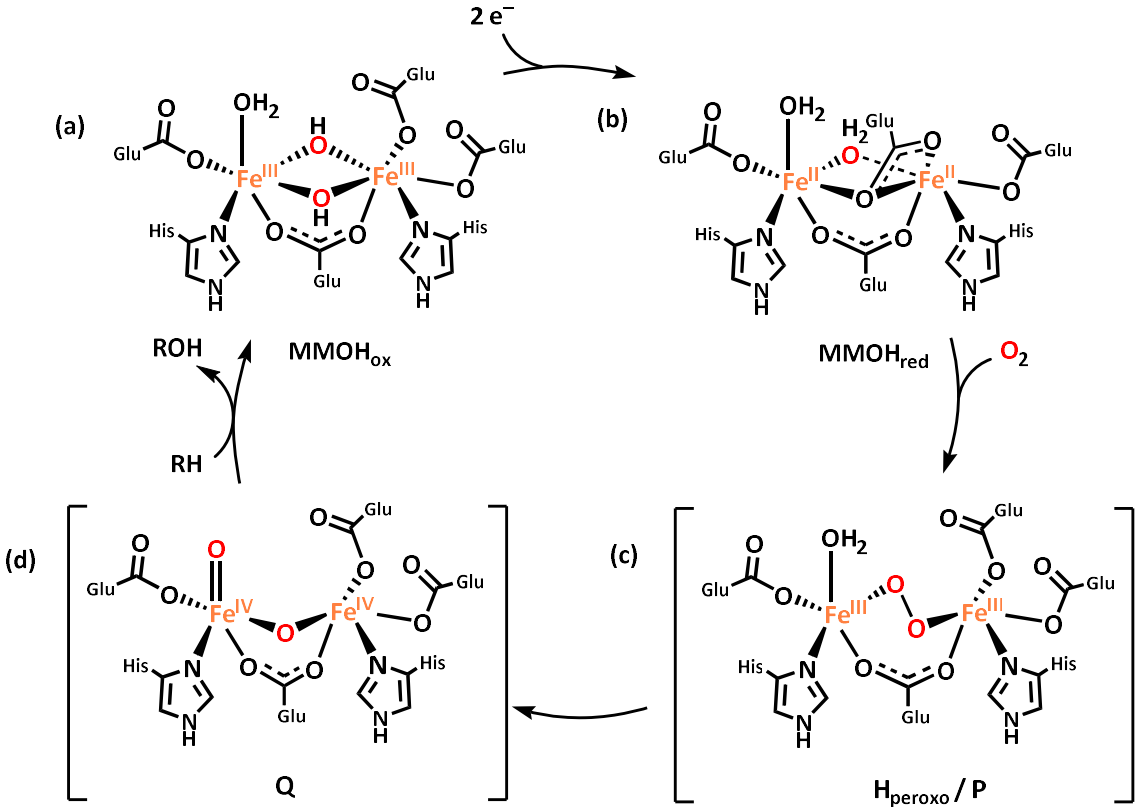

Scheme 1.1. Proposed cycle of sMMO. (a) Representative structure of the resting state $Fe^{III}Fe^{III}$ $MMOH_{ox}$[28] and of (b) $Fe^{II}Fe^{II}$ $MMOH_{red}$[31] based on crystal structure data. Subtle differences in the identity of the bridging ligands have been observed depending on protein purification and data collection temperature.[30] (c) Following reaction with dioxygen, the first spectroscopically detected intermediate H_{peroxo} (Mc)/P (Mt) is proposed to be a diiron(III) peroxo species based on absorption and ^{57}Fe Mössbauer spectroscopic features.[24] (d) Decay forms intermediate Q, which oxygenates methane. Q was originally proposed to be a diiron(IV) bis-μ-oxo diamond-core structure (as shown) has been more recently suggested to be in equilibrium with a more reactive open-core structure.[23]

computational studies[39,42] and synthetic models of Q comparing open-core and diamond-core structures suggest that an open-core motif with a mono-μ-oxo and a terminal Fe^{IV}=O may be operative during methane oxidation, as this form is found to be more reactive than bis-μ-oxo diamond cores (*vide infra*). One proposed possibility is that intermediate Q exists as an equilibrium

[42] Castillo, R. G.; Banerjee, R.; Allpress, C. J.; Rohde, G. T.; Bill, E; Que, L., Jr.; Lipscomb, J. D.; DeBeer, S. *J. Am. Chem. Soc.* **2017**, *139*, 18024–18033.

between a diamond-core and open-core structure, thereby protecting the active site from oxidation until substrate is present, at which point the diiron center opens to the more reactive form.[23,43]

1.2.2 Ribonucleotide Reductase

Ribonucleotide reductase (RNR) is an enzyme essential for DNA replication and repair by converting nucleotides to the corresponding deoxynucleotides in all organisms.[44,45] There are four defined classes of RNR; Class I RNR, the most thoroughly investigated, is found in all eukaryotes and microorganisms and features a diiron active site in the β subunit (R2 protein) of its $\alpha_2\beta_2$ structure.[46,47] Structural characterization by X-ray crystallography has indicated two unique binding sites for the iron centers. In the reduced form, the five-coordinate iron(II) centers (as verified by ^{57}Fe Mössbauer spectroscopy, **Table 1.1**)[48] are 3.9 Å apart, bridged by two glutamate residues and each featuring carboxylate and histidine moieties ($R2_{red}$, **Scheme 1.2a**).[49] Activation of dioxygen ultimately results in oxidation to the diiron(III) active R2 form, in which a carboxylate-shift and formation of an oxo bridge and water molecule from dioxygen are observed (**Scheme1.2d**).[46,47,50] Furthermore, a shortening of the Fe–Fe distance to 3.2-3.3 Å and an Fe–O–

[43] Xue, G.; Pokutsa, A.; Que, L., Jr. *J. Am. Chem. Soc.* **2011**, *133*, 16657–16667.

[44] Stubbe, J.; van der Donk, W. A. *Chem. Rev.* **1998**, *98*, 705–762.

[45] Stubbe, J.; Nocera, D. G.; Yee, C. S.; Chang, M. C. Y. *Chem. Rev.* **2003**, *103*, 2167–2202.

[46] Eklund, H.; Uhlin, U.; Färnegårdh, M.; Logan, D. T.; Nordlund, P. *Prog. in Biophys. Mol. Biol.* **2001**, *77*, 177–268.

[47] Nordlund, P.; Sjöberg, B.-M.; Eklund, H. *Nature* **1990**, *345*, 593–598.

[48] Lynch, J. B.; Juarez-Garcia, C.; Münck, E.; Que, L. Jr. *J. Biol. Chem.* **1989**, *264*, 8091–8096.

[49] Logan, D. T.; Su, X.-D.; Åberg, A.; Regnström, K.; Hajdu, J.; Eklund, H.; Nordlund, P. *Structure* **1996**, *4*, 1053–1064.

[50] Nordlund, P.; Eklund, H. *J. Mol. Biol.* **1993**, *232*, 123–164.

Fe angle of 127-129° have been indicated by EXAFS studies.[51] ^{57}Fe Mössbauer spectroscopy studies on active R2 revealed features consistent with high-spin iron(III) centers in distinct environments, as well as a diamagnetic ground state (**Table 1.1)**.[52] Furthermore, magnetometry studies confirmed antiferromagnetic coupling between the iron(III) centers with a $J = -108$ cm^{-1}, which is reasonable for a diiron oxo-bridged species.[53]

Instrumental to this transformation is a proximal tyrosine residue, located approximately 5.3 Å from the nearest iron[45] which is found in the phenol form in $R2_{red}$ and is converted to its radical form in active R2, as evidenced by a number of EPR and isotope labeling studies.[44] The proposed mechanism of dioxygen activation involves binding of O_2 to the diiron(II) center to form a putative diiron(III) peroxo intermediate (intermediate P),[54] which thereby oxidizes a nearby tryptophan residue to form Intermediate X, assigned as a mixed-valent $Fe^{III}Fe^{IV}$ species.[46,55,56,57] Lack of crystallographic evidence due to the rapid decay of intermediate P and X have led to reliance on a number of spectroscopic and computational investigations of their structures. Intermediate P is

[51] (a) Scarrow, R. C.; Maroney, M. J.; Palmer, S. M.; Que, L., Jr.; Salowe, S. P.; Stubbe, J. *J. Am. Chem. Soc.* **1986**, *108*, 6832–6834. (b) Scarrow, R. C.; Maroney, M. J.; Palmer, S.M.; Que, L., Jr.; Roe, A. L.; Salowe, S. P.; Stubbe, J. *J. Am. Chem. Soc,* **1987**, *109*, 7857–7864.

[52] Atkin, C. L.; Thelander, L.; Reichard, P.; Lang, G. *J. Biol. Chem.* **1973**, *248*, 7464–7472.

[53] (a) Petersson, L.; Graslund, A.; Ehrenberg, A.; Sjoberg, B. M.; Reichard, P. *J. Biol. Chem.* **1980**, *255*, 6706–6712. (b) Kahn, O. in *Molecular Magnetism,* VCH **1993**.

[54] Tong, W. H.; Chen, S.; Lloyd, S. G. Edmondson, D. E.; Huynh, B. H.; Stubbe, J. *J. Am. Chem. Soc.* **1996**, *118*, 2107–2108.

[55] Friedle, S.; Reisner, E.; Lippard, S. J. *Chem. Soc. Rev.* **2010**, *39*, 2768–2779.

[56] Dassama, L. M. K.; Silakov, A.; Krest, C. M.; Calixto, J. C.; Krebs, C.; Bollinger, J. M.; Green, M. T. *J. Am. Chem. Soc.* **2013**, *135*, 16758-16761.

[57] (a) Ravi, N.; Bollinger, M. B. Jr.; Huynh, B. H.; Edmondson, D. E.; Stubbe, J. *J. Am. Chem. Soc.* **1994**, *116*, 8007 –8014. (b) Ravi, N.; Bominaar, E. L. *Inorg. Chem.* **1995**, *34*, 1040–1043.

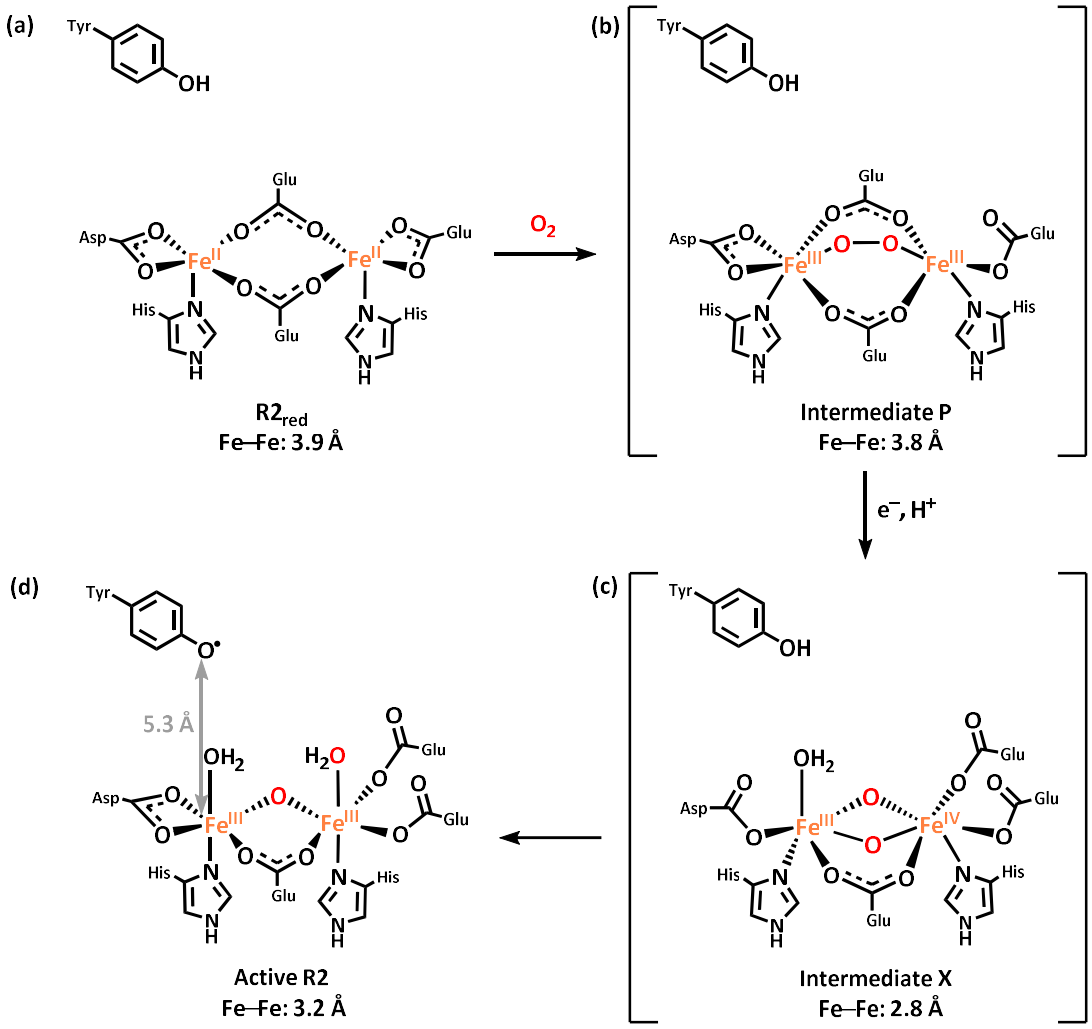

Scheme 1.2. Proposed mechanism of dioxygen activation by R2. (a) $R2_{red}$ in the diferrous state, structure determined crystallographically in *E. Coli* RNR at 1.7 Å resolution.[49] Proposed structures of (b) intermediate P[58] and (c) intermediate X[56], resulting in the (d) active diferric form with tyrosyl radical, as determined by crystallographic studies of *E. Coli* RNR at 2.2 Å resolution[46,50] and EXAFS studies for the Fe–Fe distance.[51]

proposed to contain a diferric *cis* μ-(1,2)-peroxo site based on computational models and experimentally validated structures of a mutant studied by Raman spectroscopy (**Scheme 1.2b**).[58] Recent EXAFS and computational studies of intermediate X propose assignment as a diiron bis-bridging oxo motif (**Scheme 1.2c**).[56] Intermediate X is responsible for generating the tyrosyl

[58] (a) Moënne-Loccoz, P.; Baldwin, J.; Ley, B. A.; Loehr, T. M.; Bollinger, J. M. *Biochem.* **1998**, *37*, 14659–14663. (b) Skulan, A. J.; Brunold, T. C.; Baldwin, J.; Saleh, L.; Bollinger, J. M.; Solomon, E. I. *J. Am. Chem. Soc.* **2004**, *126*, 8842–8855.

radical and is reduced to the diiron(III) active form.[55,56] Substrate reduction occurs in the α subunit of the protein, where a cysteine residue ~35 Å is oxidized by active R2 and its tyrosyl radical by long-range ET to generate a cysteine radical that is competent to perform hydrogen-atom abstraction (HAA) on the bound nucleotide substrate. [45,56] Several model compounds have been studied to date that support the current assignment and understanding of intermediate X (*vide infra*).

1.2.3 Hemerythrin

Hemerythrin (Hr) is found in numerous marine invertebrates for the function of oxygen transportation.[59] Hr is one of the three major proteins that can reversibly bind dioxygen, but its structure differs from that of the other major classes, hemoglobin and hemocyanin, by featuring a diiron active site.[60] Crystallography[61] and EXAFS[59] studies have revealed that the reduced diiron(II) form, deoxyHr, features one six-coordinate iron center and one five-coordinate iron center. The primary coordination sphere is comprised of five histidine residues, three of which are ligated to the hexa-coordinate iron and the other two to the penta-coordinate iron, plus one bridging glutamate, one bridging aspartate, and one bridging hydroxide moiety (**Scheme 1.3**). Consistent with a hydroxo-bridged diiron structure, deoxyhemerythrin is shown to exhibit weak antiferromagnetic coupling ($J \approx -14$ cm^{-1}) between two high-spin iron centers, as demonstrated by magnetic susceptibility data[62] as well as by ^{1}H NMR,[63] magnetic circular dichroism (MCD),[64]

[59] Zhang, K,; Stern, E. A.; Ellis, F. *Biochem.* **1988**, *27*, 7470–7479.

[60] Stenkamp, R. E. *Chem. Rev.* **1994**, *94*, 715–726.

[61] Holmes, M. A.; Trong, I. L.; Turley, S.; Sieker, L. C.; Stenkamp, R. E. *J. Mol. Biol.* **1991**, *218*, 583–593.

[62] Brunold, T. C.; Solomon, E. I. *J. Am. Chem. Soc*. **1999**, *121*, 8277–8287.

[63] Maroney, M. J.; Kurtz, D. M.; Nocek, J. M.; Pearce, L. L.; Que, L., Jr. *J. Am. Chem. Soc.* **1986**, *108*, 6871–6879.

[64] Reem, R. C.; Solomon, E. I. *J. Am. Chem. Soc.* **1987**, *109*, 1216–1226.

and ^{57}Fe Mössbauer spectroscopic studies (**Table 1.1**).[65,66] Furthermore, longer Fe–O bond lengths are observed by EXAFS (average 1.98 Å),[59] consistent with a μ-hydroxo unit.

The cooperativity of two irons is utilized to bind one molecule of dioxygen, however it is proposed by crystallographic[61] and spectroscopic[63,67,68] studies that dioxygen binds to the formerly five-coordinate site terminally and undergoes a two electron reduction to O_2^{2-} to form the diiron(III) oxidized form, oxyHr.[69] This results in two hexacoordinate, pseudo-octahedral centers featuring the same amino acid ligands as deoxyHr. Following the first electron transfer from iron to dioxygen, a decrease in the pK_a of the bridging hydroxide proton occurs. This allows for a proton transfer from the hydroxide and the second electron transfer from iron to dioxygen to occur concomitantly; the former is believed to be critical for stabilizing dioxygen binding in the hydrophobic pocket of the ligand.[60,69] Therefore, oxyhr contains an η^1-hydroperoxo unit bound at

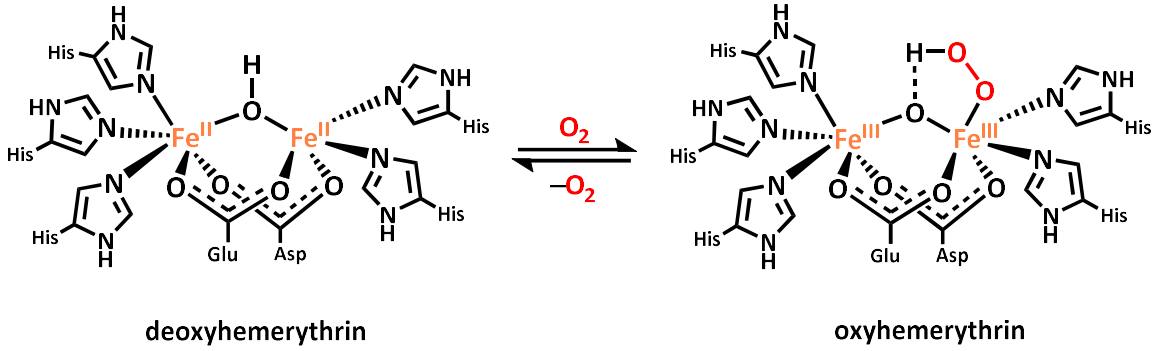

Scheme 1.3. Structures of deoxyHr and oxyHr upon reversible dioxygen binding.[60,61,69]

[65] Okamura, M. Y.; Klotz, I. M.; Johnson, C. E.; Winter, M. R. C.; Williams, R. J. P. *Biochem.* **1969**, *8*, 1951–1958.

[66] Clark, P. E.; Webb, J. *Biochem.* **1981**, *20*, 4628–4632.

[67] Dunn, J. B. R.; Shriver, D. F.; Klotz, I. M. *Proc. Natl. Acad. Sci. U.S.A.* **1973**, *70*, 2582.

[68] Gay, R. R.; Solomon, E. I. *J. Am. Chem. Soc.* **1978**, *100*, 1972–1973.

[69] Solomon, E. I.; Brunold, T. C.; Davis, M. I.; Kemsley, J. N.; Lee, S.-K.; Lehnert, N.; Neese, F.; Skulan, A. J.; Yang, Y.-S.; Zhou, J. *Chem. Rev.* **2000**, *100*, 235−349.

one iron site, as well as a formally bridging oxo ligand.[70] However, evidence for a hydrogen-bonding interaction between the μ-oxo and bound hydroperoxo has been provided by resonance Raman (ν_{O-O} = 844 cm^{-1}),[67,71] circular dichroism, and single crystal absorbance[72] spectroscopic studies. This interaction is further strengthened by the basic bent diiron μ-oxo unit, which is apt to reaccept the proton upon release of dioxygen and reduction back to the deoxyHr form.[72] The Fe–O distances decrease (average 1.82 Å)[59] and the antiferromagnetic coupling between the two high-spin iron(III) centers[65,66] of oxyHr increases substantially from deoxyHr ($J \approx -77$ cm^{-1}),[73] consistent with deprotonation to a diiron μ-oxo complex, however it should be noted that this is a lower degree of antiferromagnetic coupling between iron centers than observed in other diiron(III) enzymes featuring μ-oxo bridges,[53, 82, 85, 88] which is likely a consequence of the hydrogen-bonding interaction to the bridging oxo.[69]

1.2.4. Purple acid phosphatase

Purple acid phosphatases (PAP) are phosphohydrolases which catalyze the hydrolysis of various phosphate ester and amide substrates under acidic conditions (optimum ~4.9–6.0).[74,75] In addition to hydrolysis, mammalian PAPs have also been shown to catalyze peroxidation reactions

[70] Shlemke, A. K.; Loehr, T. M.; Sanders-Loehr, J. *J. Am. Chem. Soc.* **1984**, *106*, 4951–4956.

[71] Shlemke, A. K.; Loehr, T. M.; Sanders-Loehr, J. *J. Am. Chem. Soc*. **1986**, *108*, 2437–2443.

[72] Reem, R. C.; McCormick, J. M.; Richardson, D. E.; Devlin, F. J.; Stephens, P. J.; Mussleman, R. L.; Solomon, E. I. *J. Am. Chem. Soc.* **1989**, *111*, 4688–4704.

[73] Dawson, J. W.; Gray, H. B.; Hoenig, H. E.; Rossman, G. R.; Schredder, J. M.; Wang, R.-H. *Biochem.* **1972**, *11*, 461–465.

[74] Wilcox, D. E. *Chem. Rev.* **1996**, *96*, 2435–2458.

[75] Schenk, G.; Mitić, N.; Hanson, G. R.; Comba, P. *Coord. Chem. Rev.* **2013**, *257*, 473–482.

as an immune response[76] and have been implicated in additional biological roles such as bone resorption[77] and iron transport.[78] As members of the dinuclear metallohydrolase family, these enzymes require a dinuclear active site to function, consisting of an Fe^{III} and a divalent metal M^{II} (M^{II} = Fe in mammalian PAP and Zn or Mn in plant PAP).[75] PAPs are so-named from their characteristic purple (λ_{max} ~ 550 nm) and pink (λ_{max} ~ 510 nm) colors in their inactive oxidized ($Fe^{III}Fe^{III}$) and active reduced ($Fe^{II}Fe^{III}$) forms, respectively.[74,79]

While the overall homology between animal and plant PAPs is quite low, the primary coordination sphere of the catalytic active sites is highly conserved, as confirmed by crystal structure analysis[80,81] and corroborated by many spectroscopic studies.[82,83,84,85] At the Fe^{III} binding

[76] (a) Kaija, H.; Alatalo, S. L.; Halleen, J. M.; Lindqvist, Y.; Schneider, G.; Väänänen, H. K.; Vihko, P. *Biochem. Biophys. Res. Commun.* **2002**, *292*, 128–132. (b) Sibille, J. C.; Doi, K.; Aisen, P. *J. Biol. Chem.* **1987**, *262*, 59–62. (c) Räisänen, S. R.; Alatalo, S. L.; Ylipahkala, H.; Halleen, J. M.; Cassady, A. I.; Hume, D. A.; Väänänen, H. K. *Biochem. Biophys. Res. Commun.* **2005**, *331*, 120–126.

[77] (a) Oddie, G. W.; Schenk, G.; Angel, N. Z.; Walsh, N.; Guddat, L. W.; de Jersey, J.; Cassady, A. I.; Hamilton, S. E.; Hume, D. A. *Bone* **2000**, *27*, 575–584; (b) Ek-Rylander, B.; Flores, M.; Wendel, M.; Heinegard, D.; Andersson, G. *J. Biol. Chem.* **1994**, *269*, 14853–14856.

[78] Nuttleman, P. R.; Roberts, R. M.; *J. Biol. Chem.* **1990**, *265*, 12192–12199.

[79] Vincent, J. B.; Olivier-Lilley, G. L.; Averill, B. A. *Chem. Rev.* **1990**, *90*, 1447–1467.

[80] (a) Guddat, L. W.; McAlpine, A. S.; Hume, D.; Hamilton, S.; de Jersey, J.; Martin, J. L. *Structure* **1999**, *7*, 757–767. (b) Lindqvist, Y. Johansson, E. Kaija, H.; Vihko, P.; Schneider, G. *J. Mol.Biol.* **1999**, *291*, 135–147. (c) Sträter, N.; Jasper, B.; Scholte, M.; Krebs, B.; Duff, A. P.; Langley, D. B.; Han, R.; Averill, B. A.; Freeman, H. C.; Guss, J. M. *J. Mol. Biol.* **2005**, *351*, 233–246.

[81] Uppenberg, J.; Lindqvist, F.; Svensson, C.; Ek-Rylander, B.; Andersson, G. *J. Mol. Biol.* **1999**, *290*, 201–211.

[82] R. B. Lauffer, B. C. Antanaitis, P. Aisen, L. Que, Jr., *J Biol Chem* **1983**, *258*, 14212-14218.

[83] (a) Scarrow, R. C.; Pyrz, J. W.; Que, L., Jr. *J. Am. Chem. Soc.* **1990**, *112*, 657–665. (b) Wang, Z.; Ming, L. J.; Que, L., Jr.; Vincent, J. B.; Crowder, M. W.; Averill, B. A. *Biochem.* **1992**, *31*, 5263–5268. (c) Doi, K.; McCracken, J.; Peisach, J.; Aisen, P, *J. Biol. Chem.* **1988**, *263*, 5757–5763. (d) Antanaitis, B. C.; Peisach, J.; Mims, W. B.;Aisen, P. *J. Biol. Chem.* **1985**, *260*, 4572–4574.

[84] Antanaitis, B. C.; Strekas, T.; Aisen, P. *J. Biol. Chem.* **1982**, *257*, 3766–3770.

[85] Averill, B. A.; Davis, J. C.; Burman, S.; Zirino, T.; Sanders-Loehr, J.; Loehr, T. M.; Sage, J. T.; Debrunner, P. G. *J. Am. Chem. Soc.* **1987**, *109*, 3760–3767.

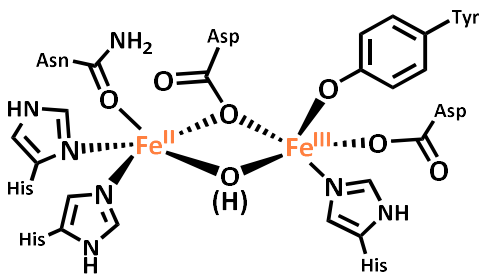

Figure 1.2. Representation of the active site of PAP, based on crystal structure analysis of the oxidized inactive form[80,81] and spectroscopic studies of both forms.[82-85] The iron centers are labelled as Fe^{II} and Fe^{III} to designate the "redox-active" and "chromophoric" sites, respectively. It is proposed that the purple oxidized diiron(III) form is bridged by an oxo moiety while the pink reduced iron(II) iron(III) form is bridged by a hydroxo moiety.[82,85,88,89]

site, known as the "chromophoric" site, aspartate, histidine, and tyrosine ligands are conserved, and it is a tyrisonate-to-iron charge transfer transition that ultimately results in the characteristic color of these proteins.[84,85,86] At the M^{II} binding site, called the "redox-active" site, two histidine and one asparagine are present regardless of M^{II} identity, and between the two metal sites is a bridging aspartate residue.[80,81] Crystallographic studies of the mammalian PAP were performed on the oxidized (purple) form and suggest the presence of a bridging oxygen ligand, assigned as a hydroxo or oxo moiety based on resolution;[80] furthermore, crystal structure analysis of plant PAP in the active form ($Zn^{II}Fe^{III}$) is also consistent with a bridging hydroxo/oxo species (**Figure 1.2**).[87]

Insight into the coupling between the two iron centers has been provided by a number of studies using techniques such as EPR spectroscopy,[85,88,89,90] magnetometry,[85,89,91] and NMR

[86] (a) Gaber, B. P.; Sheridan, J. P.; Bazer, F. W.; Roberts, R. M. *J. Biol. Chem.* **1979**, *254*, 8340–8342. (b) Yang, Y.-S.; McCormick, J. M.; Solomon, E. I. *J. Am. Chem. Soc.* **1997**, *119*, 11832–11842.

[87] Klabunde, T.; Sträter, N.; Fröhlich, R.; Witzel, H.; Krebs, B. *J. Mol. Biol.* **1996**, *259*, 737–748.

[88] Davis, J. C.; Averill, B. A. *Proc. Nat. Acad. Sci.* **1982**, *79*, 4623–4627.

[89] Day, E. P.; David, S. S.; Peterson, J.; Dunham, W. R.; Bonvoisin, J. J.; Sands, R. H.; Que, L., Jr. *J. Biol. Chem.* **1988**, *263*, 15561–15567.

[90] Debrunner, P. G.; Hendrich, M. P.; de Jersey, J.; Keough, D. T.; Sage, J. T.; Zerner, B. *Biochim. Biophys. Acta,Protein Struct. Mol. Enzymol.* **1983**, *745*, 103-106.

[91] E. Sinn, C. J. O'Connor, J. De Jersey, B. Zerner, *Inorganica Chimica Acta* **1983**, *78*, L13-L15.

spectroscopy[82] to indicate antiferromagnetic spin coupling present in both the oxidized ($Fe^{III}Fe^{III}$, $S = 0$ ground state) and reduced ($Fe^{II}Fe^{III}$, $S = {}^1/_2$ ground state) forms. Stronger antiferromagnetic interaction for the oxidized form has been elucidated in multiple studies ($J > -80$ cm^{-1}),[82,85,88] proposing the identity of the bridge to be an oxo unit, while a weaker antiferromagnetic interaction has been observed for the reduced pink form ($J < -35$ cm^{-1})[82,85,89] resulting in a predicted hydroxo-bridged species. The diagnostic rhombic EPR signals for the reduced species with molecular $S = {}^1/_2$ state with $g \sim 1.7$ ($g = 1.92, 1.77, 1.63$ for sample from bovine[88] and $g = 1.93, 1.72, 1.56$ for sample from porcine,[90] for example) are reminiscent of other $Fe^{II}Fe^{III}$ enzymatic centers, such as mixed-valent forms produced for Hr and MMO.[92] The electronic structure has been further probed by ^{57}Fe Mössbauer studies on ^{57}Fe enriched porcine samples, which suggest that the iron centers in both forms are in the high-spin state (**Table 1.1**).[90]

1.2.5 Other Diiron Enzymes

In addition to the extensively studied diiron enzymes discussed, this motif is present in many diverse enzyme active sites. For instance, several other members of the bacterial multicomponent monooxygenases family, which are responsible for the selective oxidation of a variety of hydrocarbons like methane by sMMO, also feature diiron active sites. Such examples include toluene/*o*-xylene monooxygenase (ToMOH), and phenol hydroxylase.[93] Furthermore, other classes of diiron enzymes include stearoyl-ACP Δ^9-desaturase (Δ9-D), which performs selective

[92] Que, L., Jr.; True, A. E. in *Progress in Inorganic Chemistry: Bioinorganic Chemistry, Vol. 38* (Ed.: S. J. Lippard), John Wiley & Sons. Inc **1990**.

[93] Sazinsky, M. H.; Bard, J.; Di Donato, A.; Lippard, S. J. *J. Biol. Chem.* **2004**, *279*, 30600–30610.

Table 1.1. ^{57}Fe Mössbauer parameters for diiron enzyme active sites. Data was collected at 4.2 K unless otherwise specified.

Enzyme	Form	Oxidation state	δ (Fe 1) (mm s^{-1})	$\|\Delta E_Q\|$ (Fe1) (mm s^{-1})	δ (Fe 2) (mm s^{-1})	$\|\Delta E_Q\|$ (Fe2) (mm s^{-1})	Ref.
sMMO	H_{ox} (Mc)	$Fe^{III}Fe^{III}$	0.48	0.95	0.55	1.47	32a
sMMO	H^{ox} (Mt)	$Fe^{III}Fe^{III}$	0.50	0.87	0.51	1.16	32b
sMMO	H_{red} (Mc)	$Fe^{II}Fe^{II}$	1.30	3.01	–	–	32a
sMMO	H^{red} (Mt)	$Fe^{II}Fe^{II}$	1.3	3.1	1.3	2.4-3.0	32b
sMMO	H_{peroxo} (Mc)	$Fe^{III}Fe^{III}$	0.66	1.51	–	–	35
sMMO	P (Mt)	$Fe^{III}Fe^{III}$	0.67	1.51	–	–	37
sMMO	Q (Mc)	$Fe^{IV}Fe^{IV}$	0.21	0.68	0.14	0.55	35
sMMO	Q (Mt)	$Fe^{IV}Fe^{IV}$	0.17	0.68	–	–	40
RNR	$R2_{red}$	$Fe^{II}Fe^{II}$	1.26	3.13	1.19	2.91	48
RNR	P	$Fe^{III}Fe^{III}$	0.66	1.51	–	–	54
RNR	X	$Fe^{III}Fe^{IV}$	0.55	1.0	0.36	1.0	57
RNR	Active R2	$Fe^{III}Fe^{III}$	0.53	1.65	0.45	2.45	52
Hr	deoxyHr	$Fe^{II}Fe^{II}$	1.20	2.89	–	–	65
Hr	oxyHr	$Fe^{III}Fe^{III}$	0.51	1.96	0.52	0.95	66
PAP	purple	$Fe^{III}Fe^{III}$	0.46[a]	2.12[a]	0.55[a]	1.65[a]	90
PAP	pink	$Fe^{II}Fe^{III}$	1.24[b]	2.68[b]	0.53[b]	1.84[b]	90
ferritin	peroxo	$Fe^{III}Fe^{III}$	0.62	1.08	–	–	
Δ9-D	resting	$Fe^{III}Fe^{III}$	0.54[c]	1.53[c]	–	–	94b
Δ9-D	peroxo	$Fe^{III}Fe^{III}$	0.68	1.90	0.64	1.06	94a
ferritin	peroxo	$Fe^{III}Fe^{III}$	0.62	1.08	–	–	95
hDOHH	peroxo	$Fe^{III}Fe^{III}$	0.55	1.16	0.58	0.88	96
ODP	peroxo	$Fe^{III}Fe^{III}$	0.58	1.01	–	–	97

[a] Data collected at 10 K. [b] Data collected at 60 K. [c] Corresponds to the major species.

fatty acid desaturation;[55,94] ferritin, an iron storage protein in many organisms;[95] deoxyhypusine hydroxylase (hDOHH), a key enzyme for cell proliferation regulation;[55,96] and the recently discovered oxygen-binding diiron protein (ODP) which serves as a dioxygen and iron sensor important for bacterial chemotaxis.[97] Evidence of a diiron μ-oxo dimer has been established for Δ9-D and ferritin. All of these enzymes react with O_2 to form a diiron(III) μ-(1,2)-peroxo species featuring antiferromagnetically coupled high-spin $S = {}^5/_2$ Fe^{III} centers, as determined by ^{57}Fe Mössbauer (**Table 1.1**), absorption, and resonance Raman spectroscopic studies. Comparisons of optical and Mössbauer data of H_{peroxo} / P of sMMO with these Raman-characterized enzymes has guided its assignment as a μ-(1,2)-peroxo adduct as well (in the absence of Raman data for H_{peroxo} / P).[24]

1.2.6 Nitrite Reductase

Although not formally a diiron enzyme, another important iron-dependent protein is nitrite reductase, which utilizes two heme complexes to perform the reduction of nitrite to nitric oxide. Nitrite plays a variety of important biological roles due to its involvement in the nitrogen cycle and various signaling pathways.[98] More specifically, nitrite is an important source of NO for mammalian signaling under hypoxic conditions. It is proposed that this process can be carried out by a multitude of different enzymes; in mammalian systems, these include iron (such as

[94] (a) Broadwater, J. A.; Achim, C.; Münck, E.; Fox, B. G. *Biochem.* **1999**, *38*, 12197–12044. (b) Shu, L.; Broadwater, J. A.; Achim, C.; Fox, B. G.; Munck, E.; Que, L., Jr. *J. Biol. Inorg. Chem.* **1998**, *3*, 392–400.

[95] Pereira, A. S.; Small, W.; Krebs, C.; Tavares, P.; Edmondson, D. E.; Theil, E. C.; Huynh, B. H. *Biochem.* **1998**, *37*, 9871– 9876.

[96] Vu, V. V.; Emerson, J. P.; Martinho, M.; Kim, Y. S.; Munck, E.; Park, M. H.; Que, L., Jr. *Proc. Natl. Acad. Sci. U.S.A.* **2009**, *106*, 14814–14819.

[97] Muok, A. R.; Deng, Y.; Gumerov, V. M.; Chong, J. E.; DeRosa, J. R.; Kurniyati, K.; Coleman, R. E.; Lancaster, K. M.; Li, C.; Zhulin, I. B.; Crane, B. R. *Proc. Natl. Acad. Sci.* **2019**, *116*, 14955–14960.

[98] Maia, L. B.; Moura, J. J. G. *Chem. Rev.* **2014**, *114*, 5273–5357 and references therein.

hemoglobin, myoglobin, cytochrome *c*), molybdenum (xanthene oxidase, aldehyde oxidase) or zinc (carbonic anhydrase) dependent enzymes.[98] Conversely in prokaryotes, nitrite reductase enzymes featuring iron (the cytochrome d_1-containing nitrite reductase, "Cd_1NiR") or copper (the copper-containing nitrite reductase, "CuNiR") active sites are utilized.[98] Due to their more targeted nitrite reductase function, these enzymes have been more widely studied for their role in nitrite reduction and have served as inspiration for biomimetic synthetic systems.

For Cd_1NiR, two iron centers are critical for its function: a *c*-heme center is responsible for electron transfer to the d_1-heme active site located approximately 20 Å away. It is proposed that these iron centers cycle between the diiron(III) resting state and a diiron(II) active state.[98,] Structural studies indicate that major structural rearrangements are required for the heme centers during catalysis, largely at the d_1-heme center to allow for substrate to bind. In the inactive iron(III) form, this site is hexa-coordinated but becomes penta-coordinate in the active iron(II) state by displacement of a ligand (i.e., a hydroxide[99] or a tyrosine[100] depending on the enzyme type) to yield an open coordination site for nitrite binding. In the active iron(II) form, the *c* heme center features histidine-methionine ligation, although the inactive iron(III) form ligation can vary depending on enzyme source (i.e., histidine-methionine for *Pseudomonas aeruginosa* enzyme,[101] bis-histidine for *Thiosphaera pantotropha*[100]) (**Figure 1.3**). Analogously for CuNiR, two copper centers are involved – a type-1 copper center transports electrons to the type-2 copper active site

[99] Nurizzo, D.; Cutruzzola, F.; Arese, M.; Bourgeois, D.; Brunori, M.; Cambillau, C.; Tegoni, M. *Biochem*. **1998**, *37*, 13987–13996

[100] Williams, P. A.; Fülöp, V.; Garman, E. F.; Saunders, N. F. W.; Ferguson, S. J.; Hajdu, J. *Nature* **1997**, *389,* 406–412.

[101] Nurizzo, D.; Silvestrini, M.-C.; Mathieu, M.; Cutruzzolà, F.; Bourgeois, D.; Fülöp, V.; Hajdu, J.; Brunori, M.; Tegoni, M.; Cambillau, C. *Structure* **1997**, *5*, 1157–1171.

located ~13 Å away. It is believed that Cu(I) and Cu(II) oxidation states are likely accessed in the nitrite reduction mechanism.[98,102]

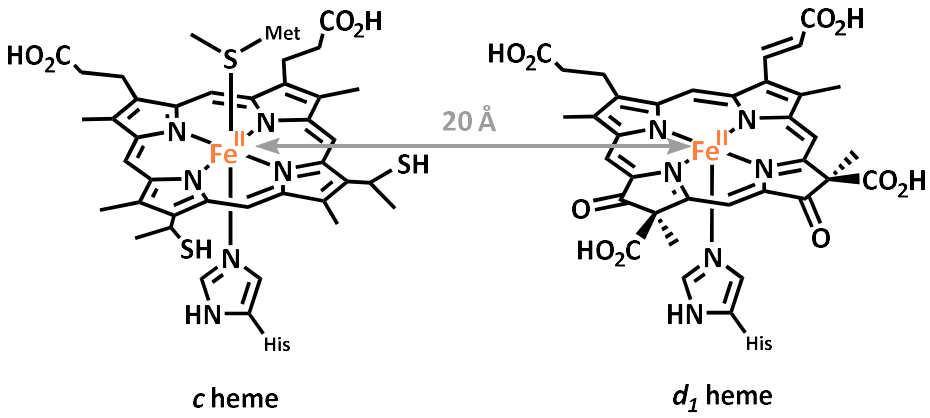

Figure 1.3. Structures of the two heme centers involved in nitrite reduction by Cd_1NIR, the *c* heme center responsible for electron transfer to the active site d_1-heme, based on crystal structure analysis in the reduced Fe(II)Fe(II) form.[99,101]

1.3 Synthetic Diiron Model Complexes

Over the last several decades, chemists have sought to synthesize model complexes as another means to better understand structure-function relationships in diiron enzymatic active sites. Of the plethora of bimetallic units that have been explored, a few key examples of both structural and functional mimics are discussed herein to share how model complexes have yielded insight into biological mechanisms, compare the electronic structure and reactivity profiles with features observed in the aforementioned enzymes, and demonstrate how this knowledge can lead to reactive synthetic models.

1.3.1 Diiron μ-Hydroxo and μ-Oxo Models

[102] Merkle, A. C.; Lehnert, N. *Dalton Trans*. **2012**, *41*, 3355–3368.

Many of the initial targets for diiron enzyme mimics featured ligands emulating those observed in nature, including hydroxo/oxo and carboxylate-bridging ligands and nitrogen-based terminal ligands. Some of the earliest hemerythrin model complexes include $[Fe^{III}_2(\mu\text{-}OH)(\mu\text{-}OAc)_2(HB(pz)_3)_2]^+$ and $[Fe^{III}_2(\mu\text{-}O)(\mu\text{-}OAc)_2\{HB(pz)_3\}_2]$ ($HB(pz)_3$ = hydrotris(1-pyrazolyl)borate) which can reversibly interconvert by protonation and deprotonation reactions reported by Lippard *et al.* in 1984 (**Figure 1.4a**). Crystallographic studies of these compounds revealed longer Fe–Fe and Fe–OH distances for the bridging hydroxide compared with the bridging oxo variant, which is consistent with observations from other diiron(III) hydroxo-bridged complexes.[103] Conversely, the Fe–O–Fe angles for the protonated and deprotonated complexes were nearly identical (**Table 1.2**). Also consistent with previous findings, solid-state magnetometry indicated a weaker antiferromagnetic coupling between the bridging hydroxo (J = –17 cm^{-1}) than for the bridging oxo (J = –121 cm^{-1}).[104]

The following year, Weiss and coworkers reported the first functional model for hemerythrin by synthesizing a diiron(II) bridging hydroxide complex, $[Fe^{II}_2(\mu\text{-}OH)(\mu\text{-}OAc)_2(Me_3TACN)_2]^+$, which can be oxidized by air to furnish the diiron(III) bridging oxo, $Fe^{III}_2(\mu\text{-}O)(\mu\text{-}OAc)_2(Me_3TACN)_2$ (Me_3TACN = *N*,*N'*,*N''*-trimethyl-1,4,7-triazacyclononane) (**Figure 1.4b**). Similarly, X-ray diffraction studies showed significantly longer Fe–Fe and Fe–OH distances for the bridging hydroxide compared with the bridging oxo variant and similar Fe–O–Fe angles for both complexes (**Table 1.2**) Furthermore, magnetic susceptibility and ^{57}Fe Mössbauer data of these compounds reveal weak antiferromagnetic coupling for the diiron(II) bridging hydroxo (J = –14 cm^{-1}) compared with stronger antiferromagnetic coupling for the diiron(III) bridging oxo (J = –

[103] Kurtz, D. M., Jr. *Chem. Rev.* **1990**, *90*, 585 –606.

[104] Armstrong, W. H.; Lippard, S. J. *J. Am. Chem. Soc.* **1984**, *106*, 4632–4633.

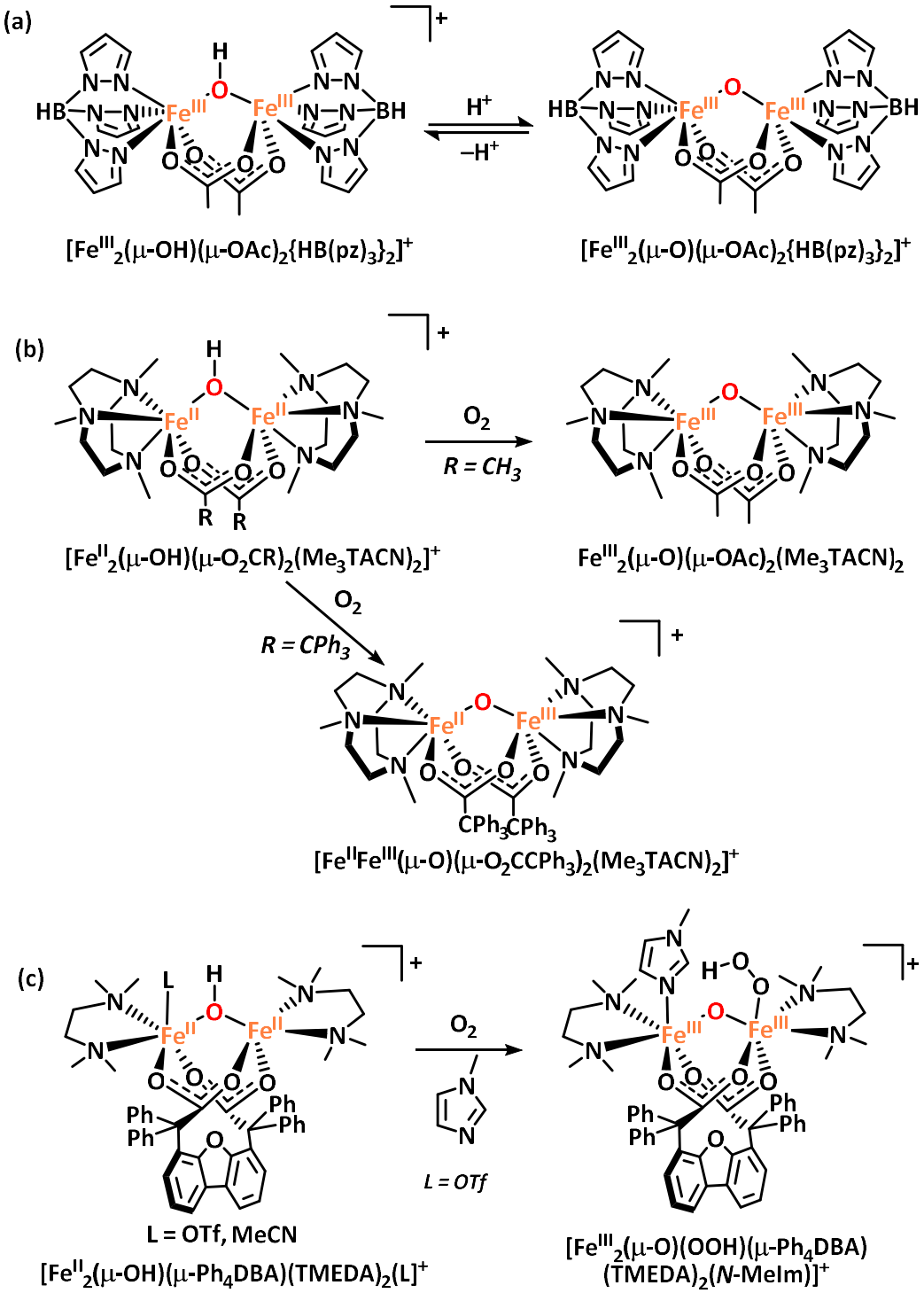

Figure 1.4. Early hemerythrin models with bridging hydroxo/oxo- and acetato- ligands. (a) Protonation-deprotonation reactivity of $[Fe^{III}_2(\mu\text{-OH})(\mu\text{-OAc})_2(HB(pz)_3)_2]^+$ and $Fe^{III}_2(\mu\text{-O})(\mu\text{-OAc})_2(HB(pz)_3)_2$.[104] (b) Oxidation reactivity of $[Fe^{II}_2(\mu\text{-OH})(\mu\text{-O}_2CR)_2(Me_3TACN)_2]^+$ to yield $Fe^{III}_2(\mu\text{-O})(\mu\text{-}O_2CR)_2(Me_3TACN)_2$ when R=CH_3[105] or $Fe^{II}Fe^{III}(\mu\text{-O})(\mu\text{-}O_2CR)_2(Me_3TACN)_2$ when R = CPh_3.[107] (c) Asymmetric coordination of the iron centers in $[Fe^{II}_2(\mu\text{-OH})(\mu\text{-Ph}_4DBA)(TMEDA)_2(L)]^+$ allows for isolation of the diiron(III) hydroxoperoxo addicut, $[Fe^{III}_2(\mu\text{-O})(OOH)(\mu\text{-Ph}_4DBA)(TMEDA)_2(N\text{-MeIm})]^+$ when L = OTf.[108]

115 cm^{-1}) (**Table 1.2**).[105,106] These metrics are consistent with those observed in diiron(II) deoxyHr and diiron(III) oxyHr (*vide supra*).

Other examples of Me_3TACN diiron complexes featuring bulkier carboxylate groups have been studied, including an example by Hagen *et al.* which allowed for the isolation of a rare mixed-valent iron(II)iron(III) μ-O complex, $[Fe^{II}Fe^{III}(\mu\text{-}O)(\mu\text{-}O_2CCPh_3)_2(Me_3TACN)_2]^+$, when utilizing the trityl ester bridging unit (**Figure 1.4b**). This compound was assigned as a Class II mixed-valent compound due to the iron sites being distinguishable by X-ray diffraction and ^{57}Fe Mössbauer studies (**Table 1.2**).[107] In 1998, Lippard *et al.* designed a dinucleating dicarboxylate ligand Ph_4DBA (DBA = dibenzofuran-4,6-diacetic acid) to afford an asymmetric coordination environment for the diiron(II) μ-OH and bis-μ-carboxylato complex, $[Fe^{II}_2(\mu\text{-}OH)(\mu\text{-}Ph_4DBA)(TMEDA)_2(OTf)]^+$ consistent with the structure of deoxyHr in which one iron center is coordinatively-unsaturated to accommodate dioxygen binding. Replacement of the triflate counterion with a solvent molecule (MeCN) allowed for study by X-ray crystallography. Reaction of the triflate complex with dioxygen in the presence of three equivalents of *N*-methylimidazole (*N*-MeIm) allowed for formation of a diiron(III) hydroperoxo complex, $[Fe^{III}_2(\mu\text{-}O)(OOH)(\mu\text{-}Ph_4DBA)(TMEDA)_2(N\text{-}MeIm)]^+$ (**Figure 1.4c**), as assigned by ^{57}Fe Mössbauer (**Table 1.2**), absorption (λ = 336, 470 nm; ε = 7300, 2200 M^{-1} cm^{-1}), and resonance Raman spectroscopy (ν_{O-O} = 844 cm^{-1}).[108] These spectroscopic features were consistent with those observed in oxyHr (*vide supra*).

---

[105] Chaudhuri, P.; Wieghardt, K.; Nuber, B.; Weiss, J. *Angew. Chem. Int. Ed. Engl.* **1985**, *24*, 778–779.

[106] Hartman, J. R.; Rardin, R. L.; Chaudhuri, P.; Pohl, K.; Wieghardt, K.; Nuber, B.; Weiss, J.; Papaefthymiou, G. C.; Frankel, R. B.; Lippard, S. J. *J. Am. Chem. Soc.* **1987**, *109*, 7387–7396.

[107] Payne, S. C.; Hagen, K. S. *J. Am. Chem. Soc.* **2000**, *122*, 6399–6410.

[108] (a) Mizoguchi, T. J.; Lippard, S. J. *J. Am. Chem. Soc.* **1998**, *120*, 11022 – 11023. (b) Du Bois, J.; Mizoguchi, T. J.; Lippard, S. J. *Coord. Chem. Rev.* **2000**, *200–202*, 443–485.

1.3.2 Diiron(III) Peroxo Models

The presence of diiron(III) peroxo intermediates in diiron active site mechanisms following reaction with dioxygen has led to great interest in the field to synthesize and characterize model systems of this type. Studies of *cis* and *trans* μ-(1,2)-peroxo complexes have ultimately contributed to understanding dioxygen reactivity in biological systems and predicting oxygen binding-modes by comparison of spectroscopic features. Dinucleating ligands such as N-Et-HPTB by Que *et al*. (N-Et-HPTB =1,3-bis(N,N-bis(1-ethylbenzimidazol-2-yl)amino)-2-hydroxypropane)[109] and Ph-BIMP by Suzuki *et al.* (Ph-BIMP = 2.6-bis[bis{2-(1-methyl4,5-diphenylimidazolyl)methyl}aminomethyl]-4-methylphenolate)[110] were metalated to afford diiron(II) μ-alkoxo, μ-carboxylato complexes that react with dioxygen to form *cis* μ-(1,2)-peroxo complexes.[111] Dioxygen addition to $[Fe^{II}_2(\mu\text{-}O_2CPh)(\text{N-Et-HPTB})]^{2+}$ at –60 °C was irreversible, leading to a product assigned as $[Fe^{III}_2(\mu\text{-}1,2\text{-}O_2)(\mu\text{-}O_2CPh)(\text{N-Et-HPTB})]^{2+}$ by ^{57}Fe Mössbauer spectroscopy (**Table 1.2**), visible absorption spectroscopy (λ_{max} = 588 nm, ε = 1500 M^{-1} cm^{-1}), and resonance Raman spectroscopy (ν_{O-O} = 900 cm^{-1}) indicating O_2 bound as a μ-(1,2)-peroxo unit.[112] Crystal structure analysis was performed on this adduct, however addition of $OPPh_3$ to the crystallization conditions was required to enhance stability of the O_2 adduct to allow crystal growth at –40 °C over the course of several weeks. In the solid-state structure, two $OPPh_3$ molecules displaced the bridging benzoate to form $[Fe^{III}_2(\mu\text{-}1,2\text{-}O_2)(PPh_3O)_2(\text{N-Et-HPTB})]^{2+}$ which showed a *cis* binding mode of the peroxide bridge.[109] Conversely, Suzuki *et al*. exploited careful ligand

[109] Dong, Y.; Yan, S.; Young, V. G., Jr.; Que, L., Jr. *Angew. Chem. Int. Ed. Engl.* **1996**, *35*, 618–620.

[110] Ookubo, T.; Sugimoto, H.; Nagayama, T.; Masuda, H.; Sato, T.; Tanaka, K.; Maeda, Y.; Okawa, H.; Hayashi, Y.; Uehara, A.; Suzuki, M. *J. Am. Chem. Soc.***1996**, *118*, 701–702.

[111] Tshuva, E. Y.; Lippard, S. J. *Chem. Rev.* **2004**, *104*, 987–1012.

[112] Ménage, S.; Brennan, B. A.; Juarez-Garcia, C.; Münck, E.; Que, L., Jr. *J. Am. Chem. Soc.***1990**, *112*, 6423–6425.

design to induce reversible reactivity of the diiron(II) starting material, $[Fe^{II}_2(\mu\text{-}O_2CPh)(Ph\text{-}BIMP)]^{2+}$ at ambient temperature. This allowed the peroxide adduct to be crystallized with greater ease, revealing $[Fe^{III}_2(\mu\text{-}O_2)(\mu\text{-}O_2CPh)(Ph\text{-}BIMP)]^{2+}$ (**Figure 1.5a**).[110]

Another synthetic strategy employed to furnish diiron(III) peroxo complexes was afforded by using hydrogen peroxide as an oxidant to diiron(III) starting materials. In this vein, Suzuki *et al.* used a tetradentate ligand featuring nitrogen- and carboxylate-donors, 6-Me_2-BPP (BPP = *N*, *N*-bis(2-pyridylmethyl)-3-aminopropionate), to synthesize the *cis* μ-(1,2)-peroxo compounds $[Fe^{III}_2(\mu\text{-}OH)(\mu\text{-}1,2\text{-}O_2)(6\text{-}Me_2\text{-}BPP)_2]^+$ and $Fe^{III}_2(\mu\text{-}O)(\mu\text{-}1,2\text{-}O_2)(6\text{-}Me_2\text{-}BPP)_2$.[113] Que and coworkers were also able to access a diiron(III) bridging-oxo bridging-peroxo complex utilizing the nitrogen-based tetradentate ligand 6-Me_3-TPA (TPA = tris(pyridylmethyl)amine), $[Fe^{III}_2(\mu\text{-}O)(\mu\text{-}1,2\text{-}O_2)(6\text{-}Me_3\text{-}TPA)_2]^{2+}$.[114]

Other reports utilized the hydrotris(pyrazolyl)borate ligand framework to synthesize peroxo

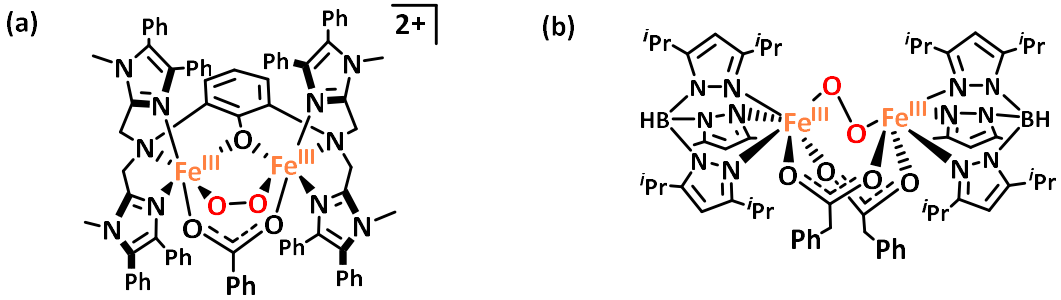

$[Fe^{III}_2(\mu\text{-}1,2\text{-}O_2)(\mu\text{-}O_2CPh)_2(\mu\text{-Ph-BIMP})]^{2+}$ $Fe^{III}_2(\mu\text{-}1,2\text{-}O_2)(\mu\text{-}O_2CCH_2Ph)_2\{HB(3,5\text{-}{}^{i}Pr_2pz)_3\}_2$

Figure 1.5. Diiron(III)-peroxo adducts, both in the (a) *cis* μ-1,2-O_2 binding mode observed in $[Fe^{III}_2(\mu\text{-}1,2\text{-}O_2)(OPPh_3)_2(N\text{-Et-HPTB})]^{2+}$,[110] and the (b) *trans* μ-1,2-O_2 adduct, $Fe^{III}_2(\mu\text{-}1,2\text{-}O_2)(\mu\text{-}O_2CCH_2Ph)_2\{HB(3,5\text{-}{}^{i}Pr_2pz)_3\}_2$.[116]

[113] Zhang, X.; Furutachi, H.; Fujinami, S.; Nagatomo, S.; Maeda, Y.; Watanabe, Y.; Kitagawa, T.; Suzuki, M. *J. Am. Chem. Soc.* **2004**, *127,* 826–827.

[114] Dong, Y.; Zang, Y.; Shu, L.; Wilkinson, E. C.; Que, L., Jr.; Kauffman, K.; Münck, E. *J. Am. Chem. Soc.* **1997**, *119*, 12683–12684.

complexes, in which two mononuclear iron(II) carboxylate compounds dimerized upon exposure to dioxygen. These complexes were relatively stable below –20 °C, above which degradation to form trinuclear iron(III) complexes occurred. Following addition of dioxygen to {HB(3,5-^{i}Pr$_2$pz)$_3$}Fe^{II}(O$_2$CCH$_2$Ph)$_2$ yielded the *trans* μ-(1,2)-peroxo diiron(III) adduct at –50 °C, [115] which was studied by ^{57}Fe Mossbauer (**Table 1.2**), resonance Raman (ν_{O-O} = 900 cm^{-1}), and absorption spectroscopy (λ_{max} = 694 nm, ε = 2650 M^{-1} cm^{-1}).[116] Crystallization at–80 °C revealed the formation of Fe$^{III}_2$(μ-1,2-O$_2$)(μ-O$_2$CCH$_2$Ph)$_2${HB(3,5-^{i}Pr$_2$pz)$_3$}$_2$ (**Figure 1.5b**). Spectroscopic comparison of this compound revealed similar ^{57}Fe Mössbauer parameters (**Table 1.2**) and optical features to H$_{peroxo}$ / P of sMMO, leading to the hypothesis that this intermediate may feature a *trans* μ-(1,2)-peroxo binding mode.[24]

1.3.3 Higher Valent Diiron Bis-μ-(Hydr)oxo Models

Key to the proposed active sites of enzymes such as RNR and sMMO is accessing higher valent diiron bis-bridging oxo centers. For RNR, intermediate X is proposed to contain a mixed-valent iron(III) iron(IV) bis-μ-O unit that is responsible for generating a tyrosine radical in the active R2 form;[56] for sMMO, intermediate Q may involve a diiron(IV) bis-μ-O as the active oxidant for hydroxylation reactivity.[22-24]

Que and coworkers have designed several of the model complexes for these proposed intermediates. Decomposition of the previously discussed diiron(III) bridging oxo, *cis* μ-(1,2)-peroxo compound, [Fe$^{III}_2$(μ-O)(μ-1,2-O$_2$)(6-Me$_3$-TPA)$_2$]$^{2+}$, gave rise to a new species assigned as the mixed-valent [Fe^{III}Fe^{IV}(μ-O)$_2$(6-Me$_3$-TPA)$_2$]$^{3+}$ (**Figure 1.6a**), providing evidence that a diiron

[115] Kitajima, N.; Tamura, N.; Amagai, H.; Fukui, H.; Moro-Oka, Y.; Mizutani, Y.; Kitagawa, T.; Mathur, R.; Heerwegh, K.; Reed, C. A.; Randall, C. R.; Que, L., Jr.; Tatsumi, K. *J. Am. Chem. Soc.* **1994**, *116*, 9071–9085.

[116] Kim, K.; Lippard, S. J. *J. Am. Chem. Soc.* **1996**, *118*, 4914–4915.

peroxo may act as an intermediate towards generating high valent diiron μ-oxo diamond core species, as is proposed in the mechanism for RNR reactivity.[56,114] Spectroscopically, this iron(III) iron(IV) species is observed to have antiferromagnetically coupled metal centers resulting in a molecular $S = ½$ spin state, confirmed by EPR and ^{57}Fe Mössbauer variable field studies.[117] The assignment of this mixed-valent product was further confirmed by an alternative synthetic route involving one electron oxidation from the diiron(III) bis-μ-oxo precursor, $[Fe^{III}_2(\mu\text{-}O)_2(6\text{-}Me_3\text{-}TPA)_2]^{2+}$, generating spectroscopic features consistent with those observed for $[Fe^{III}Fe^{IV}(\mu\text{-}O)_2(6\text{-}Me_3\text{-}TPA)_2]^{3+}$ via the original route. Resonance Raman studies were consistent with an isomerization of the diamond core to form an Fe^{III}–(μ-O)–Fe^{IV}=O motif, demonstrating the flexibility of the iron(III) iron(IV) bis-oxo diamond core.[118] Finally, reacting a diiron(II) bis-μ-hydroxo complex, $[Fe^{II}_2(\mu\text{-}OH)_2(6\text{-}Me_3\text{-}TPA)_2]^{2+}$, with dioxygen resulted in a functional model of intermediate X. First, addition of dioxygen at –40 °C, the generation of a bridging-oxo, peroxo adduct is speculated by formation of a green species with absorption features (λ = 640 nm, ε = 1100 M^{-1} cm^{-1}) and resonance Raman spectra ($\nu_{O–O}$ = 848 cm^{-1}) consistent with previous examples (*vide supra*). This metastable species is observed to slowly react with one equivalent of acid ($HClO_4$) at –30 °C to form a species with an isotropic EPR signal at g = 1.999 consistent the other mixed-valent iron(III) iron(IV) bis bridging oxo complexes generated on this platform. This proposed diiron(III,IV) bridging oxo complex converts 2,4,6-tri-*tert*-butylphenol to the corresponding phenoxyl radical, analogous to the radical reactivity observed in RNR by intermediate X to form the tyrosyl radical.[56]

[117] Dong, Y.; Que, L., Jr.; Kauffman, K.; Münck, E. *J. Am. Chem. Soc.* **1995**, *117*, 11377–11378.

[118] Zheng, H.; Yoo, S. J.; Münck, E.; Que, L., Jr. *J. Am. Chem. Soc.* **2000**, *122*, 3789–3790.

Other variants of the TPA ligand yielded similar structural diiron(III,IV) bis-μ-oxo complexes. Changing the position of the methyl group to the 5-position, $[Fe^{III}Fe^{IV}(\mu\text{-}O)_2(5\text{-}Me_3\text{-}TPA)_2]^{3+}$, largely affected the electronic structure of the unit. In this case, an $S = {}^3/_2$ EPR spectrum with g = 4.45, 3.90, and 2.01 and ^{57}Fe Mössbauer spectroscopy indicated ferromagnetic coupling in a valence-delocalized iron(III) ($S = {}^1/_2$) iron(IV) (S = 1) system.[119] Moving to more electron donating groups on the pyridine rings allowed for a similar mixed-valent iron(III) iron(IV) species, $[Fe^{III}Fe^{IV}(\mu\text{-}O)_2(L^b)_2]^{3+}$ where L^b = tris-(4-methoxy-3,5,-dimethylpyridyl-2-methyl)amine, with an overall molecular state of $S = {}^3/_2$. One electron oxidation of this species via bulk electrolysis provided access to the diiron(IV) bis-μ-oxo species, $[Fe^{IV}{}_2(\mu\text{-}O)_2(L^b)_2]^{2+}$ (**Figure 1.6b**).[120] Serving as an intermediate Q model complex, this system has elucidated a great deal of information regarding the reactivity of this proposed intermediate.

Surprisingly, these high-valent diiron bis-μ-O displayed lower reactivity for oxidation of C–H bonds (~ 3 orders of magnitude) than related mononuclear Fe^{IV}=O species. This observation indicated that bridging oxo complexes may not be as reactive as terminal oxo systems, which contrasted the original proposed mechanism for intermediate Q.[120] This possibility was further probed using nucleophilic attack of a small substrate on $[Fe^{IV}{}_2(\mu\text{-}O)_2(L^b)_2]^{2+}$ (i.e., hydroxide,[121] alcohol, or water[43]) thereby opening the core to form a terminal iron(IV)=oxo moiety (**Figure 1.6b**). Hydroxide attack resulted in a species that was far more reactive towards oxidative reactivity than its closed-core congener (2.8×10^6 more reactive towards dihydroanthracene oxidation at –80 °C) while methoxide activation led to an even more potent oxidant (2.8×10^6 more reactive for

[119] Dong, Y.; Fujii, H.; Hendrich, M. P.; Leising, R. A.; Pan, G.; Randall, C. R.; Wilkinson, E. C.; Zang, Y.; Que, L., Jr.; Fox, B. G.; Kauffman, K.; Münck, E. *J. Am. Chem. Soc.* **1995**, *117*, 2778–2792.

[120] Xue, G.; Wang, D.; De Hont, R.; Fiedler, A. T.; Shen, X.; Münck, E.; Que, L., Jr. *Proc. Nat. Acad. Sci.* **2007**, *104*, 20713–20718.

[121] Xue, G.; De Hont, R.; Munck, E.; Que, L., Jr. *Nat. Chem.* **2010**, *2*, 400–405.

Table 1.2. ^{57}Fe Mössbauer parameters coupling constants, and selected bond metrics in diiron model complexes. ^{57}Fe Mössbauer data collected at 4K unless otherwise specified.

Complex	δ (Fe1) (mm s^{-1})	$\|\Delta E_Q\|$ (Fe1) (mm s^{-1})	δ (Fe2) (mm s^{-1})	$\|\Delta E_Q\|$ (Fe2) (mm s^{-1})	J (cm^{-1})	Fe – Fe (Å)	Fe – O (Å)[a]	<Fe –O –Fe (°)[a]	Ref.
$[Fe^{III}_2(\mu\text{-}OH)(\mu\text{-}OAc)_2(HB(pz)_3)_2]^+$	–	–	–	–	–17	3.439(1)	1.960(4) 1.952(4)	123.1(2)	104
$Fe^{III}_2(\mu\text{-}O)(\mu\text{-}OAc)_2(HB(pz)_3)_2$	–	–	–	–	–121	3.1457(6)	1.780(2) 1.788(2)	123.6(1)	104
$[Fe^{II}_2(\mu\text{-}OH)(\mu\text{-}OAc)_2(Me_3TACN)_2]^+$	1.16	2.83	–	–	–14(2)	3.439(1)	1.987(8) 2.142(9)	113.2(2)	105, 106
$Fe^{III}_2(\mu\text{-}O)(\mu\text{-}OAc)_2(Me_3TACN)_2$	0.47	1.50	–	–	–115	3.12(1)	1.800(3)	119.7(1)	105, 106
$[Fe^{II}\,Fe^{III}(\mu\text{-}O)(\mu\text{-}O_2CPh_3)_2(Me_3TACN)_2]^+$	1.09	2.45	0.60	2.35	–144	3.123(1)	1.847(4) 1.800(4)	~119	107
$[Fe^{II}_2(\mu\text{-}OH)(\mu\text{-}Ph_4DBA)(TMEDA)_2(L)]^+$	1.04[b]	2.81[b]	1.33[b]	2.81[b]	–	3.1638 (5)[c]	1.959(2)[c] 1.959(2)[c]	105.12 (8)[c]	108a
$[Fe^{III}_2(\mu\text{-}O)(OOH)(\mu\text{-}Ph_4DBA)(TMEDA)_2(N\text{-}MeIm)]^+$	0.48[c]	1.03[c]	0.51[c]	1.93[c]	–	–	–	–	108b
$[Fe^{III}_2(\mu\text{-}1,2\text{-}O_2)(\mu\text{-}O_2CPh)(N\text{-}Et\text{-}HPTB)]^{2+}$	0.52	0.72	–	–	–	–	–	–	111
$[Fe^{III}_2(\mu\text{-}1,2\text{-}O_2)(\mu\text{-}O_2CPh)(Ph\text{-}BIMP)]^{2+}$	0.58[d]	0.74[d]	0.65	1.70	–	3.327(2)	2.018(5)	111.7(2)	110
$Fe^{III}_2(\mu\text{-}1,2\text{-}O_2)(\mu\text{-}O_2CCH_2Ph)_2\{HB(3,5\text{-}{}^iPr_2pz)_3\}_2$	0.66	1.40	–	–	–	4.000(4)	–	–	116
$[Fe^{III}_2(\mu\text{-}OH)(\mu\text{-}1,2\text{-}O_2)(6\text{-}Me_2\text{-}BPP)_2]^+$	0.50[e]	1.31[e]	–	–	–	3.396(1)	2.006(4) 1.943(4)	118.6(2)	113
$Fe^{III}_2(\mu\text{-}O)(\mu\text{-}1,2\text{-}O_2)(6\text{-}Me_2\text{-}BPP)_2$	0.50[e]	1.46[e]	–	–	–	3.171(1)[f]	–	–	113
$[Fe^{III}_2(\mu\text{-}O)(\mu\text{-}1,2\text{-}O_2)(6\text{-}Me_3\text{-}TPA)_2]^{2+}$	0.54	1.68	–	–	–	–	–	–	114
$[Fe^{III}Fe^{IV}(\mu\text{-}O)_2(6\text{-}Me_3\text{-}TPA)_2]^{3+}$	0.48[g]	1.6[g]	0.08[g]	0.5[g]	–	–	–	–	117
$[Fe^{III}Fe^{IV}(\mu\text{-}O)_2(5\text{-}Me_3\text{-}TPA)_2]^{3+}$	0.14	0.49	–	–	–	–	–	–	118
$[Fe^{III}Fe^{IV}(\mu\text{-}O)_2(L^b)_2]^{3+}$	0.11	0.44	–	–	–	–	–	–	119
$[Fe^{IV}_2(\mu\text{-}O)_2(L^b)_2]^{2+}$	–0.04	2.09	–	–	>80	2.73[h]	1.77[h]	–	119

[a]O = μ-oxo, hydroxo, or alkoxo; [b]L = OTf; [c]L = MeCN; [d]Data collected at 77 K. [e]Data collected at 80 K. [f]Crystal structure data exhibited extreme disorder. [g]Data collected at 150 K. [h]Distances based on EXAFS data.

the same reaction conditions). It should be noted, however, that concomitant with the structural changes upon hydroxide/methoxide activation was a spin state change of the Fe^{IV} center (from

$S = 1$ to S = 2) (**Scheme 1.6c**). A better comparison was found in a diiron(IV) mono-μ-O featuring an open core with an $S = 1$ Fe^{IV} center, which was found to be 2.7 x 10^3 more reactive.[43] These findings strongly support the notion that intermediate Q likely accesses an open-core structure during the process of activating methane.[23] Similarly, spectroscopic studies of a diiron(II) functional model of Q capable of hydroxylating cyclohexane developed by Caradonna *et al.* demonstrated a proposed $Fe^{II}Fe^{IV}$=O intermediate likely responsible for the observed reactivity.[122] These observations have led to the speculation that intermediate Q may exist in an equilibrium

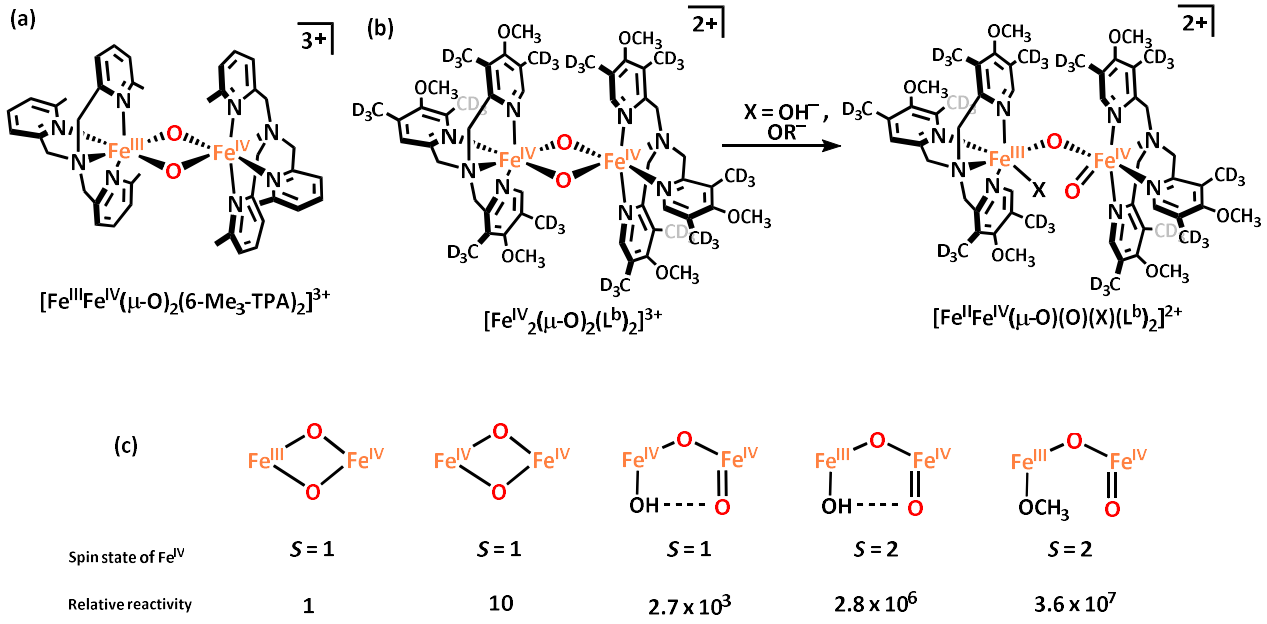

Figure 1.6. Diiron bis-μ-oxo model complexes using TPA ligand variants. (a) Using 6-Me_3-TPA, an intermediate X $Fe^{III}Fe^{IV}$ model can be achieved,[120] while (b) utilizing a more electron-deficient ligand resulted in access to the diiron(IV) species. This species could be made with methyl or deuterated methyl groups on the pyridine units; the latter was utilized when studying the reactivity of this unit. This complex was observed to be susceptible to nucleophilic attack to form an $Fe^{III}Fe^{IV}$ mono- μ-oxo complex featuring a Fe^{IV}=O moiety. (c) Directly comparing the reactivity of various high-valent iron oxo complexes with deuterated-L_b towards dihydroanthracene (–80 °C), the diiron(IV) open-core analog was observed to be three orders of magnitude more reactive than diiron(IV) diamond-core (after spin state compensation).[43,121]

[122] (a) Foster, T. L.; Caradonna, J. P. *J. Am. Chem. Soc.* **2003**, *125*, 3678–3679. (b) Rowe, G. T.; Rybak-Akimova, E. V.; Caradonna, J. P.; *Inorg. Chem.* **2007**, *46*, 10594–10606. (c) Rowe, G. T.; Rybak-Akimova, E. V.; Caradonna, J. P.; *Chem. Eur. J.* **2008**, *14*, 8303–8311.

between open- and closed-diamond core geometries in order to protect the enzyme before substrate oxidation.[43]

1.3.4 Cofacial Porphyrin Complexes

Another important class of model complexes features porphyrin ligands, similar to the ligands found in heme-based enzymes like cytochrome P450 and nitrite reductase. Bimetallic scaffolds featuring cofacial porphyrin have been studied since the 1970s for their photophysical properties,[123] catalytic abilities,[124] and host-guest applications.[125] Many strategies have been employed to tether the two macrocylic units together in a cofacial manner, including using two or more flexible linkers, such as urea,[126] ester,[127] or amide units;[128] by turning to a rigid unit, for instance anthracene or biphenylene bridges;[124,129] or even by utilizing calix[4]arene spacers or metal-metal bonds.[123] Following the initial investigations of "Pacman" complexes using rigid units by Collman[124] and Chang,[129] Nocera et al. probed the effect of cavity size imparted by the identity of the linker on the reactivity of the bimetallic unit towards oxygen-atom transfer. As such, dimethylxanthene- (DPX) and dibenzofuran- (DPD) anchored cofacial porphyrin complexes were developed. These backbones provided enhanced vertical flexibility; of note, the DPD backbone granted flexibility of >4 Å by tuning metal ligation and identity (compared with ~1 Å achieved

[123] Harvey, P. D.; Stern, C.; Gros, C. P.; Guilard, R. *Coord. Chem. Rev.* **2007**, *251*, 401–428.

[124] Collman, J. P.; Wagenknecht, P. S.; Hutchison, J. E. *Angew. Chem. Int. Ed. Engl.* **1994**, *33*, 1537–1554.

[125] (a) Tanaka, M.; Ohkubo, K.; Gros, C. P.; Guilard, R.; Fukuzumi, S. *J. Am. Chem. Soc.* **2006**, *128*, 14625–14633. (b) Nakamura, T.; Ube, H.; Shionoya, M. *Angew. Chem. Int. Ed.* **2013**, *52*, 12096–12100.

[126] Collman, J. P.; Elliott, C. M.; Halbert, T. R.; Tovrog, B. S. *Proc. Natl. Acad. Sci. USA* **1977**, *74*, 18–22.

[127] Ogoshi, H.; Sugimoto, H.; Yoshida, Z.-I. *Tetrahedron Lett.* **1977**, *2*, 169–172.

[128] Chang, C. K *J. Heterocycl. Chem.* **1977**, *14*, 1285–1288.

[129] Chang, C. K.; Liu, H, Y,; Abdalmundi, I. *J. Am. Chem. Soc.* **1984**, *106*, 2725–2726.

with anthracene or biphenyl bridges).[130] This phenomenon was termed as the "Pacman effect," in which the predisposed bite angle of the backbone in combination with the nature of ancillary ligands bound to the metal centers can drastically affect the metal–metal distance.[131]

The Pacman porphyrin complexes revealed competency for oxygenating a variety of substrates when utilizing the diiron μ-oxo photocatalysts (DPX)Fe^{III}_2O and (DPD)Fe^{III}_2O, including towards phosphites,[130] sulfides,[132] olefins, [133] and hydrocarbons,[134] the latter substrates being oxidized only by electron-deficient DPD constructs (i.e., DPDF = *meso*-tripentafluorophenyl porphyrin dibenzofuran). While both systems can oxygenate the more easily oxidized substrates (phosphites and sulfides), the DPD structure exhibited far superior efficiency (over 4 orders of magnitude more efficient) compared to the DPX congener for these transformations. Overall, the compared reactivity of these complexes demonstrated the utility of maximal vertical flexibility for oxidation of more challenging substrates. In the photocatalytic cycle, it is proposed that the diiron(III)–oxo bridge is cleaved to form a terminal iron(IV)=O along with an iron(II) center (**Scheme 1.4**).[135] The flexibility conferred by the DPD platform increased the likelihood of the photogenerated terminal oxo to access substrate rather than be out-competed by reformation of the inert diiron(III)–oxo bridge.[130, 133]

[130] Chang, C. J.; Baker, E. A.; Pistorio, B. J.; Deng, Y.; Loh, Z.-H.; Miller, S. E.; Carpenter, S. D.; Nocera, D. G. *Inorg. Chem.* **2002**, *41*, 3102–3109.

[131] Deng, Y.; Chang, C. J.; Nocera, D. G. *J, Am. Chem. Soc.* **2000**, *122*, 410–411.

[132] Pistorio, B. J.; Chang, C. J.; Nocera, D. G. *J. Am. Chem. Soc.* **2002**, *124*, 7884–7885.

[133] Rosenthal, J.; Pistorio, B. J.; Chng, L; Nocera, D. G. *J. Org. Chem.* **2005**, *70*, 1885–1886.

[134] Rosenthal, J.; Luckett, T. D.; Hodgkiss, J. M.; Nocera, D. G. *J. Am. Chem. Soc.* **2006**, *128*, 6456–6547.

[135] Hodgkiss, J. M.; Chang, C. J.; Pistorio, B. J.; Nocera, D. G. *Inorg. Chem.* **2002**, *42*, 8270–8277.

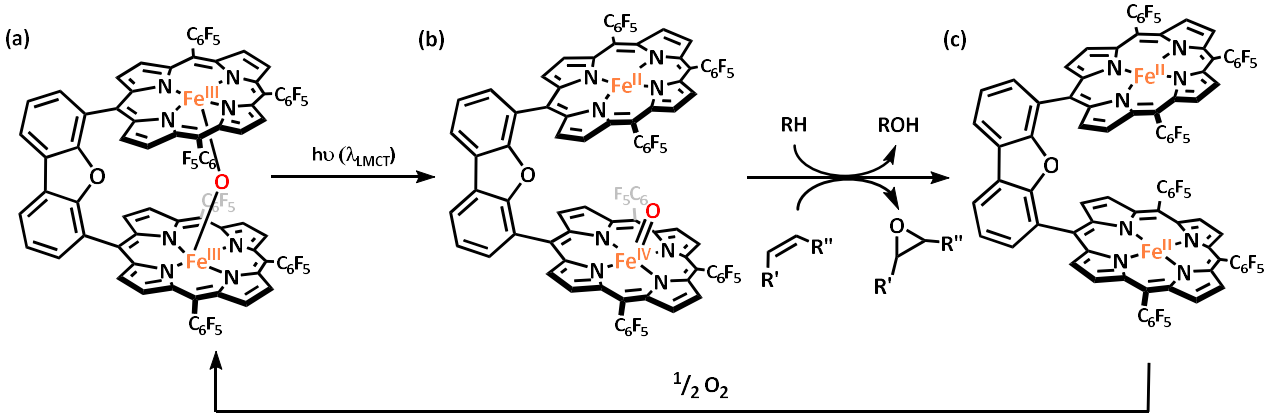

Scheme 1.4. Pacman porphyrin photocatalysts for oxidizing hydrocarbons[134] and olefins.[133] (a) (DPDF)Fe^{III}_2O starting material is thermally inert to the substrates but becomes activated upon irradiation, proposed to form (b) the PFe^{II}/PFe^{IV}=O (P = porphyrin) which serves as a potent oxidant to interact with substrate.[135] (c) (DPDF)Fe^{II}_2, the final iron-containing product, can be reconverting to the starting material with dioxygen, completing the catalytic cycle.

Dicobalt Pacman porphyrin complexes have also been studied as oxygen reduction catalysts, facilitating the selective $4e^-/4H^+$ reduction of dioxygen to water. Bimetallic redox cooperativity is utilized for administering the required electron equivalents for this transformation, and the dicobalt catalysts allow for selective catalysis by disfavoring the release of peroxo intermediates.[136,137] Dimethylxanthene- and dibenzofuran-linked dicobalt(II) cofacial bisporphyrin complexes, Co_2(DPX) and Co_2(DPD), are both selective dioxygen reduction electrocatalysts, reducing O_2 to H_2O with 72% and 80% selectivity over H_2O_2, respectively.[138,139] Furthermore, homogeneous catalysis could be achieved with these complexes using external reductants and proton sources. For instance, catalysis in the presence of ferrocene and $HClO_4$ resulted in similarly selective oxygen reduction as via electrocatalysis, and importantly the bimetallic complexes showed higher selectivity than a mononuclear porphyrin catalyst, cobalt(II) octaethylporphyrin (CoOEP).[137]

[136] Taube, H. in *Progress in Inorganic Chemistry, Vol. 34* (Ed.: S. J. Lippard), John Wiley & Sons. Inc **1986**.

[137] Rosenthal, J.; Nocera, D. G. *Acc. Chem. Res.* **2007**, *40*, 543–553.

[138] Chang, C. J.; Deng, Y.; Nocera, D. G.; Shi, C.; Anson, F. C.; Chang, C. K. *Chem. Commun.***2000,** 1355–1356.

[139] Chang, C. J.; Loh, Z.-H.; Shi, C.; Anson, F. C.; Nocera, D. G. *J. Am. Chem. Soc*. **2004**, *126*, 10013–10020.

Mechanistic studies indicate that the resting state for oxygen binding is a dicobalt-superoxide intermediate, which is protonated to eventually lead to oxygen–oxygen bond cleavage. Oxidation states up to cobalt(III) cobalt(IV) are proposed in the cycle.[137, 139]

1.4 Iron and Cobalt Dipyrrinato Complexes

Heme-based mononuclear active sites are also ubiquitous in nature, including several previously mentioned (including hemoglobin, myoglobin, nitrite reductase, and cytochrome P450). The ability of cytochrome P450 to hydroxylate strong C–H bonds of methane has garnered great attention. Extensive study of its mechanism has revealed that an iron(IV) oxo intermediate performs HAA on the substrate, forming a carbon-based radical that undergoes radical recombination to form the hydroxylated product. The observed reactivity is ascribed to the electronic structure of this intermediate, which features an open-shell $S = 1$ state, resulting in unpaired electron density along the $\pi^*_{Fe–O}$ vector that poises this enzyme for radical-type chemistry.[2, 140] Our group has designed an analogous system featuring weak field dipyrromethene ligands in place of the porphyrin unit exhibited in heme centers, allowing for lower coordinate metal species. To date, our group has demonstrated that first-row transition metals between Cr–Zn can be incorporated into this framework. In particular, late transition metals have demonstrated redox activity and catalytic competency for C–H functionalization via C–N bond formation.

To this end, amination and aziridination chemistry has been extensively studied with iron and cobalt dipyrrin catalysts. Intermolecular catalysis was observed using four-coordinate iron(II) dipyrrin complexes featuring ancillary chloride and solvent ligands. The dipyrrin motif was decorated with an aryl group at the 5-position and various organic moieties at the 1- and 9-positions. An early example featuring the ^{Ad}L variant (^{Ad}L = 5-mesityl-1,9-(adamantyl)-

[140] Groves, J. T.; McClusky, G. A. *J. Am. Chem. Soc.* **1976**, *98*, 859–861.

dipyrromethene) was metalated following lithiation with iron dichloride in diethyl ether to afford (^{Ad}L)FeCl(OEt_2). In the presence of adamantyl azide, this complex was able to aminate toluene to form benzyladamantylamine as the major product (95%) with 6.7 TON and to aziridinate styrene in 85% yield with 17 TON, both at room temperature.[141] Mechanistic studies involved a related complex, (^{Ar}L)FeCl (^{Ar}L = 5-mesityl-1,9-(2,4,6-$Ph_3C_6H_2$)-dipyrromethene), with which a key intermediate within the catalytic cycle was isolated. ^{57}Fe Mössbauer and computational studies revealed that this species was best described as a high-spin Fe^{III} center antiferromagnetically coupled to an iminyl radical,[141] a notion that was supported by follow up studies describing the enhanced reactivity of iron(III)-iminyl species over analogous iron(III)-imido complexes (**Figure 1.7a**).[142]

Furthermore, bridging imido species have also been shown to be competent for *N*-group transfer reactivity. In this case, a less sterically precluded dipyrrin ($^{t\text{Bu}}$L = 1,9-di-*tert*-butyl-5-(2,6-dichlorophenyl)-dipyrromethene) was utilized. Due to the decrease in steric hinderance, metalation of this ligand resulted in a dimeric iron bridging-chloride starting material, to which addition of 3,5-bis(trifluoromethyl)phenyl azide resulted in a diiron(III) bridging imido species (**Figure 1.7b**). The electronic structure of this dimer indicated an overall diamagnetic ground state, featuring two antiferromagnetically coupled high-spin ($S = {}^5/_2$) iron(III) centers ($J = -108.7$ cm^{-1}). Amination of toluene, cyclohexene, cyclooctene, and cyclooctadiene to the corresponding amines as well as aziridination of styrene could be achieved with 10 mol % of catalyst at room temperature.[143]

[141] King, E. R.; Hennessy, E. T.; Betley, T. A. *J. Am. Chem. Soc.* **2011**, *133*, 4917–4923.

[142] (a) Wilding, M. J. T.; Iovan, D. A.; Wrobel, A. T.; Lukens, J. T.; MacMillan, S. N.; Lancaster, K. M.; Betley, T. A. *J. Am. Chem. Soc.* **2017**, *139*, 14757–14766. (b) Wilding, M. J. T.; Iovan, D. A.; Betley, T. A. *J. Am. Chem. Soc.* **2017**, *139*, 12043–12049.

[143] Iovan, D. A.; Betley, T. A. *J. Am. Chem. Soc.* **2016**, *138*, 1983–1993.

Intramolecular amination catalysis can be achieved with an iron dipyrromethene complex featuring a modified ^{Ad}L (^{Ad}L′ = 1,9-di-adamantyl-5-(2,6-dichlorophenyl)-dipyrromethene) by incorporating the azide moiety into the substrate (**Figure 1.7c**). As such, primary, secondary, and tertiary C–H bonds four atoms away from the azide could be abstracted to form pyrrolidine products with 20 mol % of catalyst loading at 65 °C. Other N-heterocycles containing four- and six-membered rings could also be formed with this system. One necessary feature for turnover was addition of an *in situ* protecting reagent, di-*tert*-butyl decarbonate (Boc_2O), which eliminated substrate inhibition by reducing the nucleophilicity of the N-heterocyclic product.[144] More recently, our group has developed cobalt dipyrrin complexes for pyrrolidine catalysis that do not require the additional protecting group, using sterically bulky ligands such as ^{Ar}L and ^{Tr}L (^{Tr}L = 5-mesityl-1,9-(trityl)-dipyrromethene) (**Figure 1.7d**).[145] In these cases, a cobalt(I) synthon featuring an η^6-aryl interaction could be reacted directly with azide substrate to form various pyrrolidine products. In the case of (^{Ar}L)Co, room temperature catalysis could be achieved in the presence of pyridine while (^{Tr}L)Co was capable of room temperature catalysis without any additional substrates.

Oxygenation chemistry has also been explored with dipyrrin complexes in recent years. While formation of a mononuclear terminal iron oxo species has not yet been achieved, iron dipyrrin alkoxide complexes have been accessed. The addition of excess potassium *tert*-butoxide to (^{Ar}L)Fe^{II}Cl formed [K][(^{Ar}L)Fe^{II}(O^{t}Bu)$_2$] which could be oxidized with silver tetrafluoroborate ($AgBF_4$) to make (^{Ar}L)Fe^{III}(O^{t}Bu)$_2$. Reaction of (^{Ar}L)Fe^{II}Cl with *tert*-butyl peroxide (^{t}BuOO^{t}Bu)

[144] Hennessy, E. T.; Betley, T. A. *Science* **2013**, *340*, 591–595.

[145] (a) Baek, Y.; Betley, T. A. *J. Am. Chem. Soc.* **2019**, *141*, 7797–7806. (b) Baek, Y.; Hennessy, E. T.; Betley, T. A. *J. Am. Chem. Soc.* **2019**, *141*, 16944–16953.

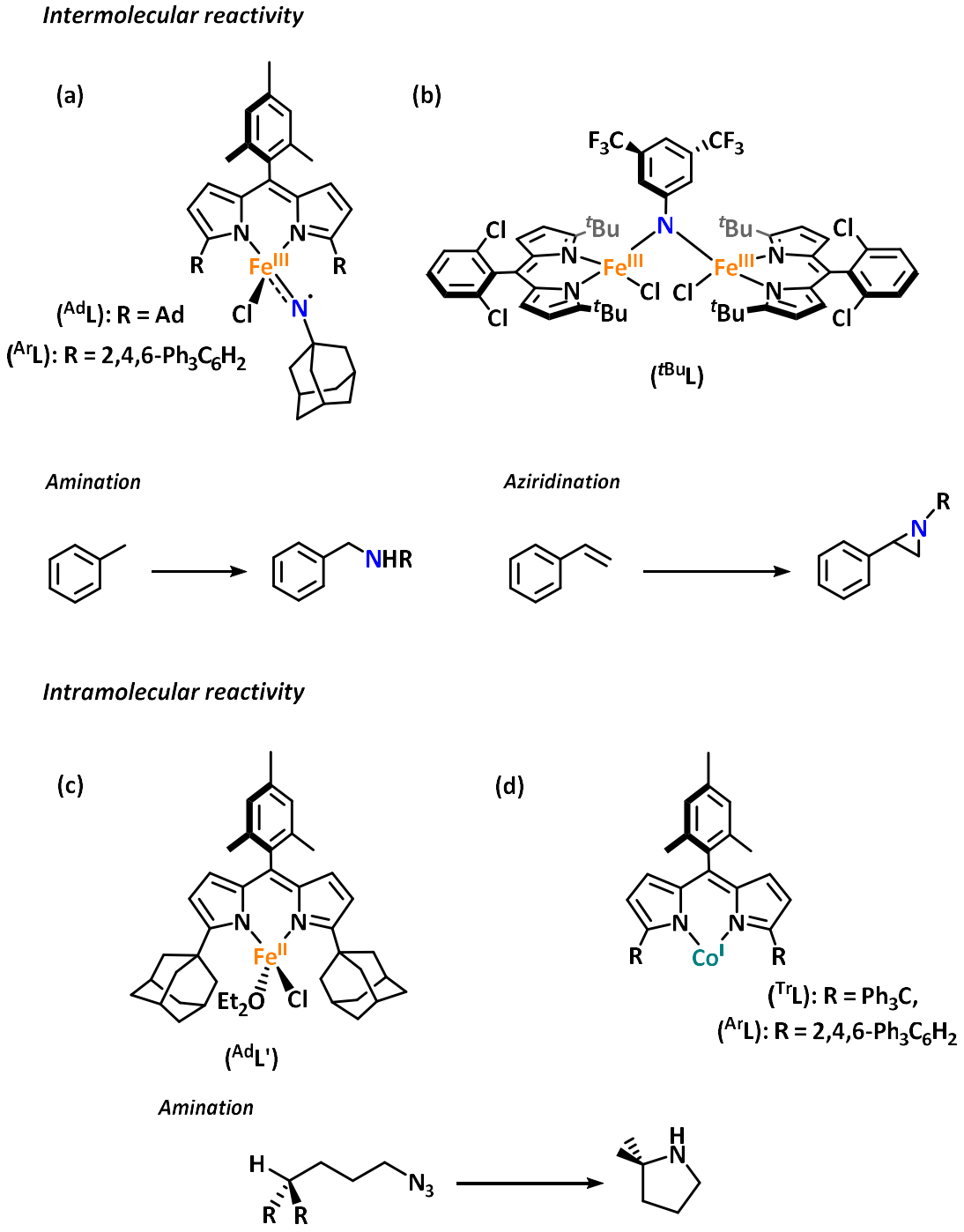

Figure 1.7. Iron and cobalt dipyrromethene catalysts developed in the Betley group. (a) Iron(III) iminyl complexes[141,142] and (b) diiron(III) bridging imido complexes[143] able to perform intermolecular amination and aziridination chemistry. (c) Iron(II)[144] and (d) cobalt(I) catalysts[145] that can facilitate intramolecular amination to form pyrrolidine products.

resulted in the mixed (^{Ar}L)Fe^{III}(O^tBu)(Cl) species.[146] Of these, the mixed alkoxide / chloride complex exhibited enhanced HAA reactivity than the bis(alkoxide) complex, which was attributed to enhanced spin density at the alkoxide unit. Modification of this system to allow for oxygen-atom transfer reactivity is underway.

1.5 Synthesis and Reactivity of Dipyrrin Iron and Cobalt Pacman Complexes

Inspired by the cooperativity exhibited by diiron enzymes, we aimed to derive a novel mimic that utilizes a bimetallic scaffold to promote metal–metal interaction and the isolation of reactive intermediates. Specifically, we proposed the use of dipyrrinato Pacman structures, wherein the dinucleating architecture can support two metals proximally oriented to maximize their ability to perform cooperative chemistry.

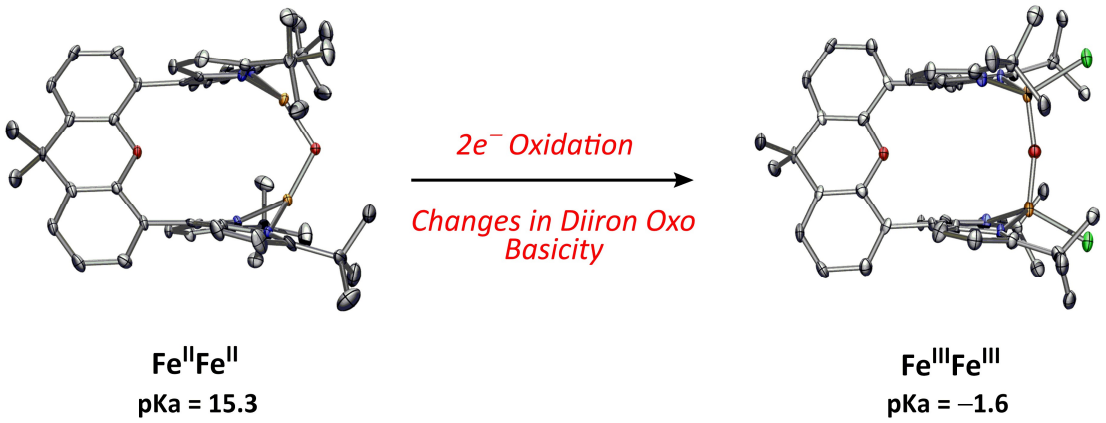

In **Chapter 2**, we demonstrate the accessibility of a series of diiron bridging hydroxo and oxo motifs in multiple oxidation states using the dipyrrin Pacman platform. Rare mixed-valent iron(II) iron(III) and diiron(II) μ-oxo complexes are possible with this ligand framework. Studying the reactivity and electronic structure of this series exemplified how metal oxidation states

[146] Kleinlein, C.; Zheng, S.-L.; Betley, T. A. *Inorg. Chem.* **2017**, *56*, 5892–5901.

influence the preference for the protonation state of the μ-(hydr)oxo bridge, consistent with findings observed in nature. Specifically, the basicity of the bridging oxo unit increases upon reduction, as evidenced by facile protonation of a diiron (II) μ-oxo complex in the presence of weak acids. Conversely, the acidity of the bridging hydroxide unit increases substantially upon oxidation, as attempts to isolate a diiron (III) μ-hydroxo species via oxidation of a diiron (II) μ-hydroxo complex resulted in loss of the hydroxide proton concomitant with oxidation. These acid/base properties were quantified through pK_a studies of their respective conjugate acids: the pK_a of the conjugate acid of the diiron (II) oxo is 15.3 while the pK_a of the conjugate acid of the diiron (III) oxo is -1.8. Both values are consistent with our experimental observations as well as the proposed mechanism of hemerythrin, which undergoes a similar pK_a change upon oxidation.

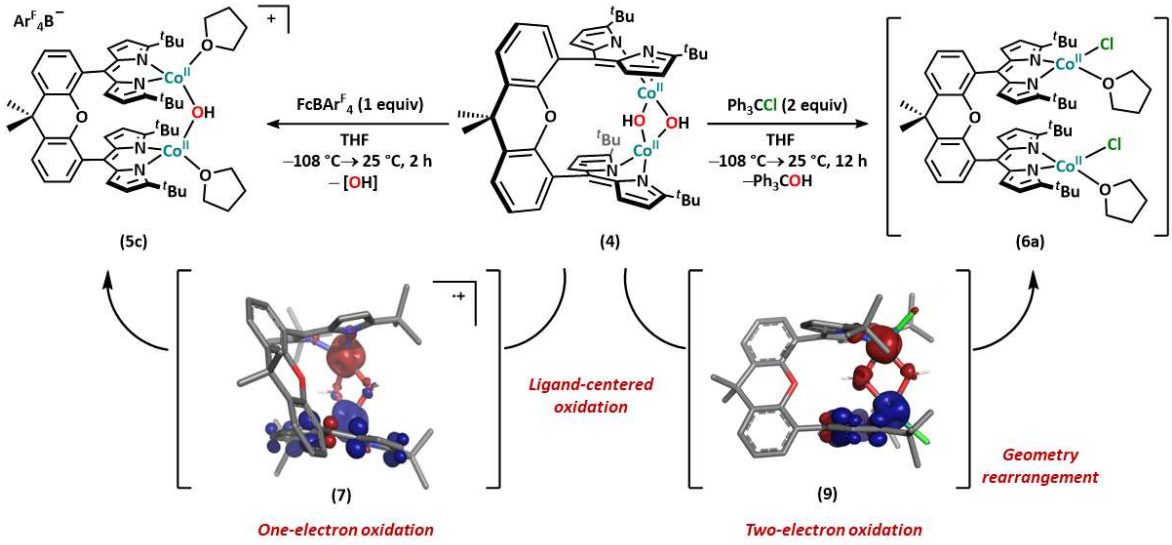

In **Chapter 3**, we extend the dipyrrin Pacman system to cobalt to explore the effects of metal identity on the reactivity of bridging hydroxide complexes. One key difference between the two platforms is the ability of the dicobalt system to support mono- and bis-hydroxide species. Furthermore, the dicobalt bis-hydroxide complex is shown to impart unique reactivity by featuring labile bridging units. This was demonstrated by interconversion to the mono-hydroxide complex

by protonation and by OH expulsion following oxidation. Rather than accessing higher valent cobalt centers, computational studies suggest that spin accumulation at the OH units may

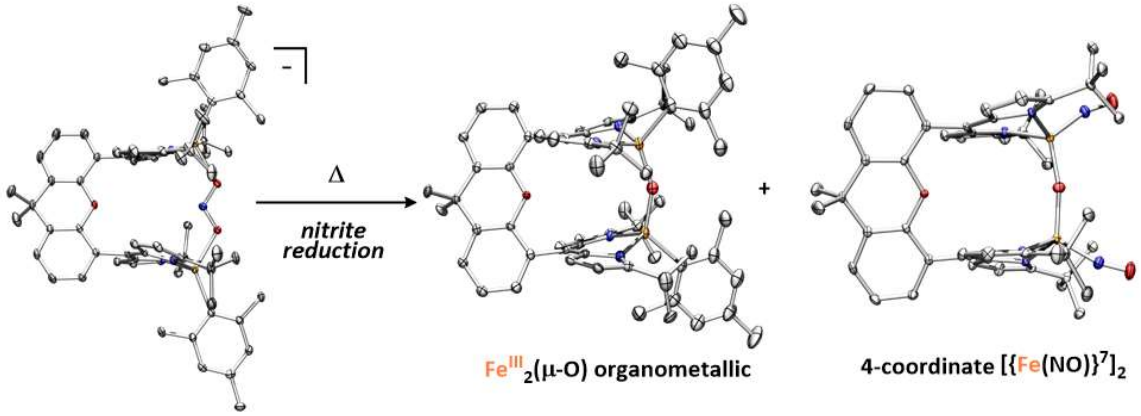

contribute to their lability. This reactivity provides a potential route to oxygen group transfer reactivity by allowing for hydroxylation of trityl radical in solution.

In **Chapter 4** we discuss how the bimetallic dipyrrin platform can be utilized to perform cooperative redox chemistry. One transformation of importance that we targeted is the reduction of oxyanions, many of which are prevalent water pollutants and whose reduction industrially is quite challenging. The two proximal iron centers in the Pacman dipyrrin model were found to be sufficient for providing the required electron equivalents for multiple reductive processes, including the reduction of nitrite to NO, deoxygenation of perhalogenate anions to halogenate species, and the overall six-electron reduction of aryl nitro compounds to the corresponding aniline species. We believe that the flexibility of the Pacman structure allows such small substrates to fit into the cavity and the proximate metal centers can work cooperatively to bear the redox load, thereby enabling reductive chemistry.

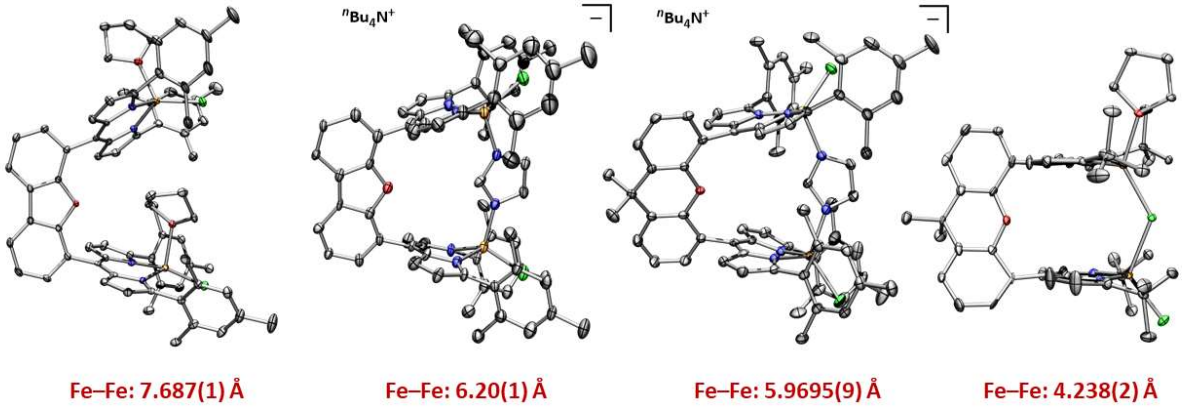

Chapter 5 covers the dipyrrin Pacman ligand design and synthesis, discussing the strategies used to tether two dipyrromethene motifs in a cofacial manner utilizing organic dibenzofuran and 9,9-dimethylxanthene backbones. Incorporation of iron into these frameworks and subsequent coordination chemistry studies are also discussed, highlighting the effect of the organic linker on the observed metal–metal distances and possible bridge sizes for different variants. Furthermore, attempts to make analogous bridging N– and S– containing moieties are discussed, which were targeted to probe the effects of bridgehead size and identity on the reactivity and electronic structure of various diiron complexes.

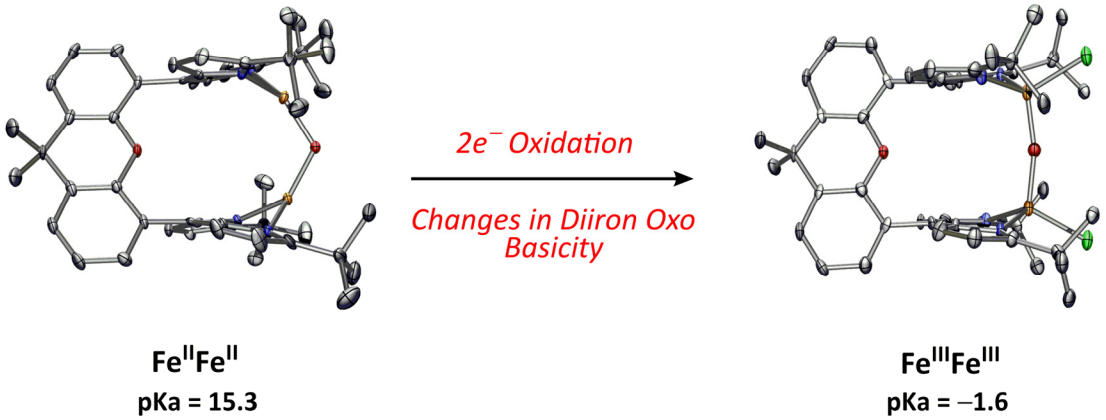

Chapter 2: Diiron Oxo Reactivity in a Weak-Field Environment[1]

2.1 Introduction

Diiron units featuring bridging oxygen ligands are important structural motifs in metalloenzymes.[2,3] For example, methane monooxygenase, ribonucleotide reductase, and hemerythrin feature diiron units which are responsible for oxygen activation or transport of dioxygen to a variety of substrates.[4] During these processes, a diiron unit which is bridged by one or two oxygen-based ligands passes through oxidation states ranging from $Fe^{II}Fe^{II}$ to $Fe^{IV}Fe^{IV}$. Synthetic model complexes featuring a μ-oxo or μ-hydroxo bridge have been

[1] This chapter was adapted from Johnson, E. J.; Kleinlein, C.; Musgrave, R.; Betley, T. A. *Chem. Sci.* **2019**, *10*, 6304–6310. © Royal Society of Chemistry, 2019.

[2] (a) L. Que, Jr., A. E. True, in *Progress in Inorganic Chemistry: Bioinorganic Chemistry, Vol. 38* (Ed.: S. J. Lippard), John Wiley & Sons. Inc **1990**. (b) Wallar, B. J.; Lipscomb, J. D. *Chem. Rev.* **1996**, *96*, 2625–2658. (c) Vincent, J. B..; Olivier-Lilley, G. L.; Averill, B. A. *Chem. Rev.* **1990**, *90*, 1447–1467.

[3] Solomon, E. I.; Brunold, T. C.; Davis, M. I.; Kemsley, J. N.; Lee, S.-K; Lehnert, N.; Neese, F.; Skulan, A. J.; Yang, Y.-S; Zhou, J. *Chem. Rev.* **2000**, *100*, 235–350.

[4] (a) Thomann, H.; Bernardo, M.; McCormick, J. M.; Pulver, S.; Andersson, K. K.; Lipscomb, J. D. Solomon, E. I. *J. Am. Chem. Soc.* **1993**, *115*, 8881–8882. (b) DeRose, V. J.; Liu, K. E.; Kurtz, D. M.; Hoffman, B. M.; Lippard, S. J. *J. Am. Chem. Soc.* **1993**, *115*, 6440–6441.

prepared in order to create functional mimics of these enzymes.[5,6] In particular, the interconversion between hydroxo- and oxo-bridged states has been of interest as it is proposed to play an important role during the catalytic cycle of metalloenzymes.[7,8] While there are many synthetic examples of diferric Fe–O–Fe units,[9] few mixed-valent Fe^{II}–O–Fe^{III} complexes[10] and Fe^{II}–O–Fe^{II} complexes have been reported.[11,12] In contrast, a variety of model complexes for both diferric and diferrous hydroxides have been synthesized.[6,13]

To better understand how the molecular oxidation state of a diiron core influences the acid-base properties of a bridging (hydr)oxo ligand, we explored the coordination and redox chemistry of a diiron unit in a cofacial dipyrrin Pacman unit. Herein, we report the synthesis and versatile reactivity of a family of diiron oxo and hydroxo complexes in three different molecular oxidation states. Reactions include acid-base chemistry as well as one and two

---

[5] (a) Friedle, S; Reisner, E.; Lippard, S. J. *Chem. Soc. Rev.* **2010**, *39*, 2768–2779. (b) Bossek, U.; Hummel, H.; Weyhermüller, T.; Bili, E.; Wieghardt, K. *Angew. Chem. Int. Ed.* **1996**, *34*, 2642–2645.

[6] Hartman, J. A. R.; Rardin, R. L.; Chaudhuri, P.; Pohl, K.; Wieghardt, K.; Nuber, B.; Weiss, J.; Papaefthymiou, G. C.; Frankel, R. B.; Lippard, S. J. *J. Am. Chem. Soc*. **1987**, *109*, 7387–7396.

[7] Jozwiuk, A.; Ingram, A. L.; Powell, D. R.; Moubaraki, B.; Chilton, N. F.; Murray, K. S.; Houser, R. P. *Dalton Trans.* **2014**, *43*, 9740–9753.

[8] Armstrong, W. H.; Lippard, S. J. *J. Am. Chem. Soc.* **1984**, *106*, 4632–4633.

[9] (a) Murray, K. S. *Coord. Chem. Rev.* **1974**, *12*, 1–35. (b) Kurtz, D. M. *Chem. Rev.* **1990**, *90*, 585–606. (c) Tshuva, E. Y.; Lippard, S. J. *Chem. Rev.* **2004**, *104*, 987–1012. (d) Shakya, R.; Powell, D. R.; Houser, R. P. *Eur. J. Inorg. Chem.* **2009**, *2009*, 5319–5327. (e) Armsttong, W. H.; Spool, G. C.; Papaefthymiou, G. C.; Frankel, R. B.; Lippard, S. J. *J. Am. Chem. Soc.* **1984**, *106*, 3653–3667. (f) Norman, R. E.; Yan, S.; Que, L., Jr. ; Backes, G.; Ling, J.; Sanders-Loehr, J.; Zhang, J. H.; O'Connor, C. J. *J. Am. Chem. Soc.* **1990**, *112*, 1554–1562. (g) Rosenthal, J.; Luckett, T. D.; Hodgkiss, J. M.; Nocera, D. G. *J. Am. Chem. Soc.* **2006**, *128*, 6546–6547.

[10] (a) Arena, F.; Floriana, C.; Chiesi-Villa, A.; Guastini, C. *J. Chem. Soc., Chem. Commun.,* **1986**, 1369–1371. (b) Payne, S. C.; Hagen, K. S. *J. Am. Chem. Soc.* **2000**, *122*, 6399–6410.

[11] Eckert, N. A.; Stoian, S.; Smith, J. M.; Bominaar, E. L.; Münck, E.; Holland, P. L. *J. Am. Chem. Soc.* **2005**, *127*, 9344–9345.

[12] Saouma, C. T.; Lu, C. C.; Day, M. W.; Peters, J. C. *Chem. Sci*. **2013**, *4*, 4042–4051.

[13] (a) Cohen, J. D.; Payne, S.; Hagen, K. S.; Sanders-Loehr, J. *J. Am. Chem. Soc.* **1997**, *119,* 2960–2961. (b) Ghosh, S. K.; Rath, S. P. *J. Am. Chem. Soc.* **2010**, *132*, 17983–17985.

electron redox chemistry, which demonstrate the intricate interplay between oxidation state, coordination environment, and reactivity.

2.2 Synthesis of a Diiron Starting Material

The dinucleating dipyrrin ligand platform was synthesized in analogy to previously reported xanthene-Pacman ligands. Reaction of 9,9-dimethylxanthene-dialdehyde with four equivalents of 2-*tert*-butylpyrrole in dry dichloromethane at 35 C affords the bis(dipyrromethene) in nearly quantitative yield. Subsequent oxidation with 2,3-dichloro-5,6-dicyanoquinone in dichloromethane at room temperature gives the corresponding bis(dipyrromethene) ($^{t\text{Bu}}$dmx)H$_2$ (($^{t\text{Bu}}$dmx)H$_2$ = 1,9-(*tert*-butyl)$_2$-5-dipyrromethene units bridged by 9,9-dimethyl-*9H*-xanthene) in 45% yield after purification.

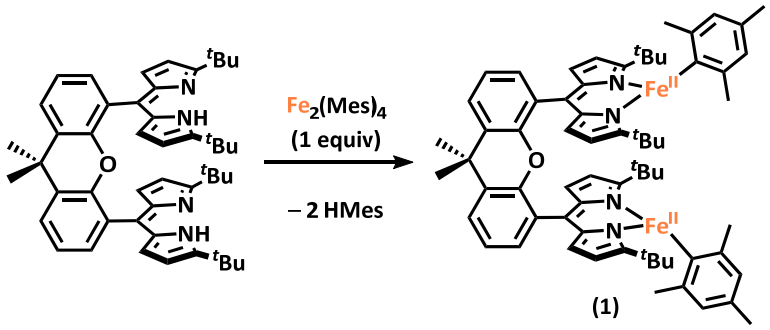

Scheme 2.1. Synthesis of ($^{t\text{Bu}}$dmx)Fe$_2$Mes$_2$ (**1**).

Formation of the diiron dipyrrin Pacman complex ($^{t\text{Bu}}$dmx)Fe$_2$(Mes)$_2$ (**1**) proceeds cleanly from the reaction of the cofacial dipyrrin Pacman ligand ($^{t\text{Bu}}$dmx)H$_2$ with Fe$_2$(Mes)$_4$ (Mes = 2,4,6-Me$_3$C$_6$H$_2$) in benzene at 65 °C for four hours (**Scheme 2.1**). The composition and purity of **1** was established by ^{1}H NMR spectroscopy, ^{57}Fe Mössbauer spectroscopy, and combustion analysis. X-ray diffraction studies on a single crystal of **1** obtained from a

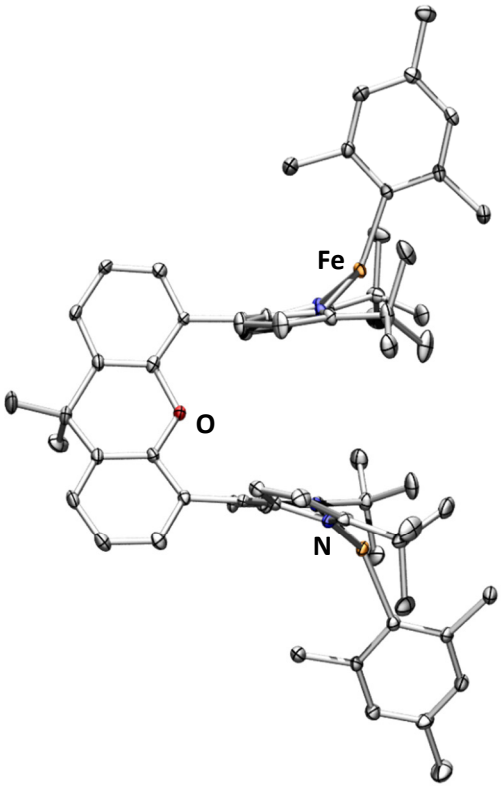

Figure 2.1. Solid state molecular structure of ($^{t\text{Bu}}$dmx)Fe$_2$(Mes)$_2$ (**1**) with thermal ellipsoids at 50% probability level. Hydrogen atoms omitted for clarity. Color scheme: Fe, orange; N, blue; C, gray; O, red.

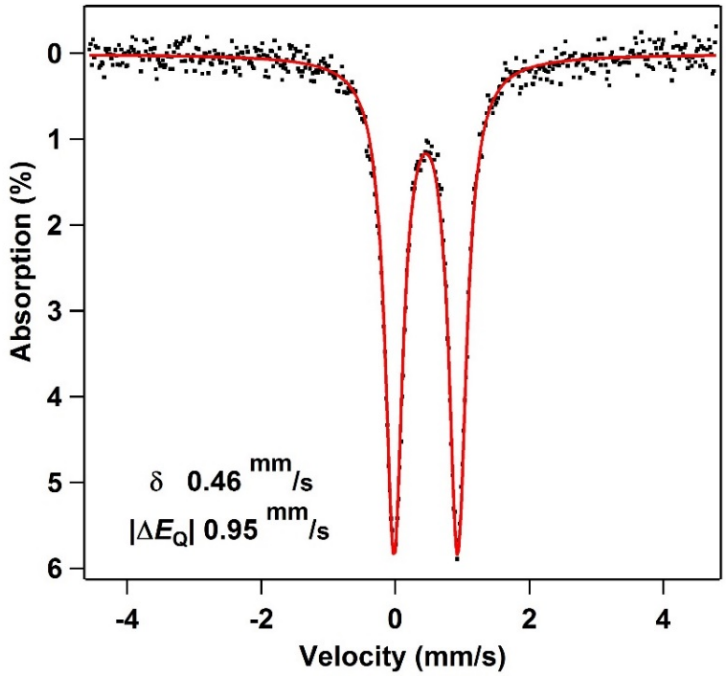

Figure 2.2. Zero-field ^{57}Fe Mössbauer spectrum of ($^{t\text{Bu}}$dmx)Fe$_2$(Mes)$_2$ (**1**). Isomer shift and quadrupole splitting are reported relative to Fe foil at room temperature.

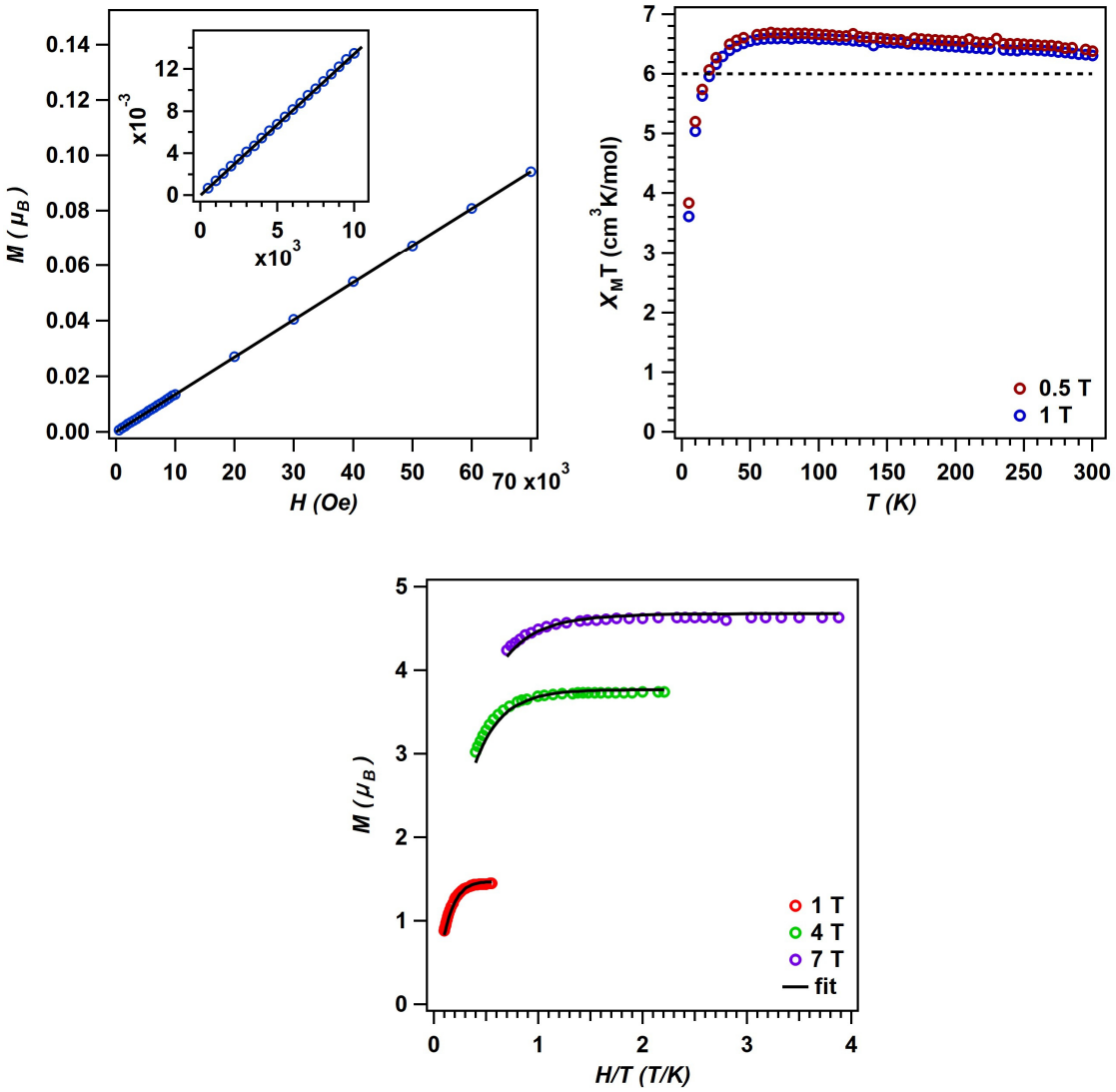

Figure 2.3. Magnetometry data for ($^{t\text{Bu}}$dmx)$Fe_2(Mes)_2$ (**1**). **(Top, left)** M vs. H at 100 K is linear, showing absence of ferromagnetic impurity even at low fields **(Top, left, inset)**. **(Top, right)**. Variable temperature magnetic susceptibility data ($\chi_M T$ vs. T) was recorded at 0.5 T and 1.0 T across the temperature range of 5 K – 300 K. At 0.5 T (red circles), $\chi_M T$ = 6.41 cm^3K/mol at 295 K and at 1.0 T, $\chi_M T$ = 6.32 cm^3K/mol at 295 K. These values exceed the spin-only value magnetic susceptibility value for two uncoupled $S = 2$ centers ($\chi_M T$ = 6.00 cm^3K/mol, dotted line) and are consistent with our hypothesis that the iron centers in this compound are non-interacting, given the large Fe–Fe distance in the solid state structure and lack of direct bridging unit. **(Bottom)** Reduced magnetization data (M vs. H/T) was collected at 3 fields (1, 4, and 7 T) over the temperature range of 1.8 K – 10 K. The data was best fit (black trace) as $S = 2$ centers with $g = 2.10$ using PHI[14] with to give the following parameters: $D = 16.8$ cm^{-1} and $|E/D| = 0.25$.

[14] Chilton, N. F.; Anderson, R. P.; Turner, L. D.; Soncini, A.; Murray, K. S. J. *Comput. Chem*. **2013**, *34*, 1164–1175.

toluene solution layered with hexanes at –35 °C revealed two non-interacting iron sites residing in a trigonal-planar geometry (**Figure 2.1**). ^{57}Fe Mössbauer analysis of **1** confirmed the presence of a single iron environment ($\delta = 0.46$ $^{mm}/_{s}$, $|\Delta E_Q| = 0.95$ $^{mm}/_{s}$) in line with other high-spin Fe^{II} complexes containing alkyl or aryl ligands (**Figure 2.2**).[15] Magnetometry data was consistent with the presence of two uncoupled $S = 2$ centers (**Figure 2.3**).

2.3 Isolation and Characterization of Diiron(II) μ-(Hydr)oxo Complexes

Diiron complex **1** is a versatile starting material for the preparation of μ-hydroxo and μ-oxo diiron complexes. Addition of one equivalent of water to **1** results in complete consumption of the starting material and formation of a new, asymmetric species, as evidenced by the presence of 18 paramagnetically shifted ^{1}H NMR resonances along with the formation of free mesitylene.[16] Cooling a concentrated diethyl ether solution of this product to –35 °C affords an orange crystalline material which was characterized by X-ray diffraction to unveil an asymmetric Pacman complex ($^{t\text{Bu}}$dmx)Fe_2(μ-OH)(Mes)(thf) (**2**) featuring a bridging hydroxide ligand (**Scheme 2.2**). One iron site remains bound to a mesitylene ligand with an Fe–O bond length of 2.045(4) Å while the second iron center is coordinated by a THF solvent molecule and exhibits a shorter Fe–O bond of 1.942(4) Å (**Figure 2.4**). The asymmetric nature of this complex is furthermore reflected by the ^{57}Fe Mössbauer spectrum which contains two quadrupole doublets ($\delta = 0.79$ $^{mm}/_{s}$, $|\Delta E_Q| = 3.22$ $^{mm}/_{s}$ and $\delta = 1.00$ $^{mm}/_{s}$, $|\Delta E_Q| = 2.95$ $^{mm}/_{s}$) (**Figure 2.5**). Solid-state FTIR spectra of **2** were collected to

[15] (a) Daifuku, S. L.; Kneebone, J. L.; Snyder, B. E. R. Neidig, M. L. *J. Am. Chem. Soc.* **2015**, *137*, 11432–11444. (b) Tondreau, A. M.; Milsmann, C.; Patrick, A. D.; Hoyt, H. M.; Lobkovsky, E.; Wieghardt, K. Chirik, P. J. *J. Am. Chem. Soc.* **2010**, *132*, 15046–15059. (c) Andres, H.; Bominaar, E. L.; Smith, J. M.; Eckert, N. A.; Holland, P. L. Münck, E. *J. Am. Chem. Soc.* **2002**, *124*, 3012–3025.

[16] Karlsson, R. *J. Chem. Eng. Data* **1973**, *18*, 290–292.

further confirm the identity of the bridging ligand as a μ-hydroxide (**Figure 2.6**). Spectra of **2** show an O–H stretching band at 3638 cm^{-1} that shifts to 2685 cm^{-1} when D_2O is used to prepare the deuterated bridging hydroxide complex ($^{t\mathrm{Bu}}$dmx)Fe_2(μ-OD)(Mes)(thf).

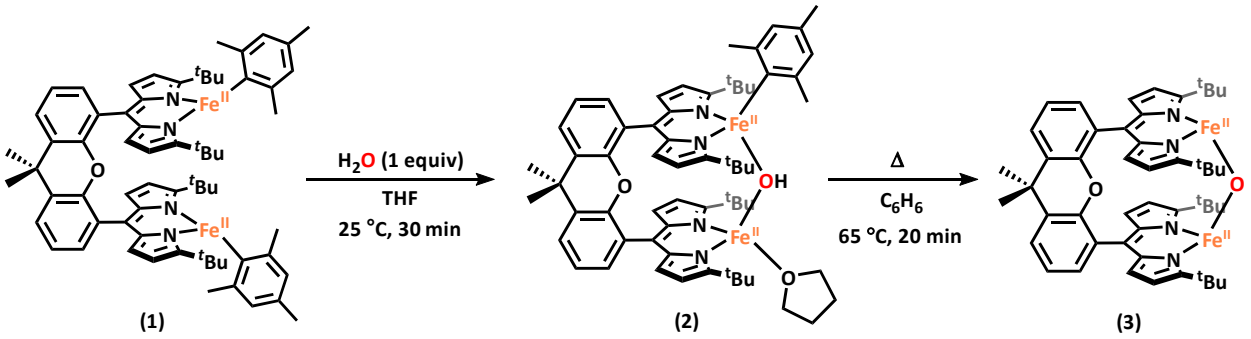

Scheme 2.2. Synthesis of ($^{t\mathrm{Bu}}$dmx)Fe_2(μ-OH)(Mes)(thf) (**2**) and ($^{t\mathrm{Bu}}$dmx)Fe_2(μ-O) (**3**).

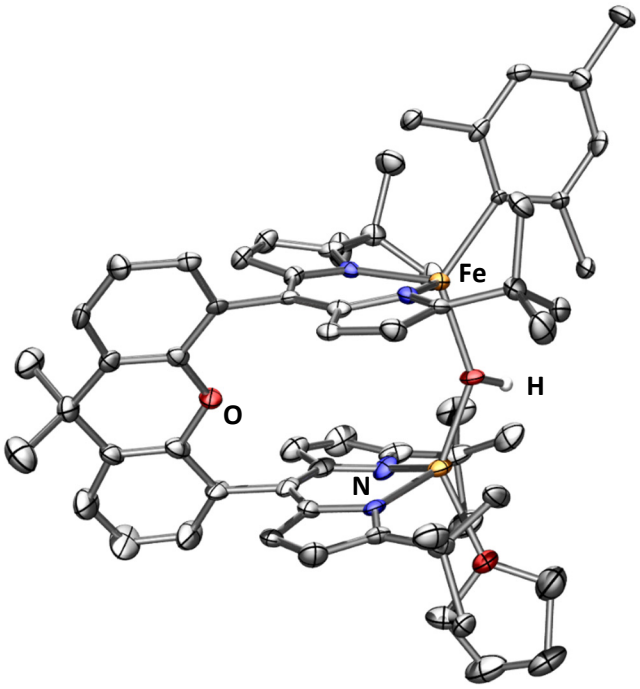

Figure 2.4. Solid state molecular structure of of ($^{t\mathrm{Bu}}$dmx)Fe_2(μ-OH)(Mes)(thf) (**2**) with thermal ellipsoids at 40% probability level. Hydrogen atoms (except the μ-hydroxo proton) omitted for clarity. Color scheme: Fe, orange; N, blue; C, gray; O, red; H, white.

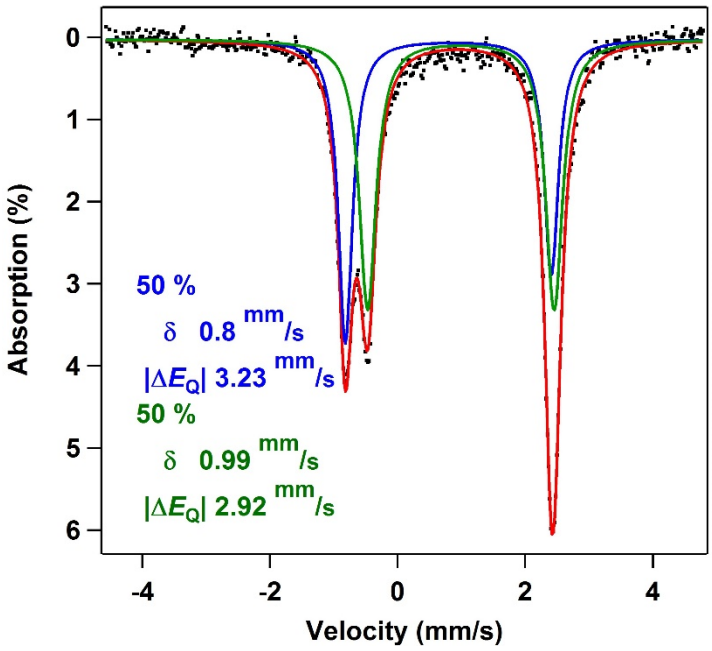

Figure 2.5. Zero-field ^{57}Fe Mössbauer spectrum of ($^{t\text{Bu}}$dmx)Fe$_2$(μ-OH)(Mes)(thf) (**2**). Isomer shift and quadrupole splitting are reported relative to Fe foil at room temperature.

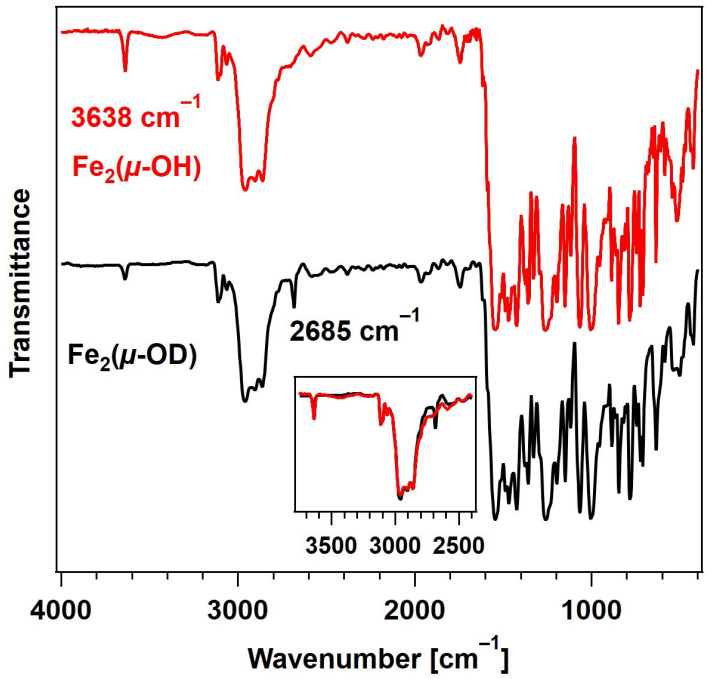

Figure 2.6. FTIR spectrum of (**Top, red**) ($^{t\text{Bu}}$dmx)Fe$_2$(μ-OH)(Mes)(thf) (**2**) and (**Bottom, black**) ($^{t\text{Bu}}$dmx)Fe$_2$(μ-OD)(Mes)(thf), with inset of overlaid spectra in region featuring OH and OD stretches.

While **2** is stable in ethereal solvents at room temperature, slow deprotonation of the bridging hydroxide ligand concomitant with release of the second mesitylene molecule is observed in non-coordinating solvents. Heating of **2** in benzene to 45 °C for 30 minutes leads to complete consumption of starting material and furnishes a new product (**3**) which is easily discernible by ^{1}H NMR spectroscopy as a C_2-symmetric species distinct from the starting material (**Scheme 2.2**). Zero-field ^{57}Fe Mössbauer analysis of **3** at 90 K (**Figure 2.7**) reveals the presence of a single iron environment with parameters ($\delta = 0.68$ $^{mm}/_{s}$, $|\Delta E_Q| = 0.87$ $^{mm}/_{s}$) similar to other three-coordinate Fe^{II} dipyrrin complexes previously synthesized.[17] The ^{57}Fe Mössbauer spectrum contains 5% of an additional species with parameters corresponding to a four-coordinate high-spin Fe^{II} compound which we assign as a small amount of an unknown bridging hydroxide species.

An X-ray diffraction study on single crystals grown from a concentrated diethyl ether solution revealed the major product **3** as a diiron complex bearing a bridging oxido ligand, ($^{t\text{Bu}}$dmx)Fe$_2$(μ-O) (**Figure 2.8**). A crystallographically imposed C_2 axis renders the two halves of the complex equivalent. The Fe–O (1.7941(17) Å) bond length is substantially shorter than the Fe–O distances in **2** (2.045(4) Å, 1.942(4) Å) and in other Fe^{II} hydroxides, and is in line with a previously reported diferrous μ-oxo species [L$^{t\text{Bu}}$Fe]$_2$O (L$^{t\text{Bu}}$ = ArNC(^{t}Bu)CHC(^{t}Bu)NAr$^-$, where Ar = 2,6-diisopropylphenyl)[11]. The Fe–O–Fe angle in **3** (116.00(14)°) deviates significantly from linearity, which is in stark contrast to the Fe–O–Fe angle of 167.55(14)° reported by Holland *et al.* for [L$^{t\text{Bu}}$Fe^{II}]$_2$O. The difference in angles for these two three-coordinate diiron (II) complexes may be due to the restraints on the coordination chemistry superimposed by the dinucleating ligand platform

[17] King, E. R.; Hennessy, E. T.; Betley, T. A. *J. Am. Chem. Soc.* **2011**, *133*, 4917–4923.

in **3**. Magnetometry studies indicated two weakly coupled high-spin iron(II) centers with $J = -53.2$ cm^{-1} present in **3** (**Figure 2.9**), consistent with values obtained by computation (**Table 2.2**).

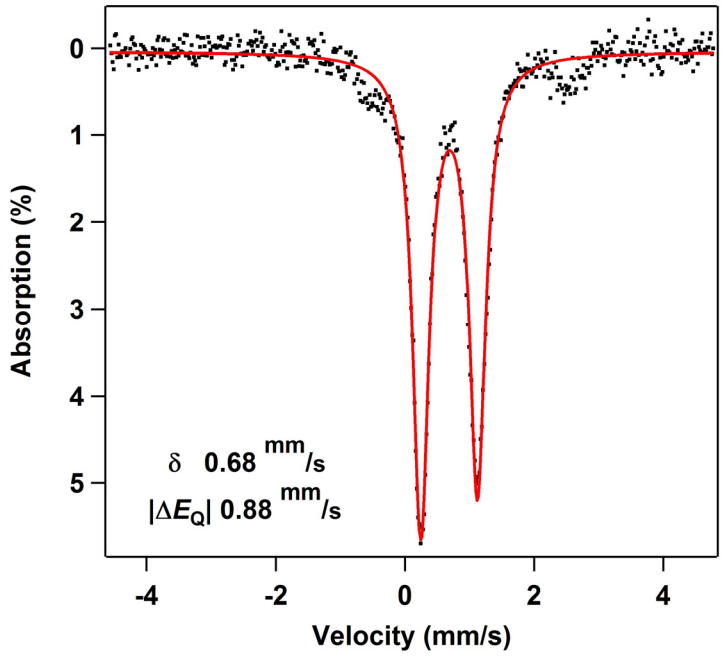

Figure 2.7. Zero-field ^{57}Fe Mössbauer spectrum of ($^{t\text{Bu}}$dmx)Fe$_2$(μ-O) (**3**). Isomer shift and quadrupole splitting are reported relative to Fe foil at room temperature.

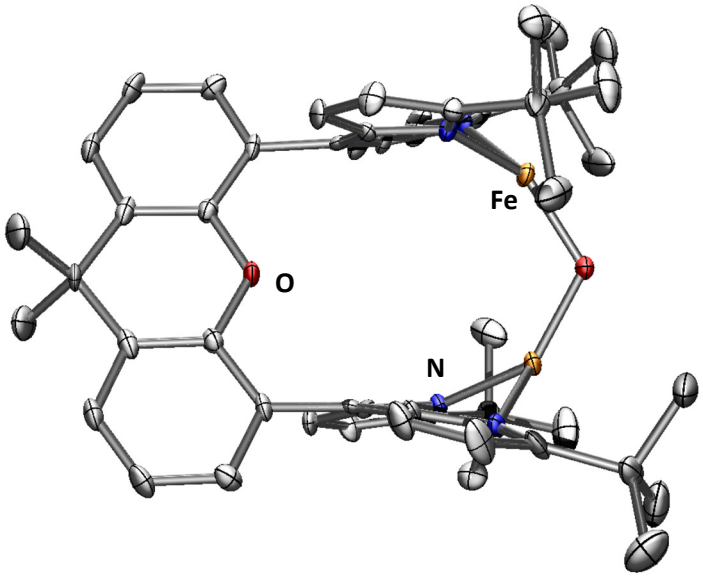

Figure 2.8. Solid state molecular structure of ($^{t\text{Bu}}$dmx)Fe$_2$(μ-O) (**3**) with thermal ellipsoids at 50% probability level. Hydrogen atoms omitted for clarity. Color scheme: Fe, orange; N, blue; C, gray; O, red.

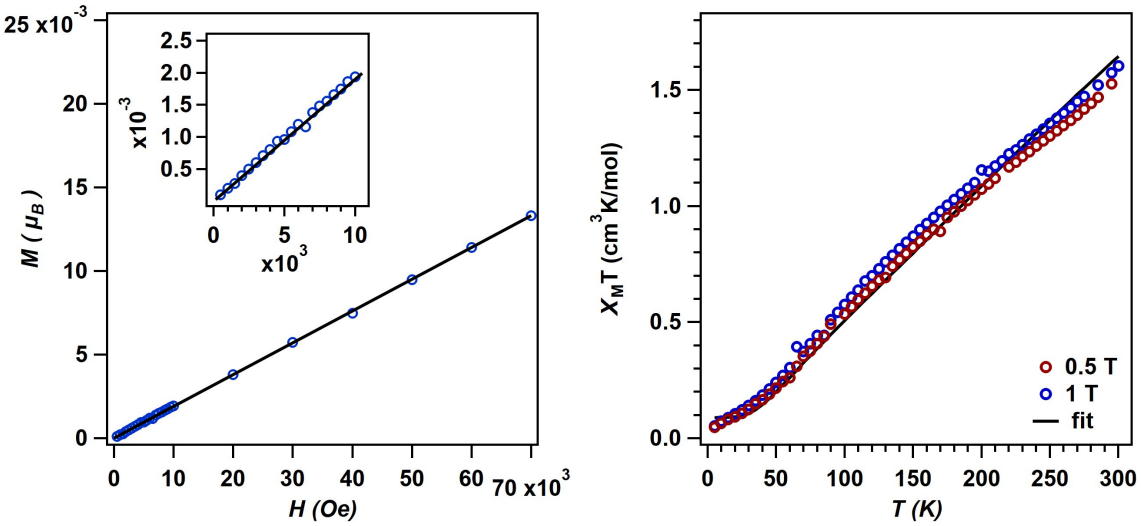

Figure 2.9. Magnetometry data for ($^{t\text{Bu}}$dmx)Fe$_2$(μ-O) (**3**). **(Left)** M vs. H at 100 K is linear, showing absence of ferromagnetic impurity even at low fields **(Left, inset)**. **(Right)** χ_MT vs. T at 0.5 T with χ_MT = 1.53 cm^{3}K/mol and 1.0 T with χ_MT = 1.57 cm^{3}K/mol at 295 K. χ_MT vs. T was best fit as two weakly coupled $S = 2$ centers using PHI[23] (black trace), including 3% of an $S = 2$ impurity, with the following parameters: $g = 1.90$, $J = -53.2$ cm^{-1}, $D = 0.64$ cm^{-1}, and $|E/D| = 0.016$.

2.4 Reactivity and Basicity of the Diiron(II) μ-Oxo

With **3** in hand, we began examining its reactivity profile. Treatment of **3** with one equivalent of a weak acid such as lutidinium tetraphenylborate results in quantitative formation of a diiron μ-hydroxide cation [($^{t\text{Bu}}$dmx)Fe$_2$(μ-OH)(thf)$_2$][BPh$_4$] (**4**) (**Scheme 2.3**). Given the observed reactivity of **3** with acids, we sought to quantify the basicity of **3** by establishing the pK_a value of its conjugate acid. Following the precedent set by Smith *et al.*, we attempted to use a combined approach of experiment and calculation to justify the reactivity of **3** with various weak acids.[18] Due to the limited solubility of **3** and many of the suitable acids in non-coordinating solvents, we selected THF as the solvent for this study. Experimentally probing the protonation of **3** proved to be challenging, as the anticipated conjugate acid product, [($^{t\text{Bu}}$dmx)Fe$_2$(μ-OH)]$^+$ (**4a**), is not stable

[18] Naito, I.; Ding, F.; Bontchev, R. P.; Wang, H.; Smith, J. M. *J. Am. Chem. Soc.* **2008**, *130,* 2716–2717.

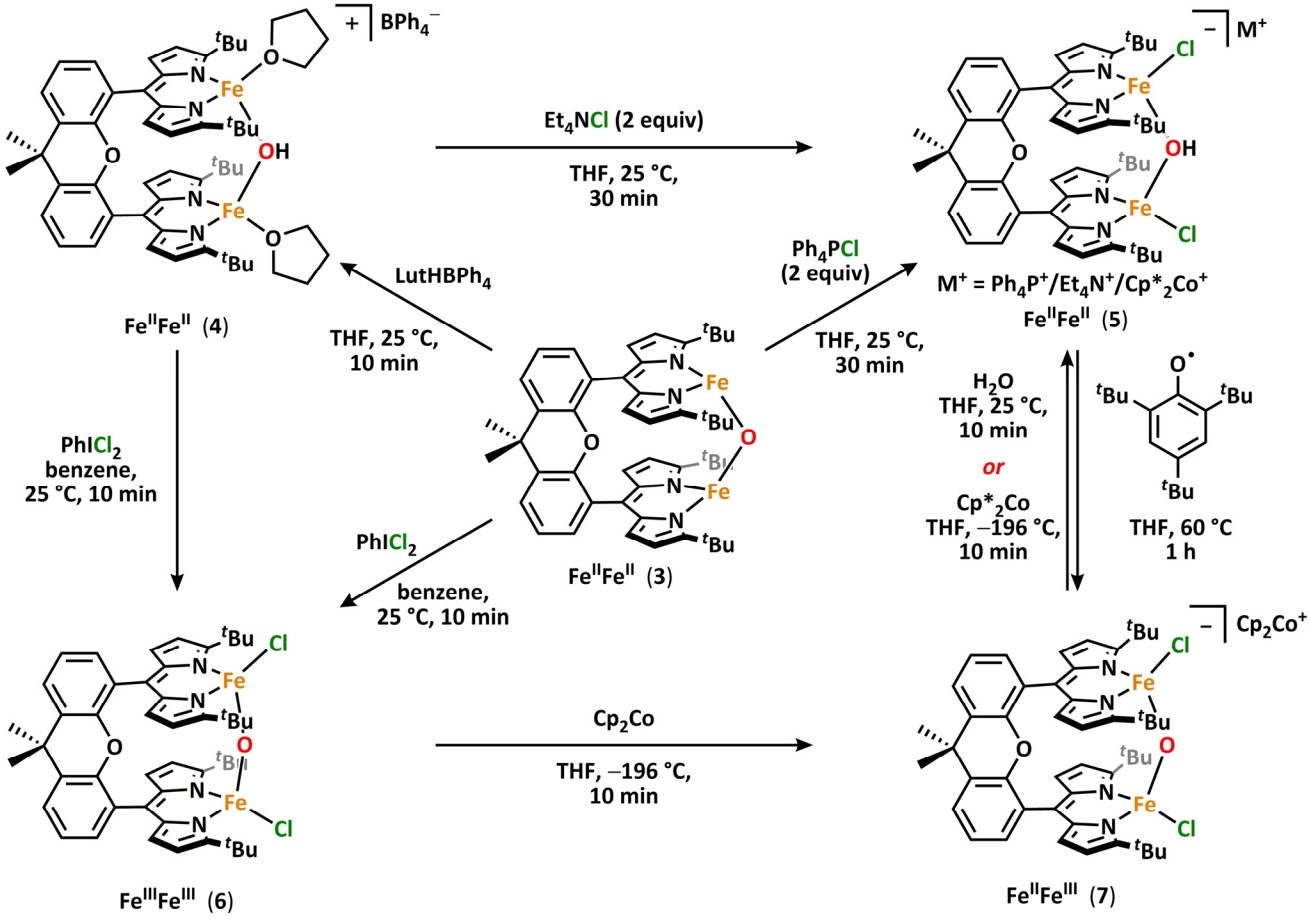

Scheme 2.3. Interconversion between diiron hydroxide and oxide species.

to reaction conditions as it may react with the generated conjugate base, in many cases leading to multiple species observed by ^{1}H NMR spectroscopy. Consequently, efforts focused on replicating the theoretical procedure used by Smith *et al*. to computationally determine the pK_a value of **4a**. Using density functional theory, the acid-base reaction shown in **Scheme 2.4** was considered, in which HA is a weak acid with reported pK_a value in THF.[19]

Since these reactions were performed in THF, we examined the stability of **3** under these reaction conditions and discovered that solvents can bind the open coordination site

[19] Ding, F.; Smith, J. M.; Wang, H. *J. Org. Chem.* **2009**, *74,* 2679–2691.

at each metal center to begin to form ($^{t\text{Bu}}$dmx)Fe$_2$(μ-O)(thf)$_2$ (**3a**) within minutes, as evidenced by ^{57}Fe Mössbauer spectroscopy (**Figure 2.10**). Thus, we modelled the acid-base reaction for both **3** and for **3a** (**Scheme 2.4**), the latter being the suspected active metal species during these reactions. The pK_a value calculated for **4a** (which is three-coordinate at iron) was 15.3(6) and upon coordination of two solvent molecules to form [($^{t\text{Bu}}$dmx)Fe$_2$(μ-OH)(thf)$_2$]$^+$ (**4**) increased to 26.8(6). We hypothesize that the coordination of a fourth ligand to each iron center results in the bridging oxo moiety adopting greater O^{2-} character, thus rendering the oxo ligand more basic. Computationally, we observe that the Fe–O covalency in **3a** decreases upon addition of the solvent ligands to **3**, reflected in a diminished Mayer bond order[20] (**3**, 0.811; **3a**, 0.798; **Table 2.1**) which results in the enhanced oxide character and basicity in **3a**. Several examples of metal oxo and nitrido complexes featuring enhanced reactivity upon coordination of additional neutral ligands[21] or increased basicity due to coordination of anionic ligands[22] have been studied. However, to our knowledge, no synthetic examples have been reported in which the change in basicity of a metal oxo species has been quantified upon coordination of neutral donors. In this case, we remarkably observe an increase in the basicity of a diiron bridging oxo complex by ten orders of magnitude upon coordination of the neutral donor THF.

---

[20] (a) Mayer, I. *Chem. Phys. Lett.* **1983,** *97*, 270–274. (b) Mayer, I. *Int. J. Quantum Chem.* **1984**, *26*, 151–154.

[21] (a) Man, W.-L.; Lam, W. W. Y.; Yiu, S.-M.; Lau, T.-C.; Peng, S.-M. *J. Am. Chem. Soc.* **2004**,*126*, 15336–15337. (b) Venkataramanan, N. S.; Rajagopal, S. *Tetrahedron.* **2006**, *62*, 5645–5651. (c) Cowley, R. E.; Eckert, N. A.; Vaddadi, S.; Figg, T. M.; Cundari, T. R.; Holland, P. L. *J. Am. Chem. Soc.* **2011**, *133*, 9796–9811.

[22] (a) Green, M. T.; Dawson, J. H.; Gray, H. B. *Science* **2004**, *304*, 1653–1656. (b) Sastri, C. V.; Lee, J.; Oh, K.; Lee, Y. J.; Lee, J.; Jackson, T. A.; Ray, K.; Hirao, H.; Shin, W.; Halfen, J. A.; Kim, J.; Que, L., Jr.; Shaik, S.; Nam, W. *Proc. Natl. Acad. Sci. U. S. A.* **2007**, *104*, 19181–19186. (c) Prokop, K. A.; de Visser, S. P;, Goldberg, D. P. *Angew. Chem., Int. Ed.* **2010**, 49, 5091–5095. (d) Stone, K. L.; Hoffart, L. M.; Behan, R. K.; Krebs, C.; Green, M. T. *J. Am. Chem. Soc.* **2006**, *128*, 6147–6153.

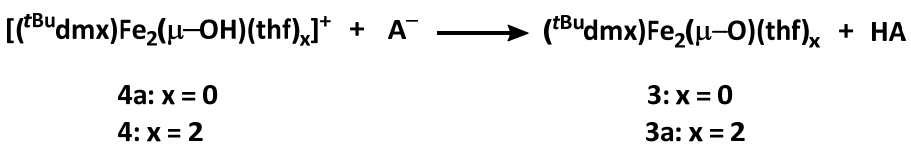

Scheme 2.4. General acid-base reaction studied to determine pK_a values of bridging hydroxides **4** and **4a**.

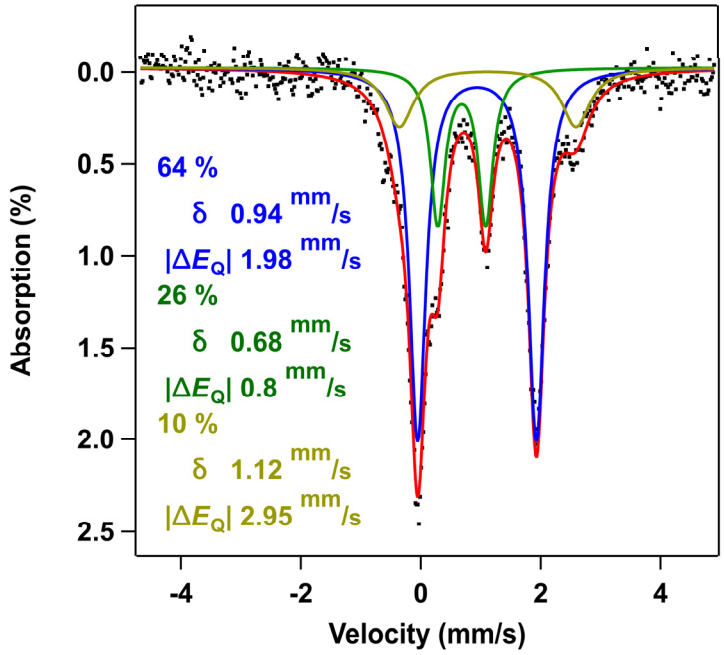

Figure 2.10. Zero-field ^{57}Fe Mössbauer spectrum of ($^{t\text{Bu}}$dmx)Fe$_2$(μ-O)(thf)$_2$ (**3a**) (blue trace) after exposing ($^{t\text{Bu}}$dmx)Fe$_2$(μ-O) (**3**) (green trace) to THF for 30 minutes. The small amount of a third species present (yellow trace) has been assigned as an impurity formed upon reaction of **3** with race water. Isomer shift and quadrupole splitting are reported relative to Fe foil at room temperature.

Table 2.1. Assessment of Fe–O covalency in **3**, **3a**, and **6**.

Complex	Fe–O distances (Å)	Mayer bond orders (Fe–O)	Orbital overlaps of UCOs
3a	1.858, 1.859[a]	0.798, 0.797	0.141–0.170
3	1.7941(17)	0.811, 0.81	0.149–0.165
6	1.7734(10)	0.947. 0.947	0.226–0.265

To further demonstrate the basicity of these diiron (II) μ-oxo complexes, we examined the reactivity of **3** upon coordination of anionic ligands. Stirring **3** in the presence of excess chloride sources such as tetraphenylphosphonium chloride in THF affords $[Ph_4P][(^{tBu}dmx)Fe_2(\mu\text{-}OH)Cl_2]$ (**5a**) in high yield (**Scheme 2.3**). The origin of the hydroxide proton in this product is unknown and protonation could not be prevented even in silylated glassware and freshly dried solvent We propose that upon coordination of chloride ligands and formation of an anticipated dianionic iron complex, the basicity of the bridging oxo increases further, resulting in instantaneous protonation. Attempts to determine the pK_a value of $(^{tBu}dmx)Fe_2(\mu\text{-}OH)Cl_2^-$ (the conjugate acid of the anticipated dianionic complex $(^{tBu}dmx)Fe_2(\mu\text{-}O)Cl_2^{2-}$) were not successful; however, based on the observed reactivity we hypothesize that this species would be more basic than **3a** and thus feature a $pK_a > 26.8$. The assignments of **4** and **5** as diiron μ-hydroxides were confirmed by X-ray diffraction studies (**Figure 2.11, Figure 2.15**), ^{57}Fe Mössbauer spectroscopy (**Figure 2.12, Figure 2.16**), and FTIR spectroscopy (**Figure 2.13, Figure 2.17**) One notable observation was that the O–H (ν = 3548 cm^{-1}) and O–D (ν = 2587 cm^{-1}) frequencies for **4** and its deuterated analogue, $[(^{tBu}dmx)Fe_2(\mu\text{-}OD)(thf)_2][BPh_4]$ in the FTIR spectrum, are lower than are often observed for such stretches,[17] which we hypothesize is due to a hydrogen-bonding interaction between the bridging hydroxide and a THF solvent molecule ($OH\text{–}O_{THF}$ 1.899(3) Å), as observed in the solid-state. Magnetometry studies indicate that **4** features antiferromagnetic coupling of two $S = 2$ iron centers with an exchange coupling $J = -13.3$ cm^{-1}, which is in line with the expected values for diiron bridging hydroxide complexes (**Figure 2.14**).[7]

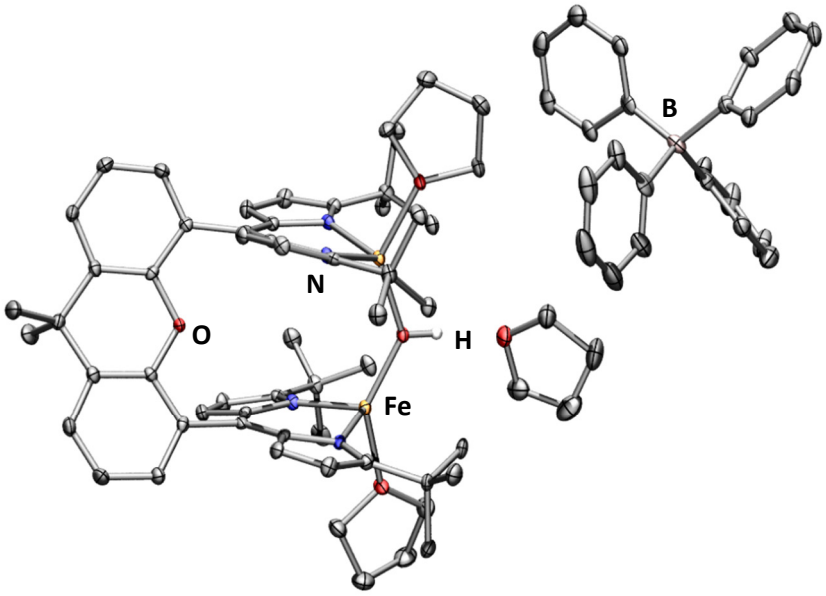

Figure 2.11. Solid state molecular structure of [($^{t\text{Bu}}$dmx)Fe$_2$(μ-OH)(thf)$_2$][BPh$_4$] (**4**) with thermal ellipsoids at 50% probability level. Hydrogen atoms (except the μ-hydroxo proton) omitted for clarity. Color scheme: Fe, orange; N, blue; C, gray; O, red; H, white.

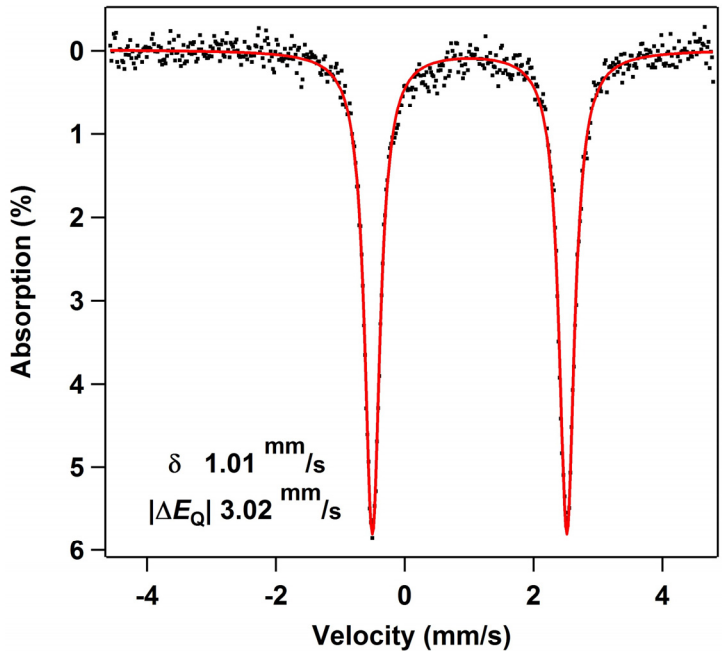

Figure 2.12. Zero-field ^{57}Fe Mössbauer spectrum of [($^{t\text{Bu}}$dmx)Fe$_2$(μ-OH)(thf)$_2$][BPh$_4$] (**4**). Isomer shift and quadrupole splitting are reported relative to Fe foil at room temperature.

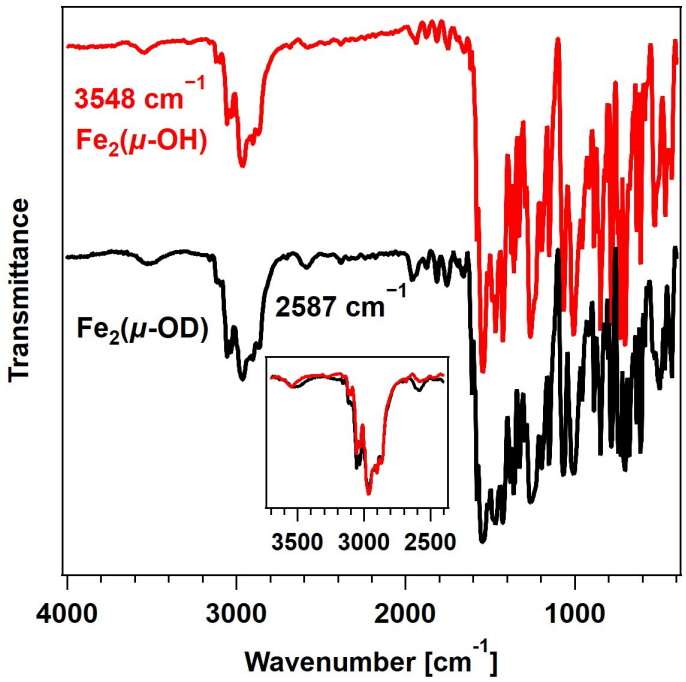

Figure 2.13. FTIR spectrum of (**Top, red**) [($^{t\text{Bu}}$dmx)Fe$_2$(μ-OH)(thf)$_2$][BPh$_4$] (**4**) and (**Bottom, black**) [($^{t\text{Bu}}$dmx)Fe$_2$(μ-OD)(thf)$_2$][BPh$_4$], with inset of overlaid spectra in region featuring OH and OD stretches.

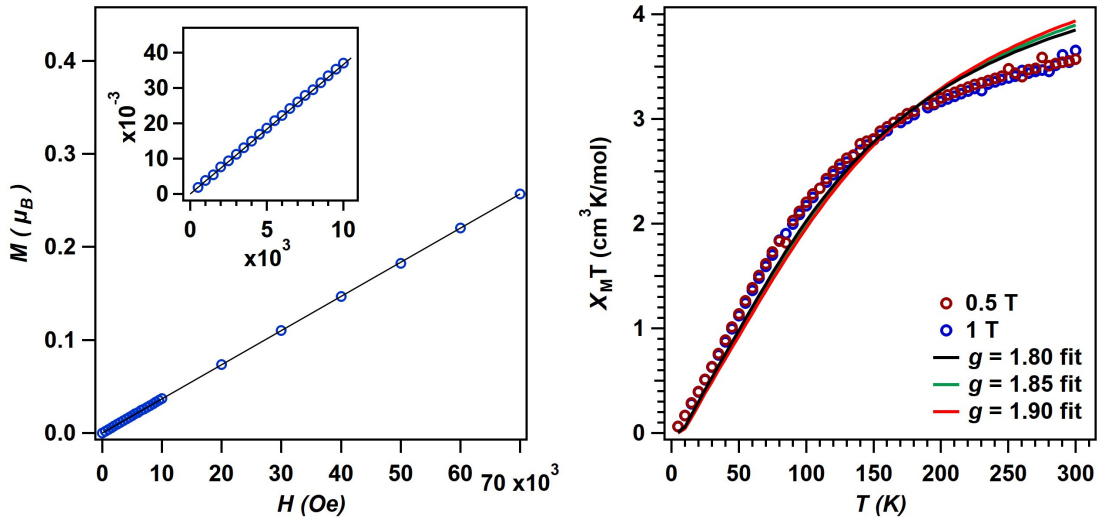

Figure 2.14. Magnetometry data for [($^{t\text{Bu}}$dmx)Fe$_2$(μ-OH)(thf)$_2$][BPh$_4$] (**4**). **(Left)** M vs. H at 100 K is linear, showing absence of ferromagnetic impurity even at low fields **(Left, inset)**. **(Right)** Variable temperature magnetic susceptibility data (χ_MT vs. T) was recorded at 0.5 T and 1.0 T across the temperature range of 5 K – 300 K. At 0.5 T (red circles), χ_MT = 3.56 cm^{3}K/mol at 295 K and at 1.0 T, χ_MT = 3.48 cm^{3}K/mol at 295 K. χ_MT vs. T was best fit as two weakly coupled $S = 2$ centers using PHI[23] (black trace) with the following parameters: $g = 1.80$, $J = -13.3$ cm^{-1}, D = 0.47 cm^{-1}, and $|E/D| = 0.23$. Due to the low g-tensor value in this fit, additional fits with $g = 1.85$ and $g = 1.90$ were attempted to confirm the presence of weak antiferromagnetic coupling by exemplifying minimally affected J coupling values: green trace, χ_MT vs. T fit parameters: $g = 1.85$, $J = -13.9$ cm^{-1}, D = 0.56 cm^{-1}, and $|E/D| = 0.11$; red trace, χ_MT vs. T fit parameters: $g = 1.90$, $J = -14.5$ cm^{-1}, D = 0.45 cm^{-1}, and $|E/D| = 0.16$.

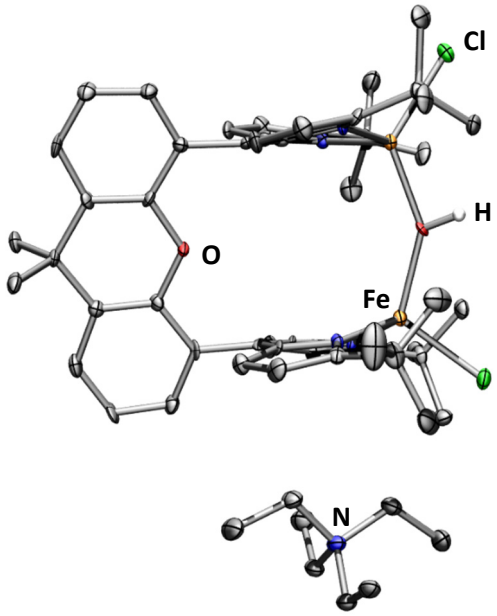

Figure 2.15. Solid state molecular structure of $[Et_4N][(^{tBu}dmx)Fe_2(\mu\text{-}OH)Cl_2]$ (**5b**) with thermal ellipsoids at 50% probability level. Hydrogen atoms (except the μ-hydroxo proton) omitted for clarity. Color scheme: Fe, orange; N, blue; C, gray; O, red; Cl, green; H, white.

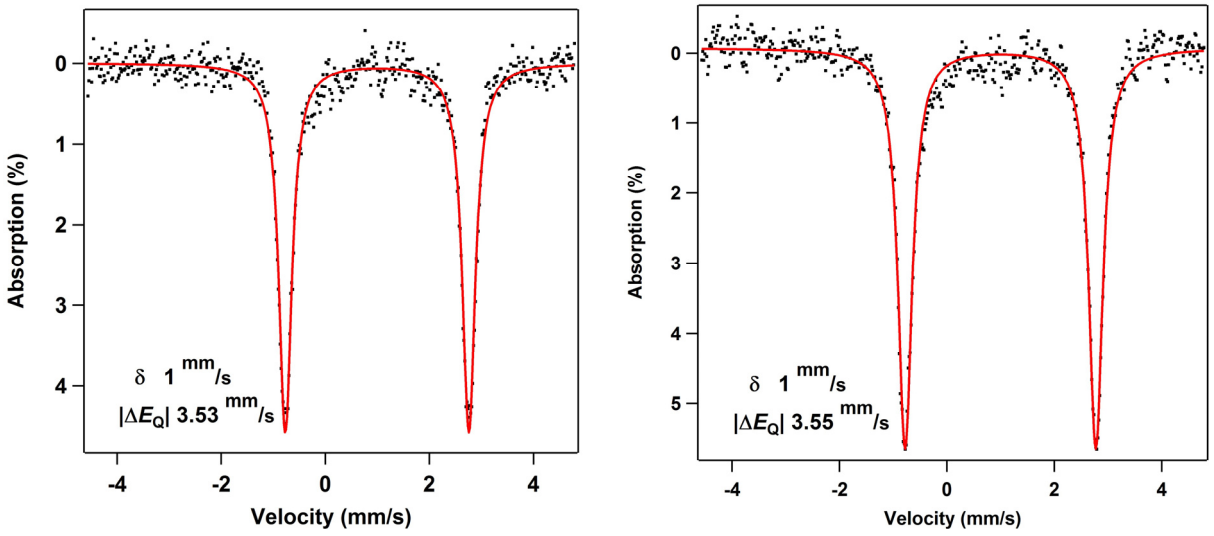

Figure 2.16. Zero-field ^{57}Fe Mössbauer spectrum of $[(^{tBu}dmx)Fe_2(\mu\text{-}OH)Cl_2]^-$ complexes, (**Left**) $[Et_4N][(^{tBu}dmx)Fe_2(\mu\text{-}OH)Cl_2]$ (**5b**) and (**Right**) $[Cp^*_2Co][(^{tBu}dmx)Fe_2(\mu\text{-}OH)Cl_2]$ (**5c**). Isomer shifts and quadrupole splitting values are reported relative to Fe foil at room temperature.

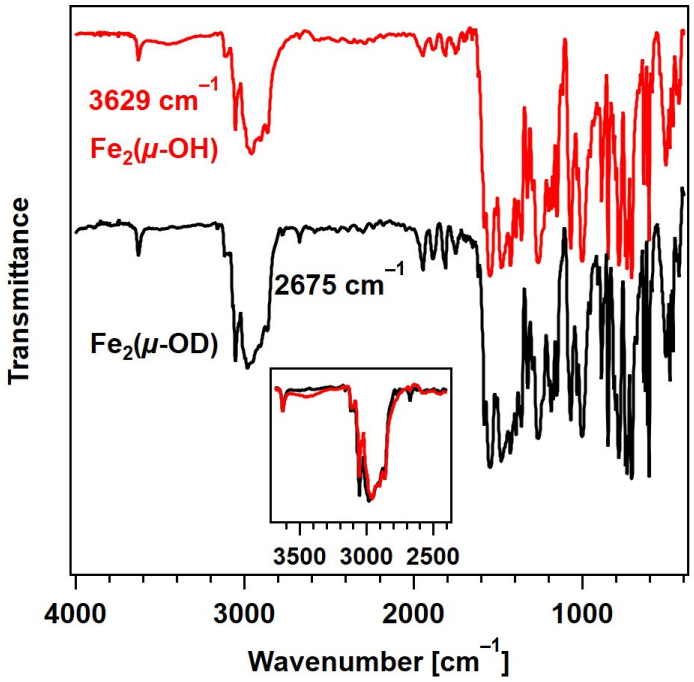

Figure 2.17. FTIR spectrum of (**Top, red**) [Et$_4$N][($^{t\text{Bu}}$dmx)Fe$_2$(μ-OH)Cl$_2$] (**5b**) and (**Bottom, black**) [Et$_4$N][($^{t\text{Bu}}$dmx)Fe$_2$(μ-OD)Cl$_2$] (bottom, black), with inset of overlaid spectra in region featuring OH and OD stretches.

2.5 Synthesis and Reactivity of a Diiron(III) μ-Oxo

Having established the basic nature of **3**, we were interested in studying its redox chemistry. Particularly, we sought to address how the acid/base properties of the oxo complexes were influenced by the oxidation states of the metal centers. Addition of one equivalent of iodobenzene dichloride to **3** in benzene resulted in an immediate color change to dark red and a new paramagnetically shifted ^{1}H NMR spectrum (**Scheme 2.3**). ^{57}Fe Mössbauer analysis of the reaction mixture revealed an iron-containing species with isomer shift and quadrupole splitting values supporting the assignment of high-spin Fe^{III} ($\delta = 0.30$ $^{mm}/_{s}$, $|\Delta E_Q| = 1.38$ $^{mm}/_{s}$) indicating formation of ($^{t\text{Bu}}$dmx)Fe$_2$(μ-O)Cl$_2$ (**6**) (**Figure 2.18**). Single crystals of **6** were grown by slow diffusion of diethyl ether into a saturated THF solution of **6** at –35 °C (**Figure 2.19**). The solid-state molecular structure of **6** features

a crystallographically imposed C_2 axis that renders both iron sites equivalent. The iron–oxygen distance of 1.7734(10) Å is in agreement with the plethora of crystallographically characterized diferric μ-oxo compounds, and the Fe–O–Fe angle of 167.1(3)° only slightly deviates from linearity.[23] Complex **6** can similarly be accessed by a two-electron oxidation of the diferrous hydroxide **4** using iodobenzene dichloride (**Scheme 2.3**). Oxidation of the hydroxide **4** does not furnish the anticipated cationic diferric bridging hydroxide species, rather the reaction product was spectroscopically identical to **6**. Loss of the hydroxide proton in **4** was confirmed using IR spectroscopy (**Figure 2.20**). Unfortunately, we were not able to identify the fate of the proton in this reaction; however, the putative diferric bridging hydroxide intermediate ($^{t\text{Bu}}$dmx)Fe$_2$(μ-OH)Cl$_2$ (**6a**) was found to be quite acidic with a computationally determined pK_a of −1.8(6), which we propose is the driving force for facile loss of the proton concomitant with oxidation to the diferric state.

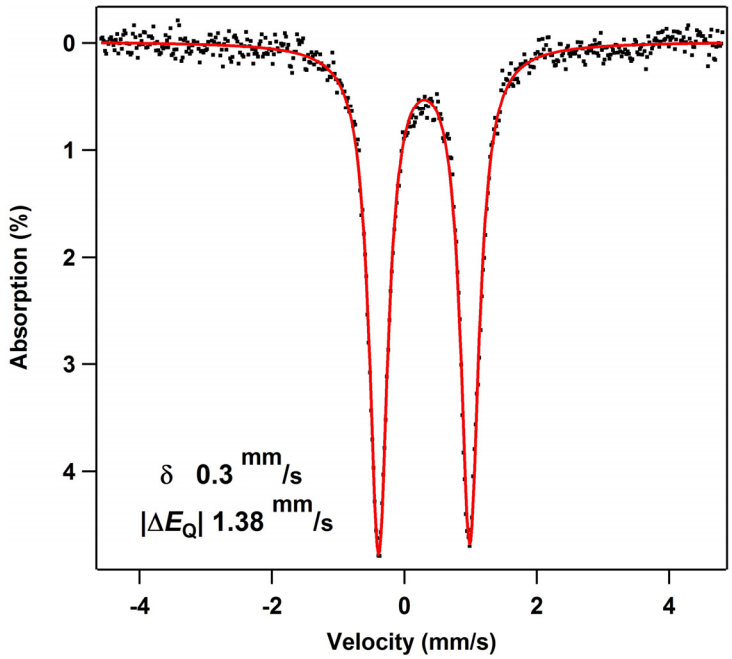

Figure 2.18. Zero-field ^{57}Fe Mössbauer spectrum of ($^{t\text{Bu}}$dmx)Fe$_2$(μ-O)Cl$_2$ (**6**). Isomer shift and quadrupole splitting are reported relative to Fe foil at room temperature.

[23] Theisen, R. M.; Shearer, J.; Kaminsky, W.; Kovacs, J. A. *Inorg. Chem.* **2004**, *43*, 7682–7690.

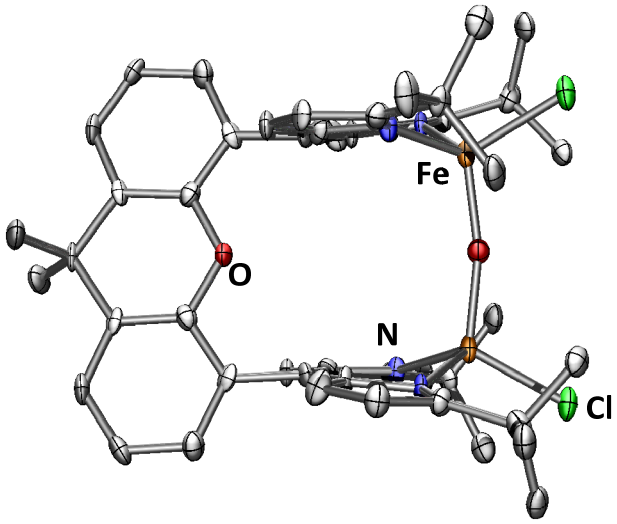

Figure 2.19. Solid state molecular structure of ($^{t\text{Bu}}$dmx)Fe$_2$(μ-O)Cl$_2$ (**6**) with thermal ellipsoids at 50% probability level. Hydrogen atoms omitted for clarity. Color scheme: Fe, orange; N, blue; C, gray; O, red; Cl, green.

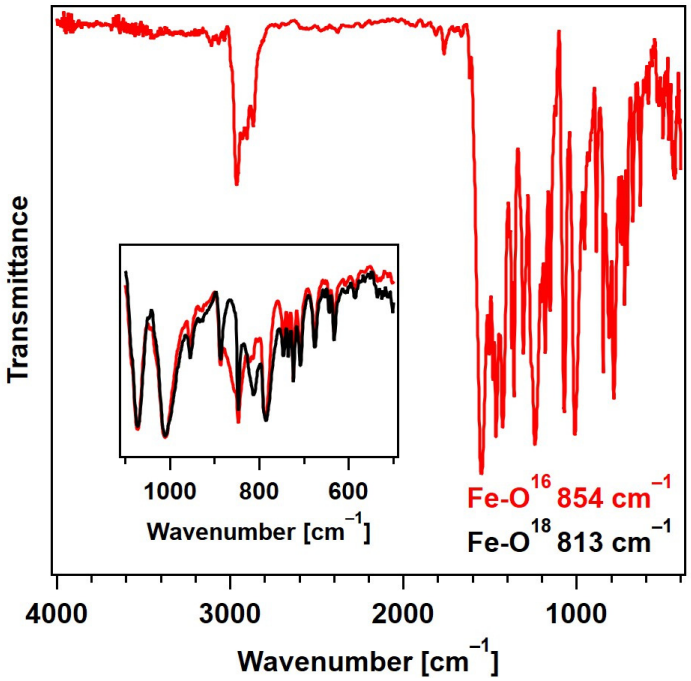

Figure 2.20. FTIR spectrum of ($^{t\text{Bu}}$dmx)Fe$_2$(μ-O)Cl$_2$ (**6**) with inset of fingerprint region for ($^{t\text{Bu}}$dmx)Fe$_2$(μ-O)Cl$_2$ (**6**) (red) and ($^{t\text{Bu}}$dmx)Fe$_2$(μ-^{18}O)Cl$_2$ (black).

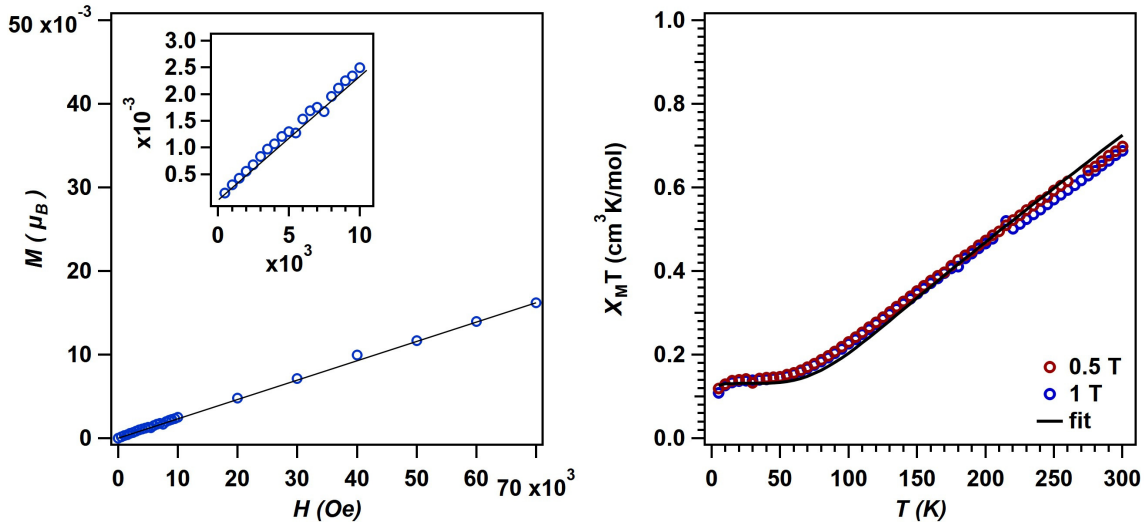

Figure 2.21. Magnetometry data for ($^{t\text{Bu}}$dmx)Fe_2(μ-O)Cl_2 (**6**). **(Left)** M vs. H at 100 K is linear, showing absence of ferromagnetic impurity even at low fields **(Left, inset)**. **(Right)**. Variable temperature magnetic susceptibility data (χ_MT vs. T) was recorded at 0.5 T and 1.0 T across the temperature range of 5 K – 300 K. At 0.5 T (red circles), χ_MT = 0.687 cm^3K/mol at 295 K and at 1.0 T (blue circles), χ_MT = 0.677 cm^3K/mol at 295 K. χ_MT vs. T was fit as two weakly coupled S = 5/2 centers using PHI[23] (black trace), including a 3% S=5/2 impurity, with the following parameters: g = 1.90, J = –122 cm^{-1}, D = 0.38 cm^{-1}, and $|E/D|$ = 0.29.

Herein, we observe a dramatic decrease in the basicity upon oxidation to the diferric state from a diferrous μ-oxo. This trend in basicity can be explained by consideration of the Fe–O covalency as a function of Fe–O–Fe angle; we hypothesize that the drastic change in Fe–O–Fe angle from the diferrous (116.00(14)°) to the diferric state (167.1(3)°) is consistent with an increase in the iron-oxygen covalency. This is supported by a combination of computational and magnetometry studies; specifically, increased Mayer bond orders upon oxidation (from 0.811 in diferrous **3** to 0.947 in diferric **6**; **Table 2.1**), enhanced orbital overlap in the unrestricted corresponding orbitals (0.149–0.165 in **3**, 0.226–0.265 in **6**; **Table 2.1**), and an increased exchange coupling constant upon oxidation to the diferric state (J ~ –60 cm^{-1} for **3**, J ~ –100 cm^{-1} for **6**; **Table 2.2**, **Figure 2.21**) Taking into account the previous comparison between **3** and **3a**, the covalency of the Fe–O interactions are not governed solely by the geometry of the linkage, but

rather are largely dictated by the electrophilicity of the iron sites within the $Fe_2(\mu\text{-}O)$ unit.[24] As such, the oxo moiety is more basic in **3a** than **3** due to THF ligation diminishing the iron electrophilicity and is more basic in **3** than **6** due to lower iron electrophilicity in the more reduced molecular oxidation state.

The foregoing results should be compared with the analysis of the relationship between the Fe–O–Fe angle, Fe–O covalency, and basicity for diiron(III) oxo complexes put forth by Solomon and coworkers. In Solomon's studies, enhanced basicity is observed with a more acute Fe–O–Fe angle due to a reduction in the Fe–O orbital overlap, thereby resulting in pronounced electron density on the bridging oxide ligand when examining an isovalent series.[3, 25] Further comparison with other diiron μ-oxo complexes corroborates this relationship, as a diiron(III) μ-oxo synthesized by Houser and coworkers[7] (Fe–O–Fe: 143.71(10), pK_a: 21.3(1)) is several orders of magnitude more basic than **6** (Fe–O–Fe: 167.1(3), pK_a: –1.8(6)) (**Table 2.2**); whereas an example by Grapperhaus and coworkers with similar core metrics to **6** (Fe–O–Fe: 168.47(13), pK_a: 6.1(3)) is less basic than the Houser example. The Grapperhaus example is more basic than **6**, which can be attributed to differences in coordination geometry; the tetrahedral iron sites in **6** are influenced more by the enhanced covalency to the oxo moiety (due to the increased iron electrophilicity) than the octahedrally coordinated iron sites in the Grapperhaus example.[26]

[24] Kahn, O. in *Molecular Magnetism,* VCH **1993**.

[25] Brown, C. A.; Remar, G. J.; Musselman, R. L.; Solomon, E. I. *Inorg. Chem.* **1995**, *34*, 688–717.

[26] Cui, J.; Mashuta, M. S.; Buchanan, R. M.; Grapperhaus, C. A. *Inorg. Chem.* **2010**, *49*, 10427–10435.

Table 2.2. Comparison of diiron μ-oxo complexes studied herein with previously studied examples.

Complex	Fe–O distances (Å)	Fe–O–Fe angle (°)	Fe–Fe distance (Å)	pK_a of conjugate acid	J_{calc} (cm^{-1})	J_{exp} (cm^{-1})	Ref.
3	1.7939(14)	116.00(14)	3.0425(10)	15.3(6)	–65.9	–53.2	1
3a[a]	1.858, 1.859	126.281	3.315	26.8(6)	–69.3	—	1
6	1.7734(10)	167.1(3)	3.5244(17)	–1.8(6)	–96.4	–122	1
$(Fe^{II})_2(\mu\text{-}O)$[b]	1.7503(4)	167.55(14)	3.4831(4)	—	~ –200 to –250	—	11
$(Fe^{II})_2(\mu\text{-}O)$[c]	1.784(9)	174.7(4)	3.573(9)	—	—	—	12
$(Fe^{II})_2(\mu\text{-}O)$[d]	1.753(2)	147.7(3)	3.367(3)	—	—	—	12
$(Fe^{III})_2(\mu\text{-}O)$[e]	1.8194(16), 1.8156(16)	143.71(10)	3.4542(7)	21.3(1)	—	0.55	7
$(Fe^{III})_2(\mu\text{-}O)$[f]	1.791(2), 1.803(2)	168.47(13)	3.5763(6)	6.1(3)	—	—	26

[a] Based on geometry-optimized structure. [b] L = (2,6-diisopropylphenyl)NC(^{t}Bu)CHC(^{t}Bu)(2,6-diisopropylphenyl). [c] L = $PhBP_3^{iPr}$. [d] L = $PhBP_3^{Ph}$. [e] L = 2,2′-(2-methyl-2-(pyridine-2-yl)propane-1,3-diyl)bis(azanediyl)bis(methylene) diphenol. [f] L = 4-((1-methyl-1*H*-imidazol-2-yl)methyl)-1-thia-4,7-diazacylononane.

2.6 Synthesis and Reactivity of a Mixed-Valent Diiron μ-Oxo

Further exploration of the redox chemistry of the diiron μ-oxo complexes studied herein was pursued. A cyclic voltammogram of **6** measured in THF revealed a quasi-reversible event at –861 mV versus $[Cp_2Fe]^{+/0}$. The peak-to-peak separation for this event varies as a function of scanrate, possibly indicating slow electron transfer rate constants. At slower scan rates, i.e. 0.02 V/s, the peak current for oxidation decreases and the redox event becomes irreversible (**Figure 2.22**). Nevertheless, these data suggest that a mixed-valent μ-oxo complex could be chemically accessible.

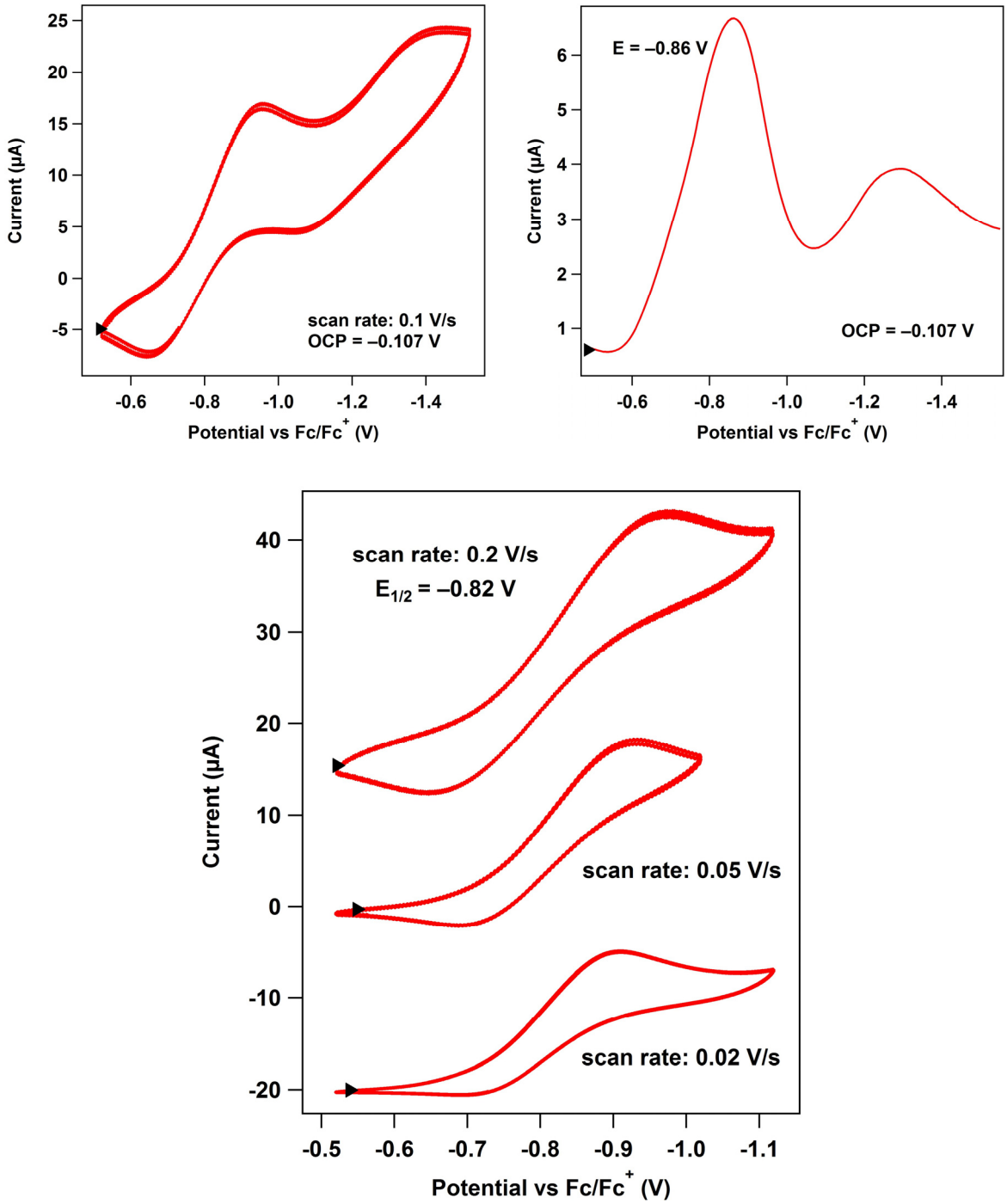

Figure 2.22. Electrochemical measurements of ($^{t\text{Bu}}$dmx)Fe_2(μ-O)Cl_2 (**6**) obtained in THF at 25 °C using a carbon working electrode and 0.1 M [^{n}Bu$_4$N][PF_6] as supporting electrolyte. (**Top, left**) Cyclic voltammogram collected at 0.1 V/s. (**Top**, **right**) Differential pulse voltammetric response. The parameters for DPV were as follows: pulse amplitude of 50 mV, step size of 4 mV, pulse width of 50 ms, and pulse period of 0.5 s. (**Bottom**) Scan rate dependence of cyclic voltammogram.

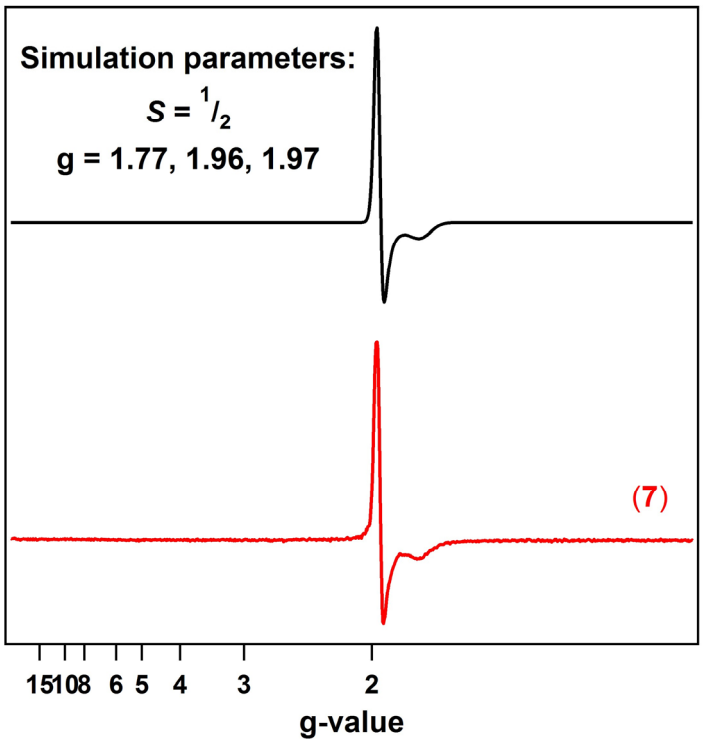

Figure 2.23. EPR spectrum of $[Cp_2Co][(^{tBu}dmx)Fe_2(\mu\text{-}O)Cl_2]$ (**7**). Spectrum collected in a frozen 2-methyltetrahydrofuran glass at 77 K. The black line represents a simulation with EasySpin.[27] Simulation parameters: $S = ½$, $g_x = 1.88$, $g_y = 1.96$, $g_z = 1.97$. Spectral broadening was accounted for by inclusion of FWHM value for the isotropic magnetic-field domain broadening, and the FWHM of the Gaussian distribution of g values.

The redox chemistry of **6** was further explored by using chemical reductants. Cp_2Co (exhibiting a reduction potential of –1.33 mV versus $[Cp_2Fe]^{+/0}$ in dichloromethane[28]) was employed to reduce **6**. Treatment of **6** with one equivalent of cobaltocene in THF for ten minutes provides access to $[Cp_2Co][(^{tBu}dmx)Fe_2(\mu\text{-}O)Cl_2]$ (**7**). A frozen solution EPR spectrum collected at 4 K displays a pseudo-axial signal with features at $g = 1.97$ and 1.77, consistent with an $S = ½$ spin state (**Figure 2.23**). Antiferromagnetic coupling of high-spin ferric and ferrous centers in **7** explains the doublet spin state and supports the formation of a mixed-valent diiron bridging oxo complex. X-ray diffraction studies on single crystals of

[27] Stoll, S.; Schweiger, A. *J. Magn. Reson.* **2006**, *178*, 42–55.

[28] Connelly, N. G.; Geiger, W. E. *Chem. Rev.* **1996**, *96*, 877–910.

7 obtained from a concentrated THF solution at 70 °C unveiled two crystallographically distinct iron sites (**Figure 2.24**); two distinct sites were further observed by ^{57}Fe Mössbauer spectroscopy, the parameters of which exhibit one center being more consistent with a high spin Fe^{II} and the other as a high spin Fe^{III} center (**Figure 2.25**). The Fe–O bond lengths (1.8034(15) Å, 1.8928(15) Å) are longer than the Fe–O bond distances in both diferrous **3** and diferric **6**, and the difference of 0.09 Å indicates a potentially localized nature. The Fe–O–Fe angle of 148.98(10)° resides in between the fairly linear Fe–O–Fe vector in the diferric state (167.1(3)°) and the significantly more acute Fe–O–Fe angle of the diferrous complex (116.00(14)°).

Upon synthesizing the mixed-valent oxo complex **7** via the method previously described, ^{1}H NMR and ^{57}Fe Mössbauer spectroscopy reveals the formation of **7** together will a small amount of hydroxide **5**. While **7** is stable at 70 °C for 12 hours and does not react with weak C–H bonds (such as those in 1,4-cyclohexadiene), this mixed valent species is protolytically sensitive. Addition of one equivalent of water to **7** leads to immediate consumption of **7** and quantitative formation of $[Cp_2Co][(^{t\text{Bu}}dmx)Fe_2(\mu\text{-}OH)Cl_2]$ (**5d**).[29] We were not able to unequivocally determine the origin of the reducing equivalent which reduces a potential mixed-valent hydroxide intermediate species to diferrous **5**, but the hydroxide generated upon proton transfer to **7** could act as a potential reductant. Alternatively, **7** can be converted to **5** by addition of one equivalent of decamethylcobaltocene (**Scheme 2.3**). These reactions demonstrate the intricate interplay between oxidation and protonation state.

[29] Carroll, J. M.; Norton, J. R. *J. Am. Chem. Soc.* **1992**, *114*, 8744–8745.

Lastly, we were able to evaluate the strength of the O–H bond in **5b** by addition of 2,4,6-tri-*tert*-butylphenoxyl radical as a hydrogen atom acceptor. Slow generation of **7** is observed upon addition of 2,4,6-tri-*tert*-butylphenoxyl radical to **5** (**Figure 2.26**), suggesting that the BDEs of the O–H bond of 5 and 2,4,6-tri-*tert*-butylphenol are comparable.[30]

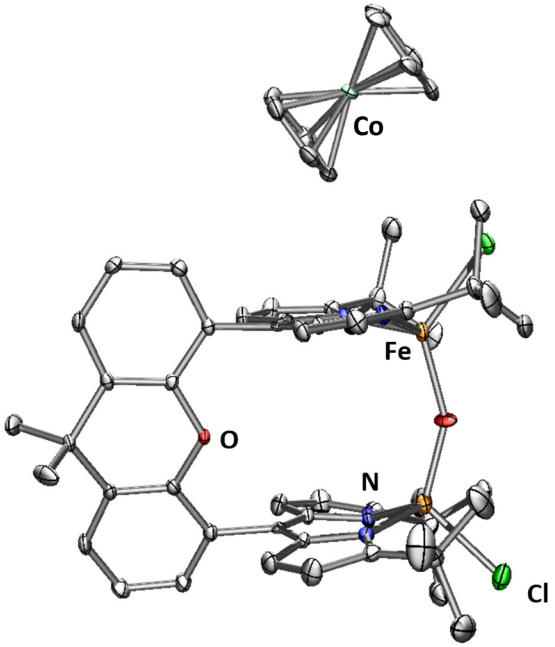

Figure 2.24. Solid state molecular structure of $[Cp_2Co][(^{tBu}dmx)Fe_2(\mu\text{-}O)Cl_2]$ (**7**) with thermal ellipsoids at 50% probability level. Hydrogen atoms omitted for clarity. Color scheme: Fe, orange; N, blue; C, gray; O, red; Cl, green; Co, aquamarine.

[30] Luo Y.-R., *Handbook of Bond Dissociation Energies in Organic Compounds*, CRC Press LLC, Boca Raton, FL, **2003**.

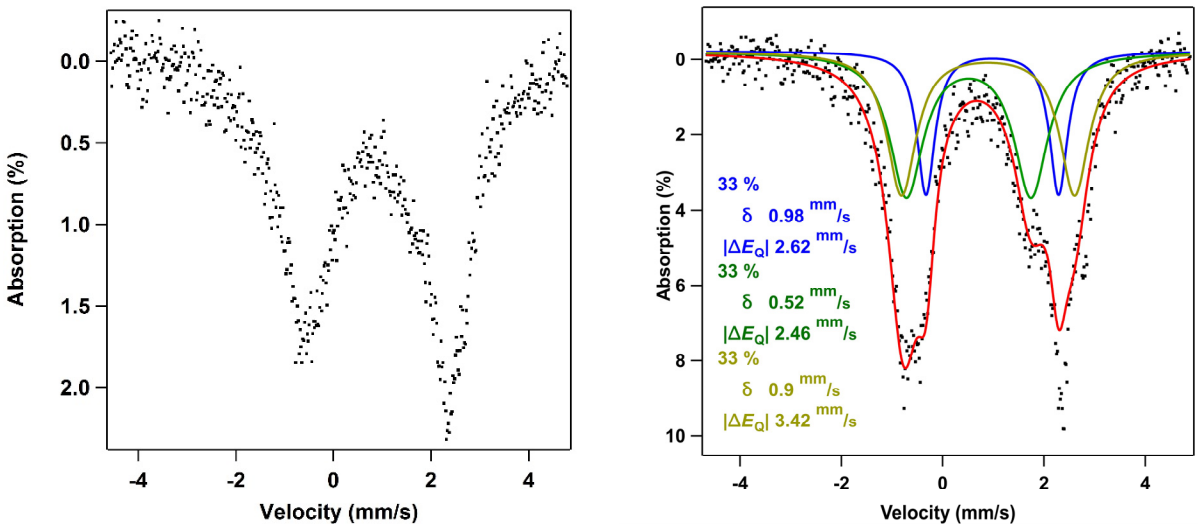

Figure 2.25. Zero-field ^{57}Fe Mössbauer spectrum of $[Cp_2Co][(^{t\text{Bu}}dmx)Fe_2(\mu\text{-}O)Cl_2]$ (**7**), (**Left**) at 90 K and (**Right**) at 4 K. Isomer shift and quadrupole splitting are reported relative to Fe foil at room temperature. The data is fit to reflect 66% of the mixed-valent complex **7**, with equal amounts of a four-coordinate high-spin Fe(II) $\delta = 0.98$ $^{mm}/_{s}$, $|\Delta E_Q| = 2.62$ $^{mm}/_{s}$) and a four-coordinate high spin Fe(III) center ($\delta = 0.52$ $^{mm}/_{s}$, $|\Delta E_Q| = 2.46$ $^{mm}/_{s}$). The remaining 33% is attributed to the formation of hydroxide **5d** by hydrolysis of **7** ($\delta = 0.90$ $^{mm}/_{s}$, $|\Delta E_Q| = 3.42$ $^{mm}/_{s}$, see **Figure 2.16** for authentic sample).

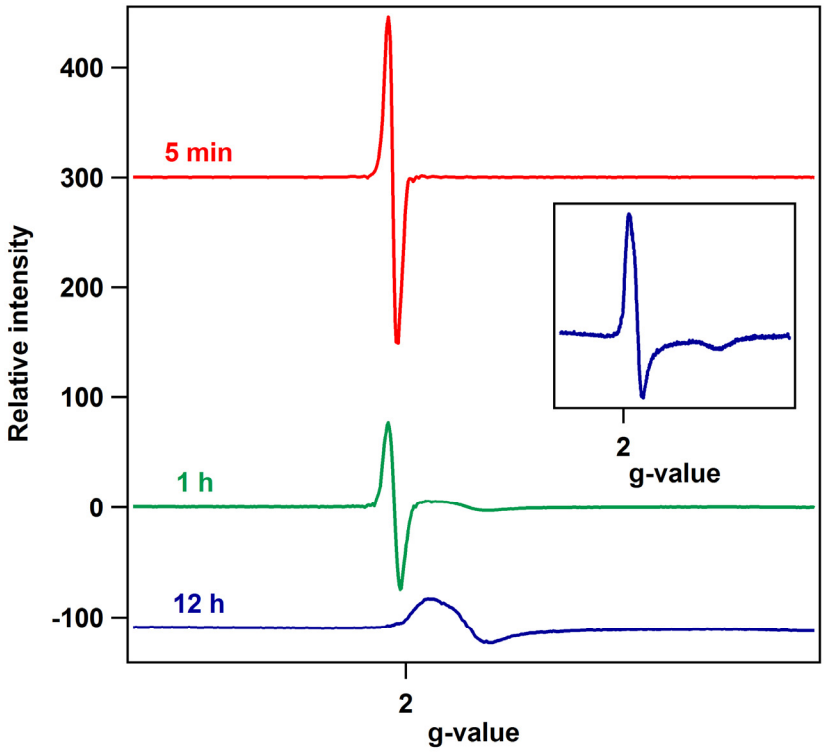

Figure 2.26. EPR reaction monitoring of $[Et_4N][(^{t\text{Bu}}dmx)Fe_2(\mu\text{-}OH)Cl_2]$ (**5b**) with 2,4,6-tri-*tert*-butylphenoxyl radical. Spectra collected in a frozen tetrahydrofuran solution at 77 K at indicated time points. Inset: Final spectrum after 12 h. Over the course of 12 h, conversion of the organic radical to the identical spectrum of **7**, with g-values of 1.95 and 1.76, was observed.

2.7 Conclusions

The Pacman ligand platform ($^{t\text{Bu}}$dmx)H_2 was selected as a template for the synthesis of dinuclear iron complexes. Reaction of ($^{t\text{Bu}}$dmx)H_2 with $Fe_2(Mes)_4$ affords a diiron complex **1** that is an excellent starting material for the introduction of bridging oxygen atoms. Our results indicate that the ($^{t\text{Bu}}$dmx)H_2 ligand serves as a preorganized scaffold to support a diiron core but is sufficiently flexible to allow for moderate structural rearrangements.

Importantly, we demonstrate that this ligand platform supports a diiron core in multiple oxidation states. As such, this system provided us with the unique opportunity to compare the reactivity of a series of diiron μ-oxo complexes in a similar coordination environment. We showcase that the diiron species have a distinct inherent preference for oxo or hydroxide bridge formation, similar to bimetallic iron enzymes in nature. While a diferrous, a mixed-valent, and a diferric μ-oxo complex could be isolated, oxidized bridging hydroxide complexes remained elusive. The acidity of the bridging hydroxide increases substantially upon oxidation (pK_a of **6a** = −1.8(6)), which precludes isolation of a diferric bridging hydroxide. Similarly, the basicity of the bridging oxygen atom increases upon reduction (pK_a of **3a** = 15.3(6)) and even further upon coordination of neutral (pK_a of **4** = 26.8(6)) or anionic ligands (pK_a of **5** is expected to be greater than 26.8).

The primary influence of changing the Fe–O–Fe bonding and, thus, its attendant covalency is the relative electrophilicity of the Fe sites within that unit. Whereas solvation of the [Fe_2(μ-O)] core results in a substantial increase of the oxo basicity relative to **3**, anation leads to oxo protonation without a discernible intermediate. Solvation and anation electrostatically reinforce the iron centers, diminishing the Fe–O interaction and increasing

oxo basicity. Oxidation of diferrous **3** to diferric **6**, on the other hand, leads to an increased covalent interaction as the iron sites are now more electrophilic following oxidation. Consequently, the oxo moiety is far less basic in the higher oxidation state complex.

Finally, we were able to isolate a rare mixed-valent diiron μ-oxo complex and observed a decomposition pathway distinct from previously reported mechanisms. Rapid disproportionation of a mixed-valent diiron oxo complex to a diferrous hydroxide together with a diferric μ-oxo complex has been described in the literature.[7] In our system, decomposition of the mixed-valent complex proceeds cleanly to diferrous hydroxide **5** without the formation of a diferric species. We believe that the reactivity showcased by the diiron complexes presented herein complements current mechanistic understanding and work is underway to elucidate the reactivity of these complexes with dioxygen.

2.8 Experimental Methods

2.8.1 General Considerations

All manipulations of metal complexes were carried out in the absence of water and dioxygen using standard Schlenk techniques, or in an MBraun inert atmosphere drybox under a dinitrogen atmosphere. Ligand and ligand precursor syntheses were carried out in air, except where noted. All glassware was oven dried for a minimum of 6 h and cooled in an evacuated antechamber prior to use in the drybox. Benzene, hexanes, tetrahydrofuran, dichloromethane and toluene were dried and deoxygenated on a Glass Contour System (SG Water USA, Nashua, NH) and stored over 4 Å molecular sieves (Strem) prior to use. Tetrahydrofuran-d_8, and D_2O were purchased from Cambridge Isotope Labs and used as received. Benzene-d_6 and dichloromethane-d_2 were purchased from Cambridge Isotope Labs, degassed and stored over 4 Å molecular sieves prior to use. Pentane and 2-methyltetrahydrofuran was purchased from Sigma-Aldrich and stored over 4 Å molecular sieves prior to use. Celite® 545 (J. T. Baker) and $MgSO_4$ were dried in a Schlenk flask for 24 h under dynamic vacuum while heating to at least 190 °C prior to drybox use. 9*H*-xanthen-9-one was purchased from TCI America. Iodobenzene and sodium hypochlorite (available chloride 10-15%) were purchased from Sigma Aldrich and cobaltocene and decamethylcobaltocene were purchased from Strem. Tetrabutylammonium chloride was purchased from Sigma-Aldrich and heated to 50 °C under high vacuum overnight prior to use. Tetraethylammonium chloride was purchased from Sigma-Aldrich and heated to 80 °C under high vacuum overnight prior to bringing into the glovebox. The solid was then recrystallized from acetonitrile layered with diethyl ether. Distilled H_2O, D_2O and H_2O^{18} were degassed by sparging with argon prior to use. Tetraphenylphosphonium chloride was purchased from Sigma Aldrich and recrystallized from an

anhydrous dichloromethane/hexanes mixture before use. KBr was purchased from International Crystal Laboratories and used without further purification. Silica gel 40–63 μm (Silicycle Inc.) and neutral aluminum oxide, Brockmann Grade I, 58–60 mesh powder (Alfa Aesar) were used as received. 2-(*Tert*-butyl)-1*H*-pyrrole[31], 9,9-dimethyl-9*H*-xanthene[32] and 9,9-dimethyl-9*H*-xanthene-4,5-dicarbaldehyde[33] were synthesized as previously reported. 2,6-Lutidinium tetraphenylborate[34] and $Fe_2(Mes)_4$[35] were synthesized following previously reported procedures.

2.8.2 Characterization and Physical Methods

^1H and ^{13}C NMR spectra were recorded on Agilent DD2 600 MHz or Varian Unity/Inova 500 MHz spectrometers. ^1H and ^{13}C NMR chemical shifts are reported relative to $SiMe_4$ using the chemical shift of residual solvent peaks as reference. Elemental analyses (%CHN) were obtained on a PerkinElmer 2400 Series II CHNS/O Analyzer.

Zero-field ^{57}Fe Mössbauer spectra were measured with a constant acceleration spectrometer (SEE Co, Minneapolis, MN) at 90 K. Isomer shifts are quoted relative to Fe foil at room temperature. Data were analyzed and simulated with Igor Pro 6 software (WaveMetrics, Portland, OR) using Lorentzian fitting functions. Samples were prepared by suspending 20–50 mg of compound in sufficient Paratone oil or by dissolving 20–40 mg in benzene and immobilizing by rapid freezing in liquid nitrogen.

Electrochemical experiments were carried out using a CH Instruments CHI660C

[31] Hennessy, E. T.; Liu, R. Y.; Iovan, D. A.; Duncan, R. A.; Betley, T. A. *Chem. Sci.* **2014**, *5*, 1526–1532.

[32] Nowick, J. S.; Ballester, P.; Ebmeyer, F., Rebek, J. *J. Am. Chem. Soc.* **1990**, *112*, 8902–8906.

[33] Chang, C. J.; Deng, Y.; Heyduk, A. F.; Chang, C. K.; Nocera, D. G. *Inorg. Chem.* **2000**, *39*, 959–966.

[34] Gronberg, K. L. C.;Henderson, R. A.; Oglieve, K. E. *J. Chem. Soc., Dalton Trans.* **1998**, 3093–3104.

[35] Hernández Sánchez, R.; Zheng, S.-L.; Betley T. A. *J. Am. Chem. Soc.* **2015**, *137*, 11126–11143.

Electrochemical Workstation. The electrolyte used was 0.1 M [^{n}Bu$_4$N][(PF$_6$] in THF. The working electrode was glassy carbon and a platinum wire was used as the counter electrode. Cyclic voltammograms were referenced against a ferrocene standard. Cyclic voltammetry was performed with scan rates of 10 mV/s to 500 mV/s.

Infrared spectra were acquired on a Varian 1000 FTIR spectrometer by pressing the samples into KBr pellets (~3–4 mg of dried sample and ~80 mg of KBr).

UV/Visible spectra were recorded on a Varian Cary 50 UV/Vis spectrometer using quartz cuvettes and a scan rate of 600 nm/min.

EPR spectra were obtained on a Bruker EleXsys E-500 CW-EPR spectrometer. Spectra were measured as frozen glass in 2-methyltetrahydrofuran at a microwave power of 0.6325–2 mW. Simulation and fitting were performed with the EasySpin 3.0.0 ToolBox for MATLAB® R2008a.[27] The spectrum was simulated by optimizing g values, the FWHM value for the isotropic magnetic-field domain broadening, and the FWHM of the Gaussian distribution of g values.

Magnetic data were collected using a Quantum Design MPMS-5S SQUID magnetometer. Measurements were obtained for finely ground microcrystalline powders restrained in a frozen eicosane matrix with polycarbonate capsules. Samples were prepared under a dry nitrogen atmosphere by packing the powder in a gel cap and adding warm liquid eicosane, which formed a solid wax upon cooling. The susceptibility data was corrected for contributions from the sample holder and eicosane, as well as the core diamagnetism of the sample using Pascal's constants.

$$\chi_M = \frac{\chi \mathrm{M}}{m \cdot H}. \quad (1)$$

Molar susceptibilities (χ_M) were calculated by converting the calculated magnetic susceptibility (χ) obtained from the magnetometer according to equation 1. The reduced magnetization data were fit using PHI.[14]

2.8.3 Synthesis

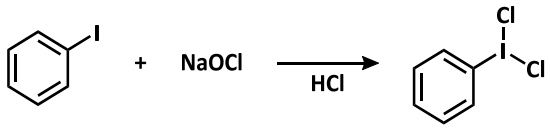

Iodobenzene dichloride: The synthesis for iodobenzene dichloride was adapted from a published procedure.[36] Iodobenzene (2.04 g, 10.0 mmol, 1.00 equiv) was dissolved in a mixture of 30 mL of sodium hypochlorite (available chloride 10–15%) and 30 mL of water. 20 mL of concentrated HCl was added dropwise to the stirring solution. A yellow solid precipitated over the course of ten minutes. The resulting yellow solid was collected by filtration, washed with water and hexanes. The solid was dissolved in dichloromethane and dried over $MgSO_4$ and filtered. The product was crystallized overnight in the dark at −35 °C. The following morning, the mother liquor was removed and the solid was brought into a nitrogen filled glovebox. It was again dissolved in dichloromethane, dried over $MgSO_4$, filtered and crystallized. The product was stored at −35 °C in the dark.

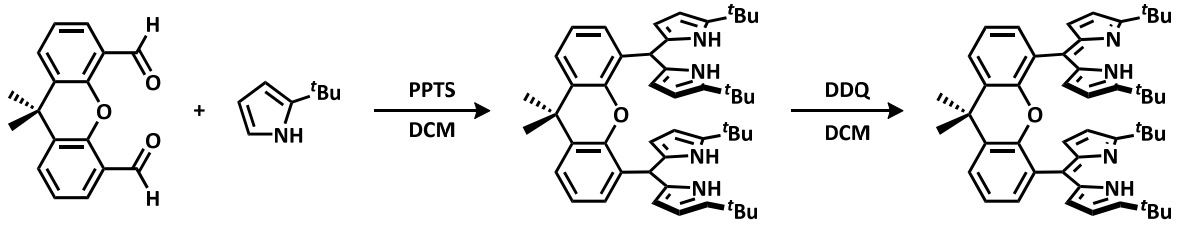

($^{t\text{Bu}}$dmx)H_2: Under inert atmosphere, a 350 mL pressure tube was charged with 2-(*tert*-butyl)-1*H*-pyrrole (6.89 g, 55.9 mmol, 4.10 equiv), 9,9-dimethyl-9H-xanthene-4,5-dicarbaldehyde (3.63 g, 13.6 mmol, 1.00 equiv) and 100 mL of dry dichloromethane. Pyridinium *p*-toluenesulfonate (685 mg, 2.73 mmol, 20.0 mol%) was added and the reaction mixture was sealed, removed from the glovebox and placed in an oil bath kept at 35 °C for 16 h. The crude reaction mixture was

[36] Zhao, X.-F.; Zhang, C. *Synthesis* **2007**, *4*, 551–557.

filtered through a plug of silica gel in a medium porosity frit (360 mL), concentrated *in vacuo* and used for the next step without further purification (9.71 g, 98.5%). The dipyrromethane (9.71 g, 13.4 mmol, 1.00 equiv) was dissolved in 200 mL of dichloromethane and 2,3-dichloro-5,6-dicyanoquinone (DDQ) (6.19 g, 27.3 mmol, 2.03 equiv) was added as a solid resulting in an immediate color change to dark brown. After stirring at room temperature for two hours, the reaction mixture was filtered through a plug of neutral alumina in a medium porosity frit (600 mL) and eluted with dichloromethane containing 1% triethylamine. Fractions containing product (TLC analysis, basic alumina, R_f (DCM) = 0.1, orange spot) were combined and the solvent was removed *in vacuo*. The resulting solid was triturated with methanol three times to remove residual triethylamine. The orange solid was recrystallized from a mixture of hot methanol/dichloromethane. The orange crystals that formed upon cooling to –10 °C were collected by filtration and washed with a small amount of methanol to give pure **($^{t\text{Bu}}$dmx)H$_2$** (4.20 g, 43.9%). ^{1}H NMR (500 MHz, C_6D_6): δ/ppm 13.25 (s, 2H), 7.17 (dd, J = 7.9, 1.6 Hz, 2H), 7.09 (dd, J = 7.5, 1.6 Hz, 2H), 6.79 (m, 2H), 6.54 (dd, J = 4.1, 0.8 Hz, 4H), 6.07 (dd, J = 4.1, 1.2 Hz, 4H), 1.50 (s, 9H), 1.40 (s, 36H). ^{13}C{^{1}H} NMR (126 MHz, C_6D_6): δ/ppm 165.05, 148.84, 140.31, 135.09, 132.40, 130.43, 128.59, 128.35, 126.51, 126.21, 122.40, 113.61, 34.69, 33.48, 32.29, 30.21. HRMS (ESI$^+$) *m/z* Calc. 719.4689 [$C_{49}H_{58}N_4O$ + H^+], Found 719.4718 [M+H]$^+$.

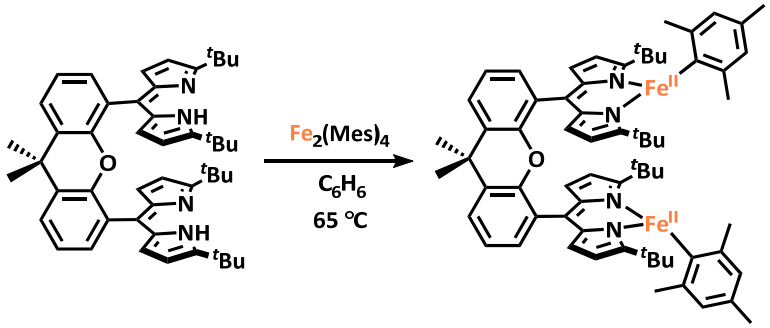

($^{t\text{Bu}}$dmx)Fe$_2$(Mes)$_2$ (1): To a 50 mL pressure vessel was added ($^{t\text{Bu}}$dmx)H$_2$ (500 mg, 695 µmol,

1.00 equiv), $Fe_2(Mes)_4$ (409 mg, 695 µmol, 1.00 equiv) and 10 mL benzene. The vessel was equipped with a magnetic stir bar, capped, removed from the glovebox and placed in an oil bath kept at 65 °C for four hours. The reaction mixture was cooled to room temperature, returned to the glovebox and filtered through Celite and the filter cake was washed with excess benzene until the eluent was nearly colorless. The solvent was frozen and removed *in vacuo* to yield a dark red powder. The residue was washed with hexanes (4×3 mL), filtered through Celite with benzene and lyophilized to yield a dark red powder (601 mg, 81.0%). Crystals suitable for X-ray diffraction were grown from a concentrated solution of toluene layered with hexanes at −35 °C. ^{1}H NMR (500 MHz, 295 K, C_6D_6): δ/ppm 134.64, 74.56, 27.63, 11.84, 8.25, 3.36, 1.23, 0.88, −2.18, −13.65. Zero-field ^{57}Fe Mössbauer (90 K) (δ, $|\Delta E_Q|$ ($^{mm}/_s$)): 0.46, *0.95* (γ = 0.16 $^{mm}/_s$). %CHN Calculated for $C_{67}H_{78}Fe_2N_4O$: C 75.42 H 7.37 N 5.25; Found: C 74.88 H 7.45 N 5.40.

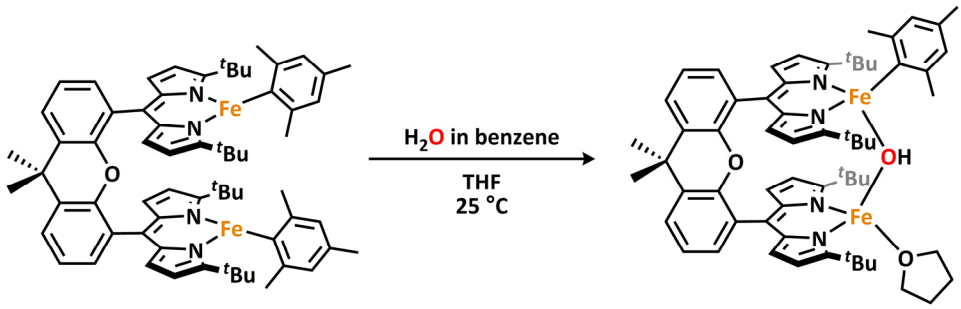

($^{t\text{Bu}}$dmx)Fe$_2$(µ-OH)(Mes)(thf) (2): In a 20 mL vial, ($^{t\text{Bu}}$dmx)Fe$_2$(Mes)$_2$ (**1**) (100 mg, 93.7 µmol, 1.00 equiv) was dissolved in 4 mL of THF. A saturated solution of water in benzene[37] (2.64 mL, 93.7 µmol, 1.00 equiv) was added dropwise to a vigorously stirred solution. The reaction mixture was stirred at room temperature for 20 minutes and concentrated *in vacuo*. The residue was recrystallized at −35 °C from 1 mL of diethyl ether. After 48 hours, the mother liquor was decanted and the residue was dried *in vacuo* to afford ($^{t\text{Bu}}$dmx)Fe$_2$(µ-OH)(Mes)(thf) (**2**) as red-brown

[37] Karlsson, R. *J. Chem. Eng. Data* 1973, *18*, 290–292.

crystals (76.0 mg, 78.3%). ^{1}H NMR (500 MHz, 295 K, THF-d_8): δ/ppm 82.43, 74.75, 72.37, 63.87, 47.17, 42.47, 37.95, 16.85, 14.29, 8.56, 6.02, 5.05, 3.35, 1.07, −1.23, −1.91, −8.08, −11.76. Zero-field ^{57}Fe Mössbauer (90 K) (δ, $|\Delta E_Q|$ ($^{mm}/_{s}$)): 0.79, *3.22;* 1*, 2.95* (γ = 0.129, 0.166 $^{mm}/_{s}$). FTIR (KBr): 3638 cm^{-1} (ν_{O-H}); 2685 cm^{-1} (ν_{O-D}). %CHN Calculated for $C_{62}H_{76}Fe_2N_4O_3$: C 71.81 H 7.39 N 5.40; Found: C 71.44 H 7.76 N 5.39.

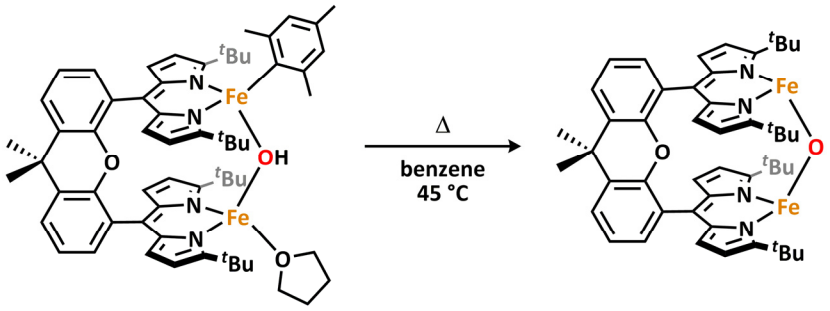

($^{t\text{Bu}}$dmx)Fe$_2$(μ-O) (3): To a J. Young tube was added ($^{t\text{Bu}}$dmx)Fe$_2$(μ-OH)(Mes)(thf) (**2**) (50 mg, 48 μmol, 1.0 equiv) and 1.5 mL of benzene. The tube was sealed, removed from the glovebox and heated to 45 °C for 30 minutes. The reaction mixture was cooled to room temperature, returned to the glovebox, transferred to a vial, frozen and concentrated *in vacuo*. The residue was dissolved in benzene and lyophilized three times to remove residual mesitylene to give ($^{t\text{Bu}}$dmx)Fe$_2$(μ-O) (**3**) as a red powder (37 mg, 91%). Crystals suitable for X-ray diffraction were grown from a concentrated diethyl ether solution at −35 °C. ^{1}H NMR (500 MHz, 295 K, C_6D_6): δ/ppm 19.51, 13.96, 8.05, 4.96, −2.27, −3.00, −6.40. Zero-field ^{57}Fe Mössbauer (90 K) (δ, $|\Delta E_Q|$ ($^{mm}/_{s}$)): 0.68, *0.88* (γ = 0.15 $^{mm}/_{s}$). %CHN Calculated for $C_{49}H_{56}Fe_2N_4O_2$: C 69.67 H 6.68 N 6.63; Found: C 70.75 H 6.76 N 6.65.

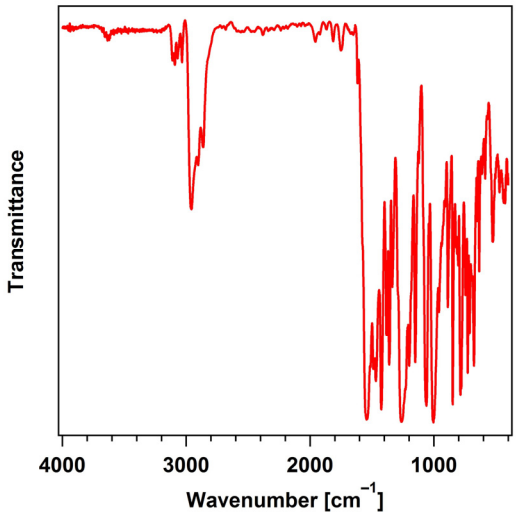

Figure 2.27. FTIR spectrum of ($^{t\text{Bu}}$dmx)Fe$_2$(μ-O) (**3**).

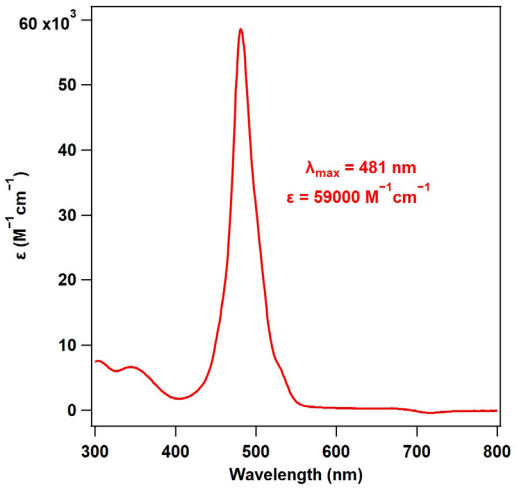

Figure 2.28. UV/Visible absorption spectrum of ($^{t\text{Bu}}$dmx)Fe$_2$(μ-O) (**3**) in THF.

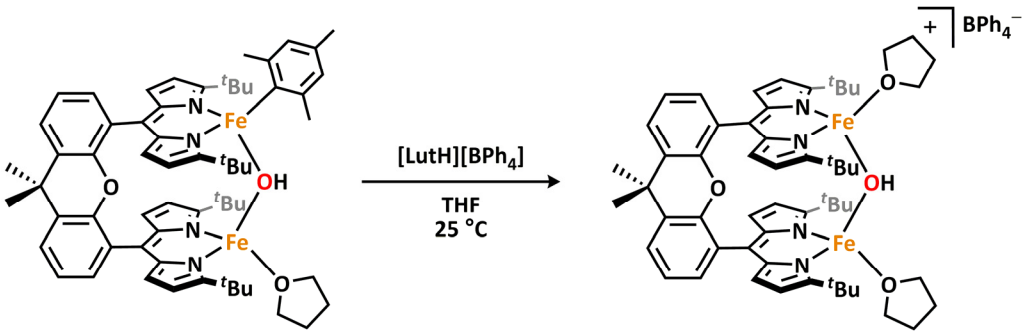

[($^{t\text{Bu}}$dmx)Fe$_2$(μ-OH)(thf)$_2$][BPh$_4$] (4): In a 20 mL vial, 2,6-lutidinium tetraphenylborate (41.2 mg, 96.4 μmol, 1.00 equiv) was dissolved in 2 mL of THF. A solution of ($^{t\text{Bu}}$dmx)Fe$_2$(μ-OH)(Mes)(thf) (**2**) (100 mg, 96.4 μmol, 1.00 equiv) in 2 mL of THF was added dropwise. The reaction mixture was allowed to stir at room temperature for 45 minutes and filtered through Celite before being concentrated *in vacuo*. The residue was washed with hexanes, filtered through Celite in THF, and concentrated *in vacuo*. The residue was taken up in minimal ether to afford a saturated solution to which drops of THF were added. This solution was filtered through Celite and recrystallized at −35 °C. After 48 hours, the mother liquor was decanted and [($^{t\text{Bu}}$dmx)Fe$_2$(μ-OH)(thf)$_2$][BPh$_4$] (**4**) was recovered as orange crystals (78.6 mg, 62.4%). ^{1}H NMR (600 MHz, 295 K, THF-d_8): δ/ppm 43.84, 28.15, 6.56, 6.28, 3.29, 2.64, 2.26, –3.04, –16.96. Zero-field ^{57}Fe Mössbauer (90 K) (δ, $|\Delta E_Q|$ ($^{mm}/_s$)): 1.01, *3.02* ($\gamma = 0.145$ $^{mm}/_s$). FTIR (KBr): 3548 cm^{-1} (ν_{O-H}); 2587 cm^{-1} (ν_{O-D}). %CHN Calculated for $C_{81}H_{93}BFe_2N_4O_4$: C 74.31 H 7.16 N 4.28; Found: C 74.66 H 7.34 N 4.31.

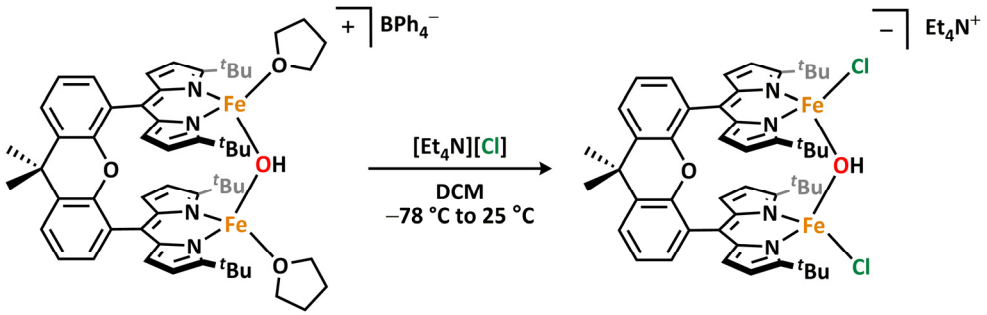

[Et$_4$N][($^{t\text{Bu}}$dmx)Fe$_2$(μ-OH)Cl$_2$] (5b): In a 20 mL vial, tetraethylammonium chloride (5.1 mg, 31 μmol, 2.0 equiv) was dissolved in 2 mL of DCM and frozen in the cold well (–78 °C). A solution of [($^{t\text{Bu}}$dmx)Fe$_2$(μ-OH)(thf)$_2$][BPh$_4$] (**4**) (20 mg, 15 μmol, 1.0 equiv) in 2 mL of DCM was added dropwise and frozen in a layer on top. The reaction mixture was thawed and allowed to stir for 10 minutes. At this point, the reaction mixture was filtered through Celite and concentrated *in vacuo*.

The residue was recrystallized at –35 °C from 4 mL of DCM layered with 1 mL of THF. After 48 hours, the mother liquor was decanted and the crystals were dried *in vacuo* to afford [Et_4N][($^{t\text{Bu}}$dmx)Fe_2(μ-OH)Cl_2] (**5b**) as an orange-brown residue (11.2 mg, 73.2%). Crystals suitable for X-ray diffraction were grown from a concentrated solution in THF upon cooling from 60 °C to room temperature. ^{1}H NMR (500 MHz, 295 K, CD_2Cl_2): δ/ppm. 40.50, 12.55, 6.31, 6.00, 4.26, 1.71, –2.44, –13.91. Zero-field ^{57}Fe Mössbauer (90 K) (δ, $|\Delta E_Q|$ ($^{mm}/_s$)): 1.00, *3.53* (γ = 0.152 $^{mm}/_s$). FTIR (KBr): 3629 cm^{-1} (ν_{O-H}); 2675 cm^{-1} (ν_{O-D}). %CHN Calculated for $C_{57}H_{77}Cl_2Fe_2N_5O_2$: C 65.40 H 7.41 N 6.69; Found: C 65.54 H 7.32 N 6.85.

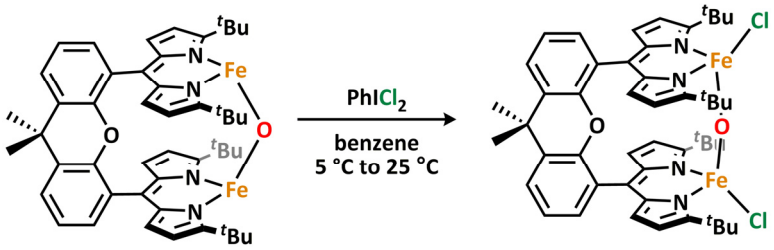

($^{t\text{Bu}}$dmx)Fe_2(μ-O)Cl_2 (6): In a 20 mL vial, iodobenzene dichloride (19.2 mg, 69.8 μmol, 1.00 equiv) was frozen in 2 mL of benzene. A solution of ($^{t\text{Bu}}$dmx)Fe_2(μ-O) (**3**) (59.0 mg, 69.8 μmol, 1.00 equiv) was added while stirring. The mixture was thawed and stirred at room temperature for ten minutes. The reaction was filtered through Celite and the filter cake washed with excess benzene until the eluent was nearly colorless. The solvent was frozen and removed *in vacuo* to yield a purple-brown powder. The residue was washed with hexanes (3×2 mL) and THF (3×0.5 mL) to give ($^{t\text{Bu}}$dmx)Fe_2(μ-O)Cl_2 (**6**) as a dark purple powder (31.2 mg, 48.8%). Crystals suitable for X-ray diffraction were grown from a concentrated solution of THF layered with diethyl ether at −35 °C. ^{1}H NMR (500 MHz, 295 K, C_6D_6): δ/ppm 13.87. Zero-field ^{57}Fe Mössbauer (90 K) (δ, $|\Delta E_Q|$ ($^{mm}/_s$)): 0.30, *1.38* (γ = 0.17 $^{mm}/_s$). %CHN Calculated for $C_{49}H_{56}Fe_2N_4O_2Cl_2$: C 64.28 H 6.17 N 6.12; Found: C 63.76 H 6.41 N 5.83.

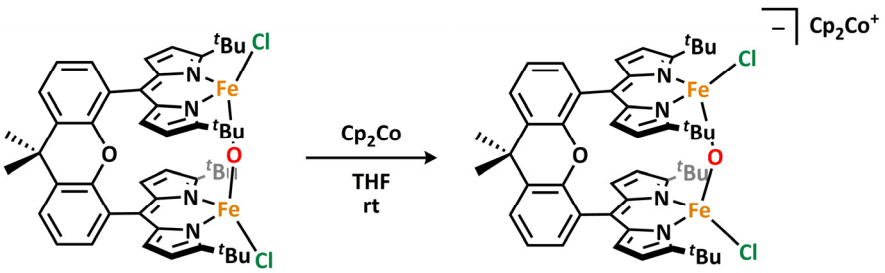

[Cp_2Co][(^{tBu}dmx)Fe_2(μ-O)Cl_2] (7): In a 20 mL vial, a solution of cobaltocene (2.7 mg, 14 mmol, 1.0 equiv) in 1 mL of THF was added dropwise to a just-thawed suspension of (^{tBu}dmx)Fe_2(μ-O)Cl_2 (**6**) (13 mg, 14 μmol, 1.0 equiv) in 2 mL of THF. The reaction mixture was stirred at room temperature for ten minutes and concentrated to give an orange solid. Crystals suitable for X-ray diffraction were grown from a concentrated solution of THF at 70 °C. ^{1}H NMR (500 MHz, 295 K, THF): δ/ppm 15.47, 8.27, 7.71, 7.19, 6.90, 1.29, 0.85.

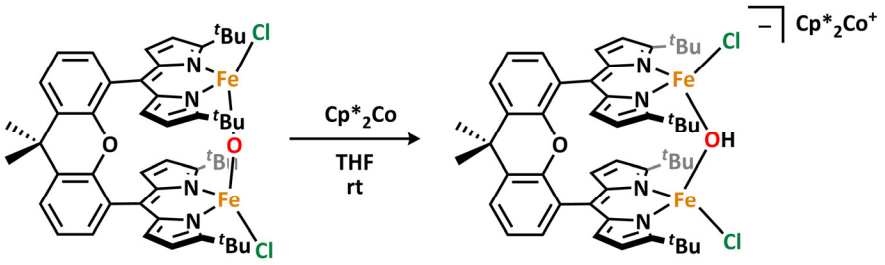

[Cp^*_2Co][(^{tBu}dmx)Fe_2(μ-OH)Cl_2] (5c): In a 20 mL vial, a solution of decamethylcobaltocene (8.6 mg, 26 μmol, 2.0 equiv) in 1 mL of THF was added dropwise to a just-thawed suspension of (^{tBu}dmx)Fe_2(μ-O)Cl_2 (**6**) (12 mg, 13 mmol, 1.0 equiv) in 2 mL of THF. The reaction mixture was stirred at room temperature for ten minutes and concentrated to give an orange solid. The solid was triturated with hexanes twice to give [Cp^*_2Co][(^{tBu}dmx)Fe_2(μ-OH)Cl_2] (**5c**) as an orange powder (12 mg, 75%). ^{1}H NMR (500 MHz, 295 K, THF): δ/ppm 38.80, 23.06, 9.36, 1.26, 0.85, −1.06, −10.35. Zero-field ^{57}Fe Mössbauer (90 K) (δ, $|\Delta E_Q|$ ($^{mm}/_s$)): 1.00, *3.55* (γ = 0.16 $^{mm}/_s$). FTIR (KBr): 3625 cm^{-1} (ν_{O-H}); 3616 cm^{-1} (ν_{O18-H}).

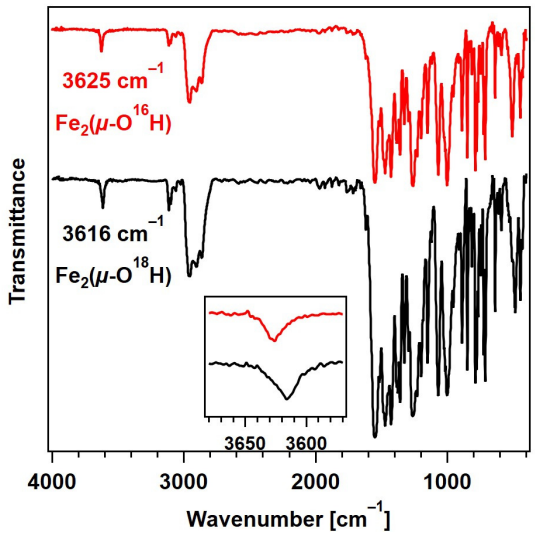

Figure 2.29. FTIR spectrum of (**Top, red**) [Cp^*_2Co][($^{t\text{Bu}}$dmx)Fe_2(μ-OH)Cl_2] (**5c**) and (**Bottom, black**) [Cp^*_2Co][($^{t\text{Bu}}$dmx)Fe_2(μ-^{18}OH)Cl_2] (bottom, black) with inset of region featuring OH stretches.

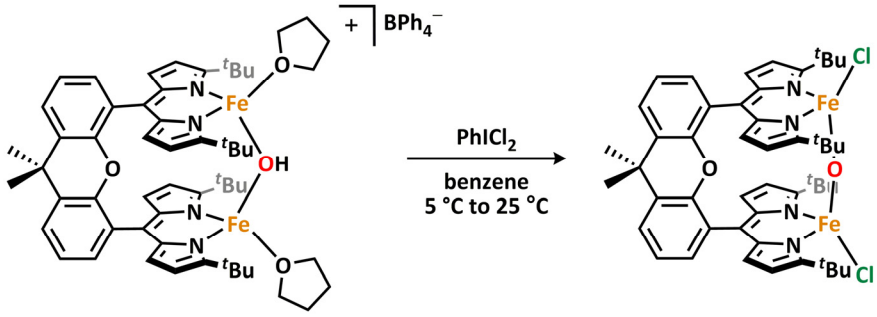

Oxidation of [($^{t\text{Bu}}$dmx)Fe_2(μ-OH)(thf)$_2$][BPh_4] (4): In a 20 mL vial, iodobenzene dichloride (12.4 mg, 45.1 μmol, 1.00 equiv) was frozen in 2 mL of benzene. A solution of [($^{t\text{Bu}}$dmx)Fe_2(*μ*-OH)(thf)$_2$][BPh_4] (**4**) (58.9 mg, 45.1 μmol, 1.00 equiv) was added while stirring. The mixture was thawed and stirred at room temperature for ten minutes. The reaction was filtered through Celite, after which the solvent was frozen and removed *in vacuo* to yield a purple-brown powder. The residue was washed with hexanes (2×2 mL) and THF (2×0.5 mL) to give ($^{t\text{Bu}}$dmx)Fe_2(μ-O)Cl_2 (**6**) as a dark purple powder (21.2 mg, 51%). Crystals suitable for X-ray diffraction were grown from a concentrated solution of diethyl ether with drops of THF at −35 °C.

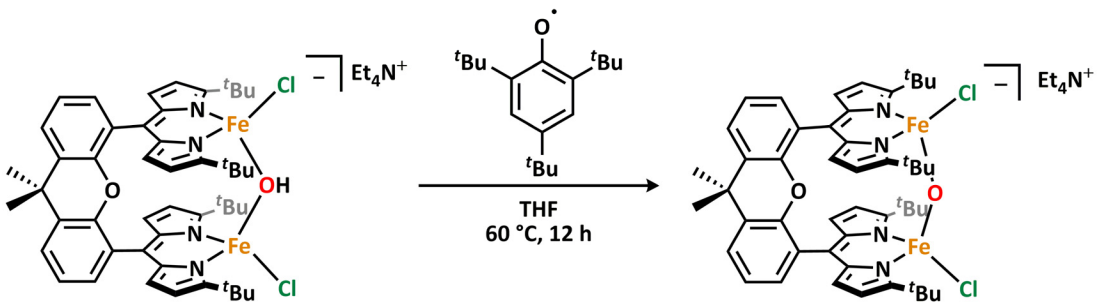

Addition of 2,4,6-tri-*tert*-butylphenoxyl radical to [Et$_4$N][($^{t\text{Bu}}$dmx)Fe$_2$(μ-OH)Cl$_2$] (5b): In a J. Young tube, 2,4,6-tri-*tert*-butylphenoxyl radical (3.7 mg, 14.1 μmol, 0.98 equiv) was combined with a 1.5 mL THF solution of [Et$_4$N][($^{t\text{Bu}}$dmx)Fe$_2$(μ-OH)Cl$_2$] (**5b**) (14.8 mg, 14.1 μmol, 1.00 equiv). ^{1}H NMR and EPR spectra were collected immediately. The reaction vessel was heated to 60 °C for 12 hours, over the course of which multiple time points were taken to monitor the reaction (**Figure 2.26**).

2.8.4 Theoretical Methods

All calculations were performed using the density functional theory and the quantum chemical program package Gaussian16[38] using the unrestricted B3LYP hybrid functional (which includes the Becke three-parameter exchange and the Lee, Yang, and Parr correlation functional) and GD3BJ dispersion of Grimme et al. with Becke-Johnson damping.[39] The SDD basis set was used in the investigation, which combines the Dunning/Huzinaga valence double-zeta basis[40] for elements up to Ar, with the Stuttgart/Dresden effective core potentials[41,42] for the remainder of the

[38] Gaussian, Inc., Revision B.01 (2016), Wallingford CT.

[39] Grimme, S.; Ehrlich, S.; Goerigk, L. *J. Comp. Chem*. **2011**, *32*, 1456–1465.

[40] Dunning, T. H., Jr.; Hay, P. J. in *Modern Theoretical Chemistry*, *Vol. 3* (Ed. H. F. Schaefer III), Plenum **1997**.

[41] Wedig, U.; Dolg, M.; Stoll, H.; Preuss, H. in *Quantum Chemistry: The Challenge of Transition Metals and Coordination Chemistry* (Ed. A. Veillard, Reidel and Dordrecht), D. Reidel Publishing Company **1986**.

[42] Bergner, A.; Dolg, M.; Kuchle, W.; Stoll, H.; Preuss, H. *Mol. Phys.,* 1993**, 80**, 1431–1441.

periodic table. This particular method and level of theory was reported by Smith *et al.* in 2008 and was found to provide appropriate accuracy in similar thermodynamic estimations of pK_a values for iron complexes.[18] Solvation of the molecular species was modelled using continuum parameters designed to describe tetrahydrofuran solvent ($\varepsilon = 7.43$). Geometry optimizations were performed in order to obtain electronic energies, followed by frequency calculations to compute zero-point energies and derive values for thermal and entropic corrections at 298.15 K.

Considering a general acid-base reaction between a bridging hydroxide species (denoted below as $[hydroxide]^+$) and a bridging oxo species (denoted as *oxo*):

$$[hydroxide]^+ + [A]^- \rightarrow oxo + HA \quad (2)$$

where HA is a weak acid whose pK_a value in THF has previously been reported.[19] The overall free energy of the reaction is thus satisfied by the relationship:

$$\Delta G = 2.303RT\,[pK_a([hydroxide]^+) - pK_a(HA)] \quad (3)$$

where $pK_a([hydroxide]^+)$ and $pK_a(HA)$ denote the pK_a values for the $[hydroxide]^+$ and HA, respectively. As described by Smith *et. al*, using this method one evaluates the relative free energy with respect to a known weak acid, HA, and thus bypasses the explicit treatment of the solvated proton.[18]

Although many experimental pK_a values for weak acids have been determined in solvents such as H_2O, dimethyl sulfoxide, and acetonitrile, unfortunately the stability of the species of interest (**3** and **4**) hindered experimental acid/base reactions under these solvation conditions. The stability of **3**/**4** in dry solvents such as benzene and diethyl ether is greatly improved, but unfortunately the poor solubility of the complexes limited effective spectroscopic evaluation of acid/base reactivity in these cases. THF is suitably solvating for both reactants and products, but

experimental pK_a values are limited in number. Smith *et al.* recently reported accurate theoretical determination of numerous pK_a values for acids in THF,[18] so we were able to use these values in order to estimate the [*hydroxide*]$^+$ pK_a theoretically.

In order to estimate the pK_a of the diiron hydroxide-bridged species **4**, it is important to define the respective conjugate base as differing simply by one proton. Experimentally, protonation of species **3** (in which binding of solvent molecules to iron is not demonstrated in the solid state structure) to yield **4** is concomitant with the binding of one THF molecule to each iron center (as featured in the solid state structure of **4**). Therefore, two options are presented in order to effectively model the acid/base reactivity of **3** and **4**:

1) Protonation of the bridging oxo **3** to yield **4a** (a model of the bridging hydroxide **4** with no THF bound). It is worth noting that experimentally, this species (**4a**) was not isolable, and it seems that THF binding upon protonation is highly favorable. In fact, addition of two THF molecules to **4a**, yielding **4**, is shown to be energetically favorable by 96 kJ mol^{-1}:

$$\mathbf{4a} + 2\ \mathrm{THF} \rightarrow \mathbf{4} \qquad \Delta G = -96\ \mathrm{kJ\ mol^{-1}}$$

The following acid-base reaction between **4a** and **3** is thus considered:

$$(^{t\mathrm{Bu}}\mathrm{dmx})\mathrm{Fe_2}(\mu\text{-}\mathrm{OH})^+ + \mathrm{A}^- \rightarrow (^{t\mathrm{Bu}}\mathrm{dmx})\mathrm{Fe_2}(\mu\text{-}\mathrm{O}) + \mathrm{HA} \qquad (4)$$

and the overall free energy of the reaction is satisfied by the relationship:

$$\Delta G = 2.303RT\ [pK_a(\mathrm{Fe_2}(\mu\text{-}\mathrm{OH})^+) - pK_a(\mathrm{HA})] \qquad (5)$$

where $pK_a(\mathrm{Fe_2}(\mu\text{-}\mathrm{OH})^+)$ and $pK_a(\mathrm{HA})$ denote the pK_a values for **4a** and HA, respectively.[14] This method was tested with a series of acids spanning a range of pK_a values (**Table 2.3**) and yielded a pK_a value for **4a** which was consistent across this series. The derived value of pK_a

by this method was shown to be 15.3(6) for ($^{t\text{Bu}}$dmx)Fe$_2$(μ-OH)$^+$ (**4a**) in THF.

2) Protonation of a bridging oxo **3a** (in which THF molecules are bound to each iron center) to yield the bridging hydroxide **4**. Again, the free energy change upon addition of two molecules of THF to **3** (yielding **3a**) was found to be energetically favorable by 30 kJ/mol, which supports experimental evidence that **3** binds THF in solution.

$$\mathbf{3} + 2\ \text{THF} \rightarrow \mathbf{3a} \qquad \Delta G = -30\ \text{kJ mol}^{-1}$$

The acid-base reaction between **4** and **3a** now takes the form:

$$(^{t\text{Bu}}\text{dmx})\text{Fe}_2(\mu\text{-OH})(\text{thf})_2^+ + \text{A}^- \rightarrow (^{t\text{Bu}}\text{dmx})\text{Fe}_2(\mu\text{-O})(\text{thf})_2 + \text{HA} \qquad (6)$$

and the free energy is satisfied by the relationship:

$$\Delta G = 2.303RT\ [pK_a(\text{Fe}_2(\mu\text{-OH})(\text{thf})_2^+) - pK_a(\text{HA})] \qquad (7)$$

where $pK_a(\text{Fe}_2(\mu\text{-OH})(\text{thf})_2^+)$ denotes the pK_a value for species **4**.

Using the same series of acids, (see **Table 2.3**), a pK_a value of 26.7(6) for **4** in THF was derived.[18]

3) Protonation of a bridging oxo **6** to yield **6a** (a model of the conjugate acid of **6**, a diferric bridging hydroxide). It is worth noting that experimentally, this species (**6a**) was not isolable, and it seems that deprotonation is highly favorable due to its negative pK_a.

The acid-base reaction between **6a** and **6** is considered:

$$(^{t\text{Bu}}\text{dmx})\text{Fe}_2(\mu\text{-OH})\text{Cl}_2^+ + \text{A}^- \rightarrow (^{t\text{Bu}}\text{dmx})\text{Fe}_2(\mu\text{-O})\text{Cl}_2 + \text{HA} \qquad (8)$$

and the free energy is satisfied by the relationship:

$$\Delta G = 2.303RT\ [pK_a(\text{Fe}_2(\mu\text{-OH})\text{Cl}_2^+) - pK_a(\text{HA})] \qquad (9)$$

where $pK_a(Fe_2(\mu\text{-}OH)Cl_2^+)$ denotes the pK_a value for species **6a**.

Using the same series of acids, (see **Table 2.3**), a pK_a value of −1.8(6) for **6a** in THF was derived.[18]

Table 2.3 Calculated pK_a values of $[(^{t\text{Bu}}\text{dmx})Fe_2(\mu\text{-}OH)]^+$ (**4a**), $[(^{t\text{Bu}}\text{dmx})Fe_2(\mu\text{-}OH)(thf)_2]^+$ (**4**), and $[(^{t\text{Bu}}\text{dmx})Fe_2(\mu\text{-}OH)Cl_2]^+$ (**6a**) with respect to different reference acids.

Reference Acid	Calculated pK_a of $Fe_2(\mu\text{-}OH)^+$ (4a)	Calculated pK_a of $Fe_2(\mu\text{-}OH)(thf)_2^+$ (4)	Calculated pK_a of $Fe_2(\mu\text{-}OH)Cl_2^+$ (6)
Lutidinium	16.1	27.6	−1.0
Benzoic Acid	15.5	27.0	−1.6
Acetic Acid	15.2	26.7	−1.9
Phenol	14.4	25.9	−2.7
2,2,2-trifluoroethanol	15.4	26.8	−1.7

To validate these findings, calculation of ^{57}Fe Mössbauer isomer shifts (δ) for complexes **3**, **3a**, **4**, **4a**, **6**, and **6a** (**Table 2.4**) were carried out as described previously[43] via linear regression of DFT calculated electron density at the nucleus to experimental values of δ. Mössbauer calculations were carried out using the ORCA 4.0.1.2 program package[44] and were initiated from spin-unrestricted single-point calculations that employed the B3LYP functional[45] with the def2-TZVP (Fe, N, O) and def2-SV(P) (C, H) basis sets.[46] Further, the def2-TSVP/J (Fe, N, Cl) and def2-SV(P)/J (C, H) auxiliary basis sets were employed to utilize the RIJCOSX approximation for

[43] Neese, F. *Inorg. Chim. Acta* **2002**, *337*, 181–192.

[44] Neese, F. *Comput. Mol. Sci.* **2012**, *2*, 73–78.

[45] (a) Becke, A. D. *J. Chem. Phys.* **1993**, *98*, 5648–5652; (b) Lee, C. T.; Yang, W. T.; Parr, R. G. *Phys Rev. B*, 1988, **37**, 785–789.

[46] Weigand, F. *Phys. Chem. Chem. Phys.* **2006**, *8*, 1057–1065.

accelerating the calculation.[47] A broken symmetry solution (see equation 10, 11 below) was used to model antiferromagnetic coupling between the iron centers, and the continuum solvation model CPCM was implemented to model the solvent as tetrahydrofuran.[48] All geometries were taken from the optimized structures used for the pK_a determinations (**Figures 2.30**–**2.32**, **Table 2.9**).

Table 2.4. Calculated Mössbauer parameters for **4a**, **4**, **3**, **3a**, **6**, and **6a**.

Complex	δ (Exp), mm/s	δ (Calc), mm/s	$\|\Delta E_Q\|$ (Exp), mm/s	$\|\Delta E_Q\|$ (Calc), mm/s
4a	--	0.80, 0.83	--	0.804, 1.01
4	1.01	1.07, 1.07	3.02	2.700, 2.700
3	0.68	0.75, 0.75	0.88	0.646, 0.648
3a	0.94	1.05, 1.05	2.01	1.821, 1.830
6	0.30	0.33, 0.33	1.38	1.081, 1.081
6a	--	0.33, 0.33	--	0.528, 0.505

The bond orders and orbital overlaps of the diiron oxo complexes were also considered using the results of the spin-unrestricted single-point calculations. Bond distance and bond order indicate that the strength of the Fe–O bonds increase from **3a** to **3** to **6** (as indicated by a shorter Fe–O distance and larger Mayer bond order), which is consistent with the trend of decreasing basicity across the series (**Table 2.1**). Furthermore, the overlap between corresponding orbitals was seen to increase across the series of **3a** to **3** to **6** (**Table 2.1**, **Table 2.6-2.9**). This value represents the overlap between orbitals involved in coupling of the system; since in this case coupling between iron centers is through the oxo bridge, this metric also provides insight into the strength of the Fe–O interactions. Each of these data is consistent with the conjecture that Fe–O covalency is increasing with decreased basicity.

[47] Neese, F.; Wennmohs, F.; Hansen, A.; Becker. U. *Chem. Phys.* **2009**, *356*, 98–109.

[48] Sinnecker, S.; Rajendran, A.; Klamt, A.; Diedenhofen, M.; Neese, F. *J. Phys. Chem. A* **2006**, *110*, 2235–2245.

Broken symmetry solutions were used to model the antiferromagnetic coupling present in these complexes. The standard notation BS(m,n) represents the (m+n) unpaired electrons within a system and net spin of $^{(m-n)}/_2$ for an antiferromagnetically coupled system.[49] As such, one fragment will bear m α electrons while the other bears n β electrons. The appropriate description for each case was as high spin iron centers (i.e., high-spin Fe^{II} for **4a**, **4**, **3**, **3a** and high spin Fe^{III} for **6**, **6a**). The exchange coupling constant J was determined from the energy difference between the high-spin and broken-symmetry states, using the spin Hamiltonian in equation S8 and formula in equation S9[50,51,52] :

$$H = -2J\overrightarrow{S_{Fe(1)}} \cdot \overrightarrow{S_{Fe(2)}}. \quad (10)$$

$$J = -\frac{E_{HS}-E_{BS}}{S^2_{max}}. \quad (11)$$

Table 2.5. Broken symmetry solution information for **4a**, **4**, **3**, **3a**, **6**, and **6a**.

Complex	Broken symmetry description	E_{HS} - E_{BS} (cm^{-1})	J (cm^{-1})
4a	BS(4,4)	162.284	–10.1
4	BS(4,4)	236.530	–14.8
3	BS(4,4)	1055.057	–65.9
3a	BS(4,4)	1107.937	–69.3
6	BS(5,5)	2408.881	–96.4
6a	BS(5,5)	442.437	–17.7

[49] Kirchner, B.**;** Wenmohs, F.; Ye, S.; Neese, F. *Curr. Opin. Chem. Biol.*2007, **11**, 134–141.

[50] Ginsberg, A.P. *J. Am. Chem. Soc.* 1980, **102**, 111–117.

[51] Noodleman, L. *J. Chem. Phys.* 1981, **74**, 5737–5743.

[52] Noodleman, L.; Davidson, E. R. *Chem. Phys.* 1986, **109**, 131–143.

Table 2.6. Orbital overlap of unrestricted corresponding orbitals (UCO) in **3a**.

Orbital	Orbital overlap
259	0.169
260	0.155
261	0.141

Table 2.7. Orbital overlap of UCOs in **3**.

Orbital	Orbital overlap
219	0.165
220	0.155
221	0.149

Table 2.8. Orbital overlap of UCOs in **6**.

Orbital	Orbital overlap
235	0.265
236	0.236
237	0.226

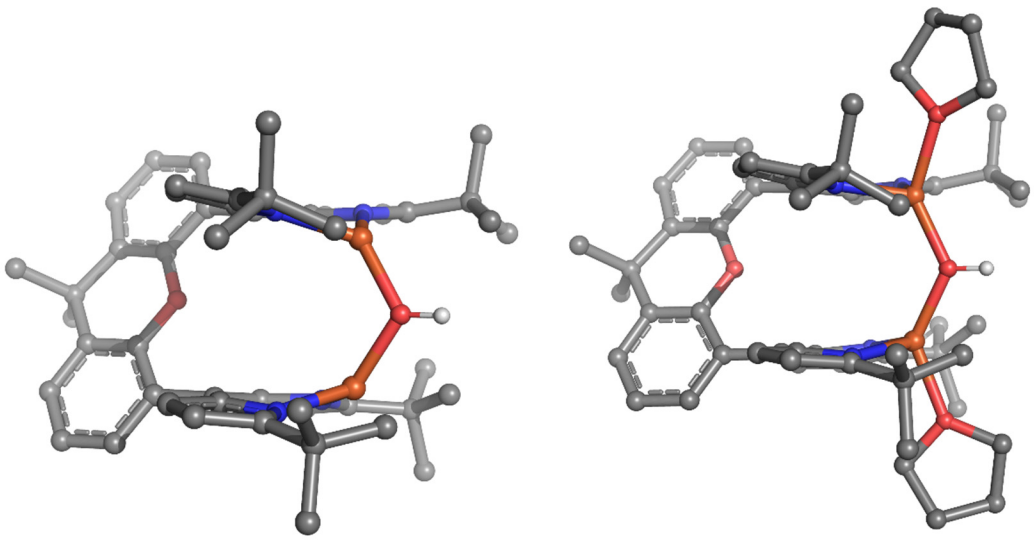

Figure 2.30. Geometry optimized structures of diiron(II) μ-hydroxo complexes. (**Left**) $[(^{t\text{Bu}}\text{dmx})\text{Fe}_2(\mu\text{-OH})]^+$ (**4a**), (**Right**) $[(^{t\text{Bu}}\text{dmx})\text{Fe}_2(\mu\text{-OH})(\text{thf})_2]^+$ (**4**). Hydrogen atoms (except the μ-hydroxo proton) omitted for clarity.

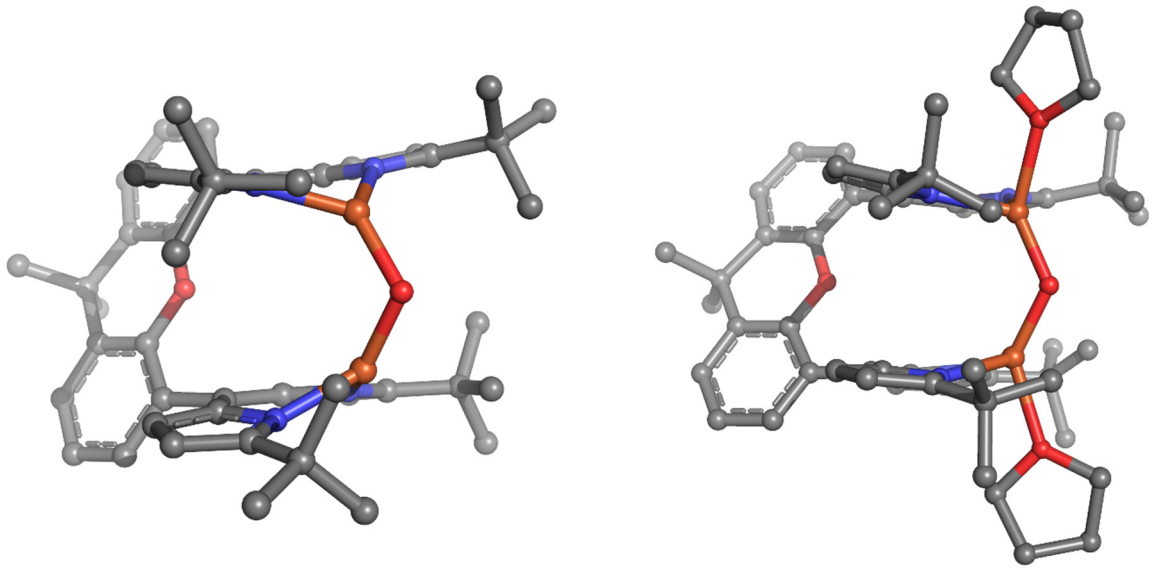

Figure 2.31. Geometry optimized structures of diiron(II) μ-oxo complexes. (**Left**) ($^{t\text{Bu}}$dmx)Fe_2(μ-O) (**3**), (**Right**) ($^{t\text{Bu}}$dmx)Fe_2(μ-O)(thf)$_2$ (**3a**). Hydrogen atoms omitted for clarity.

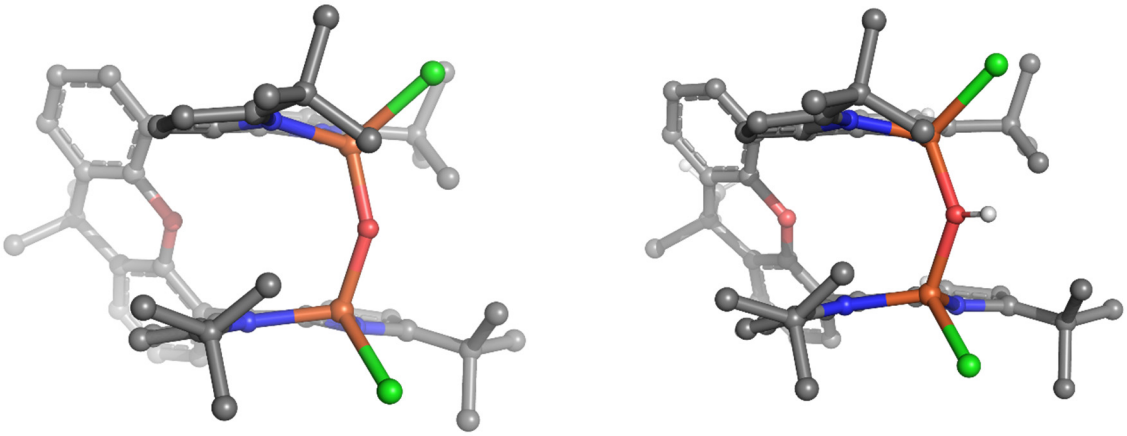

Figure 2.32. Geometry optimized structures of diiron(III) μ-(hydr)oxo dichloride complexes. (**Left**) ($^{t\text{Bu}}$dmx)Fe_2(μ-O)Cl_2 (**6**), (**Right**) [($^{t\text{Bu}}$dmx)Fe_2(μ-OH)Cl]$^+$ (**6a**). Hydrogen atoms (except the μ-hydroxo proton) omitted for clarity.

Table 2.9. Coordinates of optimized structures **4a**, **4**, **3**, **3a**, **6**, and **6a**.

[($^{t\text{Bu}}$dmx)Fe_2(μ-OH)]$^+$ (**4a**)
E = −2518.90158573 a.u.
G = −2518.028445 a.u.
Charge = +1, Multiplicity = 9

Fe	–2.13753	–0.81818	1.405085
O	–3.13079	0.066644	–0.02788
H	–4.10367	0.116254	–0.05096
O	2.698955	–0.03437	0.023025
N	–0.64515	0.049213	2.398810

N	–1.08515	2.616830	–1.09921	H	2.459333	–3.65154	2.717695
N	–0.547	–0.02325	–2.42528	C	3.311082	2.853293	–2.13018
N	–1.24961	–2.5728	1.077228	H	2.726061	3.558076	–2.71265
C	0.675715	–0.46091	2.243054	C	–1.41768	–3.44161	–3.54313
C	0.784626	0.455628	–2.26859	H	–0.55254	–3.74596	–4.14213
C	1.562912	0.388085	2.984594	H	–2.28411	–4.02183	–3.88474
H	2.631006	0.251713	3.069517	H	–1.21579	–3.69575	–2.497
C	1.177493	1.609137	–1.55276	C	4.760306	–1.13353	0.769552
C	2.513882	–1.90041	1.463952	C	–3.32574	5.173644	0.545113
C	0.335900	2.599754	–0.99855	H	–3.29111	4.585811	1.468407
C	3.434928	0.910777	–0.69491	H	–4.34175	5.569420	0.426735
C	1.041219	–1.63037	1.539397	H	–2.64623	6.025651	0.654768
C	0.171959	–2.59627	0.982671	C	–4.16133	–3.02193	0.808461
C	2.657043	1.818938	–1.44338	H	–3.97874	–2.47572	1.746301
C	–1.70657	–1.92355	–3.69909	H	–5.18342	–3.41217	0.876967
C	4.837437	0.954142	–0.66281	H	–4.12696	–2.32632	–0.03616
C	–0.57053	1.155528	3.204440	C	–1.75508	1.978489	3.677903
C	3.360459	–1.02337	0.753513	C	–1.93771	–1.59441	–5.20311
C	–0.4989	–1.135	–3.22506	H	–2.13496	–0.52379	–5.34128
C	–0.62652	–4.531	0.068651	H	–2.80017	–2.15886	–5.58005
H	–0.70179	–5.50128	–0.39954	H	–1.06082	–1.86199	–5.80352
C	0.857620	–1.39519	–3.60401	C	5.462753	2.000545	–1.37375
H	1.189165	–2.20238	–4.24066	H	6.546099	2.073660	–1.37311
C	–1.72314	–3.74707	0.549167	C	–2.98228	–1.57565	–2.90672
C	–1.52602	3.811047	–0.58651	H	–2.85041	–1.75619	–1.83593
C	0.547186	–3.81644	0.330696	H	–3.81508	–2.19797	–3.25467
H	1.558890	–4.11529	0.099627	H	–3.28965	–0.53096	–3.06812
C	5.669212	–0.10531	0.076861	C	0.791659	1.384269	3.583223
C	–3.17539	–4.19491	0.617257	H	1.141546	2.183257	4.220550
C	0.744838	3.814425	–0.35665	C	–3.56341	–4.95783	–0.67612
H	1.764151	4.085639	–0.12469	H	–3.49754	–4.30705	–1.55434
C	1.652182	–0.41535	–3.00748	H	–4.59422	–5.32313	–0.59298
H	2.723282	–0.30387	–3.09219	H	–2.91402	–5.82395	–0.84286
C	3.096350	–2.97044	2.162263	C	–2.96139	4.305607	–0.68619

C	4.494267	–3.13372	2.168136
H	4.941546	–3.9587	2.713551
C	–3.05293	1.632228	2.922565
H	–2.93878	1.774804	1.843937
H	–3.86532	2.284565	3.263204
H	–3.3785	0.600726	3.128890
C	–0.40827	4.567075	–0.10965
H	–0.45648	5.544255	0.347411
C	5.310641	–2.21414	1.490752
H	6.388752	–2.33788	1.527676
C	4.714944	2.950423	–2.08767
H	5.219737	3.748405	–2.62304
C	–3.30208	–5.15928	1.835811
H	–2.64672	–6.02935	1.715011
H	–4.33685	–5.51364	1.925314
H	–3.02623	–4.64718	2.766037
C	6.583907	–0.83318	–0.95201
H	5.980881	–1.33553	–1.71717
H	7.207474	–1.58387	–0.45435
H	7.250772	–0.12058	–1.44948
C	–1.43672	3.484570	3.469731
H	–0.55594	3.786859	4.046646
H	–2.28473	4.095086	3.804367
H	–1.24191	3.700945	2.413792
C	–3.98753	3.157549	–0.79577
H	–3.82624	2.545790	–1.69528
H	–4.99671	3.576233	–0.88457
H	–3.96613	2.516518	0.090705
C	–1.96406	1.701061	5.195391
H	–2.18102	0.639753	5.370765
H	–2.80699	2.295389	5.570623
H	–1.07053	1.968149	5.770756
C	6.549178	0.592624	1.156038
H	7.225387	1.319903	0.693247
H	7.161071	–0.14138	1.691675
H	5.921543	1.118466	1.884811
C	–3.05166	5.181980	–1.97329
H	–2.36431	6.033684	–1.91515
H	–4.07262	5.566821	–2.09158
H	–2.7952	4.592015	–2.86196

$[(^{t\text{Bu}}\text{dmx})\text{Fe}_2(\mu\text{-OH})(\text{thf})_2]^+$ (**4**)

E = −2983.86526288 a.u.

G = −2982.765575 a.u.

Charge = +1, Multiplicity = 9

Fe	1.674618	1.744587	0.318941
Fe	1.674685	–1.74454	–0.31902
O	2.552551	0.000054	–0.00012
H	3.527737	0.000078	–0.00013
O	2.376717	3.606866	0.941420
O	2.376763	–3.6068	–0.94158
O	–3.15133	–0.000062	–0.000062
N	0.085936	–1.77279	–1.56501
N	0.737628	2.393363	–1.36236
N	0.085973	1.772775	1.565050
N	0.737847	–2.39332	1.362346
C	–1.20932	–2.01988	–1.03971
C	–1.20934	2.019765	1.039861
C	–2.12515	–2.11739	–2.14317
H	–3.18525	–2.3095	–2.0637
C	–1.54998	2.176884	–0.32422
C	–3.02336	–2.27513	0.593635
C	–0.6804	2.306817	–1.42993
C	–3.84598	1.159995	–0.33231
C	–1.54985	–2.17689	0.324414
C	–0.68017	–2.30673	1.430056
C	–3.02351	2.275124	–0.59332
C	1.141058	1.535593	3.885984
C	–5.24684	1.202538	–0.40135
C	–0.02443	–1.71911	–2.92752

C	–3.84589	–1.16008	0.332490	C	1.550397	2.929659	4.442429
C	–0.02429	1.718989	2.927569	H	1.867076	3.590915	3.630033
C	0.087343	–2.75492	3.531561	H	2.384809	2.821776	5.147871
H	0.152115	–2.96167	4.589512	H	0.712911	3.404346	4.967201
C	–1.38888	1.935596	3.314132	C	3.715998	4.097774	1.378319
H	–1.76463	1.950555	4.326820	H	4.365028	4.122663	0.497064
C	1.193473	–2.68798	2.618503	H	4.104084	3.385957	2.110750
C	1.193131	2.688098	–2.61854	C	–5.8274	2.419836	–0.81719
C	–1.07482	–2.5126	2.796034	H	–6.90806	2.500264	–0.88934
H	–2.08936	–2.4837	3.165347	C	2.353086	0.883890	3.192355
C	–6.11804	–0.00016	–0.000021	H	2.066151	–0.05425	2.714392
C	2.630950	–3.07275	2.948615	H	3.139244	0.681426	3.929783
C	–1.07519	2.512803	–2.79585	H	2.793862	1.541114	2.432966
H	–2.08977	2.483958	–3.16506	C	–1.38902	–1.93591	–3.31397
C	–2.12511	2.117090	2.143398	H	–1.76484	–1.95099	–4.32663
H	–3.18524	2.309082	2.064018	C	2.953928	–2.73025	4.425213
C	–3.6338	–3.46602	1.014848	H	2.832588	–1.65971	4.620903
H	–3.018	–4.33626	1.219754	H	3.991533	–3.00743	4.649011
C	–3.63404	3.466057	–1.01427	H	2.306270	–3.28034	5.116844
H	–3.01828	4.336357	–1.21907	C	2.630577	3.072846	–2.94881
C	0.704904	0.627929	5.066346	C	1.382478	4.729432	0.958423
H	–0.12277	1.072198	5.630360	H	0.708267	4.551039	1.800760
H	1.545855	0.490580	5.758329	H	0.828714	4.671542	0.019888
H	0.388234	–0.35484	4.702362	C	–5.03564	–3.5356	1.137313
C	–5.24674	–1.20268	0.401658	H	–5.50596	–4.45956	1.459370
C	2.953398	2.730307	–4.42543	C	2.352892	–0.8839	–3.1925
H	2.832057	1.659759	–4.62107	H	2.065990	0.054194	–2.71443
H	3.990973	3.007493	–4.64935	H	3.138964	–0.68136	–3.92999
H	2.305653	3.280358	–5.11701	H	2.793763	–1.54117	–2.43321
C	3.679039	–2.38917	2.040494	C	3.452287	5.499233	1.946891
H	3.526544	–2.65034	0.988690	H	4.322461	6.151035	1.830497
H	4.680439	–2.74127	2.317284	H	3.201582	5.443995	3.011667
H	3.657949	–1.30171	2.140737	C	0.086906	2.755130	–3.53148
C	1.140806	–1.53558	–3.88604	H	0.151577	2.961941	–4.58943

C	–5.82722	–2.41993	0.817756
H	–6.90787	–2.50039	0.889977
C	–5.03589	3.535599	–1.13661
H	–5.50627	4.459591	–1.45848
C	2.745441	–4.61555	2.752729
H	2.030586	–5.14508	3.393375
H	3.758325	–4.95292	3.008329
H	2.541427	–4.88588	1.711350
C	2.232998	5.992649	1.127741
H	1.680968	6.783148	1.643635
H	2.557216	6.376456	0.154025
C	–7.01614	0.411477	1.203631
H	–6.40023	0.703005	2.062197
H	–7.66228	–0.41963	1.507444
H	–7.65954	1.256928	0.936125
C	0.704479	–0.6278	–5.06626
H	–0.12328	–1.07201	–5.63019
H	1.545329	–0.49038	–5.75835
H	0.387864	0.354939	–4.70213
C	3.678768	2.389308	–2.04078
H	3.526420	2.650545	–0.98898
H	4.680138	2.741361	–2.31773
H	3.657637	1.301835	–2.14096
C	1.550126	–2.92957	–4.44268
H	1.866939	–3.5909	–3.63039
H	2.384442	–2.82159	–5.14822
H	0.712592	–3.40424	–4.96739
C	–7.01543	–0.41204	–1.20413
H	–7.66158	0.418930	–1.50832
H	–7.65878	–1.25762	–0.93691
H	–6.39902	–0.70347	–2.06236
C	2.745087	4.615657	–2.75298
H	2.030173	5.145169	–3.39358
H	3.757948	4.953017	–3.00869
H	2.541172	4.886018	–1.71159
C	1.382526	–4.72937	–0.95854
H	0.708292	–4.55099	–1.80087
H	0.828787	–4.67147	–0.01999
C	3.716029	–4.0977	–1.37852
H	4.365091	–4.12258	–0.49729
H	4.104086	–3.38589	–2.11098
C	3.452303	–5.49917	–1.94707
H	4.322485	–6.15097	–1.8307
H	3.201559	–5.44395	–3.01184
C	2.233047	–5.99258	–1.12787
H	1.681006	–6.7831	–1.64373
H	2.557301	–6.37637	–0.15415

[($^{t\text{Bu}}$dmx)Fe_2(μ-O)] (**3**)

E = −2518.43671246 a.u.

G = −2517.574964 a.u.

Charge = 0, Multiplicity = 9

Fe	2.042842	0.847240	1.279186
O	–2.68616	–0.000012	0.000022
O	3.073001	0.000008	–0.000044
N	1.186255	2.663094	1.039236
N	0.580503	0.138543	2.481278
C	–1.63831	–0.20705	3.036343
H	–2.71084	–0.08643	3.087400
C	0.507724	–0.90559	3.355439
C	–0.86294	–1.14151	3.720333
H	–1.21099	–1.90309	4.403723
C	3.153173	4.198902	0.553260
C	–3.38527	1.015717	0.658619
C	–3.20604	3.050689	1.954022
H	–2.59879	3.777429	2.484241
C	–4.78793	1.092163	0.640682
C	–0.59214	3.897278	0.232705
H	–1.5981	4.193829	–0.02619
C	–4.6068	3.181057	1.916640

H	–5.08671	4.026551	2.399704	H	3.645514	3.634706	–1.51115
C	1.673976	3.830816	0.516978	H	3.823426	2.298462	–0.35727
C	–5.38283	2.200515	1.279685	C	–0.74327	0.609523	2.260518
H	–6.46449	2.296154	1.284808	C	–1.10435	1.727984	1.477459
C	1.681917	–1.70863	5.410979	C	–0.2286	2.683081	0.907072
H	1.790057	–0.68839	5.800352	C	–2.57877	1.956521	1.336480
H	2.516055	–2.31396	5.788983	N	1.186241	–2.66309	–1.03927
H	0.749939	–2.12893	5.805955	N	0.580431	–0.13853	–2.4813
C	–5.65786	–0.000015	0.000057	C	–1.63841	0.207034	–3.03631
C	–6.55614	0.635574	–1.10236	H	–2.71093	0.086398	–3.08734
H	–7.20332	1.410605	–0.6769	C	0.507612	0.905612	–3.35545
H	–7.19874	–0.12224	–1.56388	C	–0.86306	1.141512	–3.72031
H	–5.93985	1.091019	–1.88614	H	–1.21114	1.903105	–4.40367
C	1.693776	–1.71026	3.856537	C	3.153171	–4.19893	–0.5533
C	3.732103	3.918019	1.967004	C	–3.38529	–1.01574	–0.65856
H	3.150227	4.433165	2.741445	C	–3.20608	–3.05071	–1.95397
H	4.770671	4.269473	2.017250	H	–2.59884	–3.77745	–2.48421
H	3.733097	2.846209	2.197008	C	–4.78794	–1.09219	–0.6406
C	0.588275	4.615466	0.004897	C	–0.59214	–3.89729	–0.23273
H	0.674849	5.584330	–0.46388	H	–1.5981	–4.19385	0.026186
C	3.041494	–1.13525	3.372023	C	–4.60684	–3.18108	–1.91656
H	3.123621	–1.14282	2.279231	H	–5.08676	–4.02658	–2.39961
H	3.864101	–1.74843	3.760605	C	1.673975	–3.83082	–0.51703
H	3.189782	–0.11104	3.740237	C	–5.38285	–2.20054	–1.27959
C	3.325798	5.704698	0.237555	H	–6.46452	–2.29618	–1.28468
H	2.959685	5.946258	–0.76776	C	1.681739	1.708712	–5.411
H	4.389542	5.969229	0.279510	H	1.789929	0.688481	–5.80039
H	2.787423	6.329336	0.961411	H	2.515837	2.314088	–5.78902
C	1.532840	–3.17044	3.345999	H	0.749731	2.128967	–5.80596
H	0.616532	–3.62402	3.742282	C	–6.5561	–0.63561	1.102508
H	2.386363	–3.77992	3.671035	H	–7.20328	–1.41065	0.677070
H	1.476258	–3.19868	2.253608	H	–7.19869	0.122205	1.564041
C	3.957108	3.376927	–0.49397	H	–5.93978	–1.09105	1.886267
H	5.026187	3.608389	–0.39479	C	1.693627	1.710328	–3.85656

C	3.732144	–3.91814	–1.96705
H	3.150227	–4.43324	–2.74148
H	4.770677	–4.2697	–2.01727
H	3.733261	–2.84634	–2.19708
C	0.588283	–4.61547	–0.00493
H	0.674871	–5.58432	0.463859
C	3.041380	1.135372	–3.37208
H	3.123507	1.142892	–2.27929
H	3.863948	1.748629	–3.76063
H	3.189731	0.111198	–3.74035
C	3.325741	–5.70472	–0.23753
H	2.959579	–5.94623	0.767781
H	4.389479	–5.96928	–0.27944
H	2.787375	–6.32937	–0.96138
C	1.532633	3.170500	–3.34601
H	0.616311	3.624048	–3.7423
H	2.386136	3.780016	–3.67104
H	1.476044	3.198725	–2.25362
C	3.957119	–3.37695	0.493917
H	5.026191	–3.60846	0.394757
H	3.645500	–3.63469	1.511095
H	3.823481	–2.29849	0.357188
C	–0.74333	–0.60953	–2.26052
C	–1.10438	–1.728	–1.47746
C	–0.22861	–2.68309	–0.90709
C	–2.5788	–1.95654	–1.33644
Fe	2.042807	–0.84723	–1.27925

($^{t\text{Bu}}$dmx)Fe$_2$(μ-O)(thf)$_2$ (**3a**)

E = −2983.37141801 a.u.
G = −2982.287126 a.u.
Charge = 0, Multiplicity = 9

Fe	–1.77405	1.605064	–0.30623
Fe	–1.71329	–1.65488	0.294292
O	–2.58295	–0.04193	–0.01686
O	–2.41863	3.572097	–0.96836
O	–2.31213	–3.63576	0.960313
O	3.138393	0.044393	–0.00196
N	–0.08696	–1.74727	1.571046
N	–0.79785	2.388111	1.355348
N	–0.14138	1.743150	1.568898
N	–0.6995	–2.42308	1.356328
C	1.214635	–1.97803	1.059718
C	1.147610	2.014088	–1.04411
C	2.129704	–2.05314	2.169640
H	3.193508	–2.22892	2.097471
C	1.486540	2.182049	0.318242
C	3.047822	–2.23942	–0.551
C	0.618762	2.304104	1.424467
C	3.807561	1.217342	0.328403
C	1.569323	–2.15232	–0.29806
C	0.716133	–2.31078	–1.41039
C	2.959762	2.314498	0.583588
C	–1.17825	1.502923	–3.90374
C	5.207641	1.288301	0.398378
C	0.014305	–1.68336	2.930615
C	3.853160	–1.10829	–0.308
C	–0.02771	1.697550	–2.9277
C	–0.01029	–2.80158	–3.51524
H	–0.06037	–3.02172	–4.57191
C	1.336579	1.942975	–3.31661
H	1.710642	1.969488	–4.33044
C	–1.13089	–2.73831	–2.61167
C	–1.25063	2.681316	2.608531
C	1.136814	–2.53006	–2.77004
H	2.156055	–2.48639	–3.12556
C	6.102477	0.100596	0.002233
C	–2.55846	–3.13803	–2.96571
C	1.019028	2.516435	2.791021
H	2.034811	2.489472	3.157995

C	2.067697	2.134419	–2.14631	H	1.749963	–1.87663	4.349058
H	3.123946	2.347400	–2.06401	C	–2.88652	–2.7263	–4.42403
C	3.680273	–3.42885	–0.94163	H	–2.81812	–1.64141	–4.55115
H	3.078344	–4.31175	–1.1337	H	–3.90835	–3.04008	–4.67343
C	3.546676	3.520222	0.995477	H	–2.20702	–3.19948	–5.14234
H	2.911821	4.377555	1.197052	C	–2.6898	3.054262	2.945371
C	–0.73079	0.550150	–5.04437	C	–1.39323	4.656067	–0.97623
H	0.121340	0.958573	–5.6001	H	–0.7165	4.462571	–1.81416
H	–1.55692	0.405819	–5.75352	H	–0.84551	4.576672	–0.03578
H	–0.44368	–0.42562	–4.63955	C	5.084455	–3.48008	–1.05358
C	5.255071	–1.12899	–0.36866	H	5.570664	–4.40377	–1.35285
C	–3.01805	2.662725	4.408978	C	–2.39998	–0.94458	3.205531
H	–2.91444	1.583484	4.560367	H	–2.16558	–0.01068	2.692757
H	–4.05197	2.947284	4.642922	H	–3.18259	–0.75681	3.952132
H	–2.36155	3.173988	5.122621	H	–2.81582	–1.63575	2.465293
C	–3.61591	–2.52355	–2.02262	C	–3.4222	5.501997	–1.97878
H	–3.49871	–2.90428	–1.00451	H	–4.27296	6.181669	–1.87401
H	–4.61852	–2.80669	–2.36998	H	–3.15975	5.437200	–3.04082
H	–3.55117	–1.43398	–1.97813	C	–0.14222	2.756934	3.525670
C	–1.15312	–1.53035	3.893884	H	–0.20853	2.964910	4.583834
C	–1.54304	2.887549	–4.51376	C	5.857532	2.345516	–0.75493
H	–1.86498	3.577995	–3.72724	H	6.939864	–2.41031	–0.82056
H	–2.36358	2.776488	–5.23565	C	4.947378	3.621419	1.115560
H	–0.68354	3.330186	–5.03193	H	5.397906	4.558106	1.429892
C	–3.73164	4.107869	–1.41117	C	–2.64141	–4.69096	–2.85119
H	–4.39051	4.156669	–0.53701	H	–1.92881	–5.17558	–3.52992
H	–4.14448	3.411042	–2.145	H	–3.65342	–5.03409	–3.10562
C	5.763059	2.520569	0.804389	H	–2.41433	–5.00882	–1.82711
H	6.842017	2.624547	0.874493	C	–2.19521	5.952591	–1.14666
C	–2.42502	0.906504	–3.22429	H	–1.61166	6.728719	–1.65073
H	–2.1848	–0.01448	–2.6909	H	–2.51815	6.339754	–0.17312
H	–3.19223	0.692678	–3.97982	C	6.969555	0.515291	–1.22345
H	–2.86317	1.604743	–2.50388	H	6.331274	0.776797	–2.07542
C	1.382907	–1.87486	3.332433	H	7.630815	–0.30481	–1.52555

H	7.594998	1.381715	–0.98043
C	–0.74307	–0.59168	5.059350
H	0.103380	–0.99734	5.625732
H	–1.58543	–0.47206	5.753785
H	–0.46275	0.394776	4.676825
C	–3.7293	2.400463	2.007857
H	–3.60135	2.746191	0.978578
H	–4.73818	2.689695	2.331386
H	–3.65984	1.310433	2.001883
C	–1.49886	–2.9333	4.472161
H	–1.79095	–3.61558	3.667744
H	–2.33437	–2.85297	5.180906
H	–0.63907	–3.36627	4.998070
C	7.031092	–0.2687	1.196031
H	7.662148	0.582564	1.475140
H	7.690733	–1.10271	0.931663
H	6.437060	–0.56043	2.069831
C	–2.80598	4.602606	2.800396
H	–2.10461	5.115059	3.470340
H	–3.8253	4.929299	3.047038
H	–2.58381	4.904500	1.770644
C	–1.26886	–4.70198	0.959446
H	–0.59367	–4.50328	1.797619
H	–0.7245	–4.60704	0.018627
C	–3.61206	–4.19317	1.415762
H	–4.28165	–4.24223	0.549860
H	–4.02435	–3.50892	2.161636
C	–3.27758	–5.58849	1.966646
H	–4.11875	–6.27972	1.860261
H	–3.00913	–5.53088	3.027553
C	–2.04937	–6.01233	1.122433
H	–1.45083	–6.78432	1.615163
H	–2.37257	–6.39464	0.147046

($^{t\text{Bu}}$dmx)$Fe_2(\mu\text{-}O)Cl_2$ (**6**)

E = −3438.91434721 a.u.
G = −3438.052343 a.u.
Charge = 0, Multiplicity = 11

Fe	1.838903	0.810787	–1.5436
Cl	3.465240	1.109591	–3.153254
O	–2.885786	–0.000041	–0.000019
O	2.397485	–0.000084	–0.000111
N	0.264727	–0.053924	–2.401367
N	1.035108	2.563242	–1.039256
C	–3.581001	1.037961	–0.616181
C	–4.980826	1.122809	–0.588571
C	–1.010863	0.559835	–2.22025
C	1.556047	3.701030	–0.45635
C	–0.379791	2.589165	–0.848508
C	0.083871	–1.152504	–3.217912
C	–5.56103	2.266517	–1.177755
H	–6.641122	2.378516	–1.177435
C	–1.292977	–1.240536	–3.589477
H	–1.721043	–1.994252	–4.231679
C	–0.699359	3.752642	–0.082081
H	–1.691786	4.033480	0.237719
C	–5.852122	–0.000034	0.000095
C	1.167025	–2.09917	–3.709033
C	4.049344	3.093851	–0.202717
H	0.009398	2.857227	0.862459
H	0.049875	3.481768	–0.431196
H	0.929979	2.166358	–0.762222
C	1.968843	–0.188378	–2.973206
H	3.021084	0.041545	–3.048308
C	2.762030	1.985441	–1.2665
C	0.000845	4.171901	–0.582076
C	0.494186	4.442143	0.150072
H	0.607131	5.370071	0.687950
C	–1.301353	1.695767	–1.432277
C	–4.77123	3.263370	–1.774295

H	–5.242017	4.135443	–2.217026	C	0.084046	1.152553	3.217855
C	–3.371684	3.116153	–1.83186	C	–5.560947	–2.266529	1.178037
H	–2.759299	3.853631	–2.341027	H	–6.641039	–2.378535	1.177790
C	1.740945	–1.54585	–5.04694	C	–1.29279	1.240623	3.589447
H	0.952602	–1.47679	–5.806841	H	–1.720822	1.994345	4.231664
H	2.521928	–2.22252	–5.417874	C	–0.699307	–3.752605	0.082093
H	2.181463	–0.554837	–4.904346	H	–1.691744	–4.033434	–0.237683
C	3.213956	4.613648	–2.062489	C	1.167272	2.099126	3.708997
H	3.091591	3.769676	–2.746344	C	4.049417	–3.093876	0.202673
H	4.229141	5.013100	–2.182759	H	4.009402	–2.857161	–0.86248
H	2.497260	5.398088	–2.336769	H	5.049948	–3.481857	0.431047
C	–6.749543	–0.58054	–1.132343	H	3.930131	–2.166426	0.762265
H	–7.394248	0.198576	–1.553713	C	–1.968699	0.188489	2.973179
H	–7.394654	–1.37734	–0.745717	H	–3.020944	–0.041406	3.048308
H	–6.13368	–0.994451	–1.939122	C	–2.761944	–1.985431	1.266595
C	3.234705	5.399272	0.334766	C	3.000901	–4.171911	0.582025
H	2.609213	6.250533	0.041403	C	0.494229	–4.442105	–0.150102
H	4.282647	5.711590	0.255636	H	0.607156	–5.370028	–0.687993
H	3.029504	5.159955	1.385343	C	–1.301262	–1.695732	1.432303
C	2.293736	–2.274147	–2.671991	C	–4.771104	–3.263353	1.774568
H	2.888103	–1.36897	–2.537651	H	–5.241856	–4.135411	2.217364
H	2.980778	–3.058657	–3.01234	C	–3.371555	–3.116122	1.832043
H	1.880502	–2.57026	–1.706908	H	–2.759134	–3.85357	2.341210
C	0.548073	–3.498941	–3.972712	C	1.741305	0.545612	5.046773
H	0.090352	–3.902888	–3.062259	H	0.953037	1.476500	5.806748
H	1.339667	–4.186117	–4.295612	H	2.522362	2.222195	5.417707
H	–0.208929	–3.471242	–4.764179	H	2.181758	0.554594	4.904013
N	0.264857	0.053955	2.401324	C	3.214026	–4.613682	2.062427
N	1.035191	–2.563222	1.039235	H	3.091660	–3.769724	2.746299
C	–3.58096	–1.037996	0.616269	H	4.229214	–5.013129	2.182682
C	–4.980787	–1.122846	0.588763	H	2.497338	–5.398132	2.336697
C	–1.010751	–0.559774	2.220232	C	–6.749575	0.580434	1.132523
C	1.556108	–3.701012	0.456316	H	–7.394248	–0.198706	1.553896
C	–0.379714	–2.589138	0.848528	H	–7.394725	1.377200	0.745894

H	–6.133735	0.994378	1.939304
C	3.234732	–5.399273	–0.334836
H	2.609223	–6.250526	–0.041485
H	4.282668	–5.711616	–0.255714
H	3.029534	–5.159935	–1.38541
C	2.293896	2.274178	2.671870
H	2.888234	1.368997	2.537407
H	2.980982	3.058644	3.012229
H	1.880590	2.570390	1.706851
C	0.548402	3.498889	3.972912
H	0.090613	3.902971	3.062554
H	1.340058	4.185990	4.295823
H	–0.208525	3.471124	4.764447
Fe	1.839006	–0.81075	1.543520
Cl	3.465410	–1.109522	3.153110

$[(^{t\text{Bu}}\text{dmx})\text{Fe}_2(\mu\text{-OH})\text{Cl}_2]^+$ (**6a**)

E = −3439.34367578 a.u.

G = −3438.468656 a.u.

Charge = +1, Multiplicity = 11

Fe	1.798950	–0.854335	1.568382
Cl	3.413580	–1.131659	3.135223
O	–2.904643	0.015263	0.016520
O	2.623911	0.015858	0.006006
N	0.256155	0.051126	2.343695
N	1.031403	–2.559629	1.000183
C	–3.598463	–1.040537	0.600844
C	–4.996783	–1.129578	0.565470
C	–1.023611	–0.570995	2.176969
C	1.558491	–3.707963	0.420255
C	–0.387946	–2.584929	0.795275
C	0.078987	1.145247	3.184445
C	–5.571064	–2.290425	1.126384
H	–6.650278	–2.408462	1.123120
C	–1.288179	1.218738	3.566032
H	–1.715122	1.962279	4.220078
C	–0.694182	–3.739331	0.020229
H	–1.682077	–4.018062	–0.314549
C	–5.869335	0.005592	0.000621
C	1.161055	2.087790	3.681570
C	4.069338	–3.129625	0.241937
H	4.017792	–2.805825	–0.799506
H	5.059730	–3.567245	0.413675
H	3.998446	–2.25784	0.892515
C	–1.967897	0.165052	2.947665
H	–3.017785	–0.069921	3.036368
C	–2.774355	–2.001253	1.224012
C	2.994308	–4.19881	0.565595
C	0.502733	–4.433547	–0.199729
H	0.615088	–5.360221	–0.738937
C	–1.316656	–1.703801	1.386003
C	–4.776594	–3.298406	1.698795
H	–5.244591	–4.182304	2.119892
C	–3.377547	–3.149979	1.760261
H	–2.764042	–3.898689	2.251211
C	1.718092	1.536307	5.028370
H	0.922738	1.479852	5.781053
H	2.500589	2.209440	5.400760
H	2.151539	0.540209	4.901175
C	3.164274	–4.679282	2.040404
H	3.024636	–3.855256	2.745654
H	4.174322	–5.084681	2.176917
H	2.439036	–5.468249	2.273357
C	–6.750107	0.575893	1.151225
H	–7.395604	–0.205277	1.567487
H	–7.393556	1.382287	0.782320
H	–6.123671	0.974149	1.957657
C	3.231553	–5.405296	–0.378414
H	2.587125	–6.253888	–0.123106
H	4.271283	–5.737125	–0.28051

H	3.057783	–5.136176	–1.427333	C	–1.316017	1.697609	–1.399355
C	2.297433	2.252863	2.654641	C	–4.778297	3.277045	–1.760455
H	2.896535	1.347544	2.542926	H	–5.246369	4.151026	–2.201704
H	2.979909	3.042107	2.990031	C	–3.378667	3.130434	–1.813418
H	1.891887	2.537944	1.683108	H	–2.765269	3.868946	–2.319679
C	0.543867	3.490618	3.935316	C	1.716514	–1.512551	–5.011514
H	0.094128	3.894610	3.021265	H	0.907492	–1.46101	–5.749886
H	1.335052	4.175134	4.263156	H	2.504760	–2.166106	–5.405987
H	–0.21829	3.467542	4.721331	H	2.133819	–0.510615	–4.878127
N	0.269552	–0.064772	–2.325696	C	3.189768	4.697216	–2.018061
N	1.028582	2.567306	–1.01118	H	3.048708	3.883920	–2.735545
C	–3.59933	1.049488	–0.604306	H	4.207118	5.090210	–2.135681
C	–4.998169	1.131787	–0.583454	H	2.478656	5.498866	–2.250897
C	–1.017583	0.542119	–2.15523	C	–6.782363	–0.554928	–1.128916
C	1.551059	3.719297	–0.434265	H	–7.427191	0.232967	–1.532735
C	–0.393167	2.598941	–0.829053	H	–7.428865	–1.351786	–0.745404
C	0.098203	–1.178602	–3.141323	H	–6.178838	–0.962407	–1.94812
C	–5.573105	2.278782	–1.17167	C	3.224896	5.392963	0.410736
H	–6.652717	2.393851	–1.17625	H	2.590374	6.249355	0.157129
C	–1.275149	–1.289212	–3.492131	H	4.268124	5.718792	0.331766
H	–1.699993	–2.055799	–4.120258	H	3.033779	5.112080	1.453479
C	–0.708389	3.766388	–0.076764	C	2.346442	–2.247942	–2.6557
H	–1.700489	4.053612	0.237738	H	2.913362	–1.325554	–2.518863
C	1.191977	–2.093611	–3.663599	H	3.054034	–2.999702	–3.023737
C	4.054751	3.118553	–0.227042	H	1.962062	–2.577864	–1.690321
H	3.968133	2.759780	0.800459	C	0.601243	–3.505105	–3.929735
H	5.050832	3.559542	–0.350219	H	0.159884	–3.926417	–3.0199
H	4.005850	2.270912	–0.911019	H	1.404300	–4.171643	–4.26553
C	–1.96167	–0.230729	–2.890163	H	–0.162004	–3.488146	–4.714894
H	–3.016337	–0.014715	–2.969112	Fe	1.806923	0.865416	–1.571882
C	–2.774891	1.995991	–1.248117	Cl	3.410779	1.155703	–3.147025
C	2.992785	4.200157	–0.552032	H	3.603269	0.036338	0.020038
C	0.487658	4.457385	0.157242				
H	0.594655	5.388743	0.689443				

2.8.5 X-Ray Diffraction Techniques

Structures of **1–7** were collected on a Bruker three-circle platform goniometer equipped with an Apex II CCD and an Oxford cryostream cooling device. Radiation was from a graphite fine focus sealed tube Mo Kα (0.71073 Å) source. Crystals were mounted on a cryoloop or glass fiber pin using Paratone N oil. Structures were collected at 100 K. Data were collected as a series of φ and/or ω scans.

Data were integrated using SAINT[53] and scaled with either a numerical or multi-scan absorption correction using SADABS.[53] The structures were solved by intrinsic phasing, direct methods or Patterson maps using SHELXS-2014[54] and refined against F^2 on all data by full matrix least squares with SHELXL-2014.[54] All non-hydrogen atoms were refined anisotropically. Hydrogen atoms were placed at idealized positions and refined using a riding model. The isotropic displacement parameters of all hydrogen atoms were constrained to be 1.2 times the parameter of the atoms they were linked to (1.5 times for methyl groups). Further details on particular structures are noted below.

($^{t\text{Bu}}$dmx)Fe$_2$(Mes)$_2$ (1): The structure was solved in the triclinic space group $P\bar{1}$ with two molecules per unit cell and one molecule in the asymmetric unit. The asymmetric unit contained several strongly disordered hexanes molecules. Due to apparent low occupancy and high disorder, an acceptable model could not be refined. A solvent mask was applied in Platon to reduce unrefined electron density. (CCDC 1554783)

[53] APEX2 Software Suite; Bruker AXS: Madison, WI, 2009.

[54] Sheldrick, G. M. *Acta Crystallogr., Sect. A: Found. Crystallogr.* **2008**, *64*, 112–122.

Table 2.10. Bond metrics for **2**-**7**.

Complex	Fe–Fe (Å)	Fe–O (Å)	< Fe–O(H)–Fe (°)
($^{t\text{Bu}}$dmx)Fe_2(μ-OH)(Mes)(thf) (**2**)	3.7427(13)	2.045(4), 1.942(4)	139.7(2)
($^{t\text{Bu}}$dmx)Fe_2(μ-O) (**3**)	3.0425(10)	1.7941(17)	116.00(14)
[($^{t\text{Bu}}$dmx)Fe_2(μ-OH)(thf)$_2$][BPh_4] (**4**)	3.5933(6)	1.969(2), 1.957(2)	132.49(12)
[Et_4N][($^{t\text{Bu}}$dmx)Fe_2(μ-OH)Cl_2] (**5b**)	3.9767(12)	1.991(5), 1.999(5)	144.20(17)
($^{t\text{Bu}}$dmx)Fe_2(μ-O)Cl_2 (**6**)	3.5244(17)	1.7734(10)	167.1(3)
[Cp_2Co][($^{t\text{Bu}}$dmx)Fe_2(μ-O)Cl_2] **(7)**	3.5616(7)	1.8034(15), 1.8928(15)	148.98(10)

($^{t\text{Bu}}$dmx)Fe_2(μ-OH)(Mes)(thf) (2): The structure was solved in the monoclinic space group $P2_1/n$ with four molecules per unit cell and one molecule in the asymmetric unit. Several disordered diethyl ether solvent molecules were modeled with similarity constraints. (CCDC 1554784)

($^{t\text{Bu}}$dmx)Fe_2(μ-O) (3): The structure was solved in the monoclinic space group $C2/c$ with four molecules per unit cell and half a molecule in the asymmetric unit. (CCDC 1554786)

[($^{t\text{Bu}}$dmx)Fe_2(μ-OH)(thf)$_2$][BPh_4] (4): The structure was solved in the monoclinic space group $P2_1/c$ with four molecules per unit cell and one molecule in the asymmetric unit. Several disordered tetrahydrofuran solvent molecules were modeled with similarity constraints. (CCDC 1554785)

[Et_4N][($^{t\text{Bu}}$dmx)Fe_2(μ-OH)Cl_2] (5b): The structure was solved in the monoclinic space group *Cc* with four molecules per unit cell and one molecule in the asymmetric unit. Several disordered tetrahydrofuran solvent molecules were modeled with similarity restraints. (CCDC 1554789)

($^{t\text{Bu}}$dmx)Fe_2(μ-O)Cl_2 (6): The structure was solved in the monoclinic space group $C2/c$ with four molecules per unit cell and half a molecule in the asymmetric unit. (CCDC 1554787)

[Cp$_2$Co][($^{t\text{Bu}}$dmx)Fe$_2$(μ-O)Cl$_2$] (7): The structure was solved in the monoclinic space group $P2_1/n$ with four molecules per unit cell and one molecule in the asymmetric unit. (CCDC 1554788)

Table 2.11. X-Ray Diffraction Experimental Details for **1**-**4**.[a]

	($^{t\text{Bu}}$dmx)Fe$_2$(Mes)$_2$ (1)	($^{t\text{Bu}}$dmx)Fe$_2$(μ-OH)(Mes)(thf) (2)	($^{t\text{Bu}}$dmx)Fe$_2$(μ-O) (3)	[($^{t\text{Bu}}$dmx)Fe$_2$(μ-OH)(thf)$_2$][BPh$_4$] (4)
Moiety Formula	$C_{67}H_{78}Fe_2N_4O$	$C_{62}H_{76}Fe_2N_4O_3$; 1.677($C_4H_{10}O$)	$C_{49}H_{56}Fe_2N_4O_2$	$C_{57}H_{73}Fe_2N_4O_4$·($C_{24}H_{20}B$); 3.5(C_4H_8O)
FW	1067.03	1161.27	844.68	1561.46
λ (nm)	0.71073	0.71073	0.71073	0.71073
***T* (K)**	100(2)	100(2)	100(2)	100(2)
Crystal System	triclinic	monoclinic	monoclinic	monoclinic
Space Group (*Z*)	$P\bar{1}$ (2)	$P2_1/n$ (4)	*C*2/c (4)	$P2_1/c$ (4)
***a* (Å)**	12.6756(9)	17.416(3)	19.775(2)	18.8507(10)
***b* (Å)**	13.0518(8)	15.512(2)	12.6596(14)	21.1660(11)
***c* (Å)**	21.4971(15)	24.559(4)	18.9582(17)	21.1905(11)
α (°)	80.777(2)	90	90	90
β (°)	87.931(2)	106.397(3)	115.027(3)	95.0550(10)
γ (°)	73.976(2)	90	90	90
Volume (Å^3)	3374.0(4)	6364.9(17)	4300.5(8)	8422.0(8)
Calc. ρ (mg/m^3)	1.050	1.212	1.305	1.231
μ (mm^{-1})	0.469	0.506	0.718	0.403
Crystal Size (mm)	0.20×0.10×0.07	0.11×0.06×0.02	0.09×0.03×0.02	0.22x0.14x0.03
Reflections	12034	11474	3827	14924
Completeness (to 2θ)	99.0% 25.19°	98.9% 25.20°	99.4% 25.11	99.9% 25.06°
GOF on F^2	1.028	0.981	1.048	1.029
R1, *w*R2[a] [$I > 2\sigma(I)$]	0.0409, 0.1001	0.0836, 0.1915	0.0551, 0.1094	0.0543, 0.1574
(R1, *w*R2) [all data]	0.0623, 0.0924	0.2133, 0.1477	0.0999, 0.0959	0.0894, 0.1386

[a] $R1 = \sum||F_o| - |F_c||/\sum|F_o|$, $wR2 = \{\sum[w(F_o^2 - F_c^2)^2]/\sum[w(F_o^2)^2]\}^{1/2}$

Table 2.12. X-ray diffraction experimental details for **5**-**7**.[a]

	[Et$_4$N][($^{t\text{Bu}}$dmx)Fe$_2$(μ-OH)Cl$_2$] (5b)	**($^{t\text{Bu}}$dmx)Fe$_2$(μ-O)Cl$_2$ (6)**	**[Cp$_2$Co][($^{t\text{Bu}}$dmx)Fe$_2$(μ-O)Cl$_2$] (7)**
Moiety Formula	$C_{49}H_{57}Cl_2Fe_2N_4O_2 \cdot (C_8H_{20}N)$; $2(C_4H_8O)$	$C_{49}H_{56}Cl_2Fe_2N_4O_2$	$C_{49}H_{56}Cl_2Fe_2N_4O_2 \cdot (C_{10}H_{10}Co)$; (C_4H_8O)
FW	1189.02	915.58	1176.79
λ (nm)	0.71073	0.71073	0.71073
***T* (K)**	100(2)	100(2)	100(2)
Crystal System	monoclinic	monoclinic	monoclinic
Space Group (*Z*)	*C*c	*C*2/c (4)	$P2_1$/n (4)
***a* (Å)**	19.2846(13)	19.178(3)	12.7553(7)
***b* (Å)**	12.6737(9)	13.2068(14)	25.2117(13)
***c* (Å)**	26.2797(18)	20.033(3)	17.9429(10)
α (°)	90	90	90
β (°)	102.8790(10)	118.6000	92.873(1)
γ (°)	90	90	90
Volume (Å^3)	6261.4(7)	4454.9(11)	5762.9(5)
Calc. ρ (mg/m^3)	1.261	1.365	1.356
μ (mm^{-1})	0.598	0.815	0.923
Crystal Size (mm)	0.11x0.08x0.04	0.12×0.08×0.07	0.12×0.11×0.04
Reflections	10845	3963	10211
Completeness (to 2θ)	99.9% 25.04°	99.8% 25.11°	99.8% 25.05°
GOF on F^2	1.018	1.027	1.011
R1, *w*R2[a] [$I > 2\sigma(I)$]	0.0450, 0.0956	0.0717, 0.1862	0.0328, 0.0872
(R1, *w*R2) [all data]	0.0612, 0.0895	0.1298, 0.1593	0.0475, 0.0829

[a] $R1 = \sum\big||F_o| - |F_c|\big| / \sum|F_o|$, $wR2 = \{\sum[w(F_o^2 - F_c^2)^2] / \sum[w(F_o^2)^2]\}^{1/2}$

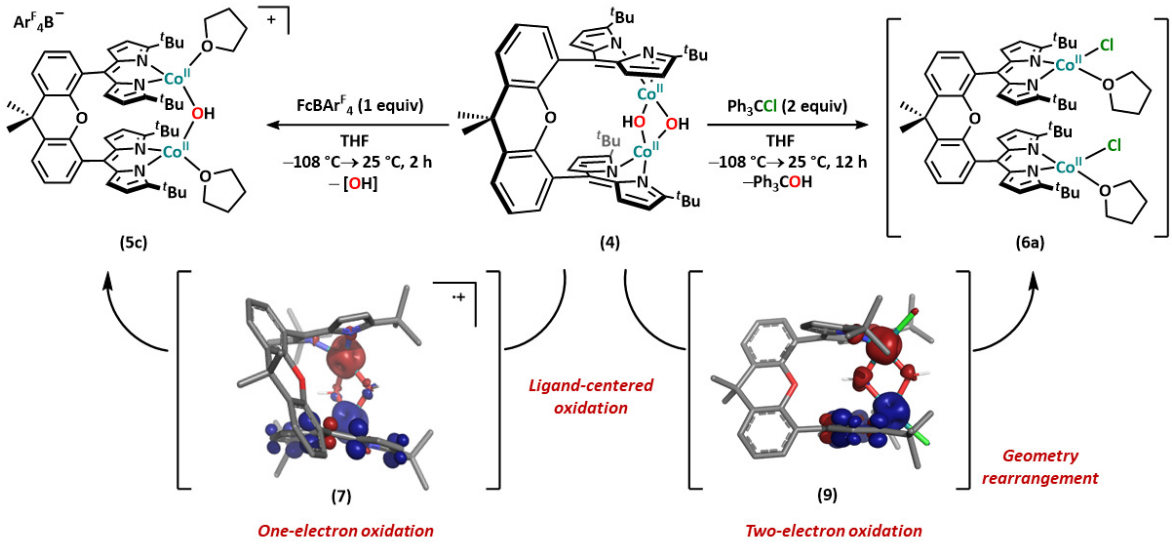

Chapter 3: Redox-Triggered Hydroxide Release from a Dicobalt Bis-Hydroxo Complex

3.1 Introduction

Polynuclear active sites are commonly employed by enzymes to promote cooperative redox chemistry. One specific class involves bimetallic active sites,[1] in which two metal centers are poised to facilitate a variety of important functions, such as promoting catalytic C–H functionalization by the diiron active site of sMMO or activating dioxygen for the reduction of ribonucleotides to the corresponding deoxyribonucleotides by diiron RNR.[2] Albeit less common in naturally occurring enzymes, dicobalt units have been studied in recent years in substituted active sites and model systems given the excellent spectroscopic handle provided by cobalt.

[1] (a) Vigato, P. A. ; Tamburini, S.; Fenton, D. E. *Coord. Chem. Rev.* **1990**, *106*, 25–170. (b) van den Beuken, E. K.; Feringa, B. L. *Tetrahedron* **1998**, *54*, 12985–13011.

[2] Tshuva, E. Y. Lippard, S. J. *Chem. Rev.* **2004**, *104*, 987–1012.

Examples include cobalt-MetAP, an enzyme responsible for cleaving key amino acid residues for protein maturation,[3,4,5] and cobalt-GpdQ, a metallophosphatase capable of hydrolyzing all three types of phosphate esters,[6] which are fully active in the dicobalt form and have been explored to better understand the electronic structure and communication between bimetallic units in such enzymes (**Figure 3.1**).[4,5] In each of these systems, the metal centers are able to communicate via hydroxo and carboxylate bridges that hold the metals in proximity. As such, bioinspired synthetic systems featuring dicobalt μ-hydroxo, oxo, and/or carboxylato ligands have been targeted to model and harness the reactivity of such active sites.[5,7,8,9] Furthermore, dicobalt complexes have been explored as molecular models of cobalt-oxo clusters shown to perform water oxidation catalysis.[(20-24)] Within these examples, as well as others with applications in coordination chemistry and catalysis, a plethora of highly-coordinated cobalt systems have been isolated, with

[3] Roderick, S. L.; Matthews, B. W. *Biochemistry* **1993**, *32*, 3907–3912.

[4] Lowther, W. T.; Orville, A. M.; Madden, D. T.; Lim, S.; Rich, D. H.; Matthews, B. W. *Biochemistry* **1999**, *38*, 7678–7688.

[5] Johansson, F. B.; Bond, A. D.; Nielson, U. G.; Moubaraki, B.; Murray, K. S.; Berry, K. J.; Larrabee, J. A.; McKenzie, C. J. *Inorg. Chem.* **2008**, *47*, 5079–5092.

[6] Hadler, K. S.; Tanifum, E. A.; Yip, S. H.-C.; Mitic, N.; Guddat, L. W.; Jackson, C. J.; Gahan, L. R.; Nguyen, K.; Carr, P. D.; Ollis, D. L.; Hengge, A. C.; Larrabee, J. A.; Schenk, G. *J. Am. Chem. Soc.***2008**, *130*, 14129–14138.

[7] Larrabee, J. A.; Johnson, W. R.; Volwiler, A. S. *Inorg. Chem.* **2009**, *48*, 8822–8829.

[8] (a) Vaiana, L.; Platas-Iglesias, C.; Esteban-Gómez, D.; Avecilla, F.; Clemente-Juan, J. M.; Real. J. A.; de B;as, A.; Rodríguez-Blas, T. *Dalton Trans.* **2005**, 2031–2037. (b) Singh, U. P.; Babbar, P.; Sharma, A. K. *Inorg. Chim. Acta*. **2005**, 358, 271–278. (c) Saunders, L. N.; Pratt, M. E.; Hann, S. E.; Dawe, L. N; Decken, A.; Kerton, F. M.; Kozak, C. M. *Polyhedron* **2012**, *46*, 53–65. (d) He, C.; Lippard, S. J. *J. Am. Chem. Soc.* **1998**, *120*, 105–113. (e) Moro-Oka, Y. *Proc. Indian Acad Sci. (Chem. Sci.)* **1999**, *111*, 413–424. (f) Qian, J.; Ma, X.; Tian, J.; Gu, W.; Shang, J.; Liu, X.; Yan, S. *J. Inorg. Biochem.* **2010**, *104*, 993–999. (g) .Hikichi, S.; Yoshizawa, M.; Sasakura, Y.; Komatsuzaki, H.; Moro-Oka, Y.; Akita, M. *Chem. Eur. J.* **2011** *7*, 5011–5028.

[9] (a) Jaynes, B. S.; Doerrer, L. H.; Liu, S.; Lippard, S. J. *Inorg. Chem.* **1995**, ***34***, 5735–5744 (b) Larsen, P. L.; Parolin, T. J.; Powell, D. R.; Hendrich, M. P; Borovik, A. S. *Angew. Chem. Int. Ed.* **2003**, *42*, 85–89. (c) Engelmann, X.; Yao, S.; Farquhar, E. R.; Szilvási, T. Kuhlmann, U.; Hildebrandt, P.; Driess, M.; Ray, K. *Angew. Chem. Int. Ed.* **2017**, *56*, 297–301. (d) DeRosha, D. E.; Mercado, B. Q.; Lukat-Rodgers, G.; Rodgers, K. R.; Holland, P. L. *Angew. Chem. Int. Ed.* **2017**, *56*, 3211–3215.

greater than 140 structurally characterized five- or six-coordinate complexes reported,[5,8,10,11,12] while far fewer examples of low coordinate dicobalt (hydr)-oxo complexes have been synthesized.[9,11,13] (38-44)

Inspired by the previous study exhibiting the capability of the Pacman dippyrin system to support low-coordinate, high-spin diiron μ-(hydr)oxo complexes in multiple oxidation states, we sought to prepare analogous dicobalt complexes and examine how the high-spin and low coordination environment impacts their reactivity. Furthermore, we were interested in investigating the effect of metal identity on the ensuing reactivity of such bimetallic μ-hydroxo

[10] (a) Dimitrou, K.; Folting, K,; Streib, W. E.; Christou, G. *J. Am. Chem. Soc.* **1993**, *115*, 6432–6433. (b) Davenport, T. C.; Ahn, H. S.; Ziegler, M. S.; Tilley, T. D. *Chem. Commun.* **2014**, *50*, 6326–6329. (c) Ishizuka, T.; Watanabe, A.; Kotani, H.; Hong, D.; Satonaka, K.; Wada, T.; Shiota, Y.; Yoshizawa, K.; Ohara, K.; Yamaguchi, K.; Kato, S.; Fukuzumi,S.; Kojima, T. *Inorg. Chem.* **2016**, *55*, 1154–1164. (d) Ullman, A. M.; Brodsky, C. N.; Li, N.; Zheng, S.-L.; Nocera, D. G. *J. Am. Chem. Soc.* **2016**, *138*, 4229–4236. (e) Brodsky, C. N.; Passard, G.; Ullman, A. M.; Jaramillo, D. E.; Bloch, E. D.; Huynh, M.; Gygi, D.; Costentin, C.; Nocera, D. G. *Dalton Trans.* **2018**, *47*, 11903–11908. (f) Mikuriya, M.; Kida, S.; Kohzuma, T.; Murase, I. *Bull. Chem. Soc. Jpn.* **1998**, 61, 2666–2668. (g) Hemmert, C.; Gornitzka, H.; Meunier, B. *New J. Chem.* **2000,** *24*, 949–951. (h) Zinn, P. J.; Sorrell, T. N.; Powell, D. R.; Day, V. W.; Borovik, A. S. *Inorg. Chem.* **2007**, *46*, 10120–10132.

[11] Volpe, M.; Hartnett, H.; Leeland, J. W.; Wills, K.; Ogunshun, M.; Duncombe, B. J.; Wilson, C.; Blake, A. J.; McMaster, J.; Love, J. B. *Inorg. Chem.* **2009**, *48*, 5195–5207.

[12] (a) Kon, H.; Nagata, T. *Dalton Trans.* **2013**, *42*, 5697–5705. (b) Reger, D. L.; Pascui, A. E.; Foley, E. A.; Smith, M. D..; Jeziershka, J.; Ozarowski, A. *Inorg. Chem.* **2014**, *53*, 1975–1988. (c) Di Giovanni, C.; Gimbert-Suriñach, C.; Nippe, M.; Benet-Buchholz, J.; Long, J. R.; Sala, X.; Llobert, A. *Chem. Eur. J.* **2016**, *22*, 361–369. (d) Mealli, C.; Midollini, S.; Sacconi, L. *Inorg. Chem.* **1975**, *14*, 2513–2521. (e) Thompson, L. K.; Niel, V.; Grove, H.; Miller, D. O.; Newlands, M. J.; Bird, P. H.; Wickramasinghe, W. A.; Lever, A. B. P. *Polyhedron* **2004**, *23*, 1175–1184. (f). Prikhod'ko, A.; Pointillart, F.; Golhen, S.; Gayrilenko, K. S.; Ouahab, L.; Kolotilov, S. V. *New J. Chem.* **2012**, *36*, 2070–2077. (g) Cappelli, C.; Duce, C.; Formica, M.; Fusi, V.; Ghezzi, L.; Giorgi, L.; Micheloni, M.; Paoli, P.; Rossi, P.; Tiné, M. R. *Inorg. Chim. Acta* **2014** *417*, 230–238. (h) Song, J.-F.; Wang, J.; Li, S.-Z.; Li, Y.; Zhou, R.-S. **2017** *1129*, 1–7. (i) *Selected examples of the >140 structurally characterized five- or six-coordinate complexes referenced above. Remaining examples can be found at:* Groom, C. R.; Bruno, I. J.; Lightfoot, M. P.; Ward, S. C. The Cambridge Structural Database. *Acta. Cryst.* **2016**, *B72*, 171–179.

[13] (a) Roy, L.; Al-Afyouni, M. H.; DeRosha, D. E.; Mondal, B.; DiMucci, I. M.; Lancaster, K. M.; Shearer, J.; Bill, E.; Brennessel, W. W.; Neese, F.; Ye, S.; Holland, P. L. *Chem. Sci.* **2019**, *10*, 918–929. (b) Khandar, A. A.; Kirschbaum, K.; Abedi, M.; Mock, K.; Tracy, G.; Spasojevic, V.; Hosseini-Yazdi, S. A. *New J. Chem.* **2015**, *39*, 2822–2831. (c) Dai, X.; Kapoor, P.; Warren, T. H. *J. Am. Chem. Soc.* **2004**, *126*, 4798–4799. (d) Sushev, V. V.; Kornev, A. N.; Min'ko, Y. A.; Belina, N. V.; Kurskiy, Y. A.; Kuznetsova, O. V.; Fukin, G. K.; Baranov, E. V.; Cherkasov, V. K.; Abakumov, G. A. *J. Organomet. Chem.* **2006**, *691*, 879–889. (e) Zhang, H.; Chen, P.; Fang, L. *Acta Cryst.* **2006**, *E62*, m934–m935. (f) Jones, C.; Schulten, C.; Rose, R. P.; Stasch, A.; Aldridge, S.; Woodul, W. D.; Murray, K. S.; Moubaraki, B.; Brynda, M.; La Macchia, G.; Gagliardi, L. *Angew. Chem. Int. Ed.* **2009**, *48,* 7406–7410. (g) Zhao, P.; Lei, H.; Ni, C.; Guo, J.-D.; Kamali, S.; Fettinger, J. C.; Grandjean, F.; Long, G. J.; Nagase, S.; Power, P. P. *Inorg. Chem.* **2015,** *54*, 8914–8922.

complexes. Herein, we report the synthesis and reactivity of low-coordinate dicobalt mono- and bis-μ-hydroxo complexes in a weak-field environment, highlighting the interconversion of these subunits via acid-base and redox reactions.

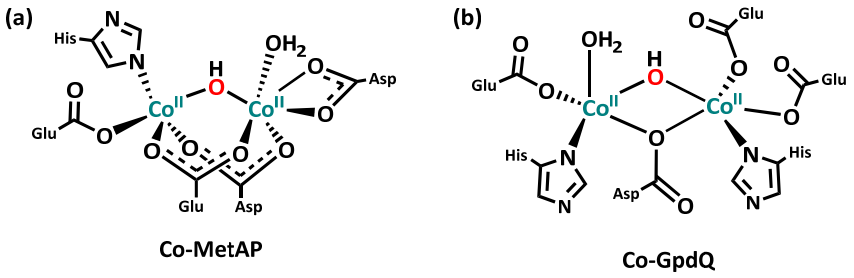

Figure 3.1. Structures of dicobalt substituted active sites featuring bridging hydroxo ligands, including (a) dicobalt(II) substituted MetAP,[4,5] and (b) dicobalt(II) substituted GpdQ.[6,7]

3.2 Synthesis and Reactivity of Dicobalt Mono-Hydroxide Species

Direct metalation of the protonated ligand ($^{t\text{Bu}}$dmx)H_2 via the cobalt(II) internal base reagent $Co[N(SiMe_3)_2]_2$ affords a suitable dicobalt(II) starting material, ($^{t\text{Bu}}$dmx)$Co_2[N(SiMe_3)_2]_2$ (**1**) (**Scheme 3.1**). X-ray diffraction (XRD) studies on single crystals grown from a saturated solution of **1** in hexanes revealed two non-interacting cobalt centers in trigonal-planar geometries located 7.0419(7) Å apart (**Figure 3.2**). Complex **1** exhibits a paramagnetic ^{1}H NMR spectrum, typical Co hyperfine structure at high g values by X-band EPR spectroscopy (**Figure 3.3**), and magnetometry

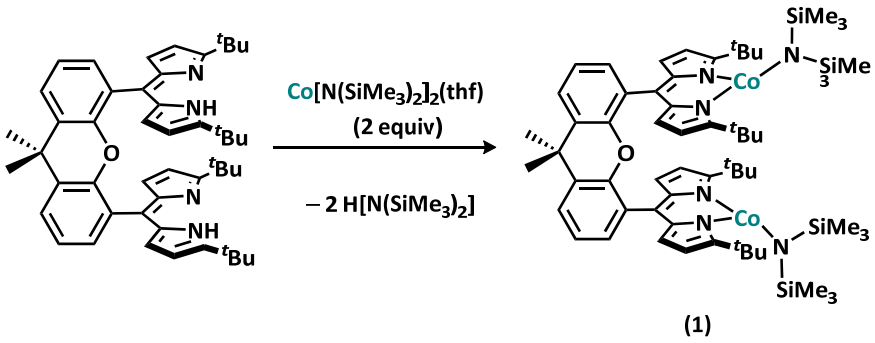

Scheme 3.1. Synthesis of dicobalt(II) starting material, ($^{t\text{Bu}}$dmx)$Co_2[N(SiMe_3)_2]_2$ (**1**).

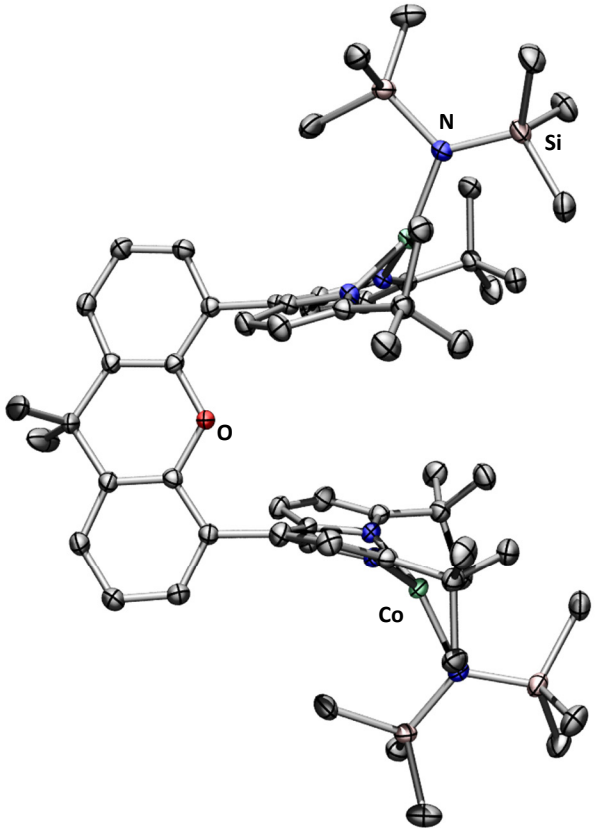

Figure 3.2. Solid state molecular structure of ($^{t\text{Bu}}$dmx)$Co_2[N(SiMe_3)_2]_2$ (**1**) with thermal ellipsoids at 50% probability level. Hydrogen atoms omitted for clarity. Color scheme: Co, aquamarine; N, blue; C, gray; O, red; Si, pink.

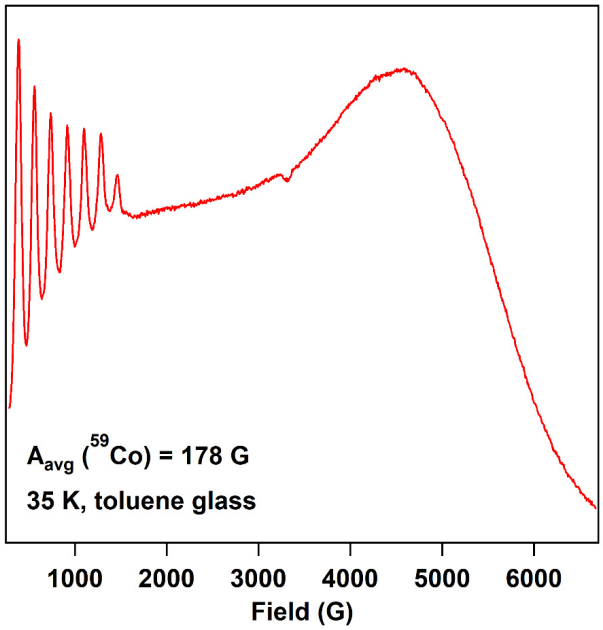

Figure 3.3. X-band EPR spectrum of ($^{t\text{Bu}}$dmx)$Co_2[N(SiMe_3)_2]_2$ (**1**). Spectrum collected in a frozen toluene glass at 35 K. The hyperfine coupling was read from the spectrum to determine the average A value of 178 G.

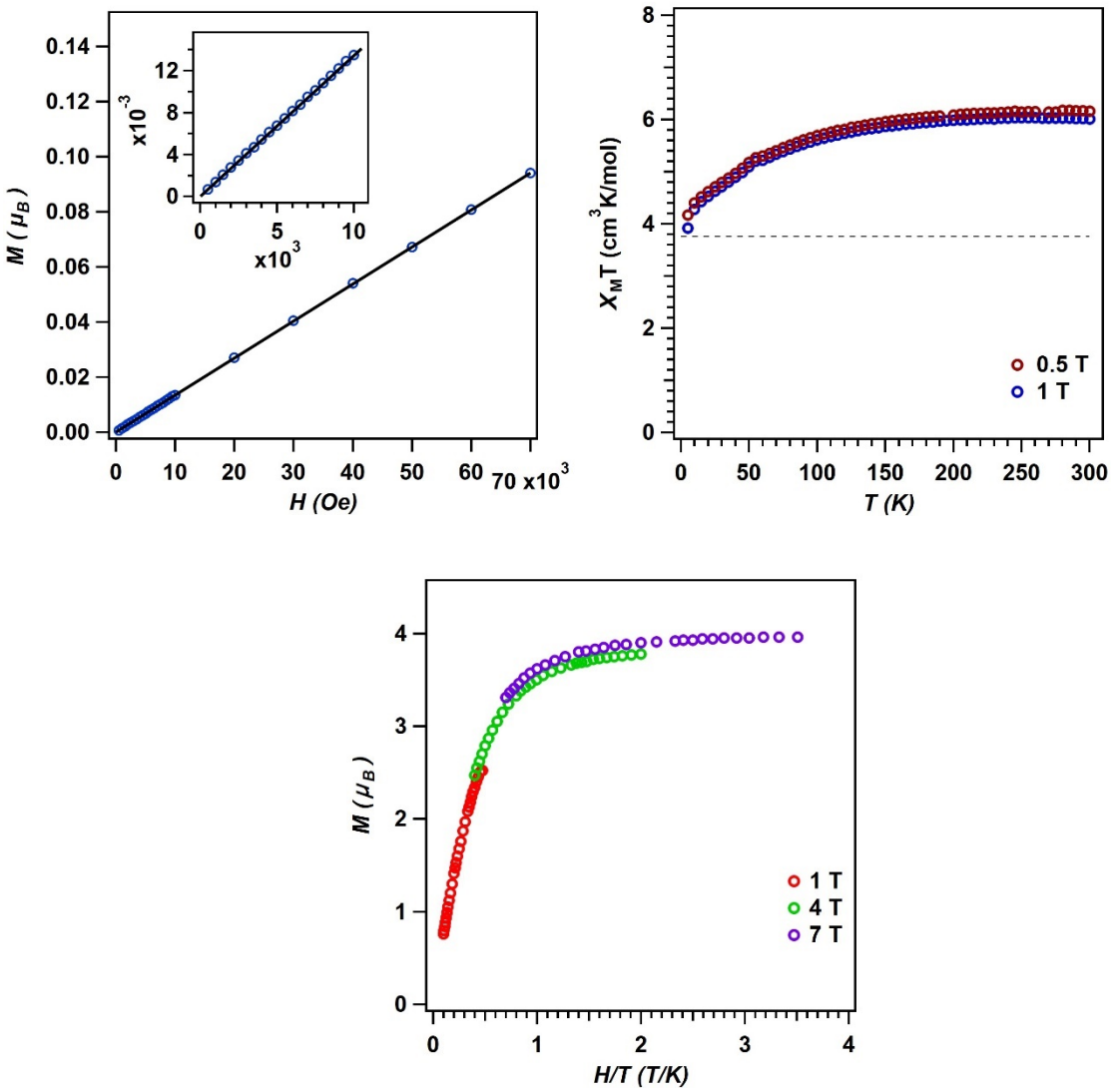

Figure 3.4. Magnetometry data for ($^{t\text{Bu}}$dmx)$Co_2[N(SiMe_3)_2]_2$ (**1**) (**Top, left**) M vs. H at 100 K is linear, showing absence of ferromagnetic impurity even at low fields **(Top, left, inset)**. **(Top, right)**. Variable temperature magnetic susceptibility data (χ_MT vs. T) was recorded at 0.5 T and 1.0 T across the temperature range of 5 K – 300 K. At 0.5 T (red circles), χ_MT = 6.16 cm^{3}K/mol at 295 K and at 1.0 T, χ_MT = 6.01 cm^{3}K/mol at 295 K. These values exceed the spin-only value magnetic susceptibility value for two uncoupled $S = {}^3/_2$ centers (χ_MT = 3.88 cm^{3}K/mol, dotted line) which is likely due to high magnetic anisotropy common for cobalt(II).[15] **(Bottom)** Reduced magnetization data (M vs. H/T) was collected at 3 fields (1, 4, and 7 T) over the temperature range of 1.8 K – 10 K.

data consistent with the presence of two non-interacting high-spin cobalt(II) centers (**Figure 3.4**).[14,15]

Akin to the synthesis of the analogous diiron bridging hydroxo complex, addition of one equivalent of water to **1** afforded a new paramagnetic species concomitant with formation of $HN(SiMe_3)_2$ (**Scheme 3.2**), as evidenced by ^1H NMR spectroscopy (**Figure 3.5**). We speculated that the paramagnetic product corresponds to a Co–hydroxo complex (**2**) based on a distinctive O–H stretch (ν = 3636 cm^{-1}) observed in the solid-state FTIR spectra of **2** and corresponding O–D stretch (ν = 2683 cm^{-1}) when D_2O was used instead (**Figure 3.6**). However, our attempts to crystallographically characterize complex **2** were unsuccessful, as the complex rapidly converts to multiple species within hours in solution or overnight in the solid state at –35 °C. Among these, we were able to crystallographically characterize one of the major decomposition products as a trimer of Pacman complexes, $[(^{t\text{Bu}}\text{dmx})Co_2(OH)(N(SiMe_3)_2)]_3$ (**3**), containing three hydroxide ligands bridging between independent Pacman units (**Scheme 3.2**, **Figure 3.8**). The solid-state FTIR spectra of the crystals of **3** revealed distinctive O–H (ν = 3624 cm^{-1}) and O–D stretches (ν = 2674 cm^{-1}) (**Figure 3.7**) from those of **2**. These data suggest that **2** contains one bound $N(SiMe_3)_2$ group as well as a mono-hydroxide unit, the latter of which could be labile and either weakly bridging or terminally-bound such that **2** is able to participate in trimerization to form **3** in solution. Complex **3** also exhibits an X-band EPR signature of high-spin cobalt(II) (**Figure 3.9**).

---

[14] (a) Baek, Y.; Das, A.; Zheng, S.-L.; Reibenspies, J. H.; Powers, D. C.; Betley, T. A. *J. Am. Chem. Soc.* **2020**, *142*, 11232–11243. (b) Kennedy, F. S.; Hill, H. A. O.; Kaden, T. A.; Vallee, B. L. *Biochem. Biophys. Res. Comm.* **1972**, *48*, 1533–1539. (c) McAlpin, J. G.; Surendranath, Y.; Dinca, M.; Stich, T. A.; Stoian, S. A.; Casey, W. H.; Nocera, D. G.; Britt, R. D. *J. Am. Chem. Soc.* **2010**, *132*, 6882–6883.

[15] (a) Palil, A. V.; Reu, O. S.; Ostrovsky, S. M.; Klokishner, S. I.; Tsukerblat, B. S.; Sun, Z.-M.; Mao, J.-G.; Prosvirin, A. V.; Zhao, H.-H.; Dunbar, K. R. *J. Am. Chem. Soc.* **2008**, *130*, 14729–14738. (b) Ostrovsky, S. M.; Falk, K.; Pelikan, J.; Brown, D. A.; Tomkowicz, Z.; Haase, W. *Inorg. Chem.* **2006**, *45*, 688–694. (c) Fortier, S.; Le Roy, J. J.; Chen, C.-H.; Vieru, V.; Murugesu, M.; Chibotaru, L. F.; Mindiola, D. J.; Caulton, K. G. *J. Am. Chem. Soc.* **2013**, *135*, 14670–14678.

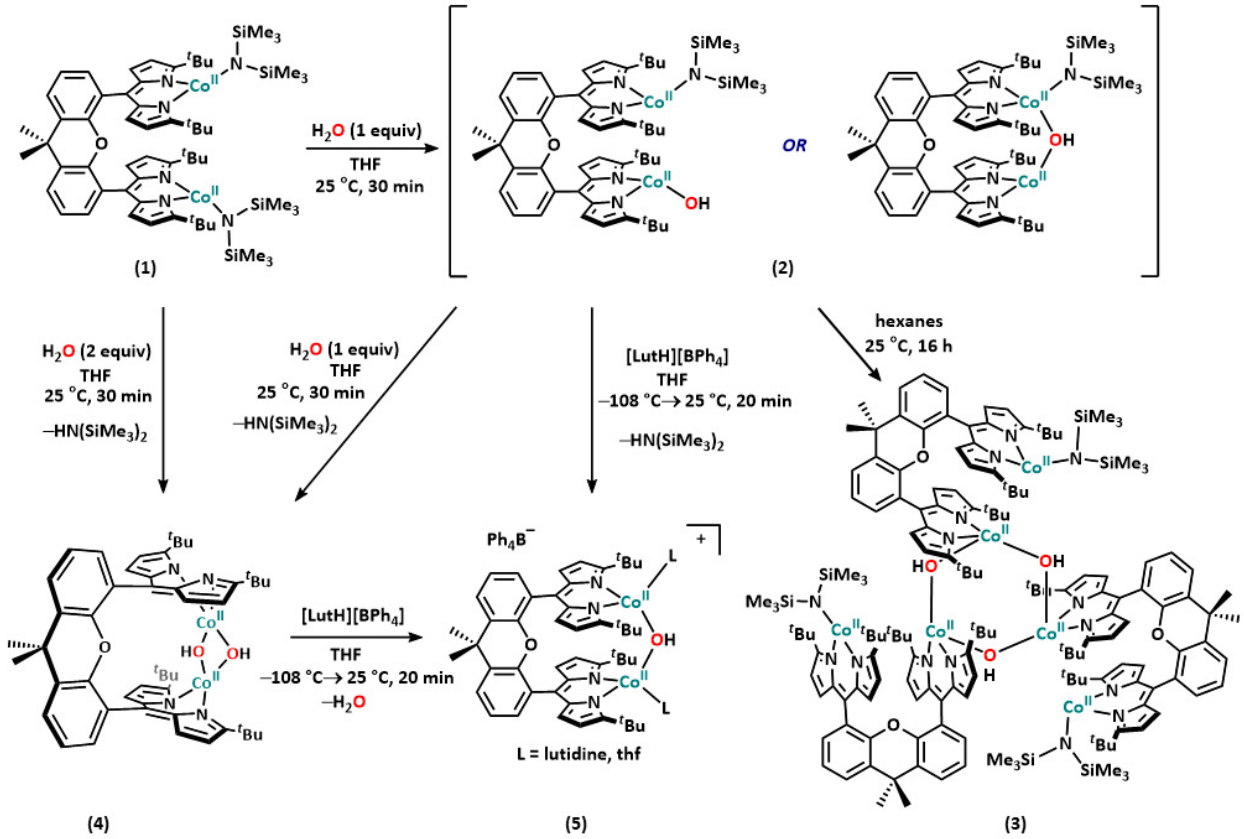

Scheme 3.2. Synthesis of mono- and bis-hydroxide complexes.

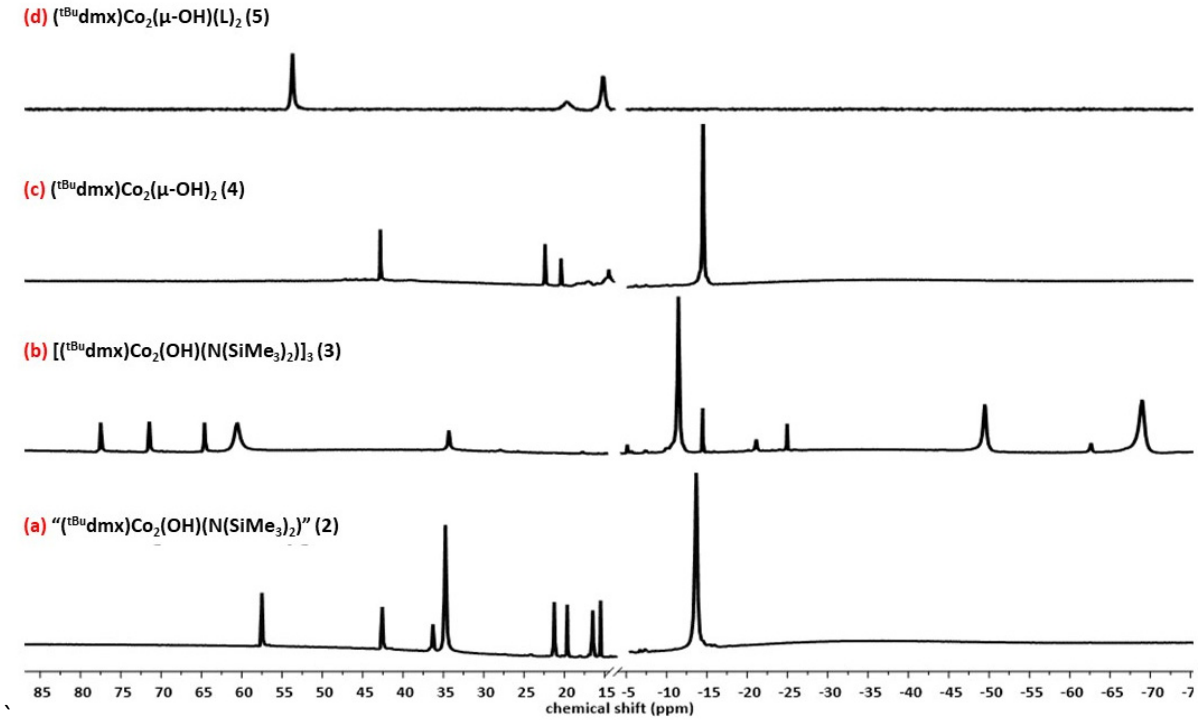

Figure 3.5. ^{1}H NMR spectra of various dicobalt hydroxide species **2**, **3**, **4**, and **5**.

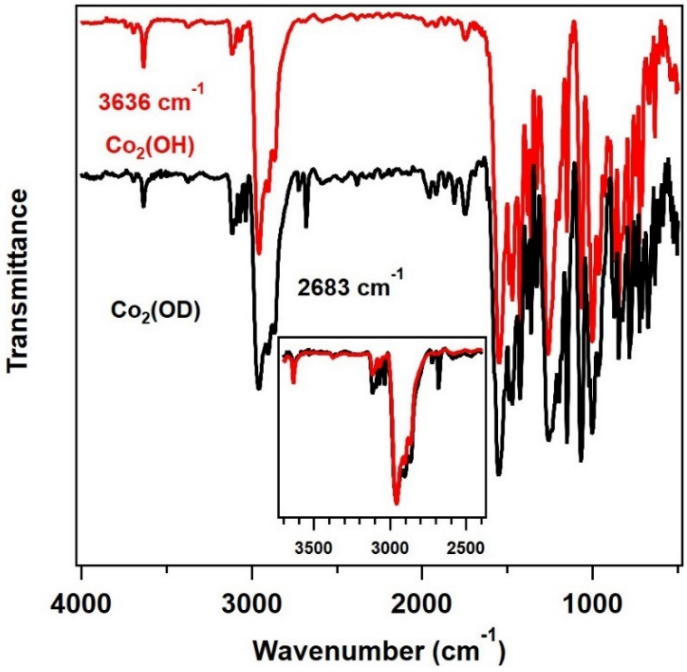

Figure 3.6. FTIR spectrum of (**Top, red**) "($^{t\text{Bu}}$dmx)Co_2(OH)[$N(SiMe_3)_2$]" (**2**) and (**Bottom, black**) "($^{t\text{Bu}}$dmx)Co_2(OD)[$N(SiMe_3)_2$]", with inset of overlaid spectra in region featuring OH and OD stretches.

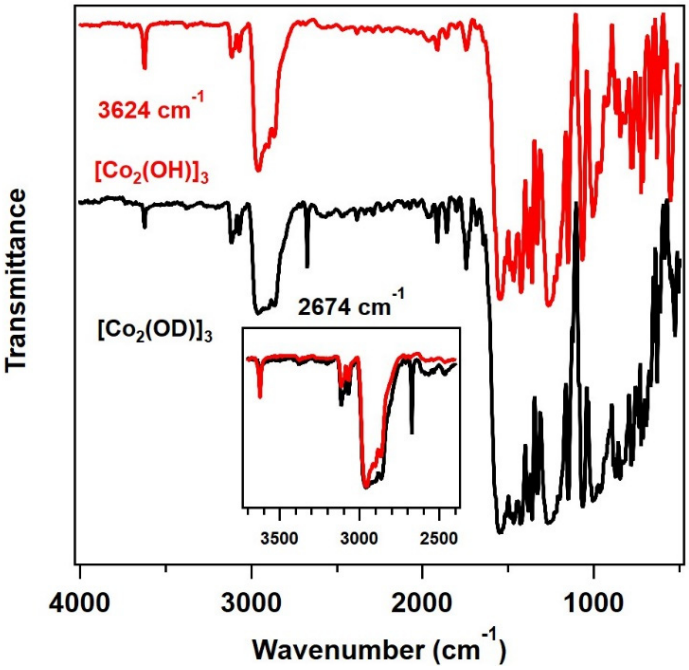

Figure 3.7. FTIR spectrum of (**Top, red**) [($^{t\text{Bu}}$dmx)Co_2(OH)($N(SiMe_3)_2$)]$_3$ (**3**) and (**Bottom**, **black**) [($^{t\text{Bu}}$dmx)Co_2(OD)($N(SiMe_3)_2$)]$_3$, with inset of overlaid spectra in region featuring OH and OD stretches.

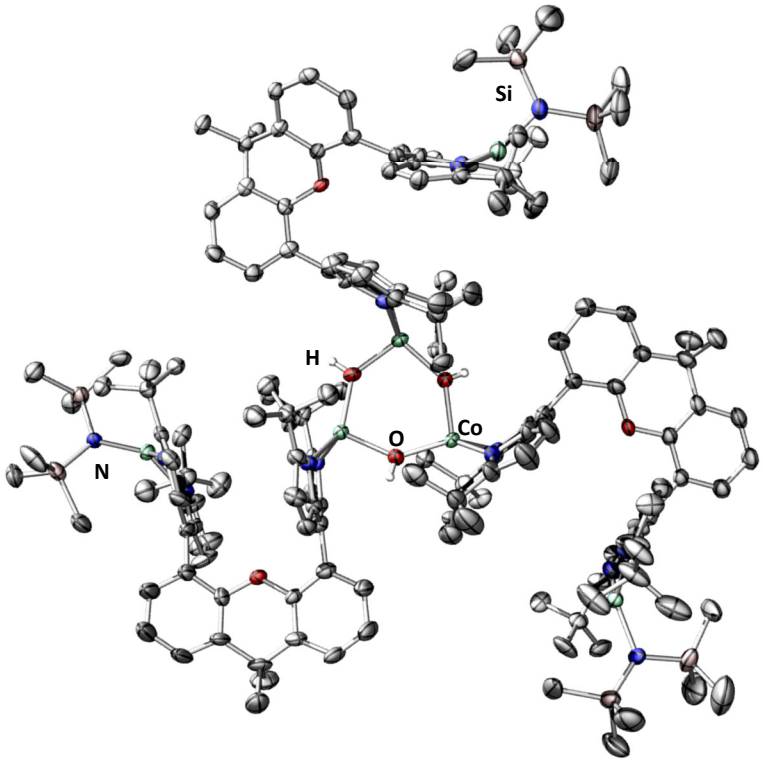

Figure 3.8. Solid state molecular structure of [($^{t\text{Bu}}$dmx)Co_2(OH)(N($SiMe_3$)$_2$)]$_3$ (**3**) with thermal ellipsoids at 40% probability level. All hydrogen atoms except for the hydroxo protons have been omitted for clarity. Color scheme: Co, aquamarine; N, blue; C, gray; O, red; Si, pink; H, white.

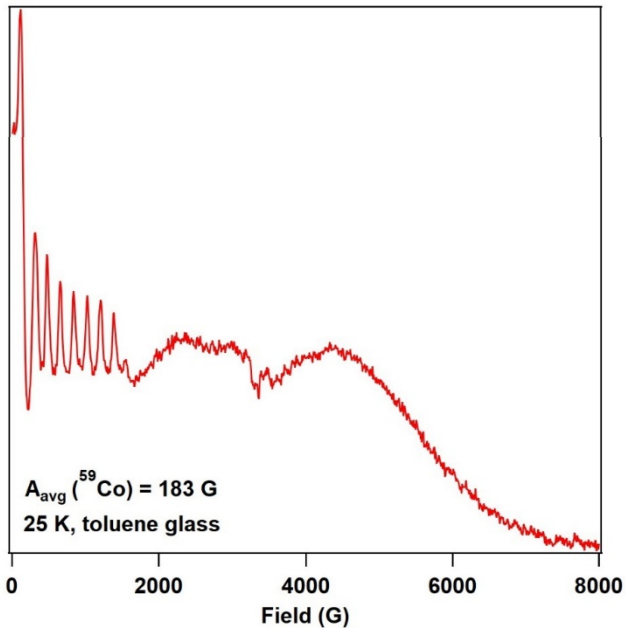

Figure 3.9. X-band EPR spectrum of [($^{t\text{Bu}}$dmx)Co_2(OH)(N($SiMe_3$)$_2$)]$_3$ (**3**). Spectrum collected in a frozen toluene glass at 25 K. The hyperfine coupling was read from the spectrum to determine the average A value of 183 G.

We reasoned that the instability of **2** could be due to the asymmetric nature of the dicobalt core. As such, we proposed that protonation of the bound $N(SiMe_3)_2$ group could help enforce a bridging hydroxo unit and further stabilize the complex. Addition of one equivalent of lutidinium tetraphenylborate to a frozen solution of **2** in THF provided clean access to a symmetric mono-μ-hydroxide salt, $[(^{t\text{Bu}}\text{dmx})Co_2(\mu\text{-OH})(L)_2][BPh_4]$ (where L = thf (**5a**) or 2,6-lutidine (**5b**)) (**Scheme 3.2**, **Figure 3.5**), along with the generation of free $HN(SiMe_3)_2$. Single crystals of this species were grown from a saturated solution in diethyl ether at –35 °C to afford the lutidine-bound structure **5b** (**Figure 3.10**), which we believe is selectively crystallized but not representative of the bulk material, as the stoichiometry of produced lutidine molecules to open coordination sites is 1:2. Using density functional theory, we confirmed that binding of 2,6-lutidine is more thermodynamically favored than THF, suggesting that when this byproduct is present, it will preferentially bind. Due to the stoichiometry requirement of lutidine, a mixture of **5a** and **5b** is anticipated to be present in solution, which is corroborated by elemental analysis results revealing the anticipated 1:1 mixture of **5a** and **5b**. These species feature broad O–H ($\nu = 3625$ cm^{-1}) and O–D ($\nu = 2683$ cm^{-1}) stretches in the FTIR spectra (**Figure 3.11**), the broadness of which we attribute to the presence of both species. Additional computational studies allowed us to determine pK_a values of the hydroxide protons for these complexes, 31.8(6) for **5a** and 29.1(6) for **5b** (**Table 3.3**), revealing the weak acidity of these protons and high basicity of the conjugate oxo bases. Isolation of these species further corroborates the assignment of complex **2** as having the formula "$(^{t\text{Bu}}\text{dmx})Co_2(OH)[N(SiMe_3)_2]$". As hypothesized, the symmetric complex **5** is significantly more stable than **2**, highlighting the role of the coordination environment in stabilizing the μ-hydroxide unit and preventing facile cluster formation.

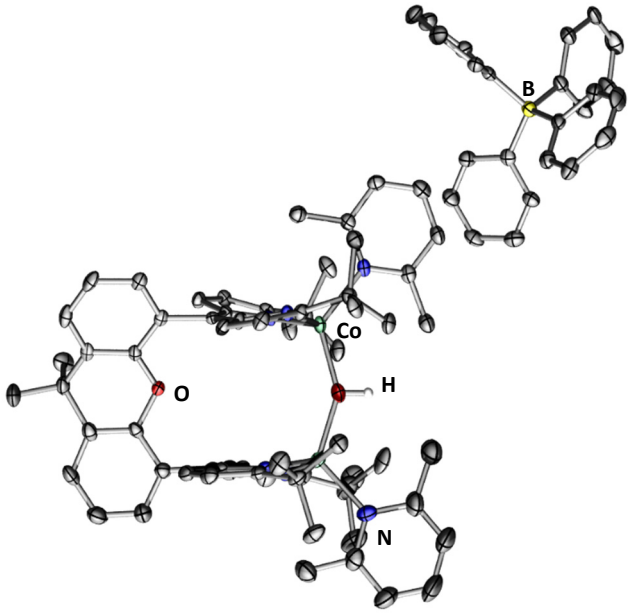

Figure 3.10. Solid state molecular structure of [($^{t\text{Bu}}$dmx)Co_2(μ-OH)(lut)$_2$][BPh_4] (**5b**) with thermal ellipsoids at 50% probability level. All hydrogen atoms except for the μ-hydroxo proton have been omitted for clarity. Color scheme: Co, aquamarine; N, blue; C, gray; O, red; B, yellow; H, white.

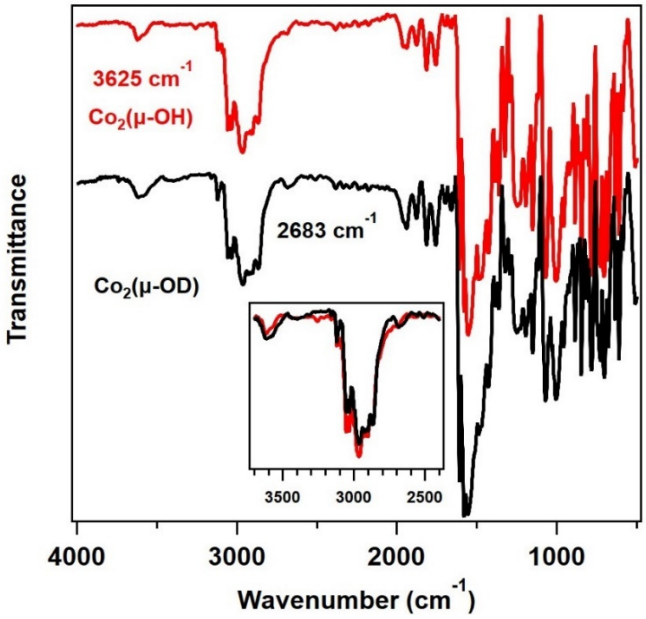

Figure 3.11. FTIR spectrum of (**Top, red**) [($^{t\text{Bu}}$dmx)Co_2(μ-OH)(L)$_2$][BPh_4] (**5a/5b**) and (**Bottom**, **black**) [($^{t\text{Bu}}$dmx)Co_2(μ-OD)(L)$_2$][BPh_4] (**5b**) with inset of overlaid spectra in region featuring OH and OD stretches. L = thf (**5a**) or 2,6-lutidine (**5b**).

3.3 Redox Reactivity of a Dicobalt Bis-Hydroxide Species

In addition to being able to synthesize mono-hydroxide species, we found that the dicobalt platform is also suitable for isolating bis-hydroxide complexes. This can be achieved by addition of a second equivalent of water to **2** or by direct addition of two equivalents of water to **1** to afford ($^{t\text{Bu}}$dmx)$Co_2(\mu\text{-}OH)_2$ (**4**), both pathways concomitant with formation of $HN(SiMe_3)_2$ (**Scheme 3.2**). Complex **4** exhibits distinctive O–H (ν = 3637 cm^{-1}) and O–D (ν = 2682 cm^{-1}) stretches (**Figure 3.13**) and ^{1}H NMR resonances (**Figure 3.5**) relative to **2**, **3**, and **5**. Single crystals suitable for XRD were grown from a saturated solution of **4** in diethyl ether with minimal THF at –35 °C. The solid-state structure exhibits two pseudo-square planar Co centers and features the shortest Co−Co distance (2.630(7) Å) observed on this system to date (**Figure 3.12**). Computational (**Table 3.1**) and magnetometry (**Figure 3.14**) studies suggest the presence of high spin cobalt(II) centers that are weakly antiferromagnetically coupled ($J \sim -20$ cm^{-1}). Furthermore, computations revealed that the hydroxide protons of complex **4** were even less acidic than for the mono-hydroxides, with pK_a values of 41.7(6) for the first deprotonation and 71.8(6) for the second deprotonation (**Table 3.3**). While stable in the solid state, complex **4** is hydrolytically sensitive, decomposing to a pentameric Co cluster (**10**) when left in solution at room temperature for multiple days (**Figure 3.15**). While indistinguishable by ^{1}H NMR spectroscopy, complex **10** features distinguishing FTIR ν_{OH} and ν_{OD} stretches (**Figure 3.16**).

Isolation of the bis-μ-hydroxide species **4** prompted us to further investigate the nature and reactivity of this species. Given the pseudo-square planar Co geometry, we anticipated that this system would be well-poised to accommodate dicobalt(III) complexes akin to the accessibility of diiron(III) oxo complexes on the iron Pacman platform. As such, we sought to explore the redox chemistry of **4**. To this end, addition of one equivalent of ferrocenium tetrakis (3,5-

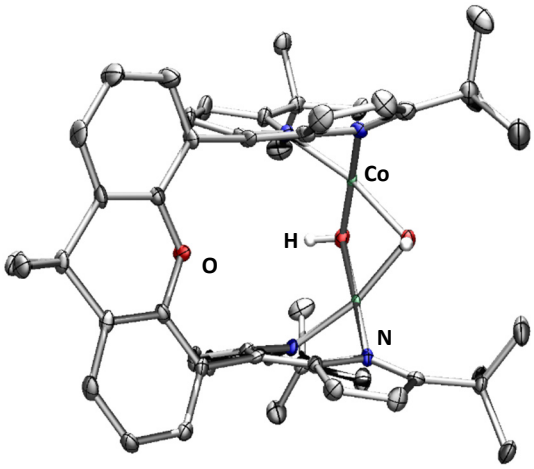

Figure 3.12. Solid state molecular structure of ($^{t\text{Bu}}$dmx)Co_2(μ-OH)$_2$ (**4**) with thermal ellipsoids at 50% probability level. All hydrogen atoms except for the μ-hydroxo protons have been omitted for clarity. Color scheme: Co, aquamarine; N, blue; C, gray; O, red; H, white.

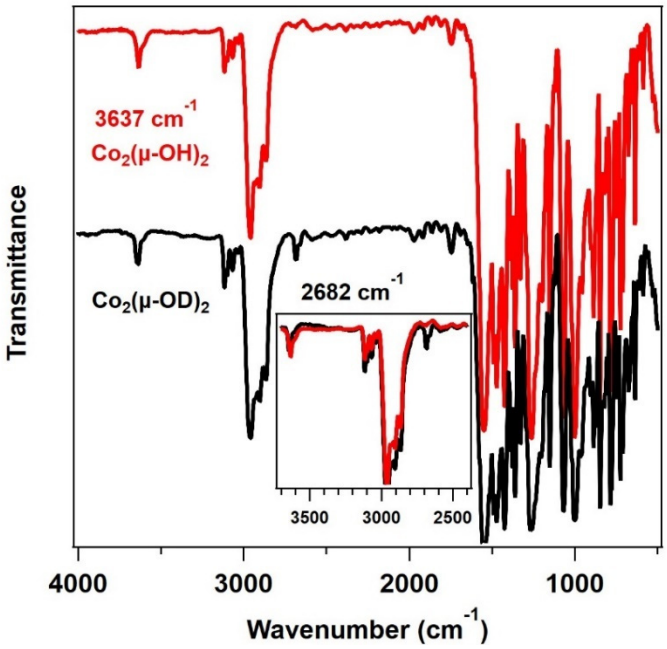

Figure 3.13. FTIR spectrum of (**Top, red**) ($^{t\text{Bu}}$dmx)Co_2(μ-OH)$_2$ (**4**) and (**Bottom**, **black**) ($^{t\text{Bu}}$dmx)Co_2(μ-OD)$_2$ with inset of overlaid spectra in region featuring OH and OD stretches.

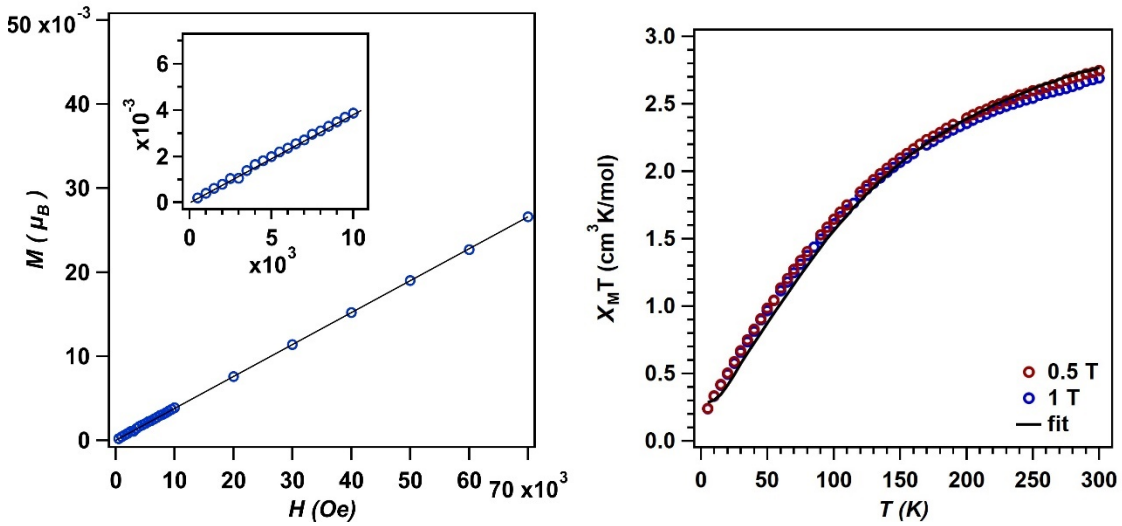

Figure 3.14. Magnetometry data for ($^{t\text{Bu}}$dmx)Co_2(μ-OH)$_2$ (**4**). **(left)** M vs. H at 100 K is linear, showing absence of ferromagnetic impurity even at low fields **(Left, inset)**. **(Right)**. Variable temperature magnetic susceptibility data (χ_MT vs. T) was recorded at 0.5 T and 1.0 T across the temperature range of 5 K – 300 K. At 0.5 T (red circles), χ_MT = 2.73 cm^{3}K/mol at 295 K and at 1.0 T, χ_MT = 2.68 cm^{3}K/mol at 295 K**.** χ_MT vs. T was best fit as two weakly coupled $S = {}^3/_2$ centers using PHI[6] (**black trace**), including 5% of an $S = {}^3/_2$ impurity, with the following parameters: g = 1.95, J = –21.2 cm^{-1}, D = 0.53 cm^{-1}, and $|E/D|$ = 0.18.

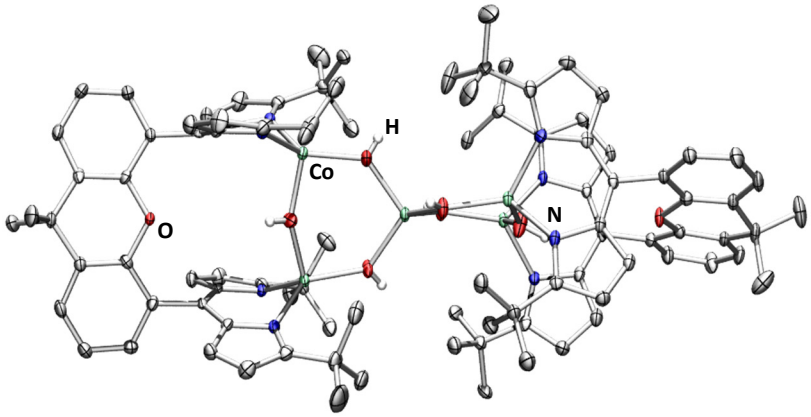

Figure 3.15. Solid state molecular structure of [($^{t\text{Bu}}$dmx)Co_2(μ-OH)]$_2$[Co(OH)$_4$] (**10**) with thermal ellipsoids at 50% probability level. All hydrogen atoms except for the μ-hydroxo protons have been omitted for clarity. Color scheme: Co, aquamarine; N, blue; C, gray; O, red; H, white.

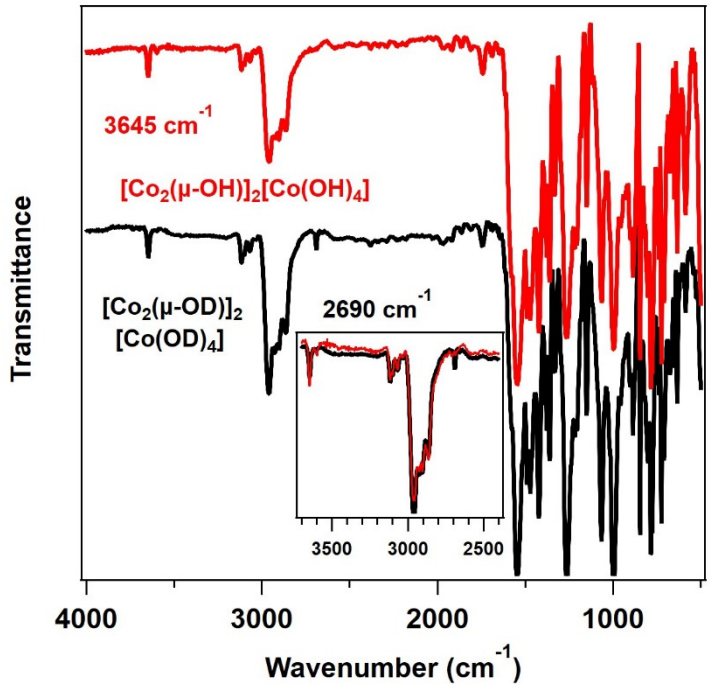

Figure 3.16. FTIR spectrum of (**Top, red**) [($^{t\text{Bu}}$dmx)Co_2(μ-OH)][$Co(OH)_4$] (**10**) and (**Bottom**, **black**) [($^{t\text{Bu}}$dmx)Co_2(μ-OD)][$Co(OD)_4$] with inset of overlaid spectra in region featuring OH and OD stretches.

bis(trifluoromethyl)phenyl) borate ($BAr^F{}_4$) to a THF solution of **4** results in loss of one of the bridging OH moieties to quantitatively form [($^{t\text{Bu}}$dmx)Co_2(μ-OH)$(thf)_2$][$BAr^F{}_4$] (**5c) (Scheme 3.3**) as evidenced by ^{1}H NMR spectroscopy (**Figure 3.17**). The oxidant is consumed in a few hours, and no detectable intermediates, nor the formation of hydrogen peroxide, are observed. Of note, the reaction does not proceed in nonpolar solvents such as benzene, even in the presence of a weak C–H bond such as 1,4-cyclohexadiene. This observation suggests the reaction likely does not involve a hydrogen atom abstraction (HAA) pathway. Furthermore, addition of an anionic borane (e.g., [Na][$BAr^F{}_4$]) to **4** resulted in no reaction, indicating that the reactivity observed does not occur via a simple salt metathesis pathway. We probed hydroxyl (OH$^\bullet$) release using trapping reagents (e.g., 5,5-dimethyl-1-pyrrolidine-*N*-oxide, DMPO, propylene oxide, PO), however we saw no evidence of OH$^\bullet$ production with these reagents. Further oxidation of **5** with outer sphere oxidants was not observed. Interestingly, we discovered that a similar transformation could occur

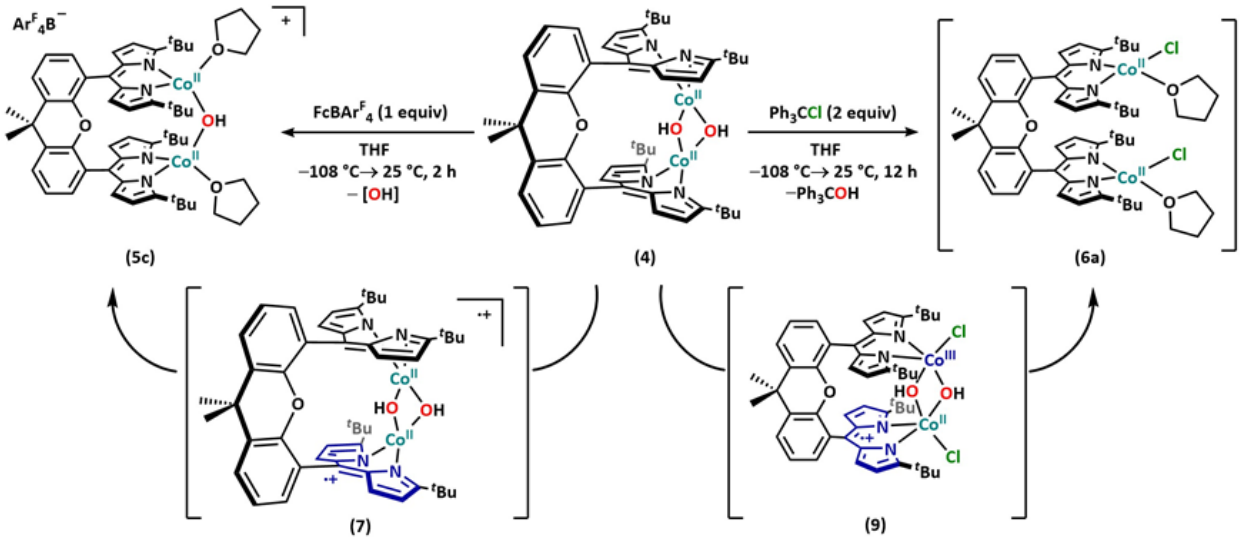

Scheme 3.3. Oxidation reactivity of ($^{t\text{Bu}}$dmx)Co$_2$(μ-OH)$_2$ (**4**).

via protonation, as addition of an acid to **4** also led to formation of **5** (likely as a mixture of **5a** and **5b**, as aforementioned) (**Scheme 3.3**). These reactions highlight the lability of the hydroxide bridges in the dicobalt bis-μ-hydroxide complex, either upon loss of an electron or introduction of a proton into the system, something that was not observed with the diiron (hydr)oxo species synthesized on this platform.

Electrochemical studies of **4** in THF show two quasi-reversible oxidative events at 461 mV and 606 mV vs. [Cp$_2$Fe]$^{+/0}$ (**Figure 3.18**), suggesting that a stronger oxidant than ferrocenium may be required to access the one- and two-electron oxidized species. To this end, more potent outer sphere oxidants were employed. New paramagnetically-shifted ^{1}H NMR spectra were observed when Ag(I) salts or thianthrenyl were reacted with **4** in THF, however the connectivity of these products has not yet been determined as single crystals suitable for crystallographic have not been achieved in either case. We had greater success when utilizing stronger inner-sphere oxidants, which provided a means to determine the final cobalt-containing species and trap the expelled OH. Addition of two equivalents of trityl chloride (Ph$_3$CCl) to **4** resulted in conversion to a new cobalt-

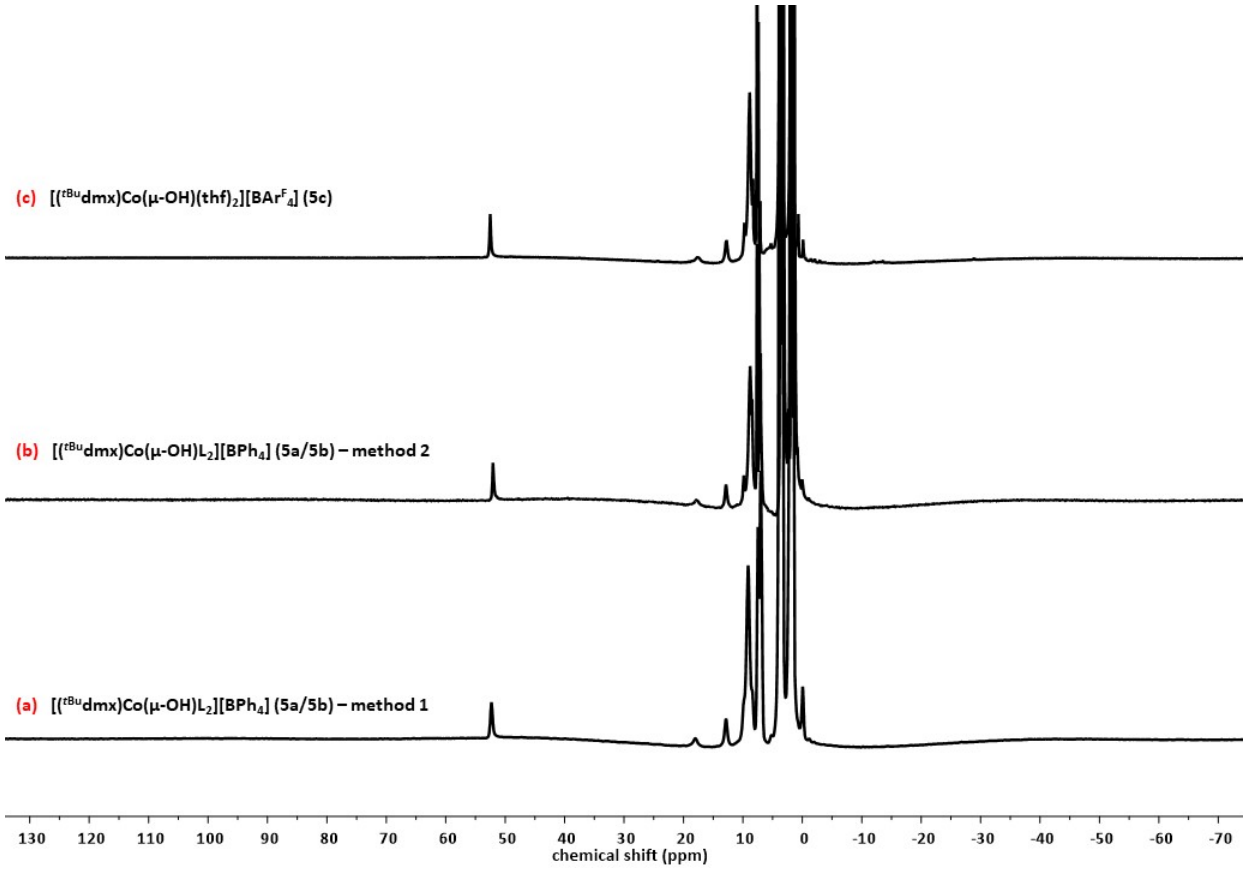

Figure 3.17. ^{1}H NMR spectra of various methods to synthesize [($^{t\text{Bu}}$dmx)Co$_2$(μ-OH)(L)$_2$]$^+$ (**5**) in THF. (a) Crude reaction mixture of 2,6-lutidinium tetraphenylborate addition to **2** to form 5a/5b. (b) Crude reaction mixture of 2,6-lutidinium tetraphenylborate addition to **4** to form **5a**/**5b**. (c) Crude reaction mixture of ferrocenium BAr$^{F}_4$ addition to **4** to form **5c**.

containing species by ^{1}H NMR, which we assign as the dicobalt(II) dichloride complex ($^{t\text{Bu}}$dmx)Co$_2$Cl$_2$(thf)$_2$ (**6a**) (**Scheme 3.3**), akin to an independently synthesized analogue ($^{t\text{Bu}}$dmx)Co$_2$Cl$_2$(py)$_2$ (**6b**) (**Figure 3.19**), along with the generation of Ph$_3$COH (42% yield relative to Ph$_3$CCl). Conversion of **4** to **6a** is also possible without a radical source via oxidation by iodobenzene dichloride (PhICl$_2$), and likewise will converge to form **6a** and Ph$_3$COH when oxidized with PhICl$_2$ in the presence of Gomberg's dimer (Ph$_3$C(C$_6$H$_5$)CPh$_2$). Previously reported

synthetic[16,17] and biological[18] examples of high-spin iron complexes with halide and oxygen-based ligands exhibit spin delocalization onto the hydr-/alkoxide ligands to allow these ligands to perform radical-type reactivity, either in the form of HAA[16] or radical recombination[17,18] with organic substrates. Therefore, we hypothesize that oxidation of **4** with Ph_3CCl oxidizes the complex to a transient oxidized species (e.g., ($^{t\text{Bu}}$dmx)$Co_2(\mu\text{-}OH)_2Cl$ (**8**) if occurring in separate one electron events, ($^{t\text{Bu}}$dmx)$Co_2(\mu\text{-}OH)_2Cl_2$ (**9**) for the two-electron oxidized product), engendering spin accumulation on the hydroxide bridges. If the oxidation is localized to the metal centers, one possible route for Ph_3COH generation could proceed by homolytic cleavage of a Co–OH bond to reduce the dicobalt core with capture of $^{\bullet}OH$ with $Ph_3C^{\bullet}$; or, alternatively, via ^{-}OH

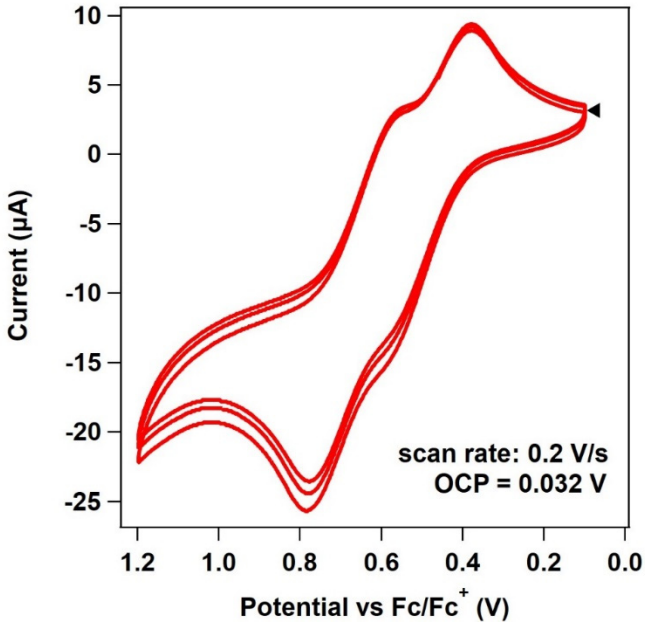

Figure 3.18. Cyclic voltammogram of data for ($^{t\text{Bu}}$dmx)$Co_2(\mu\text{-}OH)_2$ (**4**). The data were obtained at THF at 25 °C using a carbon working electrode and 0.1 M [$^{n}Bu_4N$][PF_6] as the supporting electrolyte.

[16] Kleinlein, C.; Zheng, S.-L.; Betley, T. A. *Inorg. Chem.* **2017**, *56*, 5892–5901.

[17] Yadav, V.; Rodriguez, R. J.; Siegler, M. A.; Goldberg, D. P. *J. Am. Chem. Soc.* **2020**, *142*, 7259–7264.

[18] (a) Wong, S. D.; Srnec, M.; Matthews, M. L.; Liu, L. V.; Kwak, Y.; Park, K.; Bell, C. B., III; Alp, E. E.; Zhao, J.; Yoda, Y.; Kitao, S.; Seto, M.; Krebs, C.; Bollinger, J. M., Jr.; Solomon, E. I. *Nature* **2013**, *499*, 320–321. (b) Martinez, S.; Hausinger, R. P. *J. Biol. Chem.* **2015**, *290*, 20702–20711.

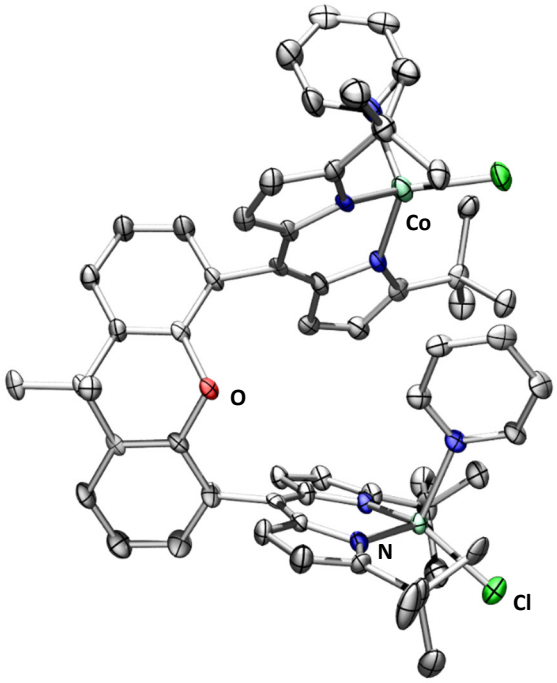

Figure 3.19. Solid state molecular structure of ($^{t\text{Bu}}$dmx)$Co_2Cl_2(py)_2$ (**6b**) with thermal ellipsoids at 50% probability level. All hydrogen atoms have been omitted for clarity. Color scheme: Co, aquamarine; N, blue; C, gray; O, red; Cl, green; H, white.

release that reacts with the $Ph_3C^{\bullet}$ followed by back electron transfer to regenerate cobalt(II). While we were not able to observe any intermediates experimentally, we propose that the intermittency of ($^{t\text{Bu}}$dmx)$Co_2(\mu\text{-}OH)_2Cl_2$ (**9**) is favored, as addition of one equivalent of Ph_3CCl to **4** resulted in unconsumed starting material and product **6a** with no evidence of a mono-substituted product.

3.4 Computational Exploration of Oxidized Intermediates

One key feature of many bimetallic active sites in nature is the ability to access multiple oxidation states to support a breadth of diverse reactivity. In the case of diiron enzymes such as sMMO and RNR, the iron centers are believed to pass through oxidation states ranging from diiron(II) to iron(III)/iron(IV) in RNR and even to diiron(IV) in sMMO.[2] In our previous studies, we demonstrated that the dipyrrin Pacman ligand platform supports diiron complexes in multiple

oxidation states including diiron(II), mixed-valent iron(II)/iron(III), and diiron(III) μ-oxo complexes. In this work, we utilized the same dinucleating ligand to synthesize novel dicobalt(II) mono- and bis-hydroxide complexes in a weak-field environment. We were curious to explore which cobalt oxidation states could be accessed, as our group has previously reported mononuclear cobalt-dipyrrin complexes ranging from cobalt(I) to cobalt(III).[19] Biologically, cobalt(III) is accessible in monometallic examples like cobalamin and nitrile hydratase;[3] however, to the best of our knowledge, the divalent state is exclusively observed for dicobalt enzymatic systems.[3-7] We anticipated that the dicobalt bis-μ-hydroxide **4** would be structurally well poised to support higher oxidation states. The close cobalt–cobalt separation could help facilitate the formation of a cobalt–cobalt bond upon oxidation to the dicobalt(III) state. However, no experimental evidence to support higher oxidation states at the metal centers was observed. Rather, reactivity suggestive of hydroxide or hydroxyl expulsion is exclusively observed following oxidative processes.

To better understand the observed reactivity, we turned to computational studies of proposed intermediates to map the reaction progression. We sought to uncover the location of oxidation, whether it is primarily metal-based or ligand-based, and if $OH^{\bullet}$ or OH^{-} release is likely invoked. To begin, we calculated the structure for the proposed one electron oxidized product $[(^{t\text{Bu}}\text{dmx})Co_2(\mu\text{-}OH)_2]^{+}$ (**7**). The Löwdin spin densities of **7** (**Figure 3.20**) determined via a broken symmetry solution (*3*,*4*) indicated that the oxidation was not formally borne out at either cobalt center, as the magnitude of spin density at cobalt (2.7, –2.7) remained equal to the magnitude of spin density at cobalt in the dicobalt(II) **4** (2.7, –2.7). Rather, the increase of spin density was observed primarily at one of the dipyrrin ligands (a sum of –1.1 for **7** versus a sum of –0.039 for **4**) (**Table 3.2**). This result suggests that neither cobalt center is accessing cobalt(III), but rather the

[19] Baek, Y.; Betley, T. A. *J. Am. Chem. Soc.* **2019**, *141*, 7797–7806.

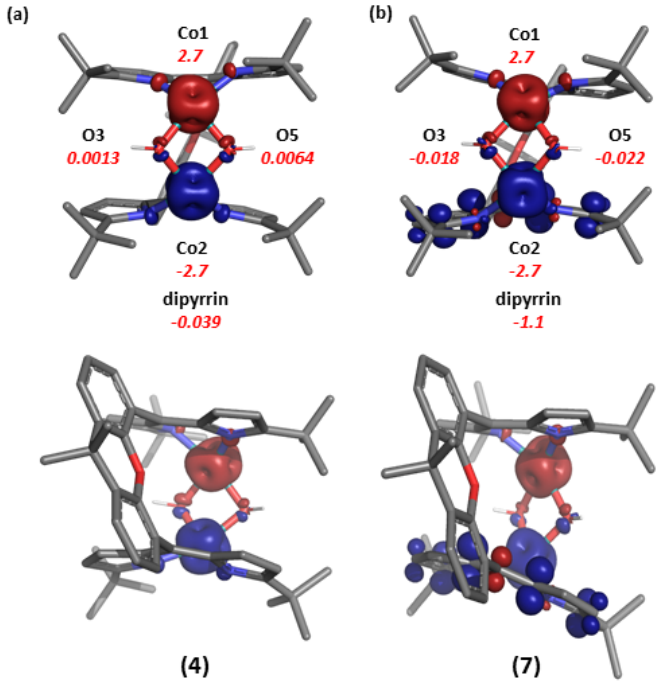

Figure 3.20. (a) Spin density plot of ($^{t\text{Bu}}$dmx)Co_2(μ-OH)$_2$ (**4**) with Löwdin spin densities of key atoms highlighted. (b) Spin density plot and key Löwdin spin densities for [($^{t\text{Bu}}$dmx)Co_2(μ-OH)$_2$]$^+$ (**7**), the proposed transient intermediate formed upon addition of an outer sphere oxidant to **4** on the path to forming the final product **5c**.

dipyrrin ligand is bearing the oxidation (**Scheme 3.3**). Many examples reporting oxidation reactivity with first-row transition metals complexes have exhibited ligand-based oxidation, where a common byproduct of this redox activity is HAA by the ligand-based radical.[20] In the present case, the proton and electron equivalents delivered to oxidized **7** go to distinct destinations: the bridging hydroxides are basic enough to protonate while the dipyrrinyl is reduced.

Akin to the oxidation of **4** by ferrocenium, potential intermediates with the inner sphere chloride oxidants were canvassed by DFT, illustrating the possibility of separate one electron events to form a putative one-electron oxidized species ($^{t\text{Bu}}$dmx)Co_2(μ-OH)$_2$Cl (**8**) and the favored two-electron oxidized ($^{t\text{Bu}}$dmx)Co_2(μ-OH)$_2$Cl$_2$ (**9**). Notably, the optimized structures of **8** and **9**

[20] (a) Ingleson, M. J.; Pink, M.; Fan, H.; Caulton, K. G. *J. Am. Chem. Soc.* **2008**, *130*, 4262-4276. (b) Sazama, G. T.; Betley, T. A. *Inorg. Chem.* **2010**, *49*, 2512-2524. (c) Kiernicki, J. J.; Zeller, M.; Szymczak, N. K. *Inorg. Chem.* **2020**, *59*, 9279-9286. (d) Creutz, S. E.; Peters, J. C. *Chem. Sci.* **2017**, *8*, 2321-2328 (2017).

show a geometric rearrangement of the [$Co_2(\mu\text{-}OH)_2$] diamond core from the edge-shared, fused square planar arrangement in **4**, orienting the bridging hydroxide ligands between the trigonal-pyramidal and Cl-bound, trigonal-bipyramidal cobalt centers in **8** and the two trigonal-bipyramidal cobalt centers in **9** (**Scheme 3.3**). The Löwdin spin density for complex **8** derived with a broken symmetry solution (*3*, *4*) (**Figure 3.21**) indicates no spin density increase at either cobalt center (2.7, -2.7). As with **7**, an increase in spin density at one dipyrrin (sum of –1.0) is observed for the monochloride **8** (**Table 3.2**). Oxidation by two electrons to form proposed two-electron oxidized **9**, with a broken symmetry solution of (*4*, *4*), reveals the first evidence of metal-based oxidation, as a substantial spin density increase at one cobalt center was identified (3.0, –2.7), accompanied by dipyrrin oxidation (-1.1) and spin density accumulation at the bridging hydroxide ligands (O5, 0.80; O3, 0.24; **Figure 3.21**, **Table 3.2**).

The foregoing results lead us to conclude that ligand oxidation is the first locus of oxidation and the second oxidizes one Co (not bound to the dipyrrin radical) to Co(III). Outer sphere oxidation of **4** to **7** likely results in net H-atom transfer to **7** (likely from THF) via hydroxide protonation and electron transfer to the dipyrrin-radical to form the product **5c**. Inner-sphere oxidation using Ph_3CCl ultimately leads to the formation of Ph_3COH and the dichloride product **6a**. Formation of Ph_3COH could potentially occur from both the one- (**8**) and two-electron (**9**) oxidation products. Following oxidation of **4** with Ph_3CCl, the trityl radical could react with a hydroxide bridge in **8**, followed by back electron transfer to the dipyrrin radical, leading to the observed Ph_3COH and partial conversion of **4** to the dichloride **6a**. We propose formation of the two-electron oxidation product **9** is favored based on the requisite stoichiometry of two equivalents of Ph_3CCl required to induce oxidation of **4** (vide supra). Trityl alcohol formation from **9** could occur by two potential routes: (1) trityl radical could react with a hydroxide bridge with back

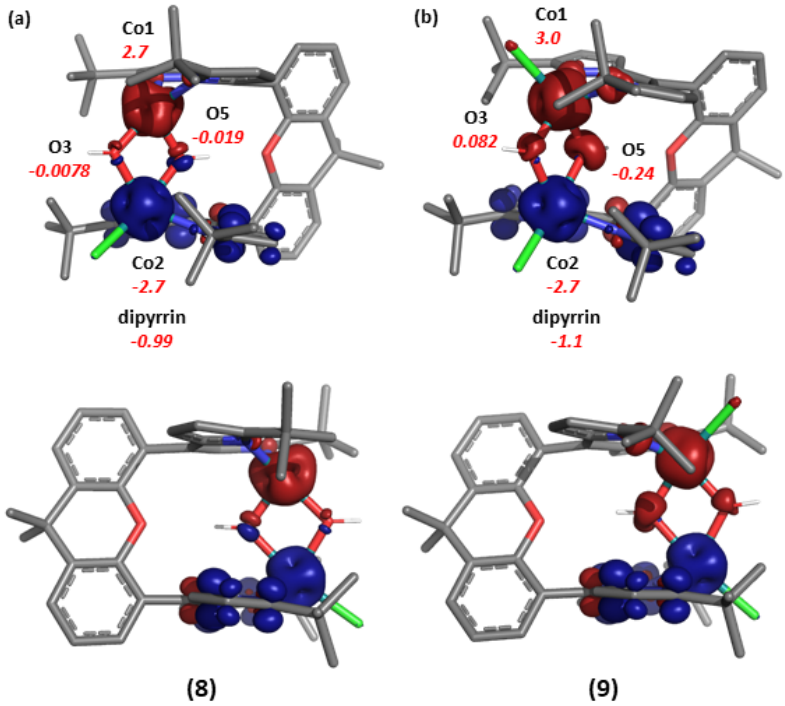

Figure 3.21. Spin density plots and Löwdin spin densities of key atoms for the proposed intermittent higher valent chloride adducts (a) ($^{t\text{Bu}}$dmx)Co_2(μ-OH)$_2$Cl (**8**) and (b) ($^{t\text{Bu}}$dmx)Co_2(μ-OH)$_2Cl_2$ (**9**). Note that both of the computationally-determined structures show a geometry change of the dicobalt bis-μ-hydroxide diamond core to becoming parallel to the dmx ligand backbone.

electron transfer to the [Co_2] core; or (2) spin accumulation at the hydroxide bridging ligands in **9** could permit a direct radical recombination between $Ph_3C^{\bullet}$ and the hydroxyl ligand.

3.5 Conclusions

In summary, the dinucleating ligand platform ($^{t\text{Bu}}$dmx)H_2 allowed for the synthesis of novel dicobalt complexes in a weak field environment. Using a protonation strategy, we were able to synthesize mono- and bis-hydroxide complexes featuring low coordination numbers. With these in hand, we have demonstrated the lability of the OH bridging units within the dicobalt bis-μ-hydroxo core, both upon redox and acid/base reactions. Specifically, upon oxidation, we propose that radical character enhancement at the bridging OH units may allow for expulsion of these bridging ligands to regenerate cobalt(II) rather than stabilizing higher valent cobalt centers. The

spin accumulation calculated for the ancillary hydroxide ligands in **9** parallels spin-accumulation on anionic ligands observed for transition-metal complexes featuring weak-field dipyrrin ligands[16,19,21] and structurally analogous β-diketiminate complexes.[22] The reactivity of the dicobalt Pacman system upon oxidation is distinct from that observed for the diiron complexes, in which the diiron(III) oxo species was found to be extremely stable (e.g., thermally robust, air-stable). The subtle shift from iron to cobalt dramatically affects the oxidation pattern we observe, as the primarily location of oxidation is dipyrrin-centered and Co(II) is preserved in the oxidized products. Furthermore, augmented radical character at the hydroxo bridges is observed upon oxidation, unveiling distinct oxygen-group transfer reactivity displayed by the dicobalt Pacman system.

[21] (a) Wilding, M. J. T.; Iovan, D. A.; Betley, T. A. *J. Am. Chem. Soc.* **2017**, *139*, 12043–12049. (b) Carsch, K. M.; Lukens, J. T.; DiMucci, I. M.; Iovan, D. A.; Zheng, S.-L.; Lancaster, K. M.; Betley, T. A. *J. Am. Chem. Soc.* **2020**, *142*, 2264–2276.

[22] Wiese, S.; Badiei, Y. M.; Gephart, R. T.; Mossin, S.; Varonka, M. S.; Melzer, M. M.; Meyer, K.; Cundari, T. R.; Warren, T. H. *Angew. Chem. Int. Ed.* **2010**, *49*, 8850–8855.

3.6 Experimental Methods

3.6.1 General considerations

All manipulations of metal complexes were carried out in the absence of water and dioxygen using standard Schlenk techniques, or in an MBraun inert atmosphere drybox under a dinitrogen atmosphere. All glassware was oven dried for a minimum of 10 h and cooled in an evacuated antechamber prior to use in the drybox. Benzene, hexanes, tetrahydrofuran, diethyl ether, and toluene were dried and deoxygenated on a Glass Contour System (SG Water USA, Nashua, NH) and stored over 4 Å molecular sieves (Strem) prior to use. Tetrahydrofuran-d_8 and D_2O were purchased from Cambridge Isotope Labs and used as received. Benzene-d_6 and dichloromethane-d_2 were purchased from Cambridge Isotope Labs, degassed and stored over 4 Å molecular sieves prior to use. Pentane, pyridine, and *tert*-butanol were purchased from Sigma-Aldrich and stored over 4 Å molecular sieves prior to use. Celite® 545 (J. T. Baker) was dried in a Schlenk flask for 24 h under dynamic vacuum while heating to at least 190 °C prior to drybox use. Trityl chloride was purchased from Aldrich and recrystallized from diethyl ether at –35 °C prior to use. $K(N(SiMe_3)_2$ was purchased from Aldrich and recrystallized from boiling toluene cooled to –35 °C prior to use. Anhydrous cobalt dichloride was purchased from Strem and used as received. Distilled H_2O and D_2O were degassed by sparging with argon prior to use. KBr was purchased from International Crystal Laboratories and heated to 80 °C under high vacuum overnight prior to use. 2,6-Lutidinium tetraphenylborate,[23] cobalt dichloride bis-pyridine,[24] ferrocenium

[23] Grönberg, K. L. C.; Henderson, R. A.; Oglieve, K. E. *J. Chem. Soc, Dalton Trans.* **1998**, 3093–3104.

[24] Allan, J. R.; Brown, D. H.; Nuttall, R. H.; Sharp, D. W. A *J. Chem. Soc. A.* **1966**, 1031–1034.

tetrakis[3,5-bis(trifluoromethyl)phenyl]borate,[25] $Co[N(SiMe_3)_2]_2(thf)$,[26] iodobenzene dichloride[27] and ($^{t\text{Bu}}$dmx)H_2[27] were synthesized following previously reported procedures.

3.6.2 Characterization and Physical Methods

^{1}H NMR spectra were recorded on Agilent DD2 600 MHz or Varian Unity/Inova 500 MHz spectrometers. ^{1}H chemical shifts are reported relative to $SiMe_4$ using the chemical shift of residual solvent peaks as reference. Elemental analyses (%CHN) were obtained on a PerkinElmer 2400 Series II CHNS/O Analyzer.

Magnetic data were collected using a Quantum Design MPMS-5S SQUID magnetometer. Measurements were obtained for finely ground microcrystalline powders restrained in a frozen eicosane matrix with polycarbonate capsules. Samples were prepared under a dry nitrogen atmosphere by packing the powder in a gel cap and adding warm liquid eicosane, which formed a solid wax upon cooling. The susceptibility data was corrected for contributions from the sample holder and eicosane, as well as the core diamagnetism of the sample using Pascal's constants.

$$\chi_M = \frac{\chi \mathrm{M}}{m \cdot H}. \quad (1)$$

Molar susceptibilities (χ_M) were calculated by converting the calculated magnetic susceptibility (χ) obtained from the magnetometer according to **equation 1**. The reduced magnetization data were fit using PHI.[28]

[25] .Chávez, I.; Alvarez-Carena, A.; Molins, E.; Roig, A.; Maniukiewicz, W.; Arancibia, A.; Arancibia, V.; Brand, H.; Manríquez. J. M. *J. Organomet. Chem.* **2000**, *601*, 126–132.

[26] Hernández Sánchez, R.; Zheng, S.-L.; Betley, T. A. *J. Am. Chem. Soc.* **2015**, *137*, 11126–11143.

[27] Johnson, E. J.; Kleinlein, C.; Musgrave, R. A.; Betley, T. A. *Chem. Sci.* **2019***, 10*, 6304–6310.

[28] Chilton, N. F.; Anderson, R. P.; Turner, L. D.; Soncini, A;. Murray, , K. S. *J. Comput. Chem.* **2013**, *34*, 1164–1175.

Infrared spectra were acquired on a Varian 1000 FT-IR spectrometer by pressing the samples into KBr pellets (~3–4 mg of dried sample and ~80 mg of KBr).

EPR spectra were obtained on a Bruker EleXsys E-500 CW-EPR spectrometer. Spectra were measured as frozen glass in toluene at a microwave power of 0.6325–2 mW.

Electrochemical experiments were carried out using a CH Instruments CHI660C Electrochemical Workstation. The electrolyte used was 0.1 M [^{n}Bu$_4$N][PF$_6$] in THF. The working electrode was glassy carbon and a platinum wire was used as the counter electrode. Cyclic voltammograms were referenced against a ferrocene standard. Cyclic voltammetry was performed with scan rates of 100 mV/s to 200 mV/s under a dinitrogen atmosphere.

3.6.3 Synthesis

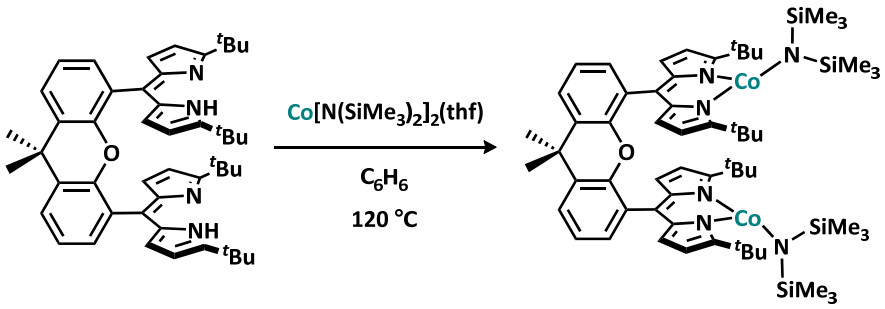

($^{t\text{Bu}}$dmx)Co$_2$[N(SiMe$_3$)$_2$]$_2$ (1): To a 35 mL pressure vessel was added ($^{t\text{Bu}}$dmx)H$_2$ (400.0 mg, 556 µmol, 1.00 equiv), Co[N(SiMe$_3$)$_2$]$_2$(thf) (502.7 mg, 1,113 µmol, 2.00 equiv) and 10 mL benzene. The vessel was equipped with a magnetic stir bar, capped, removed from the glovebox and placed in an oil bath kept at 120 °C for sixteen hours. The reaction mixture was cooled to room temperature and returned to the glovebox. The solvent was frozen and removed *in vacuo* to yield a dark red powder. The residue was washed with hexanes (4×3 mL), filtered through Celite with benzene and lyophilized to yield a dark orange-red powder (552.9 mg, 87.3%). Crystals suitable for X-ray diffraction were grown from a concentrated solution of hexanes at −35 °C. ^{1}H NMR

(500 MHz, 295 K, C_6D_6): δ/ppm 90.67, 58.19, 50.03, 16.75, 16.15, −0.51, −41.81, −42.83, −75.02. %CHN Calculated for $C_{61}H_{92}Co_2N_6OSi_4$: C 63.40 H 8.02 N 7.27; Found: C 63.62 H 7.82 N 7.26.

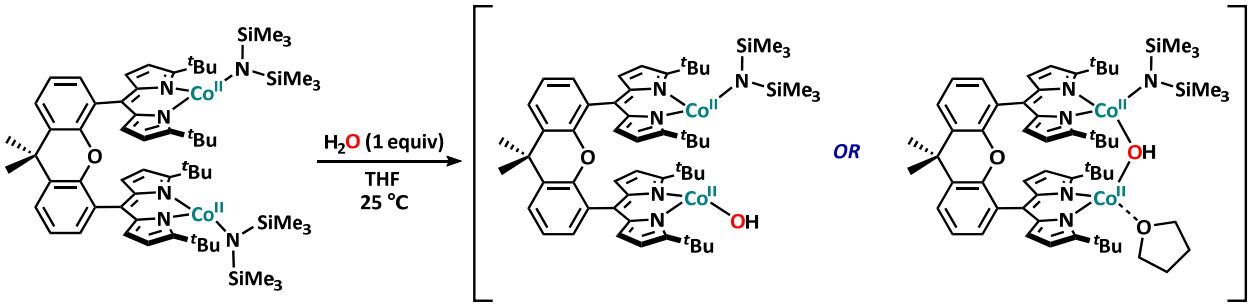

"($^{t\text{Bu}}$dmx)Co$_2$(OH)[N(SiMe$_3$)$_2$]" (2): In a 20 mL vial, ($^{t\text{Bu}}$dmx)Co$_2$[N(SiMe$_3$)$_2$]$_2$ (**1**) (20.0 mg, 17.3 µmol, 1.00 equiv) was dissolved in 1 mL of THF. A saturated solution of water in benzene[22] (0.48 mL, 17.0 µmol, 0.98 equiv) was added dropwise to a vigorously stirred solution. The reaction mixture was stirred at room temperature for 10 minutes and concentrated *in vacuo*. The assignment of this species is that it contains one N(SiMe$_3$)$_2$ group and an OH ligand, the latter which could be labile and either weakly bridging or terminally-bound such that **2** is able to participate in trimerization and form **3** in solution. This formulation is further supported by the reactivity of **2** with acids, such as addition of H_2O to form **4** or LutHBPh$_4$ to form **5a**/**5b**. ^{1}H NMR (500 MHz, 295 K, THF-d_8): δ/ppm 55.98, 40.25, 33.33, 31.66, 17.46, 15.77, 12.52, 11.42, 6.18, 5.34, −10.50. FTIR (KBr): 3636 cm^{-1} (ν_{O-H}); 2683 cm^{-1} (ν_{O-D}).

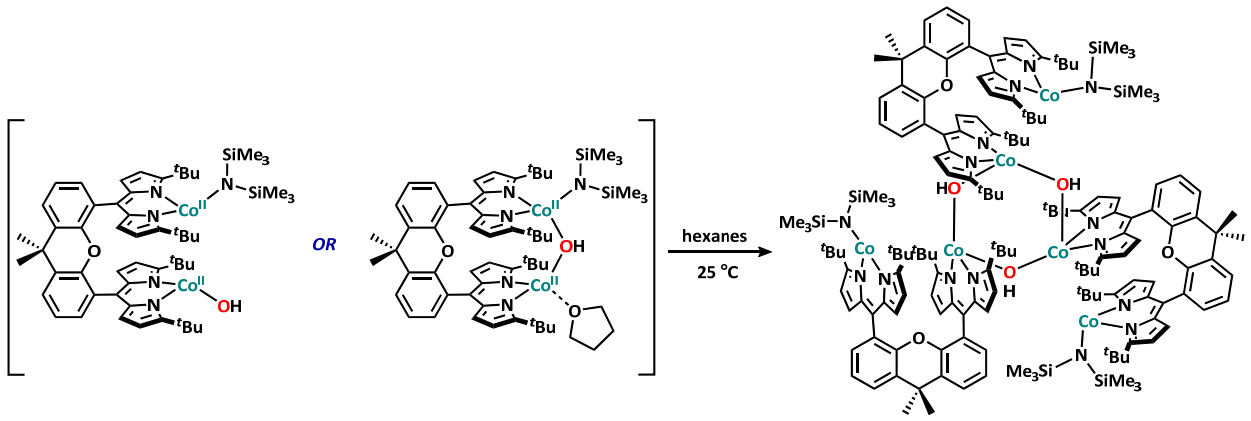

[($^{t\text{Bu}}$dmx)Co$_2$(OH)(N(SiMe$_3$)$_2$)]$_3$ (3): The crude reaction mixture of "($^{t\text{Bu}}$dmx)Co$_2$(OH)[N(SiMe$_3$)$_2$]" (**2**) (20.0 mg scale) in THF was concentrated *in vacuo*. The residue was taken up in minimal hexanes to afford brown crystals of [($^{t\text{Bu}}$dmx)Co$_2$(OH)(N(SiMe$_3$)$_2$)]$_3$ (**3**) at room temperature (20.4 mg, 39%). Conversion of complex **2** to complex **3** occurs readily in non-coordinating solvents. ^{1}H NMR (500 MHz, 295 K, C$_6$D$_6$): δ/ppm 75.28, 69.05, 62.00, 57.81, 30.74, 4.40, 2.91, −9.45, −12.56, −19.42, −23.36, −48.67, −62.24, −68.78. FTIR (KBr): 3624 cm^{-1} (ν_{O-H}); 2674 cm^{-1} (ν_{O-D}). %CHN Calculated for C$_{165}$H$_{225}$Co$_6$N$_{15}$O$_6$Si$_6$: C 65.26 H 7.47 N 6.92; Found: C 65.33 H 7.53 N 6.88.

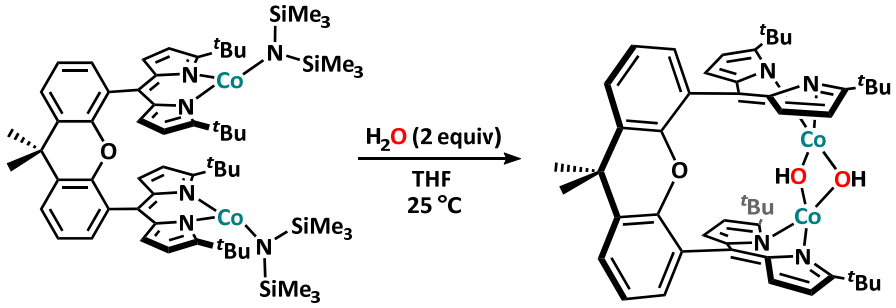

($^{t\text{Bu}}$dmx)Co$_2$(μ-OH)$_2$ (4): In a 20 mL vial, ($^{t\text{Bu}}$dmx)Co$_2$[N(SiMe$_3$)$_2$]$_2$ (**1**) (50.0 mg, 43.3 μmol, 1.00 equiv) was dissolved in 3 mL of THF. A saturated solution of water in benzene[22] (2.44 mL, 86.6 μmol, 2.00 equiv) was added dropwise to a vigorously stirred solution, effecting an immediate color change from orange-red to brown. The reaction mixture was stirred at room temperature for 20 minutes and concentrated *in vacuo*. The residue was washed with hexanes, filtered through Celite in benzene, and lyophilized to yield a brown powder (55.1 mg, 92.0%). Crystals suitable for X-ray diffraction were grown from a concentrated solution of **4** in diethyl ether with drops of THF at −35 °C. ^{1}H NMR (500 MHz, 295 K, THF-d_8): δ/ppm 42.37, 21.46, 19.05, 9.13, –0.50, –12.12. FTIR (KBr): 3637 cm^{-1} (ν_{O-H}); 2682 cm^{-1} (ν_{O-D}). %CHN Calculated for C$_{49}$H$_{58}$Co$_2$N$_4$O$_3$: C 67.73 H 6.73 N 6.45; Found: C 67.90 H 6.46 N 6.17.

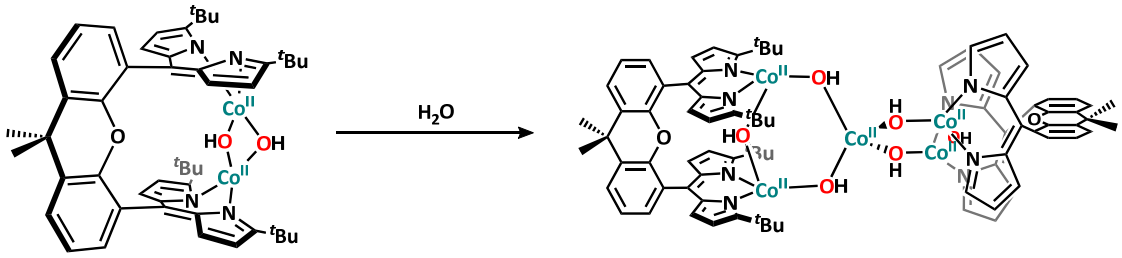

[(*t*Budmx)Co$_2$(μ-OH)]$_2$[Co(OH)$_4$] (10)** – While the targeted bis-hydroxide species was possible on the dicobalt system, we should note that sensitivity of (*t*Bu dmx)Co$_2$(μ-OH)$_2$ (**4**) to excess water can cause decomposition to a cobalt pentamer species [(*t*Bu dmx)Co$_2$(μ-OH)]$_2$[Co(OH)$_4$] (**10**). Crystals suitable for X-ray diffraction were grown from a concentrated solution of **10** in hexanes at room temperature over the course of several days. FTIR (KBr): 3645 cm^{-1} (ν_{O-H}); 2690 cm^{-1} (ν_{O-D}). While this species is not distinguishable from **4** by ^{1}H NMR spectroscopy, these species are distinguishable by FT-IR and crystallography. Furthermore, the same oxidative reactivity observed with **4** is exhibited by the analogous dicobalt bis-alkoxide species, (*t*Bu dmx)Co$_2$(O*t*Bu)$_2$(thf)$_2$ (**11**) (**Figure 3.21**). Therefore, we do not believe that the pentamer is representative of the bulk of the material highlighted in the text and is simply the decomposition product in the presence of excess water.

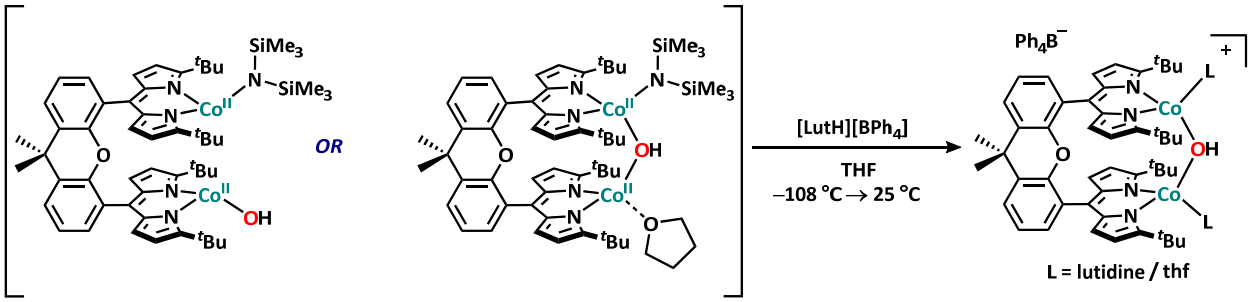

[(*t*Budmx)Co$_2$(μ-OH)L$_2$][BPh$_4$] (L = thf, 2,6-lutidine) (5a/5b) – method 1**: In a 20 mL vial, 2,6-lutidinium tetraphenylborate (9.2 mg, 21 μmol, 1.0 equiv) was dissolved in 2 mL of THF and

frozen in the cold well (–108 °C). A solution of the crude reaction mixture of "($^{t\text{Bu}}$dmx)Co$_2$(OH)[N(SiMe$_3$)$_2$]" (**2**) (20 mg scale) was added dropwise and frozen in a layer on top. The reaction mixture was thawed and allowed to stir at room temperature for 20 minutes, after which this reaction was concentrated *in vacuo*. The residue was washed with hexanes (3 mL), eluted with benzene, and concentrated *in vacuo* to afford a red-brown powder (22.4 mg, 96% - assuming a 1:1 mixture of **5a**/**5b**). *Note*: due to the instability of **2**, this reaction was performed immediately following synthesis of **2**. Crystals suitable for X-ray diffraction were grown from a concentrated solution of the product in diethyl ether at −35 °C, revealing the formation of [($^{t\text{Bu}}$dmx)Co$_2$(μ-OH)(lut)$_2$][BPh$_4$] (**5b**) due to coordination of the 2,6-lutidine byproduct to the metal centers. ^{1}H NMR (500 MHz, 295 K, THF-d_8): δ/ppm 52.31, 18.01, 12.85, 9.12, 7.47, 7.01.

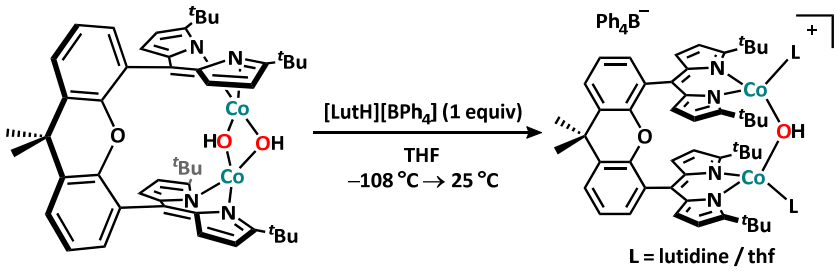

[($^{t\text{Bu}}$dmx)Co$_2$(μ-OH)L$_2$][BPh$_4$] (L = thf, 2,6-lutidine) (5a/5b) – method 2: In a 20 mL vial, 2,6-lutidinium tetraphenylborate (9.8 mg, 23.0 μmol, 1.00 equiv) was dissolved in 2 mL of THF and frozen in the cold well (–108 °C). A solution of ($^{t\text{Bu}}$dmx)Co$_2$(μ-OH)$_2$ (**4**) (20.0 mg, 23.0 μmol, 1.00 equiv) in 2 mL of THF was added dropwise and frozen in a layer on top. The reaction mixture was thawed and allowed to stir for 20 minutes, after which the crude reaction mixture was concentrated *in vacuo*. The resulting residue was washed with hexanes (3 mL), eluted with benzene, and concentrated *in vacuo* to afford a red-brown powder (30.5 mg, 98% based on 1:1 mixture of **5a** and **5b**). Crystals suitable for X-ray diffraction were grown from a concentrated solution of the product in diethyl ether plus drops of THF at −35 °C, also revealing the formation

of [($^{t\text{Bu}}$dmx)Co$_2$(μ-OH)(lut)$_2$][BPh$_4$] (**5b**) due to coordination of the 2,6-lutidine byproduct to the metal centers. ^{1}H NMR (600 MHz, 295 K, THF-d_8): δ/ppm 52.06, 17.79, 12.88, 8.80, 7.65, 7.24. FTIR (KBr): 3625 cm^{-1} (ν_{O-H}); 2683 cm^{-1} (ν_{O-D}). %CHN Calculated for $C_{81}H_{93}BCo_2N_4O_4$ (**5a**): C 73.97 H 7.13 N 4.26; %CHN Calculated for $C_{87}H_{95}BCo_2N_6O_2$ (**5b**): C 75.42 H 6.91 N 6.07; %CHN Calculated for 1:1 mixture of **5a** and **5b**: C 74.71 H 7.02 N 5.19; Found: C 74.17 H 7.05 N 5.57.

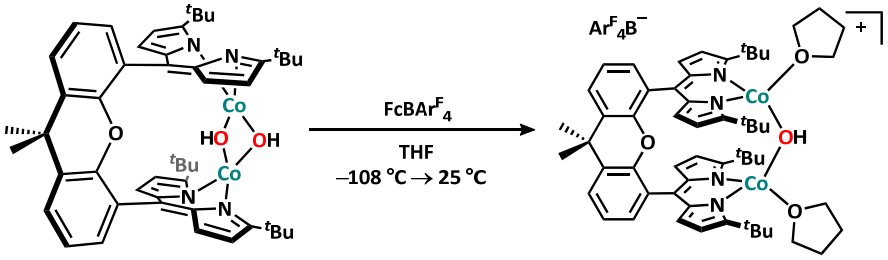

Oxidation of ($^{t\text{Bu}}$dmx)Co$_2$(μ-OH)$_2$ with FcBAr$^F_4$: In a 20 mL vial, ferrocenium tetrakis (3,5-bis(trifluoromethyl)phenyl) borate (24.1 mg, 23.0 μmol, 1.00 equiv) was dissolved in 2 mL of THF and frozen in the cold well (–108 °C). A solution of ($^{t\text{Bu}}$dmx)Co$_2$(μ-OH)$_2$ (**4**) (20.0 mg, 23.0 μmol, 1.00 equiv) in 2 mL of THF was added dropwise and frozen in a layer on top. The reaction mixture was thawed and allowed to stir for 2 hours, after which the crude reaction mixture was concentrated *in vacuo*. The resulting residue was washed with hexanes (3 mL), eluted with benzene, and concentrated *in vacuo* to afford a red-brown powder (**5c**) (41.7 mg, 97 %). ^{1}H NMR (500 MHz, 295 K, THF-d_8): δ/ppm 52.52, 17.73, 12.78, 8.88, 7.60, 7.38. See Figure S-2 for ^{1}H NMR spectra compared with **5a**/**5b**. *Note:* Performing the reaction between **4** and FcBAr$^F_4$ in the presence of 5,5-dimethyl-1-pyrrolidine-*N*-oxide (DMPO) resulted in full conversion to **5c** by ^{1}H NMR. EPR monitoring of the reaction did not reveal evidence of the DMPO/•OH radical product. Performing the reaction between **4** and FcBAr$^F_4$ in the presence of propylene oxide (PO) resulted in full conversion to **5c** by ^{1}H NMR, with no evidence of ring-opened PO product in the

diamagnetic region.The control reaction between **4** and $NaBAr^{F}_{4}$ did not show any reaction over the course of 24 hours by ^{1}H NMR. Reaction of **4** and $FcBAr^{F}_{4}$ in benzene, difluorobenzene, nor benzene in the presence of cyclohexadiene resulted in any reaction over the course of 24 hours by ^{1}H NMR.

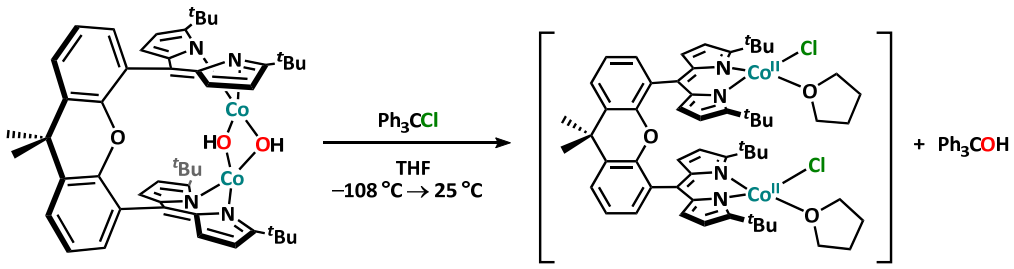

Oxidation of ($^{t\text{Bu}}$dmx)$Co_2(\mu\text{-}OH)_2$ with Ph_3CCl: In a 20 mL vial, trityl chloride (6.3 mg, 22.9 µmol, 1.99 equiv) was dissolved in 2 mL of THF and frozen in the cold well (–108 °C). A solution of ($^{t\text{Bu}}$dmx)$Co_2(\mu\text{-}OH)_2$ (**4**) (10.0 mg, 11.5 µmol, 1.00 equiv) in 2 mL of THF was added dropwise and frozen in a layer on top. The reaction mixture was thawed and allowed to stir overnight, after which the crude reaction mixture was concentrated *in vacuo*. ^{1}H NMR (cobalt-containing product) (500 MHz, 295 K, THF-d_8): δ/ppm 65.14, 46.54, 12.80, 11.81, 10.25, 5.46, 0.62, –5.28. The resulting residue was washed with pentane, filtered over celite, and concentrated *in vacuo*. Ferrocene was added as an internal standard to quantify amount of trityl alcohol (Ph_3COH) generated (2.5 mg, 42% relative to 2 equiv Ph_3CCl) ^{1}H NMR (Ph_3COH) (500 MHz, 295 K, dichloromethane-d_2): 7.26-7.33 (*m*, 15 H), 2.87 (*s*, 1 H). While suitable single crystals for X-ray diffraction of **6** from this route were not able to be grown, the ^{1}H NMR spectrum matched with that of the assigned **"($^{t\text{Bu}}$dmx)$Co_2Cl_2(thf)_2$"** (**6a**). Furthermore, addition of pyridine to the reaction mixture afforded formation of ($^{t\text{Bu}}$dmx)$Co_2Cl_2(py)_2$ (**6b**), which has been crystallographically characterized. ^{1}H NMR (600 MHz, 295 K, THF-d_8): 61.96, 32.93, 12.15, 10.98, 9.54, 8.57, –0.55, –3.05 (**Figure 3.23**).

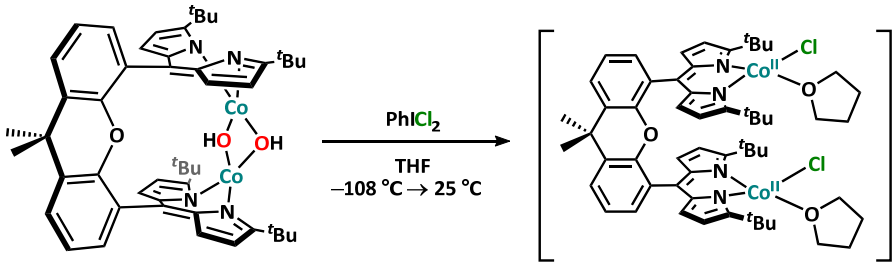

Oxidation of ($^{t\text{Bu}}$dmx)Co$_2$(μ-OH)$_2$ with PhICl$_2$: In a 20 mL vial, iodobenzene dichloride (3.2 mg, 11.5 μmol, 1.00 equiv) was dissolved in 2 mL of THF and frozen in the cold well (–108 °C). A solution of ($^{t\text{Bu}}$dmx)Co$_2$(μ-OH)$_2$ (**4**) (10.0 mg, 11.5 μmol, 1.00 equiv) in 2 mL of THF was added dropwise and frozen in a layer on top. The reaction mixture was thawed and allowed to stir for five hours, after which the crude reaction mixture was concentrated *in vacuo*. ^{1}H NMR (cobalt-containing product) (500 MHz, 295 K, THF-*d*$_8$): *δ*/ppm 65.07, 46.46, 12.20, 11.00, 9.81, 5.14, 0.81, –5.35. While suitable single crystals for X-ray diffraction of **6** from this route were not able to be grown, the ^{1}H NMR spectrum matched with that of the assigned **"($^{t\text{Bu}}$dmx)Co$_2$Cl$_2$(thf)$_2$"** (**6a**). Furthermore, addition of pyridine to the reaction mixture afforded formation of ($^{t\text{Bu}}$dmx)Co$_2$Cl$_2$(py)$_2$ (**6b**), which has been crystallographically characterized. ^{1}H NMR (500 MHz, 295 K, THF-*d*$_8$): 62.83, 32.73, 12.83, 10.11, 9.32, 7.70, –0.67, –3.15.

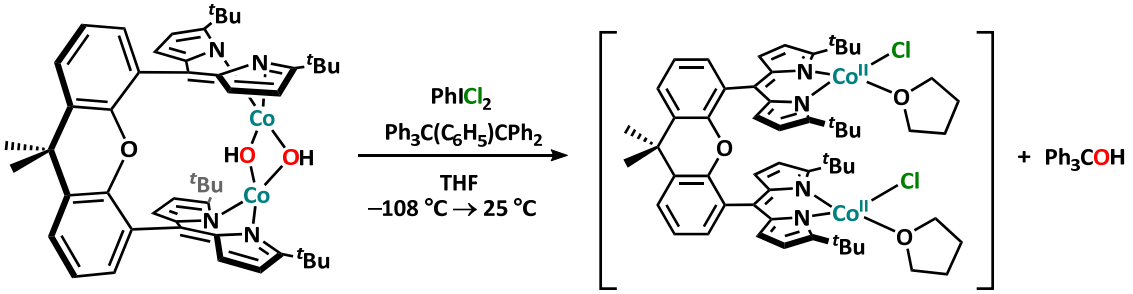

Oxidation of ($^{t\text{Bu}}$dmx)Co$_2$(μ-OH)$_2$ with PhICl$_2$ in the presence of Gomberg's Dimer: In a 20 mL vial, PhICl$_2$ (3.2 mg, 11.5 μmol, 1.00 equiv) was dissolved in 2 mL of THF and frozen in the cold well (–108 °C). A solution of ($^{t\text{Bu}}$dmx)Co$_2$(μ-OH)$_2$ (**4**) (10.0 mg, 11.5 μmol, 1.00 equiv)

in 1 mL of THF was added dropwise and frozen in a layer on top. A solution of Gomberg's dimer (5.6 mg, 11.5 µmol, 1.00 equiv) in 1 mL of THF was added dropwise and frozen in a layer on top. The reaction mixture was thawed and allowed to stir for five hours, after which the crude reaction mixture was concentrated *in vacuo*. ^{1}H NMR (cobalt-containing product) (500 MHz, 295 K, THF-d_8): δ/ppm 65.02, 46.54, 12.68, 10.94, 9.62, 5.19, 0.77, –5.46. The resulting residue was washed with pentane, filtered over celite, and concentrated *in vacuo* to reveal formation of trityl alcohol. ^{1}H NMR (Ph_3COH) (500 MHz, 295 K, dichloromethane-d_2): 7.26-7.34 (*m*, 15 H), 2.88 (*s*, 1 H).

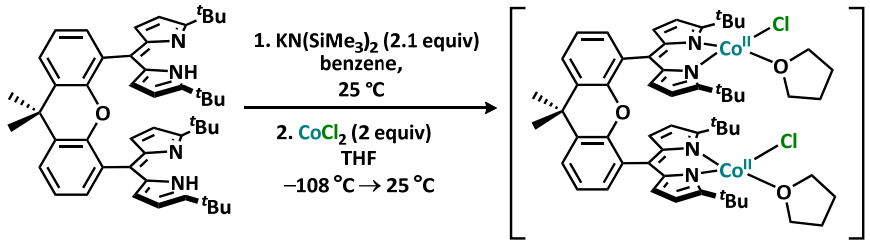

"(tBudmx)$Co_2Cl_2(thf)_2$" (6a): In a 100 mL round bottom, K(N($SiMe_3$)$_2$ (277.4 mg, 1,391 µmol, 2.10 equiv) was slowly added as a slurry in 20 mL of benzene to ($^{t\text{Bu}}$dmx)H_2 (500.0 mg, 695 µmol, 1.00 equiv) stirring in 15 mL of benzene. A color change to a slightly more brown-orange and substantial decrease in solubility were observed immediately. After stirring for 1 hour at room temperature, the crude reaction mixture was concentrated *in vacuo*. The brown-orange solid was filtered over a medium frit and washed with hexanes (2 x 20 mL) and benzene (20 mL) to afford "($^{t\text{Bu}}$dmx)K_2" (481.9 mg, 85%). In a 20 mL vial, ($^{t\text{Bu}}$dmx)K_2 (40.0 mg, 50.0 µmol, 1.00 equiv) was dissolved in 2 mL of THF and frozen in the cold well (–108 °C). A solution of $CoCl_2$ (13.0 mg, 100 µmol, 2.00 equiv) in 2 mL of THF was added dropwise and frozen in a layer on top. The reaction mixture was thawed and allowed to stir overnight, after which the crude reaction mixture was concentrated *in vacuo* to afford a brown film assigned as **"($^{t\text{Bu}}$dmx)$Co_2Cl_2(thf)_2$" (6a)**. *Note*: we assign this as the THF solvent-ligated species due to the similarity of the ^{1}H NMR spectrum

features to the pyridine-ligated species when pyridine is present, and due to the coordination of THF to the cobalt centers in the ($^{t\text{Bu}}$dmx)Co_2(O^tBu)$_2$(thf)$_2$ **(11)** species, when even bulkier O^{t}Bu groups are present. ^{1}H NMR (500 MHz, 295 K, THF-d_8): δ/ppm 65.17, 46.54, 13.16, 11.35, 10.11, 5.15, 0.78, –4.86. While suitable single crystals for X-ray diffraction of this species were not able to be grown, those by an analogous reaction to afford ($^{t\text{Bu}}$dmx)Co_2Cl_2(py)$_2$ (**6b**) were possible. Addition of pyridine to **6a** in THF yielded a distinct ^{1}H NMR spectrum that matched **6b**. ^{1}H NMR (500 MHz, 295 K, THF-d_8): δ/ppm 61.36, 32.19, 11.85, 10.12, 9.00, 7.78, –0.70, –3.31 (**Figure 3.23**).

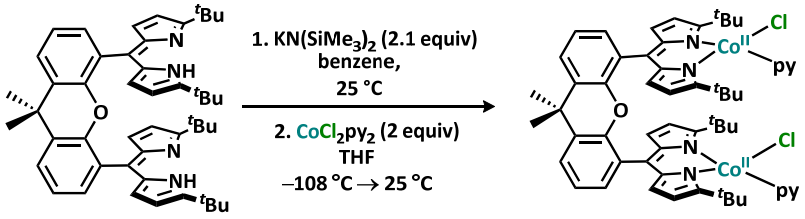

($^{t\text{Bu}}$dmx)Co_2Cl_2(py)$_2$ (**6b**): ($^{t\text{Bu}}$dmx)K_2 was synthesized in the same method described in the previous synthesis. In a 20 mL vial, ($^{t\text{Bu}}$dmx)K_2 (40.0 mg, 50.0 µmol, 1.00 equiv) was dissolved in 2 mL of THF and frozen in the cold well (–108 °C). A solution of $CoCl_2$(py)$_2$ (28.8 mg, 100 µmol, 2.00 equiv) in 2 mL of THF was added dropwise and frozen in a layer on top. The reaction mixture was thawed and allowed to stir overnight, after which the crude reaction mixture was concentrated *in vacuo*. The residue was extracted with toluene, filtered, and concentrated *in vacuo* to afford a brown film (49.5 mg, 93%). Crystals suitable for X-ray diffraction were grown from a concentrated solution of **6b** in THF with drops of diethyl ether at −35 °C. ^{1}H NMR (500 MHz, 295 K, THF-d_8): δ/ppm 61.12, 32.61, 12.22, 10.58, 9.34, 8.17, –0.55, –3.09. %CHN Satisfactory elemental analysis has not been successful due to the hydrolytic sensitivity of the molecule.

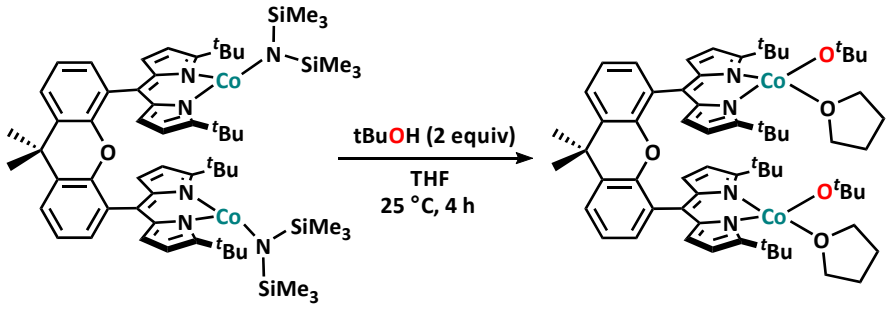

($^{t\text{Bu}}$dmx)Co$_2$(O^{t}Bu)$_2$(thf)$_2$ (11): In a 20 mL vial, *tert*-butanol (3.9 mg, 52.6 µmol, 2.02 equiv) was added to a stirring solution of ($^{t\text{Bu}}$dmx)Co$_2$[N(SiMe$_3$)$_2$]$_2$ (**1**) (30.0 mg, 26.0 µmol, 1.00 equiv) in THF. The reaction mixture was allowed to stir for 4 hours, after which the crude reaction mixture was concentrated *in vacuo* to afford a brown film. Crystals suitable for X-ray diffraction were grown from a saturated solution of **11** in diethyl ether with drops of THF at –35 °C. ^{1}H NMR (500 MHz, 295 K, THF-*d*$_8$): δ/ppm 60.53, 49.29, 23.07, 13.18, 9.48, 8.68, 6.46, –0.09, –4.28. %CHN Calculated for C$_{65}$H$_{90}$Co$_2$N$_4$O$_5$: C 69.38 H 8.06 N 4.98; Found: C 69.60 H 8.36 N 4.54.

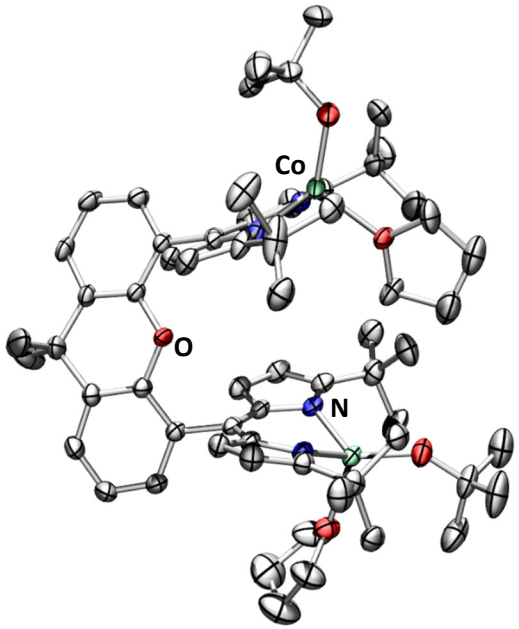

Figure 3.22. Solid state molecular structure ($^{t\text{Bu}}$dmx)Co$_2$(O^{t}Bu)$_2$(thf)$_2$ (**11**) with thermal ellipsoids at 50% probability level. Hydrogen atoms omitted for clarity. Color scheme: Co, aquamarine; N, blue; C, gray; O, red.

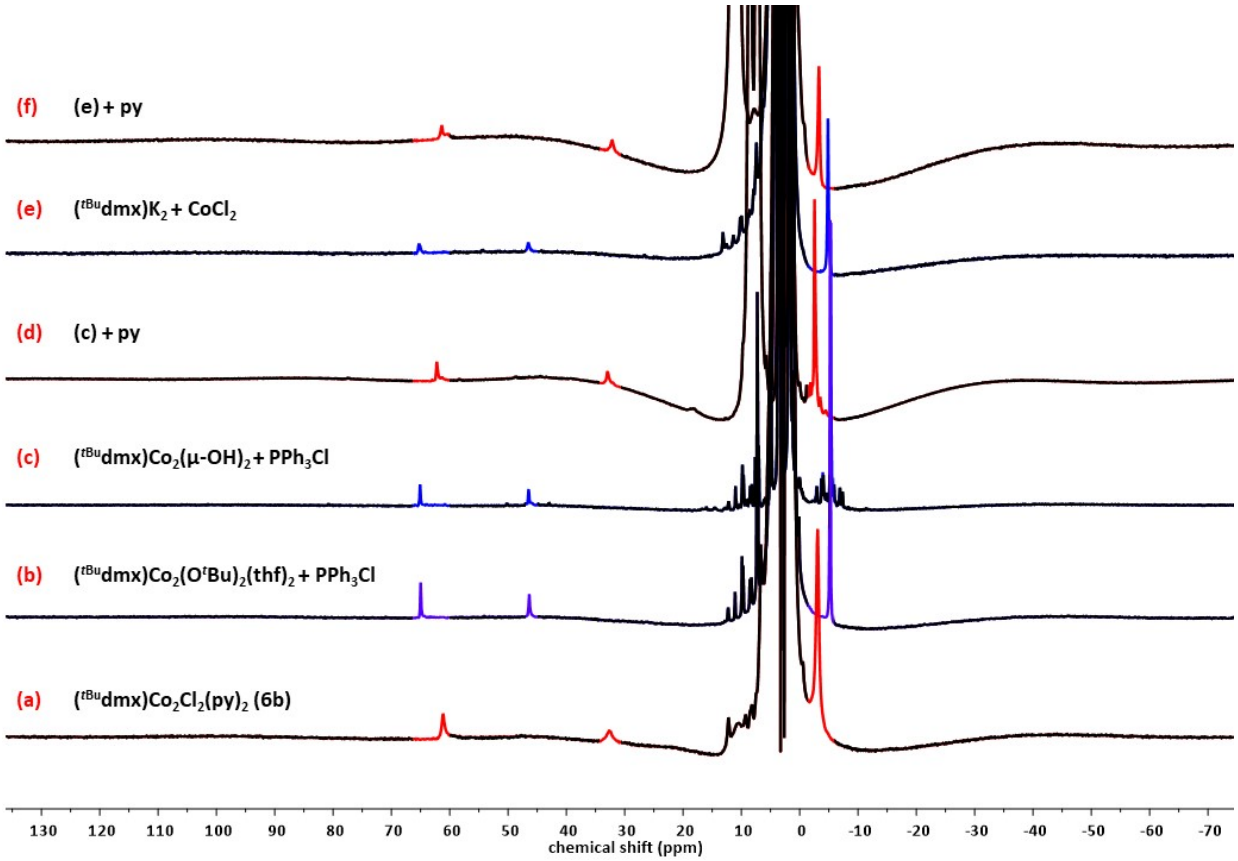

Figure 3.23. ^{1}H NMR spectra of various methods to synthesize ($^{t\text{Bu}}$dmx)Co$_2$Cl$_2$(L)$_2$ (**6**) in THF, showing "($^{t\text{Bu}}$dmx)Co$_2$Cl$_2$(thf)$_2$" (**6a**) in blue and [($^{t\text{Bu}}$dmx)Co$_2$Cl$_2$(py)$_2$ (**6b**) in red. (a) Authentic **6b** via metathesis reaction discussed above. (b) Crude reaction of Ph$_3$CCl addition to **8**, forming **6a**. (c) Crude reaction mixture of Ph$_3$CCl addition to **4**, forming **6a**. (d) Addition of pyridine to reaction mixture (c) resulted in convergence to **6b**. (e) Independent synthesis of **6a** via metathesis reaction discussed above. (f) Addition of pyridine to reaction mixture (e) resulted in convergence to **6b**.

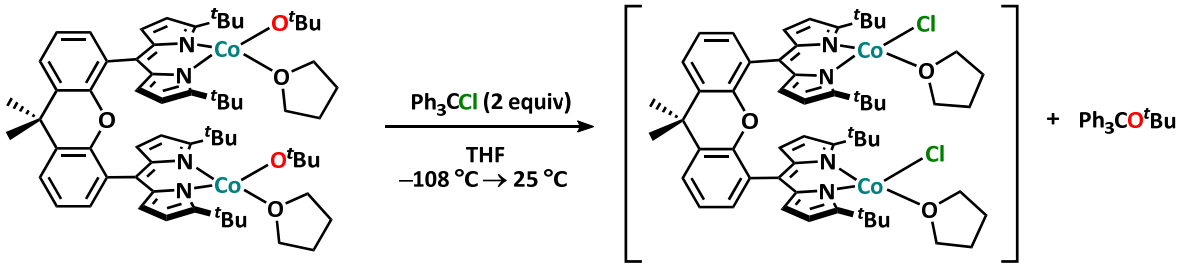

Oxidation of ($^{t\text{Bu}}$dmx)Co$_2$(O^{t}Bu)$_2$(thf)$_2$ with Trityl Chloride: In a 20 mL vial, Ph$_3$CCl (19.3 mg, 69.2 μmol, 2.01 equiv) was dissolved in 2 mL of THF and frozen in the cold well (–108 °C). A solution of ($^{t\text{Bu}}$dmx)Co$_2$(O^{t}Bu)$_2$(thf)$_2$ (**11**) (30.0 mg, 34.5 μmol, 1.00 equiv) in 2 mL of THF was added dropwise and frozen in a layer on top. The reaction mixture was thawed and allowed to stir

overnight to afford **6a**, after which the crude reaction mixture was concentrated *in vacuo*. ^{1}H NMR (500 MHz, 295 K, THF-d_8): δ/ppm 64.99, 46.37, 12.26, 11.07, 9.88, 5.22, 0.90, –5.23. See **Figure 3.23** for the ^{1}H NMR stack of this reaction and the other methods to form **6a**. The resulting residue was washed with pentane, filtered over celite, and concentrated *in vacuo*. ^{1}H NMR (Ph_3CO^tBu) (500 MHz, 295 K, dichloromethylene-d_2): 7.18-7.25 (*m*, 6 H, *m*-ArH's), 7.10-7.16 (*m*, 9 H, *o*- and *p*-ArH's), 1.31 (*t*, 9 H).

3.6.4 Theoretical Methods

All calculations were performed using the density functional theory and the quantum chemical program package Gaussian16[29] using the unrestricted B3LYP hybrid functional (which includes the Becke three-parameter exchange and the Lee, Yang, and Parr correlation functional) and GD3BJ dispersion of Grimme et al. with Becke-Johnson damping.[30] The SDD basis set was used in the investigation, which combines the Dunning/Huzinaga valence double-zeta basis[31] for elements up to Ar, with the Stuttgart/Dresden effective core potentials[32] for the remainder of the periodic table. This method and level of theory is consistent with previous studies on the analogous diiron Pacman species. Solvation of the molecular species was modelled using continuum parameters designed to describe tetrahydrofuran solvent ($\varepsilon = 7.43$). Geometry optimizations were performed in order to obtain electronic energies, followed by frequency calculations to compute zero-point energies and derive values for thermal and entropic corrections at 298.15 K.

---

[29] Gaussian, Inc., Revision B.01 (2016), Wallingford CT.

[30] Grimme, S.; Ehrlich, S.; Goerigk, L. *J. Comp. Chem*. **2011**, *32*, 1456–1465.

[31] Dunning, T. H., Jr.; Hay, P. J. in *Modern Theoretical Chemistry*, *Vol. 3* (Ed. H. F. Schaefer III), Plenum **1997**.

[32] (a) Wedig, U.; Dolg, M.; Stoll, H.; Preuss, H. in *Quantum Chemistry: The Challenge of Transition Metals and Coordination Chemistry* (Ed. A. Veillard, Reidel and Dordrecht), D. Reidel Publishing Company **1986**. (b) Bergner, A.; Dolg, M.; Kuchle, W.; Stoll, H.; Preuss, H. *Mol. Phys.,* **1993,** *80,* 1431–1441.

To look at the spin density on **4** and the proposed oxidized products **7**, **8**, and **9**, single point energy calculations were utilized on the optimized structures (**Figure 3.27, Figure 3.28**). These was carried out using the ORCA 4.0.1.2 program package[33] and were initiated from spin-unrestricted single-point calculations that employed the B3LYP functional[34] with the def2-TZVP (Co, N, O, Cl) and def2-SV(P) (C, H) basis sets.[35] Further, the def2-TSVP/J (Co, N, O, Cl) and def2-SV(P)/J (C, H) auxiliary basis sets were employed to utilize the RIJCOSX approximation for accelerating the calculation.[36] This method and level of theory is consistent with single point energy calculations performed previously on the diiron Pacman species. A broken symmetry solution was used to model the coupling present in the complexes. The standard notation BS(*m*,*n*) represents the (*m*+*n*) unpaired electrons within a system and net spin of $^{(m-n)}/_{2}$ for an antiferromagnetically coupled system.[37] As such, one fragment will bear *m* α electrons while the other bears *n* β electrons. The appropriate description for each case was as high spin cobalt centers (i.e., high spin cobalt(II) for **4**, high spin cobalt(II) cobalt(III) for **7** and **8**, and high spin cobalt (III) for **9** (**Table 3.1**)). The exchange coupling constant *J* was determined from the energy difference between the high-spin and broken-symmetry states, using the spin Hamiltonian in **equation 2** and formula in **equation 3**[38]:

$$H = -2J\overrightarrow{S_{Fe(1)}} \cdot \overrightarrow{S_{Fe(2)}} \quad (2)$$

[33] Neese, F. *WIREs Comput. Mol. Sci.* **2012**, *2*, 73-78.

[34] (a) Becke, A. D. *J. Chem. Phys.* **1993**, *98*, 5648–5652. (b) Lee, C. T.; Yang, W. T.; Parr, R. G. *Phys Rev. B*. 1988, *33*, 785–789.

[35] Weigend, F. *Phys. Chem. Chem. Phys.* **2006**, *8*, 1057–1065.

[36] Neese, F.; Wennmohs, F.; Hansen, A.; Becker. U. *Chem. Phys.* **2009**, *356*, 98–109.

[37] Kirchner, B.; Wenmohs, F.; Ye, S.; Neese, F. *Curr. Opin. Chem. Biol.* **2007**, *11*, 134–141.

[38] (a) Ginsberg, A. P. *J. Am. Chem. Soc.* **1980**, *102*, 111–117. (b) Noodleman, L. *J. Chem. Phys.* **1981**, *74*, 5737–5743. (c) Noodleman, L.; Davidson, E. R. *Chem. Phys.* **1986**, *109*, 131–143.

$$J = -\frac{E_{HS}-E_{BS}}{S^2_{max}}. \quad (3)$$

Table 3.1. Broken symmetry solution information for **4**, **7**, **8**, and **9**.

Complex	Broken symmetry description	E_{HS} - E_{BS} (cm^{-1})	J (cm^{-1})
4	BS(*3*,*3*)	172.188	–19.1
7	BS(*3*,*4*)	119.541	–9.76
8	BS(*3*,*4*)	–164.620	13.4
9	BS(*4*,*4*)	295.158	–18.1

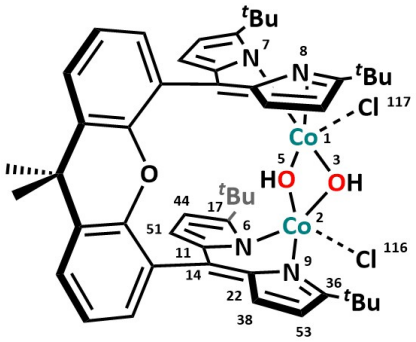

Table 3.2. Löwdin spin density values of selected atoms for **4**, **7**, **8**, and **9**, numbered as indicated in the scheme above.

	4	**7**	**8**	**9**
Co-1	2.6889	2.6897	2.6777	3.0275
Co-2	-2.6868	-2.6884	-2.6965	-2.6813
O-3	0.001328	-0.018198	0.007847	0.082123
O-5	0.006423	-0.021983	-0.018847	0.23814
N-6	-0.05252	-0.018150	-0.014010	0.000856
N-7	0.14589	0.050410	0.051084	0.004565
N-8	0.11968	0.053598	0.049307	0.053141
N-9	-0.04793	-0.008710	0.008208	-0.006191
C-11	**-0.005537**	**-0.30500**	**-0.25084**	**-0.29191**
C-14	**0.000151**	**0.13141**	**0.13251**	**0.14061**
C-17	**-0.005397**	**-0.20538**	**-0.16410**	**-0.20872**
C-22	**-0.006855**	**-0.26007**	**-0.26891**	**-0.26682**
C-36	**-0.004611**	**-0.16923**	**-0.17855**	**-0.18263**
C-38	-0.005668	0.016627	0.004548	0.008527
C-44	**-0.007928**	**-0.13144**	**-0.12613**	**-0.12611**
C-51	-0.000123	0.011613	0.008749	0.000149
C-53	**-0.008326**	**-0.12803**	**-0.13222**	**-0.13056**
dipyrrin*	-0.038503	-1.0677	-0.98823	-1.0661
Cl-116	–	–	-0.060420	-0.62727
Cl-117	–	–	–	0.14518

*dipyrrin value represents the sum of the bolded atoms of the dipyrrin, which show a significant increase in spin density between **4** and the oxidized intermediates **7**, **8**, and **9**.

To understand the solvation of complex **5**, we considered the following reactions using the optimized structures of **5**, **5a**, and **5b** (**Figure 3.25**, **Figure 3.26**) plus the optimized structures of the small molecules, THF and 2,6-lutidine. We observe that binding two 2,6-lutidine molecules to **5** is more energetically favorable than binding two THF molecules

$$\mathbf{5} + 2\ \text{THF} \rightarrow \mathbf{5a} \qquad \Delta G = -107\ \text{kJ mol}^{-1}$$

$$\mathbf{5} + 2\ (2,6\text{-lutidine}) \rightarrow \mathbf{5b} \qquad \Delta G = -149\ \text{kJ mol}^{-1}$$

This is consistent with the observation that 2,6-lutidine does indeed bind when available, as observed in the solid state structure, but due to the insufficient stoichiometry of the generated 2,6-lutidine, we hypothesize that THF solvent molecules will bind once 2,6-lutidine is no longer available.

pK_a values of the bridging hydroxide species were calculated using the same method used for the diiron Pacman complexes[5] which models the method published by Smith *et al*.[12] As such, a general acid-base reaction between a bridging hydroxide species (denoted below as $[\textit{hydroxide}]^+$) and a bridging oxo species (denoted as *oxo*) is considered:

$$[\textit{hydroxide}]^+ + [A]^- \rightarrow \textit{oxo} + HA \qquad (4)$$

where HA is a weak acid whose pK_a value in THF has previously been reported.[39] The overall free energy of the reaction is thus satisfied by the relationship:

$$\Delta G = 2.303RT\ [pK_a([\textit{hydroxide}]^+) - pK_a(HA)] \qquad (5)$$

where $pK_a([\textit{hydroxide}]^+)$ and $pK_a(HA)$ denote the pK_a values for the $[\textit{hydroxide}]^+$ and HA, respectively. As described by Smith *et. al*, using this method one evaluates the relative free energy

[39] Naito, I.; Ding, F.; Bontchev, R. P.; Wang, H.; Smith, J. M. *J. Am. Chem. Soc.* **2008**, *130,* 2716–2717.

with respect to a known weak acid, HA, and thus bypasses the explicit treatment of the solvated proton.[39]

In order to estimate the pK_a of the dicobalt hydroxide species, the acid-base reactions were considered between the dicobalt hydroxide and the respective conjugate base, which will differ simply by one proton. For the mono-hydroxides **5a** and **5b**, the acid-base reactions between complex **5a** and the corresponding deprotonated ($^{t\text{Bu}}$dmx)Co_2(μ-O)$(thf)_2$ (**12a**) (**equation 6**) and between complex **5b** and the corresponding deprotonated structure ($^{t\text{Bu}}$dmx)Co_2(μ-O)$(lut)_2$ (**12b**) (**equation 7**) were evaluated. The optimized structures of **12a** and **12b** can be found in **Figure 3.29**.

$$(^{t\text{Bu}}\text{dmx})\text{Co}_2(\mu\text{-OH})(\text{thf})_2^{+} + \text{A}^{-} \rightarrow (^{t\text{Bu}}\text{dmx})\text{Co}_2(\mu\text{-O})(\text{thf})_2 + \text{HA} \qquad (6)$$

$$(^{t\text{Bu}}\text{dmx})\text{Co}_2(\mu\text{-OH})(\text{lut})_2^{+} + \text{A}^{-} \rightarrow (^{t\text{Bu}}\text{dmx})\text{Co}_2(\mu\text{-O})(\text{lut})_2 + \text{HA} \qquad (7)$$

The overall free energy of these reactions is satisfied by the relationship:

$$\Delta G = 2.303RT\,[pK_a([\text{Co}_2(\mu\text{-OH})(L)_2]^{+}) - pK_a(HA)] \qquad (8)$$

where $pK_a([\text{Co}_2(\mu\text{-OH})(L)_2]^{+})$ denotes the pK_a value for **5a** (L = thf) or **5b** (L = 2,6 lutidine) and pK_a(HA) denotes the pK_a value of HA.[39] This method was tested with a series of acids spanning a range of pK_a values (Table S-1) and yielded pK_a values for **5a** and **5b** which was consistent across this series. The derived values of pK_a by this method was shown to be 31.8(6) for [($^{t\text{Bu}}$dmx)Co_2(μ-OH)$(thf)_2]^{+}$ (**5a**) and 29.1(6) for [($^{t\text{Bu}}$dmx)Co_2(μ-OH)$(lut)_2]^{+}$ (**5b**) in THF.

For the bis-hydroxide **4**, the acid-base reactions between complex **4** and the corresponding deprotonated [($^{t\text{Bu}}$dmx)Co_2(μ-O)(μ-OH]$^{-}$ (**13**) (**equation 9**) to demonstrate the first protonation and between complex [($^{t\text{Bu}}$dmx)Co_2(μ-O)(μ-OH]$^{-}$ (**13**) and the corresponding doubly deprotonated [($^{t\text{Bu}}$dmx)$Co_2(\mu\text{-O})_2]^{2-}$ (**14**) (**equation 10**) to represent the second deprotonation were evaluated.

The optimized structures of **13** and **14** can be found in **Figure 3.30**. It should be noted that a geometric shift of the diamond core of the mono-deprotonated complex **13** occurs and a hydrogen-bonding interaction is observed between the hydroxo-proton and the oxygen of the dimethylxanthene backbone.

$$(^{t\text{Bu}}\text{dmx})\text{Co}_2(\mu\text{-OH})_2 + \text{A}^- \rightarrow [(^{t\text{Bu}}\text{dmx})\text{Co}_2(\mu\text{-O})(\mu\text{-OH}]^- + \text{HA} \quad (9)$$

$$[(^{t\text{Bu}}\text{dmx})\text{Co}_2(\mu\text{-O})(\mu\text{-OH}]^- + \text{A}^- \rightarrow [(^{t\text{Bu}}\text{dmx})\text{Co}_2(\mu\text{-O})_2]^{2-} + \text{HA} \quad (10)$$

The overall free energy of these reactions is satisfied by the relationships:

$$\Delta G = 2.303RT\,[pK_a(\text{Co}_2(\mu\text{-OH})_2) - pK_a(\text{HA})] \quad (11)$$

$$\Delta G = 2.303RT\,[pK_a([\text{Co}_2(\mu\text{-O})(\mu\text{-OH})]^-) - pK_a(\text{HA})] \quad (12)$$

where $pK_a(\text{Co}_2(\mu\text{-OH})_2)$ denotes the pK_a value for **4**, $pK_a([\text{Co}_2(\mu\text{-O})(\mu\text{-OH})]^-)$ denotes the pK_a value for **13,** and $pK_a(\text{HA})$ denotes the pK_a value of HA.[Error! Bookmark not defined.] This method was tested with a series of acids spanning a range of pK_a values (**Table 3.3**) and yielded pK_a values for **4** and **13** which was consistent across each series. The derived values of pK_a by this method was shown to be 41.7(6) for $\text{Co}_2(\mu\text{-OH})_2$ (**4**) and 71.8(6) for $[\text{Co}_2(\mu\text{-O})(\mu\text{-OH})]^-$ (**13**) in THF.

Table 3.3. Calculated pK_a values of **5a**, **5b, 4**, and **13** with respect to different reference acids.

Reference Acid	Calculated pK_a of $[\text{Co}_2(\mu\text{-OH})(\text{thf})_2]^+$ (5a)	Calculated pK_a of $[\text{Co}_2(\mu\text{-OH})(\text{thf})_2]^+$ (5b)	Calculated pK_a of $\text{Co}_2(\mu\text{-OH})_2$ (4)	Calculated pK_a of $[\text{Co}_2(\mu\text{-O})(\mu\text{-OH})]^-$ (13)
Lutidinium	32.6	29.9	42.5	72.6
Benzoic Acid	31.9	29.3	41.9	72.0
Acetic Acid	31.6	29.0	41.6	71.6
Phenol	30.8	28.2	40.8	70.8
2,2,2-trifluoroethanol	31.8	29.2	41.7	71.8

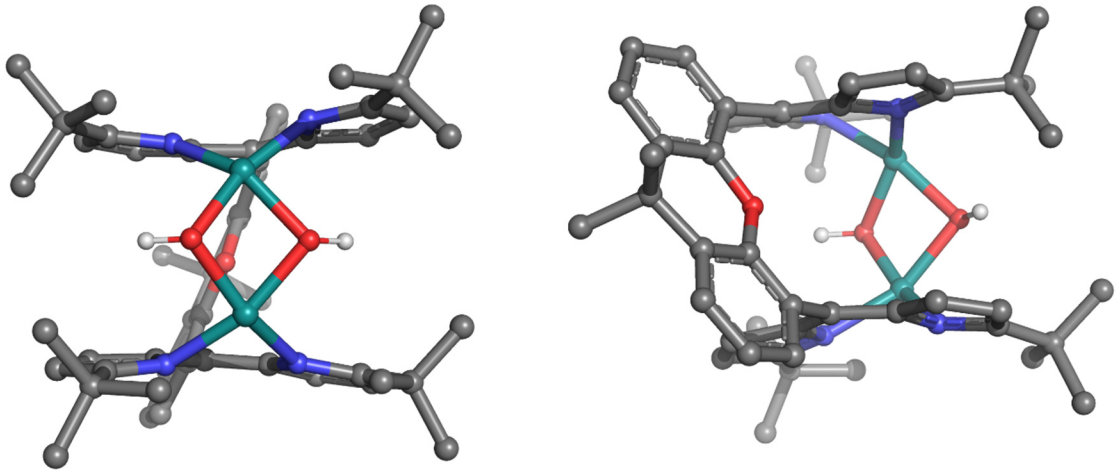

Figure 3.24. Geometry optimized structures of ($^{t\text{Bu}}$dmx)Co_2(μ-OH)$_2$ (**4**), (**Left**) Front view and (**Right**) Side view. Hydrogen atoms except for the hydroxo protons have been omitted for clarity.

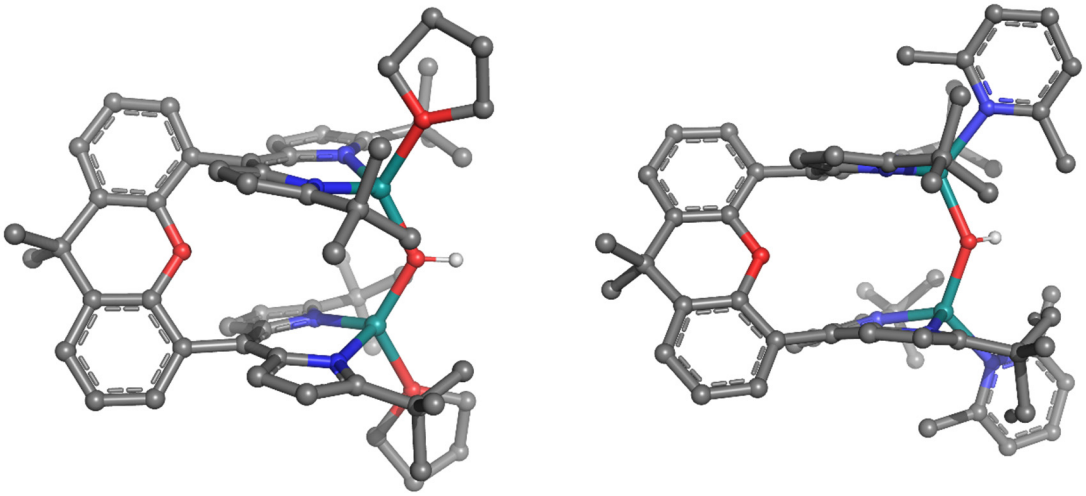

Figure 3.25. Geometry optimized structures of dicobalt(II) μ-hydroxo complexes. (**Left**) [($^{t\text{Bu}}$dmx)Co_2(μ-OH)(thf)$_2$]$^+$ (**5a**), (**Right**) [($^{t\text{Bu}}$dmx)Co_2(μ-OH)(lut)$_2$]$^+$ (**5b**). Hydrogen atoms except for the hydroxo protons have been omitted for clarity.

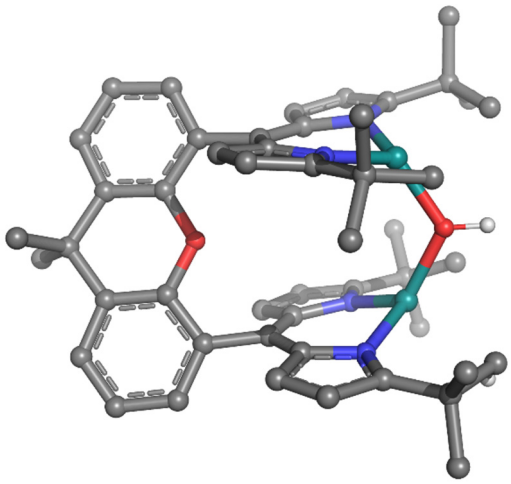

Figure 3.26. Geometry optimized structure of $[(^{t\text{Bu}}\text{dmx})\text{Co}_2(\mu\text{-OH})]^+$ (**5**). Hydrogen atoms except for the hydroxo protons have been omitted for clarity.

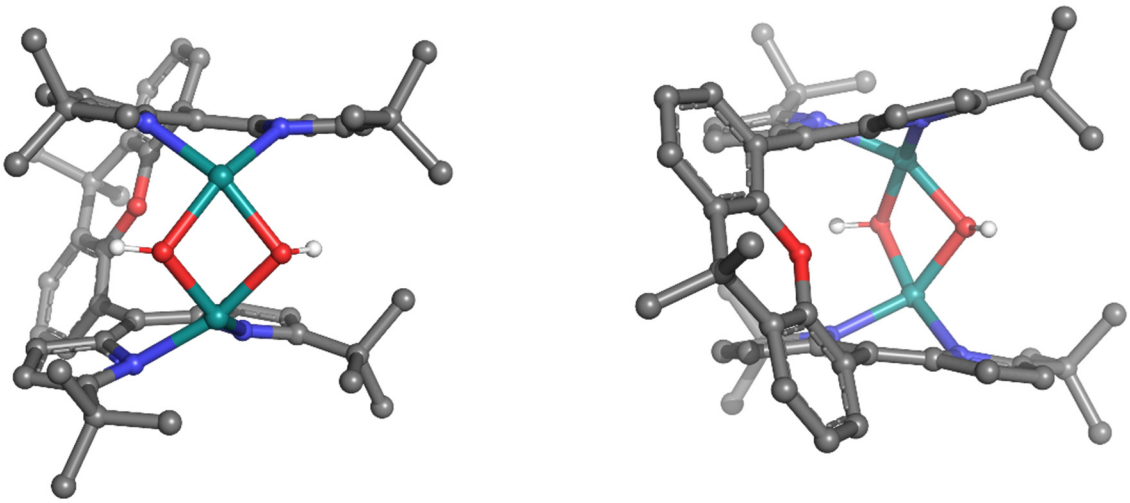

Figure 3.27. Geometry optimized structure of $[(^{t\text{Bu}}\text{dmx})\text{Co}_2(\mu\text{-OH})_2]^+$ (**7**), (**Left**) Front view and (**Right**) Side view. Hydrogen atoms except for the hydroxo protons have been omitted for clarity.

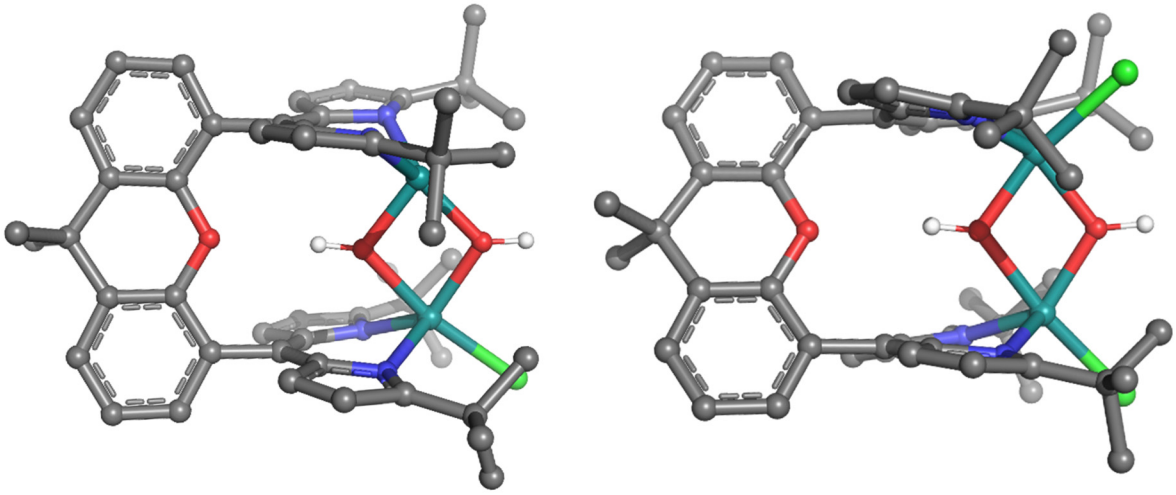

Figure 3.28. Geometry optimized structures of (**Left**) ($^{t\text{Bu}}$dmx)Co_2(μ-OH)Cl (**8**) and (**Right**) ($^{t\text{Bu}}$dmx)Co_2(μ-OH)Cl_2 (**9**). A geometric shift of the dicobalt bis-hydroxide diamond core is observed to accommodate the five-coordinate cobalt center(s) upon chloride ligation. Hydrogen atoms except for the hydroxo protons have been omitted for clarity.

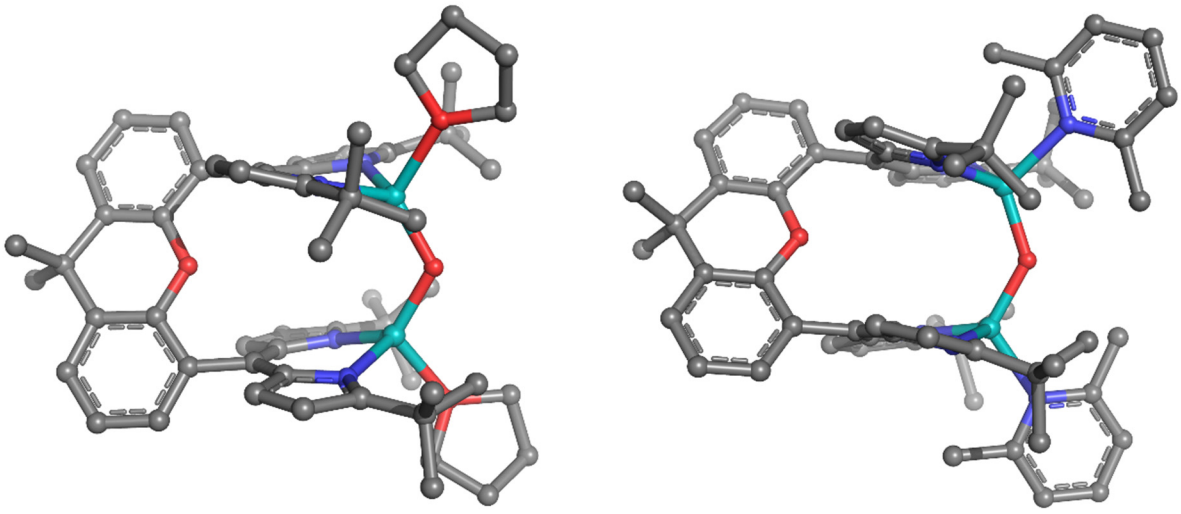

Figure 3.29. Geometry optimized structures of deprotonated dicobalt(II) mono-μ-hydroxo complexes. (**Left**) ($^{t\text{Bu}}$dmx)Co_2(μ-O)$(thf)_2$ (**12a**), (**Right**) ($^{t\text{Bu}}$dmx)Co_2(μ-O)$(lut)_2$ (**12b**). Hydrogen atoms except for the hydroxo protons have been omitted for clarity.

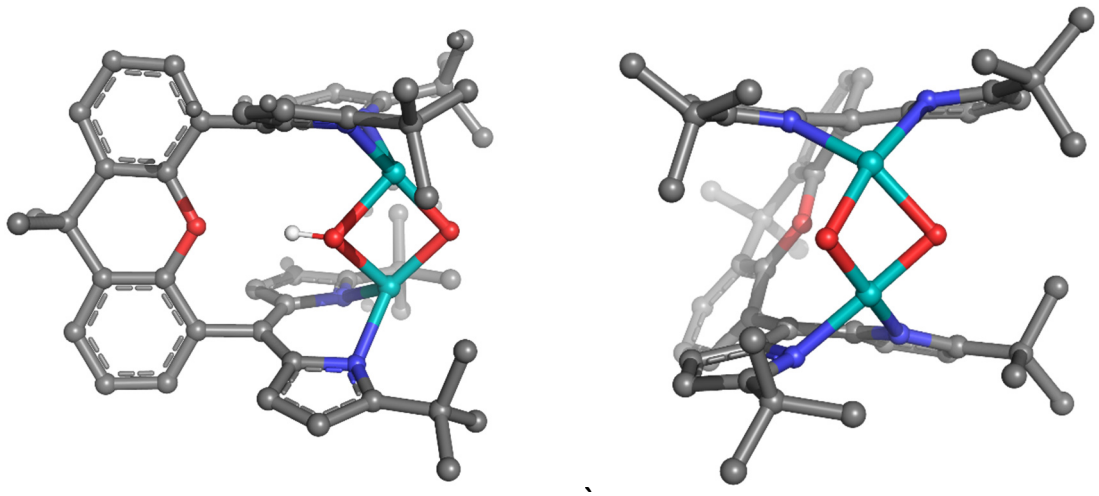

Figure 3.30. Geometry optimized structures of deprotonated dicobalt(II) bis-μ-hydroxo complexes, (**Left**) [($^{t\text{Bu}}$dmx)Co$_2$(μ-O)(μ-OH)]$^-$ (**13**); (**Right**) [($^{t\text{Bu}}$dmx)Co$_2$(μ-O)$_2$]$^{2-}$ (**14**). Hydrogen atoms except for the hydroxo protons have been omitted for clarity.

Table 3.4. Coordinates of optimized structures **4**, **5a**, **5b**, **5**, **7**, **8**, **9**, **12a**, **12b**, **13**, and **14**.

($^{t\text{Bu}}$dmx)Co$_2$(μ-OH)$_2$ (**4**)
E = −2638.71251111 a.u.
G = −2637.832731 a.u.
Charge = 0, Multiplicity = 7

Co	-1.837070	1.186985	-0.998073
Co	-1.925200	-0.979198	1.001537
O	-2.642107	-0.641197	-0.853428
O	2.718145	-0.017246	0.058445
O	-2.160665	0.995553	0.965960
N	-0.622362	-0.904911	2.551428
N	-1.033200	3.027120	-0.675351
N	-0.496227	0.794536	-2.483465
N	-1.220552	-2.819674	0.481602
C	1.230218	2.040526	-1.141461
C	0.714682	-1.216422	2.187867
C	0.374249	2.936915	-0.463692
C	0.845489	1.105623	-2.129445
C	1.079636	-2.044839	1.101949
C	1.724163	0.425184	-3.039090
H	2.803545	0.475190	-3.026004
C	-0.581466	-0.198375	3.715022
C	0.744845	3.927898	0.511381
H	1.744304	4.095330	0.885861
C	0.920868	-0.249720	-3.956991
H	1.252023	-0.840102	-4.799290
C	0.192197	-2.800380	0.302650
C	5.692630	-0.109997	0.085659
C	-1.501267	4.033994	0.112598
C	-0.449439	0.003272	-3.595361
C	2.702452	2.163056	-0.900764
C	-2.967454	0.199059	-3.994973
H	-3.268977	-0.009113	-2.965662
H	-3.772003	-0.144347	-4.657798
H	-2.868504	1.285879	-4.112176
C	4.783359	-1.297551	0.430070
C	4.864484	1.110025	-0.340777
C	-0.418133	4.618198	0.860134
H	-0.503099	5.440408	1.557041
C	-1.649263	-0.511944	-4.378783

C	-1.728864	-3.766251	-0.356439	C	-3.023908	5.980412	-0.210311
C	-2.954525	4.475970	0.179509	H	-2.403872	6.593619	0.454051
C	0.525666	-3.744067	-0.729914	H	-4.059352	6.338016	-0.139439
H	1.521385	-3.943339	-1.099244	H	-2.674362	6.130807	-1.239589
C	6.535282	0.251854	1.345526	C	-3.862417	3.669716	-0.774618
H	5.880703	0.535276	2.177917	H	-3.486217	3.693859	-1.804349
H	7.208897	1.089928	1.134186	H	-4.872661	4.098353	-0.766965
H	7.145884	-0.601643	1.660848	H	-3.946088	2.626659	-0.448320
C	0.787921	-0.013050	4.122812	C	-3.220121	-5.717213	0.013954
H	1.116883	0.500855	5.015239	H	-2.651987	-6.321390	-0.702912
C	6.643469	-0.503701	-1.083295	H	-4.257166	-6.077206	0.021256
H	7.265171	-1.362536	-0.808429	H	-2.790395	-5.874546	1.011120
H	7.313860	0.324804	-1.335806	C	-3.474024	4.298543	1.634400
H	6.065945	-0.766491	-1.977101	H	-3.460132	3.239418	1.915474
C	-3.187056	-4.206921	-0.366246	H	-4.506293	4.664772	1.709561
C	1.592563	-0.637161	3.167663	H	-2.858863	4.857720	2.349603
H	2.670963	-0.710005	3.165910	C	4.779517	3.416530	-1.174468
C	-0.666845	-4.353249	-1.131398	H	5.295496	4.326355	-1.465047
H	-0.782057	-5.131056	-1.873665	C	3.143525	-3.467974	1.228484
C	5.508115	2.303059	-0.730987	H	2.510052	-4.283773	1.562285
H	6.591624	2.361123	-0.691318	C	-1.402342	-0.255433	-5.893768
C	3.460008	1.081507	-0.397436	H	-1.308028	0.818812	-6.095859
C	3.382044	-1.183817	0.462617	H	-2.248468	-0.644149	-6.475175
C	3.379010	3.337917	-1.271568	H	-0.492652	-0.752071	-6.248434
H	2.805845	4.172553	-1.662394	C	4.539272	-3.626489	1.164568
C	5.344222	-2.541790	0.786450	H	4.992272	-4.576921	1.429096
H	6.423058	-2.663331	0.773291	C	-1.768360	-2.047181	-4.155921
C	-1.802214	0.267099	4.497245	H	-0.900433	-2.566478	-4.579925
C	-4.045254	-3.423693	0.652427	H	-2.675308	-2.434394	-4.637780
H	-3.624681	-3.492031	1.662656	H	-1.804856	-2.305300	-3.092340
H	-5.059195	-3.843405	0.673114	C	-3.126600	-0.267558	3.905316
H	-4.127509	-2.368480	0.370448	H	-3.309250	0.139699	2.905551
C	2.549713	-2.239034	0.894840	H	-3.962112	0.035797	4.549155
C	-1.671920	-0.255783	5.957401	H	-3.120426	-1.363579	3.848313
H	-1.639657	-1.352340	5.974823	C	-3.798146	-4.035296	-1.783907
H	-2.535533	0.075315	6.548644	H	-3.883327	-2.975410	-2.049778
H	-0.763388	0.121055	6.440895	H	-4.805048	-4.471475	-1.808325

H	-3.189468	-4.534409	-2.546955	H	3.228383	-2.248732	2.135489
C	-1.834228	1.821846	4.527341	C	-2.585902	-3.194749	-2.844090
H	-0.909236	2.226995	4.954418	C	2.175165	2.042832	-2.202981
H	-2.677933	2.167992	5.138669	H	3.232742	2.250864	-2.132903
H	-1.954620	2.237858	3.520613	C	1.263856	1.976580	-1.094334
H	-1.613805	1.549784	1.554850	C	-1.073791	1.338686	-3.927599
H	-2.410761	-1.321430	-1.513298	C	5.300628	-1.218662	-0.360004
				C	1.437598	1.810127	-3.361891

$[(^{t\text{Bu}}\text{dmx})\text{Co}_2(\mu\text{-OH})(\text{thf})_2]^+$ (**5a**)

E = −3027.68629177 a.u.
G = –3026.588181 a.u.
Charge = +1, Multiplicity = 7

Co	-1.570316	-1.694843	0.342533	H	1.809360	1.791070	-4.375675
Co	-1.566761	1.696798	-0.343021	C	1.607609	2.189341	0.260033
O	3.205786	-0.001421	-0.000704	C	-3.639100	-2.465646	-1.979661
N	-0.687145	-2.446766	-1.277022	H	-3.617432	-1.384886	-2.133616
N	-0.035342	-1.697268	1.604014	H	-4.638770	-2.831636	-2.244895
O	-2.501179	0.002125	0.000114	H	-3.485650	-2.675469	-0.918952
N	-0.031170	1.698279	-1.603776	C	0.734420	2.368704	1.355059
N	-0.684158	2.447818	1.277111	C	5.090854	-3.575293	-1.016466
C	3.077590	-2.296492	-0.521189	H	5.561696	-4.509921	-1.305106
C	3.899652	-1.172834	-0.294629	C	3.901260	1.168363	0.295938
C	-0.043120	-2.926618	-3.424536	C	3.080817	2.292954	0.523845
H	-0.112052	-3.190418	-4.469174	C	5.302257	1.211876	0.362381
C	-1.148479	-2.804738	-2.516959	C	5.881619	-2.449415	-0.733305
C	1.121198	-2.648994	-2.707218	H	6.962371	-2.532320	-0.799889
H	2.135103	-2.644656	-3.078840	C	6.172519	-0.003542	-0.000291
C	0.070921	-1.589621	2.965630	C	-2.715152	-4.727244	-2.584079
C	1.260012	-1.975819	1.095543	H	-2.544305	-4.955819	-1.527050
C	1.604343	-2.190412	-0.258377	H	-3.723046	-5.068439	-2.853739
C	0.731641	-2.369877	-1.353784	H	-1.986800	-5.288603	-3.180853
C	3.688934	-3.501174	-0.900244	C	-2.267344	0.670230	-3.222293
H	3.073528	-4.378083	-1.075592	H	-2.715416	1.328916	-2.473370
C	0.075895	1.591703	-2.965393	H	-3.048230	0.432625	-3.954880
C	-1.079599	-1.337193	3.926993	H	-1.953967	-0.249338	-2.726627
C	1.432473	-1.807280	3.363045	C	-1.146088	2.805347	2.516965
H	1.803708	-1.787257	4.376998	C	-0.595695	0.404244	-5.071287
C	2.170730	-2.040836	2.204753	H	-0.241437	-0.550525	-4.669678
				H	-1.429904	0.206367	-5.756766
				H	0.213354	0.858950	-5.653565
				C	-1.529441	-2.693416	4.542386

H	-0.697373	-3.185561	5.059752	H	-2.249180	3.523461	4.996726
H	-2.336025	-2.524117	5.267767	H	-3.929904	3.190457	4.553855
H	-1.900879	-3.368451	3.766112	H	-2.742421	1.868423	4.588323
C	-0.602483	-0.403812	5.071936	C	5.095760	3.567813	1.022408
H	-0.247289	0.551079	4.671479	H	5.567893	4.501261	1.312752
H	-1.437426	-0.206100	5.756558	C	7.067656	0.367115	-1.219546
H	0.205644	-0.859335	5.654865	H	6.449512	0.628382	-2.086234
C	1.123210	2.645860	2.709102	H	7.711012	1.221713	-0.982823
H	2.136772	2.639585	3.081631	H	7.713764	-0.473521	-1.496163
C	-2.888909	-2.920420	-4.339694	C	-2.709281	4.730577	2.582733
H	-2.250944	-3.520879	-4.997598	H	-2.537218	4.958712	1.525808
H	-3.931379	-3.184742	-4.556018	H	-3.716714	5.073715	2.851641
H	-2.741367	-1.864941	-4.589527	H	-1.980288	5.290598	3.179981
C	-2.272429	-0.668029	3.221109	H	-3.475304	0.002723	-0.003289
H	-2.720132	-1.325992	2.471293	O	-2.540724	3.369534	-1.103193
H	-3.053877	-0.430692	3.953194	C	-1.678701	4.592660	-1.186514
H	-1.958417	0.251733	2.726237	C	-3.921799	3.677595	-1.573589
C	-1.522980	2.694434	-4.544512	C	-2.666619	5.740877	-1.416246
H	-0.690359	3.186264	-5.061285	H	-1.119481	4.648614	-0.251036
H	-2.328725	2.524566	-5.270691	H	-0.988014	4.450132	-2.022334
H	-1.895368	3.370037	-3.769166	C	-3.815533	5.070532	-2.210937
C	5.884930	2.441136	0.737982	H	-4.217357	2.892178	-2.272771
H	6.965774	2.522254	0.805262	H	-4.581127	3.670564	-0.699703
C	-3.637069	2.470622	1.977873	H	-2.206092	6.564160	-1.969183
H	-3.618265	1.389945	2.132697	H	-3.038882	6.129704	-0.461903
H	-4.636132	2.839323	2.241663	H	-3.552425	4.991472	-3.271045
H	-3.481861	2.678998	0.917147	H	-4.755240	5.623487	-2.128682
C	7.072657	-0.374161	1.215152	O	-2.545074	-3.367832	1.101439
H	7.714982	-1.228824	0.975985	C	-1.683551	-4.591312	1.184654
H	7.720202	0.466296	1.488854	C	-3.926409	-3.675484	1.571321
H	6.458182	-0.635151	2.084523	C	-2.671913	-5.739178	1.414293
C	3.693797	3.496078	0.905183	H	-1.124339	-4.647428	0.249184
H	3.079649	4.373668	1.081524	H	-0.992800	-4.449094	2.020474
C	-0.041330	2.924649	3.425630	C	-3.820771	-5.068429	2.208729
H	-0.110756	3.187697	4.470424	H	-4.222003	-2.889924	2.270322
C	-2.583107	3.197854	2.842972	H	-4.585411	-3.668331	0.697177
C	-2.887763	2.924179	4.338345	H	-2.211764	-6.562573	1.967380

H	-3.044114	-6.127966	0.459913
H	-3.557843	-4.989427	3.268882
H	-4.760656	-5.621055	2.126298

[($^{t\text{Bu}}$dmx)Co_2(μ-OH)(lut)$_2$]$^+$ (**5b**)
E = −3216.61798430 a.u.
G = −3215.481616 a.u.
Charge = +1, Multiplicity = 7

Co	-1.239048	1.870370	-0.115262
Co	-1.313731	-1.825157	0.098087
O	3.464794	-0.013028	-0.044528
O	-1.949227	0.050491	0.300947
H	-2.898546	0.284163	0.354811
N	0.347058	2.034821	-1.289732
N	-0.410046	2.227098	1.690104
N	-0.483964	-2.122334	-1.688020
N	0.266253	-2.047464	1.299255
N	-2.572830	3.397219	-0.606101
N	-2.651109	-3.384771	0.540172
C	7.368792	-0.715072	1.013473
H	8.030258	0.034494	1.461396
H	7.999370	-1.481838	0.550522
H	6.784310	-1.183650	1.813654
C	7.283564	0.600389	-1.162893
H	6.637394	1.064946	-1.916805
H	7.914272	-0.145515	-1.659632
H	7.938365	1.372947	-0.744115
C	6.429038	-0.062525	-0.041785
C	5.575220	1.026266	0.631735
C	6.170205	2.107198	1.316976
H	7.251058	2.150011	1.413112
C	5.393255	3.137346	1.873480
H	5.875196	3.954673	2.400928
C	3.992690	3.129035	1.720364
H	3.389786	3.945326	2.105821
C	3.369006	2.078152	1.031012
C	4.175283	1.029885	0.541450
C	5.540210	-1.156265	-0.659278
C	6.099297	-2.282771	-1.299754
H	7.178074	-2.363705	-1.395206
C	5.288011	-3.308822	-1.812855
H	5.741767	-4.162925	-2.305969
C	3.888588	-3.248342	-1.659551
H	3.259568	-4.062345	-2.006299
C	3.299803	-2.146694	-1.020758
C	4.140782	-1.105732	-0.578507
C	1.905615	2.082532	0.703583
C	0.994720	2.021285	1.781071
C	1.341043	1.879440	3.165836
H	2.334493	1.688201	3.543776
C	0.166504	2.035272	3.903494
H	0.069051	1.999347	4.977565
C	-0.900641	2.267690	2.972201
C	-2.318706	2.689729	3.351641
C	-3.419632	1.971044	2.536331
H	-3.283959	2.111170	1.464599
H	-4.398340	2.392707	2.795835
H	-3.455123	0.899127	2.759844
C	-2.438819	4.222702	3.100416
H	-1.656244	4.767250	3.642208
H	-3.416156	4.581960	3.447635
H	-2.346035	4.453724	2.035796
C	-2.573485	2.411302	4.853715
H	-2.429809	1.350833	5.094552
H	-3.606065	2.682234	5.104728
H	-1.908282	3.003775	5.491798
C	1.614492	2.203613	-0.673729
C	2.570163	2.521181	-1.697545
H	3.619789	2.717698	-1.535397
C	1.888233	2.537253	-2.912617
H	2.303698	2.739558	-3.888511
C	0.517423	2.219450	-2.636989
C	-0.583119	2.137238	-3.681344
C	-0.006870	1.550452	-4.997548
H	0.763551	2.199569	-5.428362

H	-0.811913	1.450983	-5.736816	C	-0.082736	-1.693254	5.054405
H	0.427290	0.560175	-4.823039	H	0.689288	-2.363323	5.447803
C	-1.131387	3.564925	-3.968755	H	-0.888214	-1.641866	5.797721
H	-1.596980	3.998714	-3.079381	H	0.348383	-0.692516	4.939739
H	-1.888061	3.517893	-4.762827	C	-1.174319	-3.659202	3.902423
H	-0.326963	4.233531	-4.298230	H	-1.647628	-4.038069	2.992373
C	-1.723540	1.221575	-3.205991	H	-1.916808	-3.683270	4.710672
H	-1.341865	0.226165	-2.976164	H	-0.351287	-4.332587	4.169683
H	-2.489505	1.138538	-3.986520	C	-1.830652	-1.288252	3.315141
H	-2.214041	1.618806	-2.316954	H	-1.473426	-0.263524	3.175196
C	1.835545	-2.091584	-0.693380	H	-2.587425	-1.285961	4.108766
C	0.932707	-2.027192	-1.776826	H	-2.319961	-1.642053	2.405883
C	1.291634	-1.997295	-3.166254	C	-3.889027	3.172747	-0.923585
H	2.296996	-1.904218	-3.549136	C	-4.432509	1.763613	-0.935963
C	0.111641	-2.115102	-3.902004	H	-4.793614	1.509778	-1.940017
H	0.018732	-2.134684	-4.976977	H	-3.689566	1.023641	-0.638732
C	-0.972260	-2.204483	-2.966866	H	-5.288270	1.685470	-0.254390
C	-2.423319	-2.500876	-3.328379	C	-4.747933	4.240403	-1.241826
C	-3.432614	-1.733672	-2.444974	H	-5.782530	4.027423	-1.487530
H	-3.252330	-1.918321	-1.387718	C	-4.260867	5.552835	-1.234380
H	-4.450622	-2.076929	-2.667777	H	-4.912102	6.386850	-1.476335
H	-3.386448	-0.656961	-2.614745	C	-2.913351	5.772203	-0.906150
C	-2.690486	-2.142431	-4.811467	H	-2.500525	6.774125	-0.889142
H	-2.456498	-1.091854	-5.017709	C	-2.080763	4.685341	-0.597576
H	-3.749574	-2.310836	-5.041633	C	-0.626088	4.921141	-0.274083
H	-2.098892	-2.767410	-5.490209	H	-0.312028	4.350997	0.603977
C	-2.654979	-4.031118	-3.140524	H	-0.454517	5.983816	-0.083769
H	-1.934751	-4.609449	-3.731767	H	0.012548	4.615029	-1.109989
H	-3.667739	-4.295848	-3.471057	C	-3.970873	-3.194242	0.866510
H	-2.550615	-4.319043	-2.090936	C	-4.547667	-1.799392	0.920559
C	1.542203	-2.176609	0.687458	H	-4.793240	-1.533613	1.956716
C	2.507727	-2.437925	1.718982	H	-3.867400	-1.047405	0.525017
H	3.564519	-2.596272	1.564239	H	-5.479503	-1.756228	0.345715
C	1.826177	-2.456590	2.932106	C	-4.809652	-4.283806	1.165343
H	2.250079	-2.623239	3.910658	H	-5.847268	-4.094522	1.417405
C	0.441555	-2.205903	2.650093	C	-4.300049	-5.586784	1.130708
C	-0.655929	-2.204583	3.705922	H	-4.935095	-6.437212	1.357942

C	-2.950866	-5.773561	0.791254
H	-2.520113	-6.767093	0.748890
C	-2.139423	-4.665751	0.500437
C	-0.686669	-4.878217	0.153851
H	-0.399393	-4.313967	-0.736662
H	-0.500003	-5.939598	-0.028725
H	-0.038107	-4.549989	0.972654

$[(^{t\text{Bu}}\text{dmx})\text{Co}_2(\mu\text{-OH})]^+$ (**5**)

E = −2562.72279639 a.u.
G = −2561.846814 a.u.
Charge = +1, Multiplicity = 7

Co	-2.004165	-0.873201	1.468029
Co	-2.030673	0.882698	-1.375369
O	2.699544	0.010337	0.000881
N	-1.174707	-2.599818	1.063733
N	-0.540367	-0.021350	2.444497
O	-2.996450	0.036077	0.078934
N	-0.614996	-0.019220	-2.374002
N	-1.179967	2.623436	-1.097266
C	2.596082	-1.918225	1.366328
C	3.402745	-0.995848	0.666376
C	-0.575575	-4.528181	-0.011765
H	-0.662635	-5.487012	-0.500880
C	-1.661377	-3.757405	0.516115
C	0.602875	-3.817354	0.233788
H	1.608691	-4.106604	-0.032430
C	-0.454051	1.060548	3.279578
C	0.774761	-0.529187	2.256016
C	1.124759	-1.669686	1.499690
C	0.243101	-2.615643	0.928963
C	3.219204	-3.005036	1.999868
H	2.612801	-3.720738	2.545965
C	-0.564177	-1.129856	-3.175309
C	-1.619076	1.908241	3.757553
C	0.913859	1.270486	3.652560
H	1.272884	2.047254	4.312099
C	1.674541	0.290557	3.016001
H	2.742508	0.145362	3.086861
C	-3.109983	-4.211338	0.614690
C	1.584624	-0.402263	-2.956358
H	2.654906	-0.285915	-3.043415
C	0.713196	0.466625	-2.219741
C	-1.767015	-1.917139	-3.665211
C	4.803866	-1.078345	0.634672
C	0.794096	-1.386085	-3.550991
H	1.129397	-2.192447	-4.186560
C	1.096578	1.641313	-1.530724
C	-4.094585	-3.041813	0.834299
H	-4.069792	-2.335944	-0.001613
H	-5.115452	-3.433576	0.912741
H	-3.893613	-2.509008	1.774900
C	0.241248	2.633235	-1.000147
C	4.619632	-3.140066	1.955522
H	5.099634	-3.977427	2.452102
C	3.391805	0.979628	-0.727552
C	2.573157	1.879456	-1.443023
C	4.793699	1.053229	-0.733868
C	5.396786	-2.176134	1.293679
H	6.477769	-2.277385	1.295595
C	5.669209	0.004327	-0.029834
C	-3.204026	-5.180453	1.832602
H	-2.908787	-4.670776	2.758146
H	-4.234859	-5.539914	1.944728
H	-2.547812	-6.047122	1.693096
C	-3.047639	-1.598969	-2.866341
H	-3.402085	-0.576125	-3.060283
H	-3.855938	-2.268759	-3.182831
H	-2.892648	-1.736239	-1.792222
C	-1.643858	3.811376	-0.601407
C	-1.464263	-3.435688	-3.548506
H	-1.258555	-3.715256	-2.510160
H	-2.325186	-4.015020	-3.905283
H	-0.596622	-3.716063	-4.155539
C	-1.713618	1.788975	5.306152

H	-0.786740	2.120237	5.787307
H	-2.535388	2.414447	5.677504
H	-1.903989	0.750940	5.606807
C	-1.338558	3.388656	3.374666
H	-1.230129	3.500443	2.291045
H	-2.166132	4.025419	3.711703
H	-0.417729	3.749560	3.846342
C	0.627409	3.870912	-0.383379
H	1.641588	4.167537	-0.160776
C	-3.528154	-4.971972	-0.670251
H	-2.882521	-5.837134	-0.855526
H	-4.556032	-5.338875	-0.561180
H	-3.486421	-4.319340	-1.548264
C	-2.963557	1.468687	3.143635
H	-3.236681	0.458400	3.481879
H	-3.760632	2.140199	3.484211
H	-2.944506	1.506349	2.049177
C	-2.002482	-1.556544	-5.161954
H	-1.126135	-1.808959	-5.769718
H	-2.864187	-2.115695	-5.548669
H	-2.203300	-0.483914	-5.277115
C	5.376932	2.125157	-1.442158
H	6.457972	2.223894	-1.466857
C	-4.061534	3.122344	-1.031276
H	-4.031223	2.309344	-0.296611
H	-5.089069	3.503037	-1.058073
H	-3.837990	2.730724	-2.032539
C	6.521670	0.703827	1.071024
H	7.165412	-0.021796	1.580588
H	7.163747	1.475003	0.630912
H	5.874054	1.177607	1.817933
C	3.187954	2.938399	-2.130498
H	2.573466	3.636283	-2.690349
C	-0.538692	4.603465	-0.147766
H	-0.608785	5.588536	0.290353
C	-3.096153	4.261129	-0.640131
C	-3.522608	4.818134	0.744463
H	-2.850549	5.613790	1.083751
H	-4.535609	5.233949	0.677273
H	-3.523988	4.027440	1.501727
C	4.589366	3.068452	-2.121069
H	5.061509	3.886335	-2.656136
C	6.611548	-0.653896	-1.079596
H	6.029136	-1.156035	-1.860620
H	7.250563	0.098459	-1.554104
H	7.265381	-1.393783	-0.605461
C	-3.203668	5.396517	-1.701974
H	-2.896624	5.033980	-2.690862
H	-4.240893	5.749062	-1.766244
H	-2.566102	6.246887	-1.435169
H	-3.970260	-0.001972	0.067210

$[(^{t\text{Bu}}\text{dmx})\text{Co}_2(\mu\text{-OH})_2]^+$ (**7**)

E = −2638.52222645 a.u.

G = −2637.636962 a.u.

Charge = +1, Multiplicity = 8

Co	-1.975756	1.185520	-0.934174
Co	-1.943193	-1.042069	1.041213
O	-2.726103	-0.629809	-0.777735
O	2.729569	0.003370	0.027551
O	-2.064759	0.952341	1.031409
N	-0.568827	-1.021973	2.529886
N	-1.067219	3.020637	-0.579692
N	-0.531114	0.844596	-2.353596
N	-1.201377	-2.813743	0.357699
C	1.222680	2.071992	-1.026967
C	0.760268	-1.313149	2.118484
C	0.348129	2.964510	-0.381983
C	0.814709	1.112268	-1.988293
C	1.106269	-2.074792	0.979864
C	1.698761	0.378238	-2.892485
H	2.776674	0.386944	-2.853045
C	-0.498786	-0.373414	3.725455
C	0.724859	4.016226	0.561992
H	1.725451	4.197507	0.922194

C	0.897626	-0.253980	-3.807368	C	3.465316	1.122128	-0.374904
H	1.206326	-0.867352	-4.640434	C	3.401795	-1.185733	0.358582
C	0.205245	-2.775978	0.147528	C	3.349718	3.414965	-1.155101
C	5.705174	-0.079019	0.017503	H	2.769978	4.259883	-1.512946
C	-1.531816	4.048975	0.154781	C	5.368993	-2.549336	0.583913
C	-0.499835	0.076564	-3.464764	H	6.447662	-2.667916	0.554824
C	2.692555	2.218879	-0.816783	C	-1.697899	0.063259	4.555306
C	-2.992779	0.375475	-3.852391	C	-4.020110	-3.477426	0.579151
H	-3.355009	0.009247	-2.889103	H	-3.560833	-3.568300	1.570672
H	-3.777700	0.182581	-4.592418	H	-5.016388	-3.934805	0.621148
H	-2.853915	1.462325	-3.785199	H	-4.153504	-2.415899	0.343113
C	4.802356	-1.288593	0.302522	C	2.573371	-2.261076	0.740312
C	4.868294	1.156088	-0.341103	C	-1.528602	-0.505170	5.994019
C	-0.423198	4.697550	0.882056	H	-1.486199	-1.601138	5.975223
H	-0.524735	5.541249	1.548501	H	-2.380979	-0.201658	6.615081
C	-1.689881	-0.320065	-4.301953	H	-0.612924	-0.135308	6.468947
C	-1.725390	-3.716951	-0.518211	C	-3.061258	5.977484	-0.150076
C	-2.975997	4.474736	0.251251	H	-2.429625	6.606261	0.487145
C	0.519592	-3.654661	-0.946769	H	-4.097557	6.318346	-0.042627
H	1.508051	-3.830212	-1.346441	H	-2.754583	6.122711	-1.192853
C	6.548772	0.223573	1.292080	C	-3.897497	3.645931	-0.666057
H	5.895602	0.457106	2.140777	H	-3.547229	3.651418	-1.705284
H	7.214906	1.076885	1.122048	H	-4.909159	4.066122	-0.645619
H	7.167224	-0.640302	1.559089	H	-3.974878	2.611925	-0.308692
C	0.880640	-0.209583	4.110398	C	-3.150320	-5.717572	-0.175717
H	1.230415	0.255338	5.021272	H	-2.592384	-6.277758	-0.934826
C	6.654016	-0.403804	-1.173751	H	-4.176079	-6.106802	-0.145675
H	7.280777	-1.272341	-0.946650	H	-2.680648	-5.899274	0.798797
H	7.320587	0.439632	-1.382768	C	-3.436621	4.304326	1.731148
H	6.076720	-0.621917	-2.079651	H	-3.396876	3.249880	2.026098
C	-3.173240	-4.192868	-0.498536	H	-4.471599	4.653537	1.825509
C	1.661110	-0.785566	3.108403	H	-2.816020	4.887353	2.421126
H	2.738740	-0.862328	3.080818	C	4.750406	3.497675	-1.073963
C	-0.678565	-4.246746	-1.355206	H	5.255816	4.421545	-1.335510
H	-0.806502	-4.985017	-2.134646	C	3.172956	-3.505461	0.997675
C	5.494028	2.372143	-0.687643	H	2.546346	-4.340734	1.293589
H	6.577034	2.439411	-0.661590	C	-1.396185	0.103119	-5.775051

H	-1.296503	1.191895	-5.857032
H	-2.232540	-0.216589	-6.407388
H	-0.483225	-0.359901	-6.163436
C	4.568600	-3.654716	0.908816
H	5.026488	-4.616909	1.115285
C	-1.832763	-1.870846	-4.245863
H	-0.972999	-2.364118	-4.713045
H	-2.738445	-2.171609	-4.784892
H	-1.900912	-2.237251	-3.216871
C	-3.035614	-0.454731	3.981535
H	-3.241063	-0.023881	2.994906
H	-3.857393	-0.162805	4.647071
H	-3.034996	-1.549149	3.900727
C	-3.835475	-3.990170	-1.888908
H	-3.965863	-2.925201	-2.117766
H	-4.828884	-4.455732	-1.897098
H	-3.238794	-4.444465	-2.688336
C	-1.733338	1.616685	4.634262
H	-0.792333	2.013883	5.032386
H	-2.550139	1.939174	5.292598
H	-1.903107	2.061698	3.646159
H	-1.504852	1.461811	1.646030
H	-2.612128	-1.324267	-1.452350

($^{t\text{Bu}}$dmx)$Co_2(\mu\text{-}OH)_2Cl$ (**8**)

E = −3098.91654007 a.u.
G = −3098.037393 a.u.
Charge = 0, Multiplicity = 8

Co	-2.1343858	-0.7624489	1.1155910
Co	-1.4257477	0.9996170	-1.3378710
O	-2.9654487	0.2648928	-0.4167043
O	2.7732278	-0.1742690	0.1995878
O	-0.4926979	-0.0758633	-0.0503880
N	-0.2433583	0.5273244	-2.8995714
N	-1.2706835	-2.6057509	0.6947456
N	-0.8271765	-0.2452108	2.6380979
N	-0.6272997	2.8404880	-1.0629684
C	0.9331452	-1.7887280	1.6465154
C	1.1159844	0.7744625	-2.5452002
C	0.1513431	-2.5919087	0.7886075
C	0.4888319	-0.7905684	2.5350137
C	1.5540777	1.7029347	-1.5757665
C	1.3522222	-0.1023118	3.4897088
H	2.3974017	-0.3192612	3.6495347
C	-0.2488341	-0.4197624	-3.8693068
C	0.6877566	-3.6480570	-0.0640736
H	1.7367015	-3.8618549	-0.2009884
C	0.5781250	0.8364301	4.1247379
H	0.8845191	1.5297248	4.8924918
C	0.7822612	2.6862349	-0.9160456
C	5.7372044	-0.4515895	0.4658997
C	-1.6072683	-3.6294379	-0.1196824
C	-0.7780393	0.7435561	3.5522696
C	2.4108426	-2.0504992	1.6567762
C	-2.6998235	2.0801458	2.6396537
H	-2.0175200	2.5165662	1.9021965
H	-3.4575407	2.8280045	2.9041341
H	-3.2190173	1.2350179	2.1852808
C	5.0376218	0.6526067	-0.3335298
C	4.7167370	-1.3994598	1.1029894
C	-0.3880023	-4.2938408	-0.6212023
H	-0.3703868	-5.1304497	-1.3018820
C	-1.9316919	1.6563315	3.9160333
C	-0.9837284	3.9861369	-0.4179838
C	-3.0231500	-4.0995923	-0.3997716
C	1.2700019	3.7641522	-0.0995754
H	2.3003825	3.9149990	0.1893832
C	6.6585526	-1.2594616	-0.4972292
H	6.0680659	-1.7234219	-1.2956619
H	7.1913651	-2.0492493	0.0432001
H	7.4069932	-0.6053027	-0.9567285
C	1.1058561	-0.8009600	-4.1941533
H	1.3945188	-1.5234276	-4.9446322
C	6.5968266	0.1925816	1.5949222
H	7.3532046	0.8627703	1.1726038

H	7.1180011	-0.5771677	2.1742675	H	-2.5814632	-4.9548564	-2.3822702
H	5.9644756	0.7714459	2.2779531	H	-4.0495227	-5.5782809	-1.6088356
C	-2.3662833	4.6173614	-0.4986844	H	-2.4630813	-6.1321113	-1.0494912
C	1.9499114	-0.0705699	-3.3600891	C	4.2795122	-3.3684431	2.5043006
H	3.0302846	-0.0950290	-3.3332611	H	4.6523010	-4.2073041	3.0830927
C	0.1767757	4.5820988	0.1950973	C	3.8367903	2.6517415	-1.9331260
H	0.1877470	5.4990012	0.7664588	H	3.3630558	3.3980275	-2.5633014
C	5.1703950	-2.4946119	1.8677341	C	-2.8784534	0.8939800	4.8900937
H	6.2377004	-2.6641632	1.9684169	H	-3.2876098	0.0019879	4.4081108
C	3.3271586	-1.2078074	0.9869351	H	-3.7105972	1.5523604	5.1716981
C	3.6392584	0.7217836	-0.4769139	H	-2.3451445	0.6021359	5.8040066
C	2.8980354	-3.1354064	2.4027245	C	5.2323449	2.6302559	-1.7740131
H	2.1897334	-3.7809224	2.9131418	H	5.8515432	3.3727512	-2.2674468
C	5.8175723	1.6270787	-0.9912844	C	-1.4027515	2.9333624	4.6172659
H	6.8980492	1.5968579	-0.8919173	H	-0.9099113	2.7043563	5.5694853
C	-1.4989033	-1.0504290	-4.4584548	H	-2.2480636	3.5971849	4.8330036
C	-3.4841185	3.5776902	-0.7364802	H	-0.6965641	3.4778815	3.9774780
H	-3.3533992	3.0683881	-1.6981565	C	-2.7907249	-0.3461593	-3.9890182
H	-4.4558555	4.0874225	-0.7582519	H	-2.9440257	-0.4551234	-2.9103356
H	-3.5058846	2.8224633	0.0535146	H	-3.6554007	-0.7926467	-4.4965933
C	3.0275535	1.6949795	-1.2992253	H	-2.7669480	0.7245174	-4.2286307
C	-1.4238396	-0.9850139	-6.0082757	C	-2.6754539	5.4179748	0.7924027
H	-1.4169005	0.0567219	-6.3530679	H	-2.6652844	4.7704091	1.6750141
H	-2.2960854	-1.4881907	-6.4454358	H	-3.6694864	5.8756710	0.7122645
H	-0.5213496	-1.4773435	-6.3887150	H	-1.9489755	6.2236072	0.9491080
C	-3.6164500	-4.6139900	0.9477427	C	-1.5312231	-2.5405578	-4.0079574
H	-3.0045385	-5.4280649	1.3576840	H	-0.6773029	-3.0939676	-4.4165803
H	-4.6292264	-4.9980092	0.7707431	H	-2.4546672	-3.0219732	-4.3556345
H	-3.6733779	-3.8019307	1.6771203	H	-1.4870809	-2.6113143	-2.9152809
C	-3.9120809	-2.9565037	-0.9568303	H	0.4704979	-0.0148264	0.0861795
H	-3.9818332	-2.1250488	-0.2571618				
H	-4.9237702	-3.3482650	-1.1233556	($^{t\text{Bu}}$dmx)$Co_2(\mu\text{-}OH)_2Cl_2$ (**9**)			
C	-2.3440389	5.6060509	-1.7052943	E = −3559.11213910 a.u.			
H	-1.5845789	6.3842421	-1.5614605	G = −3558.229619 a.u.			
H	-3.3235581	6.0914775	-1.8094065	Charge = 0, Multiplicity = 9			
H	-2.1183082	5.0711375	-2.6360081	Co	-1.6724020	0.7455399	-1.4091805
C	-3.0165433	-5.2621151	-1.4233557	Co	-1.8612556	-0.7602558	1.4405811
				O	-2.9039069	0.1037183	-0.0306963

O	2.8572363	-0.0113586	0.0282352	H	6.1128859	1.0320939	1.9787713
O	-0.5649060	-0.1452464	-0.1282908	H	7.3896720	1.3628669	0.7874372
N	-0.3110996	-0.0517844	2.6132592	H	7.3661012	-0.1841059	1.6461345
N	-0.9705017	2.5689185	-1.0456059	C	1.2691362	1.0573223	3.8985551
N	-0.2338084	0.1425502	-2.7222194	H	1.6688282	1.7740242	4.5988073
N	-1.0216265	-2.6190647	1.0630180	C	6.7439758	-0.6474014	-1.0354544
C	1.3500428	1.7365316	-1.5663162	H	7.3805126	-1.4355019	-0.6184583
C	0.9632320	-0.6455849	2.4183628	H	7.3974942	0.1131684	-1.4758030
C	0.4455992	2.5893706	-0.9007629	H	6.1317967	-1.0822333	-1.8339138
C	1.0501257	0.7026758	-2.4759553	C	-2.9146930	-4.2019874	0.4070546
C	1.2899135	-1.7320655	1.5699326	C	1.9448240	0.0648678	3.2424000
C	2.0102061	-0.0033212	-3.2794449	H	2.9912116	-0.1870461	3.3173813
H	3.0658703	0.2195949	-3.3328970	C	-0.3452868	-4.4472118	-0.1905310
C	-0.1431103	0.9856496	3.4639282	H	-0.4319983	-5.3460316	-0.7802720
C	0.7945629	3.6944459	-0.0637875	C	5.6067058	2.1944552	-1.1676217
H	1.7982703	3.9602829	0.2338816	H	6.6882906	2.2811675	-1.1356199
C	1.3175758	-0.9883431	-3.9767266	C	3.5827889	1.0112126	-0.6215536
H	1.7312448	-1.7016823	-4.6726146	C	3.5559751	-1.0318475	0.6989431
C	0.3977205	-2.6192607	0.9415306	C	3.4646460	3.0570794	-1.9145444
C	5.8407038	-0.0235004	0.0700937	H	2.8767908	3.7861457	-2.4632310
C	-1.4741240	3.6680209	-0.3755268	C	5.5494331	-2.2324500	1.3147422
C	-0.0667967	-0.9034107	-3.5893140	H	6.6304481	-2.3308238	1.3146767
C	2.8135133	1.9578075	-1.3340142	C	-1.2136208	1.9477741	3.9209711
C	-2.1206909	-2.1923124	-2.8843854	C	-3.9319211	-3.0830450	0.0689553
H	-1.5682069	-2.5700599	-2.0174515	H	-3.9204906	-2.2935333	0.8201391
H	-2.8347298	-2.9607766	-3.2064242	H	-4.9382659	-3.5199083	0.0623407
H	-2.6981523	-1.3176661	-2.5806058	H	-3.7372644	-2.6469346	-0.9129080
C	4.9583709	-1.1165376	0.6848988	C	2.7581005	-1.9697408	1.3927985
C	4.9848067	1.0817956	-0.5618025	C	-1.8614637	1.3512911	5.2104803
C	-0.3912176	4.3651483	0.2516992	H	-2.3438568	0.3953290	4.9868299
H	-0.4837413	5.2594912	0.8471923	H	-2.6205442	2.0523508	5.5800325
C	-1.1519413	-1.8675118	-4.0444178	H	-1.1125946	1.2057816	5.9993035
C	-1.4791187	-3.7143478	0.4193412	C	-3.1221121	4.7095841	-1.9055552
C	-2.9063146	4.1920103	-0.4502515	H	-2.3883122	5.4868444	-2.1548869
C	0.7997517	-3.7631658	0.1225799	H	-4.1284617	5.1393069	-1.9962812
H	1.8145408	-3.9992601	-0.1576108	H	-3.0279309	3.8880476	-2.6215293
C	6.7326903	0.5857563	1.1925759	C	-3.9968634	3.1409883	-0.1254123

H	-3.9961393	2.3311513	-0.8525215
H	-4.9773030	3.6330415	-0.1707650
C	-3.2092952	-4.7410112	1.8445653
H	-2.5025699	-5.5330535	2.1231289
H	-4.2234740	-5.1591711	1.8649447
H	-3.1489557	-3.9281952	2.5738589
C	-3.0813641	5.3793695	0.5312235
H	-2.8860970	5.0751877	1.5671684
H	-4.1144147	5.7417758	0.4727198
H	-2.4196379	6.2172550	0.2821852
C	4.8615740	3.1875236	-1.8186649
H	5.3621945	4.0372544	-2.2717665
C	3.3786297	-3.0720839	2.0013445
H	2.7696666	-3.7925616	2.5386570
C	-1.9239189	-1.2466383	-5.2438791
H	-2.3890643	-0.3006528	-4.9560012
H	-2.7103062	-1.9386115	-5.5743181
H	-1.2440282	-1.0685543	-6.0869856
C	4.7760921	-3.2155344	1.9485995
H	5.2547493	-4.0672961	2.4207011
C	-0.5078384	-3.2011482	-4.5078979
H	0.1405327	-3.0614908	-5.3804147
H	-1.3014019	-3.9026894	-4.7930888
H	0.0830124	-3.6575187	-3.7033200
C	-2.2839702	2.1603422	2.8307688
H	-1.8203666	2.4951525	1.8993847
H	-2.9891987	2.9308770	3.1651317
H	-2.8570737	1.2518452	2.6402674
C	-3.0853200	-5.3551130	-0.6135057
H	-2.8280854	-5.0346290	-1.6305122
H	-4.1332301	-5.6750462	-0.6155676
H	-2.4729857	-6.2268306	-0.3539584
C	-0.5768689	3.3240576	4.2561850
H	0.1238711	3.2645609	5.0964487
H	-1.3740800	4.0209381	4.5396021
H	-0.0531369	3.7397657	3.3864890
H	0.4054107	-0.1696889	-0.2403264
H	-3.8698768	0.1049662	-0.1492138
H	-3.8686278	2.7190587	0.8733231
Cl	-3.3657353	1.1794358	-3.0294029
Cl	-3.5416321	-1.2191250	3.1252935

($^{t\text{Bu}}$dmx)Co_2(μ-O)(thf)$_2$ (**12a**)
E = −3027.18586474 a.u.
G = −3026.098957 a.u.
Charge = 0, Multiplicity = 7

Co	1.514474	-1.562491	-0.459730
Co	1.540570	1.557348	0.396711
O	-3.255855	-0.038522	0.085698
N	0.630680	-2.612724	1.057392
N	-0.030097	-1.591810	-1.772083
O	2.448048	-0.020717	0.010447
N	-0.004904	1.611641	1.712621
N	0.635583	2.554313	-1.117813
C	-3.135302	-2.383640	0.301026
C	-3.952979	-1.237326	0.218747
C	-0.058008	-3.372124	3.116559
H	-0.003601	-3.757323	4.124427
C	1.067061	-3.096205	2.261095
C	-1.210300	-3.042766	2.409161
H	-2.232013	-3.109018	2.752335
C	-0.160232	-1.317511	-3.108805
C	-1.328258	-1.868638	-1.272776
C	-1.660017	-2.255536	0.046378
C	-0.793256	-2.584564	1.109613
C	-3.754693	-3.622543	0.525555
H	-3.143442	-4.517502	0.587421
C	-0.126217	1.446470	3.063673
C	0.985829	-1.065515	-4.079197
C	-1.542514	-1.408490	-3.493690
H	-1.933734	-1.242072	-4.486096
C	-2.267861	-1.750598	-2.355742
H	-3.333376	-1.913966	-2.286917
C	2.506269	-3.428692	2.641784
C	-2.215628	1.970659	2.317405

H	-3.269665	2.198382	2.249066	C	0.462149	-0.335472	-5.343435
C	-1.296369	1.926772	1.210604	H	-0.025642	0.608895	-5.073753
C	0.977233	1.059547	4.038753	H	1.306551	-0.109931	-6.007655
C	-5.354945	-1.286983	0.263834	H	-0.250025	-0.950395	-5.906587
C	-1.488157	1.682649	3.467848	C	-1.158080	2.693518	-2.579439
H	-1.862183	1.631804	4.480787	H	-2.163543	2.637117	-2.970696
C	-1.641702	2.168174	-0.138655	C	2.774069	-3.027941	4.117823
C	3.553743	-2.736294	1.747346	H	2.078554	-3.517002	4.808910
H	3.402719	-1.654224	1.696747	H	3.792195	-3.329440	4.396358
H	4.558069	-2.939356	2.142499	H	2.685988	-1.947147	4.251384
H	3.506135	-3.116799	0.727365	C	2.083380	-0.185616	-3.452198
C	-0.771265	2.397861	-1.226538	H	2.461032	-0.578330	-2.507270
C	-5.156882	-3.704701	0.635063	H	2.925206	-0.087526	-4.151557
H	-5.631392	-4.665588	0.809977	H	1.683859	0.808071	-3.244683
C	-3.940810	1.139070	-0.203817	C	1.255652	2.253360	4.997864
C	-3.116141	2.266885	-0.401455	H	0.345590	2.558386	5.528317
C	-5.342144	1.187017	-0.286677	H	2.007970	1.962664	5.743253
C	-5.943046	-2.549992	0.488428	H	1.639013	3.121976	4.449866
H	-7.024278	-2.635035	0.545470	C	-5.920704	2.426774	-0.632281
C	-6.217632	-0.030828	0.056279	H	-7.001067	2.512533	-0.701156
C	2.677844	-4.974326	2.520734	C	3.620241	2.538592	-2.059092
H	2.471806	-5.313816	1.498922	H	3.716532	1.649848	-2.686397
H	3.707642	-5.256762	2.777505	H	4.582784	3.067963	-2.064568
H	1.994439	-5.500575	3.198157	H	3.418403	2.195558	-1.044480
C	2.282565	0.663120	3.326235	C	-7.225463	-0.292253	-1.099870
H	2.711015	1.515573	2.796923	H	-7.873553	-1.144125	-0.868086
H	3.016627	0.318286	4.065977	H	-7.870238	0.578392	-1.260605
H	2.116029	-0.129927	2.593093	H	-6.693157	-0.506122	-2.033847
C	1.094737	2.988577	-2.330840	C	-3.726927	3.479265	-0.758037
C	0.480079	-0.145299	4.886579	H	-3.107995	4.357576	-0.912708
H	0.257092	-1.003305	4.245103	C	0.000823	3.066633	-3.263568
H	1.256879	-0.439308	5.604902	H	0.073275	3.362476	-4.299536
H	-0.424678	0.107093	5.451593	C	2.515581	3.487248	-2.590096
C	1.582058	-2.435969	-4.510905	C	2.741310	3.692202	-4.108686
H	0.810968	-3.072359	-4.963803	H	2.080614	4.466941	-4.516435
H	2.380565	-2.280655	-5.249480	H	3.777544	4.007914	-4.283755
H	2.000043	-2.952868	-3.645849	H	2.569236	2.762183	-4.664367

C	-5.127742	3.559077	-0.881138
H	-5.595921	4.501542	-1.148669
C	-6.998694	0.275416	1.369698
H	-6.303522	0.463429	2.196248
H	-7.634004	1.159797	1.243097
H	-7.640052	-0.570732	1.642558
C	2.659035	4.865017	-1.876938
H	2.597014	4.734704	-0.794658
H	3.630981	5.314008	-2.122183
H	1.867136	5.555407	-2.193938
O	2.653204	3.177582	1.184751
C	1.890499	4.329365	1.743111
C	4.102399	3.345487	1.449232
C	2.959696	5.290039	2.289986
H	1.284499	4.745645	0.934932
H	1.232166	3.935486	2.519995
C	4.159068	4.357408	2.600248
H	4.504811	2.358837	1.689241
H	4.577280	3.728336	0.539174
H	2.607763	5.825406	3.176629
H	3.243050	6.027859	1.530424
H	4.014544	3.851283	3.561722
H	5.111535	4.894881	2.628288
O	2.740550	-2.991606	-1.408864
C	2.346844	-4.425529	-1.390394
C	4.147880	-2.845243	-1.865289
C	3.675490	-5.188857	-1.459352
H	1.772003	-4.583419	-0.476466
H	1.710878	-4.615419	-2.262026
C	4.564891	-4.254578	-2.319478
H	4.161465	-2.102819	-2.665218
H	4.735031	-2.483129	-1.015305
H	3.555024	-6.179830	-1.906713
H	4.102707	-5.308778	-0.457312
H	4.343119	-4.396425	-3.383526
H	5.632403	-4.433243	-2.161560

($^{t\text{Bu}}$dmx)Co_2(μ-O)(lut)$_2$ (**12b**)

E = −3216.13920565 a.u.

G = −3214.998133 a.u.

Charge = 0, Multiplicity = 7

Co	-1.279946	-1.704065	0.086140
Co	-1.287685	1.699203	-0.081213
O	3.472438	0.005679	-0.004850
O	-2.019446	-0.004056	0.006472
N	0.309819	-2.037769	1.300664
N	-0.434163	-2.161351	-1.707271
N	-0.432135	2.160122	1.705901
N	0.297002	2.037915	-1.301853
N	-2.630343	-3.290598	0.550163
N	-2.645570	3.286408	-0.538242
C	7.344189	0.654727	-1.086806
H	7.989713	-0.097552	-1.553896
H	7.988468	1.422927	-0.644546
H	6.734783	1.121900	-1.869090
C	7.324440	-0.651050	1.096686
H	6.700655	-1.113824	1.870237
H	7.968078	0.097155	1.572988
H	7.969306	-1.423908	0.663347
C	6.436370	0.005094	-0.001483
C	5.564927	-1.086721	-0.647763
C	6.140909	-2.192780	-1.308860
H	7.221066	-2.256848	-1.404209
C	5.344075	-3.219896	-1.842846
H	5.810361	-4.057312	-2.353129
C	3.943123	-3.181922	-1.689788
H	3.324460	-3.994516	-2.058023
C	3.337715	-2.104668	-1.026245
C	4.164687	-1.062130	-0.562494
C	5.564180	1.101954	0.634757
C	6.139050	2.210578	1.292568
H	7.219054	2.275161	1.389287
C	5.341265	3.239086	1.822423
H	5.806633	4.078490	2.330285
C	3.940357	3.199039	1.669623

H	3.320629	4.011654	2.036038	H	-0.382515	-4.398495	4.059224
C	3.336272	2.118774	1.009902	C	-1.731909	-1.249474	3.369089
C	4.164118	1.076033	0.548757	H	-1.343535	-0.230255	3.326455
C	1.871134	-2.072584	-0.701006	H	-2.511378	-1.299614	4.141717
C	0.974274	-1.990331	-1.785955	H	-2.192770	-1.465358	2.406539
C	1.339318	-1.860722	-3.171297	C	1.868870	2.080340	0.690227
H	2.340550	-1.693183	-3.541006	C	0.977564	1.994174	1.779454
C	0.167422	-1.988525	-3.916328	C	1.349165	1.872837	3.163727
H	0.076087	-1.945964	-4.991218	H	2.352563	1.710942	3.530030
C	-0.914568	-2.189624	-2.986848	C	0.180147	2.001043	3.913352
C	-2.346510	-2.557264	-3.371742	H	0.093760	1.963015	4.988860
C	-3.421884	-1.763469	-2.589090	C	-0.906455	2.194371	2.987708
H	-3.209616	-1.729190	-1.522656	C	-2.338808	2.555865	3.377074
H	-4.402403	-2.235652	-2.739891	C	-3.409838	1.742214	2.609657
H	-3.480080	-0.728737	-2.936265	H	-3.210007	1.710536	1.540800
C	-2.536638	-4.076949	-3.086597	H	-4.396695	2.197073	2.772007
H	-1.758943	-4.669391	-3.585390	H	-3.444593	0.706799	2.957341
H	-3.516265	-4.405585	-3.458956	C	-2.553093	2.328014	4.894336
H	-2.491472	-4.278660	-2.014288	H	-2.344696	1.287923	5.173195
C	-2.570641	-2.312131	-4.884894	H	-3.597413	2.547066	5.150336
H	-2.368057	-1.267589	-5.151325	H	-1.914097	2.983786	5.498292
H	-3.615329	-2.532780	-5.137952	C	-2.544810	4.069926	3.074889
H	-1.932047	-2.957300	-5.500574	H	-1.771981	4.675803	3.565042
C	1.577209	-2.191171	0.678131	H	-3.526815	4.392970	3.445926
C	2.544732	-2.512994	1.693119	H	-2.504240	4.259791	2.000429
H	3.595463	-2.698883	1.524382	C	1.567473	2.196470	-0.687181
C	1.869260	-2.548790	2.909420	C	2.527363	2.522013	-1.708304
H	2.292439	-2.759107	3.880447	H	3.578336	2.712280	-1.545772
C	0.489246	-2.241505	2.641856	C	1.844119	2.554496	-2.920425
C	-0.600084	-2.235341	3.707361	H	2.260080	2.766681	-3.894285
C	0.006973	-1.810422	5.071584	C	0.467216	2.240365	-2.643879
H	0.746132	-2.533579	5.435472	C	-0.627631	2.222005	-3.703193
H	-0.792939	-1.745545	5.820656	C	-0.035564	1.735399	-5.053373
H	0.487352	-0.828147	4.992721	H	0.727993	2.421599	-5.437650
C	-1.179466	-3.672699	3.853286	H	-0.836622	1.674766	-5.801651
H	-1.701428	-3.979916	2.944086	H	0.411358	0.740977	-4.943103
H	-1.895887	-3.700663	4.685536	C	-1.173062	3.667558	-3.894925

H	-1.666920	4.024607	-2.987239
H	-1.906891	3.681914	-4.712257
H	-0.362651	4.363450	-4.146266
C	-1.783787	1.280197	-3.324251
H	-1.419253	0.262461	-3.179092
H	-2.536373	1.277482	-4.124586
H	-2.272610	1.588191	-2.401902
C	-3.941815	-3.054027	0.873807
C	-4.455722	-1.635771	0.930325
H	-4.851859	-1.422019	1.931893
H	-3.675905	-0.905039	0.689692
H	-5.283784	-1.510922	0.219735
C	-4.823611	-4.117579	1.156190
H	-5.854096	-3.890299	1.408510
C	-4.365663	-5.439019	1.105147
H	-5.034248	-6.268251	1.316578
C	-3.020603	-5.671262	0.773969
H	-2.624711	-6.679501	0.724169
C	-2.168203	-4.587646	0.504823
C	-0.717604	-4.844232	0.179214
H	-0.397036	-4.255362	-0.683226
H	-0.562964	-5.906613	-0.031045
H	-0.077094	-4.557803	1.020116
C	-3.960557	3.048032	-0.847087
C	-4.477616	1.629952	-0.877094
H	-4.897241	1.406250	-1.866778
H	-3.693748	0.900446	-0.646556
H	-5.289086	1.513729	-0.146176
C	-4.842214	4.108862	-1.138783
H	-5.875327	3.880189	-1.378814
C	-4.380447	5.429816	-1.113509
H	-5.048545	6.257120	-1.333815
C	-3.032675	5.664089	-0.795450
H	-2.634343	6.672115	-0.763909
C	-2.180849	4.582858	-0.514323
C	-0.729367	4.842275	-0.194411
H	-0.405289	4.255333	0.668005
H	-0.576067	5.905279	0.013775
H	-0.090439	4.556164	-1.036545

[($^{t\text{Bu}}$dmx)Co_2(μ-O)(μ-OH)]$^-$ (**13**)
E = −2638.19315488 a.u.
G = –2637.321889 a.u.
Charge = –1, Multiplicity = 7

Co	1.6550081	1.4754255	0.3619223
Co	1.8872262	-1.0770692	-0.6234257
O	3.0889646	0.2595713	0.0193423
O	-2.6845328	-0.0758866	-0.0788706
O	0.4889350	0.3452186	-0.7881540
N	0.9270400	-2.1076953	-2.1165675
N	0.8533269	3.1967903	-0.4018286
N	0.5242954	1.6674101	2.0705396
N	1.2191719	-2.4551802	0.7305019
C	-1.3273037	2.3794000	0.5251568
C	-0.4488101	-2.2553793	-1.7821894
C	-0.5647724	3.0971347	-0.4271073
C	-0.8485123	1.7968439	1.7188645
C	-0.9601101	-2.3476692	-0.4668359
C	-1.6466022	1.3963182	2.8496720
H	-2.7272679	1.3972980	2.8860990
C	1.0225889	-2.0922547	-3.4673490
C	-1.0466768	3.8404989	-1.5618208
H	-2.0824297	3.9493674	-1.8503494
C	-0.7625185	1.0781630	3.8793114
H	-1.0126483	0.7613902	4.8827373
C	-0.1983376	-2.4995978	0.7124219
C	-5.6615482	-0.2897980	-0.1409073
C	1.2316961	3.9675465	-1.4536892
C	0.5742646	1.2554172	3.3614613
C	-2.8077353	2.3045574	0.3204582
C	3.1078953	1.3365570	3.3083945
H	3.1557345	0.6999274	2.4203899
H	4.0078946	1.1602237	3.9135845
H	3.1238105	2.3817895	2.9712183
C	-4.7064119	-1.4854543	-0.2020393

C	-4.8906605	1.0238649	0.0215395	C	2.2734514	-2.3670932	-5.6374390
C	0.0711157	4.3998677	-2.1910086	H	2.0705805	-3.4457498	-5.6585307
H	0.0747892	5.0342826	-3.0659263	H	3.2314351	-2.1869315	-6.1421033
C	1.8504361	1.0633467	4.1610697	H	1.4905897	-1.8584353	-6.2131792
C	1.6372342	-2.9696582	1.9158830	C	2.8262226	5.3895849	-2.7881412
C	2.6949173	4.2165590	-1.7880700	H	2.3291634	5.1613761	-3.7392897
C	-0.6519423	-2.9858236	1.9895082	H	3.8865222	5.5786189	-2.9998778
H	-1.6847113	-3.1264594	2.2773977	H	2.3872237	6.3103870	-2.3819959
C	-6.4873320	-0.2400963	-1.4622612	C	3.4896686	4.5570509	-0.5009274
H	-5.8226157	-0.1181315	-2.3252451	H	3.1017113	5.4711387	-0.0322731
H	-7.1932663	0.5978351	-1.4484498	H	4.5496270	4.7113758	-0.7436960
H	-7.0616546	-1.1635794	-1.5959167	H	3.4199539	3.7445999	0.2292431
C	-0.2866048	-2.2417427	-4.0592953	C	3.2527353	-4.0456962	3.5246912
H	-0.5042312	-2.2831908	-5.1171125	H	2.8932477	-3.4357409	4.3631150
C	-6.6253054	-0.4607464	1.0719320	H	4.3112665	-4.2745612	3.7032853
H	-7.2078518	-1.3837642	0.9816136	H	2.6942580	-4.9908119	3.5211032
H	-7.3319420	0.3739370	1.1302483	C	3.2880489	2.9291707	-2.4304126
H	-6.0584155	-0.5000954	2.0092827	H	3.2415847	2.0833190	-1.7342699
C	3.1041298	-3.2925846	2.1815808	H	4.3397583	3.0971520	-2.7024374
C	-1.2027721	-2.3273231	-3.0077289	H	2.7338705	2.6602742	-3.3385100
H	-2.2743614	-2.4545163	-3.0774243	C	-4.9639967	3.4586261	0.3172182
C	0.4920822	-3.2998949	2.7312867	H	-5.5376583	4.3768364	0.3979091
H	0.5255782	-3.7232716	3.7250369	C	-3.0223072	-3.7393797	-0.4398488
C	-5.6117395	2.2316416	0.1300238	H	-2.3606621	-4.5934363	-0.5484029
H	-6.6954352	2.2087826	0.0701846	C	1.8331311	2.0593099	5.3573325
C	-3.4851324	1.0799149	0.0920498	H	1.8098300	3.0958884	4.9971979
C	-3.3046971	-1.3403256	-0.2062949	H	2.7366368	1.9247460	5.9677196
C	-3.5640669	3.4852029	0.4212691	H	0.9579975	1.8991636	5.9989863
H	-3.0428995	4.4191279	0.6052156	C	-4.4154991	-3.9132858	-0.4055816
C	-5.2409491	-2.7869898	-0.2994227	H	-4.8469557	-4.9070845	-0.4759593
H	-6.3185177	-2.9191029	-0.2979161	C	1.8732347	-0.3862022	4.7186446
C	2.3404897	-1.8396939	-4.1839979	H	1.0424681	-0.5487009	5.4170334
C	3.5911746	-4.2165533	1.0268294	H	2.8133438	-0.5733509	5.2550937
H	2.9750078	-5.1233911	0.9635465	H	1.7759387	-1.1131466	3.9085836
H	4.6351970	-4.5131629	1.1958225	C	3.5111259	-2.5375679	-3.4464842
H	3.5253312	-3.6935981	0.0664745	H	3.6344975	-2.1397167	-2.4338226
C	-2.4511517	-2.4590471	-0.3488379	H	4.4490047	-2.3707497	-3.9928387

H	3.3375229	-3.6185358	-3.3686959
C	3.9980973	-2.0244365	2.2084721
H	3.7786213	-1.3446835	1.3766000
H	5.0548228	-2.3246586	2.1589416
H	3.8524041	-1.4670570	3.1382659
C	2.5936972	-0.3044281	-4.2075667
H	1.7911244	0.2127482	-4.7484927
H	3.5487326	-0.0837749	-4.7041083
H	2.6300760	0.0985077	-3.1912117
H	-0.4513833	0.1860481	-0.5792478

$[(^{t\text{Bu}}\text{dmx})Co_2(\mu\text{-}O)_2]^{2-}$ (**14**)

E = -2637.61159799 a.u.
G = -2636.745755 a.u.
Charge = –2, Multiplicity = 7

Co	1.7828739	1.0979089	1.0180450
Co	1.7525791	-0.8403018	-0.7610285
O	2.4658178	-0.7185708	0.9092375
O	-2.7153264	-0.0625164	-0.1127810
O	2.0785850	0.9261512	-0.9139991
N	0.5411046	-0.8420765	-2.3031443
N	1.0085396	3.0357972	0.7236802
N	0.3225506	0.8529858	2.4602193
N	1.3612287	-2.7683405	-0.5568564
C	-1.2941664	2.1003880	1.0060057
C	-0.7516550	-1.2953999	-1.9917020
C	-0.3697651	2.9574616	0.3720903
C	-0.9878187	1.2046405	2.0596044
C	-1.0442020	-2.1805840	-0.8862982
C	-1.9223676	0.5770012	2.9543336
H	-2.9989542	0.6669344	2.9050504
C	0.4891665	-0.1817072	-3.5234957
C	-0.6243790	3.9160636	-0.6749321
H	-1.5754830	4.0732225	-1.1637131
C	-1.1714208	-0.1177961	3.9052805
H	-1.5493316	-0.6920346	4.7398201
C	-0.0131487	-2.9895535	-0.2878893
C	-5.6715879	-0.1977986	-0.2207993
C	1.5665651	4.0058684	-0.0400416
C	0.2182570	0.0649527	3.5644353
C	-2.7420671	2.1987665	0.6416936
C	2.6880981	0.2728438	4.0950348
H	3.0004618	0.2461265	3.0464092
H	3.5009606	-0.1538719	4.6998959
H	2.5369395	1.3170551	4.4010555
C	-4.7462063	-1.4232344	-0.2932036
C	-4.8735196	1.0765556	0.0893581
C	0.5791554	4.5806990	-0.9220358
H	0.7535182	5.3668526	-1.6449183
C	1.3993781	-0.5620833	4.2890561
C	2.0898376	-3.7673628	0.0686365
C	3.0429991	4.3638794	0.0083297
C	-0.1177304	-4.1303243	0.5608602
H	-1.0328805	-4.5496481	0.9552074
C	-6.3834956	-0.0366784	-1.5988051
H	-5.6467882	0.1214911	-2.3951387
H	-7.0660901	0.8219901	-1.5845529
H	-6.9647153	-0.9350223	-1.8382990
C	-0.8480071	-0.1965539	-3.9930949
H	-1.1963548	0.2227970	-4.9285045
C	-6.7411847	-0.4036433	0.8912094
H	-7.3521506	-1.2896875	0.6887780
H	-7.4171333	0.4565070	0.9501026
H	-6.2584471	-0.5323248	1.8669585
C	3.6084892	-3.8831928	-0.0076997
C	-1.6345482	-0.8831156	-3.0264317
H	-2.6931684	-1.1040462	-3.0752112
C	1.2030312	-4.6281732	0.7570570
H	1.4797527	-5.5121731	1.3187865
C	-5.5375025	2.3036282	0.2974047
H	-6.6178097	2.3496331	0.1930407
C	-3.4706578	1.0622424	0.2065371
C	-3.3477455	-1.2993533	-0.3375603
C	-3.4404403	3.4037515	0.8331298
H	-2.8900276	4.2783298	1.1654217

C	-5.2944706	-2.7215954	-0.4012517	H	3.2940007	4.3251670	-2.1754685
H	-6.3719622	-2.8552231	-0.3791090	C	-4.8328857	3.4671683	0.6417059
C	1.6834882	0.4563805	-4.2250592	H	-5.3622052	4.4039417	0.7901824
C	4.1766778	-3.0907627	-1.2095701	C	-3.0689853	-3.6776604	-0.6513306
H	3.7081722	-3.4090462	-2.1494359	H	-2.4322307	-4.5343119	-0.8447270
H	5.2619685	-3.2528522	-1.2838258	C	1.0882950	-0.6564851	5.8058591
H	3.9984553	-2.0181139	-1.0868974	H	0.8906444	0.3356862	6.2339600
C	-2.4714059	-2.3966765	-0.5873335	H	1.9466523	-1.0957771	6.3317044
C	1.5228627	0.3164979	-5.7626280	H	0.2165640	-1.2933318	5.9998093
H	1.4908576	-0.7400359	-6.0616991	C	-4.4606660	-3.8429474	-0.5464210
H	2.3714839	0.7964511	-6.2711736	H	-4.8955282	-4.8366894	-0.6208697
H	0.6033323	0.7990460	-6.1164109	C	1.6317639	-1.9884518	3.7136005
C	3.1975740	5.9063042	0.0890385	H	0.7267107	-2.6041336	3.8126596
H	2.7172073	6.4003117	-0.7642591	H	2.4514489	-2.4841440	4.2561888
H	4.2618333	6.1789469	0.0840400	H	1.8952407	-1.9083784	2.6530424
H	2.7439325	6.2977571	1.0094416	C	3.0188415	-0.2120453	-3.8141490
C	3.7434662	3.7248227	1.2286073	H	3.2206158	-0.0241563	-2.7561862
H	3.2500455	4.0047522	2.1673813	H	3.8434019	0.2112267	-4.4074341
H	4.7912491	4.0525342	1.2684270	H	2.9911577	-1.2972402	-3.9832420
H	3.7380179	2.6305541	1.1525766	C	4.2442457	-3.3303717	1.2987983
C	4.0074974	-5.3743561	-0.1761427	H	3.9040652	-2.2990025	1.4372716
H	3.6339402	-5.9839952	0.6557367	H	5.3433402	-3.3660854	1.2381226
H	5.1027499	-5.4715350	-0.2016079	H	3.9235019	-3.9267766	2.1639167
H	3.6008027	-5.7863992	-1.1096399	C	1.7427636	1.9656645	-3.8564118
C	3.7185645	3.8361623	-1.2893707	H	0.8360201	2.4808741	-4.2034271
H	3.5435190	2.7584935	-1.3754916	H	2.6180496	2.4454430	-4.3235863
H	4.7987797	4.0404431	-1.2622868	H	1.8141331	2.0459886	-2.7683207

3.6.5 X-Ray Diffraction Techniques

All structures were collected on a Bruker three-circle platform goniometer equipped with an Apex II CCD and an Oxford cryostream cooling device. Radiation was from a graphite fine focus sealed tube Mo Kα (0.71073 Å), a graphite fine focus sealed tube Cu Kα (1.54178 Å) source, or synchrotron radiation at Argonne National Laboratory Advance

Photon Course, ChemMatCARS. Crystals were mounted on a cryoloop or glass fiber pin using Paratone N oil. Structures were collected at 100 K. Data were collected as a series of φ and/or ω scans.

Data were integrated using SAINT[40] and scaled with either a numerical or multi-scan absorption correction using SADABS.40 The structures were solved by intrinsic phasing, direct methods or Patterson maps using SHELXS-2014[41] and refined against F^2 on all data by full matrix least squares with SHELXL-2014.41 All non-hydrogen atoms were refined anisotropically. Hydrogen atoms were placed at idealized positions and refined using a riding model. The isotropic displacement parameters of all hydrogen atoms were constrained to be 1.2 times the parameter of the atoms they were linked to (1.5 times for methyl groups). Further details on particular structures are noted below.

($^{t\text{Bu}}$dmx)Co$_2$[N(SiMe$_3$)$_2$]$_2$ (1): The structure was solved in the monoclinic space group *C*2/*c* with two molecules per unit cell and half a molecule in the asymmetric unit. (CCDC 1995464)

[($^{t\text{Bu}}$dmx)Co$_2$(OH)(N(SiMe$_3$)$_2$)]$_3$ (3): The structure was solved in the triclinic space group *P*$\bar{1}$ with two molecules per unit cell and one molecule in the asymmetric unit. Several ^{t}Bu and SiMe$_3$ groups in the ligand exhibited positional disorder and were modeled with similarity constraints and restraints. The asymmetric unit contained several strongly disordered hexanes molecules. Due to apparent low occupancy and high disorder, an acceptable model could not be refined. A solvent mask was applied in Platon to reduce unrefined electron density. (CCDC 1995465)

[40] APEX2 Software Suite; Bruker AXS: Madison, WI, 2009.

[41] Sheldrick, G. M. *Acta Crystallogr., Sect. A: Found. Crystallogr.* **2008**, *64*, 112–122.

($^{t\text{Bu}}$dmx)$Co_2(\mu\text{-}OH)_2$ (4): The structure was solved in the triclinic space group $P\bar{1}$ with two molecules per unit cell and one molecule in the asymmetric unit. (CCDC 1995466)

[($^{t\text{Bu}}$dmx)$Co_2(\mu\text{-}OH)(lut)_2$][$BPh_4$] (5b): The structure was solved in the monoclinic space group $P2_1/c$ with four molecules per unit cell and one molecule in the asymmetric unit. The asymmetric unit contained several strongly disordered diethyl ether solvent molecules. Due to apparent low occupancy and high disorder, an acceptable model could not be refined. A solvent mask was applied in Platon to reduce unrefined electron density. (CCDC 1995467)

($^{t\text{Bu}}$dmx)$Co_2Cl_2(py)_2$ (6): The structure was solved in the triclinic space group $P\bar{1}$ with two molecules per unit cell and one molecule in the asymmetric unit. A full data set was not able to be collected due to crystal degradation, resulting in poor data quality and requiring similarity restraints and constraints. The asymmetric unit contained several strongly disordered hexanes molecules. Due to apparent low occupancy and high disorder, an acceptable model could not be refined. A solvent mask was applied in Platon to reduce unrefined electron density. (CCDC 1995468)

[($^{t\text{Bu}}$dmx)$Co_2(\mu\text{-}OH)]_2$[$Co(OH)_4$] (10): The structure was solved in the triclinic space group $P\bar{1}$ with two molecules per unit cell and one molecule in the asymmetric unit. One of the ^{t}Bu groups in the ligand exhibited positional disorder and were modeled with similarity constraints and restraints. The asymmetric unit contained one strongly disordered benzene molecule. Due to apparent low occupancy and high disorder, an acceptable model could not be refined. A solvent mask was applied in Platon to reduce unrefined electron density. (CCDC 1995469)

($^{t\text{Bu}}$dmx)Co$_2$(O^{t}Bu)$_2$(thf)$_2$ (11): The structure was solved in the monoclinic space group *P2$_1$/n* with four molecules per unit cell and one molecule in the asymmetric unit. Positional disorder exhibited by one of the ^{t}Bu groups in the ligand, and partial occupancy of an ether molecule bound to Co1 in place of the tetrahydrofuran were modeled with similarity restraints. (CCDC 1995470)

Table 3.5. Bond metrics of **3**, **4**, **5b**, and **11**.

Complex	Co–Co (Å)	Co–O (Å)	< Co–OH–Co (°)
[($^{t\text{Bu}}$dmx)Co$_2$(OH)(N(SiMe$_3$)$_2$)]$_3$ (3)	3.6229(3); 3.6228(2); 3.6154(2)	1.93501(15), 1.97359(13); 1.91535(14), 1.95968(12); 1.92566(11), 1.96276(16)	135.912(4); 138.420(3); 136.799(3)
($^{t\text{Bu}}$dmx)Co$_2$(μ-OH)$_2$ (4)	2.63665(19)	1.88506(14), 1.88005(15); 1.86691(13), 1.87552(15)	89.583(4); 88.900(4)
[($^{t\text{Bu}}$dmx)Co$_2$(μ-OH)(lut)$_2$][BPh$_4$] (5b)	3.7530(8)	1.951(3), 1.974(3)	145.9(2)
($^{t\text{Bu}}$dmx)Co$_2$(O^{t}Bu)$_2$(thf)$_2$ (11)	6.7471(9)	1.843(3), 1.869(3)	—

Table 3.6. X-ray diffraction experimental details.[a]

	($^{t\text{Bu}}$dmx)Co$_2$[N(SiMe$_3$)$_2$]$_2$ (1)	**[($^{t\text{Bu}}$dmx)Co$_2$(OH)(N(SiMe$_3$)$_2$)]$_3$ (3)**:	**($^{t\text{Bu}}$dmx)Co$_2$(μ-OH)$_2$ (4)**
Moiety Formula	$C_{30.50}H_{46}CoN_3O_{0.50}Si_2$	$C_{165}H_{225}Co_2N_{15}O_6Si_6$	$C_{58}H_{67}Co_2N_4O_3$; 1.5(C_6H_6)
FW	577.81	3036.71	986.01
λ (nm)	1.54178	0.71073	0.41328
***T* (K)**	100(2)	100(2)	100(2)
Crystal System	monolinic	triclinic	triclinic
Space Group (*Z*)	*C*2/*c* (4)	$P\bar{1}$ (2)	$P\bar{1}$ (2)
***a* (Å)**	25.4659 (13)	18.2568(15)	12.489(1)
***b* (Å)**	13.3489 (7)	22.965(2)	14.3018(12)
***c* (Å)**	20.0477 (10)	24.2037(19)	14.5945(13)
α (°)	90	71.535(2)	89.752(2)
β (°)	111.003 (3)	70.039(2)	86.374(2)
γ (°)	90	80.369(3)	75.283(2)
Volume (Å^3)	6362.3 (6)	9027.3(14)	2516.0(4)
Calc. ρ (mg/m^3)	1.206	1.117	1.301
μ (mm^{-1})	5.13	0.630	0.170
Crystal Size (mm)	0.20×0.10×0.04	0.25×0.23×0.02	0.10×0.04×0.03
Reflections	6095	31942	8503
Completeness (to 2θ)	96.3% 72.46°	99.1% 25.12°	95.3% 14.26°
GOF on F^2	1.054	1.020	0.963
R1, *w*R2[a] [*I* > 2σ(*I*)]	0.0331, 0.0903	0.0967, 0.2148	0.0543, 0.1336

[a] $R1 = \sum\big||F_o| - |F_c|\big|/\sum|F_o|$, $wR2 = \{\sum[w(F_o^2 - F_c^2)^2]/\sum[w(F_o^2)^2]\}^{1/2}$

Table 3.7. X-ray diffraction experimental details.[a]

	[($^{t\text{Bu}}$dmx)Co$_2$(μ-OH)(lut)$_2$][BPh$_4$] (5b)	**($^{t\text{Bu}}$dmx)Co$_2$Cl$_2$(py)$_2$ (6b)**	**[($^{t\text{Bu}}$dmx)Co$_2$(μ-OH)]$_2$[(Co(OH)$_4$] (10)**	**($^{t\text{Bu}}$dmx)Co$_2$(O^{t}Bu)$_2$(thf)$_2$ (11)**
Moiety Formula	$C_{63}H_{75}Co_2N_6O_2 \cdot C_{24}H_{20}B$	$C_{59}H_{66}Cl_2Co_2N_6O \cdot$	$C_{98}H_{118}Co_5N_8O_8$; $2(C_6H_6)$	$C_{64.68}H_{89.08}Co_2N_4O_5$; $0.325(CH_3)$
FW	1385.35	1063.93	1986.86	1197.44
λ (nm)	0.71073	0.71073	0.71073	1.54178
***T* (K)**	100(2)	100(2)	100(2)	100(2)
Crystal System	monoclinic	triclinic	triclinic	monoclinic
Space Group (*Z*)	$P2_1/c$ (4)	$P\bar{1}$ (2)	$P\bar{1}$ (2)	$P2_1/n$ (4)
***a* (Å)**	11.6341(7)	14.154(2)	14.7208(9)	12.332(1)
***b* (Å)**	18.7505(11)	14.249(3)	18.2332(11)	25.737(2)
***c* (Å)**	37.3530(18)	15.040(2)	20.6722(12)	21.1236(15)
α (°)	90	77.017(5)	82.406(2)	90
β (°)	96.489(2)	78.469(5)	87.128(2)	90.179(3)
γ (°)	90	86.109(5)	73.701(2)	90
Volume (Å^3)	8096.2(8)	2895.2(8)	5278.4(6)	6704.4(9)
Calc. ρ (mg/m^3)	1.137	1.220	1.250	1,186
μ (mm^{-1})	0.458	0.708	0.827	4.271
Crystal Size (mm)	0.26x0.22x0.05	0.25x0.13x0.05	0.17x0.07x0.04	0.10x0.02x0.02
Reflections	14263	9520	18647	11895
Completeness (to 2θ)	99.2% 25.07°	92.9% 25.07°	99.3% 25.08°	99.8% 66.86°
GOF on F^2	1.029	0.968	1.004	1.037
R1, *w*R2[a] [$I > 2\sigma(I)$]	0.0666, 0.1568	0.1085, 0.2563	0.0507, 0.1036	0.0635 0.1861

[a] $R1 = \sum||F_o| - |F_c||/\sum|F_o|$, $wR2 = \{\sum[w(F_o^2 - F_c^2)^2]/\sum[w(F_o^2)^2]\}^{1/2}$

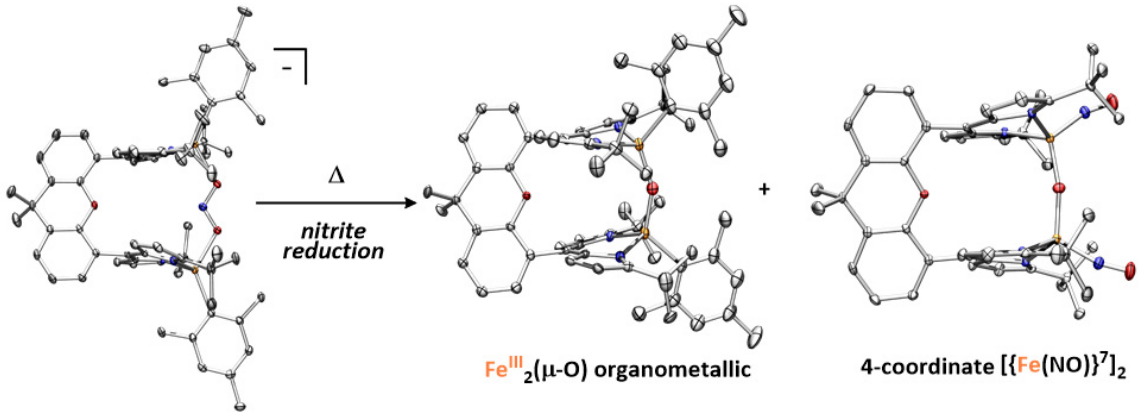

Chapter 4: Nitrite Reduction by a Bimetallic Dipyrrin Pacman Iron Complex

4.1 Introduction

Nitrite is a key member of the nitrogen biogeochemical cycle, in which it is reduced to NO by various metalloenzymes in the global recycling of nitrogen. Furthermore, this process is employed by bacteria as a method of aerobic respiration known as denitrification.[1] Dissimilatory nitrite reductase enzymes featuring copper (CuNIR) and iron (Cd_1NIR) utilize two metal centers to accomplish this reactivity; one metal performs electron transport to provide the necessary electron equivalent to the substrate-binding and catalytic metal site.[2,3] In Cd_1NIR, these include a *c* heme (electron transfer) and a d_1 heme (nitrite binding and reduction) site located approximately 20 Å apart that are able to work cooperatively through

[1] (a) Averill, B. A. *Chem. Rev.* **1996**, *96*, 2951–2964. (b) Wasser, I. M.; de Vries, S.; Moënne-Loccoz, P.; Schröder, I.; Karlin, K. D. *Chem. Rev.* **2002**, *102*, 1201–1234.

[2] Moura, I.; Moura, J. J. G. *Curr. Opin. Chem. Biol.* **2001**, *5*, 168–175.

[3] Maia, L. B.; Moura, J. J. G. *Chem. Rev.* **2014**, *114*, 5273–5357.

protein conformational changes.[4] Many reports have also established the role of nitrite reduction to NO in mammalian, plant, and bacterial signaling pathways.[3] NO is an important signaling molecule for many physiological processes, and its biosynthesis from nitrite has been recently discovered under hypoxic conditions when the more traditional method of formation via L-arginine and dioxygen[5] is no longer possible.[3] Nitrite reduction to NO in eukaryotic systems for signaling purposes is possible using various metalloproteins, including iron (such as hemoglobin,[6,7] myoglobin,[8,7] cytochrome *c*[8]), molybdenum (xanthine oxidase,[9,10] aldehyde oxidase[10,11]) or zinc (carbonic anhydrase[12]) dependent enzymes. Environmentally,

[4] (a) Nurizzo, D.; Silvestrini, M.-C-.; Mathieu, M.; Cutruzzolà, F.; Bourgeois, D.; Fülöp, V.; Hajdu, J.; Brunori, M.; Tegoni, M.; Cambillau, C. *Structure.* **1997**, *5*, 1157–1171. (b) Sutherland, J.; Greenwood, C.; Peterson, J.; Thomson, A. J. *Biochem. J.* **1986**, *233*, 893–898.

[5] (a) Moncada, S.; Palmer, R. M. J.; Higgs, E. A. *Pharmacol. Rev.* **1991**, *43*, 109–142. (b) Stuehr, D. J. *Biochim. Biophys. Acta* **1999**, *1411*, 217–230.

[6] (a) Doyle, M. P.; Pickering, R. A.; DeWeert, T. M.; Hoekstra, J. W.; Pater, D. *J. Biol. Chem.* **1981**, *256*, 12393–12398. (b) Huang, Z.; Shiva, S.; Kim-Shapiro, D. B.; Patel, R. P.; Ringwood, L. A.; Irby, C. E.; Huang, K. T.; Ho, C.; Hogg, N.; Schecter, A. N.; Gladwin, M. T. *J. Clin. Invest.* **2005***, 115*, 2099–2107. (c) Salhany, J. M. *Biochem.* **2008**, *47*, 6059–6072.

[7] Gladwin, M. T.; Kim-Shapiro, D. B. *Blood* **2008**, *112*, 2636–2647. and references therein.

[8] Basu, S.; Azarova, N. A.; Font, M. D.; King, S. B.; Hogg, N.; Gladwin, M. T.; Shiva, S.; Kim-Shapiro, D. B. *J. Biol. Chem.* **2008**, *283*, 32590–32597.

[9] (a) Zhang, Z.; Naughton, D.; Winyard, P. G.; Benjamin, N.; Blake, D. R.; Symons, M. C. *Biochem. Biophys. Res. Commun.* **1998**, *249*, 767–772. (b) Godber, B. L. J.; Doel, J. J.; Sapkota, G. P.; Blake, D. R.; Stevens, C. R.; Eisenthal, R.; Harrison, R. *J. Biol. Chem.* **2000**, *275*, 7757–7763. (c) Li, H.; Samouilov, A.; Liu, X.; Zweier, J. L. *J. Biol. Chem.* **2001**, *276*, 24482–24489.

[10] Li, H.; Cui, H.; Kundu, T. K.; Alzawahra, W.; Zweier, J. L. *J. Biol. Chem.* **2008**, *283*, 17855–17963.

[11] Li, H.; Kundu, T. K.; Zweier, J. L. *J. Biol. Chem.* **2009**, *284*, 33850–33858.

[12] Aamand, R.; Dalsgaard, T.; Jensen, F. B.; Simonsen, U.; Roepstorff, A.; Fago, A. *Am. J. Physiol. Heart Circ. Physiol.* **2009**, *297*, H2068–H2074.

nitrite removal from drinking water (and alkaline nuclear waste) is critical as this oxyanion is toxic to humans.[13,14]

A diverse group of synthetic systems capable of nitrite reduction has been reported, including homogenous transition metal[15,16,17,18,19,20,21] or lanthanide complexes[22] and electrocatalytically active transition metal complexes,[23] as well as studies on heterogeneous

[13] Cervantes, F. J.; De la Rosa, D. A.; Gómez, J. *Bioresour. Technol.* **2001**, *79*, 165–170.

[14] Rosca, V.; Duca, M.; de Groot, M. T.; Koper, M. T. M. *Chem. Rev.* **2009**, *109*, 2209–2214

[15] (a) Yamaji, M.; Hama, Y.; Miyazaki, Y.; Hoshino, M. *Inorg. Chem.* **1992**, *31*, 932–934. (b) Suslick, K. S.; Watson, R. A. *Inorg. Chem.* **1991**, *30*, 912–919.

[16] (a) López, J. P.; Heinemann, F. W.; Prakash, R.; Hess, B. A.; Horner, O.; Jeandey, C.; Oddou, J.-L.; Latour, J.-M.; Grohmann, A. *Chem. Eur. J.* **2002**, *8*, 5709–5722. (b) Ching, W.-M.; Chuang, C.-H.; Wu, C.-W.; Peng, C.-H.; Hung, C.-H. *J. Am. Chem. Soc.* **2009**, *131*, 7952–7953. (c) Harris, T. D.; Betley, T. A. *J. Am. Chem. Soc.* **2011**, *133*, 13852–13855. (d) Tsou, C.-C.; Yang, W.-L.; Liaw, W.-F. *J. Am. Chem. Soc.* **2013**, *135*, 18758–18761. (e) Uyeda, C.; Peters, J. C. *J. Am. Chem. Soc.* **2013**, *135*, 12023–12031. (f) Kwon, Y. M.; Delgado, M.; Zakharov, L. N.; Seda, T.; Gilbertson, J. D. *Chem. Commun.* **2016**, *52*, 11016–11019. (g) Burns, K. T.; Marks, W. R.; Cheung, P. M.; Seda, T.; Zakharov, L. N.; Gilbertson, J. D. *Inorg. Chem.* **2018**, *57*, 9601–9610.

[17] Villar-Acevedo, G.; Nam, E.; Fitch, S.; Benedict, J.; Freudenthal, J.; Kaminsky, W.; Kovacs, J. A. *J. Am. Chem. Soc.* **2011**, *133*, 1419–1427.

[18] (a) Patra, A. K.; Afshar, R. K.; Rowland, J. M.; Olmstead, M. M.; Mascharak, P. K. *Angew. Chem. Int. Ed. Engl.* **2003**, *42*, 4517–4521. (b) Afshar, R. K.; Eroy-Reveles, A. A.; Olmstead, M. M.; Mascharak, P. K. *Inorg. Chem.* **2006**, *45*, 10347–10354. (c) Tsai, F.-T.; Kuo, T.-S.; Liaw, W.-F. *J. Am. Chem. Soc.* **2009**, *131*, 3426–3427. (d) Tsai, F.-T.; Chen, P.-L.; Liaw, W.-F. *J. Am. Chem. Soc.* **2010**, *132*, 5290–5299.

[19] (a) Khin, C.; Heinecke, J.; Ford, P. C. *J. Am. Chem. Soc.* **2008**, *130*, 13830–13831. (b) Kurtikyan, T. S.; Hovhannisyan, A. A.; Kretskii, A. V.; Ford, P. C. *Inorg. Chem.* **2009**, *48*, 11236–11241. (c) Heinecke, J.; Ford, P. C. *J. Am. Chem. Soc.* **2010**, *132*, 9240–9243. (d) Tsai, F.-T.; Lee, Y.-C.; Chiang, M.-H.; Liaw, W.-F. *Inorg. Chem.* **2013**, *52*, 464–473. (e) Shi, K.; Mathivathanan, L.; Boudalis, A. K.; Turek, P.; Chakraborty, I.; Raptis, R. G. *Inorg. Chem.* **2019**, *58*, 7537–7544.

[20] Matson, E. M.; Park, Y. J.; Fout, A. R. *J. Am. Chem. Soc.* **2014**, *136*, 17398–17401.

[21] Petel, B. E.; Matson, E. M. *Chem. Commun.* **2020**, *56*, 555–558.

[22] Lewis, A. J.; Carroll, P. J.; Schelter, E. J. *J. Am. Chem. Soc.* **2013**, *135*, 511–518.

[23] (a) Barkley, M. H.; Meyer, T. J. *J. Am. Chem. Soc.* **1986**, *108*, 5876–5885. (b) Barkley, M. H.; Rhodes, M. R.; Meyer, T. J. *Inorg. Chem.* **1987**, *26*, 1746–1750. (c) Rhodes, M. R.; Barkley, M. H.; Meyer, T. J. *Inorg. Chem.* **1991**, *30*, 629–635. (d) Taniguchi, I.; Nakashima, N.; Matsushita, K.; Yasukouchi, K. *J. Electroanal. Chem.* **1987**, *224*, 199–209. (e) Xiang, Y.; Zhou, D.-L.; Rusling, J. F. *J. Electroanal. Chem.* **1997**, *424*, 1–3. (f) Xu, S.; Kwon, H.-Y.; Ashley, D. C.; Chen, C.-H.; Jakubikova, E.; Smith, J. M. *Inorg. Chem.* **2019**, *58*, 9443–9451.

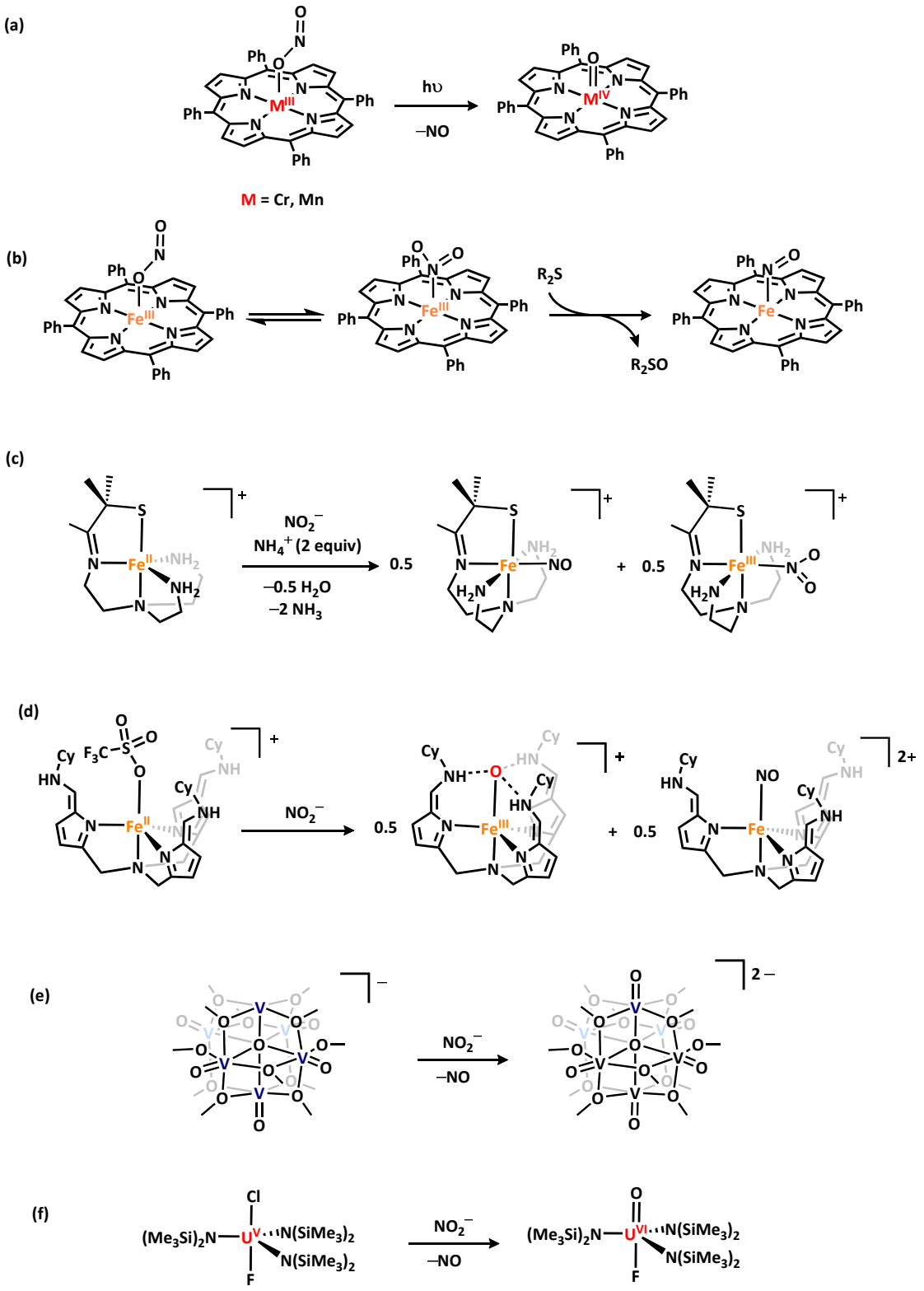

Figure 4.1. Selected examples of nitrite reduction facilitated by transition metal complexes. Many previous examples requiring (a) photolysis,[15] (b) the addition of oxophilic substrates such as thioethers,[19b] or the addition of one or (c) more equivalents of acid per nitrite equivalent to induce bond activation[17] have been reported. (d-f) The few examples enabling nitrite reduction without additional substrates are also shown.[20,21,22]

reduction mediated by various metal electrodes.[14] Electrocatalysis typically leads to a variety of nitrogen-containing reduced products, including nitrous oxide, dinitrogen, hydroxylamine, and ammonia.[14] Conversely, the majority of homogeneous examples featuring transition metal centers require photolysis,[15] protonation,[16,17] or the addition of oxygen abstraction reagents (such as phosphines[18] or thiols/thioethers[19]) to initiate nitrite activation and reduction (**Figure 4.1a-c**). The minority of systems that do not require such additives instead take advantage of the thermodynamic driving force of forming a favorable metal–oxo (M=Fe[20] or V[21]) or lanthanide–oxo (Ln=U)[22] unit to facilitate NO bond scission (**Figure 4.1d-f**). In the case of the iron complex, a tripodal ligand system featuring azafulvene-amine ligands provided secondary-sphere hydrogen bonding stabilization to the generated iron(III)–oxo.[20] The other examples involved making a V^{V}=O utilizing an oxygen-deficient polyoxovanadate cluster[21] or a U^{VI}=O from a uranium(V) bis-amide precursor.[22]

We now report a bimetallic complex that is competent for nitrite reduction without requiring additional reagents by forming iron bridging-oxo species following thermolytic N–O bond cleavage. We note that the previously developed bimetallic system is suitable for orienting two metals in proximity and displays the accessibility of bridging oxo moieties on the diiron platform in multiple oxidation states.[24] Herein, we extend our studies to explore how two proximal iron centers can be utilized for cooperative redox chemistry, forming stable bridging-oxo products that drive the system's competency for nitrite reduction.

[24] Johnson, E. J.; Kleinlein, C. K.; Musgrave, R. A.; Betley, T. A. *Chem. Sci.* **2019**, *10*, 6304–6310.

4.2 Synthesis of Diiron Nitrite Adducts

The previously discussed diiron(II) organometallic species, ($^{t\text{Bu}}$dmx)Fe$_2$(Mes$_2$ (**1**), features two high-spin S = 2 iron(II) centers held 6.7562(7) Å apart (**Figure 2.1).** By tuning the primary coordination sphere of the metal ions within the ($^{t\text{Bu}}$dmx) ligand scaffold, we observe large vertical flexibility (ΔFe–Fe > 3.5 Å) consistent with the "Pacman effect" exploited by Nocera and coworkers for oxygenation of organic substrates.[25] The large cleft between metal centers in the starting material coupled with the flexibility of the Pacman unit led us to hypothesize that this species could be suitable for performing cooperative substrate reduction chemistry. Specifically, this bimetallic unit confers sufficient space for small molecule substrates to bind between metal centers in the open pocket, while the ligand scaffold should allow for moderate geometrical changes to facilitate stabilization of intermediates en route to substrate activation. Furthermore, these bimetallic complexes can distribute the redox load to facilitate cooperative chemistry. With these principles in mind, we sought to test our hypothesis by targeting anionic nitrite reduction.

Addition of one equivalent of tetrabutylammonium nitrite ([^{n}Bu$_4$N][NO$_2$]) at room temperature in THF results in an immediate color change from orange to brown, concomitant with a distinctive paramagnetically shifted ^{1}H NMR spectrum and ^{57}Fe Mössbauer spectrum with parameters consistent with four-coordinate high spin iron(II) centers (δ = 0.75 mm s^{-1}, $|\Delta E_Q|$ = 3.15 mm s^{-1}, **Figure 4.2**). We assign the product as the diiron(II) nitrite adduct [^{n}Bu$_4$N][($^{t\text{Bu}}$dmx)Fe$_2$(NO$_2$)(Mes)$_2$] (**2a**). While **2a** provided crystal quality insufficient for

[25] (a) Rosenthal, J.; Pistorio, B. J.; Chng, L; Nocera, D. G. J. Org. Chem. 2005, 70, 1885–1886. (b) Rosenthal, J.; Luckett, T. D.; Hodgkiss, J. M.; Nocera, D. G. J. Am. Chem. Soc. 2006, 128, 6456–6547. (c) Deng, Y.; Chang, C. J.; Nocera, D. G. J. Am. Chem. Soc. 2000, 122, 410–411.

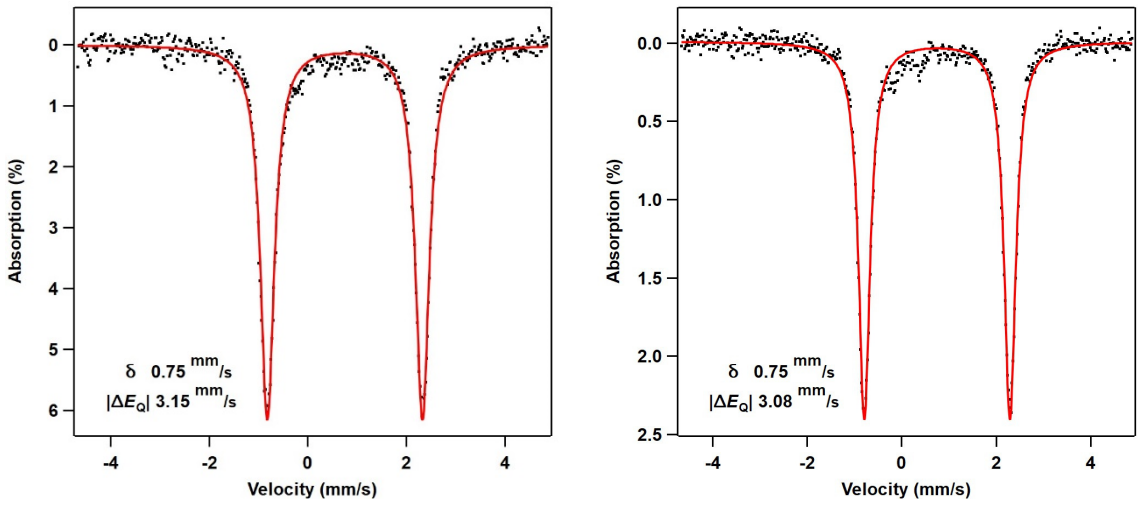

Figure 4.2. Zero-field ^{57}Fe Mössbauer spectrum of [($^{t\text{Bu}}$dmx)Fe$_2$(κ^2-O$_2$N)(Mes)$_2$]$^-$ complexes, (**Left**) [^{n}Bu$_4$N][($^{t\text{Bu}}$dmx)Fe$_2$(κ^2-O$_2$N)(Mes)$_2$] (**2a**) and (**Right**) [Na(15-crown-5)$_2$][($^{t\text{Bu}}$dmx)Fe$_2$(κ^2-O$_2$N)(Mes)$_2$] (**2b**). Isomer shifts and quadrupole splitting values are reported relative to Fe foil at room temperature.

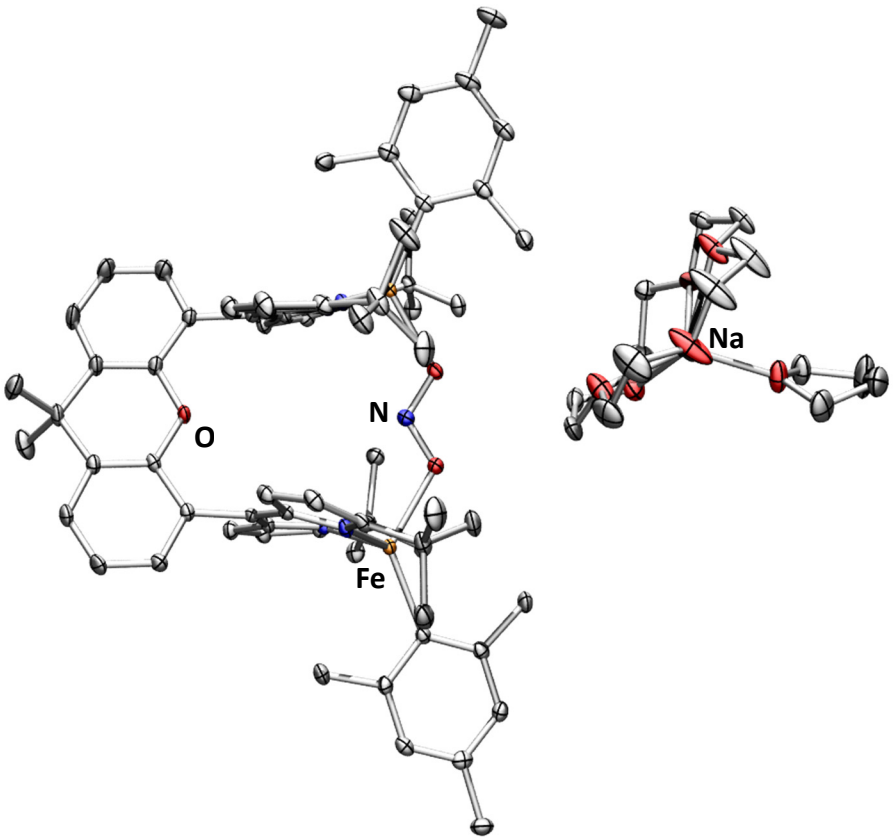

Figure 4.3. Solid state molecular structure of [Na(15-crown-5)(thf)][($^{t\text{Bu}}$dmx)Fe$_2$(κ^2-O$_2$N)(Mes)$_2$] (**2b**). with thermal ellipsoids at 50% probability level. Hydrogen atoms omitted for clarity. Color scheme: Fe, orange; N, blue; C, gray; O, red; Na, turquoise.

single crystal X-ray diffraction analysis, the sodium analogue afforded crystals of higher quality. As such, heating one equivalent of [Na][NO_2] and two equivalents of 15-crown-5 with (**1**) in THF to 45 °C overnight resulted in formation of a similar paramagnetically shifted ^{1}H NMR spectrum and ^{57}Fe Mössbauer spectrum as **2a** (δ = 0.75 mm s^{-1}, $|\Delta E_Q|$ = 3.08 mm s^{-1}, **Figure 4.2**). Single crystals suitable for crystallography were grown from a concentrated solution in diethyl ether plus drops of THF at –35 °C to reveal the nitrite adduct, [Na(15-c-5)(thf)][($^{t\text{Bu}}$dmx)Fe$_2$(κ^2-O$_2$N)(Mes)$_2$] (**2b**) (**Figure 4.3**).

4.3 Nitrite Activation and Reduction via Thermolysis

Heating the nitrite adduct **2a** to 80 °C in THF results in a color change from brown to red and convergence to a paramagnetically-broadened ^{1}H NMR spectrum. Solid state FTIR spectroscopy reveals the growth of strong features at 1730 and 1781 cm^{-1} (**Figure 4.4**), which shift to 1699 and 1755 cm^{-1} when the $^{15}NO_2$ adduct [Na][($^{t\text{Bu}}$dmx)Fe$_2$(κ^2-O$_2$^{15}N)(Mes)$_2$] (**2c**) is thermolyzed (**Figure 4.5**), consistent with formation of an iron-nitrosyl complex. The ^{57}Fe Mössbauer spectrum is indicative of oxidation to high spin iron(III) centers. The broad spectrum is best fit as two equimolar diiron(III) centers (δ = 0.21 mm s^{-1}, $|\Delta E_Q|$ = 1.81 mm s^{-1} ; δ = 0.32 mm s^{-1}, $|\Delta E_Q|$ = 1.10 mm s^{-1}, **Figure 4.6**). The identity of these species has been assigned by single crystal X-ray diffraction and spectroscopic studies to reveal an overall one electron reduction of the NO_2^- anion (**Scheme 4.1**). A similar spectrum was observed for [Na][NO_2] thermolysis as well (**Figure 4.7**).

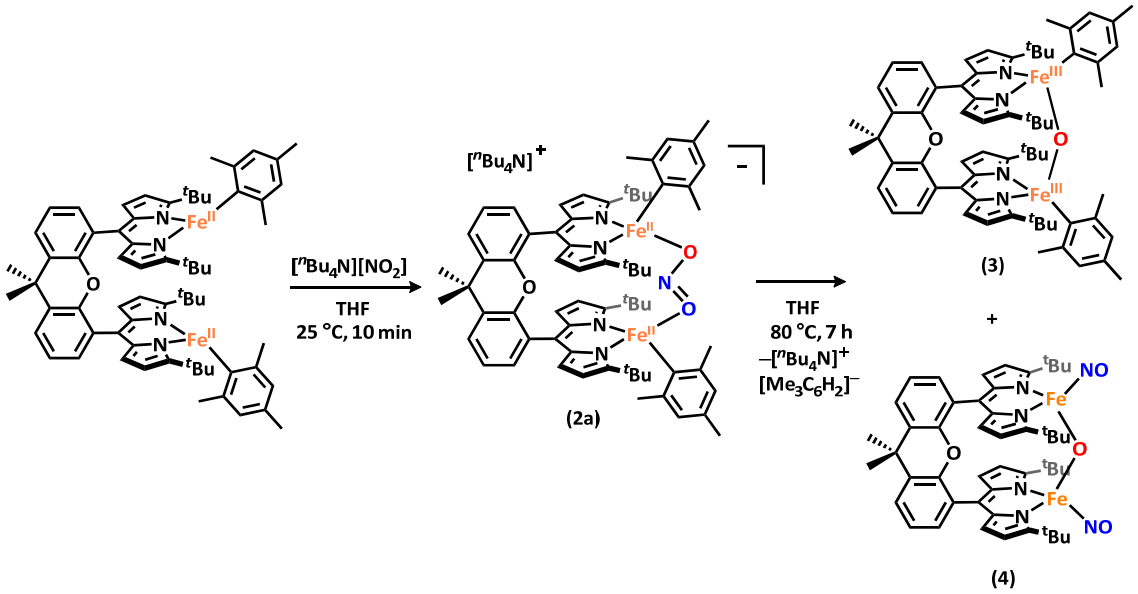

Scheme 4.1. Nitrite reduction facilitated by the diiron(II) Pacman complex **1**.

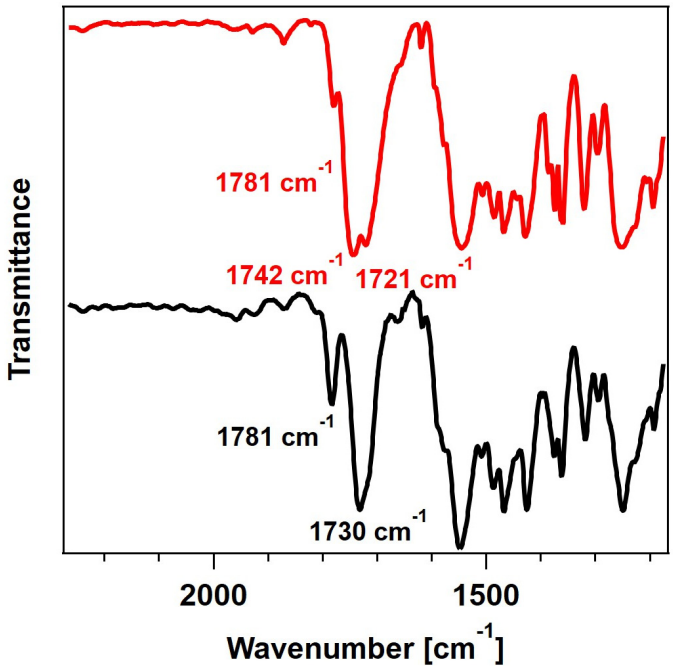

Figure 4.4. FTIR spectrum of ($^{t\text{Bu}}$dmx)Fe$_2$(μ-O)(NO)$_2$ (**4**) (top, red) via authentic synthesis route and ($^{t\text{Bu}}$dmx)Fe$_2$(μ-O)(NO)$_2$ (**4**) (bottom, black) via thermolysis route zoomed to show NO stretch region.

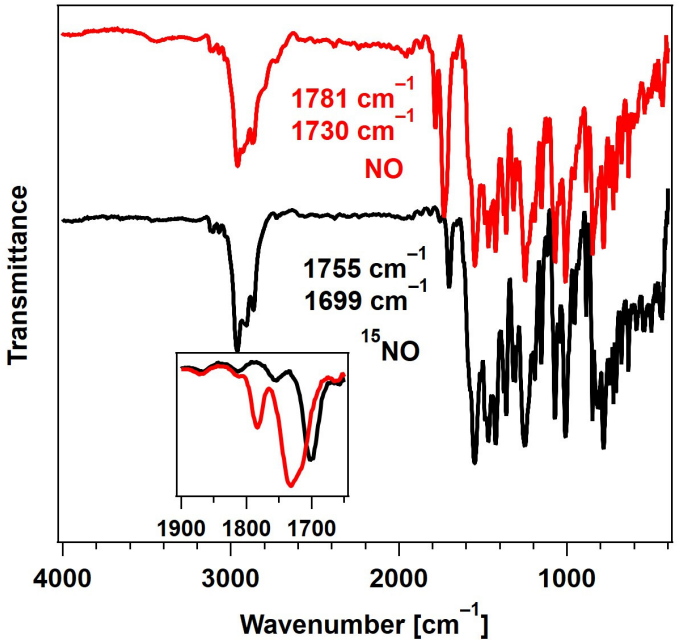

Figure 4.5. FTIR spectrum of ($^{t\text{Bu}}$dmx)Fe$_2$(μ-O)(NO)$_2$ (**4**) (top, red) and ($^{t\text{Bu}}$dmx)Fe$_2$(μ-O)(^{15}NO)$_2$ (bottom, black) via thermolysis route with inset of overlaid spectra in region featuring NO and ^{15}NO stretches.

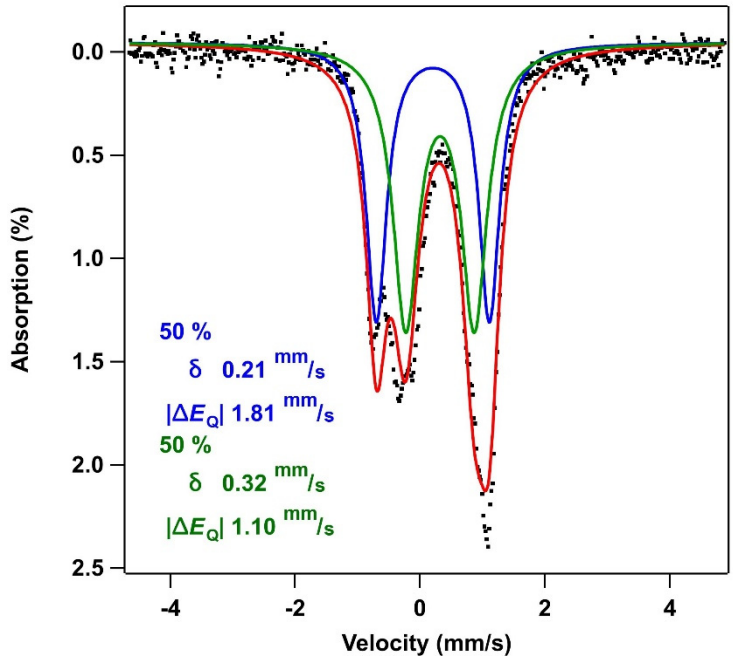

Figure 4.6. Zero-field ^{57}Fe Mössbauer spectrum of reaction mixture resulting from heating **2a**, forming a 1:1 mixture of **3** (blue trace) and **4** (green trace). Isomer shift and quadrupole splitting values are reported relative to Fe foil at room temperature.

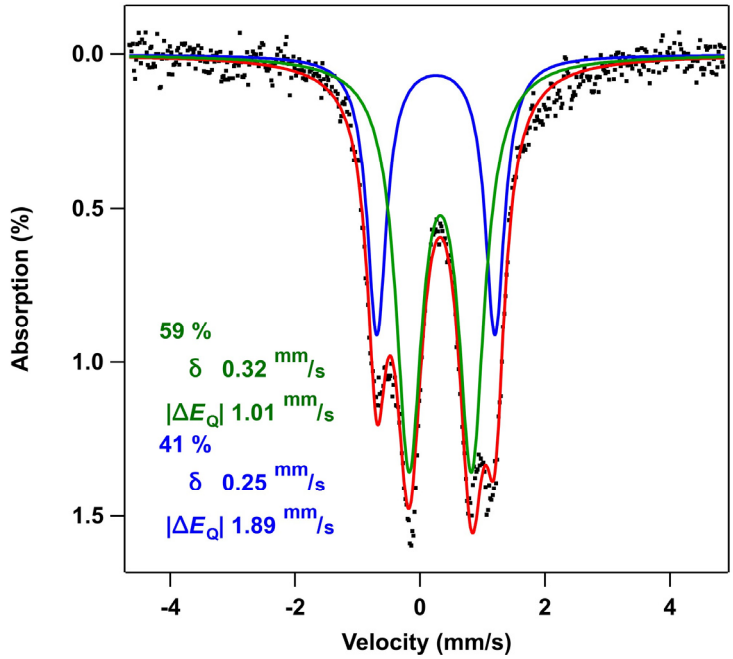

Figure 4.7. Zero-field ^{57}Fe Mössbauer spectrum of reaction mixture resulting from heating **2b**, forming a 1:1 mixture of **3** (blue trace) and **4** (green trace). Isomer shift and quadrupole splitting values are reported relative to Fe foil at room temperature.

4.4 Synthesis and Characterization of Nitrite Reduction Products

From a saturated solution of the nitrite thermolysis reaction mixture in toluene layered with hexanes at –35 °C, single crystals of one of the major species ($^{t\text{Bu}}$dmx)Fe$_2$(μ-O)Mes$_2$ (**3**) were grown to reveal trapping of the released oxygen atom from nitrite within the diiron cleft (**Figure 4.8**). Notably, the Fe–O distances observed within diiron(III) **3** (Fe–O : 1.7945(12) Å) are consistent with and only slightly elongated from those noted for ($^{t\text{Bu}}$dmx)Fe$_2$(μ-O)Cl$_2$ (**12**) from Chapter 2 (Fe–O : 1.7734(10) Å), while the Fe–C bond distances for **3** (Fe–C : 2.017(4) Å) are also slightly elongated relative to the diiron(II) organometallic species **1** (Fe–C : 2.032(3) Å, 2.041(4) Å). The diiron(III) (μ-O) organometallic species **3** has been shown to correspond to one set of doublets in the reaction ^{57}Fe Mössbauer spectrum (δ = 0.23 mm s^{-1}, $|\Delta E_Q|$ = 1.83 mm s^{-1}, **Figure 4.9**), as confirmed by independent synthesis of **3** by addition of

(dbabh)NO (dbabh = 2,3:5,6-Dibenzo-7-azabicyclo[2.2.1]hepta-2,5-diene) to **1** and is further corroborated by computational studies predicting the ^{57}Fe Mössbauer parameters (δ = 0.24 mm s^{-1}, $|\Delta E_Q|$ = 1.63 mm s^{-1}, **Table 4.2**). From a stoichiometry perspective, one equivalent of **3** should be formed per molecule of nitrite reduced, corresponding with the formation of one equivalent of NO. The diamagnetic region of the ^{1}H NMR spectrum of the thermolysis reaction of **2a** further reveals the formation of ^{n}Bu$_3$N, butene, and mesitylene (HMes). To balance this reaction, we hypothesize that the tetrabutylammonium counterion and mesityl groups are lost as [^{n}Bu$_4$N][Me$_3$C$_6$H$_2$], upon which the mesityl anion deprotonates the ^{n}Bu$_4$N in a Hoffman degradation to form the observed products.[26]

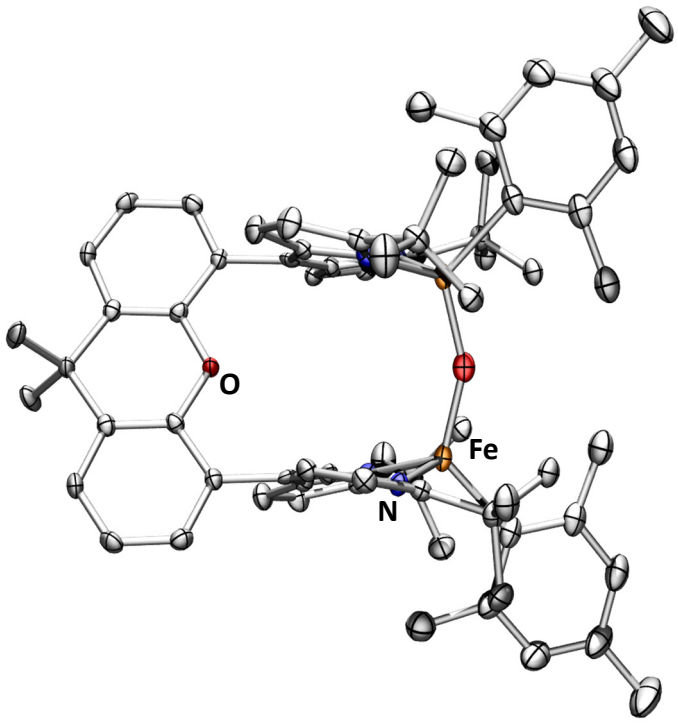

Figure 4.8. Solid state molecular structure of ($^{t\text{Bu}}$dmx)Fe$_2$(μ-O)(Mes)$_2$ (**3**) with thermal ellipsoids at 40% probability level. Hydrogen atoms omitted for clarity Color scheme: Fe, orange; N, blue; C, gray; O, red.

[26] Aube, J.; Fehl, C.; Liu, R.; McLeod, M. C.; Motiwala, H. F. *Comprehensive Organic Synthesis*, 2014, **2**, 598–635.

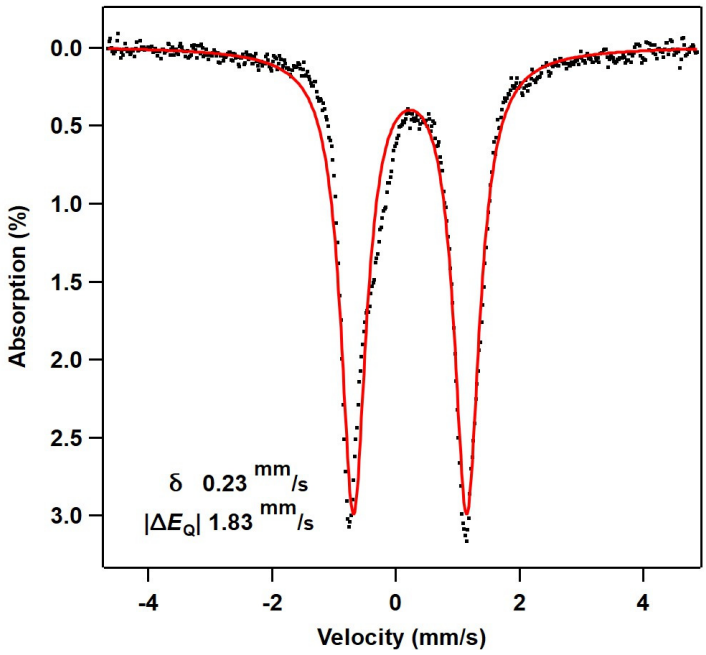

Figure 4.9. Zero-field ^{57}Fe Mössbauer spectrum of ($^{t\text{Bu}}$dmx)Fe$_2$(μ-O)(Mes)$_2$ (**3**). Isomer shift and quadrupole splitting values are reported relative to Fe foil at room temperature.

The second major species resulting from nitrite thermolysis is assigned as ($^{t\text{Bu}}$dmx)Fe$_2$(μ-O)(NO)$_2$ (**4**). Complex **4** could be synthesized directly using the previously reported diiron(II) μ-O complex ($^{t\text{Bu}}$dmx)Fe$_2$(μ-O) (**5**)[24] via the addition of two equivalents of the NO transfer reagent Ph$_3$CSNO.[27] The product was verified by solid state FTIR spectroscopy (ν_{NO} = 1721, 1742 and 1781 cm^{-1}, **Figure 4.4**) and ^{57}Fe Mössbauer spectroscopy (δ = 0.32 mm s^{-1}, $|\Delta E_Q|$ = 1.07 mm s^{-1}, **Figure 4.10**). The overall stoichiometry of the products as equimolar symmetric products, as indicated by the ^{57}Fe Mössbauer spectrum of the thermolysis reaction in **Figure 4.6**, is consistent with the overall reduction of NO_2^- to NO; for each molecule of nitrite reduced, the excised oxygen forms a bridge between the iron centers. The remaining NO is then able to displace mesityl to form **4**. While we are representing these products as symmetric, a crystal grown from a saturated solution of the **2a** thermolysis reaction

[27] Tonzetich, Z. J.; McQuade, L. E.; Lippard, S. J. *Inorg. Chem.* **2010**, *49*, 6338–6348.

in hexanes at –35 °C indicated that the asymmetric species (in which one mesitylene and one NO are bound to the same diiron molecule (($^{t\text{Bu}}$dmx)Fe$_2$(μ-O)(Mes)(NO) (**6**)) is also possible (**Figure 4.11**). While many dipyrrin Pacman species are often symmetric, complex **6** may be representative of an intermediate between **3** and **4** or may indicate that a mixture of the symmetric **3**, symmetric **4**, and asymmetric **6** are all present following nitrite reduction. In either case, the ^{57}Fe Mössbauer spectrum in **Figure 4.6** would be expected to show the same distribution of iron centers.

Single crystals suitable for X-ray diffraction analysis were produced from a saturated solution of **4** in THF layered with hexanes at –35 °C to reveal the diiron bis-nitrosyl ($^{t\text{Bu}}$dmx)Fe$_2$(μ-O)(NO)$_2$ (**4**; **Figure 4.12**). This structure features relatively bent Fe–N–O angles (164.3898(7)°), Fe–N bond lengths of 1.73707(7) Å, and N–O bond lengths of 1.16806(6) Å. Metal nitrosyl complexes are typically characterized using the Enemark-

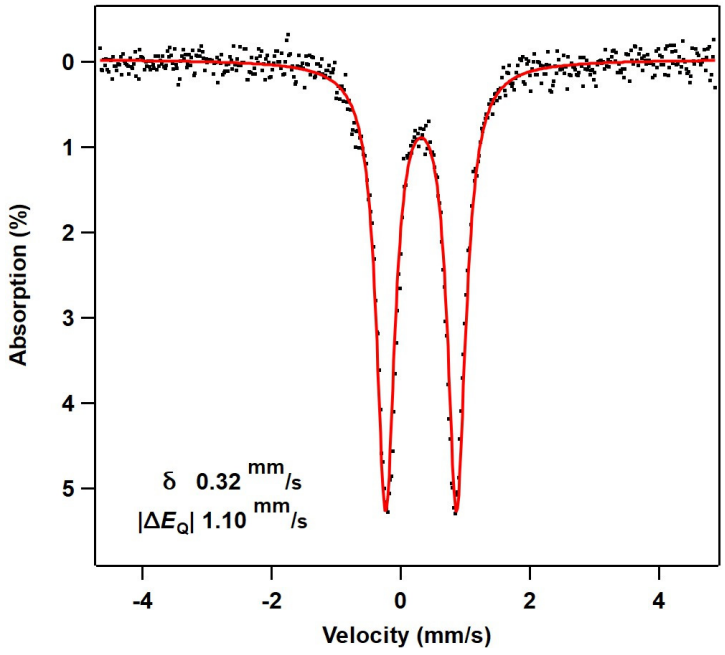

Figure 4.10. Zero-field ^{57}Fe Mössbauer spectrum of ($^{t\text{Bu}}$dmx)Fe$_2$(μ-O)(NO)$_2$ (**4**). Isomer shift and quadrupole splitting values are reported relative to Fe foil at room temperature.

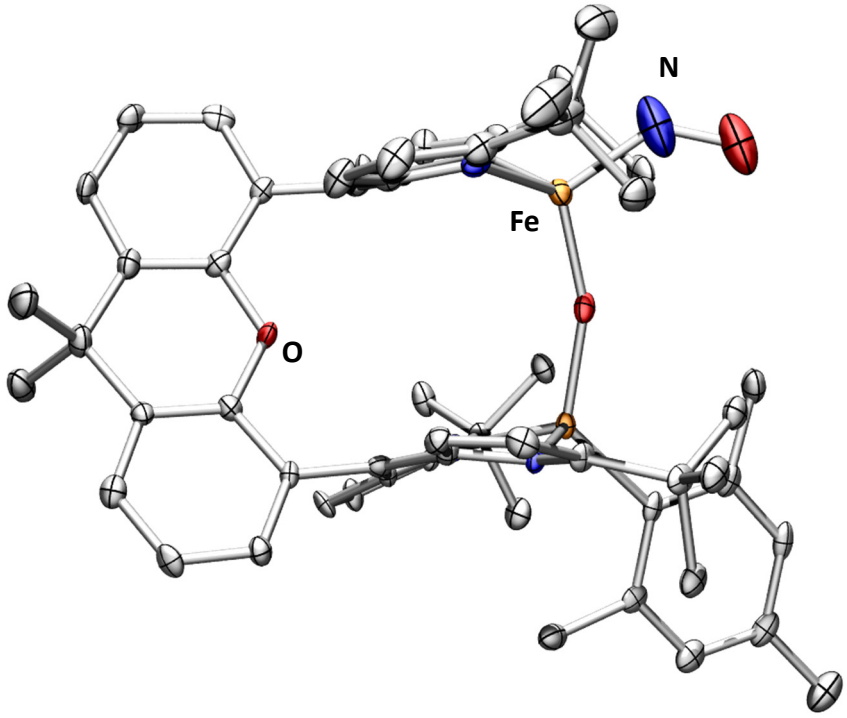

Figure 4.11. Solid state molecular structure of ($^{t\text{Bu}}$dmx)Fe$_2$(μ-O)(Mes)(NO) (**6**) with thermal ellipsoids at 40% probability level. Hydrogen atoms omitted for clarity Color scheme: Fe, orange; N, blue; C, gray; O, red.

Feltham notation {MNO}^{n} rather than formal oxidation state assignments due to the large degree of delocalization within the highly covalent metal-nitrosyl bond, where *n* is the total number of M d electrons and NO π^* electrons.[28] In the case of **4**, each iron nitrosyl unit is assigned as an {Fe(NO)}^{7} unit, meaning the formal oxidation levels could span (Fe$^{\text{I}}$)(NO$^+$), (Fe$^{\text{II}}$)(NO$^\bullet$), or (Fe$^{\text{III}}$)(NO$^-$).[29] Where complex **4** falls within this spectrum can be achieved by considering its spectral and structural properties. FTIR spectroscopy has been used to study many metal nitrosyl complexes, and the ν_{NO} stretching frequencies of **4** are consistent with

[28] (a) Enemark, J. H.; Feltham, R. D. *Coord. Chem. Rev.* **1974**, *13*, 339–406. (b) McCleverty, J. A. *Chem. Rev.* **2004**, *104*, 403–418.

[29] Thomas, D. J.; Lehnert, N. in R*eference Module in Chemistry, Molecular Sciences and Chemical Engineering*, (J. Reedijk, Ed.), Elsevier **2017**.

those observed for other (Fe^{III})(NO^-) species (ν_{NO} = 1710–1810 cm^{-1}).[17,30,31] Furthermore, this formulation is supported by the ^{57}Fe Mössbauer doublet, which is consistent with a four-coordinate high spin iron(III) center being present,[32,33] as well as the Fe–N–O unit bond metrics observed in the solid state structure.[31,34] Many compounds with the (Fe^{III})(NO^-) formulation are overall $S = {}^3/_2$, featuring a high spin iron(III) ($S = {}^5/_2$) antiferromagnetically coupled to a triplet NO^- ($S = 1$).[30,35] Following suit, computational studies of **4** showed it can be modelled as having two antiferromagnetically coupled $S = {}^3/_2$ Fe(NO) units (J = –213 cm^{-1}, **Table 4.4**) and that this model simulates the observed ^{57}Fe Mössbauer parameters (δ = 0.32 mm s^{-1}, $|\Delta E_Q|$ = 0.66 mm s^{-1}) and ν_{NO} stretching frequencies (1721 and 1742 cm^{-1} **Table 4.3**). While multiple examples of five- or six-coordinate diiron di-nitrosyl [{Fe(NO)}^{7}]$_2$ complexes have been reported previously,[36] complex **4** represents a rare four-coordinate [{Fe(NO)}^{7}]$_2$ species. In these higher coordinate diiron bis-nitrosyl species, the two metal centers are also modelled as antiferromagnetically coupled $S = {}^3/_2$ {Fe(NO)}^{7} centers that show similar bond

[30] Hauser, C.; Glaser, T.; Bill, E.; Weyhermiller, T.; Wieghardt, K. *J. Am. Chem. Soc.* **2000**, *122*, 4352–4365.

[31] Feig, A. L.; Bautista, M. T.; Lippard, S. J. *Inorg. Chem.* **1996**, *35*, 6892–6898.

[32] Harrop, T. C.; Song, D.; Lippard, S. J. *J. Am. Chem. Soc.* **2006**, *128*, 3528–3529.

[33] (a) Kleinlein, C. K.; Zheng, S.-L.; Betley, T. A. *Inorg. Chem.* **2017**, *56*, 5892–5901. (b) Iovan, D. A.; Betley, T. A. *J. Am. Chem. Soc.* **2016**, *138*, 1983–1993.

[34] (a) Chiou, Y.-M.; Que, L., Jr. *Inorg. Chem.* **1995**, *34*, 3270–3278. (b) Westre, T. E.; Di Cicco, A.; Filipponi, A.; Natoli, C. R.; Hedman, B.; Solomon, E. I.; Hodgson, K. O. *J. Am. Chem. Soc.* **1994**, *116*, 6757–6768. (c) Ray, M.; Golombek, A. P.; Hendrich, M. P.; Yap, G. P. A.; Liable-Sands, L. M.; Rheingold, A. L.; Borovik, A. S. *Inorg. Chem.***1999**, *38*, 3110–3115. (d) Jackson, T. A.; Yikilmaz, E.; Miller, A.-F.; Brunold, T. C. *J. Am. Chem. Soc.* **2003**, *125*, 8348–8363.

[35] (a) Zhang, Y.; Pavlosky, M. A.; Brown, C. A.; Westre, T. E.; Hedman, B.; Hodgson, K. O.; Solomon, E. I. *J. Am. Chem. Soc.* **1992**, *114*, 9189–9191. (b) Brown, C. A.; Pavlosky, M. A.; Westre, T. E.; Zhang, Y.; Hedman, B.; Hodgson, K. O.; Solomon, E. I. *J. Am. Chem. Soc.* **1995**, *117*, 715–732.

[36](a) Zheng, S.; Berto, T. C.; Dahl, E. W.; Hoffman, M. B.; Speelman, A. L.; Lehnert, N. *J. Am. Chem. Soc.* **2013**, *135*, 4902–4905. (b) Van Stappen, C.; Lehnert, N. *Inorg. Chem.* **2018**, *57*, 4252–4269. (c) Jana, M.; White, C. J.; Pal, N.; Demeshko, S.; Cordes, C.; Meyer, F.; Lehnert, N.; Majumdar, A. *J. Am. Chem. Soc.* **2020**, *142*, 6600–6616. (d) Hopmann, K. H.; Noodleman, L.; Ghosh, A. *Chem.* **2010**, *16*, 10397–10408.

metrics and spectroscopic signatures as **4**. However, these examples exhibit a weaker antiferromagnetic coupling between iron centers ($J \approx -20$ cm^{-1} for species with one bridge, $J \approx -100$ cm^{-1} with two bridges), likely due to the metal centers being coupled through carboxylato- and/or alkoxo- bridges, rather than an oxo bridge in **4**.[36] As discussed in chapter 2, the coupling observed in the diiron(III) μ-oxo dichloride **12** was ~ –100 cm^{-1}, showing stronger antiferromagnetic coupling than the diiron(II) μ-oxo **5** (~ –60 cm^{-1}), further supporting the formulation that the iron centers in **4** as being more iron(III) in character.

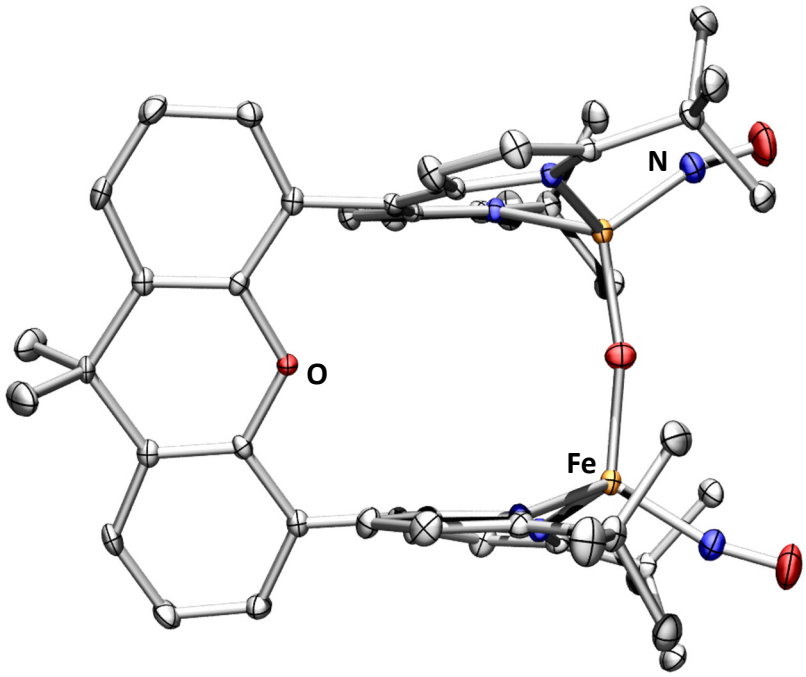

Figure 4.12. Solid state molecular structure of ($^{t\text{Bu}}$dmx)Fe$_2$(μ-O)(NO)$_2$ (**4**) with thermal ellipsoids at 50% probability level. Hydrogen atoms omitted for clarity Color scheme: Fe, orange; N, blue; C, gray; O, red.

4.5 Mechanistic Studies of Nitrite Reduction

Gratifyingly, the nitrite reduction by **1** occurs without the addition of external electron or proton equivalents and does not require an oxophilic substrate to induce reduction, as was observed in many other cases previously reported. We believe that this system is reminiscent of the other reported systems that enable nitrite reduction without additional substrates, which

utilize the thermodynamic driving force of metal-oxo formation to facilitate NO bond scission.[20,22] In this case, formation of a diiron(III) μ-oxo complex is likely the driving force, consistent with our previous findings (as discussed in Chapter 2) that bridging oxo complexes in the diiron(III) oxidation state are remarkably stable.

Efforts toward probing the mechanism to explain the formation of **3**, **4**, and **6** are summarized in **Scheme 4.2**. Although the solid-state molecular structure of **2a** indicates the nitrite binds in a κ^2-O_2N fashion, computational studies indicate that isomerization to a μ-ONO form (**7**) appears feasible via thermal activation ($\Delta G^{\ddagger}$ = 6.6 kcal/mol, **Table 4.5**). Following O–NO bond scission, we hypothesize that a one-electron oxidized diiron μ-oxo (**8**) is formed upon release of NO$^{\bullet}$. Subsequent outer sphere electron transfer can occur from **8** to yield NO^- concomitant with complex **3**. This proposal is supported by cyclic voltammetry data of complex **3** ($E_{1/2}$ = –2.73 V vs $[Cp_2Fe]^{+/0}$, **Figure 4.13**), whose potential is more cathodically-shifted than the reduction potential reported for NO$^{\bullet}$ ($E_{1/2}$ = –0.68 V vs NHE in H_2O,[37] converted to ~ –1.47 V vs $[Cp_2Fe]^{+/0}$, see equation 3 and 4 for details), suggesting that nitric oxide could be readily reduced by **3**. In light of a recent report of a dipyrrin Pacman dichromium system which shows ligand reduction by KC_8,[38] it should be noted that we do not know the locus of reduction towards complex **3**, which could be metal-based (as suggested by **Scheme 4.2**) or could be ligand-based.

Presuming NO^- is formed, we propose that complex **3** undergoes ligand metathesis in which NO displaces mesityl anion to release $[^nBu_4N][Me_3C_6H_2]$ to form the asymmetric

[37] Bartberger, M. D.; Lui, W.; Ford, E.; Miranda, K. M.; Switzer, C.; Fukuto, J. M.; Farmer, P. J.; Wink, D. A.; Houk, K. N. *Proc. Natl. Acad. Sci. U.S.A.* **2002**, *99*, 10958–10963.

[38] Carsch, K. M.; Lukens, J. T.; Elder, S. E.; Dogutan, D. K.; Nocera, D. G.; Yang, J.; Zheng, S.-L.; Daniel, T.; Betley, T. A. *Acta Cryst.*., **2021**, *C77*, 161–166.

species complex **6**. A second equivalent of NO^- (generated by activation of a second equivalent of nitrite in **2a**/**7** and back-electron transfer from **8** to form **3**) can displace the other mesitylene group of complex **6** to make the bis-nitrosyl species **4**. Experimental evidence in support ofthis route is found by reacting complex **3** with two equivalents of [K][NO] (produced by Ph_3CSNO treated with KC_8). The final product had FTIR (ν_{NO} = 1731, 1736 and 1781 cm^{-1}, **Figure 4.14**) and ^{57}Fe Mössbauer spectroscopic (δ = 0.33 mm s^{-1}, $|\Delta E_Q|$ = 1.18 mm s^{-1}, **Figure 4.15**) features consistent with the generation of **4**. Furthermore, monitoring the addition of one equivalent of [NO^-] to **3** by ^{57}Fe Mössbauer spectroscopy showed the generation of an equimolar amount of the $\{Fe(NO)\}^7$ center (δ = 0.32 mm s^{-1}, $|\Delta E_Q|$ = 1.10 mm s^{-1}, **Figure 4.15**) with the starting material iron(III) center (δ = 0.25 mm s^{-1}, $|\Delta E_Q|$ = 1.99 mm s^{-1},) consistent with either the full conversion of **3** to **6** or partial conversion to complex **4**. These data are consistent with the overall mechanism displayed in **Scheme 4.2** and can explain how each of these species (**3**, **4**, and **6**) is formed during the nitrite reduction process facilitated by this system.

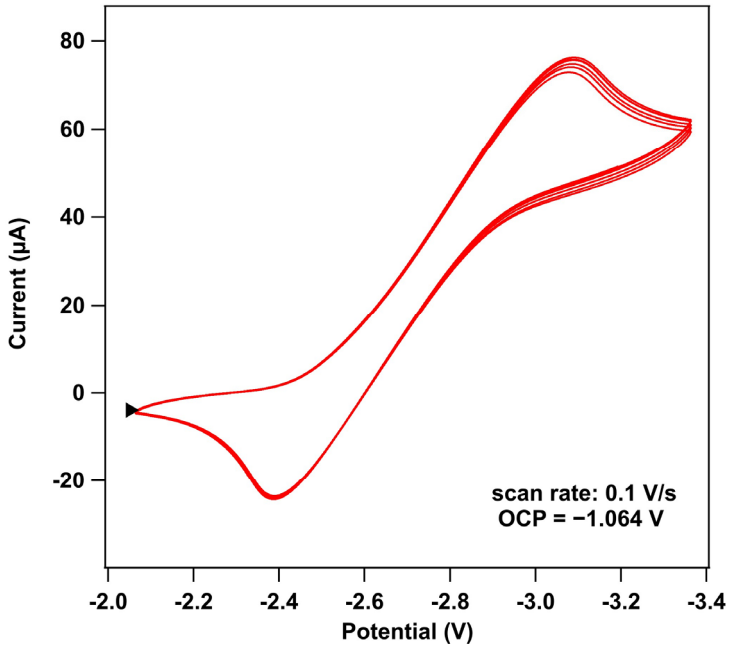

Figure 4.13. Cyclic voltammogram of ($^{t\text{Bu}}$dmx)Fe_2(µ-O)$(Mes)_2$ (**3**). The data were obtained in THF at 25 °C using a carbon working electrode and 0.1 M [$^n Bu_4N$][PF_6] as supporting electrolyte.

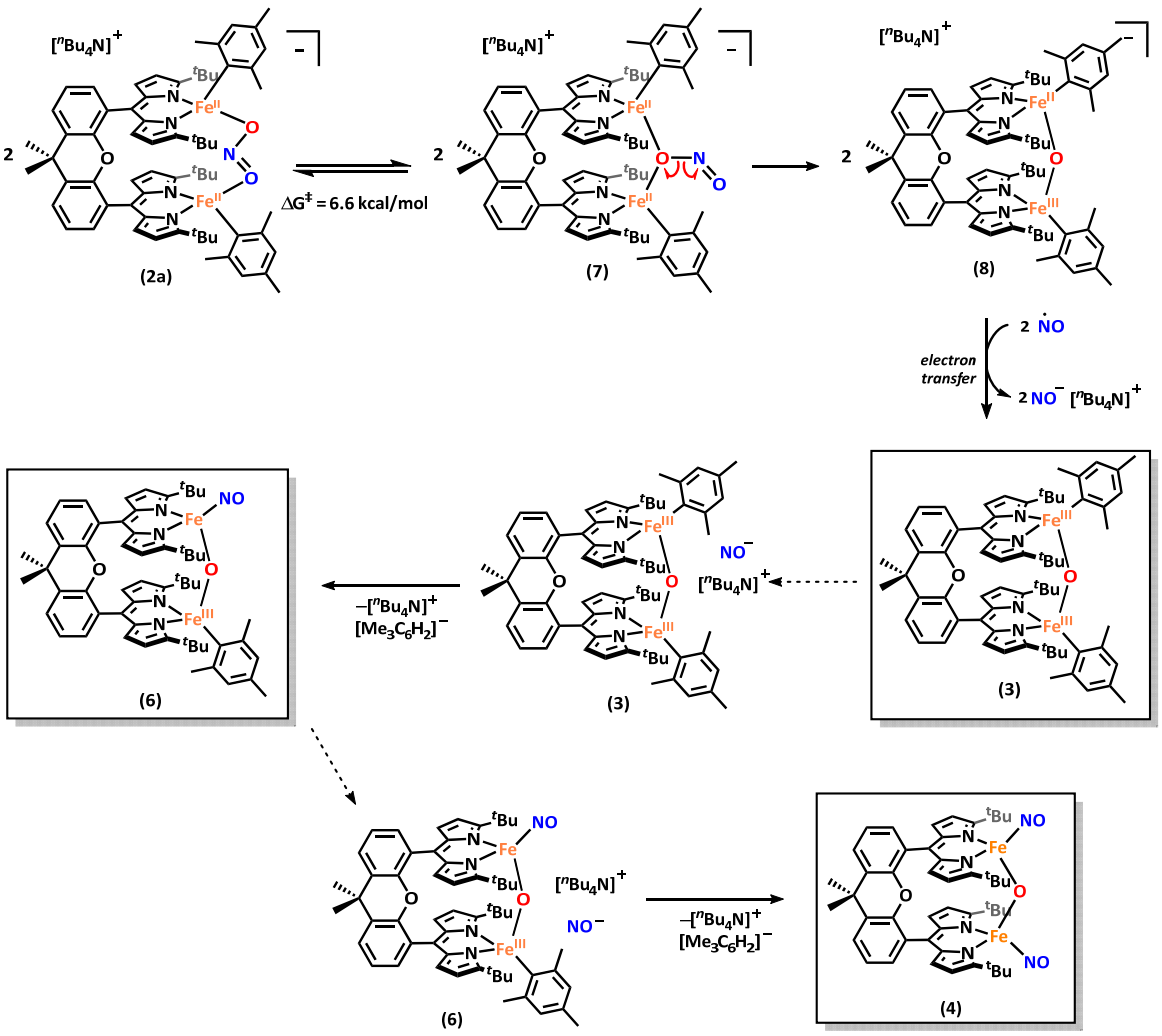

Scheme 4.2. Proposed nitrite reduction pathway from **2a** to form complexes **3**, **4**, and **6**.

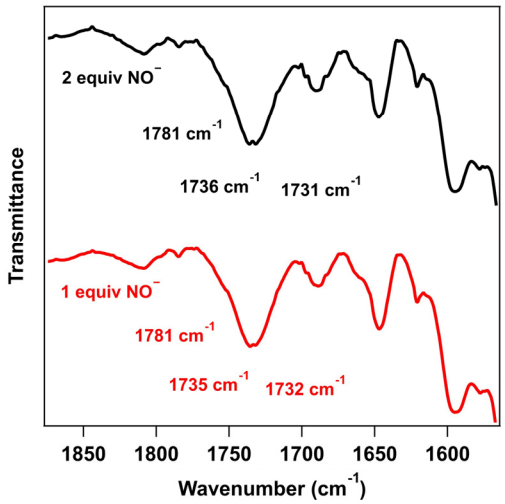

Figure 4.14. FTIR spectrum of ($^{t\text{Bu}}$dmx)Fe_2(μ-O)$(Mes)_2$ (**3**) + [K][NO] reactions, (top, red) with two equivalents of [NO^-] and (bottom, black) with one equivalent of [NO^-] zoomed to show NO stretch region.

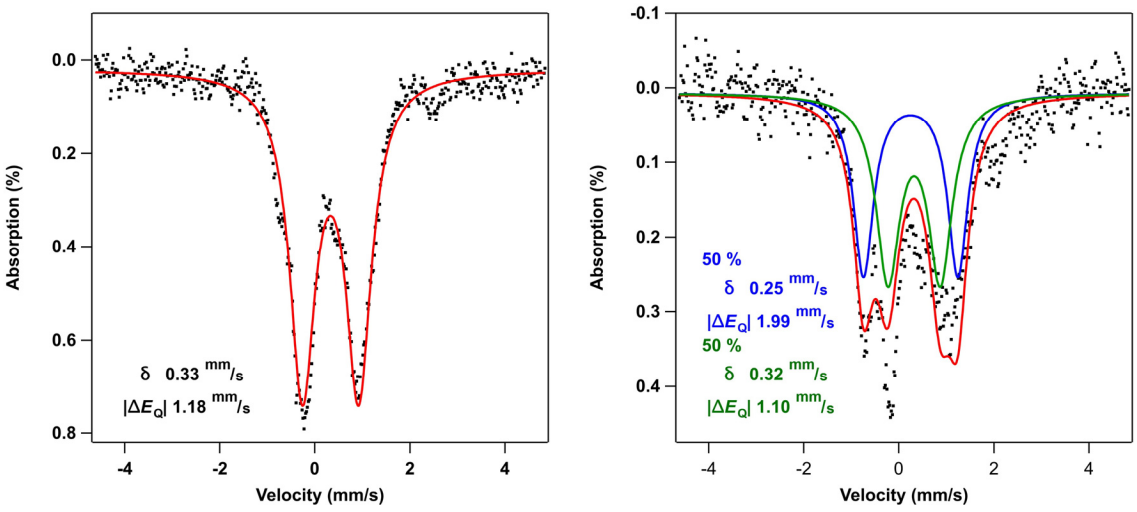

Figure 4.15. Zero-field ^{57}Fe Mössbauer spectrum of ($^{t\text{Bu}}$dmx)Fe$_2$(μ-O)(Mes)$_2$ (**3**) + [K][NO] reactions, (**Left**) with two equivalents of [K][NO$^-$] and (**Right**) with one equivalent of [K][NO$^-$]. Isomer shifts and quadrupole splitting values are reported relative to Fe foil at room temperature.

4.6 Perhalogenate Deoxygenation

In addition to being able to facilitate the one electron reduction of nitrite, we hypothesized that the iron-substituted dipyrrin Pacman scaffold could effect other substrate reduction processes. Thus, we pursued the reduction and deoxygenation reactions of other oxyanions and found promising results with perhalogenates such as periodate and perchlorate. Addition of one equivalent of tetrabutylammonium periodate [^{n}Bu$_4$N][IO$_4$] to **1** results in an immediate color change to red and conversion at room temperature to a significantly paramagnetically-broadened ^{1}H NMR species and evidence of [^{n}Bu$_4$N][Me$_3$C$_6$H$_2$] in the diamagnetic region. ^{57}Fe Mössbauer spectroscopy reveals oxidation to two equimolar diiron(III) species, one of which is assigned as **3** (50% δ = 0.20 mm s^{-1}, $|\Delta E_Q|$ = 1.80 mm s^{-1}, 50% δ = 0.33 mm s^{-1}, $|\Delta E_Q|$ = 1.39 mm s^{-1}; **Figure 4.16**). Furthermore, single crystals of the product mixture grown from a saturated diethyl ether solution at –35 °C confirmed the formation of complex **3** during this process. In an analogous fashion to the nitrite reduction sequence to form NO, we propose that deoxygenation of periodate forms iodate, and thus

assign that the other product as the potential iodate adduct ($^{t\text{Bu}}$dmx)Fe$_2$(μ-O)(IO$_3$)$_2$ (**7**) (**Scheme 4.3**). An independent route to synthesizing **7** was achieved by IO_3^- metathesis with complex **3**, releasing [K][Me$_3$C$_6$H$_2$] as indicated by ^{1}H NMR spectroscopy and the generation of a new doublet in the ^{57}Fe Mössbauer spectrum displaying parameters consistent with those observed in the product mixture (δ = 0.36 mm s^{-1}, $|\Delta E_Q|$ = 1.40 mm s^{-1}) along with remnant starting material (δ = 0.19 mm s^{-1}, $|\Delta E_Q|$ = 1.87 mm s^{-1}, **Figure 4.17**). Full conversion to **7** by this route was not achieved even when excess [K][IO$_3$] was used, and single crystals of this proposed iodate adduct suitable for XRD studies were never produced. Therefore, the binding mode of the potential iodate ligand is not known.

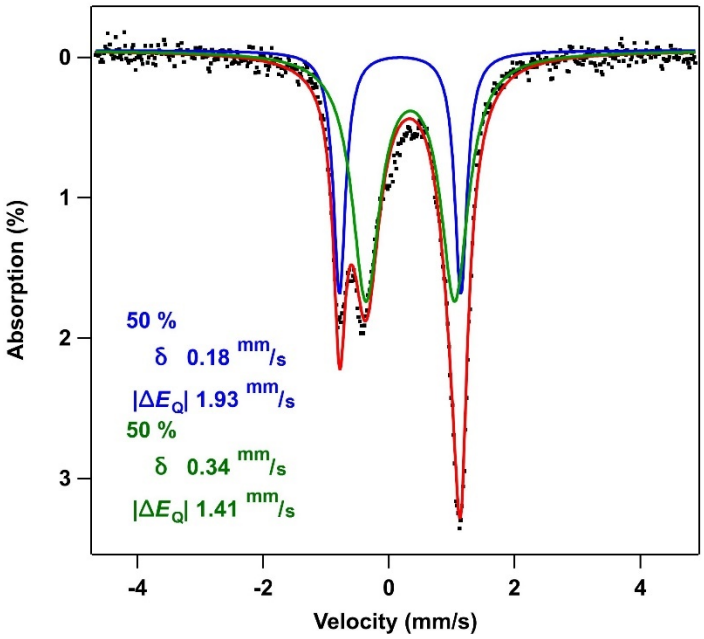

Figure 4.16. Zero-field ^{57}Fe Mössbauer spectrum of reaction mixture resulting from heating **1** in the presence of [^{n}Bu$_4$N][IO$_4$], forming a 1:1 mixture of **3** (blue trace) and **"7"** (green trace). Isomer shift and quadrupole splitting values are reported relative to Fe foil at room temperature.

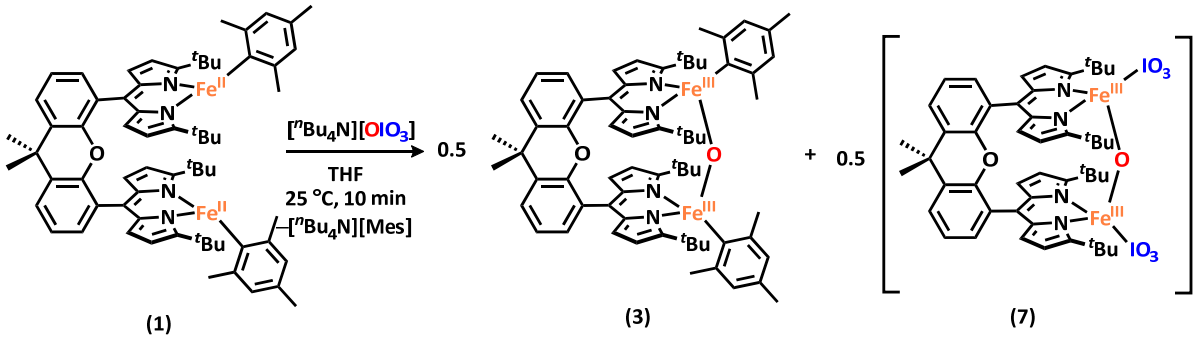

Scheme 4.3. Periodate reduction sequence.

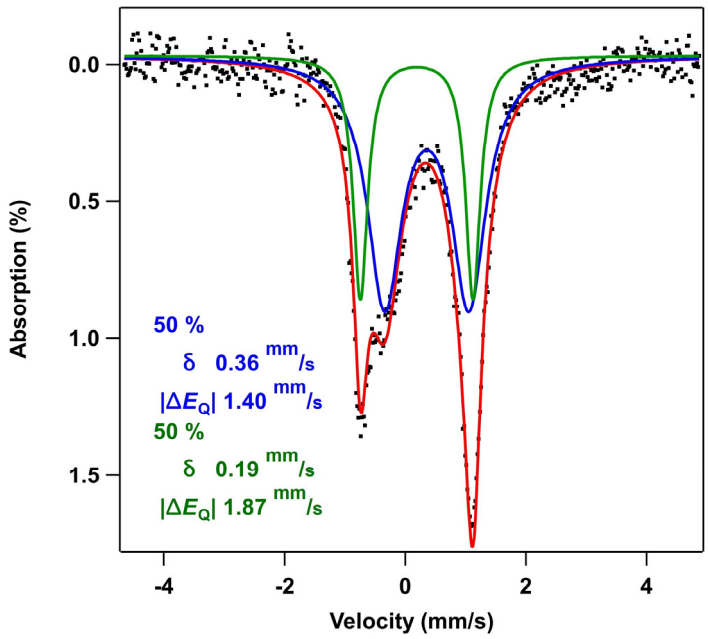

Figure 4.17. Zero-field ^{57}Fe Mössbauer spectrum of "($^{t\text{Bu}}$dmx)Fe$_2$(μ-O)(IO$_3$)$_2$" (**7**) (blue trace) with 50% unreacted starting material (green trace).

Analogous to the periodate reduction, perchlorate reduction by **1** was also observed; however, due to the greater stability of the perchlorate anion,[39] this transformation required heat for activation and full conversion. Addition of one equivalent of tetrabutylammonium perchlorate at room temperature [^{n}Bu$_4$N][ClO$_4$] to **1** resulted in the generation of a symmetric four-coordinate iron(II) species after several hours (δ = 0.81 mm s^{-1}, $|\Delta E_Q|$ = 3.14 mm s^{-1},

[39] Cox, M. M.; Moore, J. W. *J. Phys. Chem.* **1970**, *74*, 627–631.

Figure 4.18), which we assign as a perchlorate adduct (**8**). Heating this reaction to 65 °C overnight resulted in consumption of the starting material **1** and evidence of perchlorate reduction occurring to start to generate iron(III) centers (**Figure 4.18**). Full transformation to diiron(III) species was achieved by heating **8** to 90 °C overnight (**Figure 4.19**), which we propose results in formation of **3** and a potential chlorate adduct ($^{t\text{Bu}}$dmx)Fe$_2$(μ-O)(ClO$_3$)$_2$ (**9**) (**Scheme 4.4**). ^{1}H NMR spectroscopy reveals the formation of ^{n}Bu$_3$N, butene, and mesitylene (HMes) similar to the byproducts of nitrite thermolysis. Analogously, treating **3** with excess [K][ClO$_3$] serves as an independent route to generate **9** in ~50% yield by ^{57}Fe Mössbauer spectroscopy (δ = 0.37 mm s^{-1}, $|\Delta E_Q|$ = 1.31 mm s^{-1}, **Figure 4.20**). As with the proposed iodate adduct **7**, the proposed perchlorate adduct **8** and chlorate adduct **9** were not crystallized, so the binding mode of these oxyanions has not yet been discerned.

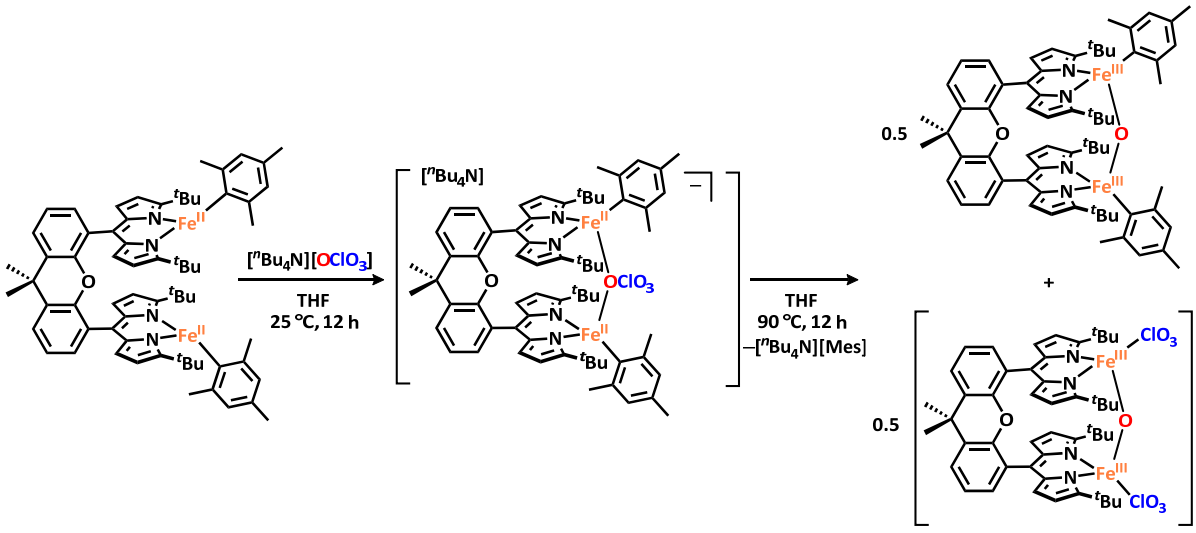

Scheme 4.4. Perchlorate reduction sequence, likely forming intermediate perchlorate adduct before thermolysis.

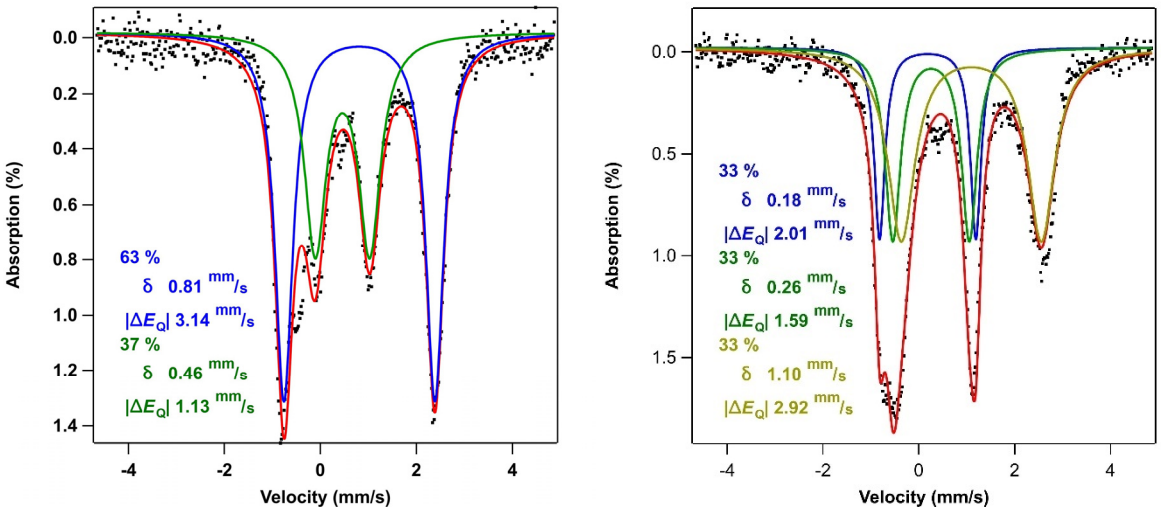

Figure 4.18. Zero-field ^{57}Fe Mössbauer spectrum of reaction mixture resulting from treating **3** with [^{n}Bu$_4$N][ClO$_4$], (**Left**) at room temperature and (**Right**) at 65 °C. There is evidence of a diiron(II) perchlorate adduct (**8**) in each spectrum (**Left, blue**) (**Right**, **yellow**), as well as leftover starting material at room temperature (**Left, green**) and formation of oxidized products upon moderate heating (**Right, blue** and **green**).

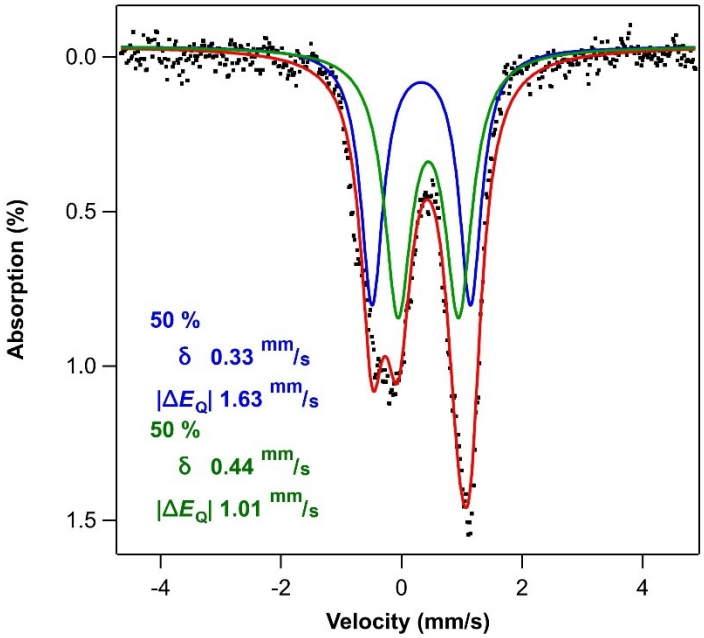

Figure 4.19. Zero-field ^{57}Fe Mössbauer spectrum of reaction mixture resulting from heating **1** to 90 °C in the presence of [^{n}Bu$_4$N][ClO$_4$], forming a 1:1 mixture of **3** (blue trace) and **"9"** (green trace). Isomer shift and quadrupole splitting values are reported relative to Fe foil at room temperature.

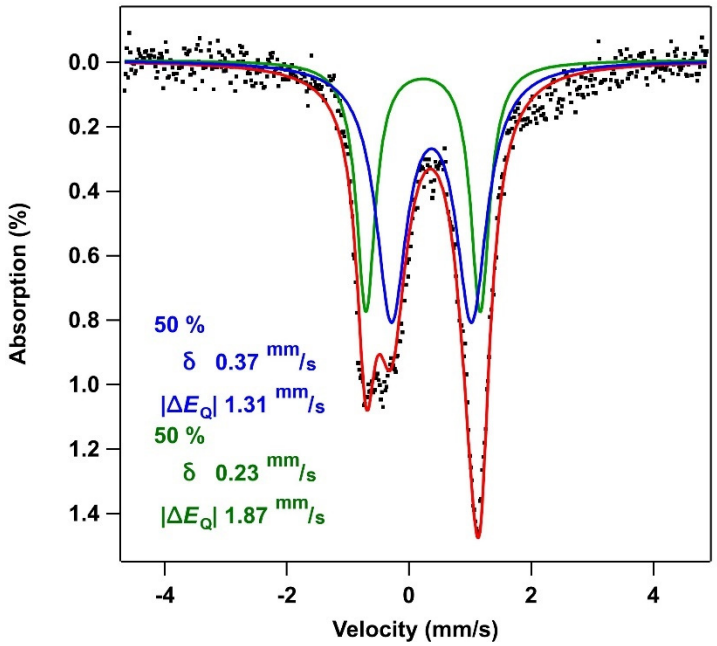

Figure 4.20. Zero-field ^{57}Fe Mössbauer spectrum of "($^{t\text{Bu}}$dmx)Fe$_2$(μ-O)(ClO$_3$)$_2$" (**9**) (blue trace) with 50% unreacted starting material (green trace).

4.7 Aryl-Nitro Reduction

In addition to reduction of inorganic nitrite, we discovered that the diiron system is also capable of reducing organic aryl-nitro substrates. Direct evidence of this reduction is observed with substrates such as *para*-nitroaniline and *para*-nitrophenol. As such, when one equivalent of substate is heated alongside one equivalent of **1**, a color change to dark red and conversion to new paramagnetically shifted ^{1}H NMR spectra are observed within a few hours. ^{57}Fe Mössbauer spectroscopy reveals formation of a common oxidized diiron(III) major species (δ = 0.33 mm s^{-1}, $|\Delta E_Q|$ = 1.38 mm s^{-1}, 65% for *para*-nitroaniline and δ = 0.34 mm s^{-1}, $|\Delta E_Q|$ = 1.30 mm s^{-1}, 91% for *para*-nitrophenol) as well as formation of **3** as the minor species (δ = 0.23 mm s^{-1}, $|\Delta E_Q|$ = 1.83 mm s^{-1}, 35% for *para*-nitroaniline and δ = 0.18 mm s^{-1}, $|\Delta E_Q|$ = 1.83 mm s^{-1}, 9% for *para*-nitrophenol) (**Figure 4.21**, **4.22)**. Single crystals suitable for X-ray diffraction revealed a similar structure for the major product; for the *para*-nitroaniline

reaction, single crystals were grown from toluene at –35 °C to disclose the formation of the tetramer $[(^{t\text{Bu}}\text{dmx})\text{Fe}^{\text{III}}_2(\mu\text{-O})(\kappa^2\text{–NHPhNH})]_2$ (**10**) (**Figure 4.23**), while for the *para*-nitrophenol reaction, crystals formed from a concentrated toluene solution layered with hexanes at –35 °C afford the formation of a similar tetramer $[(^{t\text{Bu}}\text{dmx})\text{Fe}^{\text{III}}_2(\mu\text{-O})(\text{NHPhOH})]_2$ (**11**) (**Figure 4.25**). Solid state FTIR spectroscopy reveals the growth of $\nu_{\text{N–H}}$ features at 1730 and 1781 cm^{-1}, respectively (**Figure 4.24**).

In these reactions, we hypothesize that reduction of the nitro group to an amino group results in an acidic group on each side of the arene (i.e., furnishing *para*-phenylenediamine for *para*-nitroaniline or *para*-aminophenol for *para*-nitrophenol), which can in turn protonate and displace the iron–mesityl unit to yield the major final products. While both of the nitroarene substrates feature an acidic moiety *para*- to the nitro group, exploration of a similar transformation with substrates lacking this additional acidic group (i.e., nitrobenzene and *para*-fluoronitrobenzene) have revealed promising similarities, as indicated by the formation

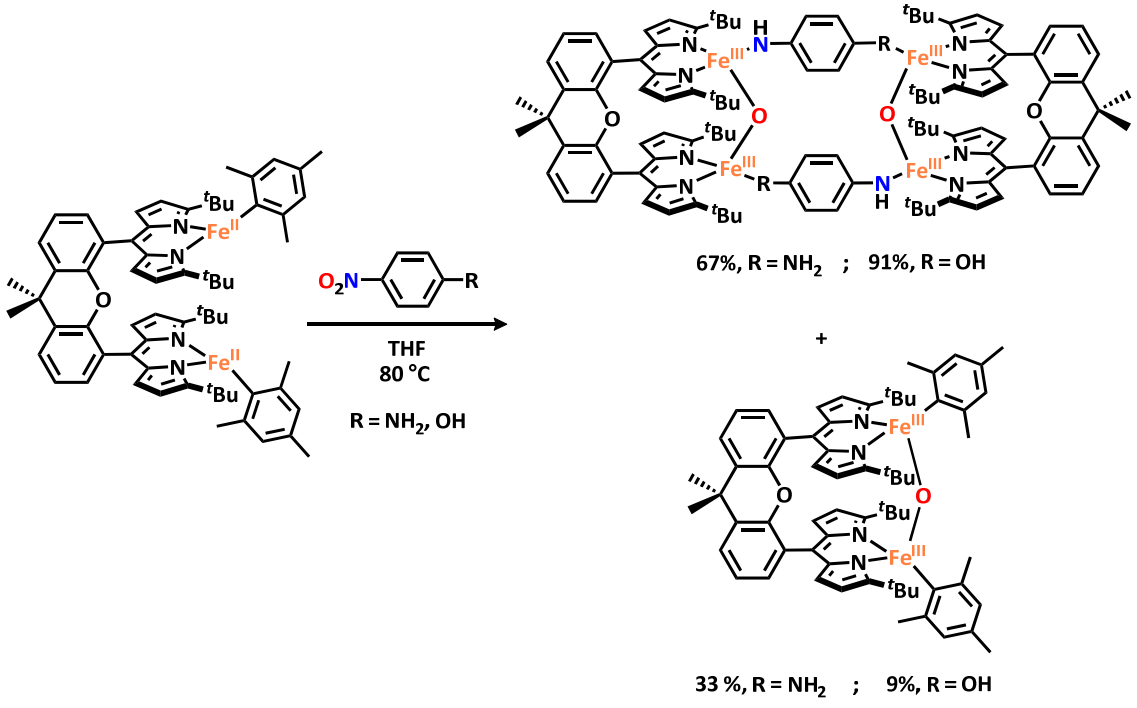

Scheme 4.5. Ditopic aryl-nitro substrate reduction by **1**.

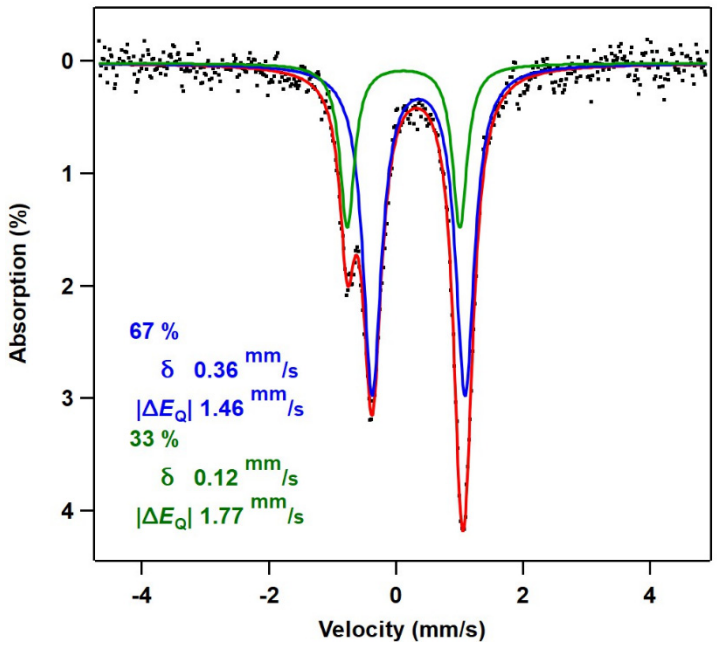

Figure 4.21. Zero-field ^{57}Fe Mössbauer spectrum of reaction mixture resulting from heating **1** in the presence of *para*-nitroaniline, forming a 2:1 mixture of [($^{t\text{Bu}}$dmx)Fe$_2$(μ-O)(κ^2-NHPhNH)]$_2$ (**10**) (blue trace) and **3** (green trace). Isomer shift and quadrupole splitting values are reported relative to Fe foil at room temperature.

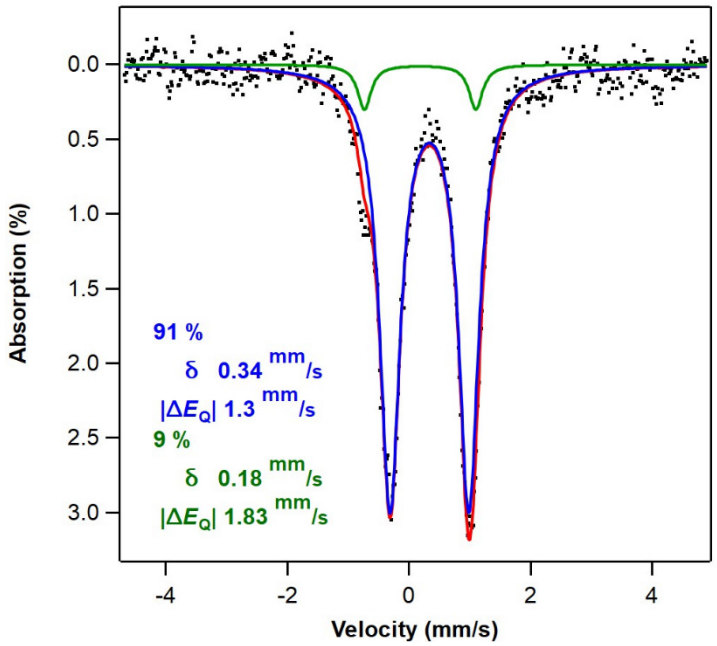

Figure 4.22. Zero-field ^{57}Fe Mössbauer spectrum of reaction mixture resulting from heating **1** in the presence of *para*-nitrophenol, forming primarily [($^{t\text{Bu}}$dmx)Fe$_2$(μ-O)(κ^2-NHPhOH)]$_2$ (**11**) (blue trace) with a small amount of **3** (green trace). Isomer shift and quadrupole splitting values are reported relative to Fe foil at room temperature.

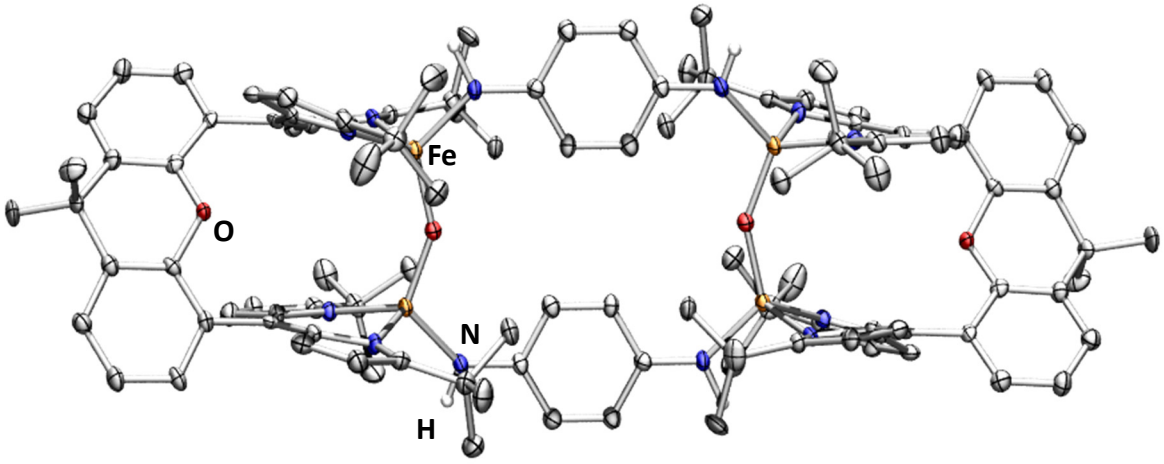

Figure 4.23. Solid state molecular structure of [($^{t\text{Bu}}$dmx)Fe$_2$(μ-O)(κ^2-NHPhNH)]$_2$ (**10**) with thermal ellipsoids at 50% probability level. Hydrogen atoms (except anilido-protons) omitted for clarity. Color scheme: Fe, orange; N, blue; C, gray; O, red; H, white.

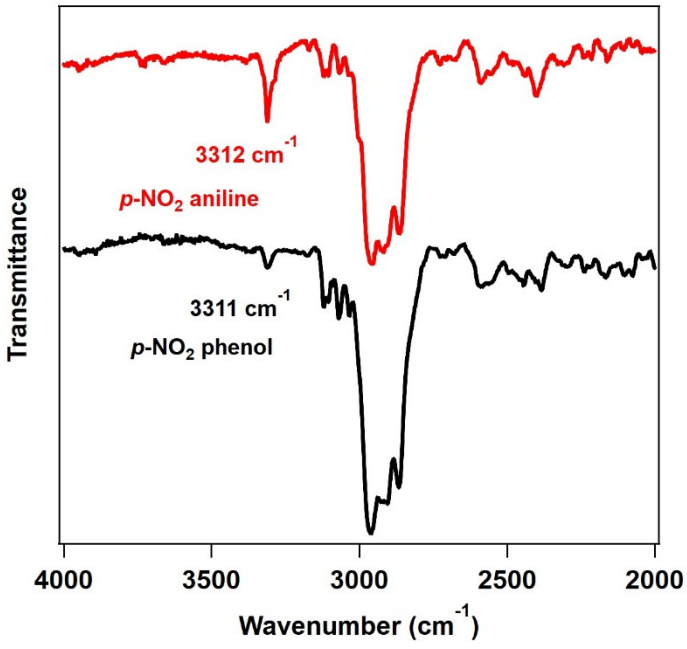

Figure 4.24. FTIR spectrum of [($^{t\text{Bu}}$dmx)Fe$_2$(μ-O)(κ^2-NHPhNH)]$_2$ (**10**) (top, red) formed and [($^{t\text{Bu}}$dmx)Fe$_2$(μ-O)(κ^2-NHPhOH)]$_2$ (**11**) (bottom, black) formed by aryl-nitro reduction by **1**, zoomed to show NH stretch region.

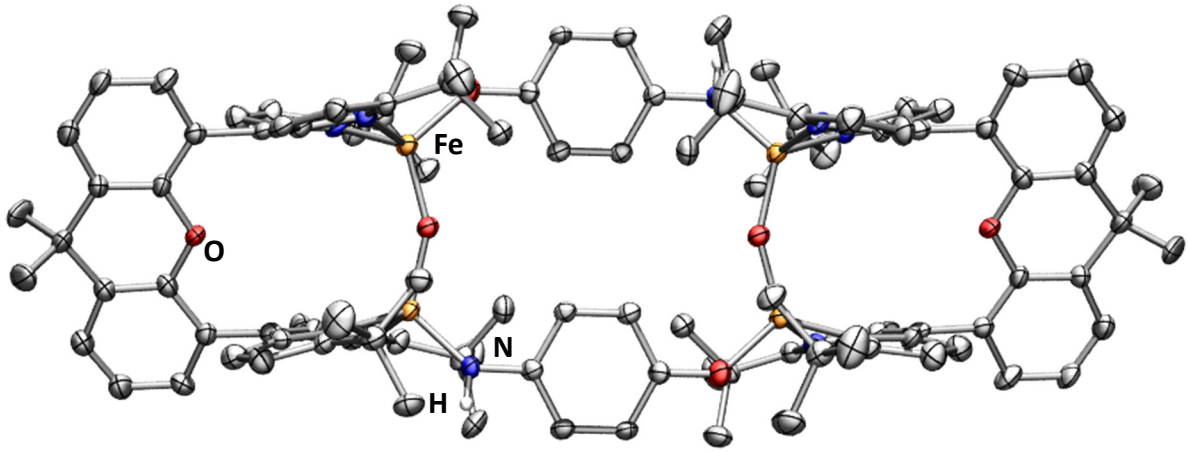

Figure 4.25. Solid state molecular structure of [($^{t\text{Bu}}$dmx)Fe$_2$(μ-O)(κ^2-NHPhOH)]$_2$ (**11**) with thermal ellipsoids at 40% probability level. Hydrogen atoms (except anilido-protons) omitted for clarity. Color scheme: Fe, orange; N, blue; C, gray; O, red; H, white.

of similar diiron(III) species detected by ^{57}Fe Mössbauer spectroscopy (**Figure 4.26**) and evidence of N–H stretches by IR spectroscopy (**Figure 4.27**). However single crystals from these reaction mixtures were not achieved and thus, the connectivity of the proposed diiron(III) aniline-containing products of these reactions has not been determined.

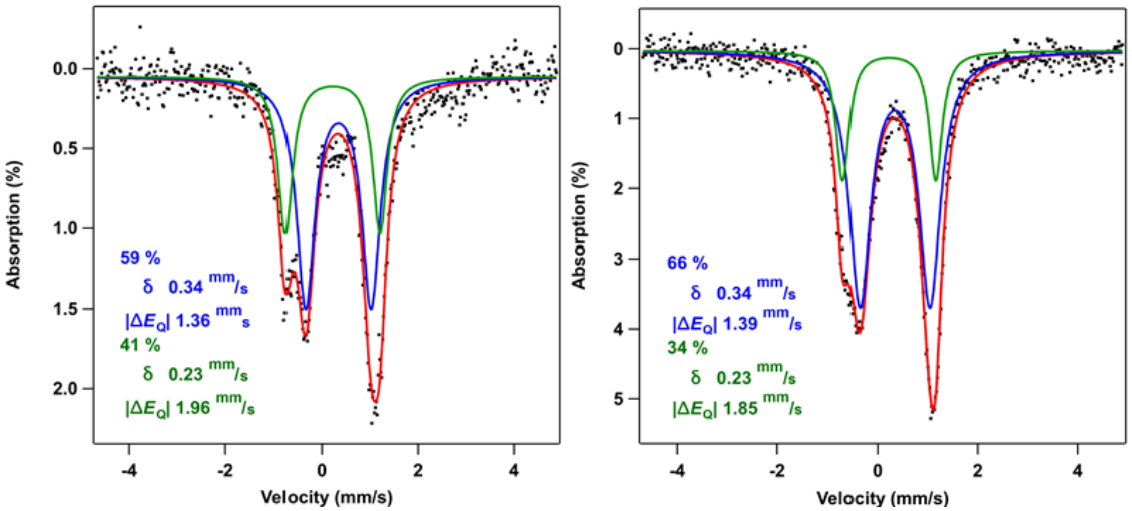

Figure 4.26. Zero-field ^{57}Fe Mössbauer spectrum of reaction mixture resulting from heating **1** in the presence of monotopic nitrophenol substrates, (**Left**) with nitrobenzene and (**Right**) with *para*-fluoronitrobenzene. In both cases, a major diiron(III) species is observed (blue traces) along with formation of **3** (green traces). Isomer shift and quadrupole splitting values are reported relative to Fe foil at room temperature.

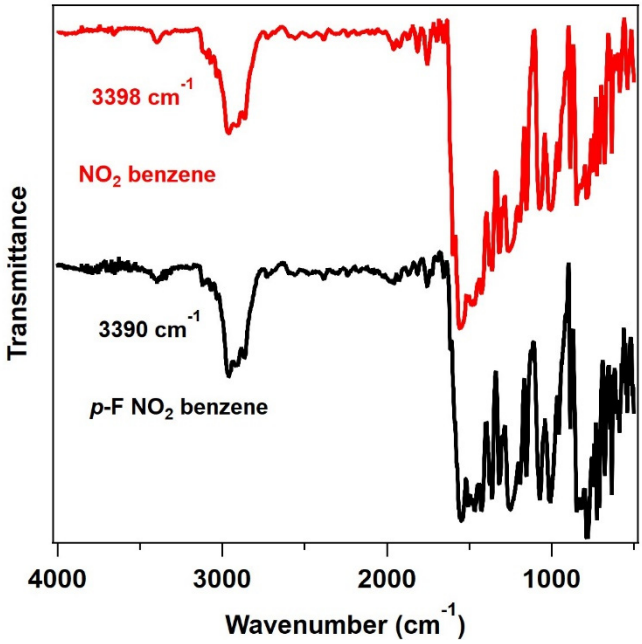

Figure 4.27. FTIR spectrum of reaction products resulting from heating **1** in the presence of monotopic nitrophenol substrates, (**Top, red**) with nitrobenzene and (**Bottom, black**) with *para*-fluoronitrobenzene, exhibiting broad N–H stretches.

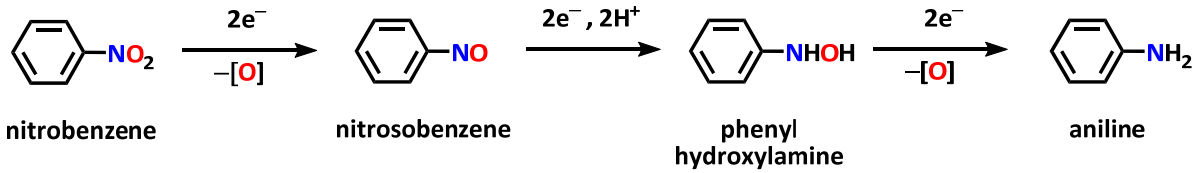

Scheme 4.6. A common nitrobenzene reduction pathway.[40]

Formally, the reduction of an aryl-nitro group to the corresponding aniline species is an six-electron process, which could go through a nitrosobenzene intermediate (**Scheme 4.6**).[40] To test if this intermediate was operative during the reduction process with **1**, we monitored the reaction between complex **3** and nitrosobenzene and observed formation of the same diiron(III) major product (δ = 0.36 mm s^{-1}, $|\Delta E_Q|$ = 1.35 mm s^{-1}) observed upon reduction of nitrobenzene by **1** (δ = 0.34 mm s^{-1}, $|\Delta E_Q|$ = 1.36 mm s^{-1}) along with unreacted starting material **3** (**Figure 4.28**). Albeit incomplete, the indication that complex **3** can react with

[40] Agrawal, A.; Tratnyek, P. G. *Environ. Sci. Technol.* **1995**, *30*, 153–160.

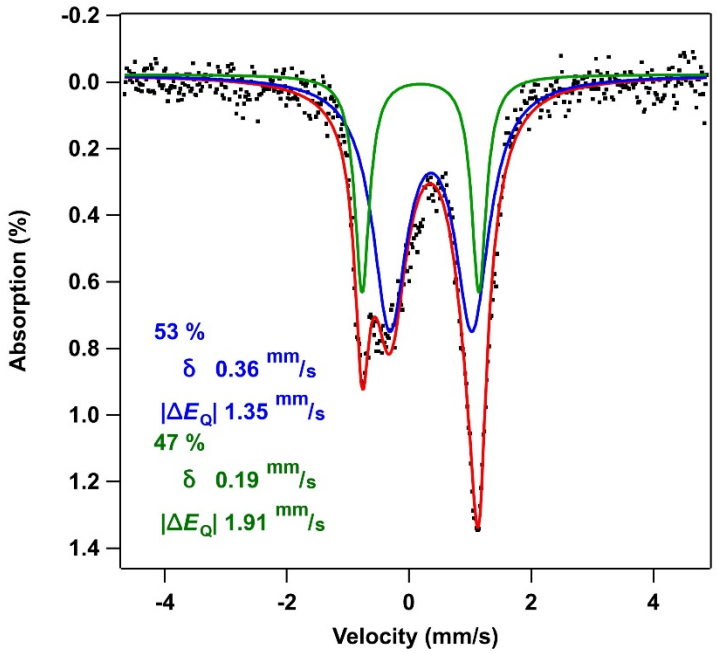

Figure 4.28. Zero-field ^{57}Fe Mössbauer spectrum of reaction products from heating **3** in the presence of nitrosobenzene, exhibiting formation of similar diiron(III) species observed in **Figure 4.26** (blue trace) and unreacted starting material **3** (green trace). Isomer shift and quadrupole splitting values are reported relative to Fe foil at room temperature.

nitrosobenzene to afford a similar product may provide some evidence for the mechanism by which nitrobenzene reduction occurs. Similar to the observations in the other deoxygenation reactions discussed, it appears that activation of substrate and formation of the diiron(III) μ-oxo species **3** occurs first, which can then further react with the generated nitrosobenzene to afford the final product.

When considering the overall stoichiometry of the reactions in **Scheme 4.5**, there remains outstanding questions regarding the charge and mass balance of these transformations. Specifically, there is inconsistency between the equivalents of substrate reduced related to the number of metal centers represented in the product mixtures, as well as unaccounted electrons to achieve this six-electron process. Further experiments with the *para*-nitroaniline substrate were performed to study these inconsistencies more closely. Firstly, it was discovered that full conversion of **1** to products **3** and **10** was observed with as little as

0.33 equivalents of substrate. Monitoring the reactions of 0.33 equivalents, 0.50 equivalents and 0.67 equivalents relative to **1** revealed approximately the same distribution of iron-containing products by ^{57}Fe Mössbauer spectroscopy (**Figure 4.29**). Of these, 0.50 equivalents would explain the stoichiometry required to fully consume the *para*-nitroaniline, but 0.33 equivalents should not be sufficient to consume all of **1**. Even so, reduction of 0.50 equivalents of *para*-nitroaniline by **1** would be expected to result in a 1:1 distribution of Mössbauer doublets (corresponding to 0.5 equivalents of the tetramer **10** and one equivalent of the dimer **3** per two equivalents of **1**, **Scheme 4.7**). The observation of a different ratio of Fe-containing products may be accounted for by consideration of the electron equivalents required for this reduction. When considering the reaction with 0.50 equivalents of substrate in **Scheme 4.7**, four electrons are accounted for by the four iron(II) centers being oxidized to four iron(III) centers, meaning two additional electron equivalents required. We hypothesize that a third undetected iron product could count account for these additional electrons. To probe this hypothesis, we performed the reduction of 0.50 equivalents of *para*-nitroaniline in the presence of two equivalents of nickelocene to serve as an external electron source. We observed the anticipated equimolar distribution of products (**Figure 4.29**), suggesting that by providing the remaining two electron equivalents, diiron **1** was fully converted to **10** and **3**. With this information, we can conclude that diiron **1** contributes two electrons per dimer, consistent with the observation of accessing diiron(III) with this platform but not yet seeing evidence of the accessibility of higher valent iron(IV) centers.

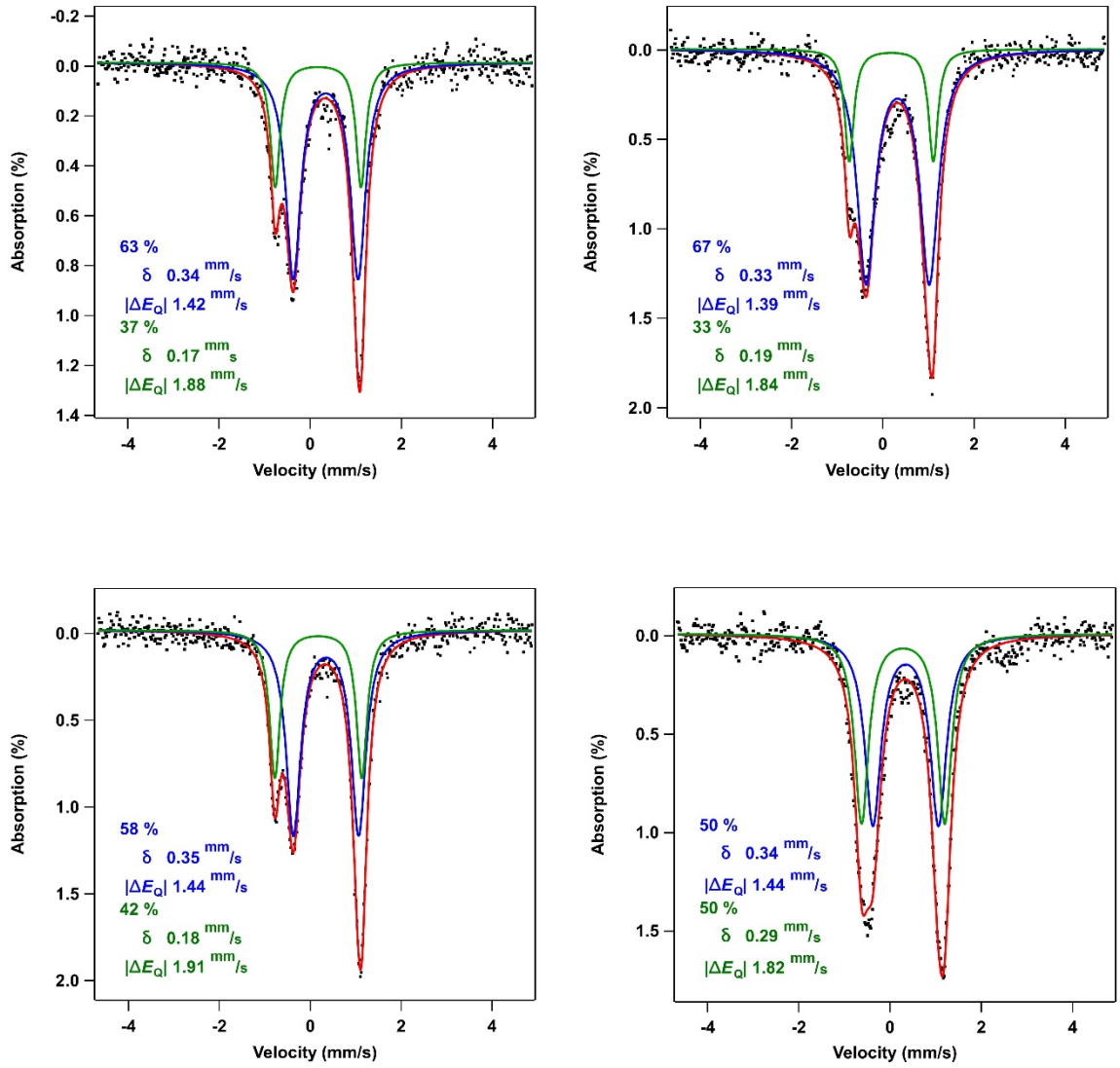

Figure 4.29. Zero-field ^{57}Fe Mössbauer spectrum of reaction products from reducing substoichiometric amounts of *para*-nitroaniline by **1**, (**Top**, **left**) 0.33 equivalents *para*-nitroaniline relative to **1**, (**Top**, **right**) 0.50 equivalents *para*-nitroaniline, (**Bottom**, **left**) 0.67 equivalents *para*-nitroaniline, (**Bottom**, **right**) 0.50 equivalents *para*-nitroaniline with two equivalents of external reductant, nickelocene. In each case, the blue trace corresponds to the tetramer **10** and the green trace corresponds to **3**.

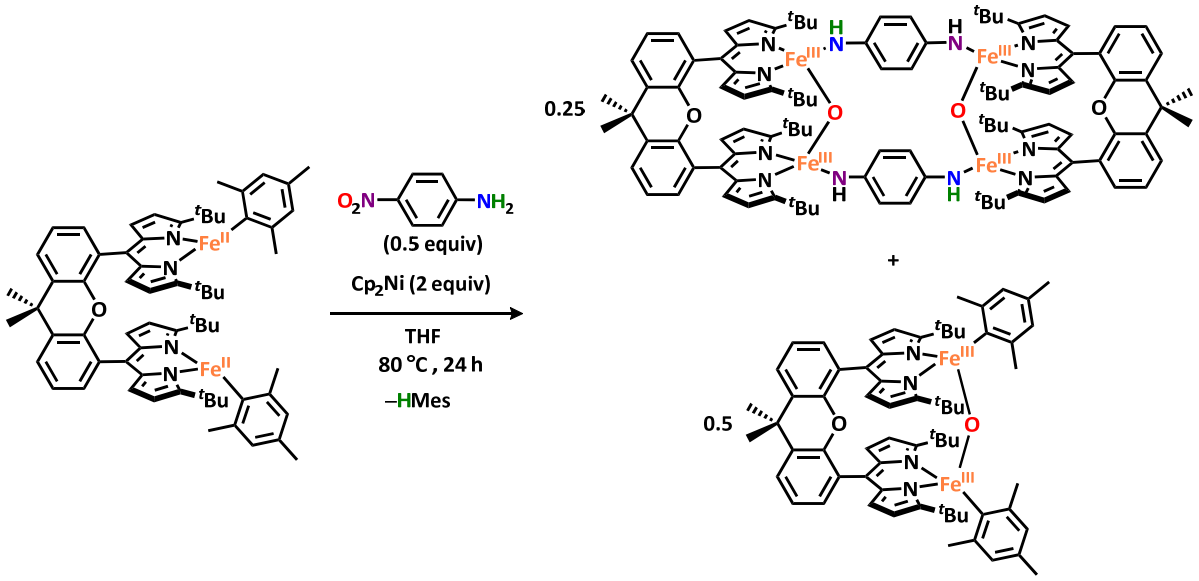

Scheme 4.7. Stoichiometry of products observed with 0.5 equivalents of substrate in the presence of an external reductant.

4.8 Conclusions

Herein, we have described how the diiron organometallic species **1** facilitates the reduction of various small molecules including nitrite to NO, perhalogenate species to halogenate complexes, and aryl-nitro compounds to yield anilines. Gratifyingly, the dipyrrin Pacman system takes advantage of the facile formation of diiron μ-oxo species to serve as a driving force, thereby eliminating the need of other additives to assist in bond scission. We believe that the utilization of two metals in concert enables the activation and ultimate deoxygenation of substrates. The major products of nitrite reduction are a diiron(III) μ-oxo complex **3** and a diiron bis-nitrosyl species, complex **4**. Metal nitrosyl complexes have been extensively studied by bioinorganic chemists, as they serve as models for enzyme active sites binding O_2.[34] To the best of our knowledge, only one prior four-coordinate monometallic iron nitrosyl has been studied,[32] and complex **4** is the first four-coordinate diiron di-nitrosyl species with the electronic structure $[\{Fe(NO)\}^7]_2$. Extensive study of **4** indicates it is best described

as having two antiferromagnetically-coupled (Fe^{III})(NO^{-}) centers. A mixed organometallic-nitrosyl species **6** has also been isolated and may represent either an intermediate between **3** and **4** or could be another major product of nitrite reduction.

Furthermore, multielectron processes can also be performed by **1**. Specifically, evidence suggesting the two-electron reduction of perhalogenate substrates periodate and perchlorate to the corresponding halogenate species has been discussed. Finally, reduction of ditopic nitrobenzene derivatives *para*-nitroaniline and *para*-nitrophenol by **1** results in formation of tetrameric species [($^{t\text{Bu}}$dmx)Fe_2(μ-O)(κ^2-NHPhNH)]$_2$ (**10**) and [($^{t\text{Bu}}$dmx)Fe_2(μ-O)(κ^2-NHPhOH)]$_2$ (**11**) along with generation of **3**. The overall mechanism of this formal six-electron reduction is still not well understood, however various experiments discussed herein suggest that each dimeric **1** provides two electrons toward this reduction. Targeting higher valent iron(IV) centers may be required for using this bimetallic scaffold to target challenging multielectron reductions requiring three or more electrons.

4.9 Experimental Methods

4.9.1 General conditions

All manipulations of metal complexes were carried out in the absence of water and dioxygen using standard Schlenk techniques, or in an MBraun inert atmosphere drybox under a dinitrogen atmosphere. All glassware was oven dried for a minimum of 6 h and cooled in an evacuated antechamber prior to use in the drybox. Benzene, hexanes, tetrahydrofuran, diethyl ether and toluene were dried and deoxygenated on a Glass Contour System (SG Water USA, Nashua, NH) and stored over 4 Å molecular sieves (Strem) prior to use. Tetrahydrofuran-d_8 was purchased from Cambridge Isotope Labs and used as received. Benzene-d_6 was purchased from Cambridge Isotope Labs, degassed and stored over 4 Å molecular sieves prior to use. Celite® 545 (J. T. Baker) was dried in a Schlenk flask for 24 h under dynamic vacuum while heating to at least 190 °C prior to drybox use. Tetrabutylammonium nitrite, tetrabutylammonium periodate, and tetrabutylammonium perchlorate were purchased from Sigma-Aldrich and recrystallized from THF layered with hexanes at –35 °C. Sodium nitrite ($NaNO_2$) and potassium iodate were purchased from Oakwood Chemical, sodium nitrite 15-N ($Na^{15}NO_2$) was purchased from Santa Cruz Biotechnology, potassium bromide was purchased from International Crystal Laboratories, and potassium chlorate, *para*-nitroaniline, *para*-nitrophenol, and nitrosobenzene were purchased from Sigma-Aldrich, all of which were used without further purification. 15-crown-5 was purchased from Sigma-Aldrich, degassed, and stored over 4 Å molecular sieves prior to use. Nitrobenzene was bought from Sigma-Aldrich and degassed prior to use. *para*-fluoronitrobenzene was purchased from Sigma-Aldrich and recrystallized from hot hexanes (~85 °C) cooled to – 35°C overnight. Nickelocene

was purchased from Strem Chemicals and recrystallized from diethyl ether layered with hexanes at –35 °C prior to use. 2,3:5,6-Dibenzo-7-azabicyclo[2.2.1]hepta-2,5-diene (dbabhNO)[41] and tritylthionitrite,[42] were synthesized following previously reported procedures.

4.9.2 Characterization and Physical Methods

^{1}H NMR spectra were recorded on Agilent DD2 600 MHz or Varian Unity/Inova 500 MHz spectrometers. ^{1}H chemical shifts are reported relative to $SiMe_4$ using the chemical shift of residual solvent peaks as reference. ^{19}F NMR spectra were recorded on a Varian Unity/Inova 500 MHz spectrometer. ^{19}F chemical shifts are reported relative to the resonance of neat $BF_3•(et_2O)_2$.

Elemental analyses (%CHN) were obtained on a PerkinElmer 2400 Series II CHNS/O Analyzer.

Zero-field ^{57}Fe Mössbauer spectra were measured with a constant acceleration spectrometer (SEE Co, Minneapolis, MN) at 90 K. Isomer shifts are quoted relative to Fe foil at room temperature. Data were analyzed and simulated with Igor Pro 6 software (WaveMetrics, Portland, OR) using Lorentzian fitting functions. Samples were prepared by dissolving 20–40 mg of sample in benzene and immobilizing by rapid freezing in liquid nitrogen.

Electrochemical experiments were carried out using a CH Instruments CHI660C

[41] Carpino, L. A.; Padukula, R. E.; Barr, D. E.; Hall, F. H.; Krause, J. G.; Dufresne, R. F.; Thoman, C. J. *J. Org. Chem.* 1988, **11**, 2565–2572.

[42] Melzer, M. M.; Mossin, S.; Cardenas, A. J. P.; Williams, K. D.; Zhang, S.; Meyer, K.; Warren, T. H. *Inorg. Chem.* 2012, **16**, 8658–8660.

Electrochemical Workstation. The electrolyte used was 0.1 M (^{n}Bu$_4$N)(PF$_6$) in THF. The working electrode was glassy carbon and a platinum wire was used as the counter electrode. Cyclic voltammograms were referenced against a ferrocene standard. Cyclic voltammetry was performed with scan rates of 10 mV/s to 500 mV/s.

Infrared spectra were acquired on a Varian 1000 FTIR spectrometer by pressing the samples into KBr pellets (~3–4 mg of dried sample and ~80 mg of KBr).

4.9.3 Synthesis

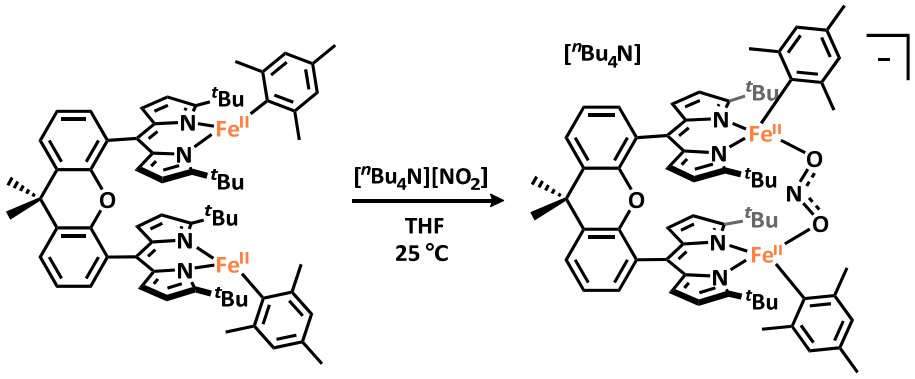

[^{n}Bu$_4$N][($^{t\text{Bu}}$dmx)Fe$_2$(κ^2-O$_2$N)(Mes)$_2$] (2a): In a 20 mL vial, tetrabutylammonium nitrite (10.8 mg, 37.4 µmol, 1.00 equiv) was dissolved in 1 mL of THF. A solution of ($^{t\text{Bu}}$dmx)Fe$_2$(Mes)$_2$ (**1**) (40.0 mg, 37.5 µmol, 1.00 equiv) in 2 mL of THF was added dropwise. The solution was allowed to stir for 10 minutes at room temperature and concentrated *in vacuo*. The residue was washed with hexanes (2 mL), filtered through Celite with benzene, and lyophilized to yield a brown powder (45.2 mg, 89.2 %).^{1}H NMR (600 MHz, 295 K, THF-d_8): δ/ppm 101.57, 97.93, 90.41, 87.00, 48.79, 31.02, 7.27, 6.39, 5.41, 0.35, −7.19, −8.05. Zero-field ^{57}Fe Mössbauer (90 K) (δ, $|\Delta E_Q|$ ($^{mm}/_s$)): 0.75, *3.15* (γ = 0.170 $^{mm}/_s$).

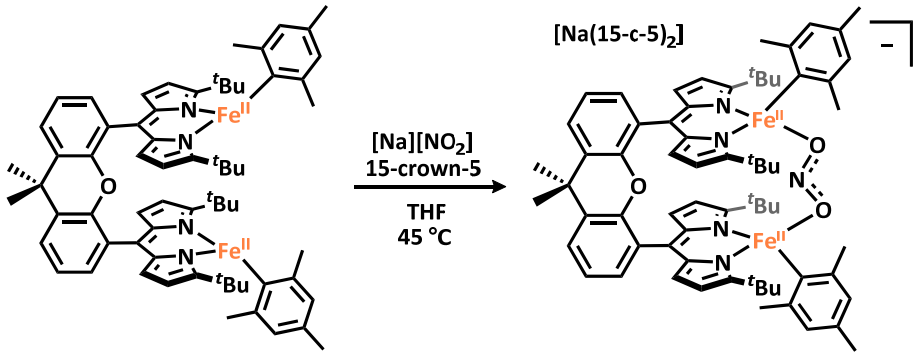

[Na(15-c-5)$_2$][($^{t\text{Bu}}$dmx)Fe$_2$(κ^2-O$_2$N)(Mes)$_2$] (2b): To a J. Young tube was added ($^{t\text{Bu}}$dmx)Fe$_2$(Mes)$_2$ (**1**) (40.0 mg, 37.5 µmol, 1.00 equiv), sodium nitrite (2.6 mg, 37.7 µmol, 1.01 equiv), 15-crown-5 (16.6 mg, 75.4 µmol, 2.01 equiv), and 2 mL of THF. The tube was sealed, removed from the glovebox, and heated to 45 °C for 24 hours. The reaction mixture was cooled to room temperature, returned to the glovebox, transferred to a vial, and concentrated *in vacuo*. The residue was recrystallized from a saturated solution of **2b** in diethyl ether plus drops of THF at –35 °C (45.1 mg, 76.3 %). Crystals suitable for X-ray diffraction were grown from a concentrated solution of **2b** in diethyl ether plus drops of THF at –35 °C. Note that in this solid state structure, sodium is encapsulated by one THF solvent molecule and one crown ether to sodium ([Na(15-c-5)(thf)][($^{t\text{Bu}}$dmx)Fe$_2$(κ^2-O$_2$N)(Mes)$_2$]), however CHN analysis is consistent with full sodium encapsulation by two crown ethers upon bulk recrystallization ([Na(15-c-5)$_2$][($^{t\text{Bu}}$dmx)Fe$_2$(κ^2-O$_2$N)(Mes)$_2$]). ^{1}H NMR (500 MHz, 295 K, THF-d_8): δ/ppm 102.45, 99.82, 91.13, 87.92, 49.09, 31.05, 7.08, 6.36, 5.31, 0.25, −7.49, −8.41. Zero-field ^{57}Fe Mössbauer (90 K) (δ, $|\Delta E_Q|$ ($^{mm}/_s$)): 0.75, *3.08* (γ = 0.170 $^{mm}/_s$). %CHN Calculated for $C_{87}H_{118}Fe_2N_5NaO_{13}$: C 66.28 H 7.54 N 4.44; Found: C 66.20 H 7.55 N 4.75.

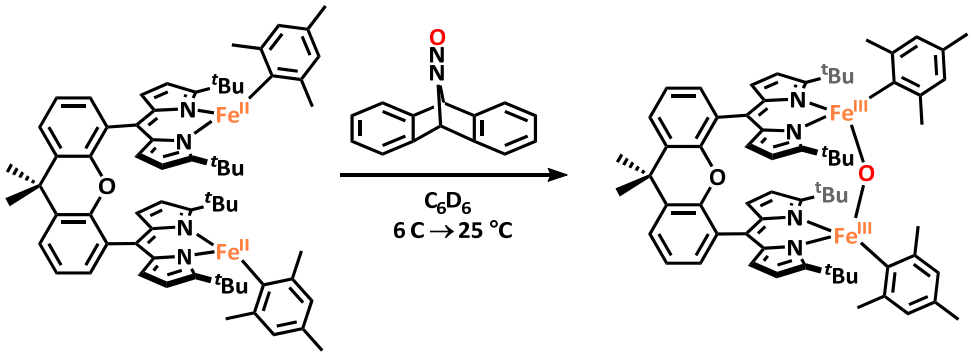

($^{t\mathrm{Bu}}$dmx)Fe$_2$(μ-O)(Mes)$_2$ (3): In a 20 mL vial, ($^{t\mathrm{Bu}}$dmx)Fe$_2$(Mes)$_2$ (**1**) (40.0 mg, 37.5 μmol, 1.00 equiv) was dissolved in 1.5 mL of C_6D_6 and frozen in the cold well (5 °C). A solution of 2,3:5,6-Dibenzo-7-azabicyclo[2.2.1]hepta-2,5-diene (dbabhNO) (16.3 mg, 37.6 μmol, 1.00 equiv) in C_6D_6 was added dropwise and frozen in a layer on top. The reaction mixture was thawed and allowed to stir for 5 hours. At this point, the reaction mixture was filtered through Celite before the solvent was frozen and concentrated *in vacuo* to yield a red powder. The powder was washed with hexanes (2 mL) to remove residual anthracene, filtered through Celite with benzene and lyophilized to yield ($^{t\mathrm{Bu}}$dmx)Fe$_2$(μ-O)(Mes)$_2$ (**3**) as a red powder (38.9 mg, 96%). Crystals suitable for X-ray diffraction were grown from the reaction mixture resulting from thermolysis of **2** (see below). ^{1}H NMR (500 MHz, 295 K, C_6D_6): δ/ppm 16.11, 10.83. Zero-field ^{57}Fe Mössbauer (90 K) (δ, $|\Delta E_Q|$ ($^{mm}/_s$)): 0.23, *1.83* (γ = 0.250 $^{mm}/_s$). %CHN Calculated for $C_{67}H_{78}Fe_2N_4O_2$: C 74.30 H 7.26 N 5.17; Found: C 74.32 H 7.28 N 5.14.

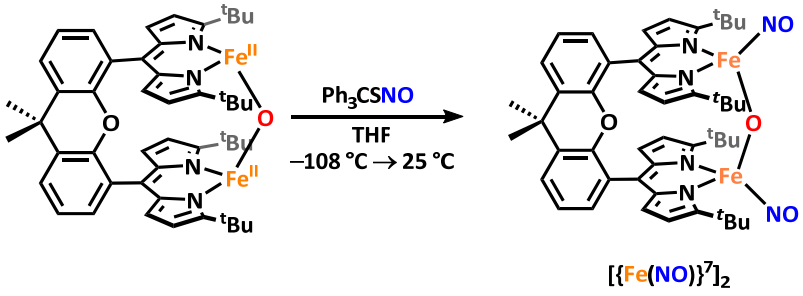

($^{t\text{Bu}}$dmx)Fe$_2$(μ-O)(NO)$_2$ (4): In a 20 mL vial, ($^{t\text{Bu}}$dmx)Fe$_2$(μ-O) (20.0 mg, 23.7 μmol, 1.00 equiv) was dissolved in 1 mL of THF and frozen in the cold well (–108 °C). A solution of tritylthionitrite (14.5 mg, 47.5 μmol, 2.00 equiv) in 1 mL of THF was added dropwise and frozen in a layer on top. The reaction mixture was thawed and allowed to stir for 40 minutes. At this point, the reaction mixture was filtered through Celite and concentrated *in vacuo*. The resulting red residue was washed with hexanes (2 mL) to remove residual ditrityl disulfide, filtered through Celite with benzene and lyophilized to yield ($^{t\text{Bu}}$dmx)Fe$_2$(μ-O)(NO)$_2$ (**4**) as a red powder (20.8 mg, 97%). Crystals suitable for X-ray diffraction were grown from a concentrated THF solution of **4** layered with hexanes at −35 °C. ^{1}H NMR (500 MHz, 295 K, C_6D_6): δ/ppm 9.23, 1.93. Zero-field ^{57}Fe Mössbauer (90 K) (δ, $|\Delta E_Q|$ ($^{mm}/_s$)): 0.32, *1.07* (γ = 0.168 $^{mm}/_s$). FTIR (KBr): 1721 cm^{-1}, 1742 cm^{-1}, 1781 cm^{-1} (ν_{N-O}). %CHN Calculated for $C_{49}H_{56}Fe_2N_6O_4$: C 65.05 H 6.24 N 9.29; Found: C 65.01 H 6.22 N 9.31.

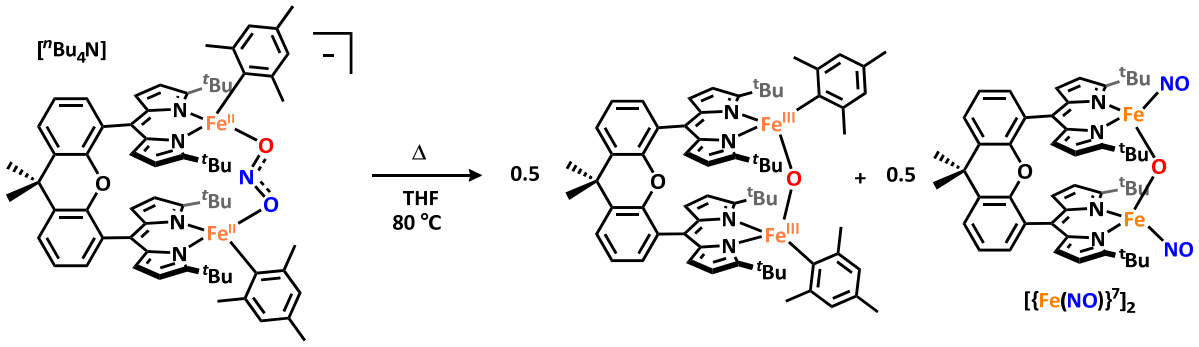

Thermolysis of [^{n}Bu$_4$N][($^{t\text{Bu}}$dmx)Fe$_2$(NO$_2$)(Mes)$_2$] (2a): To a J. Young tube was added [^{n}Bu$_4$N][($^{t\text{Bu}}$dmx)Fe$_2$(NO$_2$)(Mes)$_2$] (**2**) (30.0 mg, 22.1 μmol) and 1.5 mL of THF. The tube was sealed, removed from the glovebox, and heated to 80 °C for seven hours. The reaction mixture was cooled to room temperature, returned to the glovebox, transferred to a vial, and concentrated *in vacuo*. The red residue was washed with pentane, filtered through Celite, and the rest eluted with benzene to yield a reddish powder (21.4 mg total, ~95% yield). Crystals

suitable for X-ray diffraction were grown from a concentrated toluene solution of the resulting mixture layered with hexanes at −35 °C to reveal the formation of **3**. In another batch, crystals suitable for X-ray diffraction were grown from a concentrated hexanes solution at −35 °C to reveal the formation of **6.** ^{1}H NMR (500 MHz, 295 K, C_6D_6); (**3**): δ/ppm 15.77, 11.00; (**4**): δ/ppm 9.75, 1.99; ($^{n}Bu_3N$): δ/ppm 2.38 (*t*, 6 H), 1.39 (*m*, 6 H), 1.35 (*m*, 6 H), 0.93 (*t*, 12 H); (butene): δ/ppm 6.07 (*m*, 1 H), 5.80 (*m*, 1 H), 5.02 (*m*, 1 H), 1.92 (*m*, 2 H), 0.88 (*t*, 3 H); (HMes): δ/ppm 6.74 (*s*, 3 H), 2.16 (*s*, 9 H). Zero-field ^{57}Fe Mössbauer (90 K) (δ, $|\Delta E_Q|$ ($^{mm}/_{s}$)): 0.25, *1.89;* 0.32, *1.10* (γ = 0.253, 0.187 $^{mm}/_{s}$). Zero-field ^{57}Fe Mössbauer (90 K) (δ, $|\Delta E_Q|$ ($^{mm}/_{s}$)): 0.21, *1.81;* 0.32, *1.10* (γ = 0.200, 0.248 $^{mm}/_{s}$). FTIR (KBr): 1730 cm^{-1}, 1781 cm^{-1} (ν_{N-O}).

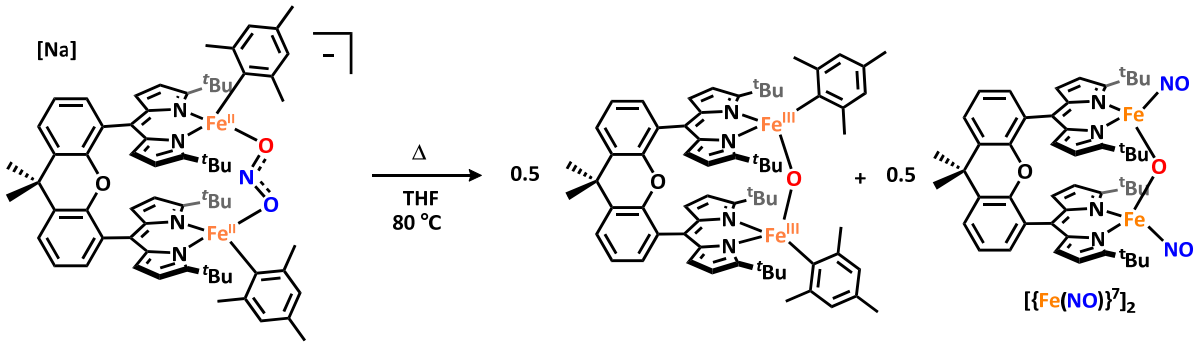

Thermolysis of [Na][($^{t\text{Bu}}$dmx)Fe$_2$(^{15}NO$_2$)(Mes)$_2$] (2c): To a J. Young tube was added [Na][($^{t\text{Bu}}$dmx)Fe$_2$(^{15}NO$_2$)(Mes)$_2$] (**2c**) (20.0 mg, 12.7 μmol) and 1.5 mL of THF. The tube was sealed, removed from the glovebox, and heated to 80 °C for twenty-four hours. The reaction mixture was cooled to room temperature, returned to the glovebox, transferred to a vial, and concentrated *in vacuo*. The red residue was washed with pentane, filtered through Celite, and the rest eluted with THF to yield a red film (12.2 mg, ~97%). ^{1}H NMR (500 MHz, 295 K, THF); (**3**, THF fraction): δ/ppm 15.85, 10.86; (**4**, THF fraction): δ/ppm 9.84; ([$Me_3C_6H_2$]$^{-}$ pentane fraction): δ/ppm 7.27 (*s*, 1 H), 6.68,(*s*, 1 H), 2.17,(*s*, 3 H), 1.25 (*s*, 9 H). Zero-field

^{57}Fe Mössbauer (90 K) (δ, $|\Delta E_Q|$ ($^{mm}/_s$)): 0.25, *1.89;* 0.32, *1.10* (γ = 0.253, 0.187 $^{mm}/_s$). FTIR (KBr): 1701 cm^{-1}, 1757 cm^{-1} (ν_{15N-O}).

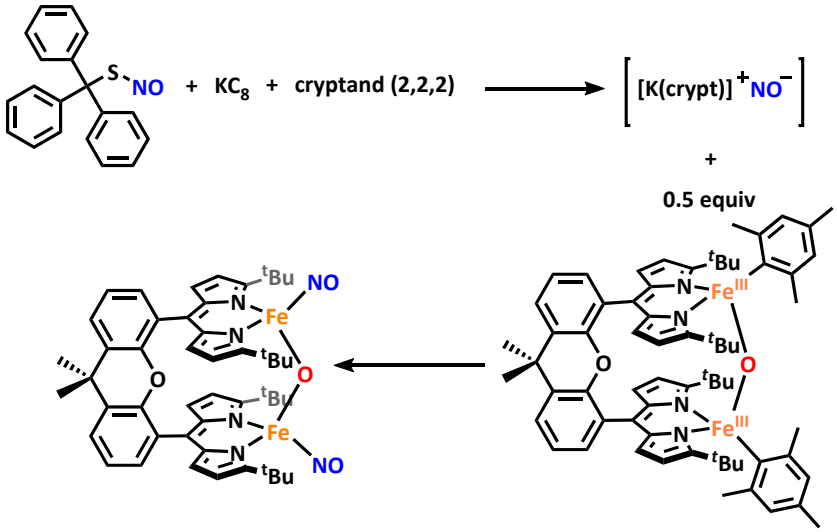

Reaction of ($^{t\text{Bu}}$dmx)Fe$_2$(μ-O)(Mes)$_2$ (3) with prereduced TrSNO (2 equiv): A taped 20 mL vial (to protect the light-sensitive tritylthionitrite) was charged with potassium graphite (7.6 mg, 56.2 μmol, 2.00 equiv) and frozen in 1 mL of THF in the cold well (–35 °C). A layer of [2.2.2]-cryptand (21.2 mg, 56.3 μmol, 2.00 equiv) in 1 mL of THF was added and frozen on top. To this, a solution of tritylthionitrite (17.2 mg, 56.3 μmol, 2.00 equiv) in 2 mL of THF was added dropwise and the reaction mixture was stirred as it thawed to room temperature. A color change from green to clear was observed as the TrSNO was reduced. A solution of ($^{t\text{Bu}}$dmx)Fe$_2$(μ-O)(Mes)$_2$ (**3**) (30.0 mg, 28.1 μmol, 1.00 equiv) in 2 mL of THF was added dropwise and stirred for three hours. The reaction mixture was concentrated *in vacuo*. The red residue was taken up in benzene and lyophilized. ^{1}H NMR (600 MHz, 295 K, THF) (**4**, THF fraction): *δ*/ppm 9.84; ([Me$_3$C$_6$H$_2$]$^-$, pentane fraction): *δ*/ppm 7.26 (*s*, 1 H), 6.84,(*s*, 1 H), 2.45,(*s*, 3 H), 1.26 (*s*, 9 H).Zero-field ^{57}Fe Mössbauer (90 K) (δ, $|\Delta E_Q|$ ($^{mm}/_s$)): 0.33, *1.18* (γ = 0.325 $^{mm}/_s$). FTIR (KBr): 1731 cm^{-1}, 1736 cm^{-1}, 1781 cm^{-1} (ν_{N-O}).

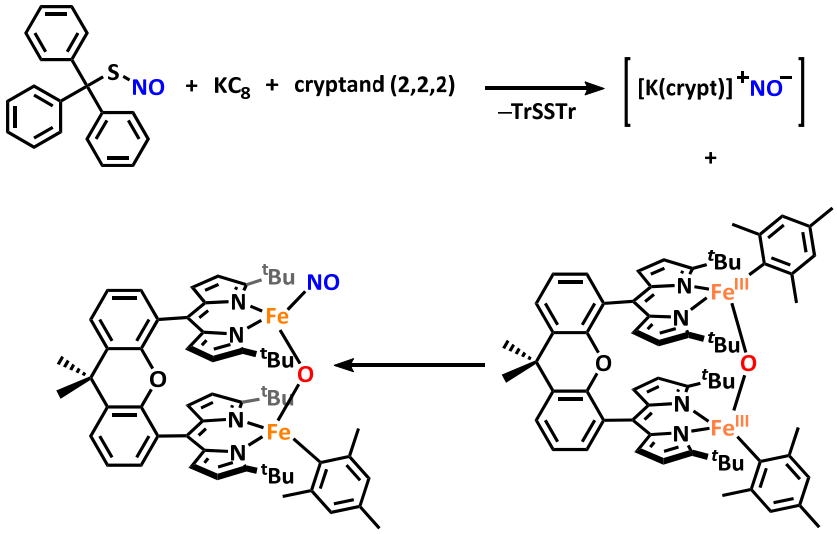

Reaction of ($^{t\text{Bu}}$dmx)Fe$_2$(μ-O)(Mes)$_2$ (3) with prereduced TrSNO (1 equiv): A taped 20 mL vial (to protect the light-sensitive tritylthionitrite) was charged with potassium graphite (3.8 mg, 28.1 μmol, 1.00 equiv) and frozen in 1 mL of THF in the cold well (–35 °C). A layer of [2.2.2]-cryptand (10.6 mg, 28.2 μmol, 1.00 equiv) in 1 mL of THF was added and frozen on top. To this, a solution of tritylthionitrite (8.6 mg, 28.1 μmol, 1.00 equiv) in 2 mL of THF was added dropwise and the reaction mixture was stirred as it thawed to room temperature. A color change from green to clear was observed as the TrSNO was reduced. A solution of ($^{t\text{Bu}}$dmx)Fe$_2$(μ-O)(Mes)$_2$ (**3**) (30.0 mg, 28.1 μmol, 1.00 equiv) in 2 mL of THF was added dropwise and stirred for three hours. The reaction mixture was concentrated *in vacuo*. The red residue was taken up in benzene and lyophilized. Zero-field ^{57}Fe Mössbauer (90 K) (δ, $|\Delta E_Q|$ ($^{mm}/_s$)): 0.25, *1.99;* 0.32, *1.10* (γ = 0.255, 0.299 $^{mm}/_s$). FTIR (KBr): 1732 cm^{-1}, 1735 cm^{-1}, 1781 cm^{-1} (ν_{N-O}).

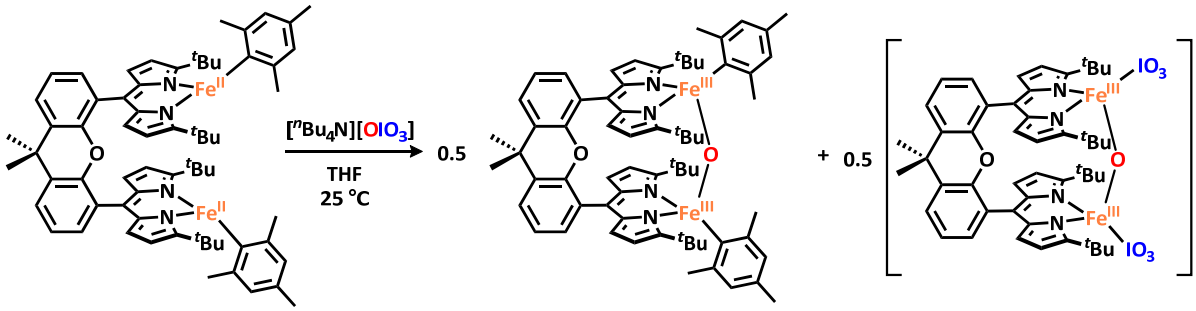

Reduction of IO_4^- with 1: In a 20 mL vial, tetrabutylammonium periodate (24.4 mg, 56.3 µmol, 1.00 equiv) was dissolved in 1 mL of THF. A solution of ($^{t\text{Bu}}$dmx)Fe$_2$(Mes)$_2$ (**1**) (60.0 mg, 56.2 µmol, 1.00 equiv) in 2 mL of THF was added dropwise. The solution was allowed to stir for 10 minutes at room temperature and concentrated *in vacuo*. The residue was washed with hexanes (2 mL), filtered through Celite with benzene, and lyophilized to yield a red powder (58.5 mg, 91.4 % assuming 1:1 mixture of proposed products). Single crystals were grown from a concentrated diethyl ether solution at −35 °C to reveal the formation of **3**. ^{1}H NMR (600 MHz, 295 K, THF-d_8): (metal complexes) δ/ppm 15.27, 10.68; ([^{n}Bu$_4$N][Me$_3$C$_6$H$_2$]) δ/ppm 7.27 (*s*, 1 H), 6.71, (*s*, 1 H), 2.38 (*t*, 8 H), 2.21,(*s*, 3 H), 1.39 (*m*, 8 H), 1.35 (*m*, 8 H), 1.02 (*s*, 9 H), 0.93 (*t*, 16 H). Zero-field ^{57}Fe Mössbauer (90 K) (δ, $|\Delta E_Q|$ ($^{mm}/_s$)): 0.18, *1.93*; 0.34, *1.41* (γ = 0.118, 0.266 $^{mm}/_s$).

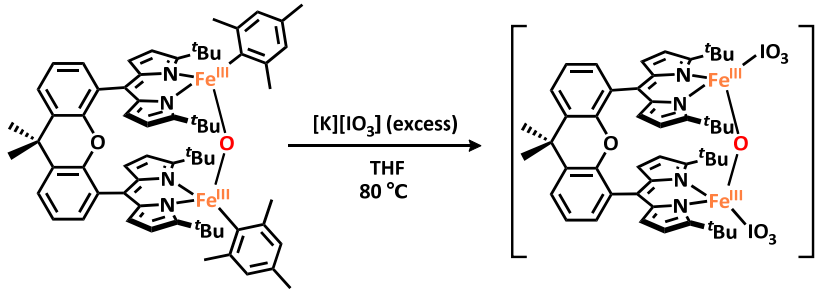

"($^{t\text{Bu}}$dmx)Fe$_2$(µ-O)(IO$_3$)$_2$" (7): To a J. Young tube was added ($^{t\text{Bu}}$dmx)Fe$_2$(µ-O)(Mes)$_2$ (**3**) (10.0 mg, 9.2 µmol, 1.00 equiv), [K][IO$_3$] (**2c**) (8.0 mg, 37.3 µmol, 4.06 equiv), and 1.5 mL of THF. The tube was sealed, removed from the glovebox, and heated to 80 °C for twenty-

four hours. The reaction mixture was cooled to room temperature, returned to the glovebox, transferred to a vial, and concentrated *in vacuo*. The red residue was washed with pentane, filtered through Celite, and the rest eluted with THF to yield a red film. ^{1}H NMR (500 MHz, 295 K, THF-d_8): ([$Me_3C_6H_2$]$^-$) δ/ppm 7.97 (*s*, 1 H), 7.40, (*s*, 1 H), 2.18,(*s*, 3 H), 1.28 (*s*, 9 H). Zero-field ^{57}Fe Mössbauer (90 K) (δ, $|\Delta E_Q|$ ($^{mm}/_{s}$)): 0.36, *1.40;* 0.19, *1.87* (γ = 0.340, 0.144 $^{mm}/_{s}$).

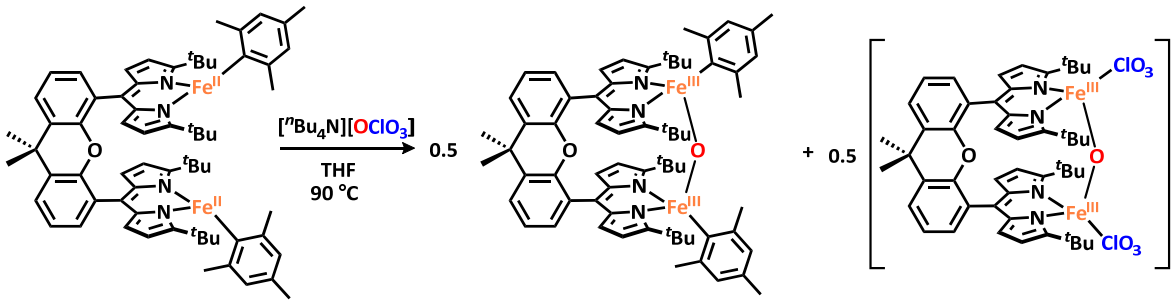

Reduction of ClO_4^- with 1: To a J. Young tube was added ($^{t\text{Bu}}$dmx)$Fe_2(Mes)_2$ (**1**) (35.0 mg, 32.7 µmol, 1.00 equiv), tetrabutylammonium perchlorate (11.2 mg, 32.8 µmol, 1.00 equiv), and 1.5 mL of THF. The tube was sealed, removed from the glovebox, and heated to 90 °C for twelve hours. The reaction mixture was cooled to room temperature, returned to the glovebox, transferred to a vial, and concentrated *in vacuo*. The residue was washed with hexanes (2 mL), filtered through Celite with benzene, and lyophilized to yield a red powder (29.4 mg, 85.8 % assuming 1:1 mixture of proposed products). ^{1}H NMR (600 MHz, 295 K, THF-d_8): (metal complexes) δ/ppm 15.75, 10.76; ($^{n}Bu_3N$): δ/ppm 2.19 (*t*, 6 H), 1.39 (*m*, 6 H), 1.27 (*m*, 6 H), 0.96 (*t*, 12 H); (butene): δ/ppm 6.13 (*m*, 1 H), 5.93 (*m*, 1 H), 5.41 (*m*, 1 H), 1.92 (*m*, 2 H), 0.88 (*t*, 3 H); (HMes): δ/ppm 6.74 (*s*, 3 H), 2.10 (*s*, 9 H). Zero-field ^{57}Fe Mössbauer (90 K) (δ, $|\Delta E_Q|$ ($^{mm}/_{s}$)): 0.18, *1.93*; 0.34, *1.41* (γ = 0.118, 0.266 $^{mm}/_{s}$).

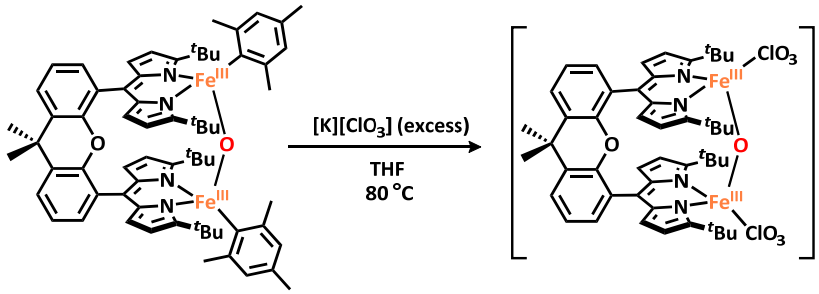

"($^{t\text{Bu}}$dmx)Fe$_2$(μ-O)(ClO$_3$)$_2$" (9): To a J. Young tube was added ($^{t\text{Bu}}$dmx)Fe$_2$(μ-O)(Mes)$_2$ (**3**) (10.0 mg, 9.2 μmol, 1.00 equiv), [K][ClO$_3$] (**2c**) (8.0 mg, 37.3 μmol, 4.06 equiv), and 1.5 mL of THF. The tube was sealed, removed from the glovebox, and heated to 80 °C for twenty-four hours. The reaction mixture was cooled to room temperature, returned to the glovebox, transferred to a vial, and concentrated *in vacuo*. The red residue was washed with pentane, filtered through Celite, and the rest eluted with THF to yield a red film. ^{1}H NMR (500 MHz, 295 K, THF-d_8): ([Me$_3$C$_6$H$_2$]$^-$) δ/ppm 7.98 (*s*, 1 H), 7.41, (*s*, 1 H), 2.19,(*s*, 3 H), 1.28 (*s*, 9 H). Zero-field ^{57}Fe Mössbauer (90 K) (δ, $|\Delta E_Q|$ ($^{mm}/_s$)): 0.37, *1.31;* 0.23, *1.87* (γ = 0.305, 0.186 $^{mm}/_s$).

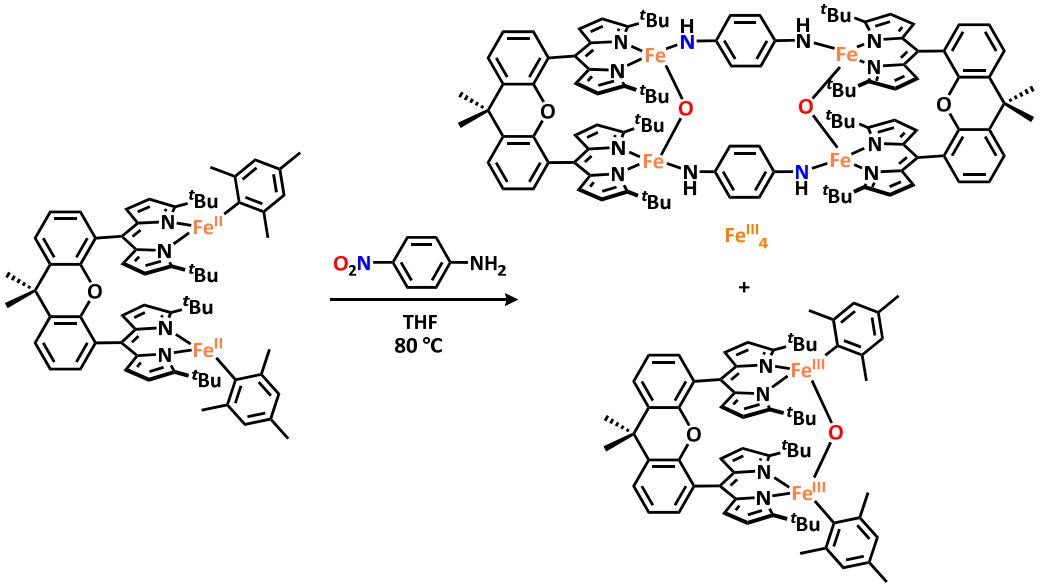

Reduction of *para*-nitroaniline with 1: To a J. Young tube was added ($^{t\text{Bu}}$dmx)Fe$_2$(Mes)$_2$ (**1**)

(40.0 mg, 37.5 µmol, 1.00 equiv), *para*-nitroaniline (5.2 mg, 37.6 µmol, 1.00 equiv), and 1.5 mL of THF. The tube was sealed, removed from the glovebox, and heated to 80 °C for five hours. The reaction mixture was cooled to room temperature, returned to the glovebox, transferred to a vial, and concentrated *in vacuo*. The residue was taken up in benzene, frozen, and lyophilized to yield a red powder . Single crystals were grown from a saturated solution in toluene layered at –35 °C. ^{1}H NMR (600 MHz, 295 K, C_6D_6): (**3**) δ/ppm 15.09; (**10**) δ/ppm 10.77, 9.85; (HMes): δ/ppm 6.70 (*s*, 3 H), 2.18 (*s*, 9 H). Zero-field ^{57}Fe Mössbauer (90 K) (δ, $|\Delta E_Q|$ ($^{mm}/_{s}$)): 0.36, *1.46*; 0.12, *1.77* (γ = 0.176, 0.138 $^{mm}/_{s}$). FTIR (KBr): 3312 cm^{-1} (ν_{N-H}). Stoichiometry experiments with 0.33, 0.50, 0.67 equivalents of substrate followed the same procedure (except heated for twenty-four hours) and were conducted on 20.0 mg scales.

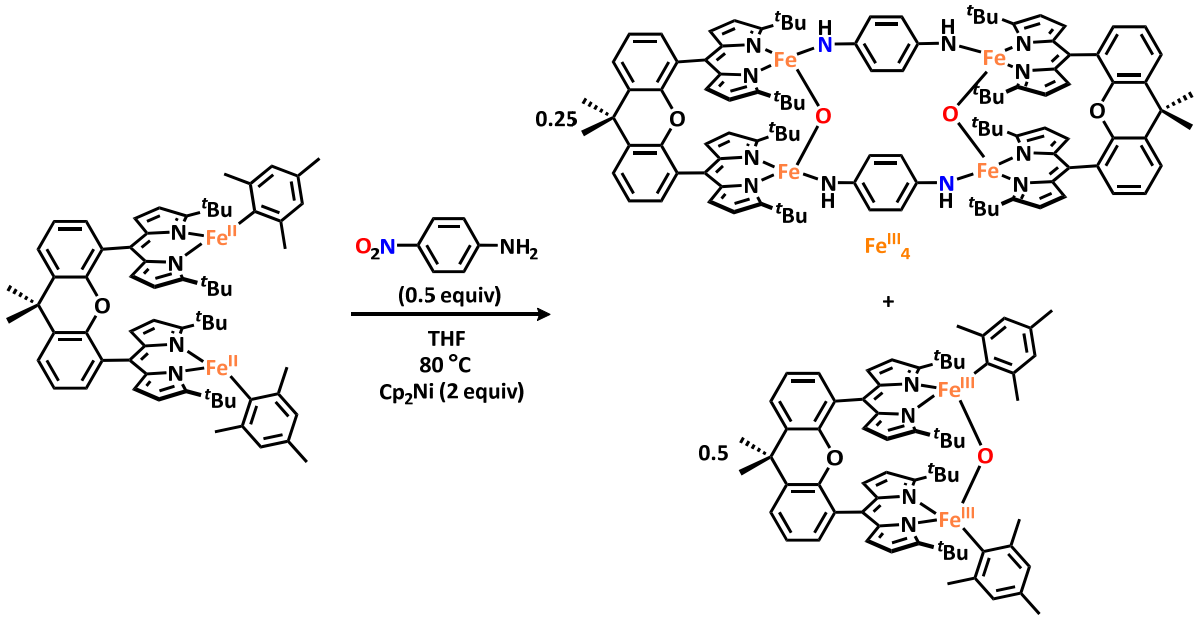

Reduction of *para*-nitroaniline with 1 in the presence of Cp_2Ni: To a J. Young tube was added ($^{t\text{Bu}}$dmx)Fe$_2$(Mes)$_2$ (**1**) (20.0 mg, 18.7 µmol, 1.00 equiv), *para*-nitroaniline (1.3 mg, 9.41 µmol, 0.50 equiv), nickelocene (7.2 mg, 38.1 µmol, 2.04 equiv) and 1.5 mL of THF. The tube was sealed, removed from the glovebox, and heated to 80 °C for twenty-four hours. The

reaction mixture was cooled to room temperature, returned to the glovebox, transferred to a vial, and concentrated *in vacuo*. The residue was taken up in benzene, frozen, and lyophilized to yield a red powder. ^{1}H NMR (600 MHz, 295 K, THF): (**3**) δ/ppm 15.77; (**10**) δ/ppm 10.87, 9.86. Zero-field ^{57}Fe Mössbauer (90 K) (δ, $|\Delta E_Q|$ ($^{mm}/_{s}$)): 0.34, *1.44*; 0.29, *1.82* (γ = 0.214, 0.184 $^{mm}/_{s}$).

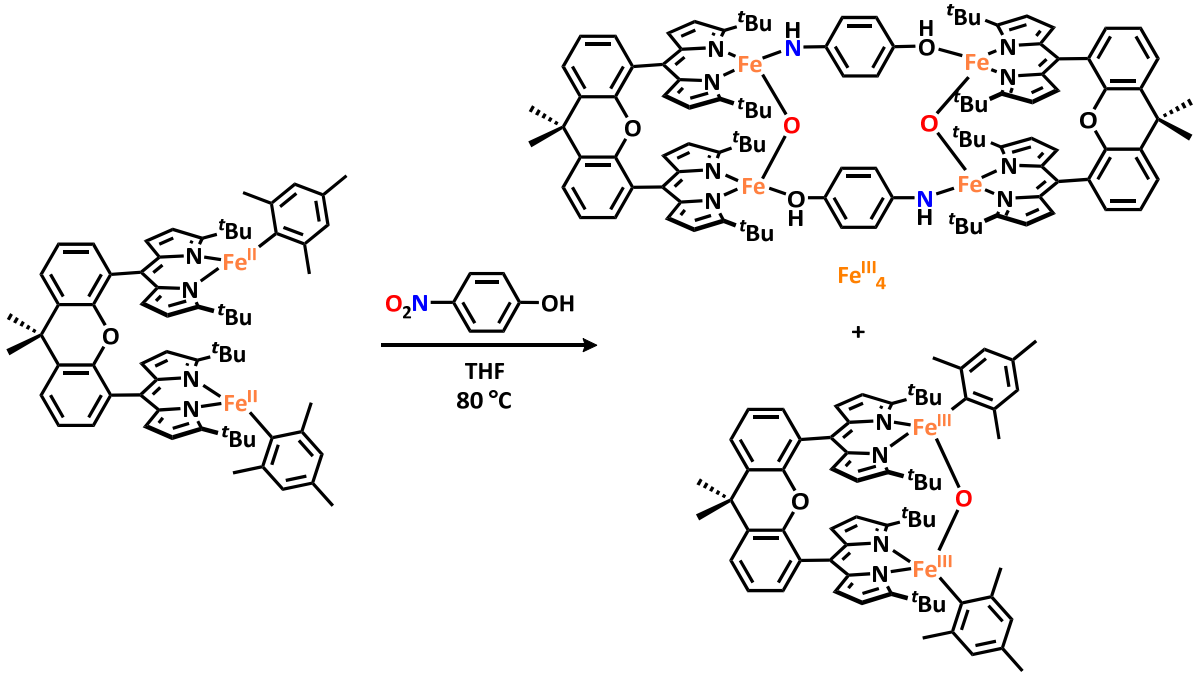

Reduction of *para*-nitrophenol with 1: To a J. Young tube was added ($^{t\text{Bu}}$dmx)Fe$_2$(Mes)$_2$ (**1**) (25.0 mg, 23.4 µmol, 1.00 equiv), *para*-nitrophenol (3.3 mg, 23.7 µmol, 1.01 equiv), and 1.5 mL of THF. The tube was sealed, removed from the glovebox, and heated to 80 °C for twenty-four hours. The reaction mixture was cooled to room temperature, returned to the glovebox, transferred to a vial, and concentrated *in vacuo*. The residue was washed with hexanes (2 mL), filtered through Celite with benzene, and lyophilized to yield a red powder . Single crystals were grown from a saturated solution in toluene layered with hexanes at –35 °C. ^{1}H NMR (500 MHz, 295 K, THF-d_8): (**3**) δ/ppm 15.27; (**11**) δ/ppm 14.24, 13.69; (HMes): δ/ppm 6.70

(*s*, 3 H), 2.18 (*s*, 9 H). Zero-field ^{57}Fe Mössbauer (90 K) (δ, $|\Delta E_Q|$ ($^{mm}/_s$)): 0.34, *1.30*; 0.18, *1.83* (γ = 0.201, 0.109 $^{mm}/_s$). FTIR (KBr): 3311 cm^{-1} (ν_{N-H}).

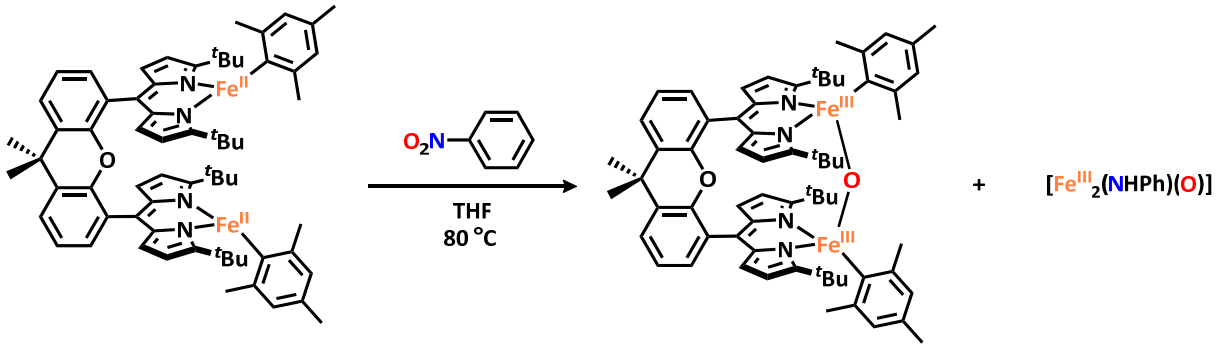

Reduction of nitrobenzene with 1: To a J. Young tube was added ($^{t\text{Bu}}$dmx)Fe$_2$(Mes)$_2$ (**1**) (40.0 mg, 37.5 µmol, 1.00 equiv), *para*-fluoronitroaniline (5.3 mg, 37.6 µmol, 1.00 equiv), and 1.5 mL of THF. The tube was sealed, removed from the glovebox, and heated to 80 °C for twenty-four hours. The reaction mixture was cooled to room temperature, returned to the glovebox, transferred to a vial, and concentrated *in vacuo*. The residue was taken up in benzene, frozen, and lyophilized to yield a red powder. ^{1}H NMR (500 MHz, 295 K, C_6D_6): (metal complexes) *δ*/ppm 15.88, 10.55, 9.82; (HMes): *δ*/ppm 6.68 (*s*, 3 H), 2.14 (*s*, 9 H). Zero-field ^{57}Fe Mössbauer (90 K) (δ, $|\Delta E_Q|$ ($^{mm}/_s$)): 0.34, *1.38*; 0.23, *1.96* (γ = 0.258, 0.157 $^{mm}/_s$). FTIR (KBr): 3398 cm^{-1} (ν_{N-H}).

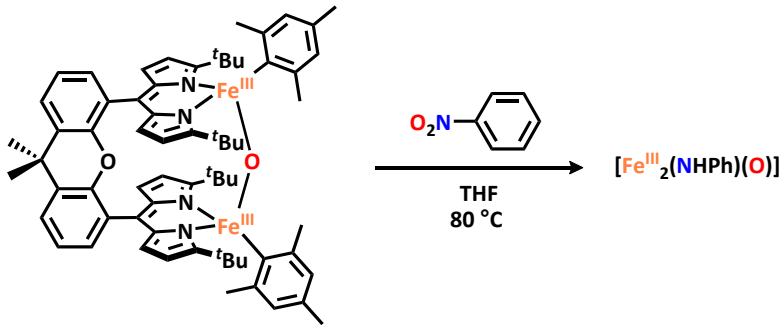

Reaction of nitrosobenzene with 3: To a J. Young tube was added ($^{t\text{Bu}}$dmx)Fe$_2$(Mes)$_2$ (**1**) (10.0 mg, 9.23 µmol, 1.00 equiv), nitrosobenzene (5.3 mg, 37.6 µmol, 1.00 equiv), and 1.5

mL of THF. The tube was sealed, removed from the glovebox, and heated to 80 °C for twenty-four hours. The reaction mixture was cooled to room temperature, returned to the glovebox, transferred to a vial, and concentrated *in vacuo*. The residue was taken up in benzene, frozen, and lyophilized to yield a red powder. ^{1}H NMR (500 MHz, 295 K, C_6D_6): (metal complexes) δ/ppm 15.79, 10.83, 10.53; (HMes): δ/ppm 6.68 (*s*, 3 H), 2.14 (*s*, 9 H). Zero-field ^{57}Fe Mössbauer (90 K) (δ, $|\Delta E_Q|$ ($^{mm}/_{s}$)): 0.36, *1.35*; 0.19, *1.91* (γ = 0.340, 0.145 $^{mm}/_{s}$).

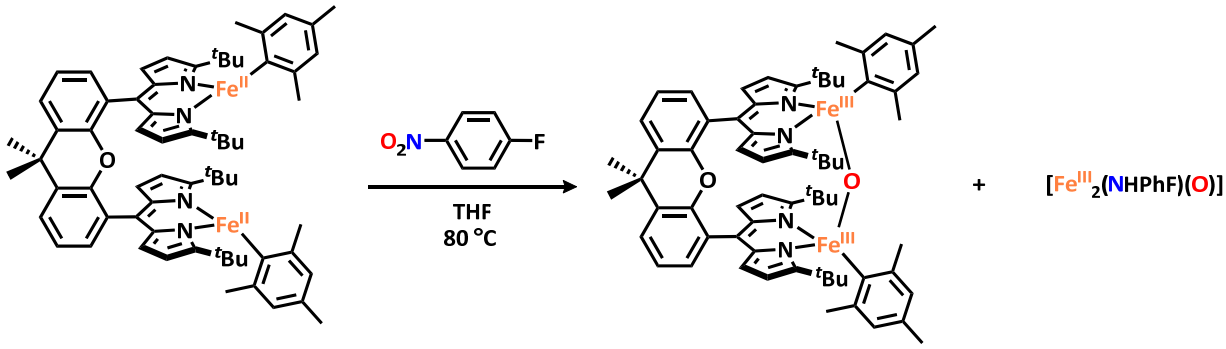

Reduction of *para*-fluoronitrobenzene with 1: To a J. Young tube was added ($^{t\text{Bu}}$dmx)Fe$_2$(Mes)$_2$ (**1**) (40.0 mg, 37.5 µmol, 1.00 equiv), *para*-fluoronitroaniline (5.3 mg, 37.6 µmol, 1.00 equiv), and 1.5 mL of THF. The tube was sealed, removed from the glovebox, and heated to 80 °C for twenty-four hours. The reaction mixture was cooled to room temperature, returned to the glovebox, transferred to a vial, and concentrated *in vacuo*. The residue was taken up in benzene, frozen, and lyophilized to yield a red powder. ^{1}H NMR (500 MHz, 295 K, THF-d$_8$): (metal complexes) δ/ppm 15.44, 10.93, 9.91; (HMes): δ/ppm 6.70 (*s*, 3 H), 2.18 (*s*, 9 H). ^{19}F NMR (500 MHz, 295 K, THF-d$_8$) δ/ppm –129.26. Zero-field ^{57}Fe Mössbauer (90 K) (δ, $|\Delta E_Q|$ ($^{mm}/_{s}$)): 0.34, *1.39*; 0.23, *1.85* (γ = 0.258, 0.157 $^{mm}/_{s}$). FTIR (KBr): 3390 cm^{-1} (ν_{N-H}). Stoichiometry experiments with 0.33, 0.50, and 0.67 equivalents of substrate were performed following the same procedure and scale. These revealed full consumption of starting material by 0.50 equivalents, producing a similar ratio of iron-

containing products by Zero-field ^{57}Fe Mössbauer (90 K): 0.33 equiv, (δ, $|\Delta E_Q|$ ($^{mm}/_s$)): 0.34, *1.59*; 0.14, *1.87;* 1.28, *2.46* (γ = 0.291, 0.108, 0.300 $^{mm}/_s$); 0.50 equiv (δ, $|\Delta E_Q|$ ($^{mm}/_s$)): 0.35, *1.46*; 0.16, *1.88* (γ = 0.306, 0.125 $^{mm}/_s$); 0.67 equiv ((δ, $|\Delta E_Q|$ ($^{mm}/_s$)): 0.33, *1.39*; 0.24, *1.92* (γ = 0.189, 0.144 $^{mm}/_s$) (**Figure 4.30**).

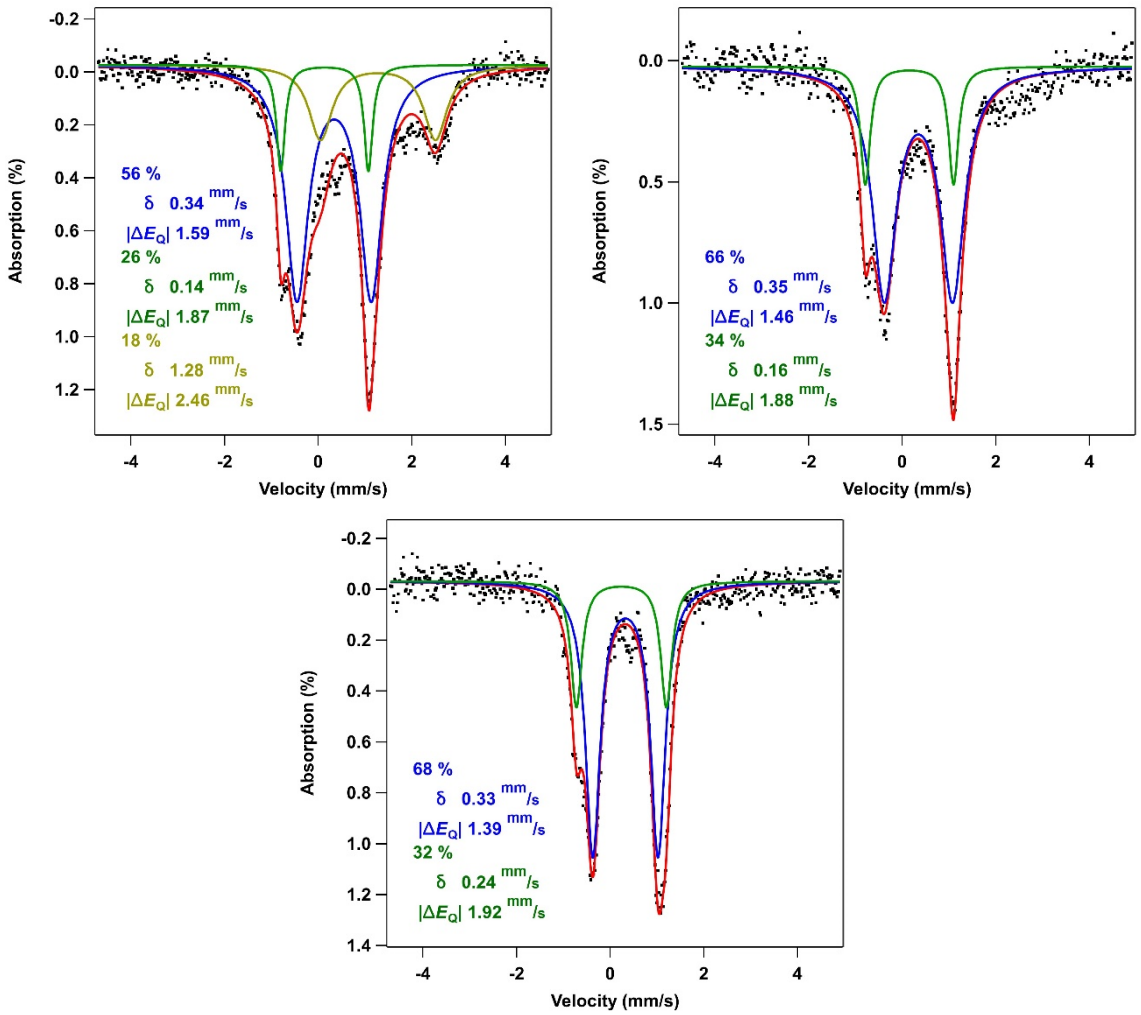

Figure 4.30. Zero-field ^{57}Fe Mössbauer spectrum of reaction products from reducing substoichiometric amounts of *para*-fluoronitrobenzene by **1**, (**Top**, **left**) 0.33 equivalents *para*-nitroaniline relative to **1**, (**Top**, **right**) 0.50 equivalents *para*-nitroaniline, (**Bottom**) 0.67 equivalents *para*-nitroaniline. In each case, the blue trace corresponds to the novel metal-containing product, the green trace corresponds to **3**, and the yellow trace in the 0.33 equivalent reaction likely corresponds to a symmetric Fe(II) intermediate during nitrobenzene reduction.

4.9.4 Theoretical Methods

All calculations were performed using the density functional theory and the quantum

chemical program package Gaussian16[43]. Solvation of all molecular species was modelled using continuum parameters designed to describe tetrahydrofuran solvent (ε = 7.43). Geometry optimizations were performed in order to obtain electronic energies, followed by frequency calculations to compute zero-point energies and derive values for thermal and entropic corrections at 298.15 K. To validate the optimized structures, calculation of ^{57}Fe Mössbauer isomer shifts (δ) for complexes **2**, **3**, **4**, **7**, and **8** were carried out as described previously[44] via linear regression of DFT calculated electron density at the nucleus to experimental values of δ. Mössbauer calculations were carried out using the ORCA 4.0.1.2 program package[45] and were initiated from spin-unrestricted single-point calculations that employed the B3LYP functional[7] with the def2-TZVP[9] (Fe, N, O) and def2-SV(P)[10] (C, H) basis sets. Further, the def2-TSVP/J (Fe, N, Cl) and def2-SV(P)/J (C, H) auxiliary basis sets were employed to utilize the RIJCOSX approximation for accelerating the calculation.[46] A broken symmetry solution (see below for more details) was used to model antiferromagnetic coupling between the iron centers, and the continuum solvation model CPCM was implemented to model the solvent as tetrahydrofuran.[47]

The optimizations for structures **2**, **3**, and **7** utilized the unrestricted B3LYP hybrid functional (which includes the Becke three-parameter exchange and the Lee, Yang, and Parr

[43] Gaussian, Inc., Revision B.01 (2016), Wallingford CT.

[44] Neese, F. *Inorg. Chim. Acta*, 2002, **337**, 181–192.

[45] Neese, F. in *The ORCA program system*, Wiley Interdiscip. Rev.: Comput. Mol. Sci., 2012, vol. 2, pp. 73.

[46] Neese, F.; Wennmohs, F.; Hansen, A.; Becker, U. *Chem. Phys.* **2009**, *356*, 98–109.

[47] Sinnecker, S.; Rajendran, A.; Klamt, A.; Diedenhofen, M.; Neese, F. *J. Phys. Chem. A*, 2006, **110**, 2235–2245.

correlation functional)[48] and GD3BJ dispersion of Grimme et al. with Becke-Johnson damping[49], with which the def2-TZVP (Fe, N, O) and def2-SV(P) (C, H) basis sets[50] were utilized. This method and level of theory was found to have good agreement with the crystallographic data and furthermore was consistent with the functional and basis sets selected for predicting ^{57}Fe Mössbauer parameters (**Table 4.1**, **Table 4.2**). The calculated Mössbauer parameters for **7 (**δ: 0.89, 0.91 mm/s; $|\Delta E_Q|$: 2.532, 2.428 mm/s) were consistent with those expected for four-coordinate, high-spin iron(II) centers but were less consistent with the experimental values observed, further confirming the connectivity of **2** as containing a κ^2-ONO binding mode.

Table 4.1. Calculated bond metrics and Mössbauer parameters for **2**.

	Optimized structure	**Crystallographic structure / Experimental data**
N–O (Å)	1.18281, 1.18282	1.16777(6)
Fe–O(NO) (Å)	1.70193, 1.70201	1.73726(7)
∠Fe–O–NO (Å)	153.56229, 153.44188	164.3898(7)
Fe–O (Å)	1.81903, 1.81911	1.77483(9)
Fe–Fe (Å)	142.7657	166.2066(10)
δ (mm/s)	0.81, 0.82	0.75
$\|\Delta E_Q\|$ (mm/s)	2.685, 2.544	3.15

[48] (a) Becke, A. D. *J. Chem. Phys.*, **1993**, *98*, 5648–5652; (b) Lee, C. T.; Yang, W. T.; Parr, R. G. *Phys Rev. B*, **1988**, *37*, 785–789.

[49] Grimme, S.; Ehrlich, S. Goerigk, L. *J. Comp. Chem*. **2011**, *32*, 1456–1465.

[50] Weigend, F.; Ahlrichs, R. *Phys. Chem. Chem. Phys.* **2005**, *7*, 3297–3305.

Table 4.2. Calculated bond metrics and Mössbauer parameters for **3**.

	Optimized structure		Crystallographic structure /
	uB3LYP[a]	**uBP86**[b]	**Experimental data**
Fe–C (Å)	2.06828	2.04317	2.0675(4)
Fe–O (Å)	1.83163, 1.83164	1.85071	1.7943(3)
∠Fe–O–Fe (°)	144.251	140.401	152.528(3)
Fe–Fe (Å)	3.48644	3.48260	3.4859(5)
δ (mm/s)	0.24, 0.24	0.22, 0.22	0.23
$\|\Delta E_Q\|$ (mm/s)	1.632, 1.633	1.581, 1.581	1.83

[a] using def2-TZVP (Fe, N, O) and def2-SV(P) (C, H) basis sets ; selected level of theory
[b] using def2-TZVP (Fe), 6-311G(d) (C, N, O) and 6-31G(d) (H) basis sets as a comparison to theory used for **4**

For the optimization of the molecular structure of **4**, the unrestricted BP86 hybrid functional (which includes Becke's 1988 exchange functional and Perdew's 1981 local correlational functional)[51] was employed with the def2-TZVP[9] (Fe), 6-311G(d)[52] (C, N, O) and 6-31G(d)[53] (H) basis sets, as this particular method and level of theory was reported by Van Stappen and Lehnert in 2008 to provide appropriate accuracy in modeling iron nitrosyl complexes.[54] Following the protocol reported in this paper, fragments were used to describe the broken symmetry state of the system, treating each $\{Fe(NO)\}^7$ unit as separate fragments of $S = {}^3/_2$ and a charge of +2. To complete the structure, the remaining ligands were provided separate fragments, the bridging oxo (O^{2-}) with S = 0 and a charge of –2 and the $^{t\text{Bu}}(\text{dmx})^{2-}$ with S = 0 and a charge of –2, arriving at an overall neutral state. The resulting optimized structure was found to have good agreement with the crystallographic data for **4**. Furthermore, the predicted ν_{NO} and ^{57}Fe Mössbauer parameters derived from this model were also in good

[51] (a) Becke, A. D. Phys Rev. A 1988, **38**, 3098–3100. (b) Perdew, J. P. *Phys. Rev. B* 1986, **33**, 8822–8824.

[52] Krishnan, R.; Binkley, J. S;. Seeger, R.; People, J. A. *J. Chem. Phys.* 1980, **72**, 650–654 .

[53] Ditchfield, R.; Hehre, W. J.; People, J. A. *J. Chem. Phys.* 1971, **54**, 724–728.

[54] Van Stappen, C.; Lehnert, N. *Inorg. Chem.* **2018**, *57*, 4252–4269.

agreement with the experimental data, in comparison to other methods (**Table 4.3**).

Table 4.3. Calculated bond metrics, vibrational stretching frequencies, and Mössbauer parameters for **4**.

	Optimized structure			Crystallographic / Experimental
	uBP86[a]	**uB3LYP 1**[b]	**uB3LYP 2**[c]	**Data**
N–O (Å)	1.18281, 1.18282	1.17068	1.17360	1.16806(6)
Fe–NO (Å)	1.70193, 1.70201	1.78767	1.79400	1.73707(7)
∠Fe–N–O (Å)	153.562, 153.442	155.736, 155.729	152.25341, 152.25318	164.3898(7)
Fe–O (Å)	1.81903, 1.81911	1.81762	1.82262	1.77478(9)
∠Fe–O–Fe (°)	142.765	148.167	145.12309	166.2166(10)
Fe–Fe (Å)	3.44777	3.49587	3.47770	3.52392(18)
ν_{NO} (cm^{-1})	1705.49, 1729.86	1774.59, 1794.28	1779.09, 1798.27	1730, 1781
δ (mm/s)	0.32, 0.32	0.43, 0.43	0.43, 0.43	0.32
$\lvert\Delta E_Q\rvert$ (mm/s)	0.660, 0.662	0.565, 0.565	0.513, 0.513	1.10

[a] using def2-TZVP (Fe), 6-311G(d) (C, N, O) and 6-31G(d) (H) basis sets ; selected level of theory
[b] using def2-TZVP (Fe, N, O) and def2-SV(P) (C, H) basis sets as a comparison to the theory used for **2**/**3**
[c] using def2-TZVP (Fe), 6-311G(d) (C, N, O) and 6-31G(d) (C, H) basis sets as an intermediate for *a* and *b*

Broken symmetry solutions were used to model the antiferromagnetic coupling present in these complexes. The standard notation BS(*m*,*n*) represents the (*m*+*n*) unpaired electrons within a system and net spin of $^{(m-n)}/_2$ for an antiferromagnetically coupled system.[55] As such, one fragment will bear *m* α electrons while the other bears *n* β electrons. The appropriate description for each case was as high spin iron centers (i.e., high-spin Fe^{II} for **2** and **7**; high spin Fe^{III} for **3**; high spin Fe^{III} antiferromagnetically coupled to NO^- for **4**). The exchange coupling constant *J* was determined from the energy difference between the high-spin and

[55] Kirchner, B.**;** Wenmohs, F.; Ye, S.; Neese, F. *Curr. Opin. Chem. Biol.*2007, **11**, 134–141.

broken-symmetry states, using the spin Hamiltonian in equation 1 and formula in equation 2[56,57,58]:

$$H = -2J\overrightarrow{S_{Fe(1)}} \cdot \overrightarrow{S_{Fe(2)}} \quad (1)$$

$$J = -\frac{E_{HS}-E_{BS}}{S^2_{max}}. \quad (2)$$

Table 4.4. Broken symmetry solution information for **2**, **3**, and **4**.

Complex	Broken symmetry description	E_{HS} - E_{BS} (cm^{-1})	J (cm^{-1})
2	BS(*4*,*4*)	13.437	–0.84
7	BS(*4*,*4*)	48.991	–3.06
3	BS(*5*,*5*)	2535.639	–101.43
4	BS(*3*,*3*)	1923.655	–213.74

[56] Ginsberg, A.P. *J. Am. Chem. Soc.* 1980, **102**, 111–117.

[57] Noodleman, L. *J. Chem. Phys.* 1981, **74**, 5737–5743.

[58] Noodleman, L.; Davidson, E. R. *Chem. Phys.* 1986, **109**, 131–143.

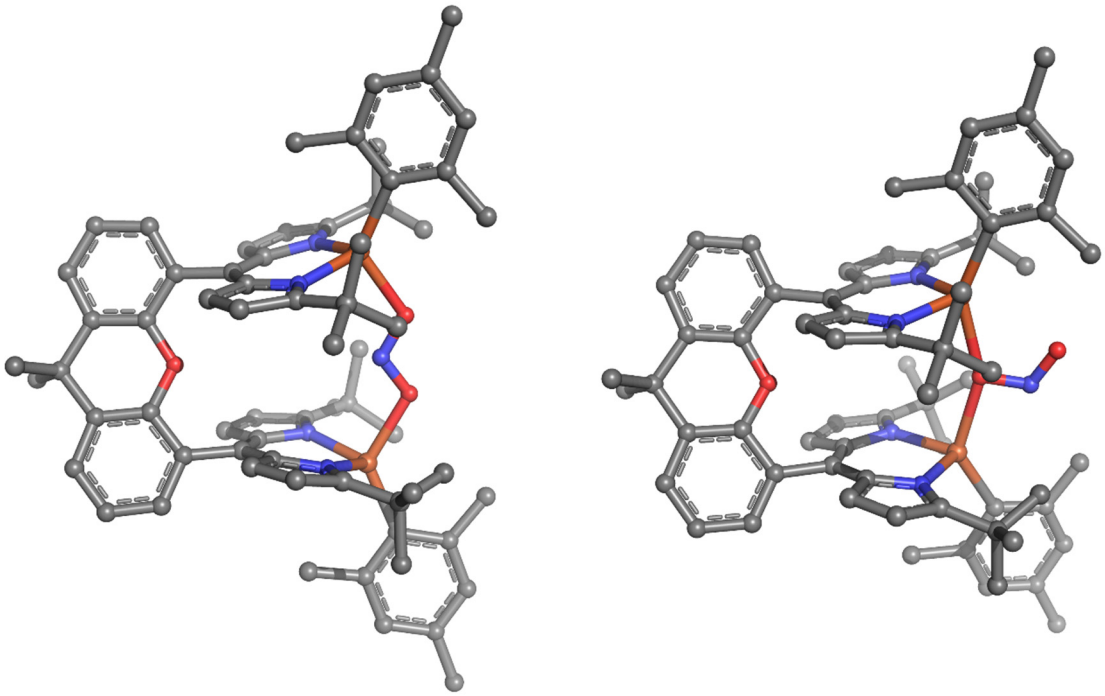

Figure 4.31. Geometry optimized structures of diiron(II) nitrite adducts. (**Left**) [($^{t\text{Bu}}$dmx)Fe$_2$(κ^2-O$_2$N)(Mes)$_2$]$^-$ (**2a**), (**Right**) [($^{t\text{Bu}}$dmx)Fe$_2$(μ-ONO)(Mes)$_2$]$^-$ (**7**). Hydrogen atoms omitted for clarity.

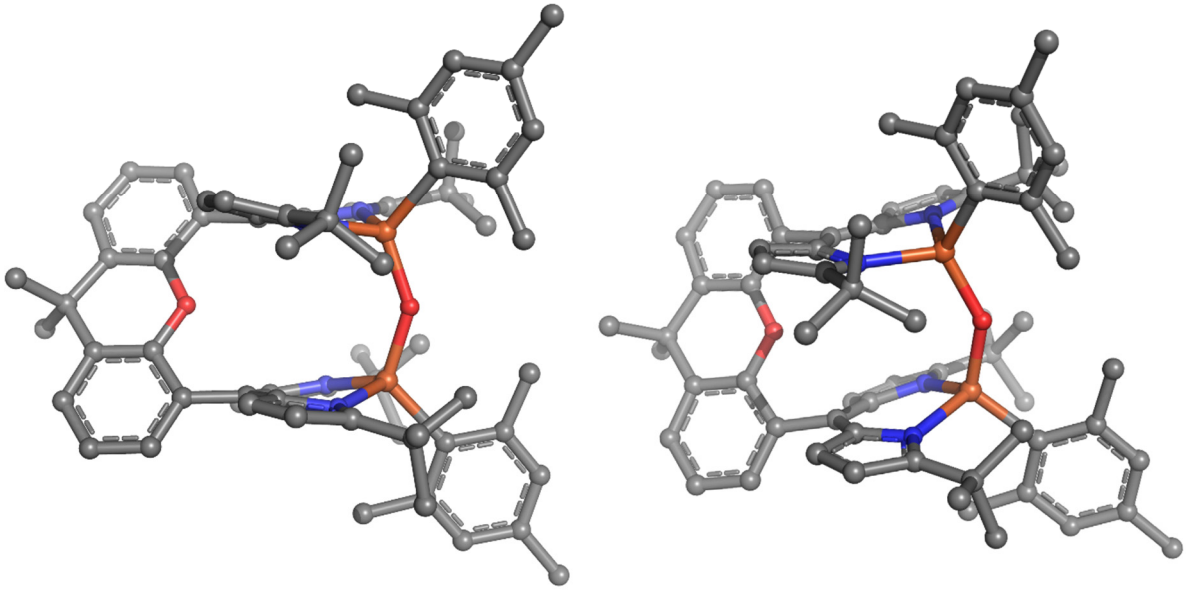

Figure 4.32. Geometry optimized structures of ($^{t\text{Bu}}$dmx)Fe$_2$(μ-O)(Mes)$_2$ (**3**), (**Left**) using uB3LYP functional with def2-TZVP (Fe, N, O) and def2-SV(P) (C, H) basis sets and (**Right**) using uBP86 functional with def2-TZVP (Fe), 6-311G(d) (C, N, O) and 6-31G(d) (H) basis sets. Hydrogen atoms omitted for clarity.

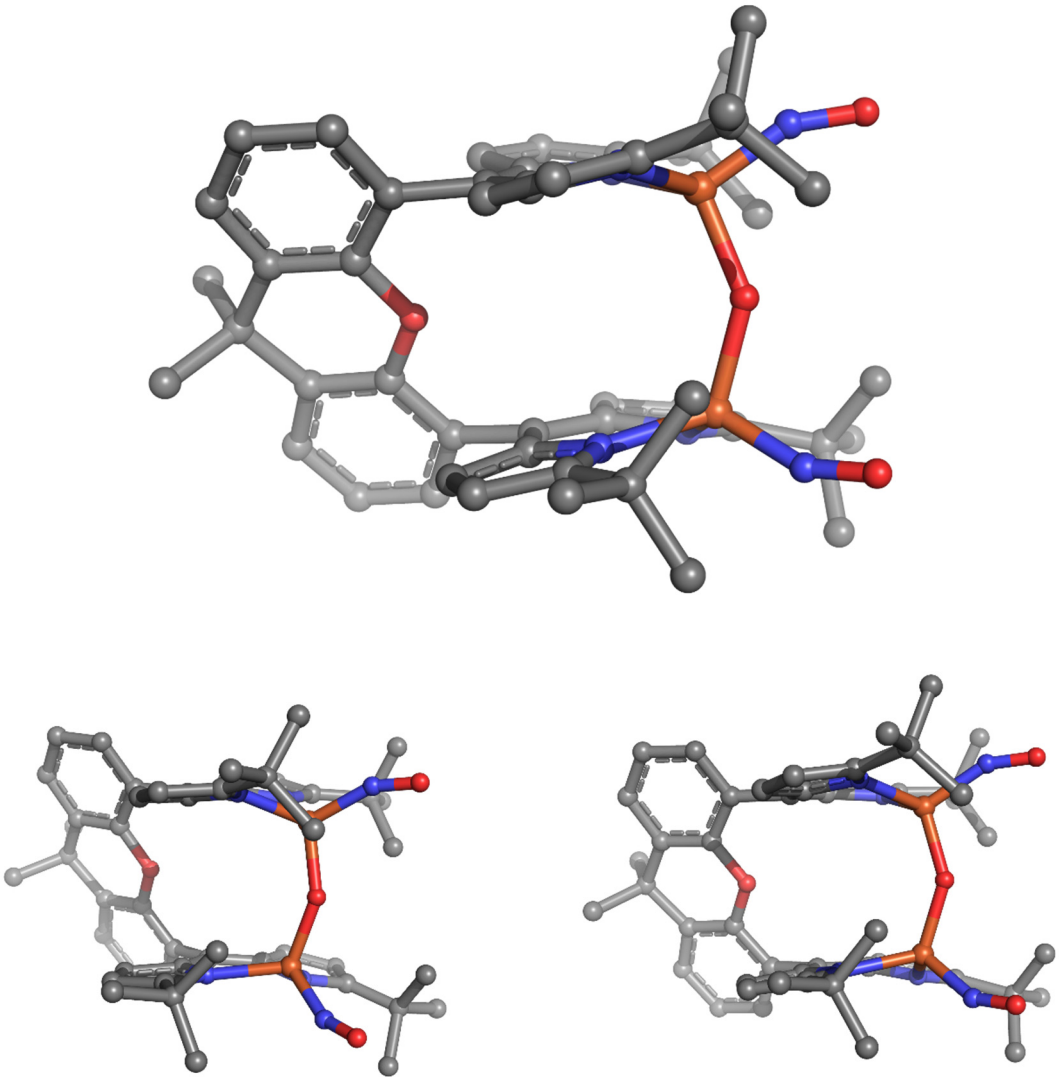

Figure 4.33. Geometry optimized structures of ($^{t\text{Bu}}$dmx)Fe$_2$(μ-O)(NO)$_2$ (**4**), (**Top**) using uBP86 functional with def2-TZVP (Fe), 6-311G(d) (C, N, O) and 6-31G(d) (H) basis sets, (**Left**)) using uB3LYP functional with def2-TZVP (Fe, N, O) and def2-SV(P) (C, H) basis sets, and (**Right**) using uB3LYP functional with def2-TZVP (Fe), 6-311G(d) (C, N, O) and 6-31G(d) (H) basis sets.

Table 4.5. Coordinates of optimized molecular structures for complexes **2**, **3**, **4**, and **7**.

$[(^{t\text{Bu}}\text{dmx})\text{Fe}_2(\kappa^2\text{-ONO})]^-$ (**2**)

E = −5625.83230378 a.u.
G = −5624.659102 a.u.
Charge = –1, Multiplicity = 9

Fe	-2.7737829	-1.2945869	-0.0381536
Fe	2.8253494	-1.3953970	0.3438797
O	-1.0471063	-2.4348805	0.3596647
O	1.0390159	-2.5067908	0.5379193
O	0.1029655	3.4881258	-0.0817951
N	2.2988076	0.2243156	1.5246187
N	-2.1577398	0.1508469	-1.3832435
N	-2.7572369	-0.0887064	1.6504576
N	2.4995390	-0.4730283	-1.4878232
N	0.0287407	-1.7985573	0.3072732
C	2.2430454	0.3864515	2.8588276
C	1.2458259	4.1046599	-0.5096194
C	-2.4017157	1.8425773	2.8414020
H	-2.1467902	2.8744062	3.0749616
C	2.2840835	1.7869008	-0.4319816
C	4.7512102	-2.1543489	0.4958427
C	2.3306729	3.2469591	-0.7691683
C	-2.4211093	1.2652480	1.5334861
C	2.3334664	1.4979089	0.9455518
C	2.2787673	1.7768659	3.1883701
H	2.2486038	2.2027610	4.1891098
C	-2.7443000	0.8374321	3.7293475
H	-2.8230665	0.9222618	4.8110012
C	1.3383446	5.4920099	-0.6769197
C	7.1672878	-1.7765418	0.2164407
H	7.9919857	-1.0927256	-0.0213753
C	5.0580448	-3.4972254	0.8196407
C	2.2699650	0.9067151	-1.5295662
C	-2.1168834	1.4922745	-0.9849646
C	-6.1470974	-4.0051593	-0.9190031
H	-6.2963717	-5.0813774	-1.0716443
C	0.1982593	6.4271706	-0.2703623
C	7.4600299	-3.1143800	0.5240488
C	-4.6187518	-2.1358655	-0.4648349
C	-2.9776000	-0.3404114	2.9537698
C	-5.7477594	-1.2748363	-0.5425293
C	2.3465912	2.4712412	1.9935404
H	2.3866658	3.5508781	1.8619699
C	-2.1767944	3.4682831	0.4656750
C	6.3881059	-3.9587303	0.8245518
H	6.5921336	-5.0088044	1.0693777
C	-3.5376438	-1.6478552	3.4949339
C	2.0337314	-0.7456732	3.8515362
C	3.5111281	3.7964755	-1.2768801
H	4.3520116	3.1300551	-1.4853161
C	5.8498348	-1.2997484	0.2005355
C	-2.2077074	1.9743685	0.3350274
C	-4.8512242	-3.5162109	-0.6725231
C	2.0836845	1.2957419	-2.8927323
H	1.8616454	2.3034975	-3.2385458
C	2.4943113	-0.9242440	-2.7540812
C	-3.2919360	-1.7380874	5.0135013
H	-2.2155364	-1.6697688	5.2491887
H	-3.6671338	-2.7038945	5.3955038
H	-3.8166101	-0.9380011	5.5627411
C	-1.9617443	2.3049257	-2.1520076
H	-1.9020930	3.3912194	-2.1717987
C	-5.5765381	0.2204851	-0.3632940
H	-5.1441032	0.4594321	0.6246554
H	-6.5367891	0.7572996	-0.4564723
H	-4.8788987	0.6368533	-1.1119777
C	-1.0345230	5.6202678	0.1412859
C	-7.2544084	-3.1532273	-0.9786778

C	-1.0234113	4.2201202	0.1707018	H	-2.8962565	-4.2176388	-0.0025193
C	-7.0305336	-1.7806704	-0.7933456	H	-3.2486373	-4.5571992	-1.7027966
H	-7.8823040	-1.0909841	-0.8460790	C	2.4749122	-0.3046305	5.2605524
C	2.5461277	6.0050908	-1.1761564	H	3.5376217	-0.0038555	5.2727228
H	2.6513304	7.0835813	-1.3168162	H	2.3461482	-1.1400489	5.9713927
C	-2.9062137	-2.8789301	2.8263981	H	1.8730507	0.5418305	5.6320805
H	-3.1646032	-2.9280154	1.7575630	C	-3.3468725	4.1522734	0.8102174
H	-3.2960863	-3.8000438	3.2947130	H	-4.2434154	3.5728184	1.0438324
H	-1.8086874	-2.8740049	2.9165815	C	-2.0629033	-1.1442652	-3.5641251
C	-2.0198879	0.1199632	-2.7211367	C	2.9050030	-2.3298572	-3.1697580
C	-1.3449395	-0.8985132	-4.9059139	C	0.5215772	-1.0710928	3.8821376
H	-1.8631970	-0.1375572	-5.5139090	H	-0.0719320	-0.1891167	4.1762281
H	-1.3211583	-1.8331827	-5.4937870	H	0.3168681	-1.8855635	4.6017873
H	-0.3061220	-0.5649792	-4.7431507	H	0.1659295	-1.3874368	2.8896788
C	-1.8925709	1.4473244	-3.2346094	C	8.8868749	-3.6106815	0.5355369
H	-1.7590387	1.7239410	-4.2782034	H	9.3999476	-3.3944690	-0.4201475
C	3.9745786	-4.4842989	1.2068162	H	8.9339776	-4.7002094	0.7053854
H	3.8543493	-4.5292492	2.3063910	H	9.4801101	-3.1223006	1.3322508
H	4.2140521	-5.5079746	0.8661248	C	2.8180493	-2.0102397	3.4706279
H	2.9929989	-4.2056613	0.7926998	H	2.4594069	-2.4431424	2.5248001
C	-5.0623501	-1.6617002	3.2308986	H	2.6809361	-2.7837624	4.2469838
H	-5.5506907	-0.7904055	3.7023724	H	3.8953726	-1.8066712	3.3615900
H	-5.5141108	-2.5801221	3.6499769	C	2.4527469	-3.4034240	-2.1687801
H	-5.2708476	-1.6379373	2.1488605	H	2.9396138	-3.2677841	-1.1911335
C	2.2148812	0.1495567	-3.6580759	H	2.7454790	-4.4025433	-2.5366738
H	2.1353081	0.0757123	-4.7406178	H	1.3622364	-3.3927030	-2.0187752
C	3.6202185	5.1732008	-1.4900830	C	-2.2312923	6.2665577	0.4889222
H	4.5480594	5.5984391	-1.8820249	H	-2.2688486	7.3586887	0.4886469
C	5.6082072	0.1529165	-0.1590140	C	4.4502549	-2.3562460	-3.2633589
H	5.0582134	0.2422424	-1.1130763	H	4.8117155	-1.6059463	-3.9886232
H	6.5542786	0.7137189	-0.2575514	H	4.7963621	-3.3531693	-3.5943816
H	4.9882810	0.6611331	0.6003829	H	4.9031825	-2.1413965	-2.2814397
C	-3.7034768	-4.5052038	-0.6948423	C	-3.3755899	5.5489022	0.8341599
H	-4.0356854	-5.5265995	-0.4362928	H	-4.2943539	6.0764815	1.1040952

C	2.3125792	-2.6702884	-4.5514183
H	1.2111631	-2.6059456	-4.5421384
H	2.5944549	-3.6998928	-4.8345710
H	2.6893171	-1.9956600	-5.3386837
C	0.6688088	7.2871125	0.9284570
H	0.9374006	6.6435189	1.7836133
H	-0.1274552	7.9791018	1.2529288
H	1.5535750	7.8884509	0.6573761
C	-0.1716670	7.3450938	-1.4596308
H	0.6926358	7.9526402	-1.7758995
H	-0.9822909	8.0410031	-1.1867322
H	-0.5071002	6.7446305	-2.3224728
C	-1.3672170	-2.3113726	-2.8480388
H	-0.3455964	-2.0343041	-2.5436396
H	-1.3126609	-3.1894321	-3.5155824
H	-1.9169025	-2.6237009	-1.9471899
C	-3.5378555	-1.5127211	-3.8444618
H	-4.0789900	-1.7086207	-2.9044212
H	-3.5910474	-2.4206797	-4.4740592
H	-4.0508065	-0.6928622	-4.3779973
C	-8.6485874	-3.6859569	-1.2119838
H	-9.2100046	-3.0548974	-1.9247980
H	-9.2360470	-3.7079166	-0.2733110
H	-8.6272852	-4.7152061	-1.6102886

($^{t\text{Bu}}$dmx)Fe$_2$(μ-O)(Mes)$_2$ (**3**)

Functional: uB3LYP

Basis sets: def2-TZVP (Fe, N, O) and def2-SV(P) (C, H)

E = −5495.73542531 a.u.

G = −5494.561818 a.u.

Charge = 0, Multiplicity = 11

Fe	-1.1611807	1.7416850	0.0732399
O	3.6096899	0.0000608	-0.0000759
O	-1.7233635	-0.0000046	0.0001607
N	-0.2996560	1.9992835	1.9059336
N	0.4808861	2.1055651	-1.0711780
C	7.4358478	0.7812566	-0.9976239
C	6.5478027	0.0000678	-0.0000932
C	5.6755732	0.9992724	0.7676056
C	6.2418499	2.0141413	1.5565204
C	5.4515468	2.9647666	2.2045132
C	4.0617338	2.9430262	2.0469955
C	3.4593391	1.9547151	1.2642828
C	4.2820638	0.9742136	0.6740051
C	2.0005937	1.9753962	0.9315231
C	1.0909645	1.8218742	1.9928425
C	1.4277026	1.6123529	3.3616026
C	0.2508982	1.7059017	4.0872864
C	-0.8028895	1.9556255	3.1606258
C	-2.2454337	2.2678224	3.5373758
C	-3.2761074	1.5513194	2.6480956
C	-2.4464294	3.7970614	3.4061027
C	-2.5028089	1.8604451	5.0012582
C	1.7231338	2.2199908	-0.4288981
C	2.6839997	2.6453855	-1.3915786
C	2.0203045	2.7819143	-2.5974173
C	0.6590242	2.4310844	-2.3736247
C	-0.4148365	2.4630084	-3.4470095
C	0.2089276	2.0690635	-4.8039047
C	-0.9809928	3.8979279	-3.5571968
C	-1.5473829	1.4808696	-3.1417542
C	-2.4881058	3.2859250	-0.2906076
C	-2.0090605	4.6200384	-0.1685094
C	-0.5710227	4.9247287	0.1953090
C	-2.8666553	5.6974447	-0.4194516
C	-4.2031048	5.5070544	-0.8039359
C	-5.1037667	6.6901264	-1.0627432
C	-4.6642182	4.1950492	-0.9285473
C	-3.8329021	3.0897232	-0.6750955

C	-4.4403173	1.7109215	-0.8237502	H	-5.2715102	7.2752679	-0.1389279
H	-5.7040450	4.0209553	-1.2296189	H	-4.6580844	7.3810067	-1.8017125
H	-2.4829944	6.7193822	-0.3185847	H	-6.0892227	6.3727741	-1.4433406
H	7.3282992	2.0675264	1.6624782	H	-3.6973638	0.9123754	-0.6898215
H	5.9214326	3.7418368	2.8129467	H	-5.2400742	1.5506376	-0.0761942
H	3.4366467	3.7124045	2.5064851	H	-4.9035870	1.5883312	-1.8200369
H	8.0868832	1.4974835	-0.4684865	N	-0.2996776	-1.9991782	-1.9058799
H	8.0846456	0.0955309	-1.5686102	N	0.4809316	-2.1055974	1.0712276
H	6.8116985	1.3438011	-1.7127580	C	7.4359813	-0.7810664	0.9973619
H	2.4292227	1.4270203	3.7436803	C	5.6755699	-0.9991882	-0.7677203
H	0.1438362	1.6090447	5.1644312	C	6.2418397	-2.0140900	-1.5565970
H	-3.1690548	1.8370482	1.5937419	C	5.4515312	-2.9647535	-2.2045275
H	-3.1924706	0.4584801	2.7148794	C	4.0617215	-2.9430211	-2.0469777
H	-4.2939162	1.8445214	2.9588432	C	3.4593350	-1.9546763	-1.2643013
H	-1.7094616	4.3453335	4.0187963	C	4.2820624	-0.9741331	-0.6740993
H	-2.3440956	4.1207485	2.3590027	C	2.0005974	-1.9753523	-0.9315023
H	-3.4588601	4.0730724	3.7526518	C	1.0909504	-1.8218308	-1.9928086
H	-2.3001116	0.7878123	5.1624649	C	1.4276853	-1.6123374	-3.3615726
H	-1.8818502	2.4403791	5.7046945	C	0.2508692	-1.7058291	-4.0872433
H	-3.5597122	2.0506584	5.2558438	C	-0.8029228	-1.9554768	-3.1605704
H	3.7364394	2.8373462	-1.1944707	C	-2.2454963	-2.2675377	-3.5373170
H	2.4502371	3.0950337	-3.5460292	C	-3.2760922	-1.5507508	-2.6481769
H	0.9625802	2.7999869	-5.1415222	C	-2.4467045	-3.7967306	-3.4058453
H	0.6841389	1.0751452	-4.7467965	C	-2.5027714	-1.8603258	-5.0012639
H	-0.5814332	2.0294230	-5.5741315	C	1.7231761	-2.2199513	0.4289248
H	-1.4809401	4.2006727	-2.6244583	C	2.6840780	-2.6453191	1.3915832
H	-0.1782108	4.6232088	-3.7774678	C	2.0203992	-2.7819550	2.5974150
H	-1.7222898	3.9446619	-4.3758753	C	0.6590990	-2.4311760	2.3736548
H	-1.1548530	0.4667402	-2.9941039	C	-0.4147606	-2.4633271	3.4470341
H	-2.1078118	1.7709046	-2.2429829	C	0.2090491	-2.0698736	4.8040473
H	-2.2671583	1.4644692	-3.9775018	C	-0.9810493	-3.8982304	3.5567757
H	-0.2273012	4.3233292	1.0522377	C	-1.5472171	-1.4809857	3.1421012
H	0.1089297	4.6962062	-0.6444948	H	7.3282874	-2.0674681	-1.6625768
H	-0.4436142	5.9901701	0.4499234	H	5.9214109	-3.7418472	-2.8129357

H	3.4366318	-3.7124305	-2.5064118
H	8.0870156	-1.4972535	0.4681700
H	8.0847886	-0.0953027	1.5682910
H	6.8119275	-1.3436481	1.7125500
H	2.4292108	-1.4270574	-3.7436620
H	0.1437971	-1.6089504	-5.1643853
H	-3.1691130	-1.8363213	-1.5937739
H	-3.1922914	-0.4579344	-2.7151389
H	-4.2939365	-1.8438536	-2.9589021
H	-1.7098043	-4.3451817	-4.0184599
H	-2.3444292	-4.1202994	-2.3587034
H	-3.4591687	-4.0726454	-3.7523727
H	-2.2999083	-0.7877469	-5.1626184
H	-1.8818805	-2.4404526	-5.7046011
H	-3.5596961	-2.0504164	-5.2558519
H	3.7365219	-2.8372344	1.1944552
H	2.4503527	-3.0951181	3.5460026
H	0.9626293	-2.8009792	5.1414311
H	0.6843616	-1.0759859	4.7472520
H	-0.5813027	-2.0303976	5.5742917
H	-1.4810599	-4.2006261	2.6239570
H	-0.1783283	-4.6236575	3.7767856
H	-1.7223227	-3.9451549	4.3754653
H	-1.1545863	-0.4668526	2.9947480
H	-2.1077008	-1.7706830	2.2432550
H	-2.2669666	-1.4647693	3.9778745
Fe	-1.1611651	-1.7416851	-0.0731515
C	-2.4880462	-3.2859641	0.2906600
C	-2.0089777	-4.6200656	0.1684974
C	-0.5709291	-4.9247172	-0.1953053
C	-2.8665697	-5.6974974	0.4193383
C	-4.2030405	-5.5071475	0.8037693
C	-5.1037052	-6.6902476	1.0624402
C	-4.6641734	-4.1951572	0.9284554
C	-3.8328559	-3.0898042	0.6751268
C	-4.4402795	-1.7110219	0.8239356
H	-5.7040157	-4.0210984	1.2294947
H	-2.4828945	-6.7194245	0.3184205
H	-0.2272265	-4.3233248	-1.0522473
H	0.1090151	-4.6961528	0.6444933
H	-0.4434856	-5.9901598	-0.4498970
H	-5.2714060	-7.2753128	0.1385687
H	-4.6580489	-7.3811871	1.8013699
H	-6.0891795	-6.3729345	1.4430228
H	-3.6974039	-0.9124451	0.6897664
H	-5.2402983	-1.5507947	0.0766501
H	-4.9032156	-1.5884267	1.8203801

($^{t\mathrm{Bu}}$dmx)Fe_2(μ-O)$(Mes)_2$ (**3**)

Functional: uBP86

Basis sets: def2-TZVP (Fe), 6-311G(d) (C, N, O) and 6-31G(d) (H)

E = −5498.48849601 a.u.

G = −5497.355640 a.u.

Charge = 0, Multiplicity = 11

Fe	-1.1763848	1.7391817	0.0862986
O	3.5943442	-0.0000142	0.0000092
O	-1.8033025	0.0000281	0.0000295
N	-0.3174511	1.9665148	1.9132000
N	0.4690920	2.0550976	-1.0470920
C	7.4379733	0.7983955	-0.9866875
C	6.5482222	-0.0000491	0.0000029
C	5.6750343	0.9878416	0.7841381
C	6.2399482	1.9935151	1.5906014
C	5.4456139	2.9347180	2.2547806
C	4.0527618	2.9152538	2.0969851
C	3.4513124	1.9362362	1.2964801
C	4.2784716	0.9639183	0.6923659
C	1.9941293	1.9459301	0.9594851
C	1.0775071	1.7816716	2.0155278

C	1.4049841	1.5696163	3.3897635	H	-3.1703159	1.7754931	1.5865008
C	0.2195416	1.6703614	4.1100396	H	-3.2401625	0.4286886	2.7520684
C	-0.8330198	1.9220520	3.1782288	H	-4.3222345	1.8441507	2.9368665
C	-2.2751108	2.2478505	3.5377676	H	-1.7327996	4.3357494	3.9857762
C	-3.3042567	1.5223066	2.6498024	H	-2.3528258	4.0795683	2.3209911
C	-2.4665962	3.7789348	3.3754038	H	-3.4828761	4.0627390	3.7067350
C	-2.5468461	1.8663073	5.0085125	H	-2.3625121	0.7915120	5.1863124
C	1.7162885	2.1894276	-0.4029587	H	-1.9204948	2.4495870	5.7067935
C	2.6702493	2.6541954	-1.3596928	H	-3.6034464	2.0775641	5.2510295
C	2.0022794	2.7961691	-2.5674508	H	3.7207619	2.8663294	-1.1562139
C	0.6445825	2.4112137	-2.3562228	H	2.4292145	3.1356654	-3.5119095
C	-0.4303767	2.4406966	-3.4264992	H	0.9590224	2.7674248	-5.1178915
C	0.1940376	2.0439531	-4.7857313	H	0.6546095	1.0422775	-4.7287345
C	-0.9980727	3.8789600	-3.5375155	H	-0.5974838	2.0190503	-5.5567275
C	-1.5656707	1.4599200	-3.1179259	H	-1.5004185	4.1798417	-2.6032543
C	-2.4611748	3.2857246	-0.2771198	H	-0.1954384	4.6056288	-3.7583829
C	-1.9464854	4.6128511	-0.1608137	H	-1.7391523	3.9206969	-4.3576999
C	-0.5044491	4.8839337	0.2146067	H	-1.1740993	0.4428362	-2.9688491
C	-2.7772603	5.7104915	-0.4293125	H	-2.1248728	1.7557219	-2.2156539
C	-4.1168975	5.5476296	-0.8269078	H	-2.2847369	1.4446809	-3.9574293
C	-4.9866176	6.7500549	-1.1097121	H	-0.1862117	4.2774051	1.0805798
C	-4.6136724	4.2434583	-0.9433591	H	0.1770689	4.6311628	-0.6193920
C	-3.8128983	3.1180434	-0.6702525	H	-0.3537699	5.9491702	0.4618878
C	-4.4481390	1.7493897	-0.8053059	H	-5.1477209	7.3499544	-0.1938377
H	-5.6580401	4.0943044	-1.2538962	H	-4.5160898	7.4196407	-1.8534986
H	-2.3680516	6.7266429	-0.3350636	H	-5.9760367	6.4507253	-1.4958521
H	7.3296841	2.0470705	1.6961101	H	-3.7104322	0.9382189	-0.6915994
H	5.9154157	3.7046304	2.8758973	H	-5.2274750	1.6022495	-0.0325151
H	3.4241967	3.6804520	2.5649558	H	-4.9439501	1.6382622	-1.7878535
H	8.0889083	1.5050057	-0.4427034	N	-0.3175036	-1.9664562	-1.9131993
H	8.0867097	0.1185411	-1.5664676	N	0.4690421	-2.0551100	1.0470929
H	6.8141418	1.3725514	-1.6935696	C	7.4379321	-0.7985274	0.9867046
H	2.4062658	1.3819674	3.7794116	C	5.6750072	-0.9879093	-0.7841410
H	0.1058441	1.5765320	5.1901556	C	6.2398949	-1.9935861	-1.5906181

C	5.4455370	-2.9347637	-2.2548045	H	-3.4828818	-4.0626984	-3.7068537
C	4.0526860	-2.9152701	-2.0970024	H	-2.3625870	-0.7913788	-5.1862587
C	3.4512613	-1.9362492	-1.2964823	H	-1.9205052	-2.4494130	-5.7068160
C	4.2784452	-0.9639569	-0.6923595	H	-3.6034762	-2.0774707	-5.2510551
C	1.9940781	-1.9459193	-0.9594853	H	3.7206938	-2.8664259	1.1561780
C	1.0774564	-1.7816213	-2.0155238	H	2.4291420	-3.1358307	3.5118615
C	1.4049324	-1.5695292	-3.3897535	H	0.9589714	-2.7677525	5.1178360
C	0.2194895	-1.6702585	-4.1100322	H	0.6546304	-1.0425582	4.7288374
C	-0.8330710	-1.9219801	-3.1782293	H	-0.5974980	-2.0193502	5.5567554
C	-2.2751551	-2.2477954	-3.5377857	H	-1.5005551	-4.1798456	2.6031107
C	-3.3043275	-1.5223154	-2.6497977	H	-0.1955742	-4.6057854	3.7581833
C	-2.4666109	-3.7788907	-3.3754980	H	-1.7392505	-3.9208404	4.3575814
C	-2.5468862	-1.8661896	-5.0085145	H	-1.1740876	-0.4428864	2.9690100
C	1.7162344	-2.1894505	0.4029511	H	-2.1249193	-1.7556794	2.2157272
C	2.6701869	-2.6542732	1.3596667	H	-2.2847432	-1.4447711	3.9575289
C	2.0022146	-2.7962822	2.5674180	Fe	-1.1764300	-1.7391399	-0.0862919
C	0.6445258	-2.4112860	2.3562088	C	-2.4612417	-3.2856653	0.2771154
C	-0.4304297	-2.4408140	3.4264887	C	-1.9465480	-4.6127934	0.1608526
C	0.1940145	-2.0442178	4.7857490	C	-0.5044992	-4.8838796	-0.2145177
C	-0.9981814	-3.8790643	3.5373893	C	-2.7773214	-5.7104287	0.4293773
C	-1.5656914	-1.4599681	3.1180125	C	-4.1169647	-5.5475589	0.8269479
H	7.3296292	-2.0471649	-1.6961321	C	-4.9866847	-6.7499780	1.1097789
H	5.9153189	-3.7046793	-2.8759324	C	-4.6137458	-4.2433856	0.9433517
H	3.4241019	-3.6804489	-2.5649793	C	-3.8129714	-3.1179758	0.6702262
H	8.0888470	-1.5051617	0.4427275	C	-4.4482225	-1.7493212	0.8052229
H	8.0866856	-0.1186962	1.5664931	H	-5.6581191	-4.0942268	1.2538674
H	6.8140699	-1.3726601	1.6935786	H	-2.3681060	-6.7265815	0.3351718
H	2.4062138	-1.3818701	-3.7793975	H	-0.1862378	-4.2773693	-1.0804944
H	0.1057920	-1.5764090	-5.1901466	H	0.1769930	-4.6310872	0.6194962
H	-3.1703904	-1.7755433	-1.5865056	H	-0.3538090	-5.9491213	-0.4617701
H	-3.2402640	-0.4286914	-2.7520158	H	-5.1477801	-7.3499027	0.1939196
H	-4.3222943	-1.8441753	-2.9368827	H	-4.5161612	-7.4195429	1.8535869
H	-1.7327968	-4.3356599	-3.9858909	H	-5.9761072	-6.4506398	1.4959033
H	-2.3528464	-4.0795751	-2.3210996	H	-3.7105087	-0.9381495	0.6915709

H	-5.2274934	-1.6021839	0.0323658
H	-4.9441159	-1.6381900	1.7877283

[($^{t\text{Bu}}$dmx)Fe_2(μ-O)$(NO)_2$] (**4**)
Functional: uBP86
Basis sets: def2-TZVP (Fe), 6-311G(d) (C, N, O) and 6-31G(d) (H)
E = −5059.15791416 a.u.
G = −5058.324553 a.u.
Charge = 0, Multiplicity = 7

Fe	1.8494589	0.8733861	-1.4859536
O	-2.8970049	0.0071545	0.0108307
N	1.0171616	2.6249481	-0.9676257
N	0.2446711	0.0786577	-2.3831744
O	4.3819146	0.7692669	-2.7010535
O	2.4271853	0.0043552	0.0039784
N	3.2431691	0.9763353	-2.4573118
C	-0.3686654	2.6279257	-0.7106761
C	-2.7527021	2.0430143	-1.1173622
C	-3.5810582	1.0633323	-0.5281094
C	-1.0237555	0.6351466	-2.1286243
C	-1.3121733	-1.0954322	-3.5668547
H	-1.7463512	-1.8388664	-4.2357626
C	1.5437613	3.7530477	-0.4074230
C	0.0713209	-0.9637077	-3.2488768
C	1.2009537	-1.7861922	-3.8389780
C	-0.6759977	3.7742543	0.0856714
H	-1.6673144	4.0408978	0.4543115
C	-1.2982640	1.7468156	-1.3004257
C	-1.9931784	-0.0995091	-2.8802534
H	-3.0640861	0.1055028	-2.9095599
C	-4.9776471	1.1538904	-0.5099844
C	2.9864173	4.1940045	-0.5980702
C	-5.8495397	0.0011110	0.0037360
C	-5.5424657	2.3335871	-1.0294133
H	-6.6320655	2.4528122	-1.0274363
C	3.2149469	5.5591913	0.0837176
H	2.5621877	6.3420598	-0.3425506
H	4.2636504	5.8724309	-0.0657364
H	3.0308435	5.5020408	1.1718046
C	0.5125853	4.4764264	0.2640841
H	0.6397929	5.4136882	0.8066132
C	3.2426370	4.3619334	-2.1174869
H	3.0755206	3.4202854	-2.6639089
H	4.2855290	4.6857467	-2.2890028
H	2.5658959	5.1262562	-2.5403653
C	-3.3548678	3.2045968	-1.6181865
H	-2.7277424	3.9702035	-2.0872841
C	2.1799006	-2.2531159	-2.7467532
H	2.5986737	-1.4235492	-2.1550886
H	3.0215009	-2.8002168	-3.2099116
H	1.6686383	-2.9272202	-2.0390812
C	3.9920009	3.1881746	0.0108796
H	3.9565060	3.2251935	1.1121317
H	5.0168681	3.4492730	-0.3099670
H	3.7883650	2.1472273	-0.2851899
C	-4.7471813	3.3561359	-1.5583104
H	-5.2160546	4.2630961	-1.9544092
C	1.9284192	-0.9315950	-4.9078963
H	1.2381579	-0.6752053	-5.7317693
H	2.7796862	-1.4977942	-5.3290278
H	2.3124227	0.0088371	-4.4816637
C	0.6347296	-3.0472778	-4.5267212
H	0.0646686	-3.6683624	-3.8124017
H	1.4691702	-3.6549216	-4.9203852
H	-0.0234580	-2.7925674	-5.3763099
C	-6.7663242	-0.4826014	-1.1482481
H	-7.4182957	0.3357103	-1.5004703
H	-7.4161167	-1.3089264	-0.8107499
H	-6.1628994	-0.8392804	-2.0009897

N	1.0220600	-2.6200868	0.9651794
N	0.2313321	-0.0845171	2.3885139
C	-0.3611574	-2.6243206	0.6943473
C	-2.7501279	-2.0531033	1.0947867
C	-3.5791147	-1.0648586	0.5203131
C	-1.0315126	-0.6535126	2.1343011
C	-1.3334900	1.0555214	3.5950594
H	-1.7732226	1.7858066	4.2747639
C	1.5569966	-3.7423779	0.4013916
C	0.0493650	0.9467461	3.2657261
C	1.1705489	1.7843169	3.8507000
C	-0.6574132	-3.7636522	-0.1160945
H	-1.6440489	-4.0289903	-0.4979691
C	-1.2980042	-1.7550682	1.2901754
C	-2.0057569	0.0591581	2.9004943
H	-3.0738388	-0.1599221	2.9327525
C	-4.9750916	-1.1626682	0.4879975
C	2.9986007	-4.1813829	0.6046196
C	-5.5379890	-2.3546179	0.9808473
H	-6.6271149	-2.4778048	0.9709865
C	3.2355967	-5.5449649	-0.0774306
H	2.5792426	-6.3292986	0.3405570
H	4.2830624	-5.8573727	0.0821312
H	3.0627293	-5.4859311	-1.1672625
C	0.5345230	-4.4622059	-0.2871588
H	0.6693999	-5.3948297	-0.8358317
C	3.2409247	-4.3514114	2.1260613
H	3.0687120	-3.4104815	2.6721617
H	4.2822863	-4.6752651	2.3065431
H	2.5605105	-5.1164059	2.5417621
C	-3.3506504	-3.2269716	1.5683919
H	-2.7232504	-3.9990027	2.0264463
C	2.1389986	2.2625726	2.7538874
H	2.5719417	1.4370367	2.1666414
H	2.9716318	2.8265732	3.2129499
H	1.6158066	2.9241826	2.0428628
C	4.0084766	-3.1726815	0.0072839
H	3.9868286	-3.2102923	-1.0942976
H	5.0301434	-3.4303986	0.3408121
H	3.7976691	-2.1323326	0.3003549
C	-4.7417697	-3.3834320	1.4960696
H	-5.2092948	-4.2995484	1.8721807
C	1.9136770	0.9409953	4.9177583
H	1.2304791	0.6773861	5.7452214
H	2.7597080	1.5185317	5.3340588
H	2.3074793	0.0046970	4.4914001
C	0.5905009	3.0388254	4.5391441
H	0.0096917	3.6515850	3.8263243
H	1.4184537	3.6576571	4.9290880
H	-0.0610573	2.7766870	5.3915604
C	-6.7123391	0.4980917	1.1920708
H	-7.3601414	-0.3120185	1.5706243
H	-7.3616969	1.3349195	0.8798191
H	-6.0694408	0.8455801	2.0194821
Fe	1.8434562	-0.8652705	1.4913161
O	4.3712036	-0.7511849	2.7139724
N	3.2338335	-0.9633034	2.4680935

[($^{t\text{Bu}}$dmx)Fe$_2$(μ-O)(NO)$_2$] (**4**)
Functional: uB3LYP
Basis sets: def2-TZVP (Fe, N, O) and def2-SV(P) (C, H)
E = −5057.02899816 a.u.
G = −5056.166398 a.u
Charge = 0, Multiplicity = 7

Fe	-1.8587950	-0.9454093	-1.4700673
O	2.8910298	-0.0000217	0.0001915
N	-1.0040668	-2.7069777	-0.9062901
N	-0.2533930	-0.2121070	-2.4802549
O	-4.3999188	-1.0705046	-2.8517869

O	-2.3570850	-0.0003793	0.0004293	H	-2.6785477	1.2795373	-2.3755206
N	-3.2785430	-1.1742075	-2.5320176	H	-2.9824742	2.6959371	-3.4021601
C	0.3779140	-2.6704252	-0.6655009	H	-1.6596211	2.7187060	-2.1957955
C	2.7478515	-2.0652234	-1.0811291	C	-3.9631809	-3.2164686	0.1178441
C	3.5653427	-1.0679577	-0.5127163	H	-3.9023541	-3.1281553	1.2131748
C	1.0109346	-0.7412717	-2.1818282	H	-4.9880545	-3.5316481	-0.1450523
C	1.2989704	0.9173549	-3.6923396	H	-3.7992127	-2.2113457	-0.2972259
H	1.7304025	1.6303781	-4.3901871	C	4.7433125	-3.3859771	-1.4746086
C	-1.5086587	-3.7819354	-0.2626473	H	5.2149527	-4.3008061	-1.8426579
C	-0.0833428	0.7809840	-3.3808284	C	-1.9448565	0.6967870	-5.0379790
C	-1.2117489	1.5829051	-4.0051440	H	-1.2571881	0.3963326	-5.8476784
C	0.7056352	-3.7493182	0.2075951	H	-2.7880248	1.2520698	-5.4872703
H	1.7002814	-3.9767848	0.5849884	H	-2.3426057	-0.2197424	-4.5759364
C	1.2907413	-1.8006448	-1.2929216	C	-0.6416501	2.8132081	-4.7377362
C	1.9803075	-0.0311370	-2.9503082	H	-0.0704029	3.4592547	-4.0487360
H	3.0511153	-0.2223208	-2.9551236	H	-1.4700770	3.4092059	-5.1585268
C	4.9592669	-1.1627384	-0.4823924	H	0.0187887	2.5249659	-5.5727799
C	-2.9484327	-4.2549615	-0.4058458	C	6.7214751	0.4724073	-1.1741289
C	5.8313434	0.0001975	0.0002018	H	7.3720253	-0.3445945	-1.5291904
C	5.5295245	-2.3512523	-0.9666521	H	7.3709622	1.3089362	-0.8651779
H	6.6159642	-2.4684703	-0.9530773	H	6.0987587	0.8112696	-2.0196581
C	-3.1570912	-5.5563895	0.3909325	N	-1.0046139	2.7067199	0.9063640
H	-2.5003316	-6.3658498	0.0290609	N	-0.2523420	0.2124258	2.4803712
H	-4.2024057	-5.8938435	0.2816206	C	0.3772306	2.6704821	0.6647071
H	-2.9616683	-5.4056846	1.4666170	C	2.7476022	2.0662347	1.0795042
C	-0.4692856	-4.4450676	0.4516459	C	3.5651891	1.0686678	0.5117333
H	-0.5813516	-5.3377302	1.0619708	C	1.0116098	0.7423318	2.1816921
C	-3.2109479	-4.5525009	-1.9003379	C	1.3008406	-0.9155835	3.6927566
H	-3.0769999	-3.6547840	-2.5231711	H	1.7327841	-1.6280644	4.3908428
H	-4.2435122	-4.9198551	-2.0386569	C	-1.5099267	3.7812950	0.2626464
H	-2.5153437	-5.3268440	-2.2686647	C	-0.0815679	-0.7803149	3.3811893
C	3.3549650	-3.2355325	-1.5460569	C	-1.2093950	-1.5830381	4.0055111
H	2.7331355	-4.0149294	-1.9926488	C	0.7040657	3.7490933	-0.2090649
C	-2.1874302	2.0915962	-2.9315617	H	1.6983964	3.9766789	-0.5872173

C	1.2906776	1.8013457	1.2921211
C	1.9814965	0.0331309	2.9503833
H	3.0521761	0.2250483	2.9550876
C	4.9590819	1.1638214	0.4808268
C	-2.9497472	4.2539468	0.4066472
C	5.5291628	2.3529607	0.9637581
H	6.6155749	2.4704121	0.9498705
C	-3.1591824	5.5553485	-0.3899692
H	-2.5024199	6.3649601	-0.0284402
H	-4.2045220	5.8925318	-0.2800614
H	-2.9643315	5.4047306	-1.4657696
C	-0.4711997	4.4444685	-0.4525478
H	-0.5839096	5.3368796	-1.0631226
C	-3.2115079	4.5513644	1.9012958
H	-3.0770662	3.6536409	2.5240146
H	-4.2440628	4.9185280	2.0401859
H	-2.5158441	5.3258137	2.2692875
C	3.3545517	3.2371616	1.5431032
H	2.7326647	4.0167867	1.9892141
C	-2.1848403	-2.0921535	2.9319071
H	-2.6766971	-1.2802880	2.3762282
H	-2.9793346	-2.6972624	3.4024446
H	-1.6566897	-2.7186286	2.1958302
C	-3.9645342	3.2152089	-0.1165067
H	-3.9045188	3.1271580	-1.2119019
H	-4.9893189	3.5299722	0.1472351
H	-3.7998850	2.2100546	0.2982126
C	4.7428265	3.3879496	1.4709904
H	5.2143375	4.3032474	1.8380386
C	-1.9430150	-0.6975711	5.0385363
H	-1.2555113	-0.3968423	5.8482735
H	-2.7858267	-1.2534594	5.4877480
H	-2.3413454	0.2187984	4.5766768
C	-0.6384407	-2.8130909	4.7378600
H	-0.0668698	-3.4586830	4.0487018
H	-1.4664429	-3.4096650	5.1586705
H	0.0219168	-2.5245543	5.5728662
C	6.7178021	-0.4728768	1.1770142
H	7.3680416	0.3435899	1.5339102
H	7.3672793	-1.3100722	0.8697969
H	6.0923902	-0.8111615	2.0207864
Fe	-1.8584510	0.9448829	1.4706656
O	-4.3991722	1.0691278	2.8531257
N	-3.2779046	1.1732359	2.5331010

[($^{t\text{Bu}}$dmx)Fe_2(μ-O)$(NO)_2$] (**4**)
Functional: uB3LYP
Basis sets: def2-TZVP (Fe), 6-311G(d) (C, N, O) and 6-31G(d) (H)
E = −5058.77715464 a.u.
G = −5057.912965 a.u.
Charge = 0, Multiplicity = 7

Fe	-1.8658140	-0.9634772	-1.4475418
O	2.8874240	0.0000254	-0.0000200
N	-0.9910232	-2.7150777	-0.8751440
N	-0.2644009	-0.2403742	-2.4776417
O	-4.4331539	-1.0712286	-2.7588873
O	-2.4120255	-0.0000208	-0.0000089
N	-3.2961330	-1.2081361	-2.5024271
C	0.3938742	-2.6705687	-0.6450894
C	2.7535701	-2.0616392	-1.0828757
C	3.5651435	-1.0679665	-0.5123991
C	1.0045527	-0.7614281	-2.1806588
C	1.2766443	0.8621043	-3.7242078
H	1.7015662	1.5569131	-4.4350621
C	-1.4803697	-3.7954292	-0.2245190
C	-0.0993938	0.7365225	-3.3999588
C	-1.2293025	1.5278037	-4.0271337
C	0.7333543	-3.7443439	0.2233947
H	1.7265242	-3.9663442	0.5896793

C	1.2946150	-1.8063139	-1.2861078	C	-0.6645824	2.7375541	-4.7944105
C	1.9623947	-0.0675067	-2.9706027	H	-0.0920390	3.3958504	-4.1309860
H	3.0274521	-0.2548210	-2.9804751	H	-1.4920355	3.3173360	-5.2186611
C	4.9543082	-1.1583633	-0.4874688	H	-0.0172052	2.4285859	-5.6221997
C	-2.9135149	-4.2811965	-0.3563302	C	6.7145643	0.4791958	-1.1698972
C	5.8250101	0.0000467	-0.0000111	H	7.3603390	-0.3307915	-1.5247451
C	5.5257624	-2.3374380	-0.9800048	H	7.3581448	1.3073313	-0.8550326
H	6.6065128	-2.4488270	-0.9705418	H	6.0973016	0.8207171	-2.0076991
C	-3.1029800	-5.5873580	0.4348742	N	-0.9910715	2.7150603	0.8751261
H	-2.4436538	-6.3815337	0.0671098	N	-0.2643977	0.2403523	2.4776140
H	-4.1377044	-5.9316735	0.3275848	C	0.3938254	2.6705748	0.6450658
H	-2.9070091	-5.4401009	1.5031562	C	2.7535328	2.0616785	1.0828512
C	-0.4306139	-4.4460508	0.4776966	C	3.5651251	1.0680180	0.5123823
H	-0.5286058	-5.3354492	1.0847461	C	1.0045437	0.7614319	2.1806172
C	-3.1888163	-4.5766823	-1.8475009	C	1.2766901	-0.8620910	3.7241608
H	-3.0639520	-3.6847570	-2.4657332	H	1.7016328	-1.5568841	4.4350186
H	-4.2148341	-4.9431484	-1.9723847	C	-1.4804376	3.7954151	0.2245213
H	-2.5007344	-5.3449350	-2.2190296	C	-0.0993548	-0.7365420	3.3999310
C	3.3608356	-3.2213101	-1.5571211	C	-1.2292191	-1.5278460	4.0271586
H	2.7439918	-3.9946058	-2.0055152	C	0.7332825	3.7443531	-0.2234233
C	-2.1886578	2.0681877	-2.9562536	H	1.7264462	3.9663697	-0.5897144
H	-2.6684931	1.2822612	-2.3699016	C	1.2945814	1.8063301	1.2860757
H	-2.9833809	2.6526496	-3.4352623	C	1.9624166	0.0675046	2.9705161
H	-1.6539376	2.7169516	-2.2561225	H	3.0274732	0.2548261	2.9803551
C	-3.9347130	-3.2585064	0.1812256	C	4.9542885	1.1584338	0.4874648
H	-3.8629165	-3.1764802	1.2687300	C	-2.9135763	4.2811912	0.3563848
H	-4.9495319	-3.5890517	-0.0697474	C	5.5257227	2.3375143	0.9800101
H	-3.7940610	-2.2566032	-0.2278463	H	6.6064712	2.4489199	0.9705522
C	4.7451552	-3.3668342	-1.4919415	C	-3.1030712	5.5873336	-0.4348445
H	5.2154917	-4.2715101	-1.8667202	H	-2.4437129	6.3815106	-0.0671402
C	-1.9794985	0.6257882	-5.0314223	H	-4.1377849	5.9316658	-0.3275042
H	-1.3087197	0.3132216	-5.8401187	H	-2.9071648	5.4400452	-1.5031339
H	-2.8202632	1.1742188	-5.4736906	C	-0.4306950	4.4460533	-0.4777003
H	-2.3706829	-0.2741399	-4.5514319	H	-0.5287002	5.3354633	-1.0847307

C	-3.1888081	4.5767215	1.8475597
H	-3.0639110	3.6848165	2.4658135
H	-4.2148211	4.9431884	1.9724812
H	-2.5007109	5.3449883	2.2190309
C	3.3607783	3.2213545	1.5571095
H	2.7439200	3.9946395	2.0055023
C	-2.1885696	-2.0683600	2.9563361
H	-2.6684781	-1.2825125	2.3699395
H	-2.9832394	-2.6528425	3.4354081
H	-1.6538287	-2.7171374	2.2562353
C	-3.9348088	3.2584972	-0.1810952
H	-3.8630647	3.1764425	-1.2686013
H	-4.9496118	3.5890614	0.0699166
H	-3.7941495	2.2566031	0.2279957
C	4.7450966	3.3668974	1.4919445
H	5.2154167	4.2715787	1.8667307
C	-1.9794367	-0.6258309	5.0314313
H	-1.3086565	-0.3132067	5.8401042
H	-2.8201668	-1.1742858	5.4737353
H	-2.3706721	0.2740635	4.5514210
C	-0.6643997	-2.7375175	4.7944815
H	-0.0918532	-3.3958236	4.1310693
H	-1.4918009	-3.3173177	5.2188086
H	-0.0169966	-2.4284616	5.6222183
C	6.7146113	-0.4790763	1.1698497
H	7.3603751	0.3309280	1.5246781
H	7.3582070	-1.3071932	0.8549681
H	6.0973826	-0.8206140	2.0076697
Fe	-1.8658266	0.9634418	1.4475253
O	-4.4331723	1.0711741	2.7588643
N	-3.2961517	1.2080881	2.5024050

$[(^{t\text{Bu}}\text{dmx})\text{Fe}_2(\mu\text{-ONO})]^-$ (**7**)

E = −5625.82580647 a.u.

G = −5624.648567 a.u.

Charge = –1, Multiplicity = 9

Fe	-2.1588480	-1.3186693	-0.0408617
O	-0.1582009	3.5736208	-0.0610885
N	-2.2376678	-0.2856424	1.7719328
N	-2.1004210	0.3449944	-1.2676244
C	-0.7627533	7.3496046	-1.2368489
C	-0.1514175	6.5102466	-0.0895233
C	-1.2558445	5.6462407	0.5307875
C	-2.3823987	6.2135542	1.1494988
C	-3.4110236	5.4205742	1.6624169
C	-3.3499096	4.0267850	1.5421476
C	-2.2520222	3.4246860	0.9249786
C	-1.2126578	4.2516612	0.4629553
C	-2.1777592	1.9527553	0.6486843
C	-2.0727262	1.1067194	1.7691929
C	-1.9426215	1.5523705	3.1210570
C	-2.0669728	0.4328860	3.9258477
C	-2.2754899	-0.6841537	3.0569396
C	-2.7063626	-2.0697632	3.5201435
C	-2.1431649	-3.2056669	2.6560194
C	-4.2523984	-2.1145100	3.4390134
C	-2.2687110	-2.3021105	4.9792701
C	-2.2707575	1.6172983	-0.7155454
C	-2.5540392	2.5356607	-1.7754140
C	-2.5425359	1.8084536	-2.9521017
C	-2.2533929	0.4538151	-2.5984039
C	-2.1955324	-0.7085913	-3.5736726
C	-1.6009169	-0.2315535	-4.9148242
C	-3.6327154	-1.2271294	-3.8147488
C	-1.3215956	-1.8451946	-3.0315927
C	-3.9382775	-2.3842561	-0.3923370
C	-5.1483067	-1.6383257	-0.3234084
C	-5.1392998	-0.1491788	-0.0416774
C	-6.3966660	-2.2422814	-0.5472927

C	-6.5129514	-3.6019185	-0.8540514	H	-1.2210332	-2.6427857	-3.7879158
C	-7.8620922	-4.2496765	-1.0572828	H	-4.5032871	0.0979513	0.8233812
C	-5.3296995	-4.3435070	-0.9357734	H	-4.7338532	0.4172776	-0.8985768
C	-4.0695529	-3.7635078	-0.7092577	H	-6.1570298	0.2289588	0.1589795
C	-2.8640325	-4.6735198	-0.8204018	H	-8.2679840	-4.6464324	-0.1058138
H	-5.3899431	-5.4104872	-1.1835965	H	-8.6025335	-3.5299547	-1.4489899
H	-7.3059215	-1.6314995	-0.4852521	H	-7.8026658	-5.0986577	-1.7612152
H	-2.4610964	7.3009908	1.2283691	H	-2.1230472	-4.2873992	-1.5392335
H	-4.2740927	5.8910553	2.1412110	H	-2.3281967	-4.7605111	0.1389834
H	-4.1648597	3.3978350	1.9090475	H	-3.1568403	-5.6879990	-1.1434407
H	-1.5670907	8.0045758	-0.8601230	N	2.1269709	-0.3293215	-1.7163917
H	0.0032630	7.9898067	-1.7073547	N	1.9414904	0.3447410	1.2893674
H	-1.1881002	6.6911151	-2.0133565	C	0.4373205	7.4486015	0.9902268
H	-1.7751171	2.5806772	3.4352529	C	0.9725294	5.6289462	-0.6478801
H	-2.0341383	0.4047116	5.0127393	C	2.1192635	6.1806746	-1.2425153
H	-2.4538906	-3.1004632	1.6062482	C	3.1608413	5.3741875	-1.7055717
H	-1.0450200	-3.2446326	2.6943281	C	3.0921072	3.9842608	-1.5541339
H	-2.5348347	-4.1744807	3.0132001	C	1.9719709	3.3961486	-0.9619540
H	-4.7024041	-1.3015192	4.0358877	C	0.9193665	4.2355190	-0.5572690
H	-4.5870391	-2.0096417	2.3936145	C	1.9163139	1.9297874	-0.6490266
H	-4.6270490	-3.0793825	3.8284589	C	1.9055374	1.0544805	-1.7518212
H	-1.1760774	-2.1890997	5.0911468	C	1.8024420	1.4624238	-3.1185161
H	-2.7602129	-1.6005521	5.6744829	C	1.9936068	0.3305775	-3.8915374
H	-2.5417532	-3.3253579	5.2922209	C	2.2123950	-0.7566140	-2.9887673
H	-2.7420979	3.6018374	-1.6634203	C	2.6523060	-2.1526806	-3.4048279
H	-2.7162576	2.1875546	-3.9576352	C	2.1234441	-3.2465373	-2.4677447
H	-2.2360316	0.5310495	-5.3970025	C	4.2000368	-2.1802377	-3.3794705
H	-0.5934426	0.1932343	-4.7694856	C	2.1675284	-2.4560962	-4.8364544
H	-1.5195051	-1.0849452	-5.6119839	C	1.9765283	1.6240379	0.7247388
H	-4.0834071	-1.5855053	-2.8749753	C	2.1335442	2.5779016	1.7799177
H	-4.2732557	-0.4279738	-4.2282442	C	2.1826542	1.8660465	2.9646590
H	-3.6179793	-2.0653741	-4.5364362	C	2.0620965	0.4840177	2.6213583
H	-0.3196059	-1.4816982	-2.7617090	C	2.1368135	-0.6707587	3.6047842
H	-1.7735288	-2.3086044	-2.1398669	C	1.5489209	-0.2377969	4.9630615

C	3.6191951	-1.0651348	3.7987923
C	1.3407354	-1.8783299	3.0970812
H	2.2026498	7.2659400	-1.3433742
H	4.0403133	5.8314320	-2.1670020
H	3.9189025	3.3456910	-1.8750389
H	1.2243335	8.0948819	0.5659798
H	-0.3432000	8.1045982	1.4118104
H	0.8784311	6.8616764	1.8139485
H	1.6020797	2.4751663	-3.4627204
H	1.9876473	0.2733814	-4.9778236
H	2.5078391	-3.1216573	-1.4433515
H	1.0243571	-3.2541125	-2.4264571
H	2.4653245	-4.2367262	-2.8164215
H	4.6172515	-1.4096232	-4.0515883
H	4.5746116	-1.9950784	-2.3593464
H	4.5700271	-3.1679013	-3.7124434
H	1.0702463	-2.3661324	-4.9152792
H	2.6220940	-1.7766929	-5.5771734
H	2.4492680	-3.4868318	-5.1155373
H	2.2018501	3.6574617	1.6613406
H	2.2898087	2.2731828	3.9682684
H	2.1336950	0.5772699	5.4223848
H	0.5058521	0.1023478	4.8496920
H	1.5613734	-1.0912597	5.6644797
H	4.0669067	-1.3855319	2.8438722
H	4.2029584	-0.2130285	4.1899574
H	3.6998605	-1.8993132	4.5209258
H	0.3086167	-1.5902161	2.8506714
H	1.7961257	-2.3241097	2.1973157
H	1.3170553	-2.6721541	3.8638865
Fe	2.2446400	-1.3358177	0.1083814
C	4.2223615	-2.0518582	0.3861716
C	5.2815119	-1.1188829	0.1883299
C	5.0079607	0.3311497	-0.1519827
C	6.6292644	-1.4947441	0.3166778
C	7.0045242	-2.7995266	0.6502942
C	8.4569030	-3.2018214	0.7465145
C	5.9760531	-3.7207856	0.8674916
C	4.6204027	-3.3701967	0.7420831
C	3.6104503	-4.4645240	1.0097106
H	6.2368715	-4.7491384	1.1465139
H	7.4110776	-0.7423121	0.1551397
H	4.3994729	0.4253568	-1.0657409
H	4.4433964	0.8347514	0.6503587
H	5.9463433	0.8916914	-0.3064197
H	8.8453201	-3.5520725	-0.2301708
H	9.0923573	-2.3551128	1.0613713
H	8.6024187	-4.0267821	1.4662922
H	2.8658373	-4.1587783	1.7613160
H	3.0354290	-4.7184646	0.1046845
H	4.1049378	-5.3841685	1.3690005
O	-0.0114137	-1.8852124	0.0331311
N	-0.1996268	-3.1660860	0.1437051
O	0.8057915	-3.8121153	0.3428358

Conversion of reported NO• Reduction Potential from aqueous conditions referenced versus NHE to organic solvents referenced versus $[Cp_2Fe]^{+/0}$:The standard calomel electrode (SCE) is defined as +0.242 V versus the normal hydrogen electrode (NHE).[59] Thus, the reported reduction potential of NO• **(**$E_{1/2}$ **=** –0.68 V vs NHE in H_2O)[60] is

$$0.242\ V - (-0.68\ V) = -0.922\ V \text{ vs SCE in } H_2O \quad (3)$$

The reduction potential of the $[Cp_2Fe]^{+/0}$ couple related to SCE is reported in various organic solvents, however it is still not well-known for aqueous conditions. For instance, $E_{1/2}$ of $[Cp_2Fe]^{+/0}$ is ~ 0.55 V vs SCE in THF (reported as –0.56 V[61] and 0.547 V[62]) but can range from 0.382 V to 0.580 V depending on the solvent conditions.[61,62] Using the referenced value for THF, the estimated reduction potential for NO• vs $[Cp_2Fe]^{+/0}$ in THF is

$$-0.922\ V - (0.55\ V) = -1.472\ V \text{ vs } [Cp_2Fe]^{+/0} \text{ in THF} \quad (4)$$

However, we note that due to the large solvent effects, this value could be between –1.304 V to –1.502 V vs $[Cp_2Fe]^{+/0}$ to represent the wide window of various organic solvents. Regardless, a reduction potential in this range is still less cathodically-shifted than that observed for **3** and is in a range that would easily be reduced by KC_8.

4.9.5 X-Ray Diffraction Techniques

Structures of **2a–6** were collected on a Bruker three-circle platform goniometer equipped with an Apex II CCD and an Oxford cryostream cooling device. Radiation was from a graphite

[59] Sawyer, D. T.; Sobkowiak, A.; Roberts, J. L/ *Electrochemistry for Chemists.* 2nd edition, pp. 192.

[60] Bartberger, M. D.; Lui, W.; Ford, E.; Miranda, K. M.; Switzer, C.; Fukuto, J. M.; Farmer, P. J.; Wink, D. A.; Houk, K. N. *Proc. Natl. Acad. Sci. U.S.A.* **2002**, *99*, 10958–10963.

[61] Connelly, N. G.; Geiger, W. E. *Chem. Rev.***1996**, *96*, 877–910.

[62] Aranzaes, J. R.; Daniel, M.-C.; Astruc, D. *Can. J. Chem.* **2006**, *84*, 288–299.

fine focus sealed tube Mo Kα (0.71073 Å) source. Crystals were mounted on a cryoloop or glass fiber pin using Paratone N oil. Structures were collected at 100 K. Data were collected as a series of φ and/or ω scans.

Data were integrated using SAINT[63] and scaled with either a numerical or multi-scan absorption correction using SADABS.[63] The structures were solved by intrinsic phasing, direct methods or Patterson maps using SHELXS-2014[64] and refined against F^2 on all data by full matrix least squares with SHELXL-2014.[64] All non-hydrogen atoms were refined anisotropically. Hydrogen atoms were placed at idealized positions and refined using a riding model. The isotropic displacement parameters of all hydrogen atoms were constrained to be 1.2 times the parameter of the atoms they were linked to (1.5 times for methyl groups). Further details on particular structures are noted below.

[Na(15-c-5)(thf)][($^{t\text{Bu}}$dmx)Fe$_2$(κ^2-O$_2$N)(Mes)$_2$] (2b): The structure was solved in the triclinic space group $P\bar{1}$ with four molecules per unit cell and half of a molecule in the asymmetric unit. The asymmetric unit contained strongly disordered tetrahydrofuran solvent molecules. Due to apparent low occupancy and high disorder, an acceptable model could not be refined. A solvent mask was applied in Platon to reduce unrefined electron density.

($^{t\text{Bu}}$dmx)Fe$_2$(μ-O)(Mes)$_2$ (3): The structure was solved in the rhombohedral space group $R\bar{3}\,c$ with twenty four molecules per unit cell and two-thirds of a molecule in the asymmetric unit. The asymmetric unit contained several strongly disordered toluene molecules. Due to apparent low occupancy and high disorder, an acceptable model could not be refined. A solvent mask was applied in Platon to reduce unrefined electron density.

[63] APEX2 Software Suite; Bruker AXS: Madison, WI, 2009.

[64] Sheldrick, G. M. *Acta Crystallogr., Sect. A: Found. Crystallogr.* **2008**, *64*, 112–122.

($^{t\text{Bu}}$dmx)Fe$_2$(μ-O)(NO)$_2$ (4): The structure was solved in the monoclinic space group $C2/c$ with four molecules per unit cell and half a molecule in the asymmetric unit.

($^{t\text{Bu}}$dmx)Fe$_2$(μ-O)(NO)(Mes) (6): The structure was solved in the triclinic space group $P\bar{1}$ with two molecules per unit cell and one molecule in the asymmetric unit. The NO unit displayed moderate disorder that was modelled using a similarity constraint. The asymmetric unit also contained strongly disordered hexanes solvent molecules. Due to apparent low occupancy and high disorder, an acceptable model could not be refined. A solvent mask was applied in Platon to reduce unrefined electron density.

[($^{t\text{Bu}}$dmx)Fe$_2$(μ-O)(κ^2-NHPhNH)]$_2$ (10): The structure was solved in the triclinic space group $P\bar{1}$ with four molecules per unit cell and two molecules in the asymmetric unit. The asymmetric unit contained strongly disordered toluene solvent molecules. Due to apparent low occupancy and high disorder, an acceptable model could not be refined. A solvent mask was applied in Platon to reduce unrefined electron density.

[($^{t\text{Bu}}$dmx)Fe$_2$(μ-O)(κ^2-NHPhOH)]$_2$ (11): The structure was solved in the monoclinic space group $P2_1/c$ with two separate crystals grown from the same conditions, (1) with eight molecules per unit cell and two molecule in the asymmetric unit and (2) with two molecules per unit cell and half of molecule in the asymmetric unit. In both cases, the asymmetric unit contained strongly disordered toluene solvent molecules and positional disorder between the *para*-"N"H and "O" on the arenes. Due to apparent low occupancy and high disorder of the solvent molecules, an acceptable model could not be refined. A solvent mask was applied in Platon to reduce unrefined electron density.

Table 4.6. X-ray diffraction experimental details.[a]

	[Na(15-c-5)(et$_2$o)] [($^{t\text{Bu}}$dmx)Fe$_2$(κ^2-O$_2$N)(Mes)$_2$] (2a)	($^{t\text{Bu}}$dmx)Fe$_2$(μ-O)(Mes)$_2$ (3)	($^{t\text{Bu}}$dmx)Fe$_2$(μ-O)(NO)$_2$ (4)
Moiety Formula	$C_{40.5}H_{53}FeN_{2.5}Na_{0.5}O_{4.5}$	$C_{50.25}H_{58.5}Fe_{1.5}N_3O_{1.5}$	$C_{49}H_{56}Fe_2N_6O_4$
FW	714.203	812.27	904.69
λ (nm)	0.71073	0.71073	0.71073
***T* (K)**	100(2)	100(2)	100(2)
Crystal System	triclinic	rhombohedral	monoclinic
Space Group (*Z*)	$P\bar{1}$ (4)	$R\bar{3}$ *c* (24)	*C*2/c (4)
***a* (Å)**	15.1806(14)	25.268(5)	19.0746(9)
***b* (Å)**	15.2328(14)	25.268(5)	13.3184(7)
***c* (Å)**	19.3334(19)	51.350(19)	19.9923(12)
α (°)	105.038(3)	90	90
β (°)	104.557(3)	90	118.1182(13)
γ (°)	101.613(3)	120	90
Volume (Å^3)	4005.5(7)	28393(14)	4479.5(4)
Calc. ρ (mg/m^3)	1.184	1.140	1.341
μ (mm^{-1})	0.424	0.504	0.699
Crystal Size (mm)	0.28×0.13×0.05	0.14×0.04×0.02	0.22×0.12×0.08
Reflections	14365	5616	5313
Completeness (to 2θ)	97.8% 27.51°	99.1% 25.14°	98.8% 27.93°
GOF on F^2	1.023	1.023	1.044
R1, *w*R2[a] [$I > 2\sigma(I)$]	0.0536, 0.1313	0.0521, 0.1183	0.0508, 0.1116

[a] $R1 = \sum\big||F_o| - |F_c|\big|/\sum|F_o|$, $wR2 = \{\sum[w(F_o^2 - F_c^2)^2]/\sum[w(F_o^2)^2]\}^{1/2}$

Table 4.7. X-ray diffraction experimental details.[a]

	($^{t\text{Bu}}$dmx)Fe$_2$(μ-O)(NO)(Mes) (6)	[($^{t\text{Bu}}$dmx)Fe$_2$(μ-O)(κ^2-NHPhNH)]$_2$ (10)	[($^{t\text{Bu}}$dmx)Fe$_2$(μ-O)(κ^2-NHPhNH)]$_2$ (11)
Moiety Formula	$C_{58}H_{67}Fe_2N_5O_3$	$C_{110}H_{120}Fe_4N_{12}O_{45}$	0.25 ($C_{110}H_{122}Fe_4N_{10}O_6$)
FW	993.86	1901.66	475.91
λ (nm)	0.71073	0.71073	0.71073
T (K)	100(2)	100(2)	100(2)
Crystal System	triclinic	triclinic	monoclinic
Space Group (Z)	$P\bar{1}$ (2)	$P\bar{1}$ (4)	$P2_1/c$ (8)
a (Å)	11.5822(10)	16.137(2)	12.4486(3)
b (Å)	14.9935(14)	16.151(2)	26.3549(8)
c (Å)	18.8312(15)	16.447(2)	22.8922(6)
α (°)	92.319(3)	77.887(2)	90
β (°)	103.625(3)	61.602(20	96.833(2)
γ (°)	105.335(3)	89.001(2)	90
Volume (Å^3)	3046.5(5)	3669.8(8)	7457.2(3)
Calc. ρ (mg/m^3)	1.083	1.237	0.848
μ (mm^{-1})	0.518	0.448	3.366
Crystal Size (mm)	0.30×0.22×0.27	0.27×0.08×0.06	0.12×0.10×0.08
Reflections	6529	8404	8869
Completeness (to 2θ)	99.2% 25.17°	98.6% 25.14°	99.3% 66.93°
GOF on F^2	1.036	1.014	1.057
R1, *w*R2[a] [$I > 2\sigma(I)$]	0.0814, 0.1924	0.0554, 0.1583	0.0827, 0.2906

[a] $R1 = \sum\big||F_o| - |F_c|\big|/\sum|F_o|$, $wR2 = \{\sum[w(F_o^2 - F_c^2)^2]/\sum[w(F_o^2)^2]\}^{1/2}$

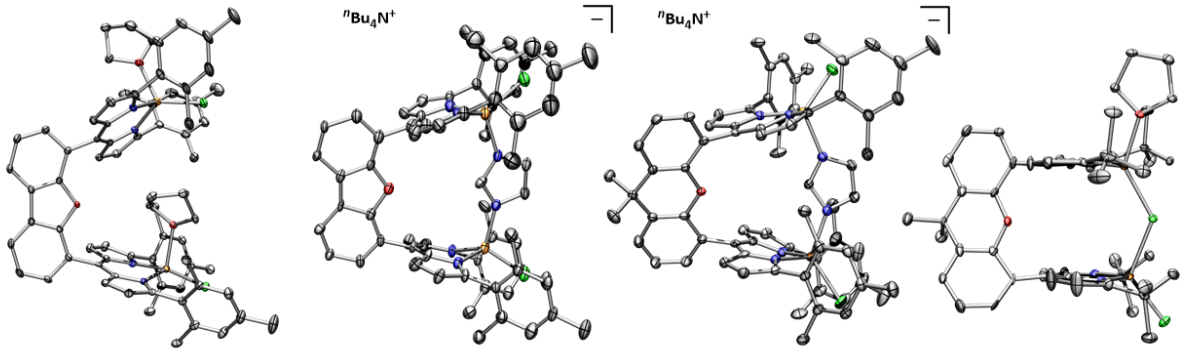

Chapter 5: Exploring the Coordination Chemistry of the Dipyrrin Pacman Platform

5.1 Introduction

Cofacial bimetallic complexes tethered by organic linkers often demonstrate a Pacman effect, in which the predisposed bite angle of the backbone in combination with the nature of the ancillary ligands bound to the metal centers can drastically affect the metal–metal distance.[1] The flexibility of the backbone in these complexes allows the metal–metal contact to expand or contract, a feature which has been shown by Nocera *et al.* to enable oxygenation reactivity.[2] Analogous themes are observed in biology, as secondary coordination sphere and allosteric effects are seen to influence the flexibility of enzyme active sites to help promote reactivity.[3] To assess the flexibility of the dipyrrin Pacman system, we sought to target various coordination complexes

[1] Chang, C. J.; Baker, E. A.; Pistorio, B. J.; Deng, Y.; Loh, Z.-H.; Miller, S. E.; Carpenter, S. D.; Nocera. D. G. *Inorg. Chem.* **2002**, *41*, 3102–3109.

[2] Chang, C. J.; Loh, Z.-H.; Shi, C.; Anson, F. C.; Nocera, D. G. *J. Am. Chem. Soc.* **2004**, *126*, 10013–10020.

[3] Das, A.; Hessin, C.; Ren, Y.; Murr, M. D.-E. *Chem. Soc. Rev.* **2020**, *49*, 8840 – 8867.

using the dibenzofuran (dbf) and dimethylxanthene (dmx) backbones, evaluating the modulation in iron–iron separation and motifs accessible on the ligand platform.

5.2 Comparison of Dibenzofuran and Dimethylxanthene Scaffolds[4]

Several Pacman dipyrrin complexes featuring either a dmx or a dbf backbone and different functional groups on the 1- and 9-positions of the dipyrrin units were synthesized following literature precedent.[5] Direct metalation of the Pacman ligand structure can be achieved using iron precursors containing an internal base (i.e., tetramesityldiiron (Fe_2Mes_4) or iron bis(trimethylsilyl)amide ($Fe[(N(SiMe_3)_2]_2$) metalating reagents), a strategy that was previously discussed for the (^{tBu}dmx)H_2 platform (**Chapter 2.2**) and can be applied to another dmx-bridged ligand, (^{Mes}dmx)H_2 (**Scheme 5.1, Scheme 5.2**), as well as to dbf-bridged ligands, (^{tBu}dbf)H_2 and (^{Mes}dbf)H_2 (**Scheme 5.3**). The novel metalated complexes (**1-7**) were characterized using ^{1}H NMR spectroscopy, as well as ^{57}Fe Mössbauer spectroscopy and single crystal X-ray diffraction in some cases.

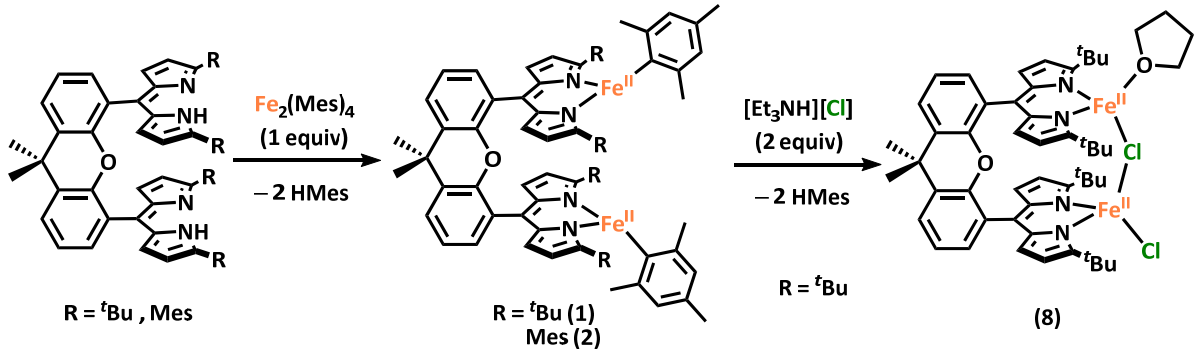

Scheme 5.1. Metalation and coordination chemistry of (^{R}dmx)Fe_2Mes_2 species, yielding an example of a monoatomic-bridged complex accessible using this ligand backbone variant.

[4] This work was done in collaboration with Dr. Claudia Kleinlein and Chastity Li, with contributions from Dr. Kurtis Carsch.

[5] Rosenthal, J.; Nocera, D. G. *Acc. Chem. Res.* **2007**, *40*, 543–553.

Metalation of (^{Mes}dmx)H$_2$ with (Fe[(NSiMe$_3$)$_2$]$_2$) proceeded at 100 °C in benzene to afford (^{Mes}dmx)Fe$_2$[N(SiMe$_3$)$_2$]$_2$ (**4**). Single crystals of **4** grown from a saturated solution in ether layered with hexanes at –35 °C revealed a large iron–iron distance of 7.9931(5) Å due to the bulky amide groups pulling the irons ~0.81 Å out of the dipyrrin plane away from each other (**Figure 5.1**). A similar effect was observed for dmx complex **1**, in which the mesitylene groups displace the irons ~0.73 Å away from the cavity (**Figure 2.1**). Single crystals of the dbf variant (^{Mes}dbf)Fe$_2$(Mes)$_2$ (**6**) revealed an even larger iron–iron distance than the comparable iron–mesitylene complex **1** (7.7592(3) Å for **6**, 6.7562(7) Å for **1**), directly exhibiting the effect of the larger bite angle of the dbf backbone on metal–metal distance (**Figure 5.2**). ^{57}Fe Mössbauer analysis of a few of these complexes (**1**, ($^{t\text{Bu}}$dbf)Fe$_2$(Mes)$_2$ (**5**), and **6**) were all consistent with the presence of symmetric species containing three-coordinate, high-spin ferrous centers (**Figure 2.1, Figures 5.3-5.4**).

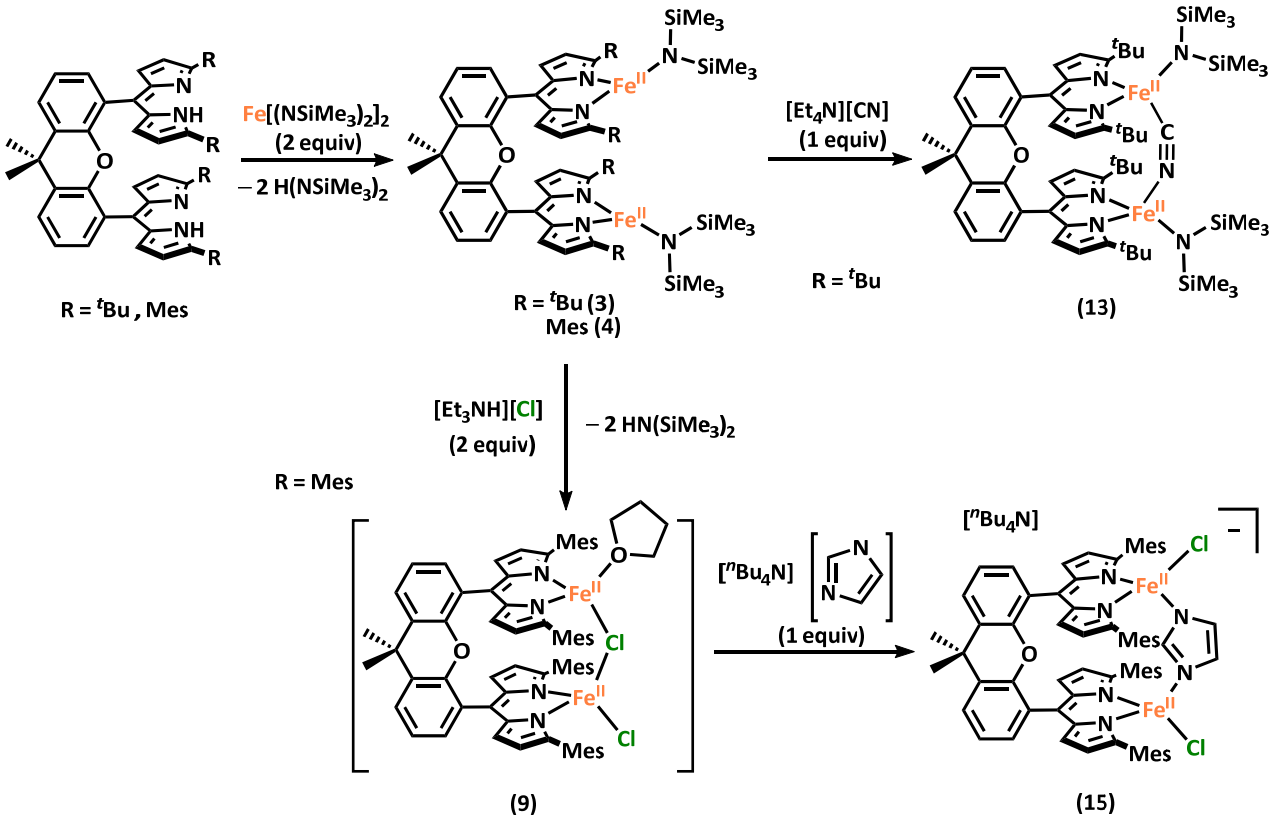

Scheme 5.2. Metalation and coordination chemistry of (^{R}dmx)Fe$_2$[N(SiMe$_3$)$_2$]$_2$ species, yielding examples of diatomic-bridged and triatomic-bridged complexes accessible on this ligand variant.

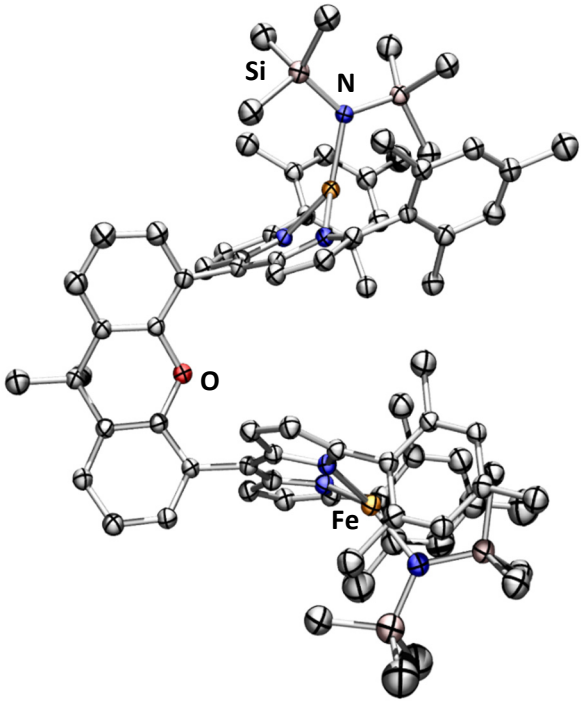

Figure 5.1. Solid state molecular structure of (^{Mes}dmx)Fe$_2$[N(SiMe$_3$)$_2$]$_2$ (**4**) with thermal ellipsoids at 40% probability level. Hydrogen atoms omitted for clarity. Fe = orange, N = blue, C = gray, O = red, Si = pink.

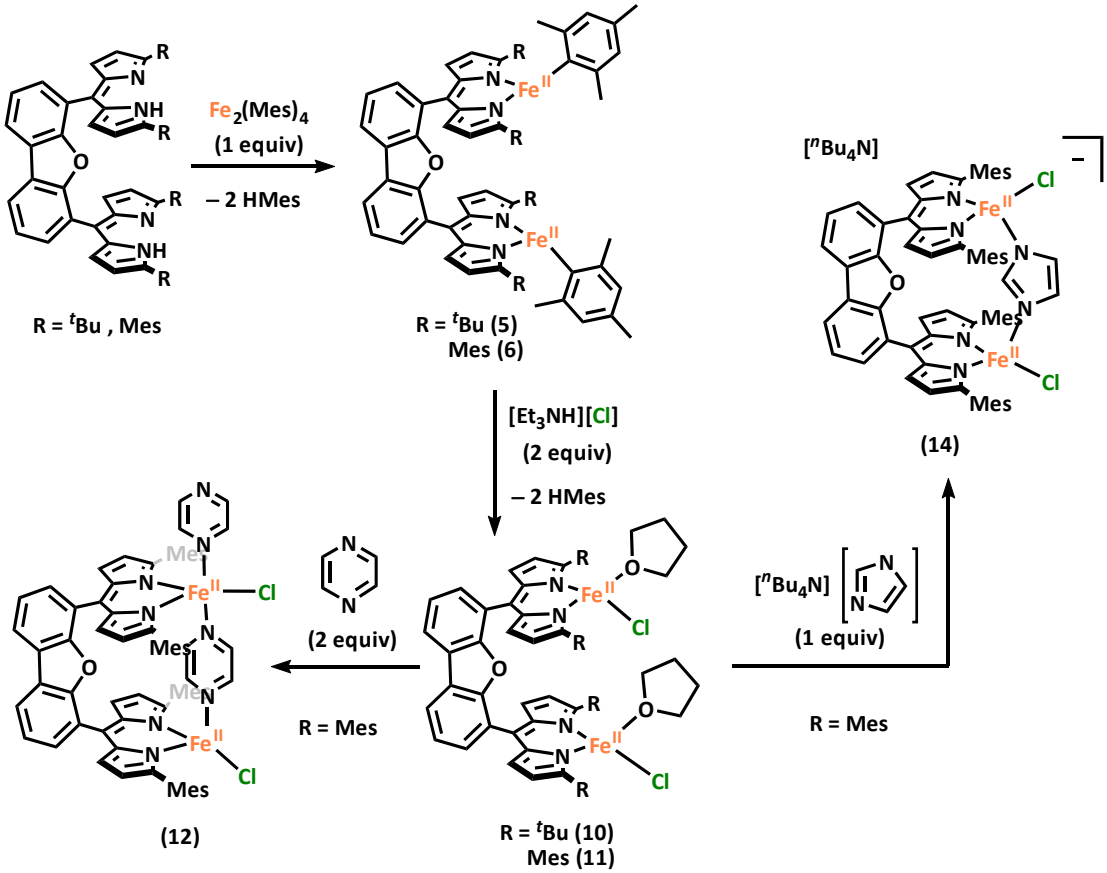

Scheme 5.3. Metalation and coordination chemistry of (^{R}dbf)Fe$_2$(Mes)$_2$ species, yielding examples of triatomic- and tetratomic- bridged complexes accessible with this ligand backbone.

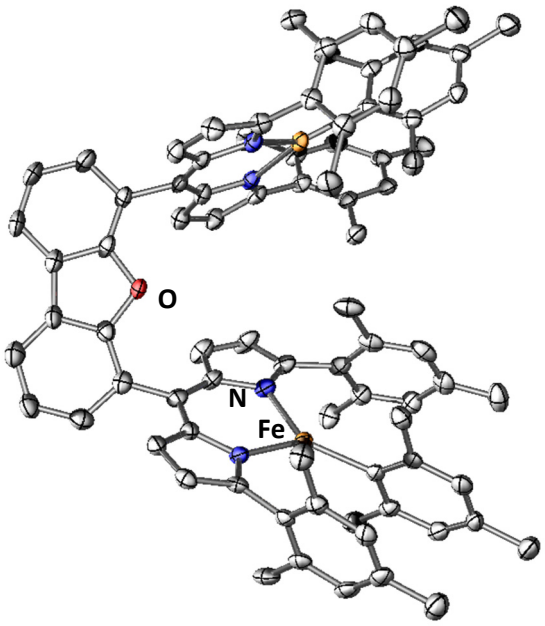

Figure 5.2. Solid state molecular structure of (^{Mes}dbf)Fe$_2$Mes$_2$ (**6**) with thermal ellipsoids at 50% probability level. Hydrogen atoms and solvent molecules omitted for clarity. Fe = orange, N = blue, C = gray, O = red.

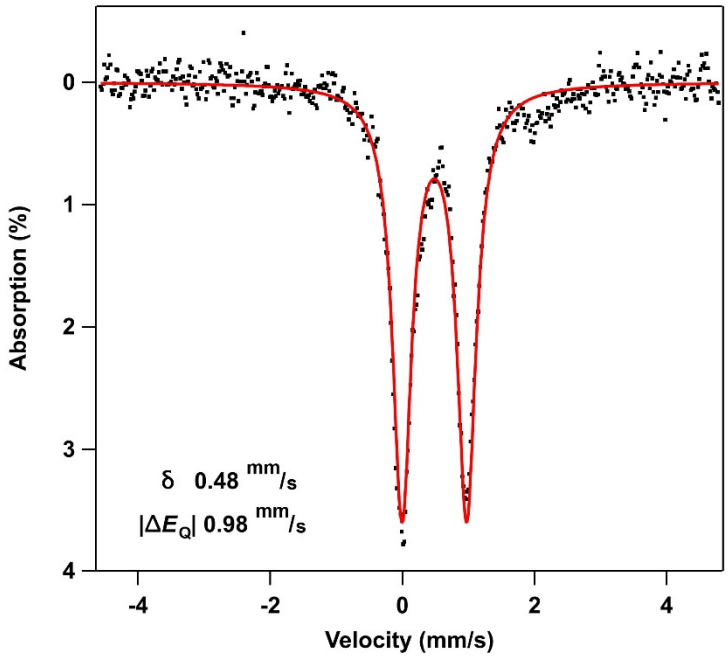

Figure 5.3. Zero-field ^{57}Fe Mössbauer spectrum of ($^{t\text{Bu}}$dbf)Fe$_2$Mes$_2$ (**5**). Isomer shift and quadrupole splitting are reported relative to Fe foil at room temperature.

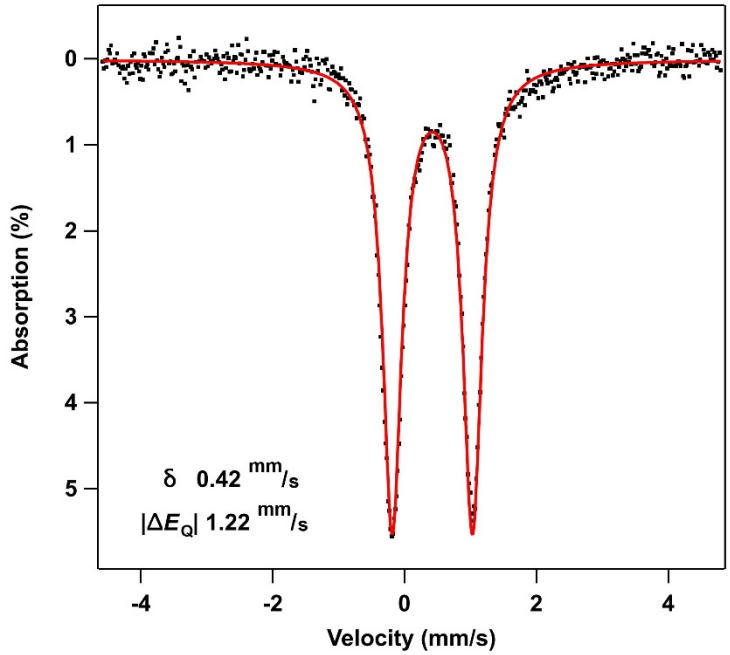

Figure 5.4. Zero-field ^{57}Fe Mössbauer spectrum of (^{Mes}dbf)Fe$_2$Mes$_2$ (**6**). Isomer shift and quadrupole splitting are reported relative to Fe foil at room temperature.

With suitable iron starting materials in hand, we employed a protonolysis strategy to synthesize a variety of substituted Pacman complexes. For instance, the addition of non-coordinating acids with chloride counterions provided access to diiron dichloride complexes. Treatment of **1** with two equivalents of triethylammonium chloride resulted in synthesis of ($^{t\text{Bu}}$dmx)Fe$_2$(μ-Cl)(Cl)(thf) (**8**) (**Scheme 5.1**). Crystallographic analysis of **8** reveals that each iron center is unique and four-coordinate, in which one bridged and one terminal chloride is present (**Figure 5.5**). Furthermore, complex **8** features a contracted iron–iron distance of 4.238(2) Å relative to the starting material. Conversely, the presence of symmetric four-coordinate irons is observed for the dibenzofuran derivatives, ($^{t\text{Bu}}$dbf)Fe$_2$Cl$_2$(thf)$_2$ (**10**) and (^{Mes}dbf)Fe$_2$Cl$_2$(thf)$_2$ (**11**) (**Scheme 5.3**). X-ray crystallographic studies of **10** and **11** demonstrate that terminally bound chloride and one bound tetrahydrofuran molecule complete the metal coordination spheres (**Figure**

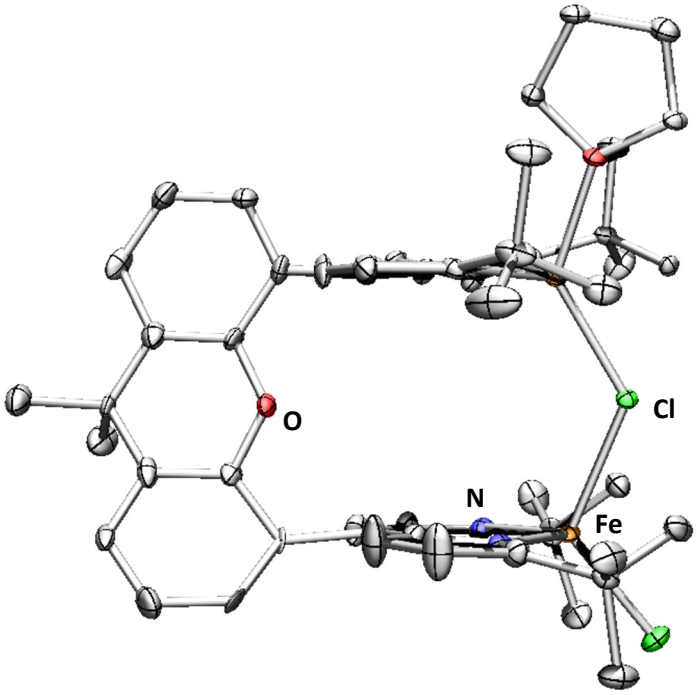

Figure 5.5. Solid state molecular structure of ($^{t\text{Bu}}$dmx)Fe_2(μ-Cl)(Cl)(thf) (**8**) with thermal ellipsoids at 50% probability level. Hydrogen atoms omitted for clarity. Fe = orange, N = blue, C = gray, O = red, Cl = green.

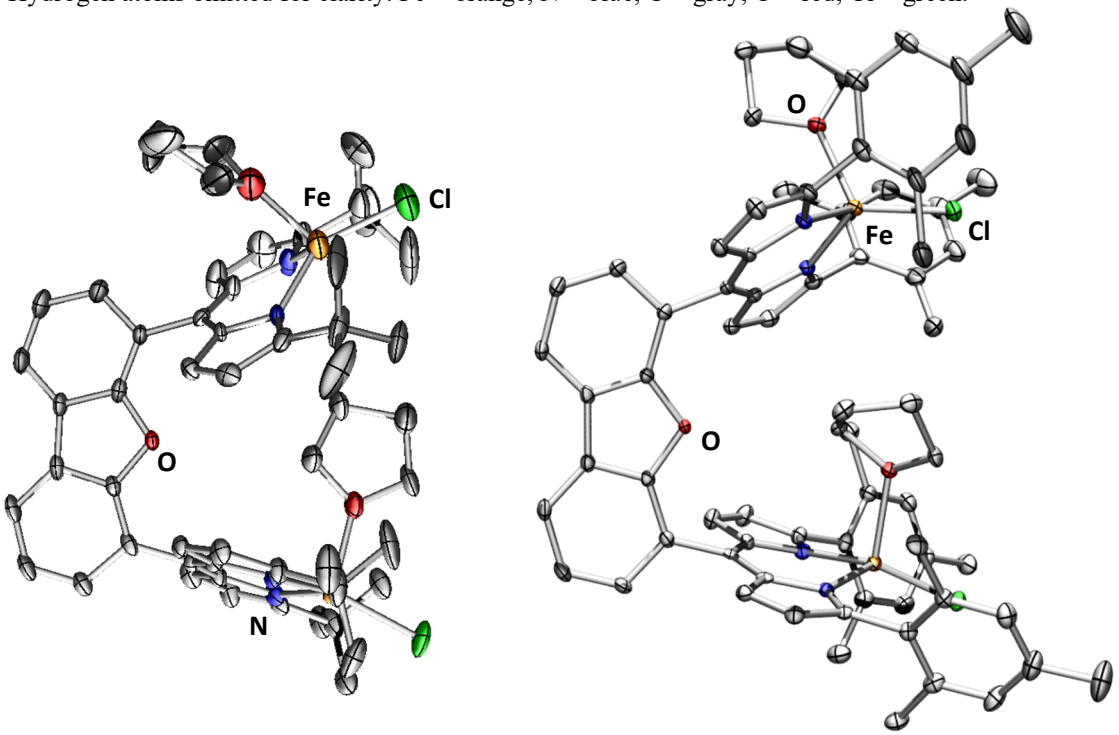

Figure 5.6. Solid state molecular structures of (**Left**) ($^{t\text{Bu}}$dbf)$Fe_2Cl_2(thf)_2$ (**10**) and (**Right**) ($^{\text{Mes}}$dbf)$Fe_2Cl_2(thf)_2$ (**11**) with thermal ellipsoids at 30 and 50% probability level, respectively. Hydrogen atoms and solvent molecules omitted.

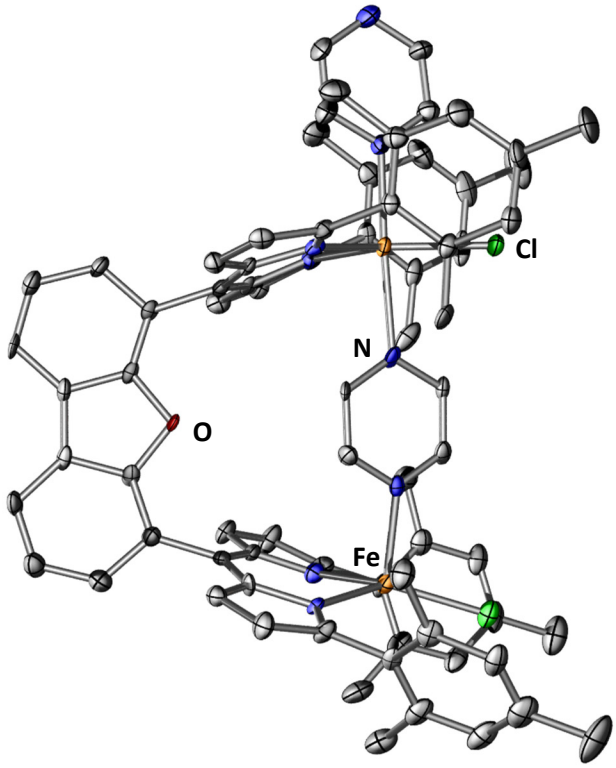

Figure 5.7. Solid state molecular structure of (^{Mes}dbf)Fe_2Cl_2(pyrazine)$_2$ (**12**) with thermal ellipsoids at 50% probability level. Hydrogen atoms omitted for clarity. Fe = orange, N = blue, C = gray, O = red, Cl = green.

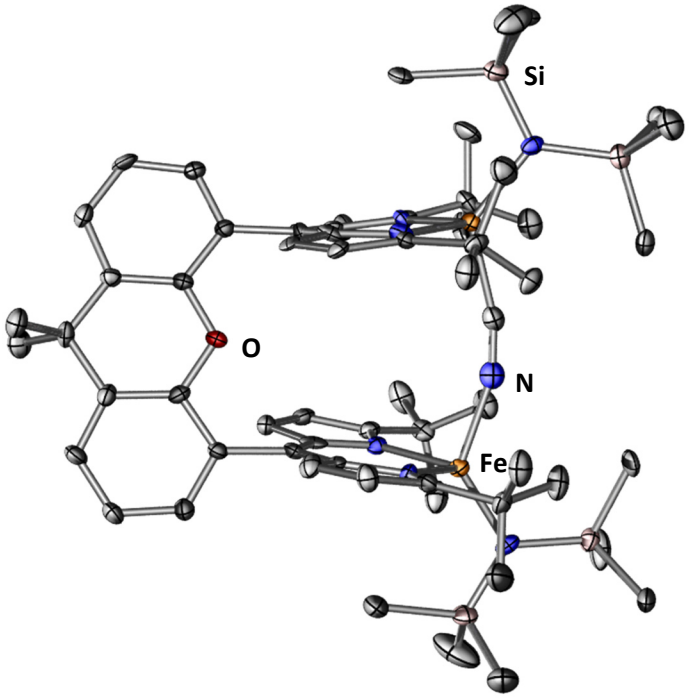

Figure 5.8. Solid state molecular structure of [Et_4N][(^{tBu}dmx)Fe_2(μ-CN){N($SiMe_3$)$_2$}$_2$] (**13**) with thermal ellipsoids at 50% probability level. Hydrogen atoms and counterion, and solvent molecules omitted for clarity. Fe = orange, N = blue, C = gray, O = red, Si = pink.

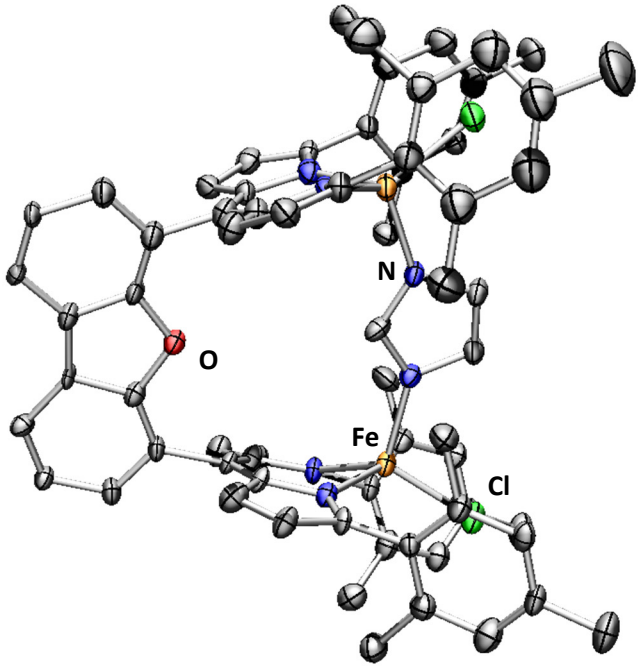

Figure 5.9. Solid state molecular structure of [^{n}Bu$_4$N][(^{Mes}dbf)Fe$_2$Cl$_2$(imidazolate)] (**14**) with thermal ellipsoids at 40% probability level. Hydrogen atoms, counterion, and solvent atoms omitted for clarity. Fe = orange, N = blue, C = gray, O = red, Cl = green.

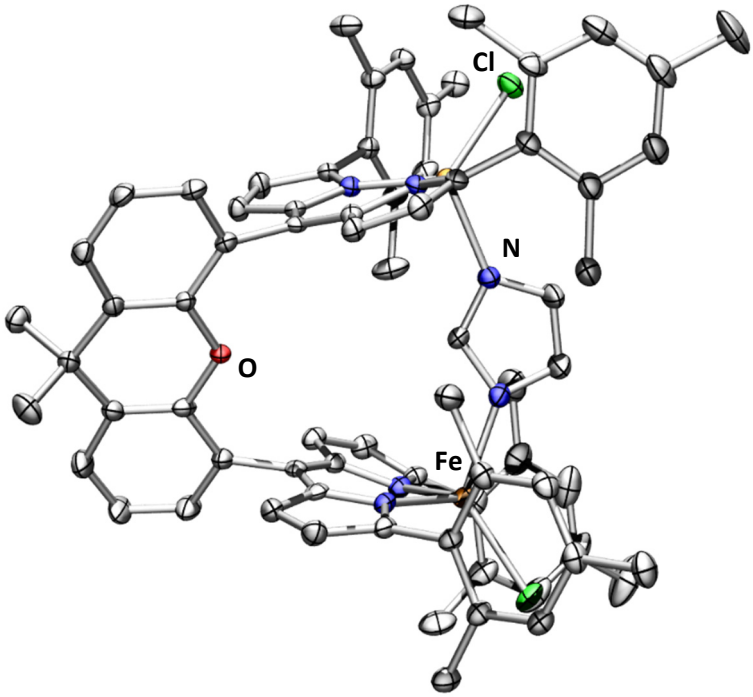

Figure 5.10. Solid state molecular structure of [^{n}Bu$_4$N][(^{Mes}dmx)Fe$_2$Cl$_2$(imidazolate)] (**15**) with thermal ellipsoids at 50% probability level. Hydrogen atoms, counterion, and solvent atoms omitted for clarity. Fe = orange, N = blue, C = gray, O = red, Cl = green.

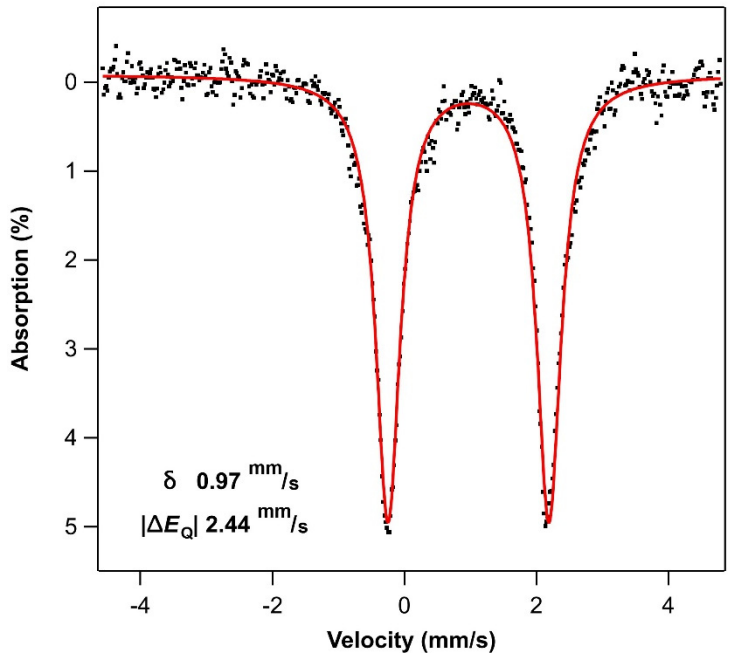

Figure 5.11. Zero-field ^{57}Fe Mössbauer spectrum of ($^{t\text{Bu}}$dbf)Fe$_2$Cl$_2$(thf)$_2$ (**10**). Isomer shift and quadrupole splitting are reported relative to Fe foil at room temperature.

5.6). These species display expanded metal–metal distances (7.8906 Å for **10**, 7.6872(13) Å for **11**) compared to **8** due to their lack of bridging moieties, which we attribute to the bite angle of the dbf backbone. The ^{57}Fe Mössbauer spectrum of **10** corroborates this formulation by exhibiting one quadrupole doublet consistent with high-spin iron(II) centers (**Figure 5.11**). Addition of the neutral ligand pyrazine to **10** demonstrates that the dbf backbone can accommodate four-membered bridges (**Scheme 5.2**). Crystallographic studies of ($^{\text{Mes}}$dbf)Fe$_2$Cl$_2$(pyrazine)$_2$ (**12**) reveal a slight contraction in the metal–metal distance to 7.282(9) Å upon addition of the bridge (**Figure 5.7**). Conversely, in addition to monoatomic bridges, the dmx platform allows for diatomic bridged species, as indicated by addition of tetraethylammonium cyanide to **3** which yielded [Et$_4$N][($^{t\text{Bu}}$dmx)Fe$_2$(μ-CN){N(SiMe$_3$)$_2$}$_2$] (**13**) (**Figure 5.8**, **Scheme 5.2**).

Further manipulation of the dichloride compounds revealed that both backbones converge on their ability to accommodate triatomic bridges. As such, addition of tetrabutylammonium

imidazolate to diiron dichloride species allowed for the installation of imidazolate to form the ate complexes, [^{n}Bu$_4$N][(^{Mes}dbf)Fe$_2$Cl$_2$(imidazolate)] (**14**) and [^{n}Bu$_4$N][(^{Mes}dmx)Fe$_2$Cl$_2$(imidazolate)] (**15**)**.** In the case of the dibenzofuran complex **14**, the iron centers are pulled inward, out of the dipyrrin plane by 0.6 Å on average (**Figure 5.9**). As such, this shows the limitations of the dibenzofuran-bridged Pacman complexes to force the iron centers into proximity. In contrast, for the **15** featuring the dimethylxanthene backbone, the two dipyrromethene units are pushed apart from each other, yet the complex still exhibits a contracted Fe–Fe distance (5.9695(9) Å) as compared to the dibenzofuran case (6.20(1) Å). This direct comparison further supports the hypothesis that the bite angle of the dmx bridge promotes shorter Fe–Fe distances than the dibenzofuran backbone (**Figure 5.10**).

Throughout these studies, we have demonstrated the ability of the dipyrrin Pacman complexes to modulate the iron–iron distance by more than 3.65 Å by manipulating bite angle of the backbone and the primary coordination sphere surround the iron centers. These results were instrumental in guiding our other studies, illuminating the motifs possible on each ligand framework and displaying the flexibility of these compounds that could be utilized for bimetallic reactivity.

5.3 Series of Diiron Bridging Azide Adducts

Previous work in our group has demonstrated the first diiron bridging imido complex that is competent for hydrogen-atom abstraction (HAA) and performs C–H amination.[6] This result inspired the synthesis of the Pacman platform as a means of dimerizing two dipyrrin complexes to allow for bimetallic reactivity. We sought to add bridging N-containing units to our list of single-

[6] Iovan, D. A.; Betley, T. A. *J. Am. Chem. Soc.* **2016**, *138*, 1983–1993.

atom bridged complexes and to compare the reactivity within the series of Pacman structures, as well as with the dimeric imido that was previously reported.

Numerous strategies were employed to target bridging imido complexes. While protonolysis strategies using substituted anilines and oxidative addition strategies with various aryl azides did not prove fruitful, clean reactivity was observed when using inorganic azides and trityl azide, which we hypothesized could be used to make bridging nitride complexes. One equivalent of potassium azide ([K][N_3]) and cryptand (2,2,2) were added to a solution of **1** in THF and heated to 70 °C for 12 hours, yielding a new product **16** by ^{1}H NMR spectroscopy and a color change to brown. ^{57}Fe Mössbauer spectroscopy indicated a symmetric species featuring high spin Fe^{II} centers (**Figure 5.12**); meanwhile, solid-state FTIR spectroscopy showed a distinctive N_3 stretch at 2094 cm^{-1} (**Figure 5.13**), suggesting the azide unit was still intact and bound to the complex, as the N_3 stretch in free KN_3 appears at 2031 cm^{-1}. Single crystals suitable for XRD were grown from a saturated solution of **16** in diethyl ether with minimal THF at –35 °C and confirmed its identity as the symmetric bridging azide complex, [K(2,2,2)][($^{t\text{Bu}}$dmx)Fe^{II}_2(κ^2-N_3)(Mes)$_2$] (**Figure 5.14**, **Scheme 5.4**). Complex **15** proved to be extremely robust, as treatment with heat, light, or Lewis acids failed to induce loss of dinitrogen to afford the desired monoatomic nitrogen bridge.

Attempts to induce N_3 decomposition to yield the targeted bridging nitrido complex via chemical oxidation or reduction were also unsuccessful. The N_3 moiety was conserved upon oxidation of **15**, as shown when treating a frozen THF solution with one equivalent of ferrocenium tetraphenylborate ($FcBPh_4$) afforded a new azide stretch in the FTIR solid state spectrum at 2111 cm^{-1} (**Figure 5.13**). ^{1}H NMR spectroscopic studies revealed that the same product (**16**) was formed when **1** was treated with trityl azide (Ph_3CN_3) in the presence of a weak C–H bond donor such as 1,4-cyclohexadiene (CHD), concomitant with Gomberg's dimer ($Ph_3C(C_6H_5)CPh_2$)

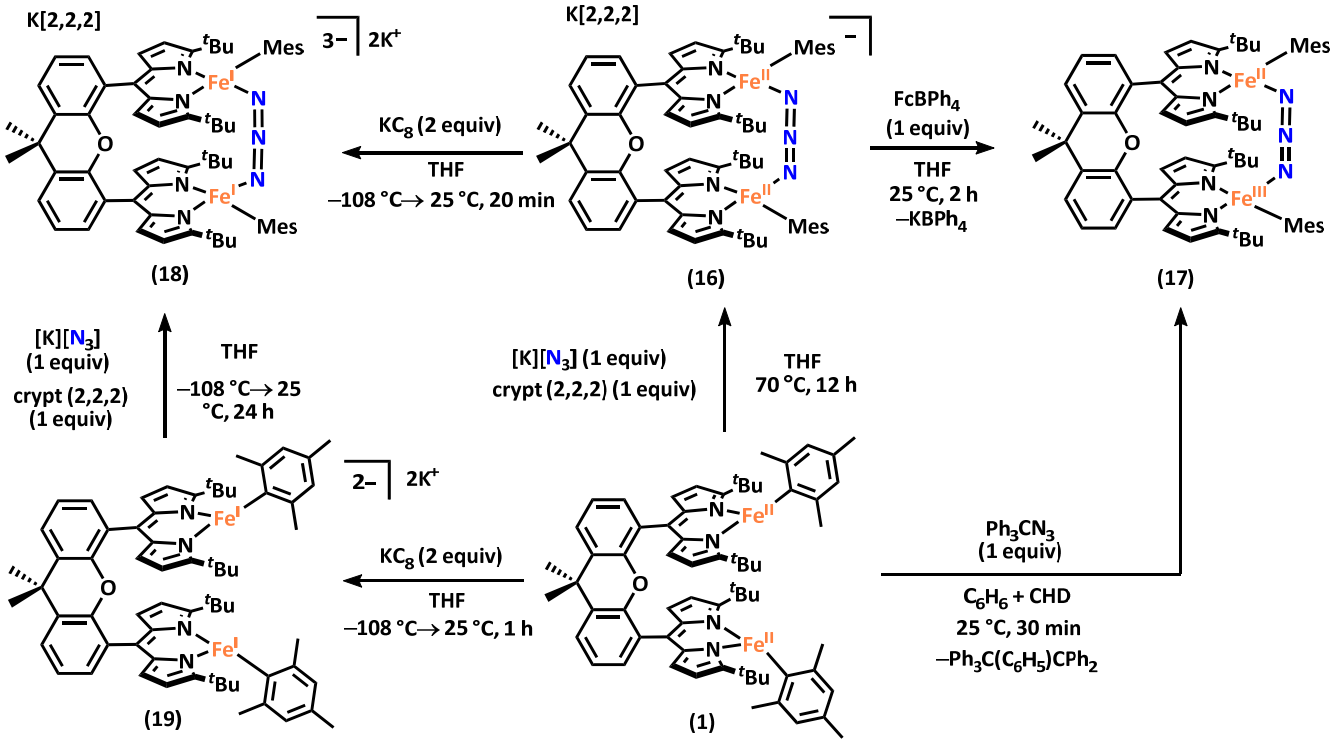

Scheme 5.4. Synthesis of various bridging azide adducts.

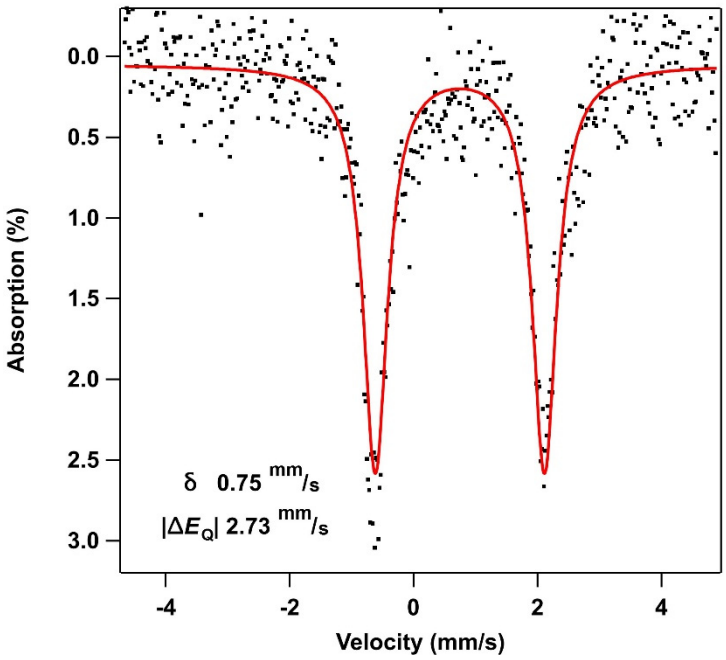

Figure 5.12. Zero-field ^{57}Fe Mössbauer spectrum of [K(2,2,2)][($^{t\text{Bu}}$dmx)Fe$_2$(κ^2-N$_3$)Mes$_2$] (**16**). Isomer shift and quadrupole splitting are reported relative to Fe foil at room temperature.

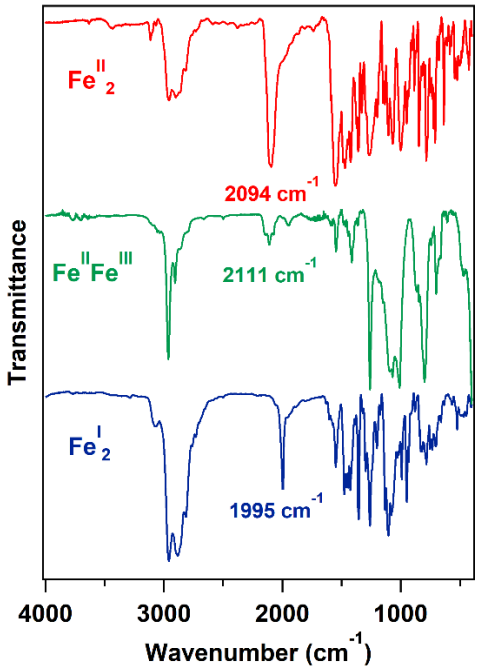

Figure 5.13. FTIR spectrum of various azide adducts. (**Top**, **red**) [K(2,2,2)][($^{t\text{Bu}}$dmx)Fe$_2$(κ^2-N$_3$)(Mes)$_2$] (**16**), (**Middle**, **green**) [K][($^{t\text{Bu}}$dmx)Fe^{II}Fe^{III}(κ^2-N$_3$)(Mes)$_2$] (**17**), (**Bottom**, **blue**) [K(2,2,2)][K]$_2$[($^{t\text{Bu}}$dmx)Fe$_2$(κ^2-N$_3$)(Mes)$_2$] (**18**).

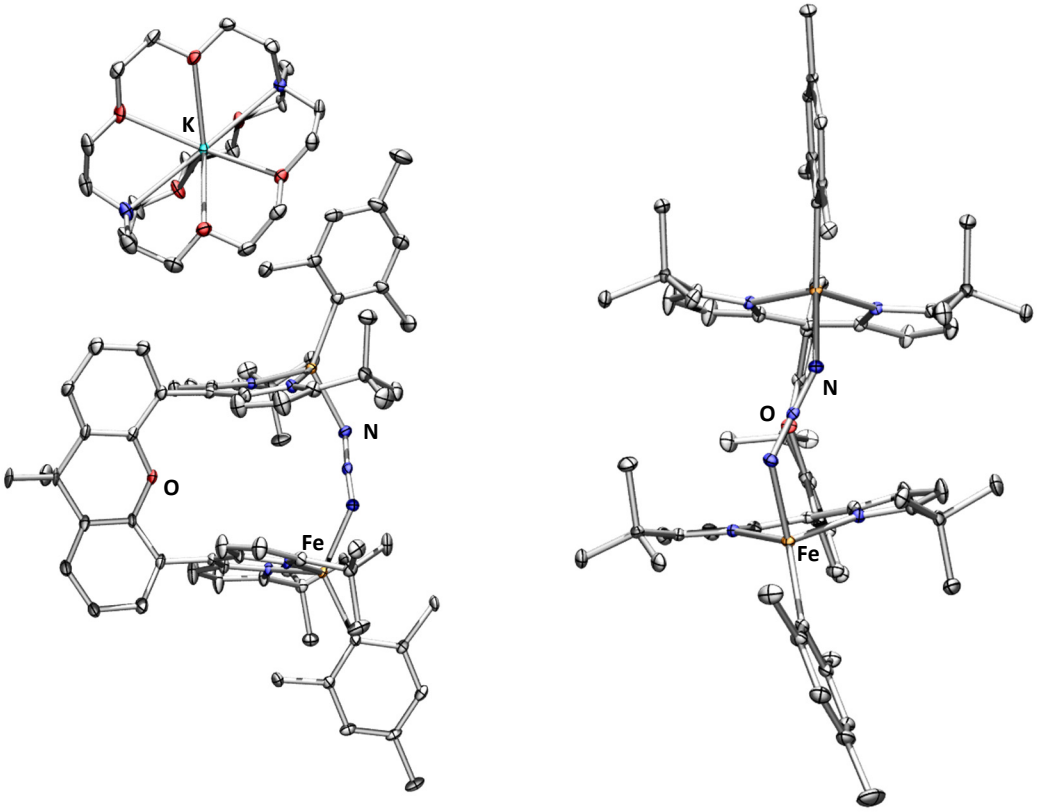

Figure 5.14. Solid state molecular structure of [K(2,2,2)][($^{t\text{Bu}}$dmx)Fe$_2$(κ^2-N$_3$)(Mes)$_2$] (**16**); (**Left**) front view, (**Right**) side view, with thermal ellipsoids at 30% probability level. Hydrogen atoms in both cases and counterion (on right image) omitted for clarity. Fe = orange, N = blue, C = gray, O = red, K = turquoise.

formation as the byproduct. The ^{57}Fe Mössbauer spectrum of the product **16** exhibited two quadrupole doublets, indicative of a mixed-valent species (**Figure 5.15**), and the X-band EPR spectrum of **16** showed a pseudo-axial signal consistent with an overall $S = {}^1/_2$ formulation (**Figure 5.16**). Single crystals were grown from pentane at 25 °C to reveal formation of the one-electron oxidized product, ($^{t\text{Bu}}$dmx)Fe$^{\text{II}}$Fe$^{\text{III}}$(κ^2-N$_3$)(Mes)$_2$ (**16**) (**Figure 5.17**, **Scheme 5.4**). Although the ^{57}Fe Mössbauer spectrum of **16** suggests moderate oxidation state localization within the mixed-valent core, it should be noted that the bond metrics of the primary coordination sphere of the metals are far less distinct (Fe(1)–N$_{\text{azide}}$ = 2.0011(6) Å, Fe(2)–N$_{\text{azide}}$ = 2.0211(9) Å, **Table 5.1**) than was observed for the mixed-valent diiron μ-oxo complex discussed in chapter 2 (Fe(1)–O = 1.8032(16) Å, Fe(2)–O = 1.8928(16) Å, **Table 2.10**). These data combined suggest that **16** is likely best described as a Robin-Day class II mixed-valence compound.[7]

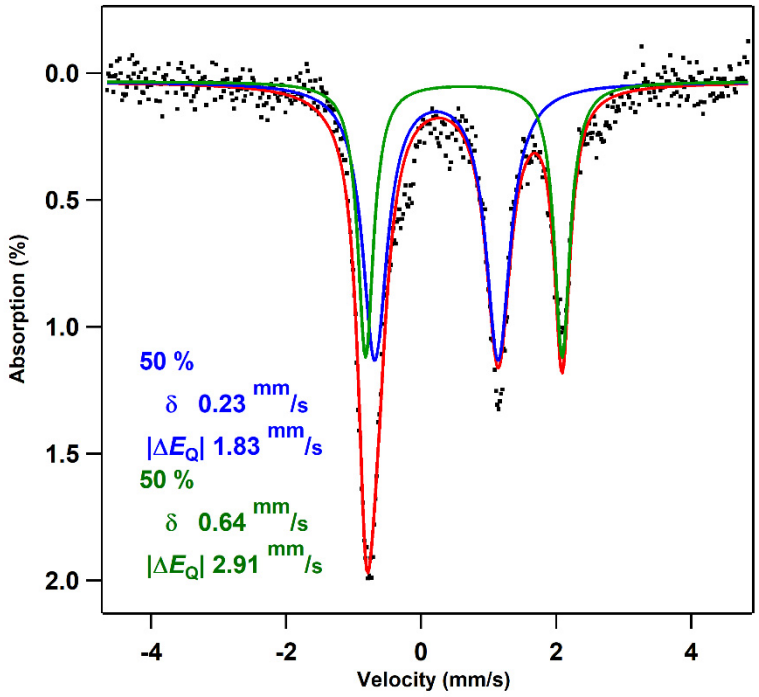

Figure 5.15. Zero-field ^{57}Fe Mössbauer spectrum of ($^{t\text{Bu}}$dmx)Fe$^{\text{II}}$Fe$^{\text{III}}$(κ^2-N$_3$)Mes$_2$ (**17**). Isomer shift and quadrupole splitting are reported relative to Fe foil at room temperature.

[7] Robin, M. B.; Day, P. in *Advances in Inorganic Chemistry and Radiochemistry*, *Vol 10*. (Ed.: Emeléus, H., Sharpe, A. G.) Academic Press **1967**.

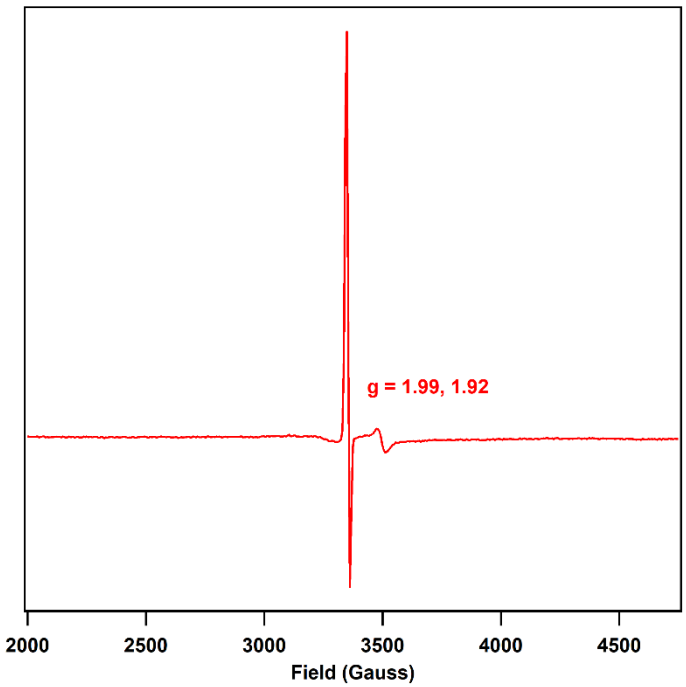

Figure 5.16. X-band EPR spectrum of ($^{t\text{Bu}}$dmx)Fe$^{\text{II}}$Fe$^{\text{III}}$(κ^2-N$_3$)(Mes)$_2$ (**17**). Spectrum was collected in a frozen toluene glass at 77 K.

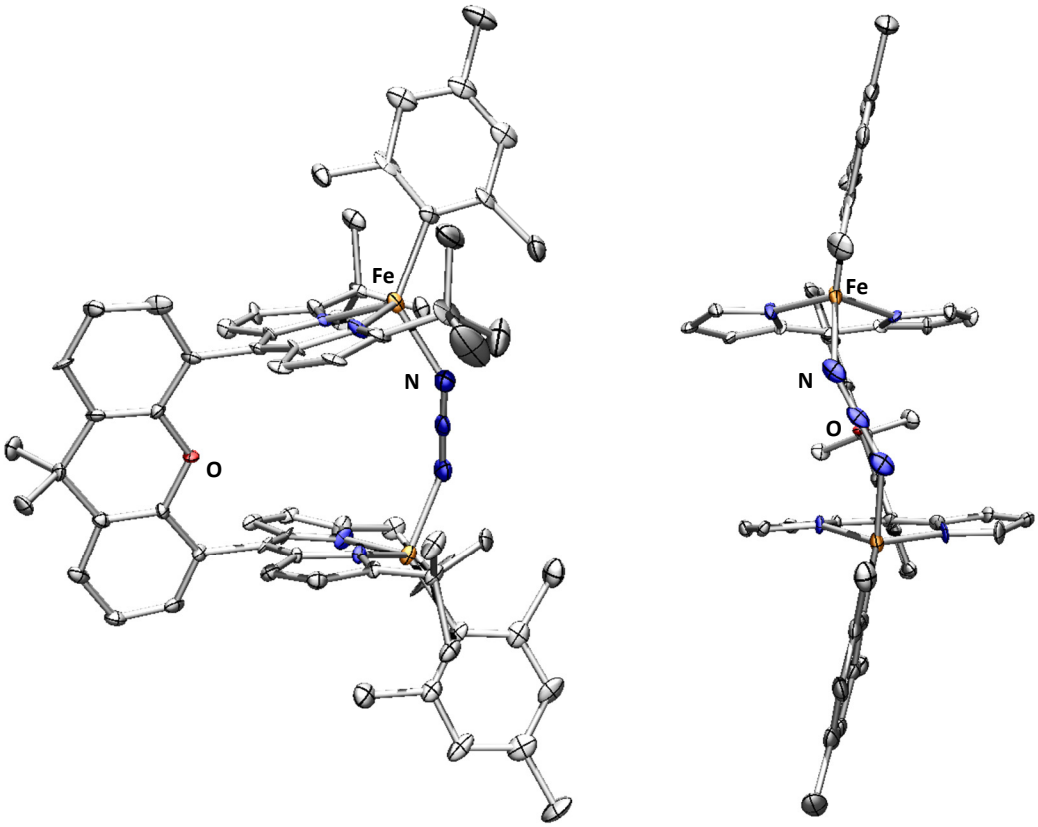

Figure 5.17. Solid state molecular structure of ($^{t\text{Bu}}$dmx)Fe$^{\text{II}}$Fe$^{\text{III}}$(κ^2-N$_3$)(Mes)$_2$ (**17**); (**Left**) front view, (**Right**) side view, with thermal ellipsoids at 40% probability level. Hydrogen atoms and solvent molecules omitted in both views, and ^{t}Bu ligand arms omitted in the side view for clarity. Fe = orange, N = blue, C = gray, O = red.

Reduction of **15** was also attempted to induce azide activation. Ungratifyingly, addition of two equivalents of potassium graphite (KC_8) to a frozen solution of **15** in THF resulted in formation of [K(2,2,2)][K]$_2$[($^{t\text{Bu}}$dmx)Fe$^{\text{I}}_2$Mes$_2$(κ^2-N$_3$)] (**17**), in which the azide moiety remained intact by observation of a distinctive N_3 stretch at 1995 cm^{-1} (**Figure 5.13**) and further confirmation by X-ray diffraction on single crystals grown in a saturated solution of **17** in THF layered with *n*-hexanes at –35 °C (**Figure 5.18**). A slight elongation in the Fe–$N_{dipyrrin}$ bond distances is observed upon reduction from **16** (average: 2.060 Å) to **18** (average: 2.0676 Å) with a slight contraction of the Fe–N_{azide} (average: 2.085 for **16**, average: 2.0441 for **18**) and Fe–C_{Mes} (average: 2.073 for **16**, average: 2.0431 for **18**), possibly consistent with metal-based reduction; however, it should be noted that due to poor crystal quality, it is difficult to make any assignments based on bond metrics alone.

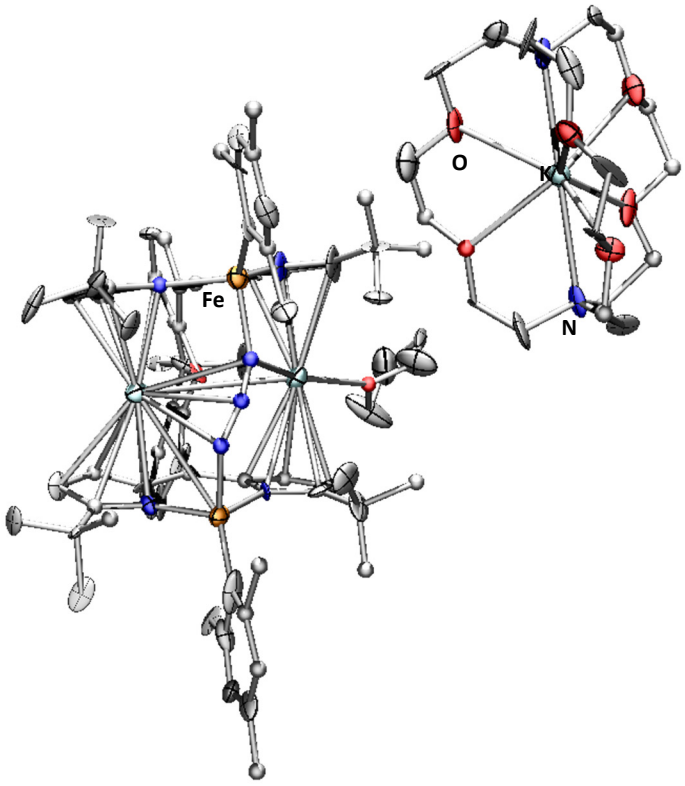

Figure 5.18. Solid state molecular structure of [K(2,2,2)][K]$_2$[($^{t\text{Bu}}$dmx)Fe$_2$(κ^2-N$_3$)(Mes)$_2$] (**18**), side view, with thermal ellipsoids at 30% probability level. Hydrogen atoms and solvent molecules (other than thf ligated to potassium) are omitted for clarity. Due to poor crystal quality, some atoms are isotropically refined. Fe = orange, N = blue, C = gray, O = red, K = turquoise.

Table 5.1. Comparison of bond metrics of diiron κ^2-azide complexes.

Complex	Fe–N_{azide} distances (Å)	Fe–$N_{dipyrrin}$ distances (Å)	Fe–C_{Mes} distances (Å)	Fe–Fe distance (Å)	N–N–N angle (°)	dmx bend angle (°)
16	2.067(5) 2.103(5)	2.074(5) 2.053(5) 2.055(4) 2.058(4)	2.079(6) 2.067(5)	5.7074(11)	175.4(5)	116.0(4)
17	2.0211(9) 2.0011(6)	2.0248(6) 2.0307(7) 2.0207(6) 2.0288(8)	2.0321(6) 2.0261(8)	5.660(3)	166.606(3)	118.74(3)
18	2.0441(4) 2.0440(4)	2.0922(4) 1.9786(4) 2.0969(4) 2.1027(4)	2.0313(3) 2.0549(2)	5.9410(12)	177.0875(17)	112.566(14)

Another route was attempted by first reducing **1** by two electrons to attempt to synthesize a diiron(I) synthon, $[K]_2[(^{t\text{Bu}}\text{dmx})Fe_2Mes_2]$ (**19**) (**Scheme 5.4**), which we assign based on novel ^{1}H NMR and ^{57}Fe Mössbauer spectra (**Figure 5.19**). Due to the lack of crystallographic characterization of **19** and recent work reporting ligand reduction in an analogous dichromium Pacman system, we note the likelihood that the locus of reduction for **19** could also be ligand-borne.[8] Ungratifyingly, treatment of **18** with $[K][N_3]$ and cryptand (2,2,2) also afforded **17** (**Scheme 5.4**), as verified by ^{1}H NMR spectroscopy. Zero-field ^{57}Fe Mössbauer spectroscopy of **17** by this route also indicated the ambiguity of the location of reduction ($\delta = 0.85$ $^{mm}/_{s}$, $|\Delta E_Q| = 2.17$ $^{mm}/_{s}$), possibly consistent with subtle changes in parameters upon reduction observed in other iron dipyrrin complexes[9] but also possibly in line with iron(II) centers as well.

[8] Carsch, K. M.; Lukens, J. T.; Elder, S. E.; Dogutan, D. K.; Nocera, D. G.; Yang, J.; Zheng, S.-L.; Daniel, T.; Betley, T. A. *Acta Cryst.*., **2021**, *C77*, 161–166.

[9] Wilding, M. J. T.; Iovan, D. A.; Betley, T. A. *J. Am. Chem. Soc.* **2017**, *139*, 12043–12049.

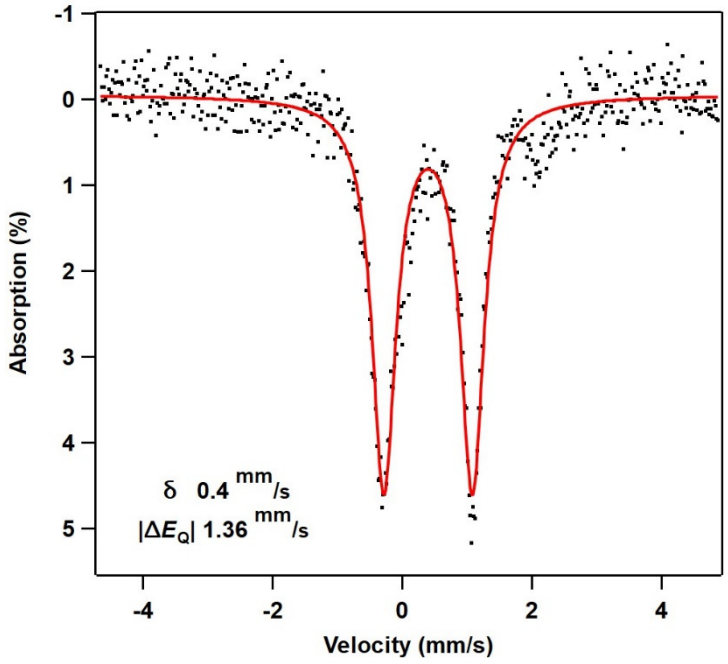

Figure 5.19. Zero-field ^{57}Fe Mössbauer spectrum of $[K]_2[(^{tBu}dmx)Fe_2(Mes)_2]$ (**19**). Isomer shift and quadrupole splitting are reported relative to Fe foil at room temperature.

Given the propensity for azides to bridge the two metal centers in the Pacman system, the addition of azides does not appear to be a viable strategy to form the desired monoatomic μ-N moiety. Although many cases of metal–azide complexes are able to undergo photoloysis, thermolysis, or oxidative reactions to release dinitrogen, there is extensive precedence for transition-metal clusters, extended solids, and coordination polymers featuring bridging azide moieties in this end-to-end fashion.[10] Combined with the results presented in the previous section, we have further demonstrated the facile accommodation of triatomic nitrogen-containing bridges within the dmx Pacman scaffold through the series of bridging azide adducts discussed here.

[10] (a) Banerjee, A.; Banerjee, S.; Gómez García, C. J.; Benmansour, S.; Chattopadhyay, S. *ACS Omega* **2019**, *10*, 20634–20643. (b) Escuer, A.; Aromi, G. *Eur. J. Inorg. Chem.* **2006**, 4721–4736. (c) Thompson, L. K.; Tandon, S. S. *Comments Inorg. Chem.* **1996**, *18*, 125–144. (d) Chen, Z.-L.; Jiang, C.-F.; Yan, W.-H.; Liang, F.-P.; Batten, S. R. *Inorg. Chem.* **2009**, *48*, 4674–4684. (e) Kahn, O. in *Molecular Magnetism,* VCH **1993**.

5.3 Targeting Bridging (Hydro)sulfido Complexes

Iron sulfur clusters are among some of the most versatile enzymatic cofactors as they are active towards various functions including electron transfer, hydrogenase activity, and nitrogenase reactivity.[11] Accordingly, synthetic models featuring polynuclear iron clusters with sulfur-based ligands have been long-time targets by bioinorganic chemists to uncover how these motifs can provide the necessary reactivity. Given the accessibility of diiron bridging (hydr)oxo complexes on the dipyrrin Pacman platform, we proposed that a diiron μ-S(H) could also be feasible with the system. Furthermore, synthesizing a bridging (hydro)sulfide species could allow us to study the effects of a larger bridging atom on the resulting metal–metal interaction and reactivity by comparing to the analogous bridging (hydr)oxide series.

One equivalent of sodium hydrosulfide ([Na][SH]) and two equivalents of 15-crown-5 were added to a solution of **1** in THF (**Scheme 5.5**). After stirring overnight, a color change to brown and evidence of a new species by ^{1}H NMR was observed. Single crystals of this species were grown from a saturated solution in toluene to reveal the formation of the symmetric anionic complex, [Na(15-crown-5)$_2$][($^{t\text{Bu}}$dmx)Fe$_2$(μ-SH)(Mes)$_2$] (**20**) (**Figure 5.20**). ^{57}Fe Mössbauer spectroscopy of **20** was consistent with a single high spin Fe^{II} environment, and the solid-state FTIR spectrum showed a weak S–H stretch at 2589 cm^{-1}. Targeting an isostructural species to compare with the diiron(II) (μ-OH) complexes, we sought removal of the mesitylene units via additions of various acids (i.e., lutidinium tetraphenylborate, triethylammonium chloride, and lutidinium triflate) but ungratifying saw only demetallation with these strong acids. Turning to weaker acids, such as *para*-methoxyphenol, elicited no reaction with **20**. Moreover, heating **20** showed degradation to many unidentified iron-containing products. Lastly, deprotonation to form

[11] Brzóska, K.; Meczyńska, S.; Kruszewski, M. *Acta Biochim. Pol.* **2006**, *53*, 685–691.

the corresponding μ-sulfido, which could serve as a comparison with the diiron(III) μ-oxo organometallic species discussed in Chapter 4, was attempted with bases such as triethylamine but did not show any reaction toward the desired product. Therefore, no direct comparisons between the bridging O and bridging S platforms has been made at this point.

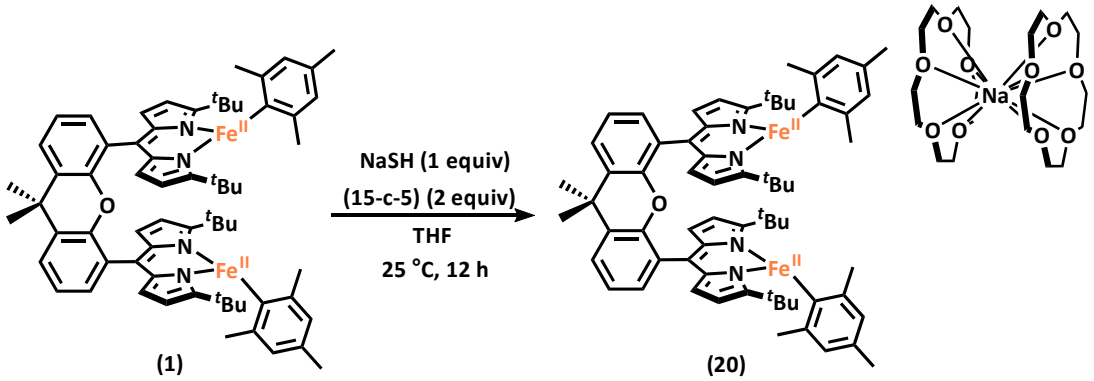

Scheme 5.5. Synthesis of diiron bridging hydrosulfide **20**.

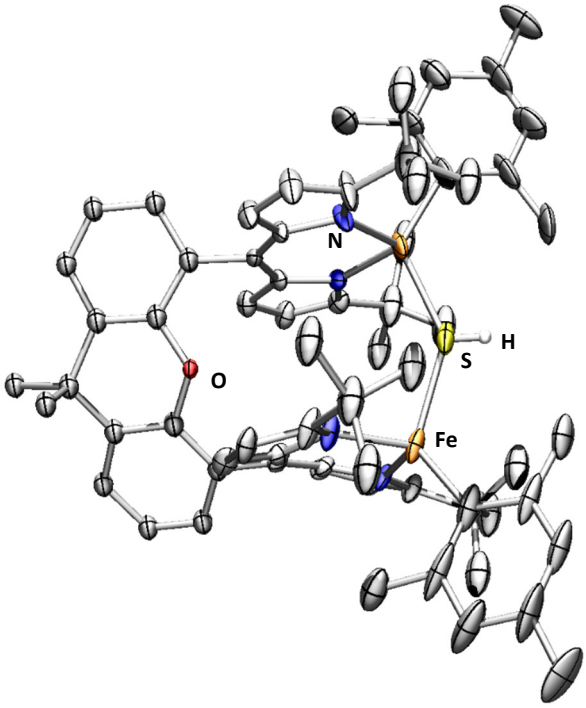

Figure 5.20. Solid state molecular structure of [Na(15-crown-5)$_2$][($^{t\text{Bu}}$dmx)Fe$_2$(μ-SH)(Mes)$_2$] (**20**) with thermal ellipsoids at 20% probability level. Hydrogen atoms (other than μ-hydrosulfido proton), counterion, and solvent molecules are omitted for clarity. Fe = orange, N = blue, C = gray, O = red, S = yellow, H = white.

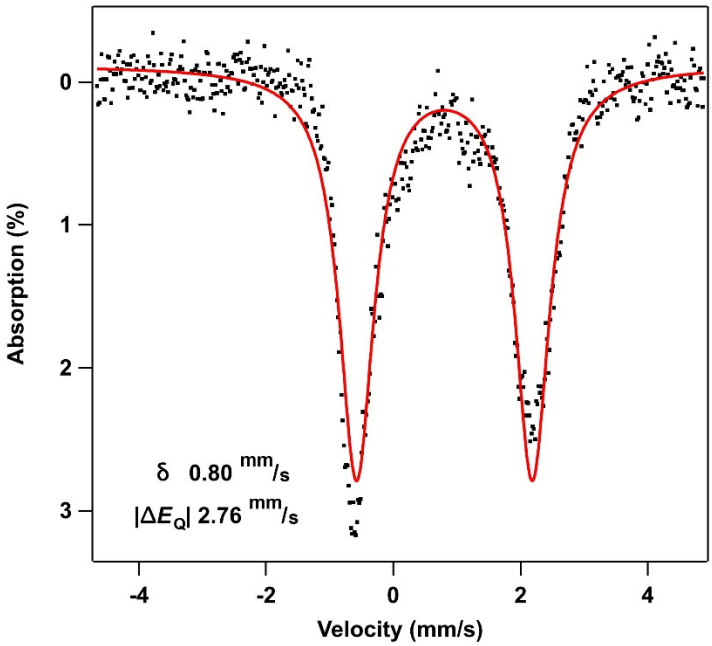

Figure 5.21. Zero-field ^{57}Fe Mössbauer spectrum of [Na(15-crown-5)$_2$][($^{t\text{Bu}}$dmx)Fe$_2$(μ-SH)(Mes)$_2$] (**20**). Isomer shift and quadrupole splitting are reported relative to Fe foil at room temperature.

5.5 Conclusions

These fundamental studies of the coordination chemistry of the novel dipyrrin Pacman ligand platform allowed us to canvas the reactivity of the available diiron starting materials and provided key information regarding targetable endpoints in later studies. Direct comparisons of the effects of the backbone and organic groups decorating the dipyrrin indicated the metal–metal distances and binding motifs possible for various combinations. We utilized this information to direct which to pursue with our targets monoatomic-bridged adducts. Furthermore, knowledge that anionic monoatomic (i.e., SH^-) and triatomic (i.e., N_3^-) ligands will readily bind between the metal centers in **1** was crucial for the pursuit of small molecule reduction reactivity with anions such as nitrite, perchlorate, and periodate discussed in Chapter 4.

5.6 Experimental Methods

5.6.1 General Considerations

All manipulations of metal complexes were carried out in the absence of water and dioxygen using standard Schlenk techniques, or in an MBraun inert atmosphere drybox under a dinitrogen atmosphere. Ligand and ligand precursor syntheses were carried out in air, except where noted. All glassware was oven dried for a minimum of 10 h and cooled in an evacuated antechamber prior to use in the drybox. Benzene, hexanes, tetrahydrofuran, diethyl ether, dichloromethane and toluene were dried and deoxygenated on a Glass Contour System (SG Water USA, Nashua, NH) and stored over 4 Å molecular sieves (Strem) prior to use. Tetrahydrofuran-d_8 was purchased from Cambridge Isotope Labs and used as received. Benzene-d_6 was purchased from Cambridge Isotope Labs, degassed, and stored over 4 Å molecular sieves prior to use. Pentane, dichloroethane, and *n*-hexane were purchased from Sigma-Aldrich and stored over 4 Å molecular sieves prior to use. Pyrazine and 15-crown-5 were purchased from Sigma-Aldrich, degassed, and stored over 4 Å molecular sieves prior to use. 1,4-cyclohexadiene was purchased from Sigma-Aldrich, dried over calcium hydride, and distilled, then stored at –35 °C under inert atmosphere. Celite® 545 (J. T. Baker) was dried in a Schlenk flask for 24 h under dynamic vacuum while heating to at least 190 °C prior to drybox use. Pyridinium *p*-toluenesulfonate, 2,3-dichloro-5,6-dicyanoquinone, triethylammonium chloride, tetraethylammonium cyanide, potassium azide, cryptand (2,2,2), and sodium hydrosulfide were purchased from Sigma-Aldrich and used as received. Tetrabutylammonium imidazolate was purchased from Sigma-Aldrich and recrystallized from a saturated solution in THF layered with hexanes at –35 °C. KBr was purchased from International Crystal Laboratories and heated to 80 °C under high vacuum overnight prior to use. 2-(mesityl)-

1*H*-pyrrole,[12] 2-(*tert*-butyl)-1*H*-pyrrole,[13] 9,9-dimethyl-9H-xanthene-4,5-dicarbaldehyde,[14] dibenzofuran-4,6-dicarbaldehyde,[15] Fe_2Mes_4,[16] $Fe[N(SiMe_3)_2]_2(thf)$,[17] ferrocenium tetraphenylborate,[18] and potassium graphite[19] were synthesized following previously reported procedures. ($^{t\text{Bu}}$dmx)H_2 and ($^{t\text{Bu}}$dmx)Fe_2Mes_2 were synthesized as discussed in Chapter 2.

5.6.2 Characterization and Physical Methods

^{1}H NMR spectra were recorded on Agilent DD2 600 MHz or Varian Unity/Inova 500 MHz spectrometers. ^{1}H chemical shifts are reported relative to $SiMe_4$ using the chemical shift of residual solvent peaks as reference.

Zero-field ^{57}Fe Mössbauer spectra were measured with a constant acceleration spectrometer (SEE Co, Minneapolis, MN) at 90 K. Isomer shifts are quoted relative to Fe foil at room temperature. Data were analyzed and simulated with Igor Pro 6 software (WaveMetrics, Portland, OR) using Lorentzian fitting functions. Samples were prepared by suspending 20–50 mg of compound in sufficient Paratone oil or by dissolving 20–40 mg in benzene and immobilizing by rapid freezing in liquid nitrogen.

Infrared spectra were acquired on a Varian 1000 FTIR spectrometer by pressing the

[12] Reith, R.; Mankad, N.; Calimano, E.; Sadighi, J. *Org. Lett.* **2004**, *6*, 3981–3983.

[13] Harman, W. H.; Harris, T. D.; Freedman, D. E.; Fong, H.; Chang, A.; Rinehart, J. D.; Ozarowski, A.; Sougrati, M. T.; Grandjean, F.; Long, G. J.; Long, J. R.; Chang, C. J. *J. Am. Chem. Soc.* **2010**, *132*, 18115–18126.

[14] Chang, C. J.; Deng, Y.; Heyduk, A. F.; Chang, C. K.; Nocera, D. G. *Inorg. Chem.* **2000**, *6*, 959–966.

[15] Deng, Y.; Chang, C. J.; Nocera, D. G. *J. Am. Chem. Soc.* **2000**, *122*, 410–411.

[16] Hernández Sánchez, R.; Zheng, S.-L.; Betley, T. A. *J. Am. Chem. Soc.* **2015**, *137*, 11126–11143.

[17] Andersen, R. A.; Faegri, K. Jr.; Green, J. C.; Haaland, A.; Lappert, M. F.; Leung, W.-P.; Rypdal, K. Inorg. Chem. 1988, 27, 1782.

[18] Piglosiewicz, I. M.; Beckhaus, R.; Wittstock, G.; Saak, W.; Haase, D. *Inorg. Chem.* **2007**, *46*, 7610–7620.

[19] Wilding, M. J. T.; Iovan, D. A.; Wrobel, A. T.; Lukens, J. T.; MacMillan, S. N.; Lancaster, K. M.; Betley, T. A. *J. Am. Chem. Soc.* **2017**, *139*, 14757–14766.

samples into KBr pellets (~3–4 mg of dried sample and ~80 mg of KBr).

5.6.3 Synthesis

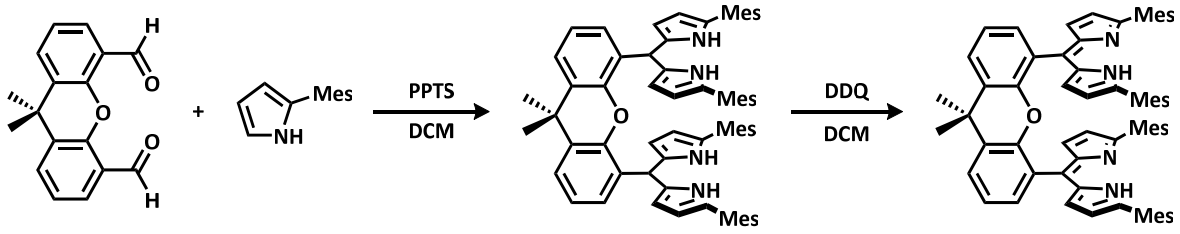

(^{Mes}dmx)H$_2$: Under inert atmosphere, a 100 mL flask was charged with 2-(mesityl)-1*H*-pyrrole (1.391 g, 1.88 mmol, 3.99 equiv), 9,9-dimethyl-9H-xanthene-4,5-dicarbaldehyde (500.0 mg, 1.88 mmol, 1.00 equiv) and 40 mL of dry dichloromethane. Pyridinium *p*-toluenesulfonate (94.4 mg, 0.38 mmol, 20.0 mol%) was added and the reaction mixture was stirred for 21 h. The crude reaction mixture was removed from the glove box and filtered through a plug of silica gel in a medium porosity frit (150 mL), concentrated *in vacuo*, and used for the next step without further purification (1.820 g, 99.4%). The dipyrromethane (1.820 g, 1.86 mmol, 1.00 equiv) was dissolved in 50 mL of dichloromethane and 2,3-dichloro-5,6-dicyanoquinone (DDQ) (1.247 g, 5.49 mmol, 2.95 equiv) was added as a solid resulting in an immediate color change to dark purplish red. After stirring at room temperature overnight, the reaction mixture was filtered through a plug of silica in a medium porosity frit (360 mL) and eluted with dichloromethane. Fractions containing product (^{1}H NMR analysis) were combined and the solvent was removed *in vacuo*. The resulting solid was washed with methanol to yield clean **(^{Mes}dmx)H$_2$** (1.20 g, 66.0%). ^{1}H NMR (500 MHz, $CDCl_3$): δ/ppm 12.43 (s, 2H), 7.56 (dd, J = 7.8, 1.5 Hz, 2H), 7.28 (dd, J = 7.0, 0.8 Hz, 2H), 7.14 (m, 2H), 6.30 (dd, J = 5.0, 1.5 Hz, 4H), 6.01 (dd, J = 4.0, 1.0 Hz, 4H), 1.94 (s, 36H), 1.54 (s, 9H).

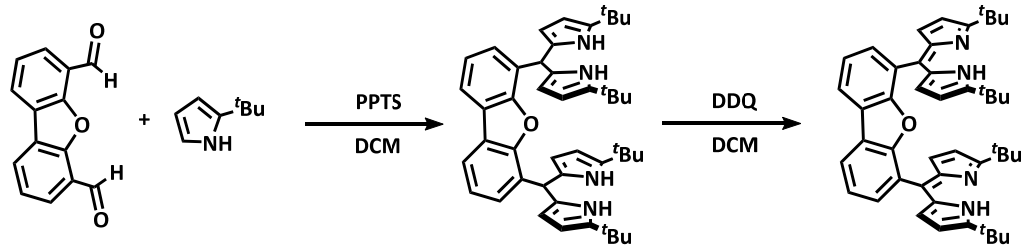

($^{t\text{Bu}}$dbf)H$_2$: Under inert atmosphere, a 350 mL pressure tube was charged with 2-(*tert*-butyl)-1*H*-pyrrole (8.43 g, 68.4 mmol, 4.20 equiv), dibenzofuran-4,6-dicarbaldehyde (3.65 g, 16.3 mmol, 1.00 equiv) and 120 mL of dry dichloromethane. Pyridinium *p*-toluenesulfonate (818 mg, 3.26 mmol, 20.0 mol%) was added and the reaction mixture was sealed, removed from the glovebox, and placed in an oil bath kept at 40 °C for 16 h. The crude reaction mixture was filtered through a plug of silica gel in a medium porosity frit (360 mL), concentrated *in vacuo*, and used for the next step without further purification (10.9 g, 98.8%). The dipyrromethane (10.9 g, 16.1 mmol, 1.00 equiv) was dissolved in 150 mL of dichloromethane and 2,3-dichloro-5,6-dicyanoquinone (DDQ) (7.39 g, 32.56 mmol, 2.02 equiv) was added as a solid resulting in an immediate color change to dark brown. After stirring at room temperature for two hours, the reaction mixture was filtered through a plug of neutral alumina in a medium porosity frit (600 mL) and eluted with dichloromethane. Fractions containing product (^{1}H NMR analysis) were combined and the solvent was removed *in vacuo*. The resulting solid was washed with methanol to yield clean **($^{t\text{Bu}}$dbf)H$_2$** (2.34 g, 21.2%). ^{1}H NMR (500 MHz, $CDCl_3$): δ/ppm 13.05 (s, 2H), 8.05 (dd, J = 7.5, 1.8 Hz, 2H), 7.48 (dd, J = 7.5, 1.5 Hz, 2H), 7.38 (m, 2H), 6.29 (dd, J = 4.0, 1.0 Hz, 4H), 6.10 (dd, J = 4.0, 0.8 Hz, 4H), 1.50 (s, 9H), 1.40 (s, 36H).

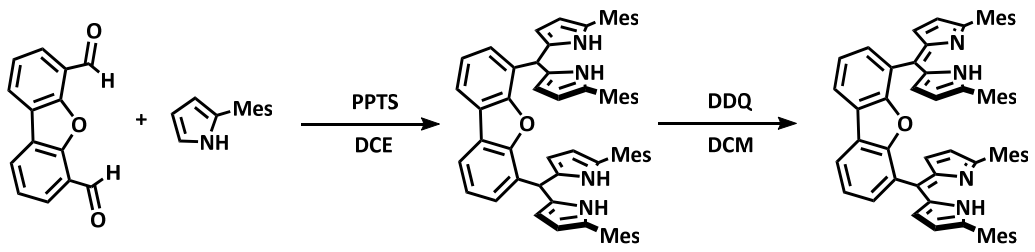

(^{Mes}dbf)H$_2$: Under inert atmosphere, a 100 mL pressure tube was charged with 2-(mesityl)-1*H*-pyrrole (2.93 g, 15.81 mmol, 4.00 equiv), dibenzofuran-4,6-dicarbaldehyde (886 mg, 3.95 mmol, 1.00 equiv) and 40 mL of dry dichloroethane. Molecular sieves and pyridinium *p*-toluenesulfonate (199 mg, 0.79 mmol, 20.0 mol%) were added and the reaction mixture was sealed, removed from the glovebox, and placed in an oil bath kept at 105 °C for 12 h. The crude reaction mixture was filtered through a plug of silica gel in a medium porosity frit (150 mL), concentrated *in vacuo,* and used for the next step without further purification (3.65 g, 99.5%). The dipyrromethane (3.65 g, 3.92 mmol, 1.00 equiv) was dissolved in 200 mL of dichloromethane and 2,3-dichloro-5,6-dicyanoquinone (DDQ) (1.79 g, 7.90 mmol, 2.02 equiv) was added as a solid resulting in an immediate color change to dark brown. After stirring at room temperature overnight, the reaction mixture was filtered through a plug of silica in a medium porosity frit (360 mL) and eluted with dichloromethane. Fractions containing product (^{1}H NMR analysis) were combined and the solvent was removed *in vacuo*. The resulting solid was washed with methanol to yield clean **(^{Mes}dbf)H$_2$** (2.68 g, 67.9%). ^{1}H NMR (600 MHz, C_6D_6): δ/ppm 13.78 (s, 2H), 8.29 (dd, J = 7.8, 1.2 Hz, 2H), 8.00 (dd, J = 7.8, 1.2 Hz, 2H), 7.65 (m, 2H), 6.67 (dd, J = 4.2, 1.8 Hz, 4H), 6.07 (dd, J = 4.2, 2.2 Hz, 4H), 1.50 (s, 9H), 1.40 (s, 36H).

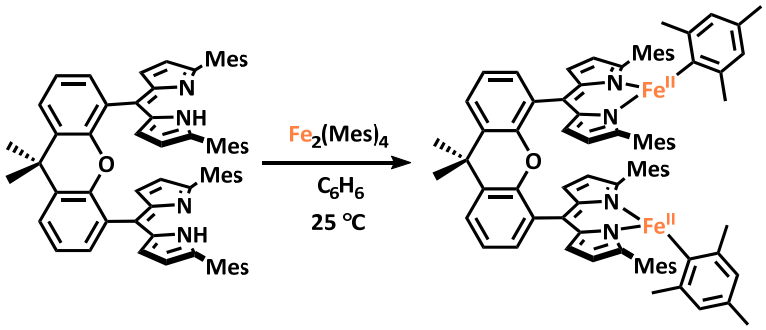

(^Mes^dmx)Fe~2~(Mes)~2~ (2): A 20 mL scintillation vial was charged with (^Mes^dmx)H~2~ (100 mg, 103 µmol, 1.00 equiv). To this was added Fe~2~(Mes)~4~ (60.0 mg, 103 µmol, 1.00 equiv) in 6 mL benzene. The reaction mixture was allowed to stir for 2 hours at room temperature. The reaction mixture was filtered through Celite and the filter cake was washed with excess benzene until the eluent was nearly colorless. The solvent was frozen and removed *in vacuo* to yield a dark red powder. The residue was washed with hexanes (2×3 mL), filtered through Celite with benzene and lyophilized to yield a dark red powder of **(^Mes^dmx)Fe~2~(Mes)~2~ (2)** (130.2 mg, 96.1%). ^{1}H NMR (500 MHz, 295 K, C_6D_6): δ/ppm 142.93, 74.16, 65.22, 15.96, 12.05, 10.18, 8.32, 2.18, −6.62, −10.38, −29.29, −86.65.

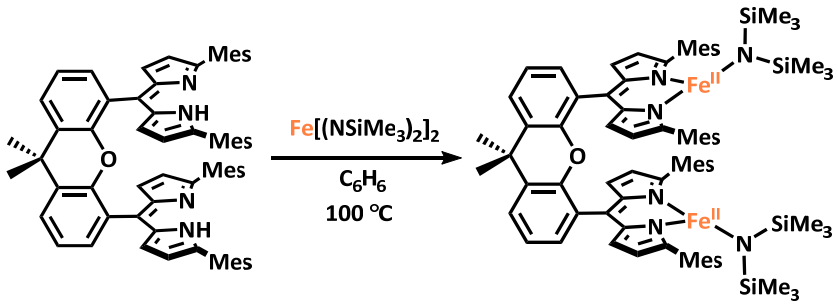

(^tBu^dmx)Fe[N(SiMe~3~)~2~]~2~ (3): To a 35 mL pressure vessel was added (^tBu^dmx)H~2~ (100 mg, 139 µmol, 1.00 equiv), Fe~2~[N(SiMe~3~)~2~]~2~ (105 mg, 278 µmol, 2.00 equiv) and 6 mL benzene. The vessel was equipped with a magnetic stir bar, capped, removed from the glovebox and placed in an oil bath kept at 100 °C for sixteen hours. The reaction mixture was cooled to room temperature, returned to the glovebox and filtered through Celite and the filter cake was washed with excess

benzene until the eluent was nearly colorless. The solvent was frozen and removed *in vacuo* to yield a dark red powder. The residue was washed with hexanes (2×3 mL), filtered through Celite with benzene and lyophilized to yield a dark red powder (150.2 mg, 93.9%). ^{1}H NMR (500 MHz, 295 K, C_6D_6): δ/ppm 69.34, 17.73, 15.78, 10.80, −14.33, −20.10, −30.10.

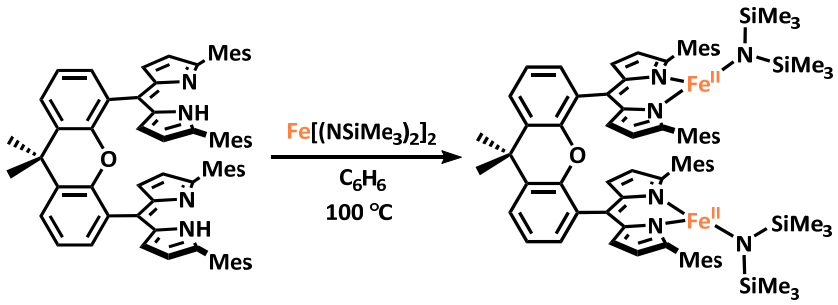

(^{Mes}dmx)Fe[N(SiMe$_3$)$_2$]$_2$ (4): To a 35 mL pressure vessel was added ($^{t\text{Bu}}$dmx)H$_2$ (100 mg, 104 μmol, 1.00 equiv), Fe$_2$[N(SiMe$_3$)$_2$]$_2$ (77.9 mg, 207 μmol, 2.00 equiv) and 6 mL benzene. The vessel was equipped with a magnetic stir bar, capped, removed from the glovebox and placed in an oil bath kept at 100 °C for twelve hours. The reaction mixture was cooled to room temperature, returned to the glovebox and filtered through Celite and the filter cake was washed with excess benzene until the eluent was nearly colorless. The solvent was frozen and removed *in vacuo* to yield a dark red powder. The residue was washed with hexanes (4×3 mL), filtered through Celite with benzene and lyophilized to yield a dark red powder (120 mg, 81.0%). Single crystals were grown from a saturated solution in diethyl ether layered with hexanes at −35 °C. ^{1}H NMR (500 MHz, 295 K, C_6D_6): δ/ppm 62.52, 61.93, 19.51, 17.53, 14.87, 2.72, −4.56, −21.71, −30.27, −30.85, −57.07.

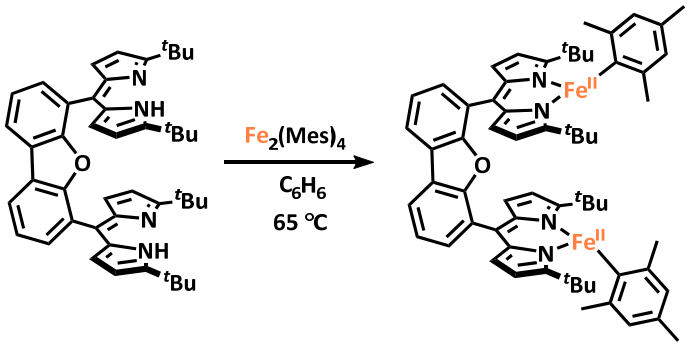

($^{t\text{Bu}}$dbf)Fe$_2$(Mes)$_2$ (5): To a 35 mL pressure vessel was added ($^{t\text{Bu}}$dbf)H$_2$ (175 mg, 259 µmol, 1.00 equiv), Fe$_2$(Mes)$_4$ (152.1 mg, 259 µmol, 1.00 equiv) and 8 mL benzene. The vessel was equipped with a magnetic stir bar, capped, removed from the glovebox and placed in an oil bath kept at 65 °C for four hours. The reaction mixture was cooled to room temperature, returned to the glovebox and filtered through Celite and the filter cake was washed with excess benzene until the eluent was nearly colorless. The solvent was frozen and removed *in vacuo* to yield a dark red powder. The residue was washed with hexanes (3×2 mL), filtered through Celite with benzene and lyophilized to yield a dark red powder (236 mg, 89.1%). ^{1}H NMR (500 MHz, 295 K, C_6D_6): δ/ppm 132.76, 131.52, 74.99, 11.50, 2.81, −3.65. Zero-field ^{57}Fe Mössbauer (90 K) (δ, $|\Delta E_Q|$ ($^{mm}/_s$)): 0.48, *0.98* (γ = 0.174 $^{mm}/_s$).

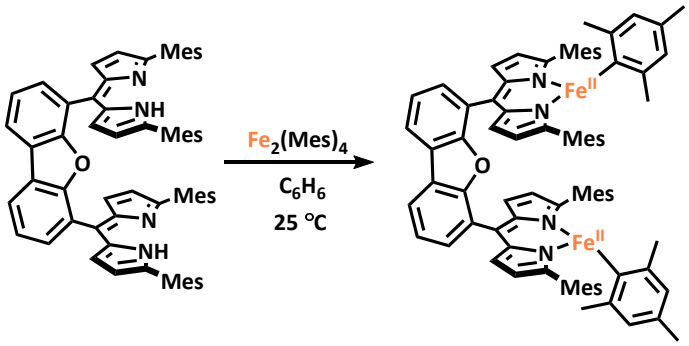

($^{\text{Mes}}$dbf)Fe$_2$(Mes)$_2$ (6): A 20 mL scintillation vial was charged with ($^{\text{Mes}}$dbf)H$_2$ (101 mg, 108 µmol, 1.00 equiv). To this was added Fe$_2$(Mes)$_4$ (63.3 mg, 108 µmol, 1.00 equiv) in 6 mL benzene. The reaction mixture was stirred for 2 hours at room temperature, after which it was filtered through

Celite and the filter cake was washed with excess benzene until the eluent was nearly colorless. The solvent was frozen and removed *in vacuo* to yield a dark red powder. The residue was washed with hexanes (2×3 mL), filtered through Celite with benzene and lyophilized to yield a dark red powder of **(^{Mes}dbf)Fe$_2$(Mes)$_2$ (6)** (131.3 mg, 95.5%). ^{1}H NMR (500 MHz, 295 K, C_6D_6): δ/ppm 147.89, 76.49, 64.53, 38.51, 25.86, 22.16, 11.08, 8.90, −2.84, −40.10, −68.59. Zero-field ^{57}Fe Mössbauer (90 K) (δ, $|\Delta E_Q|$ ($^{mm}/_s$)): 0.42, *1.22* (γ = 0.17 $^{mm}/_s$).

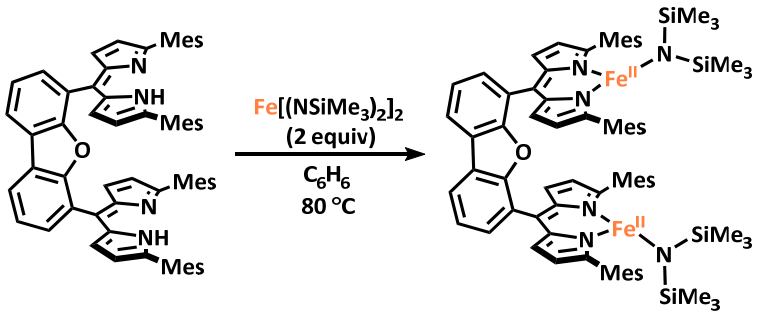

(^{Mes}dbf)Fe[N(SiMe$_3$)$_2$]$_2$ (7): To a 35 mL pressure vessel was added (^{tBu}dmx)H$_2$ (200 mg, 216 µmol, 1.00 equiv), Fe$_2$[N(SiMe$_3$)$_2$]$_2$ (163 mg, 432 µmol, 2.00 equiv) and 8 mL benzene. The vessel was equipped with a magnetic stir bar, capped, removed from the glovebox and placed in an oil bath kept at 100 °C for twelve hours. The reaction mixture was cooled to room temperature, returned to the glovebox and filtered through Celite and the filter cake was washed with excess benzene until the eluent was nearly colorless. The solvent was frozen and removed *in vacuo* to yield a dark red powder. The residue was washed with hexanes (4×3 mL), filtered through Celite with benzene and lyophilized to yield a dark red powder (272 mg, 92.8%). ^{1}H NMR (500 MHz, 295 K, C_6D_6): δ/ppm 58.76, 58.30, 24.77, 19.47, 17.13, 9.78, −2.42, −4.05, −14.72, −24.09, −37.49, −47.38.

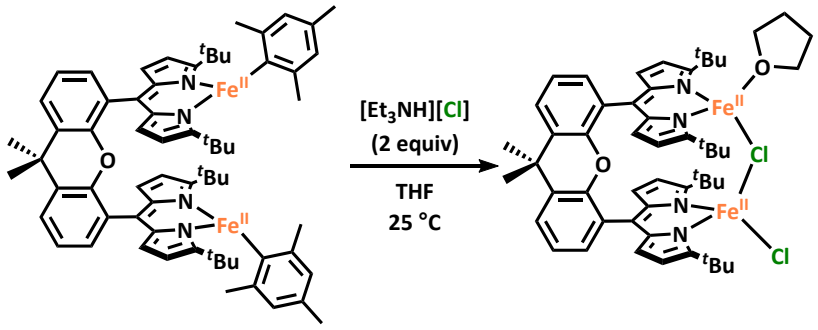

(*t*Bu dmx)Fe2(μ-Cl)(Cl)(thf) (8): In a 20 mL vial, a 2 mL THF solution of (*t*Bu dmx)Fe2(Mes)2 (**1**) (50.0 mg, 46.9 μmol, 1.00 equiv) was added to a stirring 2 mL THF solution of triethylammonium chloride (12.8 mg, 93.0 μmol, 1.98 equiv). The reaction mixture was stirred at room temperature for three hours and concentrated *in vacuo*. The residue was washed with 2 mL of hexanes, filtered through Celite, and eluted with THF. Following concentration *in vacuo*, the residue was taken up in benzene, the solvent was frozen, and the sample was lyophilized to afford (*t*Bu dmx)Fe2(μ-Cl)(Cl)(thf) (**8**) as an orange-brown solid (42.8 mg, 93.8%). Single crystals were grown from a concentrated solution of **8** in diethyl ether with drops of THF. ^{1}H NMR (500 MHz, 295 K, THF-): δ/ppm 50.54, 25.43, 16.03, 7.98, 6.97, 6.43, 0.59, −1.58, −2.31.

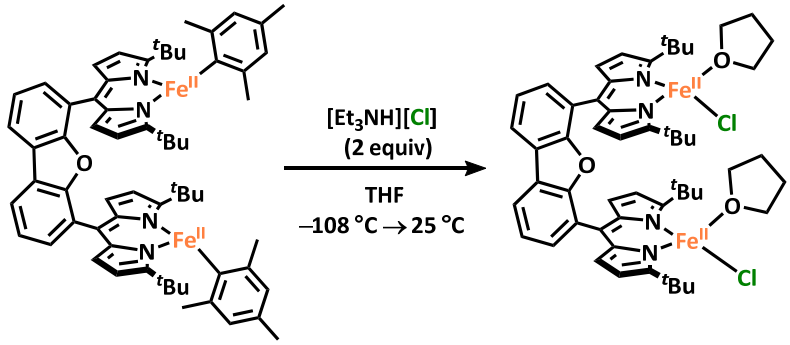

(*t*Bu dbf)Fe2Cl2(thf)2 (10): In a 20 mL vial, triethylammonium chloride (26.9 mg, 195 μmol, 2.00 equiv) was frozen in 2 mL of THF in the cold well (–78 °C). A 2 mL THF solution of (*t*Bu dbf)Fe2(Mes)2 (**5**) (100.0 mg, 97.6 μmol, 1.00 equiv) was added dropwise and the reaction mixture was allowed to thaw. The reaction mixture was stirred at room temperature for three hours

and concentrated *in vacuo*. The residue was washed with 3 mL of hexanes, filtered through Celite, and eluted with THF. Following concentration *in vacuo*, the residue was taken up in benzene, the solvent was frozen, and the sample was lyophilized to afford ($^{t\text{Bu}}$dmx)Fe$_2$Cl$_2$(thf)$_2$ (**8**) as an orange-brown solid (87.7 mg, 87.7%). A saturated THF solution of **8** layered with hexanes at –35 °C resulted in single crystals for X-ray diffraction studies. ^{1}H NMR (500 MHz, 295 K, THF): δ/ppm 50.84, 31.01, 13.97, 11.11, 9.93, 7.14, 6.55, 0.73, −1.50. Zero-field ^{57}Fe Mössbauer (90 K) (δ, $|\Delta E_Q|$ ($^{mm}/_s$)): 0.97, *2.44* (γ = 0.224 $^{mm}/_s$).

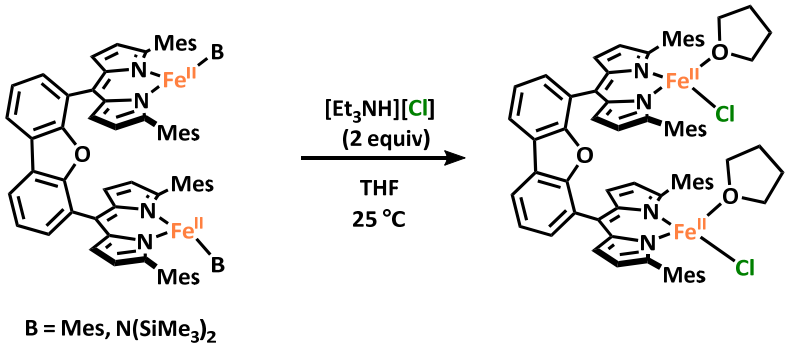

($^{\text{Mes}}$dbf)Fe$_2$Cl$_2$(thf)$_2$ (11): (*Method 1)* A 20 mL vial was charged with ($^{\text{Mes}}$dbf)Fe$_2$(Mes)$_2$ (**6**) (15.0 mg, 11.8 µmol, 1.00 equiv), to which a 2 mL THF solution of triethylammonium chloride (3.2 mg, 23.6 µmol, 2.00 equiv) was added dropwise. The reaction mixture was stirred at room temperature for two hours and concentrated *in vacuo*. The residue was washed with 4 mL of hexanes, filtered through Celite, and eluted with THF. Single crystals were achieved from a saturated THF solution of ($^{\text{Mes}}$dmx)Fe$_2$Cl$_2$(thf)$_2$ (**10**) layered with hexanes at –35 °C. (*Method 2*) To a 20 mL vial charged with ($^{\text{Mes}}$dbf)Fe$_2$[N(SiMe$_3$)$_2$]$_2$ (**7**) (150 mg, 111 µmol, 1.00 equiv) was added a 2 mL THF solution of triethylammonium chloride (30.5, 221 µmol, 1.99 equiv) dropwise. The reaction mixture was stirred at room temperature for two hours and concentrated *in vacuo*. The residue was washed with 1.5 mL of hexanes, filtered through Celite, and eluted with THF. Following concentration *in vacuo*, the residue was taken up in benzene, the solvent was frozen, and the sample was lyophilized to

afford ($^{t\text{Bu}}$dmx)Fe$_2$Cl$_2$(thf)$_2$ (**10**) as an orange-brown solid (79.6 mg, 85.2%). ^{1}H NMR (500 MHz, 295 K, THF): δ/ppm 49.43, 26.54, 23.26, 16.34, 15.05, 9.07, −11.85, −14.33.

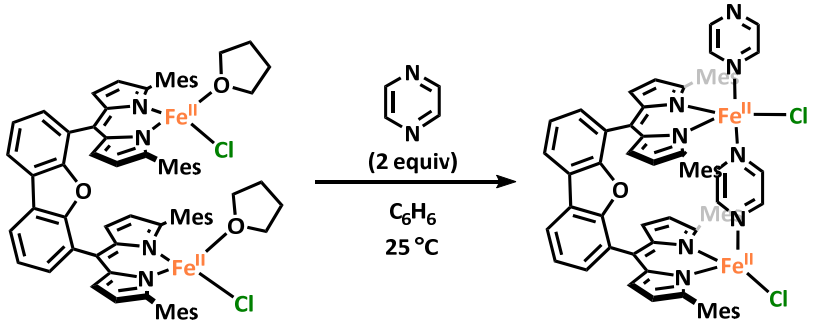

($^{\text{Mes}}$dbf)Fe$_2$Cl$_2$(pyrazine)$_2$ (12): A benzene solution of pyrazine (1.2 mg, 15.0 µmol, 1.90 equiv) was added to a 20 mL vial charged with ($^{\text{Mes}}$dbf)Fe$_2$Cl$_2$(thf)$_2$ (**11**) (10.0 mg, 8.01 µmol, 1.00 equiv). The reaction mixture was stirred at room temperature for one hour, after which the solvent was frozen and lyophilized. A saturated solution of the product mixture in toluene layered with hexanes at –35 °C afforded single crystals of ($^{\text{Mes}}$dbf)Fe$_2$Cl$_2$(pyrazine)$_2$ (**12**). ^{1}H NMR (500 MHz, 295 K, C$_6$D$_6$): δ/ppm 56.16, 36.10, 26.41, 16.28, 15.37, −18.06, −24.26.

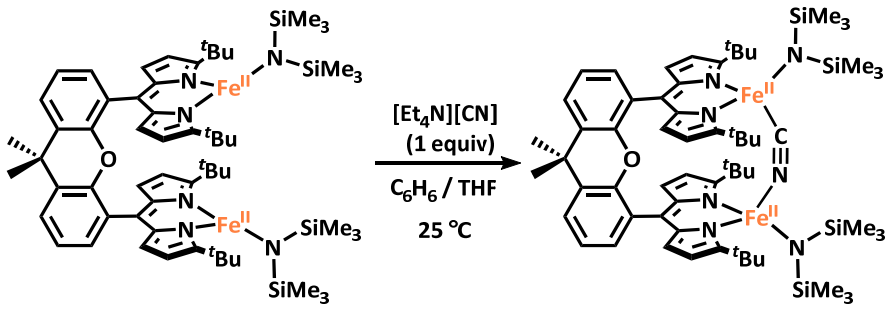

[Et$_4$N][($^{t\text{Bu}}$dmx)Fe$_2$(µ-CN){N(SiMe$_3$)$_2$}$_2$] (13): To a 20 mL vial was added ($^{t\text{Bu}}$dmx)Fe[N(SiMe$_3$)$_2$]$_2$ (**3**) (25.0 mg, 21.7 µmol, 1.00 equiv). A solution of tetraethylammonium cyanide (3.4 mg, 21.7 µmol, 1.00 equiv) in benzene with drops of THF was added dropwise. After stirring for one hour at room temperature, the reaction mixture was concentrated *in vacuo*. A saturated solution of the product mixture in THF layered with hexanes at –35 °C yielded single crystals of [Et$_4$N][($^{t\text{Bu}}$dmx)Fe$_2${N(SiMe$_3$)$_2$}$_2$(µ-CN)] (**13**). ^{1}H NMR (500 MHz, 295 K, C$_6$D$_6$):

δ/ppm 48.38, 45.82, 17.26, 15.79, 13.85, 12.11, 9.61, −5.58, −9.76.

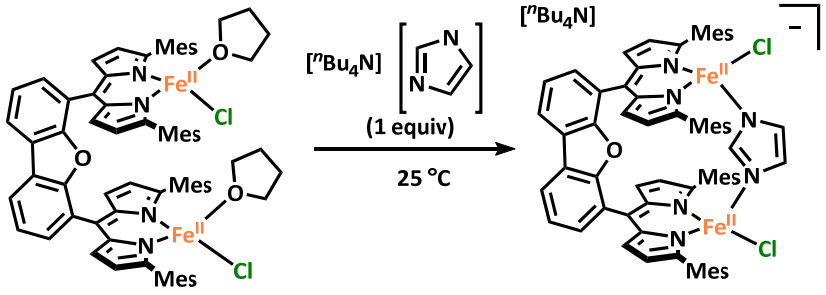

[^{n}Bu$_4$N][(^{Mes}dbf)Fe$_2$Cl$_2$(imidazolate)] (14): A THF solution of tetrabutylammonium imidazolate (9.9 mg, 32.1 µmol, 1.00 equiv) was added to a 20 mL vial containing (^{Mes}dbf)Fe$_2$Cl$_2$(thf)$_2$ (**11**) (40.0 mg, 32.1 µmol, 1.00 equiv). The reaction mixture was stirred at room temperature for thirty minutes followed by concentration *in vacuo*. A saturated solution of the product mixture in diethyl ether with drops of THF at –35 °C resulted in single crystals of [^{n}Bu$_4$N][(^{Mes}dbf)Fe$_2$Cl$_2$(imidazolate)] (**14**) suitable for diffraction. ^{1}H NMR (600 MHz, 295 K, THF): δ/ppm 41.03, 25.22, 19.99, 13.78, 12.80, 7.23, 6.11, −11.28, −20.74.

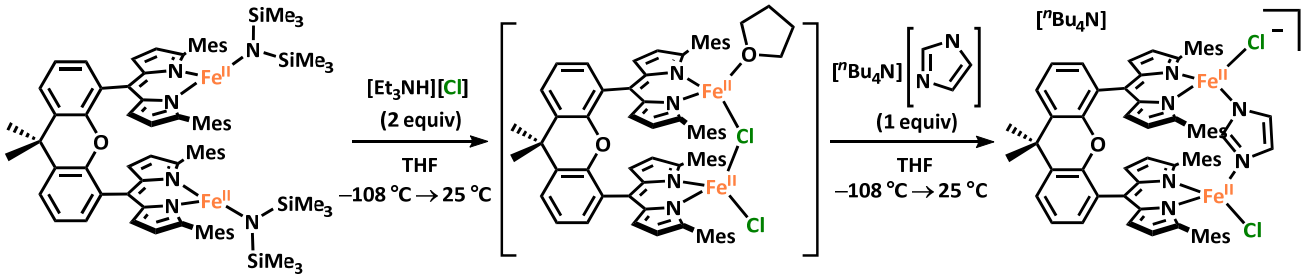

[^{n}Bu$_4$N][^{Mes}dmx)Fe$_2$Cl$_2$(imidazolate)] (15): *(Step 1)* Triethylammonium chloride (20.1, 146 µmol, 2.00 equiv) was frozen in 2 mL of THF (–78 °C) in a 20 mL vial. A 2 mL solution of (^{Mes}dmx)Fe$_2$[N(SiMe$_3$)$_2$]$_2$ (**4**) (100 mg, 73.1 µmol, 1.00 equiv) was frozen in a layer on top. The reaction mixture was thawed and stirred at room temperature for three hours and concentrated *in vacuo*. The residue was washed with 3 mL of hexanes, filtered through Celite, and eluted with

THF. Following concentration *in vacuo*, the residue was taken up in benzene, the solvent was frozen, and the sample was lyophilized to afford "($^{t\text{Bu}}$dmx)Fe$_2$Cl$_2$(thf)" (**9**) as an orange-brown solid (79.6 mg, 85.2%). Single crystals of this product were not achieved, however spectroscopic analysis indicated similarity of **9** with the analogous species **8**. ^{1}H NMR (500 MHz, 295 K, THF): δ/ppm 48.45, 29.09, 13.37, 12.84, −15.46, −19.22. Zero-field ^{57}Fe Mössbauer (90 K) (δ, $|\Delta E_Q|$ ($^{mm}/_s$)): 0.97, *2.21* (γ = 0.220 $^{mm}/_s$). *(Step 2)* A THF solution of tetrabutylammonium imidazolate (2.7 mg, 8.69 µmol, 1.00 equiv) was frozen in the cold well (–78 °C) in a 20 mL vial. To this, a solution of "($^{t\text{Bu}}$dmx)Fe$_2$Cl$_2$(thf)" (**9**) was added dropwise and the reaction mixture was allowed to thaw. After one hour at room temperature, the solvent was removed *in vacuo*. Single crystals of [^{n}Bu$_4$N][$^{\text{Mes}}$dmx)Fe$_2$Cl$_2$(imidazolate)] (**15**) were grown from a saturated solution in THF layered with hexanes at –35 °C. ^{1}H NMR (500 MHz, 295 K, C$_6$D$_6$): δ/ppm 44.30, 20.79, 19.53, 13.44, 11.78, 7.40, 4.97, −14.92, −19.95.

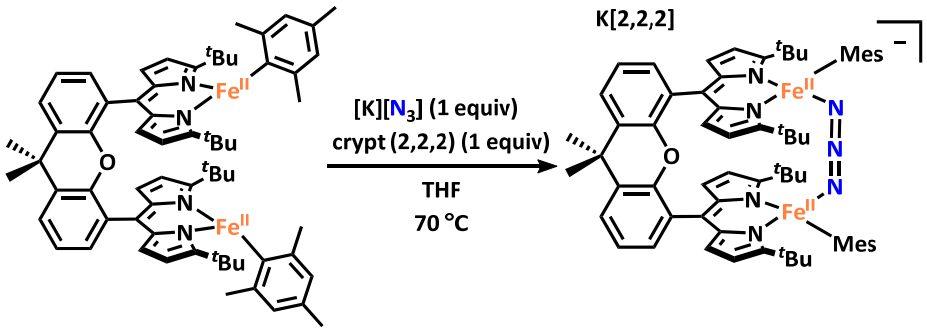

[K(2,2,2)][($^{t\text{Bu}}$dmx)Fe$^{II}_2$Mes$_2$(κ^2-N$_3$)] (16): To a J. Young tube was added ($^{t\text{Bu}}$dmx)Fe$_2$(Mes)$_2$ (**1**) (50.0 mg, 46.9 µmol, 1.00 equiv), potassium azide (3.8 mg, 46.8 µmol, 0.998 equiv), cryptand (2,2,2) (17.7 mg, 47.0 µmol, 1.00 equiv) and 1.5 mL of THF. The tube was sealed, removed from the glovebox and heated to 70 °C for fourteen hours. The reaction mixture was cooled to room temperature, returned to the glovebox, transferred to a vial and concentrated *in vacuo*. The residue was triturated with hexanes (2 x 2 mL), filtered through Celite, and eluted with THF to give

[K(2,2,2)][($^{t\text{Bu}}$dmx)Fe^{II}_2Mes$_2$(κ^2-N$_3$)] (**16**) as a brown film (74.1 mg, 95.8%). Crystals suitable for X-ray diffraction were grown from a concentrated diethyl ether solution at −35 °C. ^{1}H NMR (500 MHz, 295 K, THF-d_8): δ/ppm 96.34, 92.07, 79.48, 74.25, 46.22, 31.24, −5.66, −6.25. Zero-field ^{57}Fe Mössbauer (90 K) (δ, $|\Delta E_Q|$ ($^{mm}/_s$)): 0.75, *2.73* (γ = 0.24 $^{mm}/_s$). FTIR (KBr): 2094 cm^{-1} (ν_{N3}).

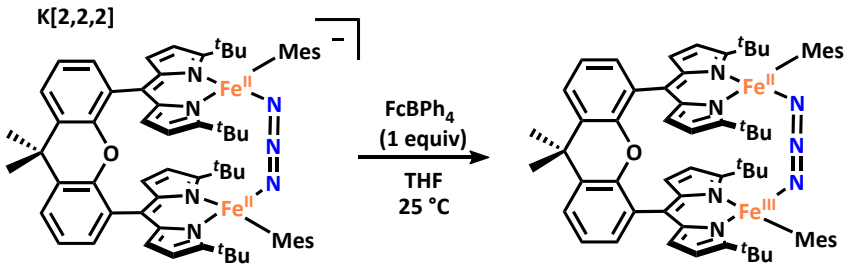

($^{t\text{Bu}}$dmx)$Fe^{II}Fe^{III}$Mes$_2$(κ^2-N$_3$) (17): *(Method 1)* To a 20 mL vial was added [K(2,2,2)][($^{t\text{Bu}}$dmx)Fe^{II}_2Mes$_2$(κ^2-N$_3$)] (**16**) (25.0 mg, 16.4 μmol, 1.00 equiv) and 1 mL of THF. A solution of ferrocenium tetraphenylborate (10.2 mg, 20.2 μmol, 1.23 equiv) in 1 mL of THF was added dropwise. After stirring for twenty minutes at room temperature, the reaction mixture was concentrated *in vacuo*. The residue was washed with 2 mL of hexanes and filtered through Celite, followed by elution with benzene and lyophilization to yield a dark brown-red powder (17.1 mg, 94.0%). ^{1}H NMR (500 MHz, 295 K, THF-d_8): δ/ppm 130.92, 117.99, 66.60, 63.04, 19.38, 12.89. FTIR (KBr): 2109 cm^{-1} (ν_{N3}).

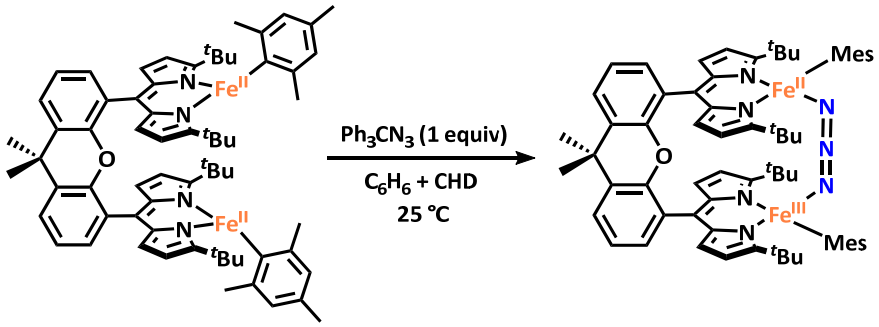

($^{t\text{Bu}}$dmx)$Fe^{II}Fe^{III}Mes_2(\kappa^2\text{-}N_3)$ (17): *(Method 2)* To a 20 mL vial was added ($^{t\text{Bu}}$dmx)$Fe^{II}_2Mes_2$ (**1**) (20.0 mg, 18.7 µmol, 1.00 equiv), trityl azide (5.3 mg, 18.6 µmol, 0.99 equiv), and 1 mL of benzene. To this was added was a solution of 1,4-cyclohexadiene (1.5 mg, 18.7 µmol, 1.00 equiv) in 1 mL of benzene, dropwise while stirring. An immediate color change to dark brown-red was observed. After stirring for twenty minutes at room temperature, the reaction mixture was concentrated *in vacuo*. The residue was washed with 2 mL of hexanes and filtered through Celite, followed by elution with benzene and lyophilization to yield a dark brown-red powder (19.7 mg, 95.0%). Single crystals were afforded from a saturated solution of **17** in pentane at 25 °C overnight. ^{1}H NMR (500 MHz, 295 K, THF-d_8): δ/ppm 130.92, 117.99, 66.60, 63.04, 19.38, 12.89. Zero-field ^{57}Fe Mössbauer (90 K) (δ, $|\Delta E_Q|$ ($^{mm}/_s$)): 0.23, *1.83*; 0.64, *2.91* (γ = 0.209, 0.158 $^{mm}/_s$). FTIR (KBr): 2106 cm^{-1} (ν_{N3}).

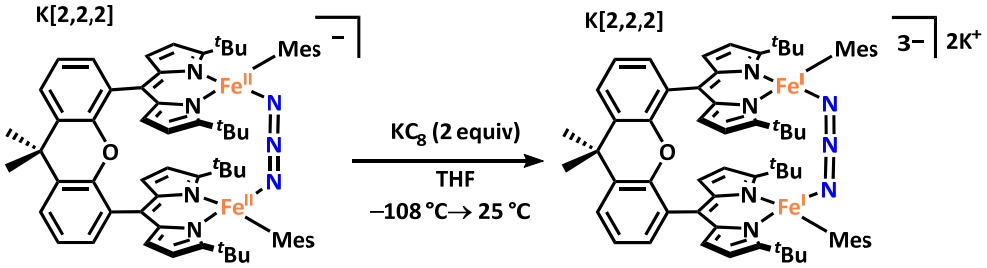

[K(2,2,2)][K]$_2$[($^{t\text{Bu}}$dmx)$Fe_2Mes_2(\kappa^2\text{-}N_3)$] (18): *(Method 1)* A THF solution of [K(2,2,2)][($^{t\text{Bu}}$dmx)$Fe^{II}_2Mes_2(\kappa^2\text{-}N_3)$] (**16**) (25.0 mg, 16.4 µmol, 1.00 equiv) was frozen in the cold well (–78 °C) in a 20 mL vial. To this, a solution of potassium graphite (4.5 mg, 33.3 µmol, 2.03 equiv) in THF was added dropwise and the reaction mixture was allowed to thaw. After twenty minutes of stirring at room temperature, the solvent was removed *in vacuo*. Single crystals of [K(2,2,2)][K]$_2$[($^{t\text{Bu}}$dmx)$Fe^{I}_2Mes_2(\kappa^2\text{-}N_3)$] (**18**) were grown from a saturated solution in THF layered with *n*-hexane at –35 °C. ^{1}H NMR (500 MHz, 295 K, THF-d_8): δ/ppm 98.04, 89.55, 79.59,

73.83, 28.17, 22.99, 9.56, 8.88, −6.17, −7.92. FTIR (KBr): 1995 cm^{-1} (ν_{N3}).

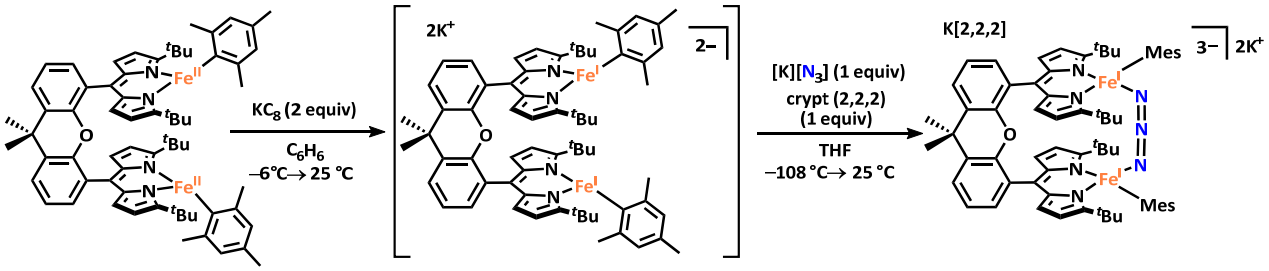

[K(2,2,2)][K]$_2$[($^{t\text{Bu}}$dmx)Fe$_2$Mes$_2$(κ^2-N$_3$)] (18): *(Method 2) (Step 1)* A 20 mL vial was charged with potassium graphite (12.7 mg, 93.9 µmol, 2.00 equiv) and frozen in 2 mL of benzene in the glovebox freezer (–35 °C). A 2 mL solution of ($^{t\text{Bu}}$dmx)Fe$^{\text{II}}_2$(Mes)$_2$ (**1**) (50.0 mg, 46.9 µmol, 1.00 equiv) was added dropwise and the reaction mixture was thawed to room temperature with stirring. A color change to purple was observed in this time. Allowed to stir for twenty minutes before filtering through Celite, freezing, and lyophilizing to afford "($^{t\text{Bu}}$dmx)Fe$^{\text{I}}_2$(Mes)$_2$" (**19**) as a purple-brown solid (51.2 mg, 95.3%). ^{1}H NMR (600 MHz, 295 K, C_6D_6): δ/ppm 107.74, 36.28, 17.61, 13.89, 5.86, −3.75, −12.17. Zero-field ^{57}Fe Mössbauer (90 K) (δ, $|\Delta E_Q|$ ($^{mm}/_s$)): 0.40, *1.36* (γ = 0.224 $^{mm}/_s$). *(Step 2)* A THF solution of "($^{t\text{Bu}}$dmx)Fe$^{\text{I}}_2$(Mes)$_2$" (**19**) (35.0 mg, 30.6 µmol, 1.00 equiv) was frozen in the cold well (–78 °C) in a 20 mL vial. To this, a solution of potassium azide (3.8 mg, 46.8 µmol, 0.998 equiv) and cryptand (2,2,2) (17.7 mg, 47.0 µmol, 1.00 equiv) in 3.0 mL of THF was added on top as the reaction mixture was thawed. After stirring for twenty minutes at room temperature, the reaction mixture was filtered through celite and the solvent was removed *in vacuo*. The resulting film was triturated with benzene to afford a brown solid (44.0 mg, 89.7%) (^{1}H NMR (500 MHz, 295 K, THF-d_8): δ/ppm 98.01, 89.55, 79.54, 73.67, 28.09, 22.70, 9.56, 8.95, −6.24, −7.99. Zero-field ^{57}Fe Mössbauer (90 K) (δ, $|\Delta E_Q|$ ($^{mm}/_s$)): 0.85, *2.17* (γ = 0.5 $^{mm}/_s$).

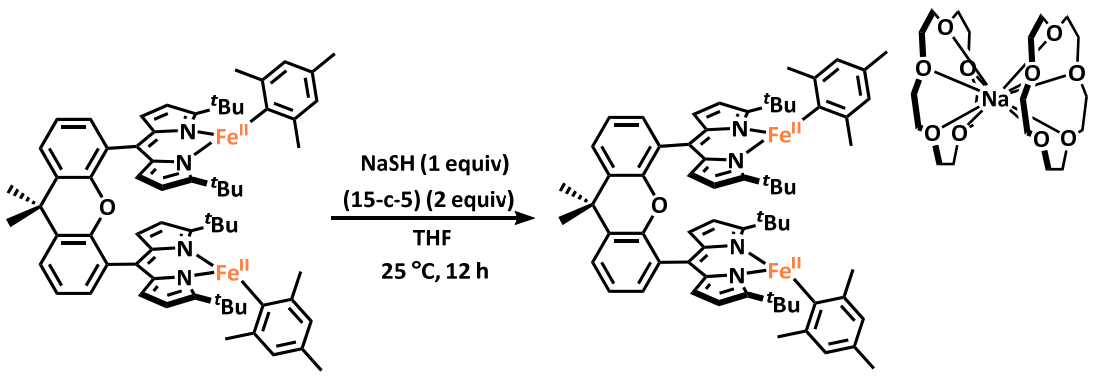

[Na(15-crown-5)$_2$][($^{t\text{Bu}}$dmx)Fe$_2$Mes$_2$(μ-SH)] (20): To a 20 mL vial was added ($^{t\text{Bu}}$dmx)Fe$^{\text{II}}_2$Mes$_2$ (**1**) (35.0 mg, 32.8 μmol, 1.00 equiv) and 1 mL of THF. A 2 mL solution of sodium hydrosulfide (1.8 mg, 32.1 μmol, 0.98 equiv) and 15-crown-5 (14.4 mg, 65.4 μmol, 1.99 equiv) in THF was added dropwise. The reaction was stirred overnight, during which time a color change to brown was observed. The reaction was filtered over celite and concentrated *in vacuo*, then triturated with benzene to afford a brown solid (45.8 mg, 90.3%). Single crystals were grown as brown plates from a saturated solution of **20** in toluene at –35 °C. ^{1}H NMR (500 MHz, 295 K, THF-d_8): δ/ppm 85.10, 78.19, 63.54, 43.41, 42.10, 20.16, 12.18, 9.29, 8.82, –1.16. Zero-field ^{57}Fe Mössbauer (90 K) (δ, $|\Delta E_Q|$ ($^{\text{mm}}/_{\text{s}}$)): 0.80, *2.76* (γ = 0.333 $^{\text{mm}}/_{\text{s}}$). FTIR (KBr): 2589 cm^{-1} (ν_{SH}).

5.6.4 X-Ray Diffraction Techniques

All structures were collected on a Bruker three-circle platform goniometer equipped with an Apex II CCD and an Oxford cryostream cooling device. Radiation was from a graphite fine focus sealed tube Mo Kα (0.71073 Å), a graphite fine focus sealed tube Cu Kα (1.54178 Å) source, or synchrotron radiation at Argonne National Laboratory Advance Photon Course, ChemMatCARS. Crystals were mounted on a cryoloop or glass fiber pin using Paratone N oil. Structures were collected at 100 K. Data were collected as a series of φ and/or ω scans.

Data were integrated using SAINT[20] and scaled with either a numerical or multi-scan absorption correction using SADABS.[20] The structures were solved by intrinsic phasing, direct methods or Patterson maps using SHELXS-2014[21] and refined against F^2 on all data by full matrix least squares with SHELXL-2014.[21] All non-hydrogen atoms were refined anisotropically. Hydrogen atoms were placed at idealized positions and refined using a riding model. The isotropic displacement parameters of all hydrogen atoms were constrained to be 1.2 times the parameter of the atoms they were linked to (1.5 times for methyl groups). Further details on particular structures are noted below.

(^{Mes}dmx)Fe$_2$[N(SiMe$_3$)$_2$]$_2$ (4): The structure was solved in the monoclinic space group *C*2/c with thirty-eight molecules per unit cell and 4.75 molecules in the asymmetric unit.

(^{Mes}dbf)Fe$_2$Mes$_2$ (6): The structure was solved in the monoclinic space group $P\bar{1}$ with four molecules per unit cell and two moleculea in the asymmetric unit.

(^{tBu}dmx)Fe$_2$(μ-Cl)(Cl)(thf) (8): The structure was solved in the monoclinic space group $P2_1/c$ with eight molecules per unit cell and two molecules in the asymmetric unit. Full molecule positional disorder was modelled with similarity constraints.

(^{tBu}dbf)Fe$_2$Cl$_2$(thf)$_2$ (10): The structure was solved in the monoclinic space group $P\bar{1}$ with thirty-five molecules per unit cell and 17.5 molecules in the asymmetric unit. Positional disorder at one of the iron centers was modelled with similarity constraints.

(^{Mes}dbf)Fe$_2$Cl$_2$(thf)$_2$ (11): The structure was solved in the rhombohedral space group $R\bar{3}$ with forty-five molecules per unit cell and 2.5 molecules in the asymmetric unit.

[20] APEX2 Software Suite; Bruker AXS: Madison, WI, 2009.

[21] Sheldrick, G. M. *Acta Crystallogr., Sect. A: Found. Crystallogr.* **2008**, *64*, 112–122.

(^{Mes}dbf)Fe_2Cl_2(pyrazine)$_2$ (12): The structure was solved in the monoclinic space group $P\bar{1}$ with four molecules per unit cell and two molecules in the asymmetric unit. Disorder within one of the dipyrrin ligands was modelled with displacement restraints.

[Et_4N][($^{t\text{Bu}}$dmx)Fe_2{$N(SiMe_3)_2$}$_2$CN] (13): The structure was solved in the monoclinic space group $P2_1/n$ with twelve molecules per unit cell and three molecules in the asymmetric unit.

[^{n}Bu_4N][(^{Mes}dbf)Fe_2Cl_2(imidazolate)] (14): The structure was solved in the monoclinic space group $P\bar{1}$ with twelve molecules per unit cell and six molecules in the asymmetric unit.

[^{n}Bu_4N][(^{Mes}dmx)Fe_2Cl_2(imidazolate)] (15): The structure was solved in the monoclinic space group $P2_1/n$ with seventeen molecules per unit cell and 4.25 molecules in the asymmetric unit.

[K(2,2,2)][($^{t\text{Bu}}$dmx)Fe_2(κ^2-N_3)$(Mes)_2$] (16): The structure was solved in the monoclinic space group $P\bar{1}$ with four molecules per unit cell and two molecules in the asymmetric unit.

($^{t\text{Bu}}$dmx)$Fe^{II}Fe^{III}$(κ^2-N_3)$(Mes)_2$ (17): The structure was solved in the monoclinic space group $P\bar{1}$ with eight molecules per unit cell and four molecules in the asymmetric unit.

[K(2,2,2)][K]$_2$[($^{t\text{Bu}}$dmx)Fe_2(κ^2-N_3)$(Mes)_2$] (18): The structure was solved in the orthorhombic space group $P2_12_12_1$ with four molecules per unit cell and one molecule in the asymmetric unit.

[Na(15-crown-5)$_2$][($^{t\text{Bu}}$dmx)Fe_2(μ-SH)$(Mes)_2$] (20): The structure was solved in the monoclinic space group $P2_1/n$ with twelve molecules per unit cell and three molecules in the asymmetric unit. Positional disorder at the encapsulated counterion was modelled with similarities constraints.